Multi-Targeting Derivatives For Alzheimer's Disease: Utilization of Quinazoline Ring Scaffolds

by

Tarek Mohamed

A thesis
presented to the University of Waterloo
in fulfillment of the
thesis requirement for the degree of
Doctor of Philosophy
in
Chemistry

Waterloo, Ontario, Canada, 2016

© Tarek Mohamed 2016

AUTHOR'S DECLARATION

I hereby declare that I am the sole author of this thesis. This is a true copy of the thesis, including any required final revisions, as accepted by my examiners.

I understand that my thesis may be made electronically available to the public.

ABSTRACT

The complex and multifaceted nature of Alzheimer's pathology has significantly hindered the discovery and development of viable therapeutics, let alone the cause and initiation of the disease. Over the past century, what was known as the 'one drug, one target' approach has only recently shifted to the multifunctional ideology. By investing, discovering and developing therapeutic options with multi-targeting capabilities, not only would patient outcomes improve, but the road to multi-targeting therapeutics can help shed new light on Alzheimer's disease (AD) pathogenesis. In order to undertake the multifunctional ideology, viable and interconnecting targets need to be identified.

As such, the work presented herein employed computer-aided drug design (CADD) to develop bicyclic small-molecules against three key targets of AD pathology – the cholinesterases (AChE and BuChE), amyloid-β (Aβ) aggregation and reactive oxygen species (ROS) generation. A chemical library of ~ 140 derivatives, based on a quinazoline (Qnz) or a pyridopyrimidine (Ppd) ring scaffold, was generated to gather structure-activity relationship (SAR) data in the target-specific assays with the goal of identifying lead multi-targeting candidates for future optimization and pre-clinical assessment. Specifically:

Chapter one provides the background information and literature survey with respect to the statistics of AD, the current hypotheses with a keen focus on cholinergic dysfunction and amyloid toxicity, and an overview of the interconnectivity observed with each of the hypotheses put forth in relation to disease pathology and progression.

Chapter two surveys the utility of the quinazoline and pyridopyrimidine scaffolds in medicinal chemistry and ties that with previously utilized templates and those found in marketed therapies to develop a AD-specific hypothesis bearing a multi-targeting focus. From that survey and hypothesis, a chemical design and development plan was generated to yield the sought-after chemical derivatives.

Chapter three is dedicated to the design, development and evaluation of the first series of compounds, which were based on a Qnz-scaffold and featured a dimethoxybenzylamine group at the C4-position (2-substituted-*N*-(3,4-dimethoxybenzyl)-quinazolin-4-amines). This series contained 13 derivatives with varying functional groups at the C2-position. The general observations from this collection revealed the lack of inhibitory activity toward BuChE and Aβ42, while AChE and Aβ40 targeting were considered moderate. The most active AChEI and ROS scavenger across the research program was discovered within this series. This chapter also included the bulk of synthetic and biochemical assessment protocols/methodologies.

Chapter four describes the design, development and evaluation of 2-substituted-*N*-benzylquinazolin-4-amines. This was primarily a measure of the 3,4-dimethoxy moiety's validity in dual-ChE targeting and anti-amyloid aggregation potential. This series also contained 12 derivatives with varying functional groups at the C2-position as well as one regioisomer. The general observations from this collection revealed on par activities toward AChE inhibition with slight improvements toward BuChE inhibition for some derivatives. In addition, the overall Aβ40/42 inhibitory profiles were also improved, although the ROS scavenging derivative was not as potent compared to its dimethoxy counterpart. That said, the first nanomolar Aβ40 inhibitor was identified within this series so was the first low-mid micromolar Aβ42 aggregation inhibitor.

Chapter five describes the design, development and evaluation of 2-substituted-*N*-(3,4-dimethoxyphenethyl)-quinazolin-4-amines. This was primarily a measure of the additional methylene group's validity in dual-ChE targeting and anti-amyloid aggregation potential. This was a larger series with 12 derivatives carrying the same functional groups at the C2-position as those in Chapters 3 and 4, a regioisomer and an additional 12 derivatives. These additional derivatives explored the addition of a chlorine atom on the Qnz-scaffold at three positions (C6-, C7-, or C8-) with the top 4 C2-groups to expand the SAR data. With respect to Chapter 3 counterparts, the general observations from this collection revealed on par activities toward AChE inhibition with slight improvements toward BuChE inhibition for some derivatives. Mixed outcomes were observed with respect to Aβ40/42 targeting capacities, while the weakest ROS scavenger was identified within this series of derivatives. More so, the outcomes of the

chloroquinazoline counterparts were not as promising as anticipated with respect to dual ChE and dual Aβ40/42 targeting, although some exceptions do apply. Interestingly, this series revealed some of the first potent and dual, non-selective Aβ aggregation inhibitors, along with the selectivity toward Aβ42 with 8-chloro-based quinazoline derivatives.

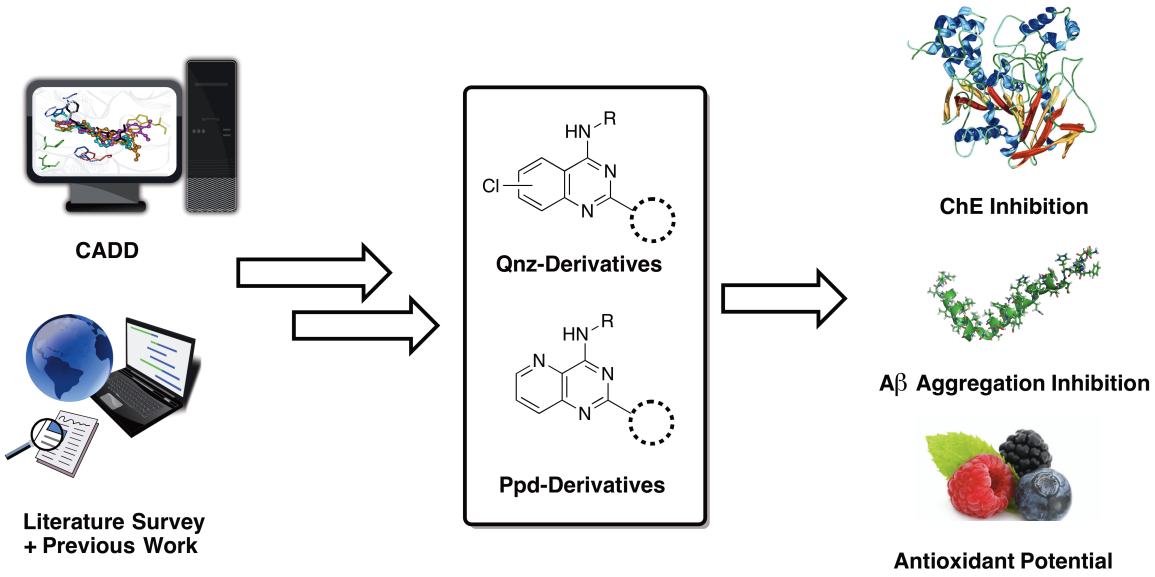
Chapter six describes the design, development and evaluation of 2-substituted-*N*-phenethylquinazolin-4-amines. This elicited a dual measure of the validity of the 3,4-dimethoxy moiety as well as the additional methylene linker in dual-ChE targeting and anti-amyloid aggregation potential with respect to the counterparts in Chapters 4 and 5. This series included the original 12 functional groups at the C2-position, two regioisomers and the additional 12 chloroquinazoline-based derivatives. With respect to Chapter 4 and 5 counterparts, the general observations from this collection revealed on par activities toward AChE inhibition with significant improvements toward BuChE inhibition for some derivatives. Mixed outcomes were observed with respect to Aβ40/42 targeting capacities, while the ROS scavenger within this series was more potent compared to its counterparts in Chapters 4 and 5. More so, the outcomes of the chloroquinazoline counterparts were more promising with respect to dual ChE and dual Aβ40/42 targeting, when compared to those in Chapter 5. Besides revealing some potent and dual, non-selective Aβ aggregation inhibitors, the most potent BuChEI was identified within this series.

Chapter seven describes the design, development and evaluation of 2,4-disubstituted pyridopyrimidines as rational counterparts to leading derivatives from Chapters 5 and 6. This series included 10 derivatives and was developed to assess iron chelation potential and assess Qnz vs. Ppd. SAR data. The derivatives here did not impart significant improvements toward AChE, but as expected, were inactive toward BuChE. Activity toward Aβ40 was of mixed outcomes, while improvements toward Aβ42 inhibition were observed. Lastly, chelation capacity was considered weak to moderate at best.

Chapter eight describes the design, development and evaluation of monosubstituted quinazoline-2,4-diamines to further investigate the regioisomeric impact on Aβ40/42 targeting as an expansion on two isomeric pairs from Chapters 4 and 6. This series discussed 30 isomeric derivatives (15 C2-amino, and 15

C4-amino) in comparison to the previously disclosed isomers. The general observations from this collection revealed that C2-amino-based isomers were more effective at targeting Aβ40 (compared to their C4-amino isomers), while the opposite was true with respect to Aβ42. The most potent Aβ40 aggregation inhibitor across the collective library was identified within this Chapter.

Chapter nine provides closing conclusions and a future works/outlook plan.



* Graphical Abstract

ACKNOWLEDGEMENTS

I would like to thank the Faculty of Science, Office of Research, the School of Pharmacy/Department of Chemistry at the University of Waterloo, Ontario Mental Health Foundation (graduate scholarship for T.M.), NSERC-Discovery (RGPIN: 03830-2014), Canada Foundation for Innovation (CFI-JELF), Ontario Research Fund (ORF), and Early Researcher Award, Ministry of Research and Innovation, Government of Ontario, Canada (PR) for financial support of the presented work.

I also acknowledge Mandeep K. Mann for her assistance with the project during her time with our research group as an NSERC-USRA. I also would like to extend my acknowledgement and appreciation to my supervisor, Dr. Praveen N. Rao, who has been a tremendous source of knowledge, support, understanding and motivation – I simply could not have asked for a better supervisor and mentor. To my co-supervisor, Dr. Gary Dmitrienko and my committee advisors, Drs. Michael Beazely, Eric Fillion and Richard Manderville, thank you for their patience and support over these past five years. A special thank you goes out to Dr. Richard Smith and Jan Vann for their help with spectral acquisitions throughout the research program and also to my graduate studies coordinators for their support and assistance with the navigation of the many administrative processes along the way.

Who can forget the friends, colleagues, weekend warriors, weeknight owls, mentees and mentors at the School of Pharmacy and other departments for their continued help, support and understanding throughout the course of my graduate programs.

Lastly, to the other graduate students and staff I met during my unique time with the Waterloo Graduate House – some of whom I consider as good and life-long friends – you also had a hand in making this come together, so thank you for the life-long stories and memories.

DEDICATION

Five years ago, I embarked on a journey to enhance my knowledge and technical skills in basic scientific research with no clear vision of what the future held (obviously). It was a very risky, yet easier, choice to make at the time and I knew it wasn't going to be easy ... If it were, then it wasn't the right path to pursue. Five years is not a substantial timeframe by many definitions but this journey was a substantially challenging one on many fronts. I was constantly challenged mentally, emotionally, financially, socially, spiritually, physically and ethically. I wanted to quit (on multiple occasions) but never had the guts to do so. I sometimes question why I stayed and why it was as hard as it was ... I'm still figuring things out.

For now, however, I'm dedicating this work to the ones who anchored, hugged, listened, supported, believed and loved me unconditionally. The ones that understood and forgave my wrong doings without hesitation or questioning of my intentions. The ones whom without their existence in my life, wouldn't have made this journey a successful one. To my loving parents and younger sister ... I am not whom I am without you. Thank you - can't even begin to express my gratitude and appreciation of your unconditional love and support.

Last, but not least, I dedicate this to myself. While I may never openly share the intimate details of my journey, amidst the challenges rose a remarkable achievement full of dedication, pride and self-worth. If I were to capture a life lesson from this to pass on to my children, it would be this ... 'Nothing in this life that's worth doing or important to you comes without hard work, dedication and perseverance. You must never quit learning and never learn quitting'

TABLE OF CONTENTS

List of Figures ..... **xiv - xxv**
List of Tables ..... **xxvi - xxvii**
List of Schemes ..... **xxviii**
List of Abbreviations ..... **xxix - xxxii**
Functional Group Nomenclature ..... **xxxiii**

Chapter 1: Background on Alzheimer's Disease ..... **1 - 36**
1.1. Introduction ..... 1 - 3
1.2. The cholinergic dysfunction hypothesis ..... 3 - 11
1.2.1. Cholinergic neurotransmission ..... 3 - 5
1.2.2. The cholinesterase (ChE) enzymes ..... 5 - 10
1.2.2.1. Acetylcholinesterase (AChE) ..... 7 - 9
1.2.2.2. Butyrylcholinesterase (BuChE) ..... 9 -10
1.2.3. Hypothesis summary ..... 10 - 11
1.3. The amyloid-β (Aβ) hypothesis ..... 11 - 31
1.3.1. Amyloid precursor protein (APP) ..... 12 - 13
1.3.2. APP metabolism and processing pathways ..... 13 - 16
1.3.3. The Aβ-peptide: Structure, function and clearance ..... 16 - 18
1.3.4. Aβ aggregation and toxicity mechanisms ..... 19 - 23
1.3.5. Aβ targeting strategies ..... 23 - 28
1.3.5.1. Upstream of Aβ production ..... 23 - 24
1.3.5.2. Downstream of Aβ production..... 24 - 29
1.3.6. Hypothesis summary ..... 30 - 31
1.4. Other factors in AD pathology ..... 31 - 35
1.4.1. Tauopathy..... 32 - 34
1.4.2. Inflammation ..... 34 - 35
1.5. Chapter conclusion ..... 36 - 37

Chapter 2: Rationale Behind the Utilization of the Quinazoline Ring Scaffold for Designing Novel AD Therapies ..... **38 - 47**
2.1. Quinazoline survey ..... 38 - 41
2.2. Template design ..... 42 - 44
2.3. Synthesis of quinazoline core template ..... 44 - 45
2.4. Target quinazoline library ..... 46 - 47

Chapter 3: Development and Evaluation of *N*-(3,4-dimethoxybenzyl)quinazolin-4-amines as Dual ChE and Aβ Aggregation Inhibitors ..... 48 - 82
3.1. Introduction 48
3.2. Hypothesis ..... 48 - 49
3.3. Results and discussions ..... 49 - 67
3.3.1. Synthesis ..... 49 - 55
3.3.2. Cholinesterase ..... 55 - 58
3.3.3. Amyloid-β aggregation ..... 58 - 62
3.3.4. Antioxidant capacity 63
3.3.5. Molecular modeling ..... 63 - 67
3.3.5.1. Cholinesterase ..... 64 - 65
3.3.5.2. Amyloid-β ..... 65 - 67
3.4. Summary 67
3.5. Experimental ..... 68 - 82
3.5.1. Chemistry ..... 68 - 78
3.5.2 Biological screening ..... 78 - 81
3.5.2.1. Human cholinesterase (hChE) assay ..... 78 - 79
3.5.2.2. Amyloid-β (Aβ) aggregation assay ..... 79 - 80
3.5.2.3. DPPH scavenging assay 81
3.5.3. Computational chemistry 82

Chapter 4: Development and Evaluation of *N*-benzylquinazolin-4-amines as Dual ChE and Aβ Aggregation Inhibitors ..... 83 - 116
4.1. Introduction 83
4.2. Hypothesis ..... 83 - 84
4.3. Results and discussions ..... 84 - 102
4.3.1. Synthesis ..... 84 - 87
4.3.2. Cholinesterase ..... 87 - 90
4.3.3. Amyloid-β aggregation ..... 90 - 96
4.3.4. Transmission electron microscopy (TEM) ..... 95 - 96
4.3.5. Antioxidant capacity ..... 96 - 97
4.3.6. Molecular modeling 97- 102
4.3.6.1. Cholinesterase ..... 97 - 99
4.3.6.2. Amyloid-β ..... 99 - 102
4.4. Summary ..... 102 - 103
4.5. Experimental ..... 103 - 116
4.5.1. Chemistry ..... 103 - 112

4.5.2. Biological screening ..... 113 - 116
4.5.2.1. Human cholinesterase (hChE) assay 113
4.5.2.2. Amyloid-β (Aβ) aggregation assay ..... 113 - 114
4.5.2.3. TEM assay and imaging ..... 114 - 115
4.5.2.4. DPPH scavenging assay ..... 115 - 116
4.5.3. Computational chemistry 116

Chapter 5: Development and Evaluation of *N*-(3,4-dimethoxyphenethyl)quinazolin-4-amines as Dual ChE and Aβ Aggregation Inhibitors ..... 117 - 159
5.1. Introduction 117
5.2. Hypothesis 118
5.3. Results and discussions ..... 118 - 141
5.3.1. Synthesis ..... 119 - 121
5.3.2. Cholinesterase ..... 121 - 127
5.3.3. Amyloid-β aggregation ..... 127 - 135
5.3.4. Transmission electron microscopy (TEM) 136
5.3.5. Antioxidant capacity 137
5.3.6. Molecular modeling ..... 137 - 141
5.3.6.1. Cholinesterase ..... 138 - 139
5.3.6.2. Amyloid-β ..... 140 - 141
5.4. Summary ..... 141 - 142
5.5. Experimental ..... 142 - 159
5.5.1. Chemistry ..... 142 - 156
5.5.2. Biological screening ..... 156 - 155
5.5.2.1. Human cholinesterase (hChE) assay 156
5.5.2.2. Amyloid-β (Aβ) aggregation assay 157
5.5.2.3. TEM assay and imaging 157- 158
5.5.2.4. DPPH scavenging assay 158
5.5.3. Computational chemistry ..... 158 - 159

Chapter 6: Development and Evaluation of *N*-phenethylquinazolin-4-amines as Dual ChE and Aβ Aggregation Inhibitors ..... 160 - 204
6.1. Introduction ..... 160 - 161
6.2. Hypothesis 161
6.3. Results and discussions ..... 162 - 185
6.3.1. Synthesis ..... 162 - 164
6.3.2. Cholinesterase ..... 165 - 171

6.3.3. Amyloid-β aggregation ..... 171 - 179
6.3.4. Transmission electron microscopy (TEM) ..... 179 - 180
6.3.5. Antioxidant capacity …..... 180 - 181
6.3.6. Molecular modeling ..... 181 - 185
6.3.6.1. Cholinesterase ..... 181 - 183
6.3.6.2. Amyloid-β ..... 184 - 185
6.4. Summary ..... 185 - 186
6.5. Experimental ..... 186 - 204
6.5.1. Chemistry ..... 186 - 201
6.5.2. Biological screening ..... 201 - 203
6.5.2.1. Human cholinesterase (hChE) assay ..... 201 - 202
6.5.2.2. Amyloid-β (Aβ) aggregation assay 202
6.5.2.3. TEM assay and imaging ..... 202 - 203
6.5.2.4. DPPH scavenging assay 203
6.5.3. Computational chemistry ..... 203 - 204

Chapter 7: Development and Evaluation of 2,4-Disubstituted Pyridopyrimidines as Dual ChE and Aβ Aggregation Inhibitors with Chelation Capacity ..... 205 - 226
7.1. Introduction 205
7.2. Hypothesis 206
7.3. Results and discussions ..... 206 - 213
7.3.1. Synthesis 207
7.3.2. Cholinesterase ..... 208 - 209
7.3.3. Amyloid-β aggregation ..... 209 - 212
7.3.4. Transmission electron microscopy (TEM) ..... 212 - 213
7.3.5. Iron chelation capacity ..... 213 - 215
7.3.6. Molecular modeling ..... 215 - 217
7.3.6.1. Cholinesterase ..... 215 - 216
7.3.6.2. Amyloid-β ..... 216 - 217
7.4. Summary ..... 217 - 218
7.5. Experimental ..... 218 - 226
7.5.1. Chemistry ..... 218 - 223
7.5.2. Biological screening 223- 226
7.5.2.1. Human cholinesterase (hChE) assay ..... 223 - 224
7.5.2.2. Amyloid-β (Aβ) aggregation assay 224
7.5.2.3. TEM assay and imaging ..... 224 - 225
7.5.2.4. Iron chelation assay ..... 225 - 226

7.5.3. Computational chemistry 226

Chapter 8: Development and Evaluation of Isomeric Monosubstituted 2,4-Diaminoquinazolines as Aβ Aggregation Inhibitors ..... 227 - 249

8.1. Introduction 227

8.2. Hypothesis 228

8.3. Results and discussions ..... 228 - 238

8.3.1. Synthesis ..... 228 - 229

8.3.2. Amyloid-β aggregation ..... 229 - 235

8.3.3. Transmission electron microscopy (TEM) 236

8.3.4. Amyloid-β molecular modeling ..... 237 - 238

8.4. Summary 239

8.5. Experimental ..... 239 - 249

8.5.1. Chemistry ..... 240 - 247

8.5.2. Biological screening ..... 247 - 246

8.5.2.1. Amyloid-β (Aβ) aggregation assay ..... 247 - 248

8.5.2.2. TEM assay and imaging 248

8.5.3. Computational chemistry ..... 248 - 249

Chapter 9: Conclusions and Future Outlook ..... 250 - 254

Appendices ..... 255 - 305

Appendix I: Sample spectra for Chapter 2 255

Appendix II: Sample spectra for Chapter 3 ..... 256 - 260

Appendix III: Sample spectra for Chapter 4 ..... 261 - 265

Appendix IV: Sample spectra for Chapter 5 ..... 266 - 276

Appendix V: Sample spectra for Chapter 6 ..... 277 - 287

Appendix VI: Sample spectra for Chapter 7 ..... 288 - 295

Appendix VII: Sample spectra for Chapter 8 ..... 296 - 305

References ..... 306 - 336

LIST OF FIGURES

Figure 1: Schematic representation of cholinergic neurotransmission mediated by acetylcholine (ACh). *Not drawn to scale.

Figure 2: Hydrolysis mechanism of ACh via the ChE catalytic triad – serine, histidine and glutamic acid. Residue numbering reflects that of human AChE (hAChE).

Figure 3: Comparison of first-generation and currently marketed ChEIs.

Figure 4: Active site outline of hAChE (1B41) showcasing the catalytic triad (green), acyl pocket (turquoise), anionic pocket (purple) and peripheral anionic site (PAS, red). Hydrogen atoms were removed to enhance clarity.

Figure 5: Comparison of active-site bound vs. dual-binding/bivalent inhibitors (yellow) of hAChE (PBD ID: 1B41). Hydrogen atoms were removed to enhance clarity. The PAS highlighted with Trp286 (red) and the active site highlighted with Trp86 (purple).

Figure 6: Active site outline of hBuChE (1P0I) showcasing the catalytic triad (green), acyl pocket (turquoise), anionic pocket (purple) and entry site (red). Hydrogen atoms were removed to enhance clarity.

Figure 7: Summary of cholinergic dysfunction in AD progression.

Figure 8: Schematic of APP structure and currently identified mutations that enhance or hinder AD pathology via the amyloid-β hypothesis. Numbering is based on APP_{770} isoform. *Not drawn to scale.

Figure 9: Schematic of APP metabolism via the non-amyloidogenic route (left) or the amyloidogenic route (right). *Not drawn to scale.

Figure 10: Amyloid-β sequence showcasing the metal-binding domain and amyloidogenic cores.

Figure 11: Reduction of amyloid-β degradation (via peptidase activity) and clearance mechanisms (via efflux receptors) propagating AD pathogenesis by increasing the amyloid-β load in the extracellular space. *Not drawn to scale.

Figure 12: Schematic of progressive decline in the management of amyloid-β structural conformation from the stable helix-kink-helix arrangement to the misfolded random coil, with or without the influence of metal-ions. The blue-dotted lines represent the essential salt bridges and hydrophobic interactions that stabilize the random coil, while the purple dotted lines represent those coordinated with the metal-ion. *Not drawn to scale.

Figure 13: Schematic of the downstream aggregation pathways of misfolded amyloid-β. Both aggregation pathways lead to plaque deposits but with different morphologies and pathological characteristics. *Not drawn to scale.

Figure 14: Transmission electron micrograph of an amyloidogenic peptide (closely related to amyloid-β) displaying the transformation of two protofilaments (A) into a dimeric-isoform (B) with the red triangles pointing to the banding pattern. The tetrameric form (C) is showcasing thicker banding indicated by the alternating white/black triangles. The morphological assessment during early-stage aggregation showcases the ~ 4–5 nm wide oligomeric structures represented above as "cross-sections" of protofilament (A).

Figure 15: Schematic overview of upstream interventions utilized to modulate amyloid-β production.

Figure 16: Schematic comparison of the varying toxicity impact (cell death) with progressive amyloid-β aggregation.

Figure 17: Schematic overview of downstream interventions utilized to modulate amyloid-β behavior and impact.

Figure 18: Commonly utilized small-molecule probes/dyes used in studying and tracking of amyloid-β aggregation in in vitro and staining studies. These compounds undergo free-rotation in solution, but once bound to amyloid their rotation capacity is restricted, attributing to their spectral red shifts.

Figure 19: Schematic overview of a typical ThT-monitored kinetic plot of amyloid-β aggregation without (black) or with a multi-mode aggregation inducer (red) or a multi-mode aggregation inhibitor (blue). The lag phase starts at t = 0 and ends at the start of the aggregation slope. The aggregation rate is indicative of how fast oligomers and protofilaments are forming. The saturation phase is the end point where fibrils are the dominant form (usually corroborated by AFM/TEM). R.F.U = Relative Fluorescence Units.

Figure 20: A brief listing of aromatic, conjugated ring systems that modulate amyloid-β aggregation. Blue-coded compounds belong to the anti-aggregatory grouping, while red-coded compounds belong to the pro-aggregatory grouping.

Figure 21: A brief recap of the amyloid cascade along with potential intervention sites.

Figure 22: A brief recap of the tauopathy cascade along with potential intervention sites.

Figure 23: A brief schematic of the ubiquitous role and presence of inflammation along the pathology timeline of AD.

Figure 24: A schematic and basic overview of the complexity tying the various cascades and mechanisms together contributing to AD pathology.

Figure 25: Naturally-occurring quinazoline and quinazolinone alkaloids.

Figure 26: A collection of marketed, in-development and patented quinazoline and related derivatives. Structures featuring the quinazoline or quinazolinone rings are indicated with red, whereas those featuring the pyridopyrimidine or related rings are indicated with blue.

Figure 27: Summary of the design strategy leading to the disubstituted quinazoline template featuring a smaller group at the C2-position to effectively generate bivalent inhibitors.

Figure 28: Overview of proposed SAR optimization on the quinazoline derivatives including template modifications.

Figure 29: Retrosynthetic pathway to the key di- or trichloroquinazoline and dichloropyrido[3,2-*d*]pyrimidine intermediates.

Figure 30: Reaction mechanisms for the cyclization and chlorination of 2-aminobenzoic acid to generate 2,4-DCQ.

Figure 31: Outline of target derivatives in this research program.

Figure 32: Mechanism for NAS reactions on the quinazoline scaffold. Coupling at the C2-position requires harsher conditions compared to C4-based coupling.

Figure 33: Mechanism for hydrazine and Pd/C driven dehalogenation via oxidative addition, β-hydrogen elimination and reductive elimination.

Figure 34: Copper-DMEDA complex mediating the amination of 2-chloro-N^4-substituted quinazoline derivatives using ammonium hydroxide.

Figure 35: Reaction mechanism toward the generation and reduction of 2-azido-N^4-substituted quinazoline derivatives.

Figure 36: Reaction mechanism toward the generation of N^4-substituted quinazoline-2-ol derivatives using formic acid and potassium formate.

Figure 37: Reaction mechanism toward the generation of N^4-substituted quinazoline-2-acetamide derivatives using acetyl chloride and acetic acid.

Figure 38: Standards utilized in the DTNB cholinesterase screening protocol. The broad inhibition window ensures representable and reliable data at both ends of the inhibition spectrum.

Figure 39: Cholinesterase metrics for 2-substituted-*N*-(3,4-dimethoxybenzyl)-quinazolin-4-amines (**5**-**18**).

Figure 40: Standards utilized in the ThT-binding assay for β-sheet aggregation monitoring.

Figure 41: Amyloid-β metrics for 14 2-substituted-*N*-(3,4-dimethoxybenzyl)-quinazolin-4-amines (**5**-**18**).

Figure 42: ThT-monitored kinetics of Aβ40 aggregation at 37 °C over a 24 hour incubation period at pH 7.4. Panel (A): Impact of 1, 5 or 25 μM of resveratrol on the aggregation kinetics of 5 μM Aβ40. Panel (B): Impact of 1, 5 or 25 μM of N^2-(1-benzylpiperidin-4-yl)-N^4-(3,4-dimethoxybenzyl)quinazoline-2,4-diamine (**6**) on the aggregation kinetics of 5 μM Aβ40. Panel (C): Impact of 1, 5 or 25 μM of N^4-(3,4-dimethoxybenzyl)-N^2-propylquinazoline-2,4-diamine (**16**) on the aggregation kinetics of 5 μM Aβ40.

Figure 43: Standards utilized in the DPPH-scavenging along with the data for selective derivatives (**9** and **10**).

Figure 44: Superimposition of docking structures. Panel (A): Binding modes of **6** (red) and **9** (green) in the active site of *h*AChE (PDB ID: 1B41). Panel (B): Binding modes of **6** (red) and **9** (green) in the active site of *h*BuChE (PDB ID: 1P0I). Hydrogens removed to enhance visibility. Black-dashed lines indicate hydrogen-bonding interactions.

Figure 45: Superimposition of docking structures. Panel (A): Binding modes of **6** (red) and **16** (turquoise) in the Aβ ($Aβ_{9-40}$ – PDB 2LMN) dimer model or fibril model [Panel (B)]. Hydrogens removed to enhance visibility. Amino acid labels to be used as a general guide as space restrictions limited complete and accurate labeling of both structures.

Figure 46: Cumulative chapter summary of 2-substituted-*N*-(3,4-dimethoxybenzyl)-quinazolin-4-amines (**5**-**18**).

Figure 47: Principles of the DTNB-assay for assessing ChE inhibition by target quinazoline derivatives.

Figure 48: Principles of the ThT assay for assessing Aβ-aggregation inhibition by target quinazoline derivatives.

Figure 49: Principles of the DPPH-scavenging assay for assessing antioxidant capacity for select quinazolines.

Figure 50: Cholinesterase metrics for 14 2-substituted-*N*-benzylquinazolin-4-amines (**19**-**31**).

Figure 51: Amyloid-β metrics for 14 2-substituted-*N*-benzylquinazolin-4-amines (**19-31**).

Figure 52: ThT-monitored kinetics of Aβ40 aggregation at 37 °C over a 24 hour incubation period at pH 7.4. Panel (A): Impact of 1, 5 or 25 μM of resveratrol on the aggregation kinetics of 5 μM Aβ40. Panel (B): Impact of 1, 5 or 25 μM of 4-(benzylamino)quinazolin-2-ol (**23**) on the aggregation kinetics of 5 μM Aβ40. Panel (C): Impact of 1, 5 or 25 μM of N-(4-(benzylamino)quinazolin-2-yl)acetamide (**26**) on the aggregation kinetics of 5 μM Aβ40.

Figure 53: ThT-monitored kinetics of Aβ42 aggregation at 37 °C over a 24 hour incubation period at pH 7.4. Panel (A): Impact of 1, 5 or 25 μM of resveratrol on the aggregation kinetics of 5 μM Aβ42. Panel (B): Impact of 1, 5 or 25 μM of N^2-benzylquinazoline-2,4-diamine (**22-iso**) on the aggregation kinetics of 5 μM Aβ42.

Figure 54: TEM assessment of Aβ40/42 morphology with or without test compounds at the end of a 24-hour, 37 °C incubation period at pH 7.4. Panel (A–C): 25 μM Aβ40 alone or at a 1:1 ratio with resveratrol or 4-(benzylamino)quinazolin-2-ol **(23)**; respectively. Panel (D–F): 25 μM Aβ42 alone or at a 1:1 ratio with resveratrol or N^2-benzylquinazoline-2,4-diamine (**22-iso**); respectively. White/black bars represent 500 nm.

Figure 55: Standards utilized in the DPPH-scavenging along with the data for 4-(benzylamino)quinazolin-2-ol (**23**).

Figure 56: Superimposition of docking structures. Panel (A): Binding modes of **20** (magenta) and **22** (red) in the active site of *h*AChE (PDB ID: 1B41). Panel (B,C): Binding modes of **22** (red) and **22-iso** (turquoise) in the active sites of *h*AChE (PDB ID: 1B41) and *h*BuChE (PDB ID: 1P0I); respectively. Hydrogens removed to enhance visibility. Black-dashed lines indicate hydrogen-bonding interactions.

Figure 57: Superimposition of docking structures. Panels (A–C): Binding modes of **22** (red) and **22-iso** (turquoise), **22** (red) and **23** (green) or **23** (green) and **26** (gold); respectively, in the Aβ ($Aβ_{9-40}$ – PDB 2LMN) dimer model or fibril model [Panels (D–F)]. Hydrogens removed to enhance visibility. Amino acid

labels to be used as a general guide as space restrictions limited complete and accurate labeling of all peptide structures.

Figure 58: Superimposition of docking structures. Panel (A): Binding modes of **23** (red) and its resonance stabilized structures (green and yellow/orange) in the Aβ ($A\beta_{9\text{-}40}$ – PDB 2LMN) dimer model or fibril model [Panel (B)]. Hydrogens removed to enhance visibility. Amino acid labels to be used as a general guide as space restrictions limited complete and accurate labeling of all peptide structures.

Figure 59: Cumulative chapter summary of 2-substituted-*N*-benzylquinazolin-4-amines (**19**-**31**) and related regioisomers.

Figure 60: Principles of the TEM imaging setup for assessing amyloid morphology with or without select derivatives.

Figure 61: Cholinesterase metrics for 14 2-substituted-*N*-(3,4-dimethoxyphenethyl)quinazolin-4-amines (**32**-**44**) and 15 2-substituted-*N*-(3,4-dimethoxyphenethyl)chloroquinazolin-4-amines (**45**-**59**).

Figure 62: Amyloid-β metrics for 14 2-substituted-*N*-(3,4-dimethoxyphenethyl)quinazolin-4-amines (**32**-**44**) and 15 2-substituted-*N*-(3,4-dimethoxyphenethyl)chloroquinazolin-4-amines (**45**-**59**).

Figure 63: ThT-monitored kinetics of Aβ40 aggregation at 37 °C over a 24 hour incubation period at pH 7.4. Panel (A): Impact of 1, 5 or 25 μM of 2,6-dichloro-*N*-(3,4-dimethoxyphenethyl)quinazolin-4-amine (**45**) on the aggregation kinetics of 5 μM Aβ40. Panel (B): Impact of 1, 5 or 25 μM of 2,7-dichloro-*N*-(3,4-dimethoxyphenethyl)quinazolin-4-amine (**46**) on the aggregation kinetics of 5 μM Aβ40. Panel (C): Impact of 1, 5 or 25 μM of 6-chloro-N^4-(3,4-dimethoxyphenethyl)-N^2,N^2-dimethylquinazoline-2,4-diamine (**51**) on the aggregation kinetics of 5 μM Aβ40. Panel (D): Impact of 1, 5 or 25 μM of 8-chloro-N^4-(3,4-dimethoxyphenethyl)-N^2,N^2-dimethylquinazoline-2,4-diamine (**59**) on the aggregation kinetics of 5 μM Aβ40.

Figure 64: ThT-monitored kinetics of Aβ42 aggregation at 37 °C over a 24 hour incubation period at pH 7.4. Panel (A): Impact of 1, 5 or 25 μM of 2,7-dichloro-*N*-(3,4-dimethoxyphenethyl)quinazolin-4-amine (**46**) on the aggregation kinetics of 5 μM Aβ42. Panel (B): Impact of 1, 5 or 25 μM of 2,8-dichloro-*N*-(3,4-dimethoxyphenethyl)quinazolin-4-amine (**47**) on the aggregation kinetics of 5 μM Aβ42. Panel (C): Impact of 1, 5 or 25 μM of 8-chloro-N^4-(3,4-dimethoxyphenethyl)-N^2-isopropylquinazoline-2,4-diamine (**57**) on the aggregation kinetics of 5 μM Aβ42. Panel (D): Impact of 1, 5 or 25 μM of 8-chloro-N^4-(3,4-dimethoxyphenethyl)-N^2,N^2-dimethylquinazoline-2,4-diamine (**59**) on the aggregation kinetics of 5 μM Aβ42.

Figure 65: TEM assessment of Aβ40/42 morphology with or without test compounds at the end of a 24-hour, 37 °C incubation period at pH 7.4. Panel (A–C): 25 μM Aβ40 alone or at a 1:1 ratio with resveratrol or 2,7-dichloro-*N*-(3,4-dimethoxyphenethyl)quinazolin-4-amine **(46)**; respectively. Panel (D–F): 25 μM Aβ42 alone or at a 1:1 ratio with resveratrol or 2,8-dichloro-*N*-(3,4-dimethoxyphenethyl)quinazolin-4-amine **(47**); respectively. White/black bars represent 500 nm.

Figure 66: Standards utilized in the DPPH-scavenging along with the data for 4-((3,4-dimethoxyphenethyl) amino)quinazolin-2-ol (**36**).

Figure 67: Superimposition of docking structures. Panel (A): Binding modes of **32** (red) and **35** (purple) in the active site of *h*AChE (PDB ID: 1B41). Panel (B): Binding modes of **40** (green) and **44** (magenta) in the active sites of *h*BuChE (PDB ID: 1P0I). Panel (C): Binding modes of **43** (blue) and **53** (gold) in the active sites of *h*BuChE (PDB ID: 1P0I). Hydrogens removed to enhance visibility. Black-dashed lines indicate hydrogen-bonding interactions.

Figure 68: Superimposition of docking structures. Panels (A and B): Binding modes of **45** (gold), **46** (red) and **47** (turquoise) in the Aβ ($Aβ_{9-40}$ – PDB 2LMN) dimer model or fibril model; respectively. Hydrogens removed to enhance visibility. Amino acid labels to be used as a general guide as space restrictions limited complete and accurate labeling of all peptide structures.

Figure 69: Cumulative chapter summary of 2-substituted-*N*-(3,4-dimethoxyphenethyl)quinazolin-4-amines (**32**-**44**) and 2-substituted-*N*-(3,4-dimethoxyphenethyl)chloroquinazolin-4-amines (**45**-**59**).

Figure 70: Cholinesterase metrics for 15 2-substituted-*N*-phenethylquinazolin-4-amines (**60**-**72**) and 15 2-substituted-*N*-phenethylchloroquinazolin-4-amines (**73**-**87**).

Figure 71: Amyloid-β metrics for 15 2-substituted-*N*-phenethylquinazolin-4-amines (**60**-**72**) and 15 2-substituted-*N*-phenethylchloroquinazolin-4-amines (**73**-**87**).

Figure 72: ThT-monitored kinetics of Aβ40 aggregation at 37 °C over a 24 hour incubation period at pH 7.4. Panel (A): Impact of 1, 5 or 25 μM of 1-(4-(phenethylamino)quinazolin-2-yl)urea (**65**) on the aggregation kinetics of 5 μM Aβ40. Panel (B): Impact of 1, 5 or 25 μM of N^2-cyclopropyl-N^4-phenethylquinazoline-2,4-diamine (**72**) on the aggregation kinetics of 5 μM Aβ40. Panel (C): Impact of 1, 5 or 25 μM of 8-chloro-N^2-isopropyl-N^4-phenethylquinazoline-2,4-diamine (**85**) on the aggregation kinetics of 5 μM Aβ40. Panel (D): Impact of 1, 5 or 25 μM of 8-chloro-N^2-cyclopropyl-N^4-phenethylquinazoline-2,4-diamine (**86**) on the aggregation kinetics of 5 μM Aβ40.

Figure 73: ThT-monitored kinetics of Aβ42 aggregation at 37 °C over a 24 hour incubation period at pH 7.4. Panel (A): Impact of 1, 5 or 25 μM of 2,7-dichloro-*N*-phenethylquinazolin-4-amine (**74**) on the aggregation kinetics of 5 μM Aβ42. Panel (B): Impact of 1, 5 or 25 μM of 2,8-dichloro-*N*-phenethyl)quinazolin-4-amine (**75**) on the aggregation kinetics of 5 μM Aβ42.

Figure 74: TEM assessment of Aβ40/42 morphology with or without test compounds at the end of a 24-hour, 37 °C incubation period at pH 7.4. Panel (A–C): 25 μM Aβ40 alone or at a 1:1 ratio with resveratrol or 8-chloro-N^2-isopropyl-N^4-phenethylquinazoline-2,4-diamine (**85**); respectively. Panel (D–F): 25 μM Aβ42 alone or at a 1:1 ratio with resveratrol or 2,7-dichloro-*N*-phenethylquinazolin-4-amine **(74**); respectively. White/black bars represent 500 nm.

Figure 75: Standards utilized in the DPPH-scavenging along with the data for 4-(phenethylamino) quinazolin-2-ol (**64**).

Figure 76: Superimposition of docking structures. Panel (A–B): Binding modes of **63** (orange) and **63-iso** (magenta) or **81** (red) and **83** (olive) in the active site of *h*AChE (PDB ID: 1B41); respectively. Panel (C): Binding modes of **63** (orange) and **63-iso** (magenta) in the active sites of *h*BuChE (PDB ID: 1P0I). Panel (D): Binding modes of **71** (green), **77** (gold), **81** (red) and **85** (blue) in the active sites of *h*BuChE (PDB ID: 1P0I). Hydrogens removed to enhance visibility. Black-dashed lines indicate hydrogen-bonding interactions.

Figure 77: Superimposition of docking structures. Panels (A and B): Binding modes of **85** (olive) and **86** (magenta) in the Aβ ($A\beta_{9\text{-}40}$ – PDB 2LMN) dimer model or fibril model; respectively. Hydrogens removed to enhance visibility. Amino acid labels to be used as a general guide as space restrictions limited complete and accurate labeling of all peptide structures.

Figure 78: Cumulative chapter summary of 2-substituted-*N*-phenethylquinazolin-4-amines (**60**-**72**) and 2-substituted-*N*-phenethylchloroquinazolin-4-amines (**73**-**87**).

Figure 79: ThT-monitored kinetics of Aβ40/42 aggregation at 37 °C over a 24 hour incubation period at pH 7.4. Panel (A): Impact of 1, 5 or 25 μM of N^2-isopropyl-N^4-phenethylpyrido[3,2-*d*]pyrimidine-2,4-diamine (**95**) on the aggregation kinetics of 5 μM Aβ40. Panel (B): Impact of 1, 5 or 25 μM of 2-chloro-*N*-(3,4-dimethoxyphenethyl) pyrido[3,2-*d*]pyrimidin-4-amine (**88**) on the aggregation kinetics of 5 μM Aβ42.

Figure 80: TEM assessment of Aβ40/42 morphology with or without test compounds at the end of a 24-hour, 37 °C incubation period at pH 7.4. Panel (A–C): 25 μM Aβ40 alone or at a 1:1 ratio with resveratrol or N^2-isopropyl-N^4-phenethylpyrido[3,2-*d*]pyrimidine-2,4-diamine (**95**); respectively. Panel (D–F): 25 μM Aβ42 alone or at a 1:1 ratio with resveratrol or 2-chloro-*N*-(3,4-dimethoxyphenethyl)pyrido[3,2-*d*]pyrimidin-4-amine **(88**); respectively. White/ black bars represent 500 nm.

Figure 81: Overall summary of the scaffold evaluation toward iron chelation capacity.

Figure 82: Superimposition of docking structures of **93** (gold) and **97** (turquoise) in the active site of *h*AChE (PDB ID: 1B41). Hydrogens removed to enhance visibility. Black-dashed lines indicate hydrogen-bonding interactions.

Figure 83: Superimposition of docking structures. Binding modes of **95** (red) and **96** (green) in the Aβ ($A\beta_{9\text{-}40}$ – PDB 2LMN) dimer model. Hydrogens removed to enhance visibility. Amino acid labels to be used as a general guide as space restrictions limited complete and accurate labeling of all peptide structures.

Figure 84: Cumulative chapter summary of 2,4-disubstituted pyridopyrimidines (**88**-**97**).

Figure 85: Principles of the ferrozine-based iron chelation assay.

Figure 86: Amyloid-β metrics for 30 2,4-diaminoquinazolines (**98**-**112**) including their regioisomers.

Figure 87: ThT-monitored kinetics of Aβ40 aggregation at 37 °C over a 24 hour incubation period at pH 7.4. Panel (A): Impact of 1, 5 or 25 μM of N^4-(3-bromobenzyl)quinazoline-2,4-diamine (**109**) on the aggregation kinetics of 5 μM Aβ40. Panel (B): Impact of 1, 5 or 25 μM of N^2-(3-bromobenzyl)quinazoline-2,4-diamine (**109-iso**) on the aggregation kinetics of 5 μM Aβ40. Panel (C): Impact of 1, 5 or 25 μM of N^4-(4-bromobenzyl)quinazoline-2,4-diamine (**110**) on the aggregation kinetics of 5 μM Aβ40. Panel (D): Impact of 1, 5 or 25 μM of N^2-(4-bromobenzyl)quinazoline-2,4-diamine (**110-iso**) on the aggregation kinetics of 5 μM Aβ40.

Figure 88: ThT-monitored kinetics of Aβ42 aggregation at 37 °C over a 24 hour incubation period at pH 7.4. Panel (A): Impact of 1, 5 or 25 μM of N^4-(3-bromobenzyl)quinazoline-2,4-diamine (**109**) on the aggregation kinetics of 5 μM Aβ42. Panel (B): Impact of 1, 5 or 25 μM of N^2-(3-bromobenzyl)quinazoline-2,4-diamine (**109-iso**) on the aggregation kinetics of 5 μM Aβ42. Panel (C): Impact of 1, 5 or 25 μM of N^4-(4-bromobenzyl)quinazoline-2,4-diamine (**110**) on the aggregation kinetics of 5 μM Aβ42. Panel (D):

Impact of 1, 5 or 25 μM of N^2-(4-bromobenzyl)quinazoline-2,4-diamine (**110-iso**) on the aggregation kinetics of 5 μM Aβ42.

Figure 89: TEM assessment of Aβ40/42 morphology with or without test compounds at the end of a 24-hour, 37 °C incubation period at pH 7.4. Panel (A–C): 25 μM Aβ40 alone or at a 1:1 ratio with resveratrol or N^4-(4-bromobenzyl)quinazoline-2,4-diamine (**110**); respectively. Panel (D–F): 25 μM Aβ42 alone or at a 1:1 ratio with resveratrol or N^2-(4-bromobenzyl)quinazoline-2,4-diamine (**110-iso**); respectively. White/black bars represent 500 nm.

Figure 90: Superimposition of docking structures. Panel (A, C): Binding modes of **109** (pink) and **109-iso** (green) in the Aβ ($Aβ_{9-40}$ – PDB 2LMN) dimer or fibril model; respectively. Panel (B, D): Binding modes of **110** (red) and **110-iso** (gold) in the Aβ ($Aβ_{9-40}$ – PDB 2LMN) dimer or fibril model; respectively Hydrogens removed to enhance visibility. Amino acid labels to be used as a general guide as space restrictions limited complete and accurate labeling of all peptide structures.

Figure 91: Cumulative chapter summary of 2,4-diaminoquinazolines (**98**-**112**) and their respective regioisomers.

Figure 92: Collective metrics for complete quinazoline-based library. Selections were based on good-moderate activity against all 4 primary targets. (Notes: As Chapter 8 diaminoquinazolines were only assessed for Aβ aggregation, they were included in the Aβ pie charts but not considered during leading candidate selection. Derivatives screened for antioxidant and chelation capacities were not identified as complete multi-targeting candidates; hence those metrics were not included here).

LIST OF TABLES

Table 1: Cholinesterase inhibition data for 2-substituted-*N*-(3,4-dimethoxybenzyl)-quinazolin-4-amines (**5**-**18**).

Table 2: Amyloid-β (Aβ40/42) inhibition data for 2-substituted-*N*-(3,4-dimethoxybenzyl)-quinazolin-4-amines (**5**-**18**).

Table 3: Cholinesterase inhibition data for 2-substituted-*N*-benzylquinazolin-4-amines (**9**-**31**) and the C4-amino regiosiomer (**22-iso**).

Table 4: Amyloid-β (Aβ40/42) inhibition data for 2-substituted-*N*-benzylquinazolin-4-amines (**9**-**31**) and the C4-amino regiosiomer (**22-iso**).

Table 5: Cholinesterase inhibition data for 2-substituted-*N*-(3,4-dimethoxyphenethyl)quinazolin-4-amines (**32**-**44**) and the C4-unsubstituted regiosiomer (**33-iso**).

Table 6: Cholinesterase inhibition data for 2-substituted-*N*-(3,4-dimethoxyphenethyl)chloroquinazolin-4-amines (**45**-**59**).

Table 7: Amyloid-β (Aβ40/42) inhibition data for 2-substituted-*N*-(3,4-dimethoxyphenethyl)quinazolin-4-amines (**32**-**44**) and the C4-unsubstituted regiosiomer (**33-iso**).

Table 8: Amyloid-β (Aβ40/42) inhibition data for 2-substituted-*N*-(3,4-dimethoxyphenethyl)chloro quinazolin-4-amines (**45**-**59**).

Table 9: Cholinesterase inhibition data for 2-substituted-*N*-phenethylquinazolin-4-amines (**60**-**72**) and the related regiosiomers (**61-iso** and **63-iso**).

Table 10: Cholinesterase inhibition data for 2-substituted-*N*-phenethylchloroquinazolin-4-amines (**73**-**87**).

Table 11: Amyloid-β (Aβ40/42) inhibition data for 2-substituted-*N*-phenethylquinazolin-4-amines (**60**-**72**) and the related regiosiomers (**61-iso** and **63-iso**).

Table 12: Amyloid-β (Aβ40/42) inhibition data for 2-substituted-*N*-phenethylquinazolin-4-amines (**73**-**87**).

Table 13: Cholinesterase inhibition data for 2,4-disubstituted pyridopyrimidines (**88**–**97**).

Table 14: Amyloid-β (Aβ40/42) inhibition data for 2,4-disubstituted pyridopyrimidines (**88**–**97**).

Table 15: Iron chelation capacity for 2,4-disubstituted pyridopyrimidines (**90**–**97**) in relation to quinazoline counterparts (**42**–**44** and **70**–**72**).

Table 16: Amyloid-β (Aβ40/42) inhibition data for 2,4-diaminoquinazolines (**98**–**112**) and their regioisomers.

LIST OF SCHEMES

Scheme 1[a] – Highlighting a few metal-free synthetic routes toward quinazoline-based derivatives.

Scheme 2[a] – Highlighting a few catalyst-dependent synthetic routes toward quinazoline-based derivatives.

Scheme 3[a] – Highlighting a few microwave or ultrasound-assisted synthetic routes toward quinazoline derivatives and intermediates

Scheme 4[a] – Synthetic route toward the 2,4-dichloroquinazoline intermediate.

Scheme 5[a] – Synthetic routes toward quinazoline-based derivatives **5**–**7**.

Scheme 6[a] – Synthetic routes toward quinazoline-based derivatives **8**–**10**.

Scheme 7[a] – Synthetic routes toward quinazoline-based derivatives **11**–**13**.

Scheme 8[a] – Synthetic routes toward quinazoline-based derivatives **14**–**18**.

Scheme 9[a] – Synthetic routes toward quinazoline-based derivatives **19** and **20**.

Scheme 10[a] – Synthetic routes toward quinazoline-based derivatives **21**–**23.**

Scheme 11[a] – Synthetic routes toward quinazoline-based derivatives **22** and **22-iso.**

Scheme 12[a] – Synthetic routes toward quinazoline-based derivatives **24**–**31**.

Scheme 13[a] – Synthetic routes toward quinazoline-based derivatives **32**, **33** and **33-iso**.

Scheme 14[a] – Synthetic routes toward quinazoline-based derivatives **34**–**36.**

Scheme 15[a] – Synthetic routes toward quinazoline-based derivatives **37**–**44**.

Scheme 16[a] – Synthetic routes toward quinazoline-based derivatives **45**–**59**.

Scheme 17[a] – Synthetic routes toward quinazoline-based derivatives **60**, **61** and **61-iso**.

Scheme 18[a] – Synthetic routes toward quinazoline-based derivatives **62**–**64** and **63-iso.**

Scheme 19[a] – Synthetic routes toward quinazoline-based derivatives **65**–**72**.

Scheme 20[a] – Synthetic routes toward quinazoline-based derivatives **73**–**87**.

Scheme 21[a] – Synthetic routes toward pyridopyrimidine-based derivatives **88**–**89**.

Scheme 22[a] – Synthetic routes toward pyridopyrimidine-based derivatives **90**–**97**.

Scheme 23[a] – Synthetic routes toward isomeric quinazoline-2,4-diamine derivatives **98–112.**

LIST OF ABBREVIATIONS

2,4-DCP = 2,4-dichloropyridopyrimidine

2,4-DCQ = 2,4-dichloroquinazoline

6-, 7-, 8-TCQ = 2,4,6- , 2,4,7-, 2,4,8-trichloroquinazoline

Aβ = Amyloid-β

ACh = Acetylcholine

AChE = Acetylcholinesterase

AChEI = Acetylcholinesterase inhibitor

ACID = APP intracellular domain

AcOH = Acetic acid

AD = Alzheimer's disease

ADAM = A disintegrin and metalloprotease

ADDLs = Amyloid-derived diffusible ligands

ADE = Amyloid-degrading enzyme

$AgBF_4$ = Silver tetrafluoroborate

Aph-1 = Anterior pharynx-defective 1

Apo ε4 = Apolpoprotein ε4

APP = Amyloid precursor protein

ATCh = Acetylthiocholine

BACE = Beta-site APP cleaving enzyme

BBB = Blood-brain barrier

BuCh = Butyrylcholine

BuChE = Butyrylcholinesterase

BuChEI = Butyrylcholinesterase inhibitor

BuOH = Butanol

$BuPAd_2$ = Di-(1-adamantyl)-*n*-butylphosphine

BuTCh = Butyrylthiocholine

CADD = Computer-aided drug design

CAS = Cationic active site

CD = Circular dichroism

ChAT = Choline acetyltransferase

ChE = Cholinesterase

ChEI = Cholinesterase inhibitor

ClogP = Partition coefficient

ColQ = AChE-associated collagen

$[Cp^*RhCl_2]_2$ = Pentamethylcyclopentadienylrhodium-(III)-chloride dimer

CT = Catalytic triad

CTF = C-terminal fragment

DAQ = Diaminoquinazoline

DCB = Dichlorobenzene

DCE = Dichloroethane

DCM = Dichloromethane

DIPEA = Diisopropylethylamine

DMA = Dimethylacetamide

DMAP = Dimethylaminopyridine

DME = Disease-modifying effect

DMEDA = Dimethylethylenediamine

DMSO = Dimethylsulfoxide

DPPH = 2,2-Diphenyl-1-picrylhydrazyl

DTBP = Di-tert-butyl peroxide

DTNB = Dithiobis-(2-nitrobenzoic acid)

EDG: Electron-donating groups

EWG: Electron-withdrawing groups

EtOAc = Ethyl acetate

EtOH = Ethanol

FAD = Familial Alzheimer's disease

FRET = Fluorescence resonance energy transfer

GPI = Glycophosphatidylinositol

HPLC = High-performance liquid chromatography

HRMS = High-resolution mass spectroscopy

Hsp = Heat-shock protein

IC_{50} = Concentration required for 50% inhibition

LCMS = Liquid-chromatography coupled to a mass spectrometer

LRP = Lipoprotein receptor-related protein

mAChR = Muscarinic acetylcholine receptor

MeCN = Acetonitrile

MeOH = Methanol

$MgSO_4$ = Magnesium sulfate

MTT = 3-(4,5-dimethylthiazol-2-yl)-2,5-diphenyltetrazolium bromide

MW = Microwave

MV = Molecular volume

nAChR = Nicotinic acetylcholine receptor

NaH = Sodium hydride

NAS = Nucleophilic aromatic substitution

NBS = N-bromosuccinimide

NFTs = Neurofibrillary tangles

NMDA = *N*-methyl-D-aspartate

NPs = Nanoparticles

NTB = 2-Nitro-5-thiobenzoic acid

PAS = Peripheral anionic site

$Pd(OAc)_2$ = Palladium-(II)-acetate

P-gp = ATP-binding cassette transporter p-glycoprotein

$PhI(OAc)_2$ = Phenyliodonium diacetate

pM = Picomolar

$POCl_3$ = Phosphoryl chloride

Ppd = Pyridopyrimidine

PRiMA = Proline-rich membrane anchor

PTA = Phosphotungstic acid

PV = Pressure vial

Qnz = Quinazoline

RAGE = Receptor for advanced glycation end products

RFUs = Relative fluorescence units

ROS = Reactive oxygen species

r.t = Room temperature

$sAPP_{\alpha/\beta}$ = Soluble APP fragment α/β

SAR = Structure-activity relationship

SGCC = Silica gel column chromatography

SI = Selectivity index

SODS = Superimposition of docked structures

τ = Tau

TEA = Triethylamine

TEM = Transmission electron microscopy

TFA = Trifluoroacetic acid

THF = Tetrahydrofuran

ThT = Thioflavin T

TLC = Thin-layer chromatography

TsOH = Toluenesulfonic acid

WHO = World Health Organizatio

FUNCTIONAL GROUP NOMENCLATURE

Ac = Acetyl

Ar = Aryl

Bn = Benzyl

*c*Pr = Cyclopropyl

DiOMe = Dimethoxy

Et = Ethyl

*i*Pr = Isopropyl

Me = Methyl

*n*Pr = normal Propyl

OMe = Methoxy

Ph = Phenyl

PhEt = Phenethyl

CHAPTER 1

• Background on Alzheimer's Disease •

1.1. Introduction

We are all unique – not only by virtue of our genetic makeup, but also by way of our neuronal framework and networking. Individuality has much to do with what one projects on the exterior as it is with what they captivate within. A life's worth of memories and experiences define our cognitive fingerprint and elicit one of our fabrics of humanity. While cancer is portrayed as a hijacker of a cell's proliferation mechanisms, Alzheimer's disease (AD) can be painted, as a hijacker of one's conscious and subconscious mind – an eraser of a substantial aspect of your self-being.

With initial documentation of its pathology dating back to 1907,[1, 2] a growing prevalence and a lack of viable cures or therapeutic options, AD has manifested a strong socioeconomic holding and an overwhelming healthcare burden on communities across the globe. To appreciate the severity of this neurodegenerative disorder, consider the following: (a) According to the World Health Organization (WHO), nearly 48 million people worldwide are living with AD and that number is anticipated to escalate to about 76 million by 2030; (b) In Canada alone, the Alzheimer's Society of Canada estimates the combined annual direct and indirect costs associated with AD to be upwards of $33 billion; (c) In the United States, the Alzheimer's Association estimates that a new patient develops AD every 67 seconds and (d) the dollar amount spent on AD research accounts for less than 0.4% of the amount spent on the disease's presumed "treatment".[3-5]

The challenges of tackling the AD dilemma are inclusive, with the lack of early detection and an overall miscomprehension of disease pathology being chief culprits. With the former, the onset of dementia symptoms typically point to a lost opportunity for any level of successful intervention as progression is well underway, while the latter simply points to the overall complexity of the neuroscience field and its ties with the normal aging process that can mask early-warning signs of dementia.[6-8] As it stands now, an

Alzheimer's diagnosis is ominously a death-sentence – no cure, no viable treatments and a losing uphill battle.

In a general sense, AD is the progressive loss of brain mass, due to neuronal cell death, that presents in the form of dementia, loss of cognitive, and eventually, motor function. Patients lose memory recall capability, the ability to perform typical daily tasks, the ability to connect and interact with surrounding environments and, ultimately, symptoms of depression and isolation surface leading to poorer health status.[9-11] AD patients typically succumb to death as a result of various infections, rather than a direct cause of dementia insults.[12] While AD generally afflicts elderly populations worldwide, it is not a gender-specific disorder and a number of genetic pre-dispositions expand its outreach to middle-aged patients as well.[13-17]

The road to understanding AD pathology has been charted with more of a retrosynthetic (or reverse discovery) tactic – starting with the end outcomes and backtracking to potential causes of said outcomes. In fact, back in 1906, the post-mortem discovery of dense proteinaceous deposits in the brain of what is now known as the first AD patient, established one of the quintessential hallmarks of AD pathology.[1, 2, 18, 19] Further classified as amyloid plaques (originating from the Aβ peptide) and neurofibrillary tangles (NFTs, originating from the tau peptide), these proteinaceous deposits still captivate a substantial amount of research focus in AD.[20-23] Clinical assessments also linked the observed regression in cognitive ability with the decline of acetylcholine (ACh, a cholinergic neurotransmitter) levels in the brains of AD patients.[9, 24-26] From these conclusions, amongst many others, a number of disease hypotheses were put forth in an attempt to explain disease progression and to identify potential interventions. Primary hypotheses included cholinergic dysfunction,[9, 24-26] amyloid-β,[16, 20, 27-30] tau protein[28, 31-37] and the multipronged reactive oxygen species (ROS),[38-40] with the foremost being the oldest and most fruitful at generating marketed AD therapeutics (e.g. Aricept™, Reminyl™ and Exelon™). That said, AD is still a cureless disorder and the aforementioned therapeutics merely offer symptomatic relief without targeting neither disease initiation nor progression.[24, 41, 42]

Therein lies one of the significant setbacks toward curing AD. It was not until recently that the research community was devoting most of its efforts with the "one-drug, one target" ideology. It is that ideology that generated currently marketed therapeutics but then again, they are not true treatments. With a

disease as complex and as misunderstood as AD, a multidimensional approach does not simply become an option but rather a mandate. By shifting focus toward multi-targeting and multifunctional therapeutics, not only are better outcomes anticipated but it could also be argued that through the development and discovery of such candidates, new light could be shone on the pathological framework.[43-50]

The good news is that this paradigm shift is well underway as more and more research endeavors are charting the relatively untested waters of multi-targeting agents as potentially being the next generation of AD treatment options.

1.2. The Cholinergic Dysfunction Hypothesis

One of the key factors of maintaining a vehicle in motion is having enough gasoline flowing to the engine – a similar principle applies to cholinergic function and in that scenario, the cholinergic "gasoline" is ACh. As one of the oldest hypotheses put forth to explain the clinical assessments tied with deteriorating cognitive ability, the cholinergic dysfunction premise is centered on ACh, its generation, actions in the CNS and metabolism.

1.2.1. *Cholinergic Neurotransmission*

There are a number of critical players that collectively contribute to the functionality of the cholinergic system. The neurotransmitter ACh is synthesized from acetyl-CoA and recycled choline by choline acetyltransferase (ChAT) and is stored in vesicles, which are released from the presynaptic neurons upon depolarization from a stimulus. Upon ACh release, it binds to nicotinic (nAChR) or muscarinic acetylcholine receptors (mAChR) to elicit the appropriate physiological response and the remaining ACh molecules are rapidly hydrolyzed by the cholinesterases (AChE or BuChE) to acetic acid (AcOH) and choline (a substrate for the choline transporters on the presynaptic neurons) (Figure 1).[9, 26, 51]

Under typical circumstances, the activity of the cholinesterases (ChEs) is a security measure against neuronal overstimulation. Chemical nerve agents, for example, induce overstimulation of the cholinergic system by paralyzing the ChEs, leading to an overwhelming concentration of ACh in the synapse.[52]

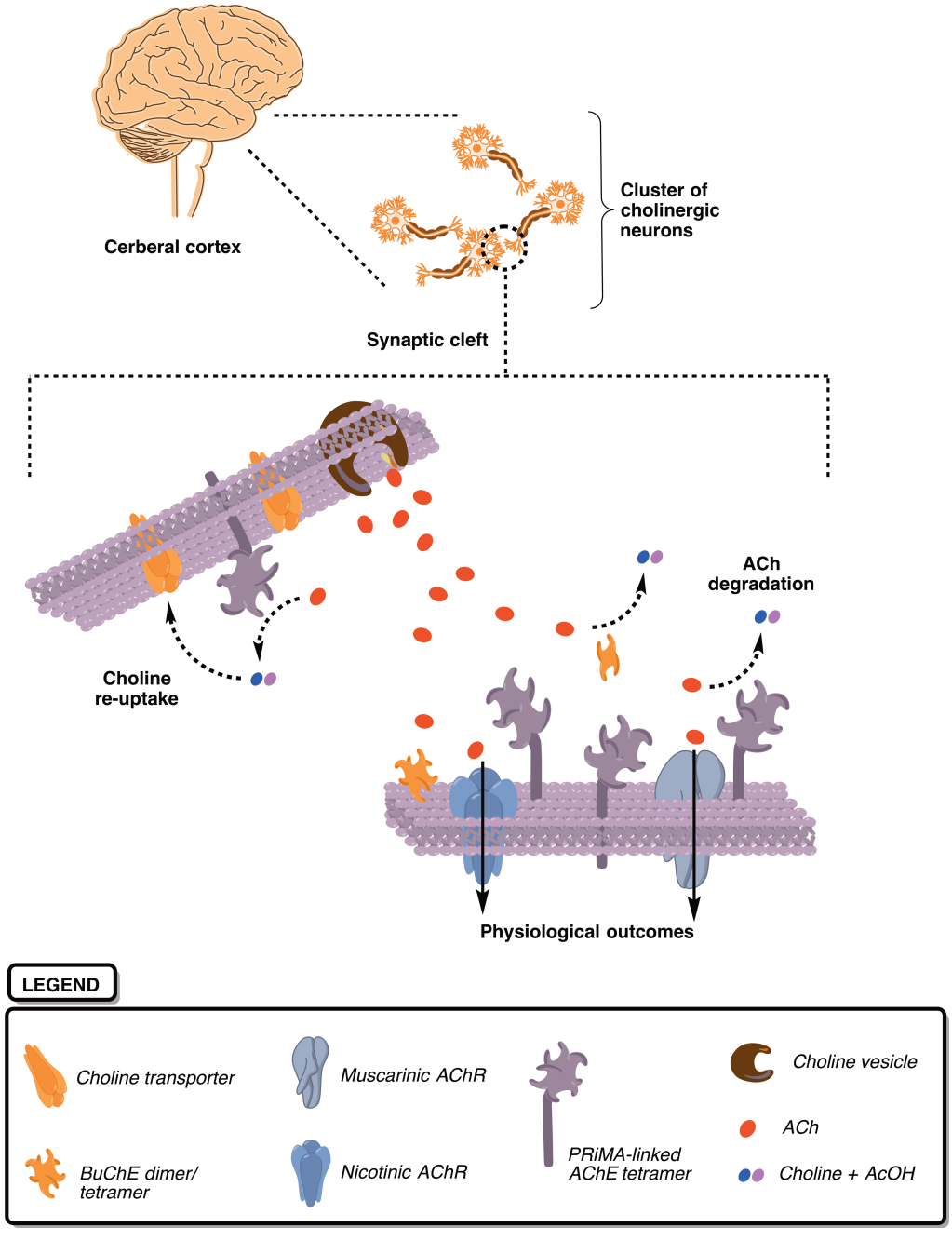


Figure 1: Schematic representation of cholinergic neurotransmission mediated by acetylcholine (ACh). *Not drawn to scale.

Transferring that concept to AD pathology, as the number of ACh-producing neurons are declining, developing reversible ChE inhibitors was meant to restore or maintain the ACh levels in the synapse of AD patients to alleviate some of the memory deficits – a symptom, not a cause of AD.

1.2.2. *The Cholinesterase (ChE) Enzymes*

While the cholinesterases play a number of diverse physiological roles, in the context of AD and the cholinergic dysfunction hypothesis, they primarily function to eliminate unbound ACh in the cholinergic synapse by hydrolyzing the neurotransmitter to acetic acid and choline, which is recycled back to pre-synaptic neurons. While the ChE isoforms (AChE/BuChE) only share about 50% sequence identity, their structure homology is relatively similar.[53, 54] Moreover, the ACh hydrolysis mechanism is shared and relies on the presence of a catalytic triad (serine, histidine and glutamic acid) with the serine hydroxyl group acting as the nucleophile. Upon binding of ACh, a tetrahedral intermediate is formed, where its eventual collapse releases choline leaving an acetylated serine residue, which is rapidly hydrolyzed back to the active state (Figure 2).[55-57]

Due to their active site variances (discussed later), their substrate specificity is unique. While AChE is capable of hydrolyzing ACh at near diffusion limits, BuChE is not as fast but it has a larger substrate pool. These variances also translate to the design of cholinesterase inhibitors (ChEIs) and explain the difficulty of successfully developing a dual, potent and non-selective ChEI.[58-60] A brief examination of previously and currently marketed ChE-based AD therapeutics, demonstrates that none are ideal with respect of effectively targeting both ChEs and at possessing multi-targeting capabilities (Figure 3).

The concept of dual-ChE targeting has more to do with disease progression than simply a mere ambition. Moreover, the overall distribution and arrangements of the ChEs in and outside of the CNS play a role in their implications with AD.

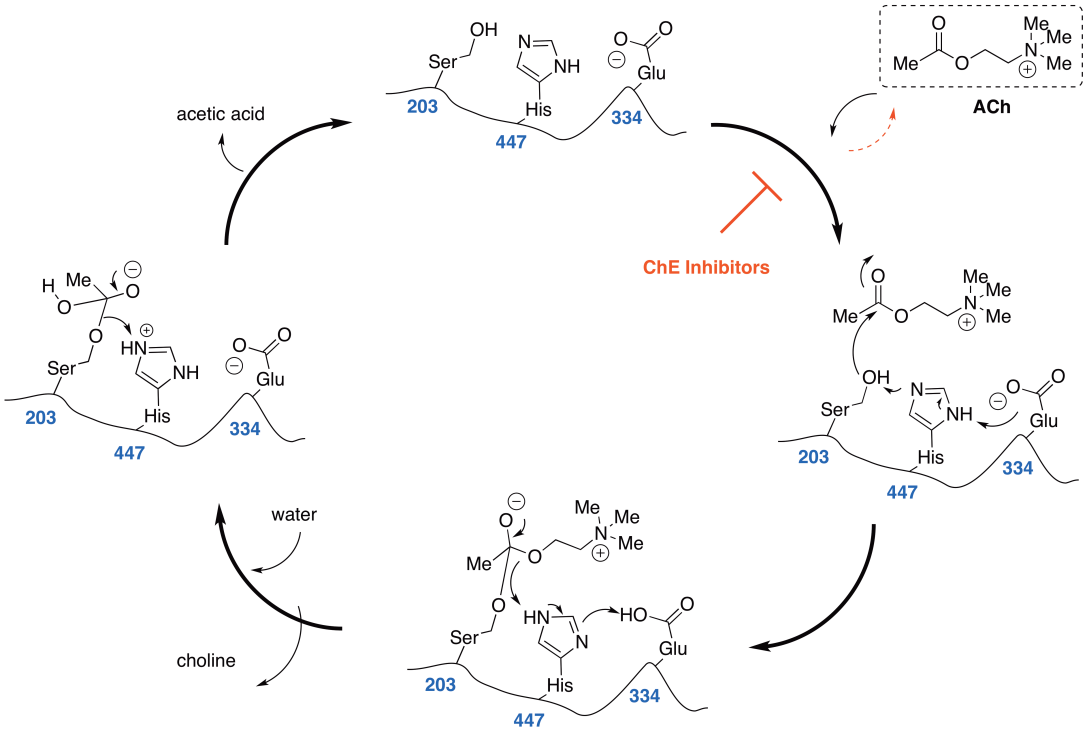


Figure 2: Hydrolysis mechanism of ACh via the ChE catalytic triad – serine, histidine and glutamic acid. Residue numbering reflects that of human AChE (hAChE).

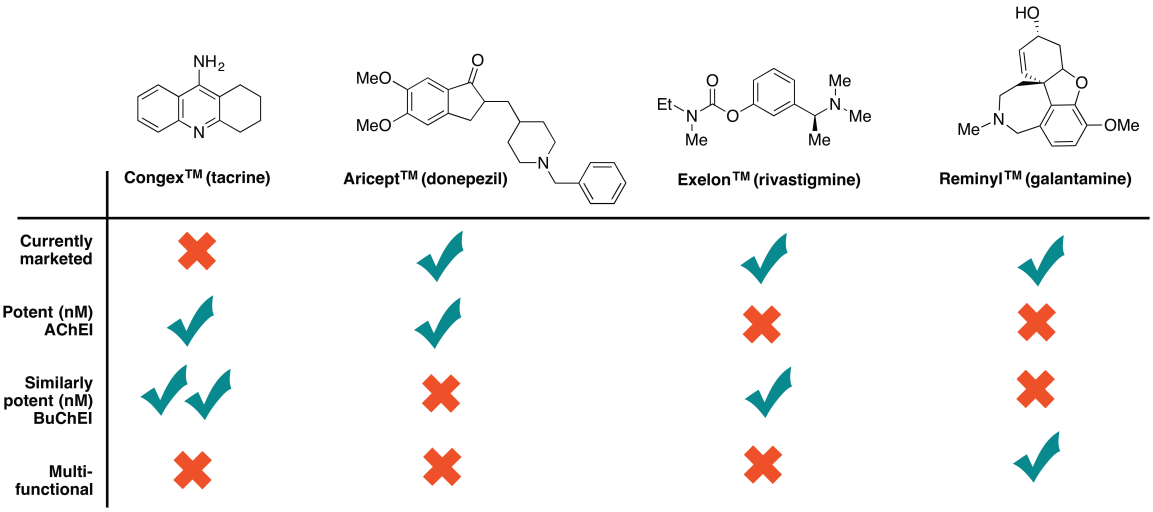


Figure 3: Comparison of first-generation and currently marketed ChEIs.

1.2.2.1. *Acetylcholinesterase (AChE)*

As the primary cholinesterase, AChE represents the prime target with respect to the cholinergic dysfunction hypothesis. In humans, this hydrolase is encoded by a single gene (*ACHE*), located on chromosome 7, which takes on two major forms based on alternative splicing. On the surface of erythrocytes, AChE is present as a dimer anchored to GPI (glycophosphatidylinositol), while in the CNS it is present as a tetramer that is either anchored to PRiMA (proline-rich membrane anchor) at the synapses or to ColQ (AChE-associated collagen) at the neuromuscular junctions.[54, 61]

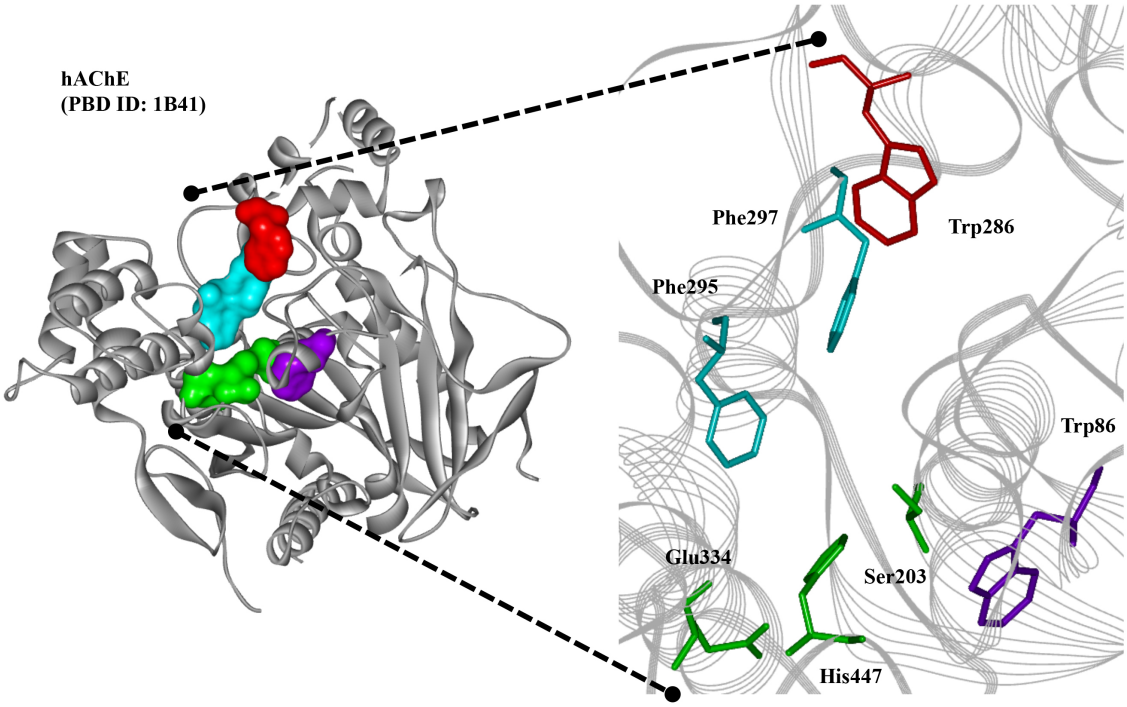


Figure 4: Active site outline of hAChE (1B41) showcasing the catalytic triad (green), acyl pocket (turquoise), anionic pocket (purple) and peripheral anionic site (PAS, red). Hydrogen atoms were removed to enhance clarity.

With respect to the core of this ChE, its active site is located at the bottom of a 20Å gorge that is lined with aromatic residues (tryptophan and tyrosine) at the entry site creating a bottleneck-like conformation that is believed to contribute to AChE's specificity. The active site's catalytic triad (green residues in Figure 4) work in tandem to hydrolyze ACh once bound and stabilized by the anionic pocket (primarily

composed of W86, purple). The phenylalanine residues of the acyl pocket (F295 and F297, turquoise residues) are essential for stabilizing the tetrahedral intermediate formed as a result of the nucleophilic attack on the ACh ester carbonyl. The discovery of a secondary "back-door" channel was believed to aid in the displacement of water molecules, which are crucial for hydrolyzing the acetylated serine residue and further attest to the astonishing ACh hydrolysis rates observed.[54, 57, 58, 62-66]

Another noteworthy mention regarding AChE is what is typically referred to as a peripheral anionic site (PAS) that is comprised of a number of tryptophan and tyrosine resides (more importantly W286, red residue).[62, 67, 68] The PAS, part of the active site gorge entry, has been well documented to act as a seeding facilitator for Aβ-peptides to form higher-order aggregates and highly toxic AChE-Aβ complexes.[69, 70] The elevated toxicity from these complexes is a result of their close proximity to many post- and pre-synaptic membrane proteins by virtue of the anchorage of the synaptic AChE isoform via PRiMA. Those findings gated the focus of ChE inhibitor development toward drug candidates featuring PAS-binding moieties – these candidates, which greatly focused on tacrine-based hybrids, were generally referred to as bivalent inhibitors (Figure 5).[71-79]

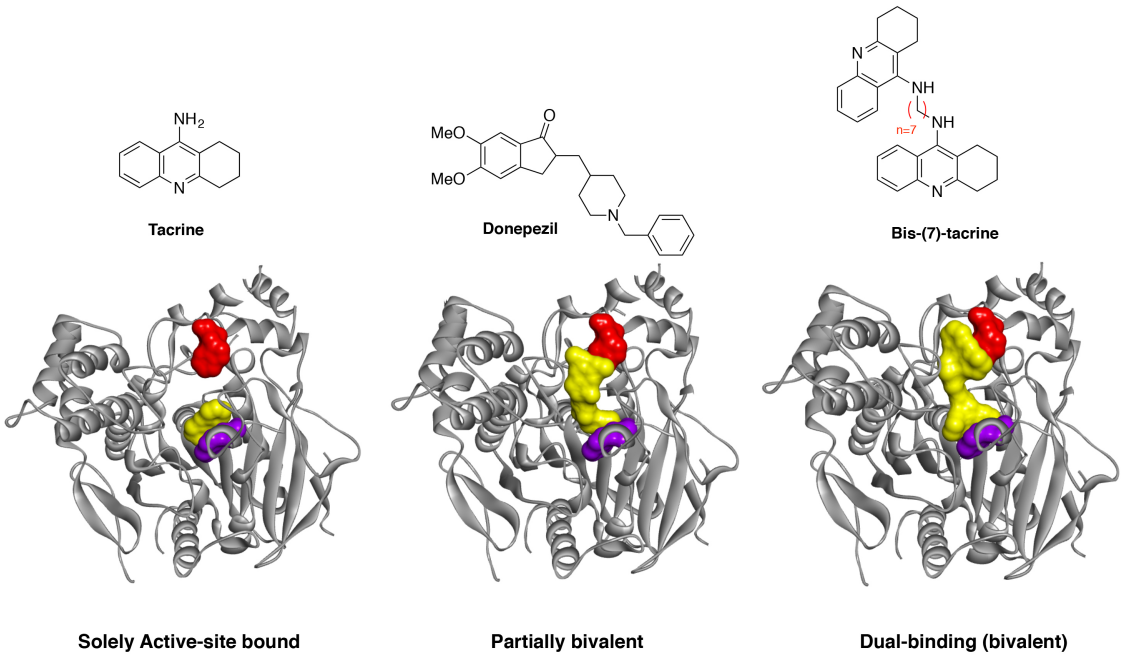


Figure 5: Comparison of active-site bound vs. dual-binding/bivalent inhibitors (yellow) of hAChE (PBD ID: 1B41). Hydrogen atoms were removed to enhance clarity. The PAS highlighted with Trp286 (red) and the active site highlighted with Trp86 (purple).

The downside of this approach is that to achieve bivalent binding, while maintaining strong inhibition at the catalytic triad, meant that these hybrid candidates were large in size and very hydrophobic in nature, which explains why no such hybrid/bivalent candidates ever made it through preclinical studies.

1.2.2.2. *Butyrylcholinesterase (BuChE)*

Unlike AChE, this pseudocholinesterase (secondary ChE) is typically not the primary target within the general cholinergic dysfunction hypothesis. That being said, it is still capable of hydrolyzing ACh and it does hold a relatively important ranking with respect to later stages of AD progression.

A single gene located on chromosome 3 encodes for this pseudocholinesterase and, just like AChE, alternative splicing yields various forms. With its wider distribution throughout the body – present in plasma, liver and the CNS – and more substrate capacity, BuChE has been suggested to play more of a general hydrolase with some detoxifying roles like the hydrolysis of cocaine and scopolamine. In plasma, BuChE is presented as a soluble tetramer while a combination of both soluble dimers/tetramers can be found in association with glial and neuronal cells.[54, 80]

The overall architecture of BuChE resembles many aspects found in AChE; however, a number of key differences do exist. Although the enzyme's catalytic triad is also 20 Å below the enzyme surface, the entry to that gorge is far less restrictive as the degree of aromatic residues in that region is far less than what is found in AChE. While the anionic pocket also contains a tryptophan residue (W82, purple, Figure 6), the acyl pocket region consists of non-aromatic residues (L286-V288) that account for BuChE's wider substrate pool. With a less hindered gorge entry and acyl domain, the overall volume capacity of BuChE is approximately 200$Å^3$ larger compared with AChE. Although BuChE is lacking a PAS at its gorge entry, some studies suggested its association with neurotoxic aggregates as part of an inflammatory response, although the underlying details are not known.[58, 59, 62, 81, 82]

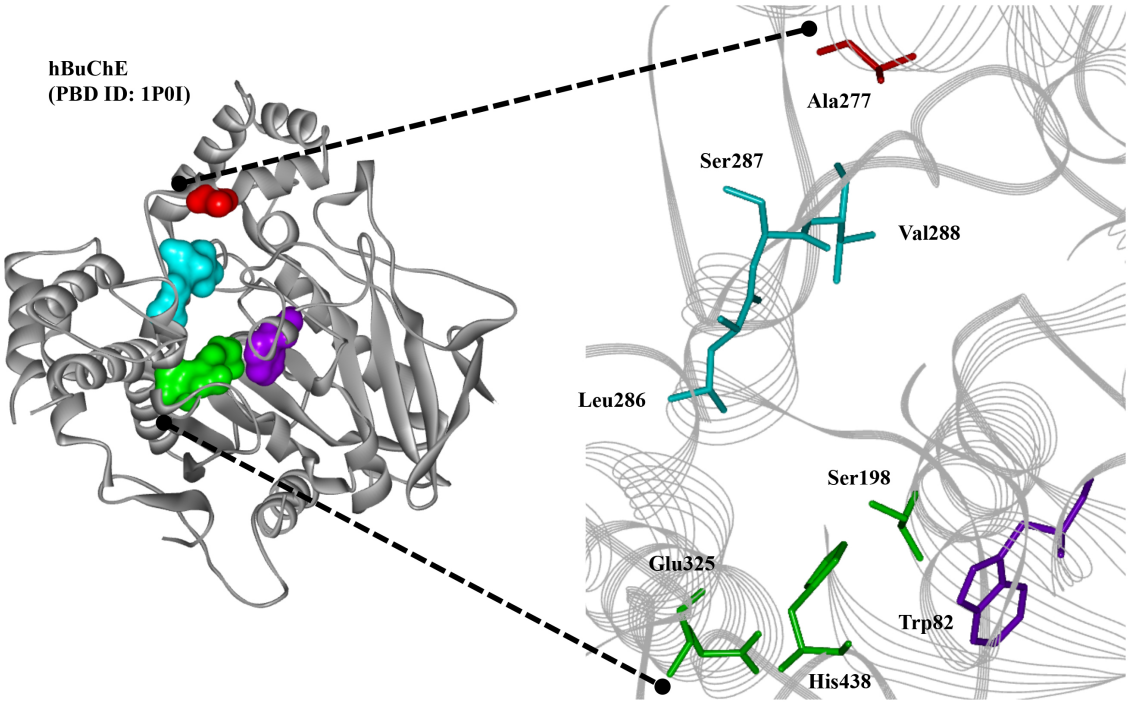


Figure 6: Active site outline of hBuChE (1P0I) showcasing the catalytic triad (green), acyl pocket (turquoise), anionic pocket (purple) and entry site (red). Hydrogen atoms were removed to enhance clarity.

Under typical circumstances, AChE is the principle ACh-degrading enzyme. However, as the neuronal cholinergic mass shrinks with AD progression, the abundance of AChE declines and that is when BuChE's presence in the CNS sparks to take-on ACh metabolism. This increase in BuChE levels may not necessarily be an up regulation of its expression but merely a result of an inflammatory response as CNS-derived BuChE is typically associated with glial cells. That shift in the ChE ratio with disease progression constitutes the mandate of developing dual ChEIs in an effort to better manage patient symptoms at various stages of AD.[83, 84]

1.2.3. *Hypothesis Summary*

The cholinergic dysfunction hypothesis is one of the oldest ever put forth to describe the pathology of AD. All factors considered, however, this hypothesis merely outlines the cause of dementia symptoms but not necessarily the roots of disease initiation. Other pathological routes are compromising the integrity of

the cholinergic branch thus shrinking the neuronal mass occurs, which disrupts the neuronal framework, reduces ACh-producing neurons and collectively, yields the dementia outcomes observed, amongst other symptoms.

That said, the ChEs are still considered valuable targets for developing the next generation of anti-dementia medications but more so, should be part of any well-rounded multi-targeting research platform as they are implicated in other hypotheses of the AD pathogenesis tree (Figure 7).

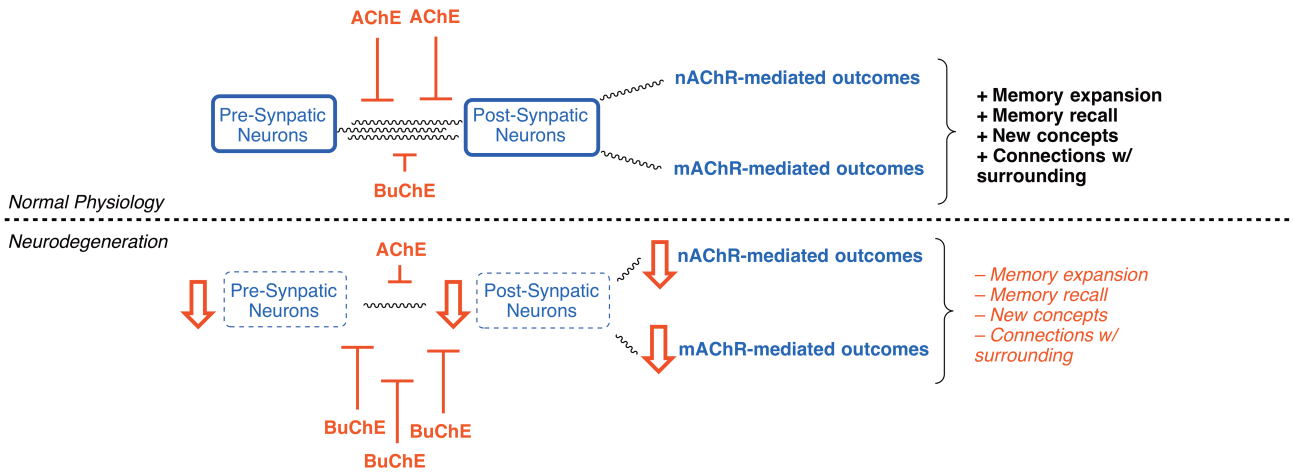


Figure 7: Summary of cholinergic dysfunction in AD progression.

1.3. The Amyloid-β (Aβ) Hypothesis

If the cholinergic dysfunction hypothesis were to be portrayed as a DeLorean DMC-12, then the Aβ-hypothesis could be depicted as the Camaro contrast – the DeLorean was a star in its prime but now, it's more of a figurative/collectable icon, and while the Camaro had its followers and fan club back then, it went off-grid for a while but recently made a stunning return and re-gained the attention of old and new fans.

What truly primes the Aβ-hypothesis is its intricate manifestation and interplay within the AD pathogenesis hierarchy. Unlike the cholinergic dysfunction hypothesis, Aβ-specific pathology has the potential, on some level, of mitigating the upstream consequences leading to neuronal cell death. The

hypothesis itself is centered on the 40–42 amino acid-long amyloid- β (Aβ) peptide, its generation, function, metabolism and off-course neurotoxic potentials, but before the main event, let's highlight the origin story.

1.3.1. *Amyloid Precursor Protein (APP)*

As the name suggests, the amyloid precursor protein (APP) is the parent peptide from which Aβ is released, under a specific metabolic sequence discussed in the proceeding section. The highly-conserved gene encoding for APP is located on chromosome 21 and, with various splicing arrangements, the translated peptide can vary largely from ~ 365–770 amino acids in length with three particular isoforms (APP_{695}, APP_{751} and APP_{770}) holding stronger interests in neuronal synapses.[29, 85, 86] A noteworthy mention regarding those three isoforms, both APP_{751} and APP_{770} contain a KPI (Kunitz Protease Inhibitor) domain, while APP_{695} (the most predominant form expressed in neurons) lacks said domain.[85, 86] While the primary role of APP is not fully understood, a number of key roles like cell adhesion, neurite growth and iron transport, to name a few, have been proposed.[29, 87, 88]

The APP, as shown in Figure 8, has a larger extracellular (N-terminal) domain as compared to its intracellular (C-terminal) domain. The N-terminal domain is comprised of the E1, containing a conserved metal binding motif and a growth factor-like domain, and E2 domains. The KPI domain, again only found in the larger APP isoforms, divides the E1 and E2 domains and two key glycosylation sites are located downstream of the E2 domain. With respect to the amyloid-β placement within APP, a larger component of its sequence exists extracellularly with ~ 30% of the sequence being embedded within the transmembrane domain.[16, 17, 86, 89-92]

Mutations within the APP gene, specifically those surrounding the amyloid sequence domain, can promote or exacerbate the development of AD by increasing the overall production of Aβ-peptides. The well characterized Swedish, Flemish, Dutch, Florida and London APP mutations (Figure 8) do in fact alter APP processing pathways in AD-favourable mechanisms. On the other hand, a rare mutation identified

within Icelandic communities has been shown to steer APP metabolism away from pathological Aβ-peptide production.[93, 94] These mutations don't include other factors such as Down's syndrome (trisomy 21) and Presenilin-1 and -2 (PS1, PS2) mutations that are also linked to disrupting the APP processing balance.[16, 89, 90]

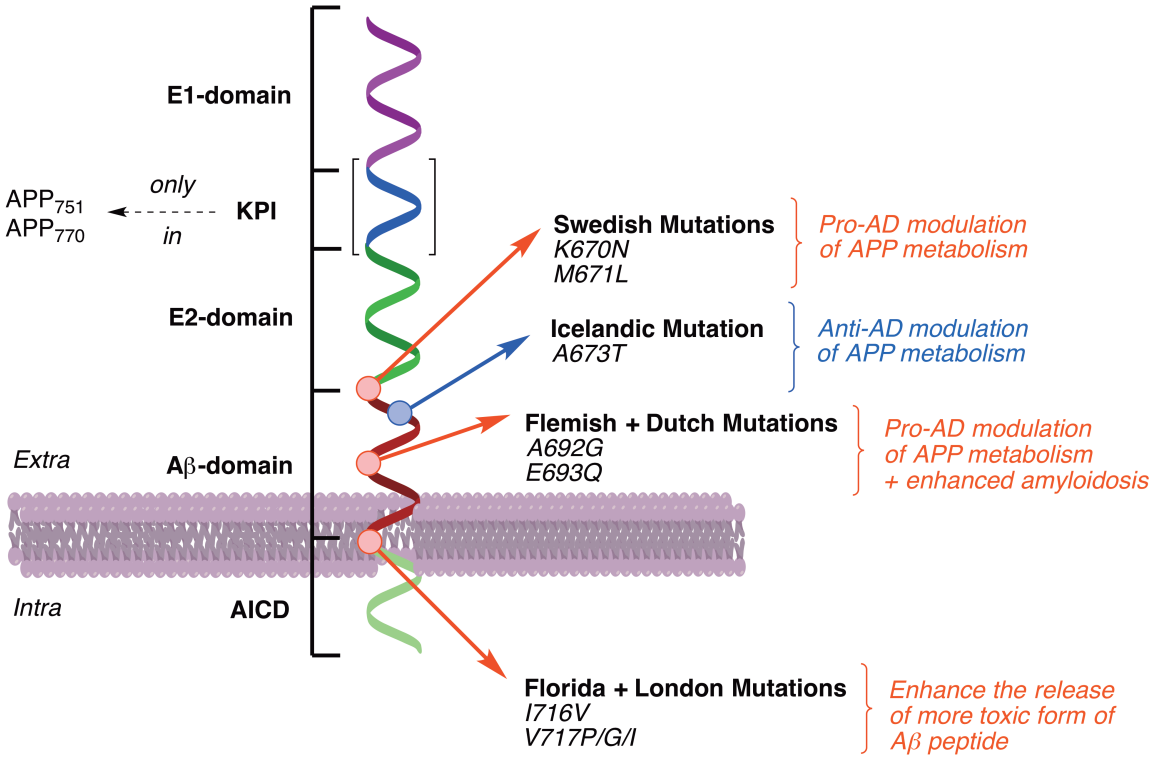


Figure 8: Schematic of APP structure and currently identified mutations that enhance or hinder AD pathology via the amyloid-β hypothesis. Numbering is based on APP_{770} isoform. *Not drawn to scale.

1.3.2. *APP Metabolism and Processing Pathways*

As with countless biological system synergies, when harmony and homeostasis are disturbed, undesirable consequences arise in multifaceted manners. The affiliation of APP with the amyloid-β hypothesis is not a direct correlation per se but more of a disruption in the metabolism of APP that result in a shift toward AD pathogenesis.

In a general context, one of two primary secretase enzymes dictate the fate of APP metabolism, while a third is simply solicited to "finish the job" or in other words, is influenced by the actions of upstream secretases. The alpha-gamma duo (α-secretase and γ-secretase) constitutes the non-amyloidogenic, non-pathological metabolic stream, while the beta-gamma duo (β-secretase and γ-secretase) elicits amyloidogenic (Aβ-release) metabolic outcomes (Figure 9).[90, 95, 96] If things were simply presented as above, then the solution becomes quite straightforward – disable the beta-gamma duo, or just β-secretase for that matter and no Aβ is formed, right?

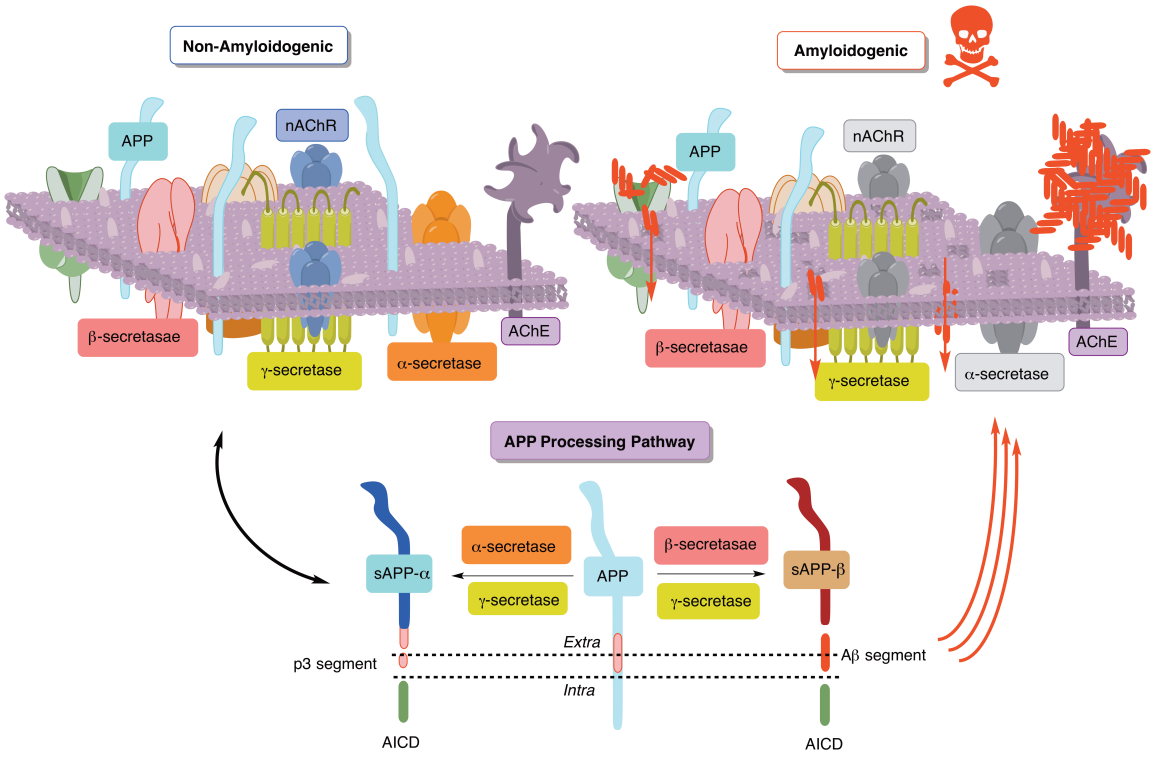


Figure 9: Schematic of APP metabolism via the non-amyloidogenic route (left) or the amyloidogenic route (right). *Not drawn to scale.

Unfortunately, it is not quite as simple as it may appear. While APP is strongly predicted to engage in a number of neuronal functions, it is under a constitutive secretory pathway due to its short half-life and ongoing secretase-based metabolism.[86] Of its two metabolic fates, the non-amyloidogenic processing route

(via α- and γ-secretase) is the most dominant form under typical circumstances. That process, initiated by α-secretase, cleaves APP near the surface of the membrane (between K687 and L688 – APP_{770} numbering) generating a large soluble peptide ($sAPP_{\alpha}$) and an 83-amino acid C-terminal fragment (CTF_{83}), while disrupting Aβ-fragment sequence.[97-99] The resulting CTF_{83} is processed by γ-secretase releasing the APP intracellular C-terminal domain (AICD) and a small 3kD peptide (p3) (Figure 9).[17, 86, 89, 90] On the other hand, the amyloidogenic metabolism of APP, via of β- and γ-secretase, is of greater interest with respect to AD pathology as the full $A\beta_{1\text{-}40\ /42}$ peptide is liberated with significant potential of inducing neurotoxic outcomes. The β-site APP cleaving enzyme (BACE or β-secretase) severs APP further upstream compared to the α-secretase cleavage site. The bond cleavage between M671 and D672 (APP_{770} numbering) generates a large soluble peptide ($sAPP_{\beta}$) and a 99-amino acid C-terminal fragment (CTF_{99}). At this point, the full Aβ-fragment sequence is still within the CTF_{99} fragment and it's the action of γ-secretase (between A713/W714 or V711/I712) that releases the AICD with the undisrupted $A\beta_{1\text{-}42}$ or $A\beta_{1\text{-}40}$ peptide, respectively (Figure 9).[17, 100-103]

Putting aside the consequences of Aβ-peptide alone for now, let's briefly examine the outcomes related to the other metabolites of APP. For starters, the $sAPP_{\alpha}$ fragment from the non-amyloidogenic pathway has been reported to enact neuroprotective benefits (via some regulatory roles with kinases like CDK5 and GSK-3β),[85, 104, 105] modulate/restrict the activity of β-secretase[106] and support neuronal plasticity.[95, 98, 107, 108] The role of the truncated Aβ-peptide (p3, released from CTF_{83}), however, is a bit of mystery. While it does not aggregate in an Aβ-type fashion, some studies have shown that p3 is capable of forming deposits/lesions, inducing apoptosis and inflammatory cytokines,[95, 109] while others, acknowledging those roles, also suggesting some potential modulation of the full length Aβ-peptide itself via p3.[110] With respect to the $sAPP_{\beta}$ fragment from the amyloidogenic pathway, it is surprisingly not as well characterized or studied as its alpha-relative. It may possess some level of a neurotrophic factor but it is far-less active compared to $sAPP_{\alpha}$;[95] however, other reports showcase it as not being a neuroprotective entity at all.[85] Lastly, the AICD (a highly conserved APP domain and a shared proteolytic product of both APP metabolic pathways) is believed to act as a transcriptional regulator as it is transported to the nucleus after $CTF_{83/99}$ processing via γ-secretase.[111] A number of studies have implicated the AICD with pro-apoptotic mechanisms, activation of GSK-3β transcription, other pro-AD pathologies[111-114] but also some anti-Aβ

activities,[115] which points to a knowledge gap regarding the full discourse of APP metabolism. The AICD also contains a key threonine residue (T668) that is susceptible to phosphorylation. The phosphorylation state of this residue also plays an important role in APP localization and its ability to interact with different adaptor proteins. As such, it is not surprising to observe high levels of phosphorylated T668-APP in AD patients compared to healthy/control groups suggesting a role for this residue in AD pathology.[86, 114]

As it looks, the APP has a lot more going on besides simply carrying the Aβ–fragment and there is a lot more to be discovered about its regulation, its function as a whole and the function of its metabolites.

1.3.3. *The Aβ Peptide: Structure, Function and Clearance*

Now that the origins of the Aβ-peptide have been described, it's time to hone in on the primary target that defines and captivates the amyloid-β hypothesis.

The final processing of CTF_{99} by γ-secretase can release Aβ-fragments ranging from 34 to 43 amino acids long, with the $Aβ_{40}$ being the more commonly liberated product and $Aβ_{42}$ being the most toxic form.[116] The native peptide, despite its size, contains a number of important domains that implicate it in AD pathology.

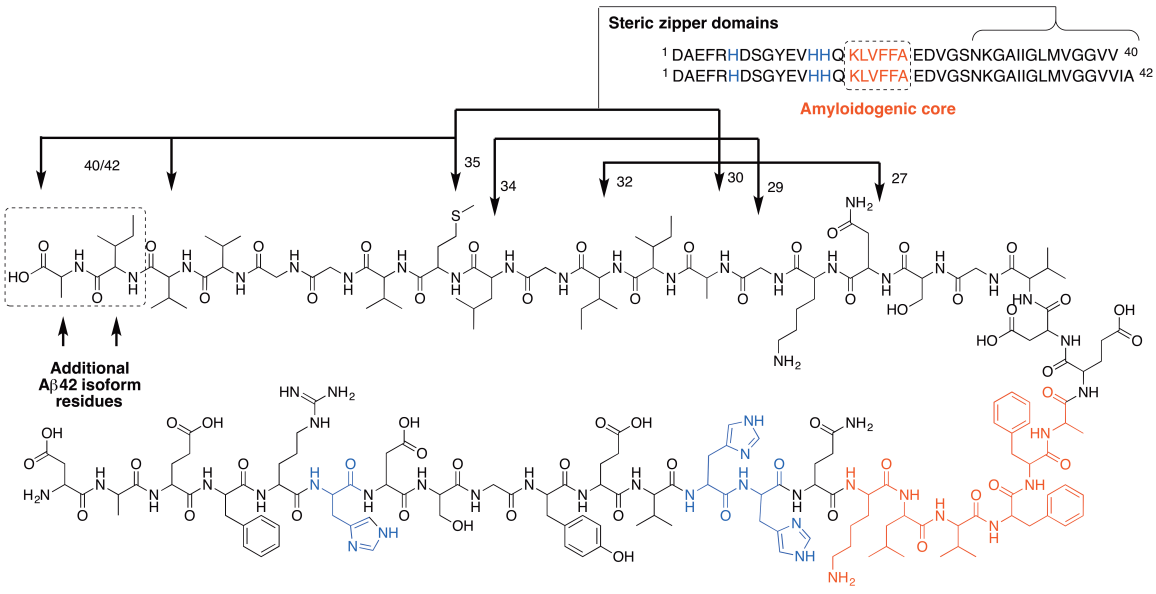


Figure 10: Amyloid-β sequence showcasing the metal-binding domain and amyloidogenic cores.

The metal-binding domain, consisting of three histidine residues (H6, H13 and H14; marked in blue in Figure 10), is known to coordinate with copper and iron metals – an interaction that is documented as a key contributor to the increase in the redox chemistry within the brain that generates ROS.[117-120] Besides the metal-binding domain, the Aβ-peptide contains a number of hydrophobic domains that naturally drive its aggregation propensity. The KLVFFA domain, shown in red in Figure 10, is one of the most studied domains on the Aβ-sequence as it is the driver of oligomer formation – the early stages of aggregation that produce the most toxic form of Aβ.[121, 122] Downstream of the KLVFFA region, closer to the C-terminal end, exists a larger stretch of hydrophobic domains (Figure 10) that are implicated in the higher-order aggregates of Aβ that facilitate the maturation of oligomers to protofibrils.[123, 124]

It's noteworthy that the Aβ-peptide itself, as a stand-alone monomer, is not toxic. In fact, non-AD patients produce Aβ on a regular basis, especially considering that the amyloidogenic APP pathway is active in non-AD patients as well. Under typical physiological conditions (and with proper regulatory control), Aβ-peptide concentrations hover around the picomolar (pM) scale with rate of clearance roughly at 1.1-fold higher than the rate of generation.[125, 126] At that concentration, the monomeric peptide serves a number of physiological functions, supported by neuronal culturing work, including neuronal support/ growth and ties to glucose metabolism.[127-129]

A big piece of the puzzle here has to deal with post-production handling and clearance of Aβ-peptides. Upon its release, is either engaged in one of its physiological functions, targeted by a variety of peptidases for degradation or trafficked outside of the brain's extracellular space. With respect to enzymatic degradation, neprilysin and insulin-degrading enzyme (both being zinc-binding proteases) are some of the more commonly affiliated peptidases. Transport of soluble Aβ-peptides out of the interstitial fluid can occur by bulk flow or by receptor-mediated efflux across the blood-brain barrier (BBB) into the bloodstream. The former, is a very slow process that accounts for 10-15%, while receptor-mediated efflux can occur via lipoprotein receptor-related protein (LRP) or ATP-binding cassette transporter p-glycoprotein (p-gp).[130-132]

Under normal conditions and circumstances, the Aβ-peptide is being produced at physiologically relevant rates and concentrations and is either cleared via peptidase- or microglial-degradation or removed out of the extracellular space, across the BBB, to the bloodstream. As mentioned earlier, the amyloid

hypothesis is based on the disruption in the management of Aβ-peptide production and post-production handling. A complex cascade of biochemical events occurs where the ratio of Aβ-peptide production to its clearance is hindered, resulting in a growing population of Aβ monomeric species. It is noteworthy that most amyloid-degrading enzymes (ADEs) were reported to have decreased levels of activity/expression in aging and AD brains, while the efflux mechanisms become greatly compromised with the increased Aβ-peptide load. The situation gets worse with the presence of receptor for advanced glycation end products (RAGE) as it works against efflux mechanisms by funneling Aβ from the blood stream into the brain's extracellular space.[131, 132] It is that offset in regulatory balance that alters Aβ-peptide structure and behavior charting a path toward neurotoxic outcomes and engaging in positive feedback loops that propagate disease progression and downstream pathogenesis (Figure 11).

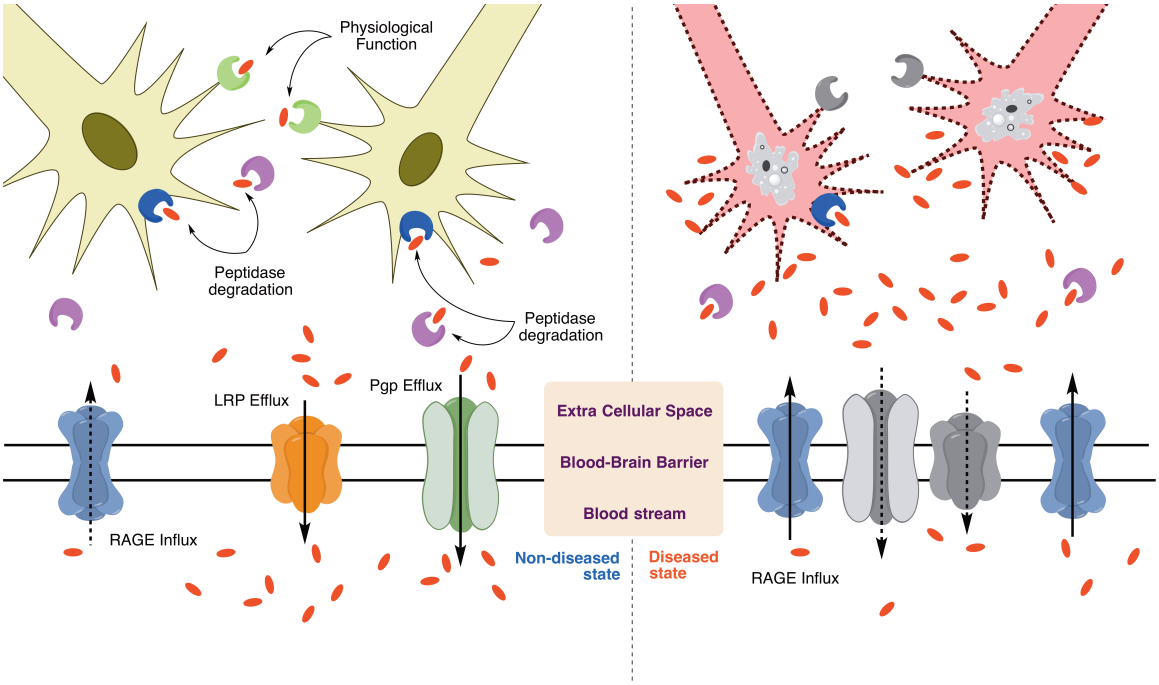


Figure 11: Reduction of amyloid-β degradation (via peptidase activity) and clearance mechanisms (via efflux receptors) propagating AD pathogenesis by increasing the amyloid-β load in the extracellular space. *Not drawn to scale.

1.3.4. *Aβ Aggregation and Toxicity Mechanisms*

It is not quite clear whether an event upstream of Aβ production sparks the imbalance between production and clearance pathways resulting in higher Aβ concentrations in the brain or if it is Aβ alone that disrupts that delicate balance, in a positive feedback manner, to propagate itself. A large part of the uncertainty here (and elsewhere along the pathology tree) has to do with the complex feedback mechanisms that regulate every aspect of this hypothesis, from APP to APP metabolites including Aβ itself and the downstream pathways.

Nonetheless, by glancing at the right-hand side of Figure 11, it is evident that the degradation and clearance mechanisms are crumbling and the concentration of Aβ has exceeded the physiological picomolar range. While concentration has a key role to play in the aggregation pathway, it is not a stand-alone contributor. The native Aβ-peptide takes on a helix-kink-helix arrangement that is initiated and maintained by the activity of molecular chaperons (e.g. heat-shock protein 70 – Hsp70). The regulatory activities of molecular chaperones, along with that of the ubiquitin-proteasome system, are crucial to ensuring an aggregate-free environment. Unfortunately, both of these mechanisms face the same fate as the ADEs and efflux receptors, which quintessentially generate the "perfect storm" of AD amyloidosis that starts with the misfolding of the native Aβ-peptide (Figure 12).[133-136]

At this point, the misfolded Aβ monomer, while non-toxic, has a very high propensity of self-association (self-induced aggregation) and that is when the floodgates of neurotoxicity are open. Recall that PAS pocket in AChE (Section 1.2.2.1) – It is a strong primer for misfolded Aβ monomer self-association as it provides a seeding location for the aggregation process. While self-induced and PAS-induced aggregation toward higher-order structures follow similar mechanisms, the Aβ monomer can also undergo a metal-ion induced misfolding arrangement, as seen in Figure 12, that is as problematic as the other conformations. Misfolded Aβ-peptides maintain their random coil structures by undergoing a number of hydrophobic, salt-bridge and coordinating (metal-ion arrangements only) interactions that stabilize the conformation and facilitate the downstream aggregation and toxicity pathways.[38, 39, 118] It is not a surprise to see the susceptibility of Aβ-peptide to metal-induced misfolding, considering it has a metal-binding domain (Figure 10). Under disease-conditions, the unfolded monomer utilizes its tri-histidine-based metal-binding

domain, along with the D1 residue, to coordinate with free copper, iron or zinc metals (Figure 12) and that plays a crucial role in stabilizing that complex.[119, 120, 137] On the other hand, non metal-ion based Aβ random coils are stabilized by a salt-bridge formed between D23 and K28 and a number of hydrophobic and stacking interactions between the 16-KLVFF-20 region and the C-terminal region (32-IGLMVGGVVIA-42) of the peptide.[138]

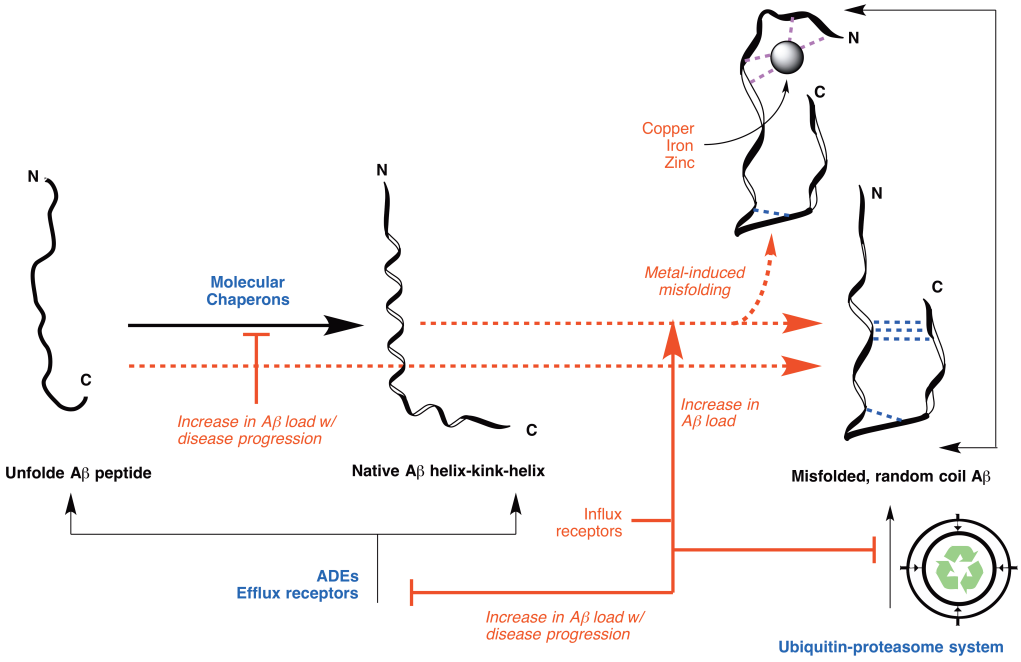


Figure 12: Schematic of progressive decline in the management of amyloid-β structural conformation from the stable helix-kink-helix arrangement to the misfolded random coil, with or without the influence of metal-ions. The blue-dotted lines represent the essential salt bridges and hydrophobic interactions that stabilize the random coil, while the purple dotted lines represent those coordinated with the metal-ion. *Not drawn to scale.

The path from a single misfolded monomer to higher-order aggregates can undoubtedly be described as an intricate dance of biochemical and biophysical interplay. There are a number of critical aggregate forms pertaining to the Aβ hierarchy, each with unique structural features and varying neurotoxicity impacts. One of the initial steps to furthering the aggregation pathway is the collapse of the stabilizing interactions within the misfolded monomer in favour of the dimeric stabilizing interactions.[139] This turnover switch occurs with both metal-bound and metal-free Aβ monomers (as shown in Figure 13) and is essentially, the first amyloidogenic structure in this process, which has been reported to be energetically

favourable compared to the native form.[119, 120, 137, 140, 141] This dimeric structure is considered the smallest seeding point in the pathway, which makes way for other misfolded monomers to join in and the evolution of the small molecular weight oligomers arise. This is, typically, where the metal-bound and metal-free aggregation path similarities end as the presence of metal-ions (like copper, iron and zinc) prevents the formation of downstream aggregate forms and the population is left as a large complex of size-variable oligomers (Figure 13). These Aβ-metal complexes contribute to the pro-inflammatory and pro-toxicity pathways in AD via redox chemistry and the increase in ROS generation.[38, 118, 120, 142, 143]

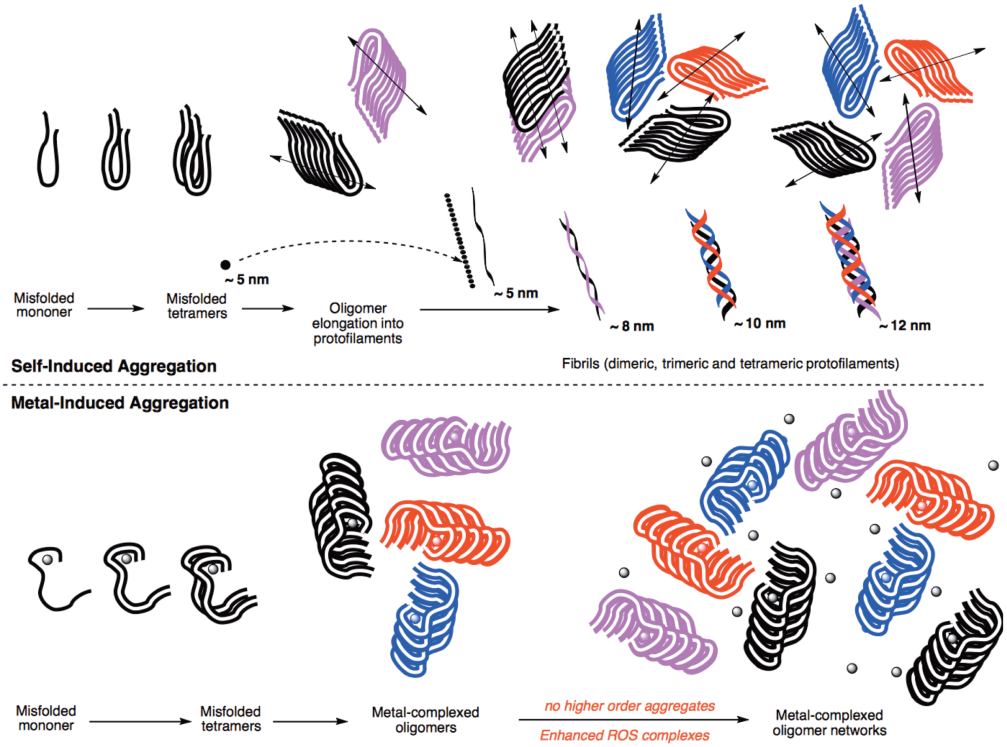


Figure 13: Schematic of the downstream aggregation pathways of misfolded amyloid-β. Both aggregation pathways lead to plaque deposits but with different morphologies and pathological characteristics. *Not drawn to scale.

Metal-free oligomers, on the other hand, continue to grow and elongate to form protofilaments. These structures can be pictured of as a growing stack of unidirectional horseshoes that average about 4-5 nm in thickness and are rich in parallel β-sheet formation.[144, 145] As the population of protofilaments increases, the

structures can propagate to form antiparallel β-sheet dimeric, trimeric, tetrameric, pentameric and oligomeric forms (as pictured in Figure 13). While protofilaments can be seen as relatively short and straight structures under transmission electron microscopy (TEM), higher-order aggregates display intriguing twist-form morphology, resulting in banding patterns observed under microscopy, (Figure 14) with a hollow-core ranging from ~ 1–5 nm internal diameter.[146-150]

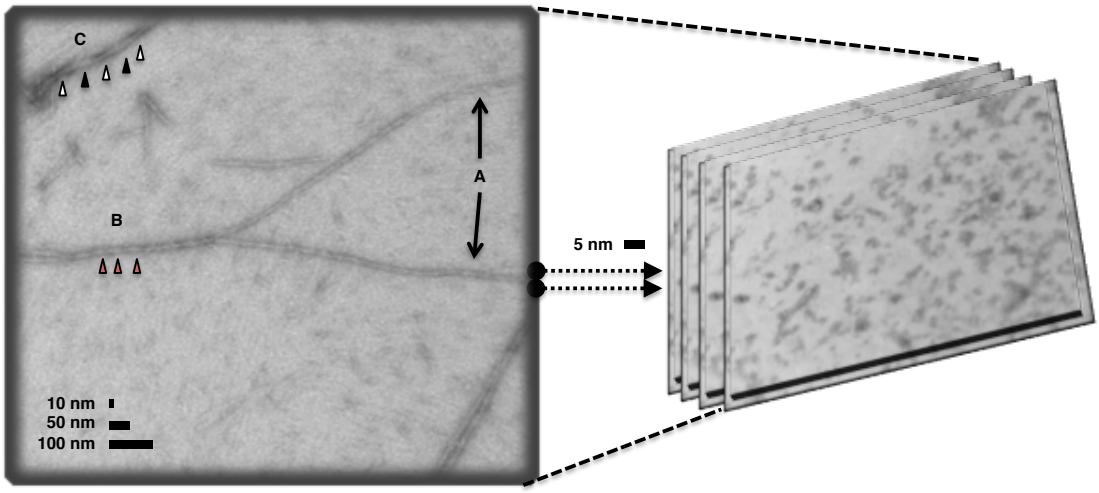


Figure 14: Transmission electron micrograph of an amyloidogenic peptide (closely related to amyloid-β) displaying the transformation of two protofilaments (A) into a dimeric-isoform (B) with the red triangles pointing to the banding pattern. The tetrameric form (C) is showcasing thicker banding indicated by the alternating white/black triangles. The morphological assessment during early-stage aggregation showcases the ~ 4–5 nm wide oligomeric structures represented above as "cross-sections" of protofilament (A).

As mentioned earlier, the various aggregate isoforms elicit a wide range of neurotoxic mechanisms, although it has been well documented that the oligomeric forms of Aβ, such as the amyloid-derived diffusible ligands (ADDLs), are the most toxic.[151-155] Besides acting as seed points for higher-order aggregates, these oligomers have been shown to disrupt cell membrane integrity via pore formation, interfere with ion channels and other membrane-bound receptors, enhance ROS generation, impact downstream regulation of gene expression, impede mitochondrial function, induce a positive feedback loop back to amyloidogenic APP metabolic regulation and more. On the other hand, higher-order aggregates are still problematic as the resulting amyloid plaques disrupt signal transduction and contribute to the

inflammatory responses, although their direct neurotoxicity impact is lower compared to oligomers and ADDLs.[27, 110, 126, 156-169]

1.3.5. *Aβ Targeting Strategies*

While the intricate layers centered on the amyloid cascade are still being peeled, what is currently known offers a diverse platform of intervening potentials for drug discovery and therapeutic developments. The common factor with these upstream or downstream interventions is the Aβ-peptide itself.

1.3.5.1. *Upstream of Aβ Production*

Recalling the biological mechanisms leading up to the release of the Aβ-peptide (Section 1.3.2), one can easily identify BACE-1 and/or γ-secretase as primary upstream targets for the management or reduction of Aβ-peptide production. In fact, these targets have taken the therapeutic spotlight for a few years, leading to the development of a number of small-molecule or peptidomimtic clinical candidates.[10, 73, 102, 170-180] While those candidates showcased potential at the pre-clinical, and some even at the early clinical stages, most ended up failing in late-stage clinical studies. While these were devastating outcomes, they painted a clear picture regarding the role of the secretases (especially γ-secretase) that extends beyond APP processing. Selectivity was also a concern, considering that β-secretase has two isoforms (BACE-1/2) and a number of other aspartate proteases, like the cathepsins, that are susceptible to eliciting side effects with inappropriate targeting. That said, BACE-1 and γ-secretase still hold a substantial mainstay and therapeutic interest that pharmaceutical companies are pursuing novel candidates at various stages of R&D and more so, on formulating properly structured clinical trials to assess validity.[181-185] Interestingly, the reinvestment in these targets has been paralleled with a re-boost in Aβ-based research from both academia and pharma as well. This further exemplifies the strong connection between AD pathology and progression with this peptide and cascade as a whole.

What about non-secretase based approaches? It does not come as a surprise that the intertwining complexity of AD signals a number of indirect approaches to the upstream interventions tied to the Aβ-

peptide. For starters, cholinesterase inhibitors have been shown to bi-directionally modulate APP processing.[186, 187] This is both an interesting and crucial find considering that current medication regimens are based primarily on cholinesterase inhibition. This modulation could be a result of some level of direct or indirect agonistic or antagonistic activity on the secretases. Additionally, certain AChR have been shown to steer APP processing toward the non-amyloidogenic pathway, increasing the release of the neuroprotective $sAPP_{\alpha}$.[98, 188] A great example of these interactions can be depicted with galantamine (Reminyl™) – a weak cholinesterase inhibitor with positive modulation of APP processing in addition to its agonistic properties on nAChRs and reported inhibition of Aβ-aggregation.[189, 190]

It is also noteworthy that the Aβ-peptide itself elicits feedback loops on its release (Figure 15) and that is a primer for the large collective effort directed at the downstream interventions discussed below.[29, 95, 110, 158, 191]

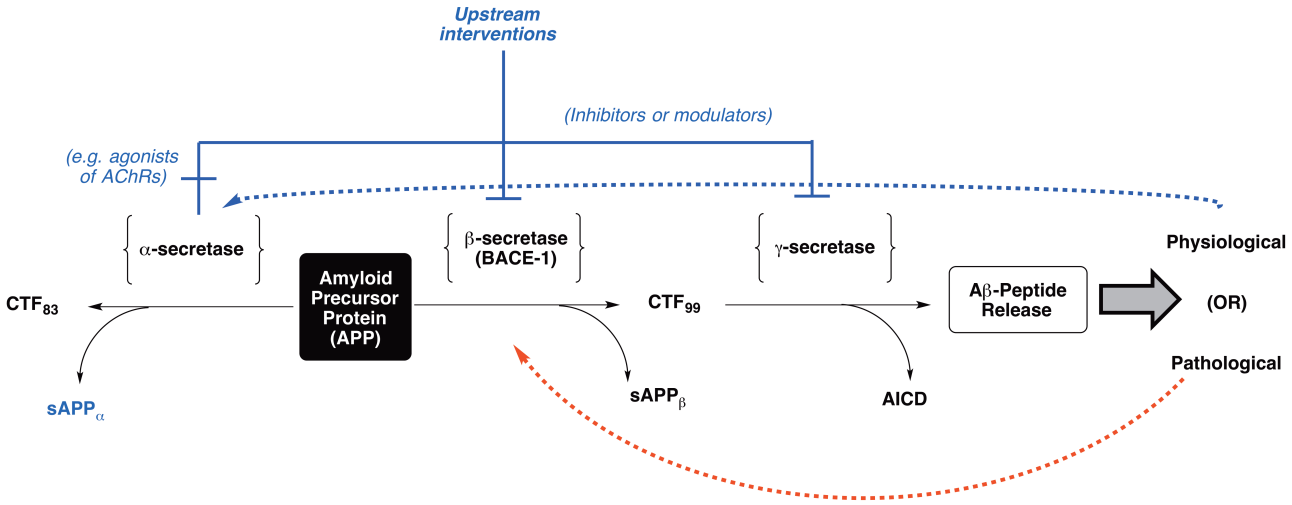


Figure 15: Schematic overview of upstream interventions utilized to modulate amyloid-β production.

1.3.5.2. *Downstream of Aβ Production*

The strategies handling the post-release of the Aβ-peptide outnumber upstream interventions. While discussing each potential strategy is beyond the scope of this thesis, these downstream interventions can

generally be grouped as strategies toward the modulation of Aβ-peptide behavior or the modulation of Aβ-prone targets. The primary focus moving forward with this section will be the modulation of Aβ-peptide behavior as it is a direct and well-studied approach.

Recalling to Section 1.3.4, the case was made to distinguish the toxicity implications along the Aβ-aggregation pathway – If plotted, it would look something like the inlay in Figure 16.[136, 155, 192] As such, it is not a surprise to come across varying opinions on which strategy (pro- or anti-aggregation of Aβ-peptide) is most effective. The reality is, neither is perfect as a stand-alone strategy because in both cases, a saturation limit will be met and the efficacy of treatment, on either end, will diminish.

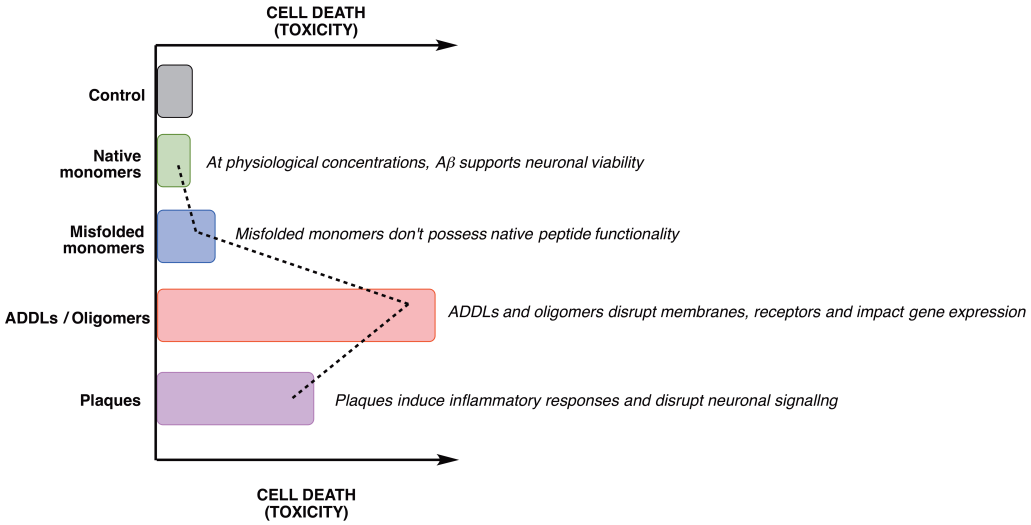


Figure 16: Schematic comparison of the varying toxicity impact (cell death) with progressive amyloid-β aggregation.

The pro-aggregation approach is based on accelerating the aggregation process of the peptide, beyond the oligomer stage, to minimize neuronal exposure to the ADDLs and cell-damaging oligomers.[193, 194] The case for a pro-aggregation strategy plays out like this: a) higher order aggregates and plaques will eventually form because an anti-aggregation treatment is not viable long-term, b) and once formed, plaques are generally localized entities and act as sponges for free-flowing oligomers and c) this strengths the case of using plaque-specific anti-bodies to engage the immune response as a scavenger of these aggregate deposits.[152, 153, 195] The issues against this strategy look like this: a) the success rate of developing a brain-penetrable anti-body are low, b) not to mention that by the time dense plaques have formed, disease

progression is far beyond repair, c) and along with mid- to advanced-stage disease progression, patients are likely to be immune-compromised, and lastly d) by that stage, any trace of Aβ-clearance activity will very likely crumble as a result of the overload. On the other hand, the anti-aggregation approach is based on preventing the oligomerization of the peptide significantly to minimize neuronal exposure to the ADDLs and cell-damaging oligomers but to also reduce plaque load and the associated inflammatory responses.[11, 196-199] The case for an anti-aggregation strategy plays out like this: a) stabilizing the monomer or even the misfolded monomer long enough can reduce the rate of oligomerization, b) and by elongating the lag-phase, cellular responses may be able to clear, correct or digest the misfolded monomers, or c) allow for other non-toxic structures to form reducing the positive-feedback loop elicited by Aβ, ADDLs and oligomeric entities. The issues against this strategy are solely based on challenges tied to the treatment's therapeutic window, half-life and overall long-term viability. In addition to those strategies, a combinational approach has started to flourish in the research community. Some groups have reported aggregation-modifiers as potential therapeutic strategies. The concept there is based on small-molecules that bind to the misfolded monomers and induce a non-typical aggregation scheme that shuttles these misfolded monomers away from neurotoxic pathways.[193, 200, 201] The concern here lies with the fate of these supposedly non-toxic, non-typical aggregates – could they not disrupt other cellular processes downstream? (Figure 17)

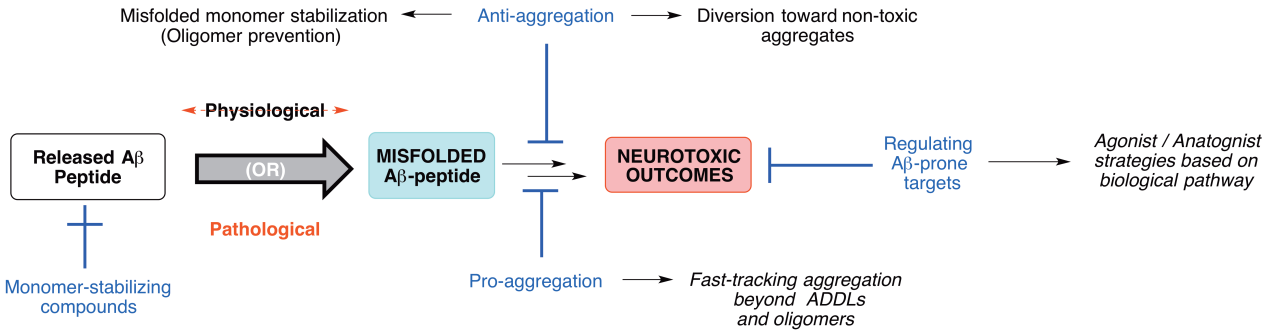


Figure 17: Schematic overview of downstream interventions utilized to modulate amyloid-β behavior and impact.

Collectively, it is quite clear that downstream interventions are not suitable as stand-alone strategies. That said, what is a common feature amongst these downstream strategies, besides the Aβ-peptide itself, is the need for one-on-one interactions between a particular molecule and Aβ. The interesting factor here though, is that these interactions are distinctive on the molecular level – while the end result is more plaques or less plaques, the road to that conclusion is specific. This phenomenon is attributed to the multi-stage aggregation process of Aβ. As showcased in Figure 13, there are multiple "access" points for a given molecule to potentially interact and even similar molecules in a chemical library might behave differently along the aggregation process. Where a molecule that binds early on in the aggregation process could delay or reduce oligomer formation, another that binds favourably at the oligomer/fibril domains could delay or reduce fibril formation.

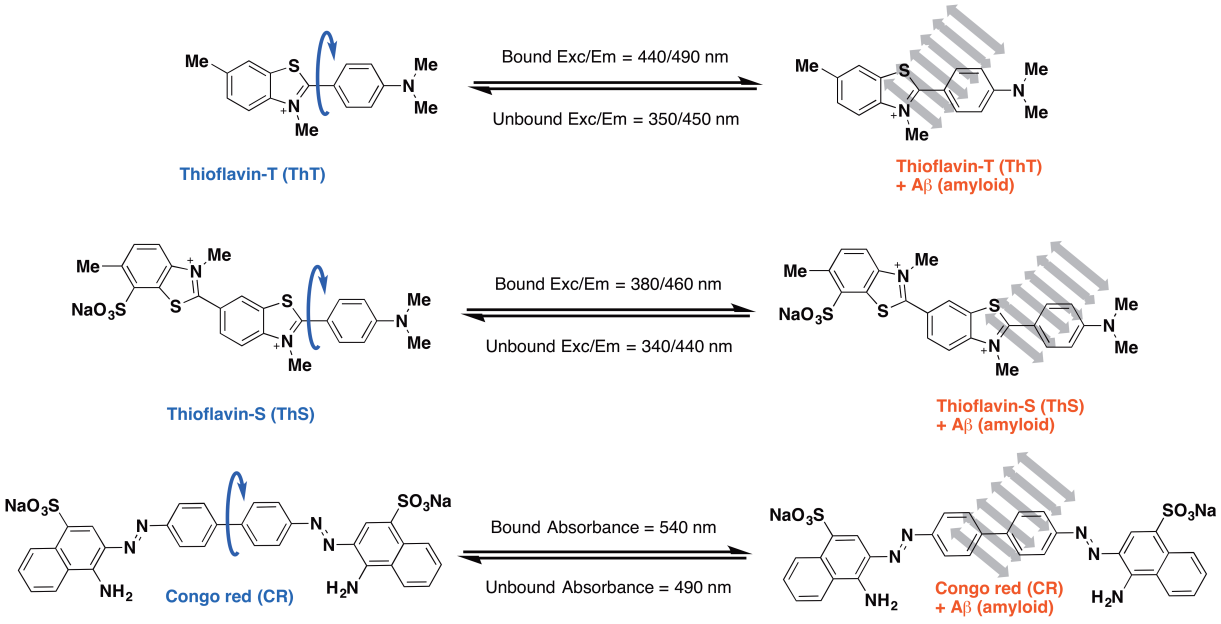


Figure 18: Commonly utilized small-molecule probes/dyes used in studying and tracking of amyloid-β aggregation in in vitro and staining studies. These compounds undergo free-rotation in solution, but once bound to amyloid their rotation capacity is restricted, attributing to their spectral red shifts.

The preferential binding or interactions of molecules with varying forms of Aβ constitute one the largest research areas in this subclass of AD research. The ability of researchers to assess molecular

interactions with Aβ, has led the way of a number of critical findings about AD and other amyloid-based diseases, like Parkinson's disease. One of the simplest and most common approaches to these studies is based on small-molecule probes or dyes, like Thioflavin-T/S (ThT/ThS) and Congo red (CR), which undergo spectrophotometric changes upon binding to amyloidogenic peptides/aggregates (Figure 18).[202-205]

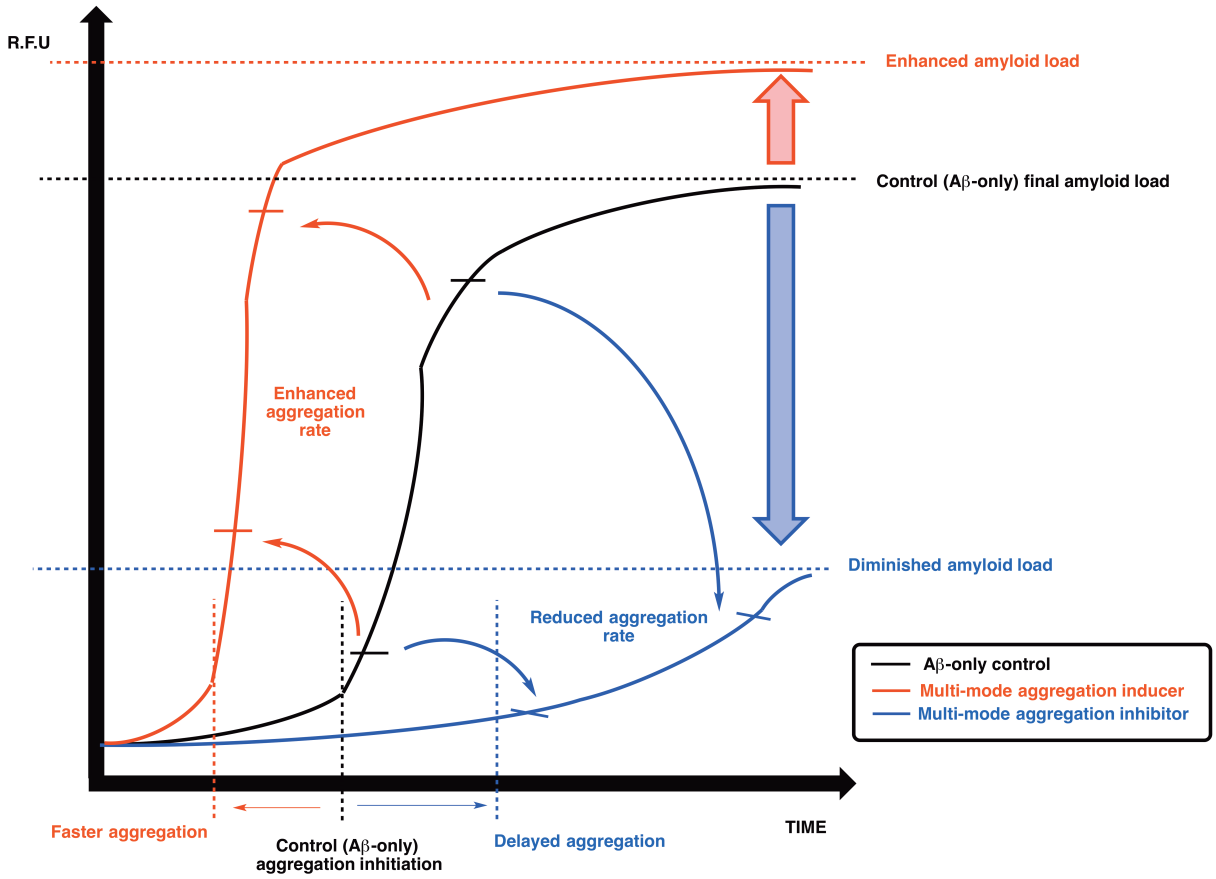


Figure 19: Schematic overview of a typical ThT-monitored kinetic plot of amyloid-β aggregation without (black) or with a multi-mode aggregation inducer (red) or a multi-mode aggregation inhibitor (blue). The lag phase starts at t = 0 and ends at the start of the aggregation slope. The aggregation rate is indicative of how fast oligomers and protofilaments are forming. The saturation phase is the end point where fibrils are the dominant form (usually corroborated by AFM/TEM). R.F.U = Relative Fluorescence Units.

While not perfect (due to specificity concerns), these probes have become essential in in vitro screening efforts to study molecular interactions with Aβ and also for amyloid staining in tissue samples.

While the histological applications are mainly qualitative, the dyes' spectrophotometric red shifts (fluorescence or absorbance based) are used to indirectly quantify the initiation, rate and extent of β-sheet/amyloid formation in solutions, in relation to assay controls. While these aggregation kinetic studies are typically corroborated with secondary experiments, like AFM (atomic force microscopy), TEM or circular dichroism (CD) spectroscopy, they have been favourably exploited to classify the modulation impact of molecular entities on Aβ-aggregation (Figure 19).[206-210]

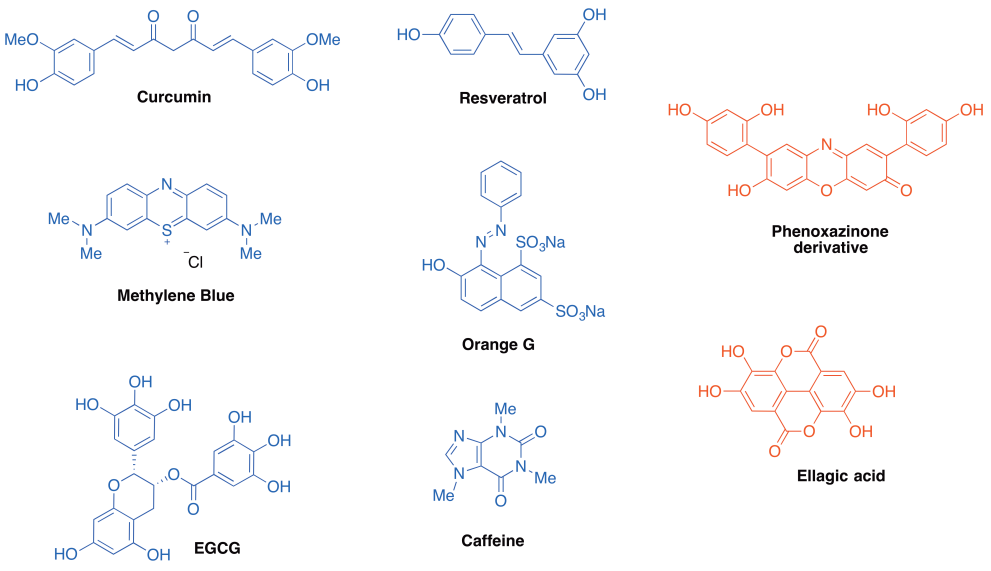


Figure 20: A brief listing of aromatic, conjugated ring systems that modulate amyloid-β aggregation. Blue-coded compounds belong to the anti-aggregatory grouping, while red-coded compounds belong to the pro-aggregatory grouping.

In a practical sense, developing aggregation modulators for the $A\beta_{40}$ isoform is easier when compared to $A\beta_{42}$, considering its slower misfolding and aggregation kinetic rates.[147, 211, 212] These properties offer a larger window of opportunity for chemical candidates to interact with the $A\beta_{40}$ isoform along the aggregation path. That said, it would be inappropriate to assume that any given $A\beta_{42}$ modulator would also impact $A\beta_{40}$ aggregation in a similar fashion. Due to the nature of these peptides, the traditional pharmacophore development approach has not been very successful as there is no defined active site and this exemplifies the diverse interactions that could modulate the aggregation process. A number of Aβ-

modulation platforms are based on naturally-sourced, phenolic compounds such as curcumin (a component of the spice turmeric), resveratrol (a phytoalexin found in grapes and berries), epigallocatechin-3-gallate (EGCG, a catechin-based antioxidant found in tea) and more.[121, 213-222] In addition, synthetic dyes, like orange G and methylene blue, are also used as pharmacological tools in drug discovery due to their anti-aggregation properties (Figure 20).[199, 223]

1.3.6. *Hypothesis Summary*

In contrast to the cholinergic dysfunction hypothesis, the amyloid cascade is not only more intricate, but is also more upstream along the pathological roadmap (Figure 21). This mainstay hypothesis is centered on the production, function, regulation and behavior of a single peptide. The Aβ-peptide, along with its precursor (APP), are physiologically relevant in the maintenance and function of the central nervous system, so complete eradication is not a viable approach. As highlighted earlier, the pathology attributed to Aβ is a consequence of the disruption and collapse of the mechanisms that regulate and maintain its positive, non-pathological outputs. The significance of this hypothesis in modern AD research is that the causation of this regulatory collapse in Aβ checkpoints is not fully comprehensible.

With our current knowledge and understanding of Aβ's upstream and downstream origins and impacts, a thorough and multidimensional approach is needed.[204] A critical aspect to a viable, long-term solution is the advancement of early-detection screening, considering that the manifestation of the amyloid hypothesis is not abrupt – it is a slow and progressive indication. Along with ongoing early-detection, a therapeutic strategy aimed at reducing the rate of Aβ production, while stabilizing the peptide to avoid misfolding-derived neurotoxicity is an asset.

Considering the collective discussion thus far, it would seem that a multi-mode Aβ-aggregation modulator, possessing some cholinesterase activity, is the key to a successful therapeutic strategy.[69, 224, 225] Unfortunately, the AD puzzle is far more complex than that. A critical piece to the proper placement of the various pathological events comes from post-mortem analyses, where AD patients' brains were showcasing large variances in the amount of amyloid plaques. This indicates that while Aβ is a major player in the

pathology of AD, its overall placement along the pathology timeline is more upstream. In addition, the number of toxic implications of ADDLs and oligomers exemplify the sheer destructive power of this cascade, which charters the path to a host of secondary hypothesis and mechanisms that further drive disease progression.[162, 167] As such, the critical aspect becomes the balance between amyloidogenic and non-amyloidogenic metabolism as it is directly related to the delicate balance between production and clearance of amyloid-β.

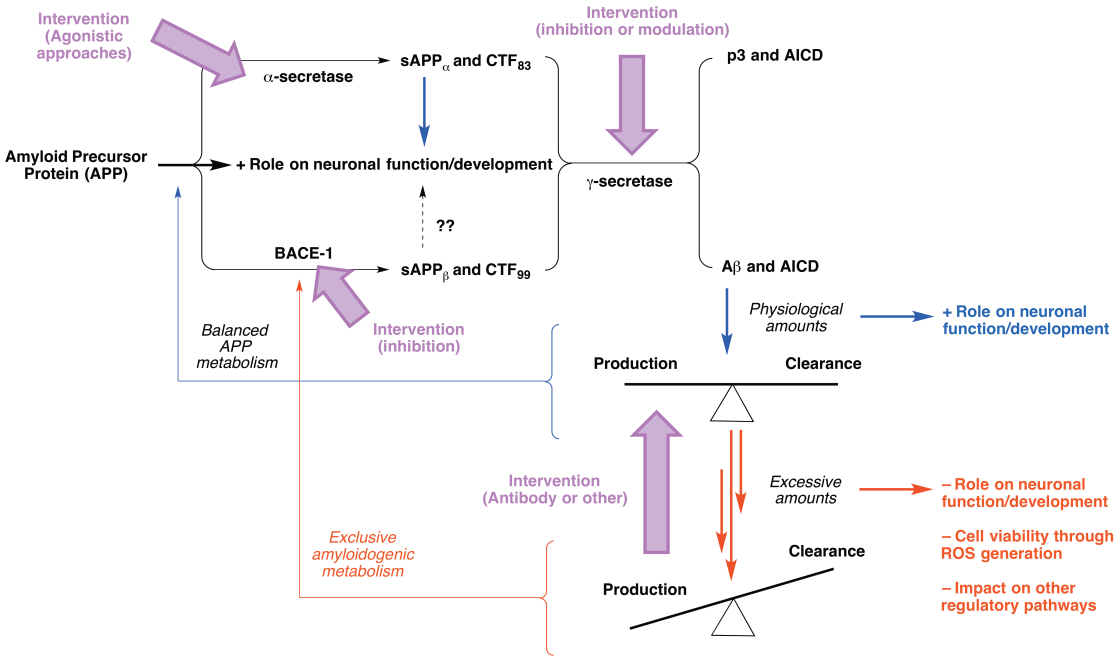


Figure 21: A brief recap of the amyloid cascade along with potential intervention sites.

1.4. Other Factors in AD Pathology

The multifaceted nature of AD pathogenesis is grounded by the principle of neuronal cell death leading to the onset of dementia symptoms. While cholinergic dysfunction is a consequence, not cause, of neuronal cell death, implications tied to the amyloid cascade, and many other factors, are responsible for said

neuronal cell death. What starts out in a localized branch of the CNS, spreads over time in prion-like fashion to other areas of the brain.[145, 226]

Although the primary focus of this thesis is linked to the cholinergic and amyloid hypotheses, it is important to address other key factors in AD pathology. Due to their impact and connectivity to the amyloid cascade, the principles of the tau and inflammatory hypotheses are briefly discussed below.

1.4.1. *Tauopathy*

If the baseline of the amyloid cascade had a relative, it would be tauopathy. This aggregation-based hypothesis is centered on the causation, formation and consequences of neurofibrillary tangles (NFTs), which are the amyloid plaque equivalent in this cascade.

Similar to the extracellular amyloid plaques, intracellular NFTs cause significant damage to the neuron by hindering regulatory and metabolic processes and destabilizing the cell's cytoskeletal framework along the way. These NFTs are comprised of hyperphosphorylated tau proteins that originate from the native, microtubule-associated tau (τ) proteins. Just as APP and Aβ are vital to neuronal function, tau proteins are crucial to maintaining neuronal integrity and axon stability and function.[32, 227] Comparable to the imbalance between Aβ production and clearance that fosters the amyloid cascade, the imbalance between tau kinases and phosphatases results in the increased rate of tau phosphorylation, which forms the basis of the tauopathy cascade.[33, 34] The excessive phosphorylation of tau (hyperphosphorylation) weakens its affinity to the neuronal microtubule assemblies and as they start to dissociate, the cellular cytoskeleton is compromised and the hyperphosphorylated tau monomers under amyloidogenic aggregation in a very similar fashion to that observed in Aβ.[31, 228] As a matter of fact, a few studies based on the amyloidogenic KLVFFA core of Aβ are often mirrored with the VQIVYK amyloidogenic core of tau. These amyloidogenic hexapeptide domains serve as a high-throughput screening model since the results are generally translatable and the screening costs are much lower.[210, 229-231]

The collapse of the neuronal cytoskeleton, combined with the persistent observations of NFTs and brain shrinkage in postmortem analysis point to tauopathy as more of a downstream pathological

mechanism, as compared to the amyloid cascade. As a matter of fact, a growing number of studies implicate the amyloid cascade with tauopathy, even though tauopathy-induced cellular damage has positive feedback input into the amyloid cascade.[36, 37, 162, 204, 228, 232, 233] Yet again, literature would demonstrate a collection of upstream and downstream intervention strategies for tauopathy,[35, 234-236] but unlike the amyloid cascade, downstream interventions upon tau hyperphosphorylation or NFT formation would not be therapeutically viable considering the extent of neurotoxicity in place at that stage. That said, it is safe to assume that interventions upstream of tau hyperphosphorylation are worthy as those are typically based on restoring the balance of kinase and phosphatase activity, although that is not without challenge, or are based on upstream/downstream interventions within the amyloid cascade (discussed earlier).

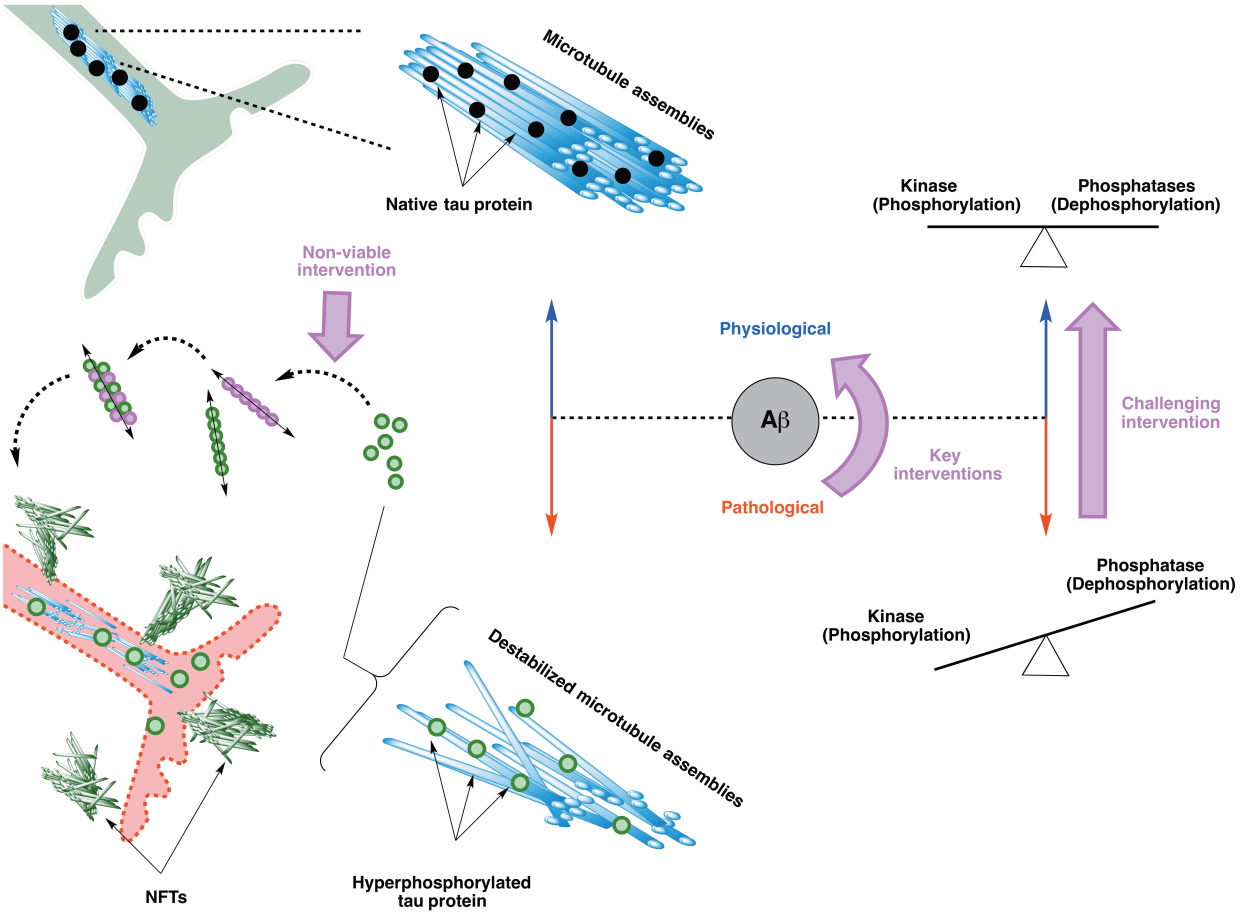


Figure 22: A brief summary of the tau cascade along with potential intervention sites.

The challenge with regulating or restoring the balance of tau phosphorylation has to do with the type of kinases involved in that process. Developing inhibitors or modulators of GSK-3β or Cdk5 is not the challenge per se, but having site-specific activity is as these kinases are well dispersed throughout the body and carry substantially critical activities – A potent, non-site specific inhibitor of GSK-3β for example could wreak havoc on healthy cellular functions.[104, 237, 238] Overall, it is best to target as far upstream as possible and with respect to tauopathy, dealing with the amyloid cascade could alleviate the need to focus on tau-related pathogenesis (Figure 22).[22, 105, 239]

1.4.2. *Inflammation*

The concept of an appropriate and physiological inflammatory response compared to ongoing and longer onset inflammation linked to disease initiation and progression is not a novel one. A large proportion of disorders, like heart disease, diabetes and cancer, include an inflammatory component and neurodegenerative diseases are no different.

With respect to AD, while the cascades discussed thus far seem to have a general placement along the pathology timeline, inflammation is a bit different. There are a few ideas that suggest the entire pathology timeline starts out with ongoing inflammatory responses, while others hypothesize that inflammation is a key component throughout the pathology timeline. Considering the causes of inflammation are vast, it could be that both schools of thought are correct – Where inflammation is a key initiator and continues to promote disease progression.[240] As such, the inflammatory hypothesis for AD is not well defined because anything from an infection, brain trauma or metabolic dysfunction could set the tone for ongoing or unsuppressed inflammation, especially in older adults. It is well documented that amyloid species (like Aβ and NFTs) induce inflammation but it is not far-fetched that further upstream inflammatory responses could offset the balance tied to Aβ production/ clearance and/or tau kinase/phosphatase activity.[109, 241, 242]

One of the primary culprits identified under the inflammatory umbrella is the *N*-methly-D-aspartate (NMDA) receptor. Elevated levels of glutamate result in the over-activation of NMDA receptors leading to a large influx of Ca^{2+} ions and this leads to excitotoxicity and neuronal degeneration.[243-245] Another

potential target, which is also implicated in Parkinson's disease, is the monoamine oxidase family of enzymes (MAO A/B). Along with the generation of peroxide radicals as part of their mechanistic activity, recent studies have reported elevated levels of MAO activity in AD patients. The elevated levels of MAO could be a response to the diminishing cholinergic mass or attributed to an increase in monoamine substrates. Regardless of the cause, that increased MAO activity contributes to the reduction of key neurotransmitters, like serotonin, leading to elevated depression levels in AD patients.[246-248] In addition, the oxygenase enzymes, COX-1/2 and 12-/15-LOX, along with the TNF-α cytokine have been implicated with pro-inflammatory mechanisms in AD.[249-253]

It is without a doubt that inflammation plays a significant role here to the point that it is considered a given. That said, literature wouldn't necessarily showcase research platforms solely targeting inflammatory responses in neurodegenerative diseases as that has much to do with the large umbrella/tent that the inflammation casts on everyday life. Alternatively, research efforts tend to be more targeted at the specific causes of inflammation – The upstream intervention strategy (Figure 23).[254]

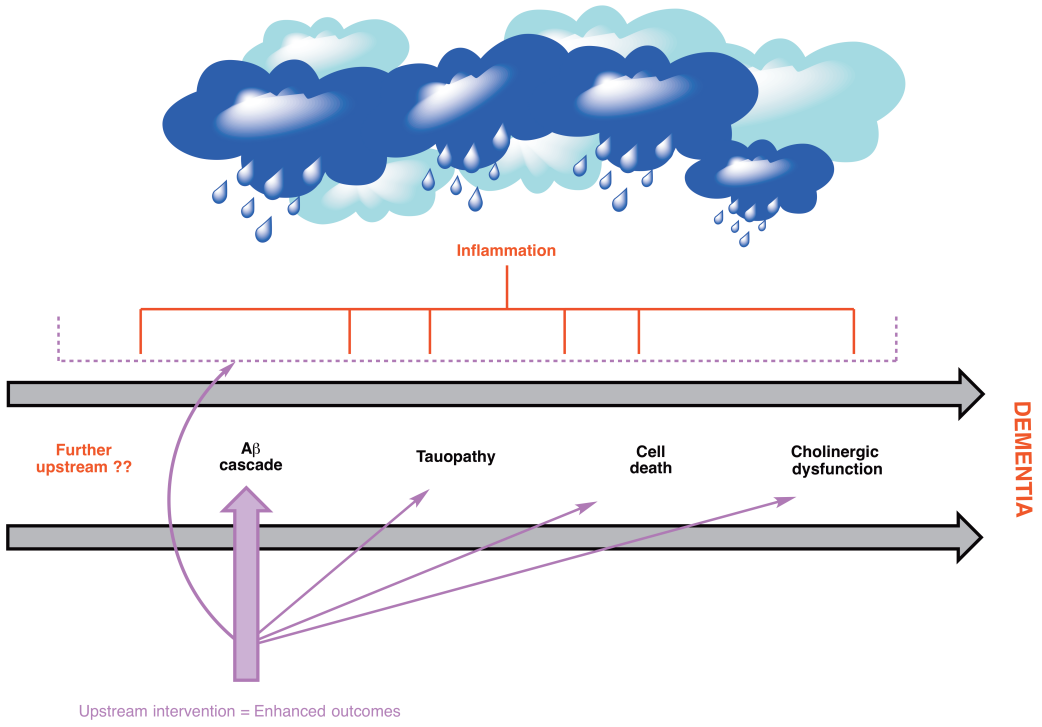


Figure 23: A brief schematic of the ubiquitous role and presence of inflammation along the pathology timeline of AD.

1.5. Chapter Conclusion

The mechanisms and cascades outlining AD pathology are not linearly associated as summarized in Figure 24. The collective research conducted over the past 100+ years has revealed a number of key hypotheses, a small handful of marketed treatments and countless failed clinical trials.

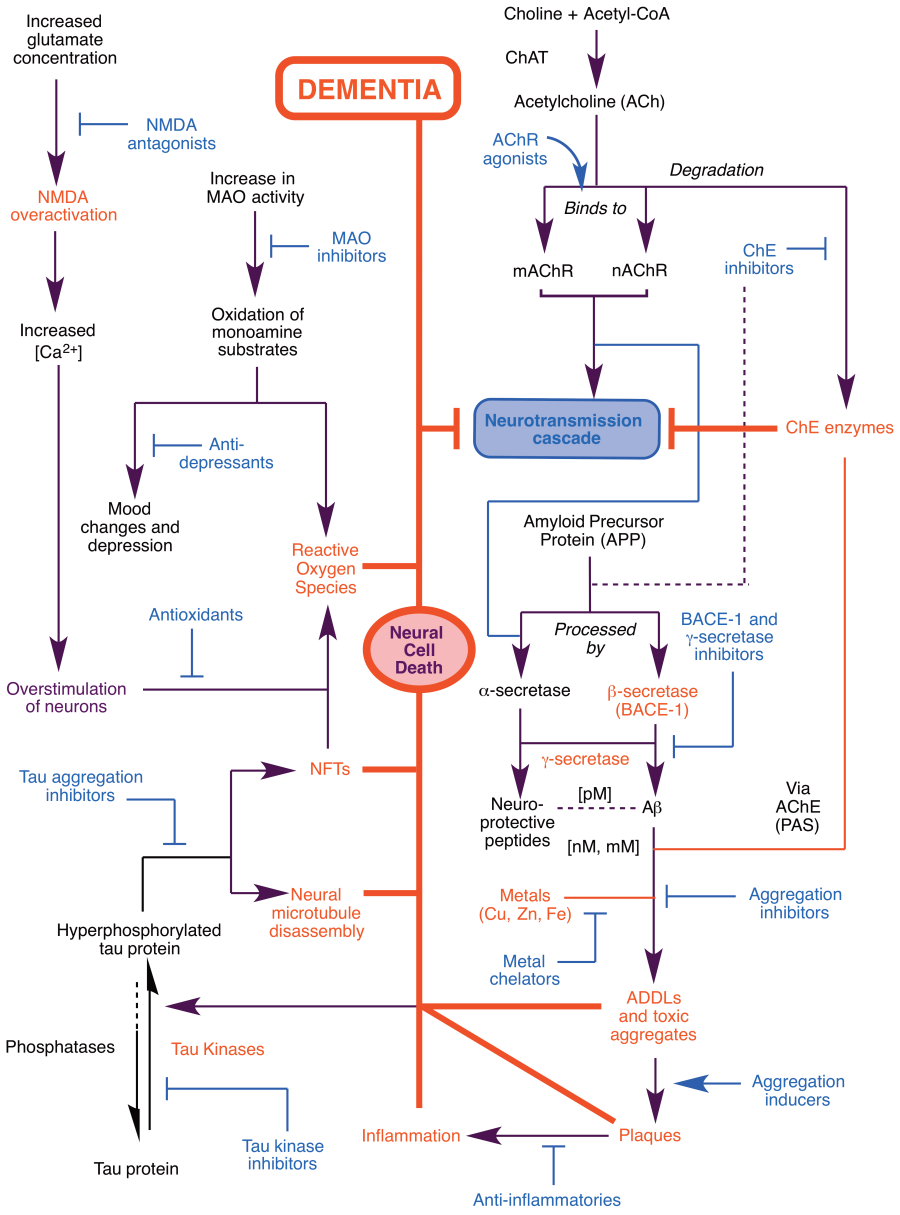


Figure 24: A schematic and basic overview of the complexity tying the various cascades and mechanisms together contributing to AD pathology.

While it would seem that there is much left to uncover with respect to AD pathology, a few primary take home messages from this chapter include: a) the fact that cholinergic dysfunction, while not directly implicated in neuronal cell death, has been linked to patients' dementia symptoms, b) not to mention that the amyloid cascade has and continues to be a high-ranking culprit due to its vast downstream implications and lastly c) the mandate for a multipronged strategy, primarily based on amyloid targeting, to inflict the most positive outcomes in the 'global' perspective of AD pathology was built.

CHAPTER 2

• Rationale Behind the Utilization of the Quinazoline Ring Scaffold for Designing Novel AD Therapies •

2.1. Quinazoline Survey

Heterocyclic ring scaffolds function as effective templates for multiple disease platforms and industry research pipelines. In a broad sense, these scaffolds are sought after for their known biological properties, applications and potential to afford novel therapeutics.

From microorganisms to plants and marine animals, nature hosts a variety of bioactive quinazoline and related heterocylics (Figure 25). Selectively produced by yeast (*C. lipolytica*) and found in a few plant species, tryptanthin, an indolequinazoline, has been reported for its anti-inflammatory and antimicrobial properties.[255] The *Aspergillus* genus of fungi are a source of multi-cyclic quinazolines, like sclerotigenin, circumdatin F and asperlicin C, with varying biological profiles.[256, 257] Initially isolated from *D. febrifuga*, the quinazoline alkaloid (+)-febrifugine has been documented for its antimalarial properties. The vasicine-related alkaloid, deoxypeganine is isolated from *J. adhatoda* and has a wide-range of biological activity including substance abuse/ dependence and Alzheimer's disease.[258] On the marine front, fumiquinazoline K is isolated from the soft coral fungus *A. fumigatus*, while the Russian brown algae *L. sachalinensis* is a known source of the carnequinazolines B and C.[259]

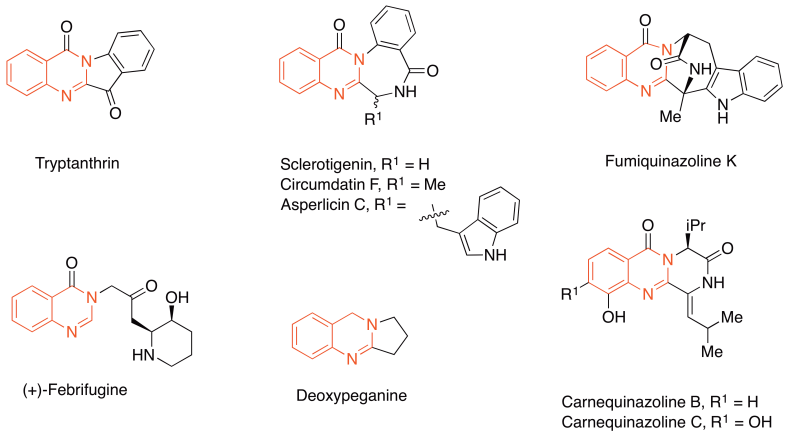


Figure 25: Naturally-occurring quinazoline and quinazolinone alkaloids.

As a privileged scaffold, the quinazoline ring system (along with its close relatives and bioisosteres) have seen numerous oncological,[260-264] microbial,[265-268] inflammatory,[269-271] anti-obesity [272-274] and neurological [73, 275-281] applications ranging from early-development to successful marketed therapies as showcased below (Figure 26).[257, 282-287] These quinazoline and quinazoline-like derivatives truly exemplify the diversity, broad utility and therapeutic potential of these scaffolds.

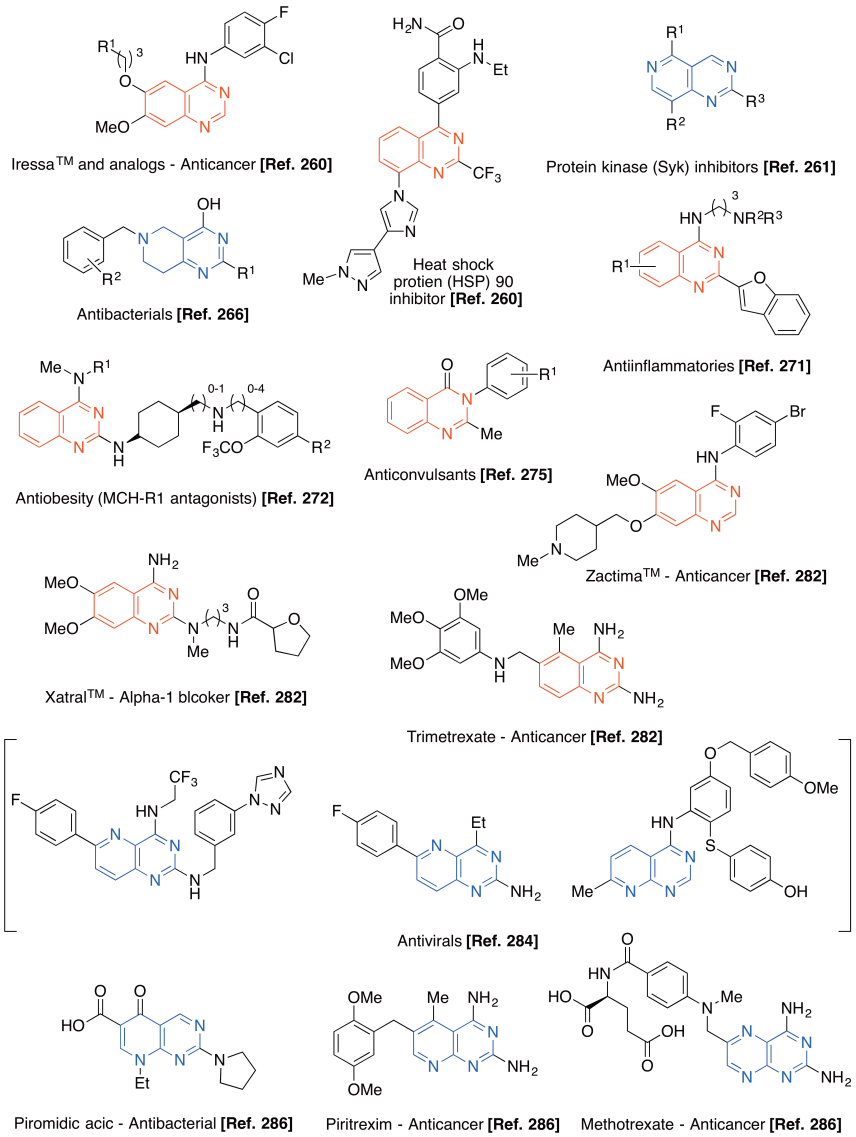
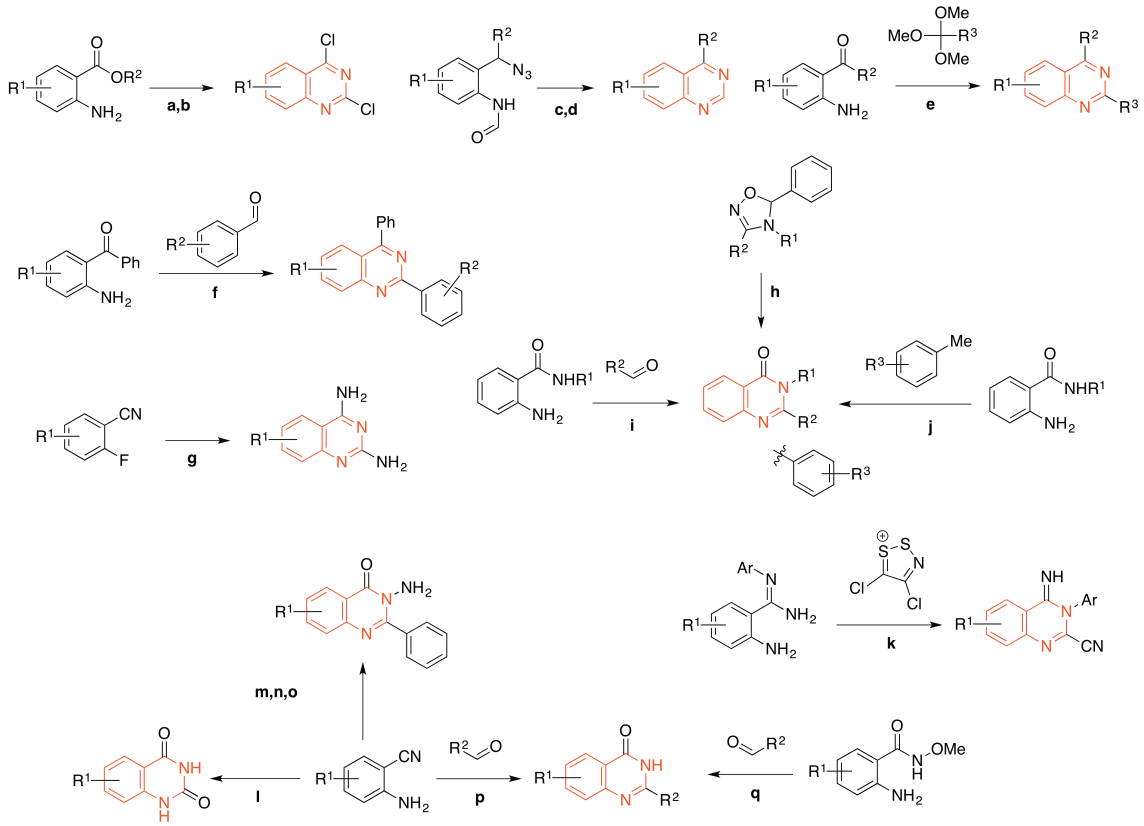


Figure 26: A collection of marketed, in-development and patented quinazoline and related derivatives. Structures featuring the quinazoline or quinazolinone rings are indicated with red, whereas those featuring the pyridopyrimidine or related rings are indicated with blue.

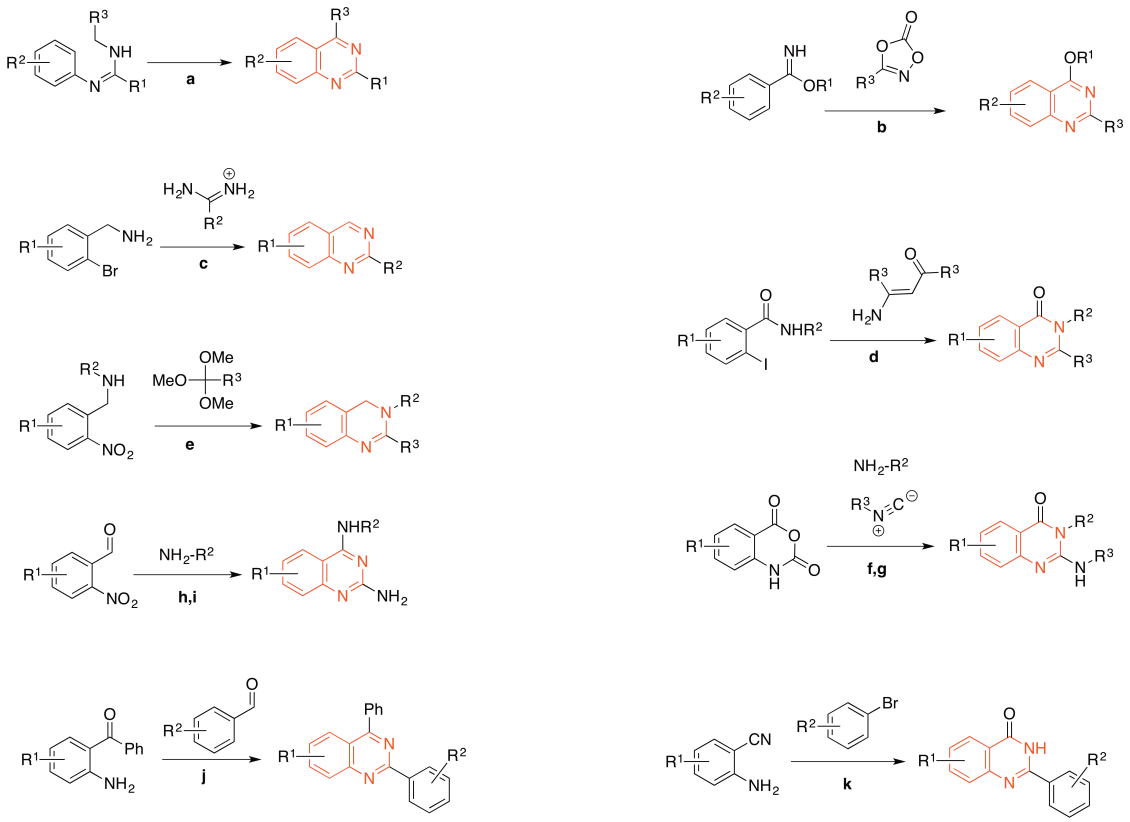
The synthetic roadmap to bioactive quinazoline molecules is strategically diverse to allow for the design and development of diverse compound libraries for the acquisition of comprehensive structure-activity relationship (SAR) data – A brief overview of these multi-approach synthetic routes are showcased below in Scheme 1 (metal-free methods)[257, 264, 269, 272, 288-291], Scheme 2 (catalyst-dependent methods)[290, 292-294] and Scheme 3 (microwave or ultrasound-aided methods).[257, 290, 293, 295] It is noteworthy that some of these methods are translatable to related heterocyclic derivatives including pyridopyrimdines and quinolones.

Scheme 1[a]



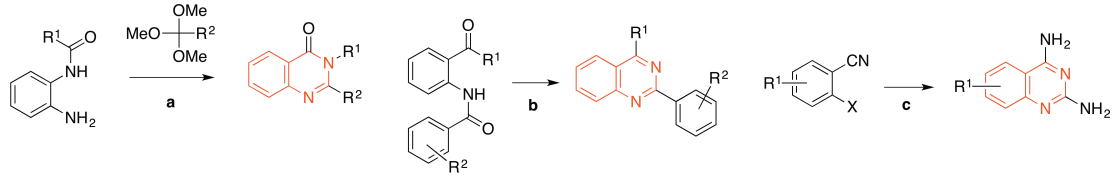
[a]**Reagents and conditions:** Highlighting a few metal-free synthetic routes toward quinazoline-based derivative. (a) Urea, pressure tube, 150–160 °C, 3–4 h.; (b) $POCl_3$, base, 0–115 °C, 5–18 h.; (c) $POCl_3$, TEA, THF, 0°C; (d) NaH, DMF, 0 °C; (e) Ammonium acetate, 110 °C; (f) Ammonium acetate, DMAP, EtOH, 40 °C; (g) Guanidine carbonate, DMA, 140 °C, 8 h; (h) DMSO, dry air, 120 °C; (i) DMSO, open flask, 100 °C; (j) DMSO, TsOH, DTBP, 100 °C, 20 h.; (k) DIPEA, DCM, 20 °C, 2 h; (l) Water, carbon dioxide, 160 °C; (m) Pyridine, benzoyl chloride; (n) Hydrazine hydrate, EtOH; (o) AcOH, EtOH; (p) Water, tripotassium phosphate, 100 °C; (q) AcOH, 100 °C.

Scheme 2[a]



[a]**Reagents and conditions:** Highlighting a few catalyst/metal-dependant synthetic routes toward quinazoline-based derivatives. (a) $PhI(OAc)_2$, toluene, 140 °C; (b) $AgBF_4$, $[Cp^*RhCl_2]_2$, DCE, 50 °C, 5 h.; (c) Pivalic acid, tripotassium phosphate, copper iodide, 1,2-DCB, 110 °C, 18 h; (d) Copper iodide, cesium carbonate, MeCN, 90 °C, 24 h; (e) $TiCl_4$-Zn, THF; (f) Toluene, amine, 100°C; (g) $Pd(OAc)_2$, silver carbonate, isocyanide; (h) Cyanamide, dry MeOH, sodium *t*-butoxide, NBS, 0–50 °C, 12 h; (i) Amine, MeOH, iron/hydrochloric acid, r.t.–60 °C, 3 h; (j) $CuFe_2O_4$, NPs, water, air 80 °C; (k) $Pd(OAc)_2$, $BuPAd_2$, potassium carbonate, carbon monoxide, DMSO, water.

Scheme 3[a]



[a]**Reagents and conditions:** Highlighting a few microwave or ultrasound-assisted synthetic routes toward quinazoline-based derivatives. (a) p-TsOH, DMA, MW; (b) Ultrasound; (c) Guanidine carbonate, potassium carbonate, MW 140 °C, 20 min.

2.2. Template Design

With its medicinal/pharmaceutical advantage, prior exploitation in AD therapeutics[279, 296-298] and diverse synthetic approaches, the platform of this thesis is based on utilizing the quinazoline ring scaffold to design novel, multi-targeting candidates focused on the modulation of Aβ-aggregation and the dual targeting of the ChE enzymes. The results of the author's prior work with a disubstituted pyrimidine ring scaffold has shown that the presence of a C4 3,4-dimethoxybenzylamine substituent provided bivalent inhibition of AChE. The lead molecule (Pyr-lead) exhibited dual ChE inhibition and anti-Aβ aggregation properties (AChE IC_{50} = 9.9 μM, BuChE IC_{50} = 11.4 μM, Percent inhibition of AChE-induced Aβ aggregation = 59.3%, percent inhibition of self-induced Aβ aggregation = 17.4% at 100 μM)[299] and the collective data from those studies influenced the design strategy showcased below (Figure 27).

As seen in the left-panel of Figure 27, the combination of the pyrimidine ring scaffold, the benzylpiperidine pharmacophore from donepezil and a 3,4-dimethoxybenzylamine at the C4-position resulted in a true bivalent ligand (Pyd-lead) that extends past donepezil for stronger interactions at the PAS of AChE (W286). When the pyrimidine scaffold was replaced with a quinazoline (Qnz-version), it became evident that the majority of the ligand was binding at and beyond the PAS in AChE (W286). While the benzylpiperidine pharmacophore was binding within the active site gorge, it was not exhibiting favourable or comparable interactions as donepezil or Pyd-lead (W86). The preliminary molecular modeling studies suggested the radical downsizing of the functional groups at the C2-position of the quinazoline scaffold with minor linker extensions at the C4-positions to be favourable. The binding interactions observed with the Qnz ligand, in the right-panel of Figure 27, support the ChE-targeting design strategy of employing smaller functional groups at the C2-position while maintaining aromatic amines at the C4-position with 1-2 methylene unit linkers.

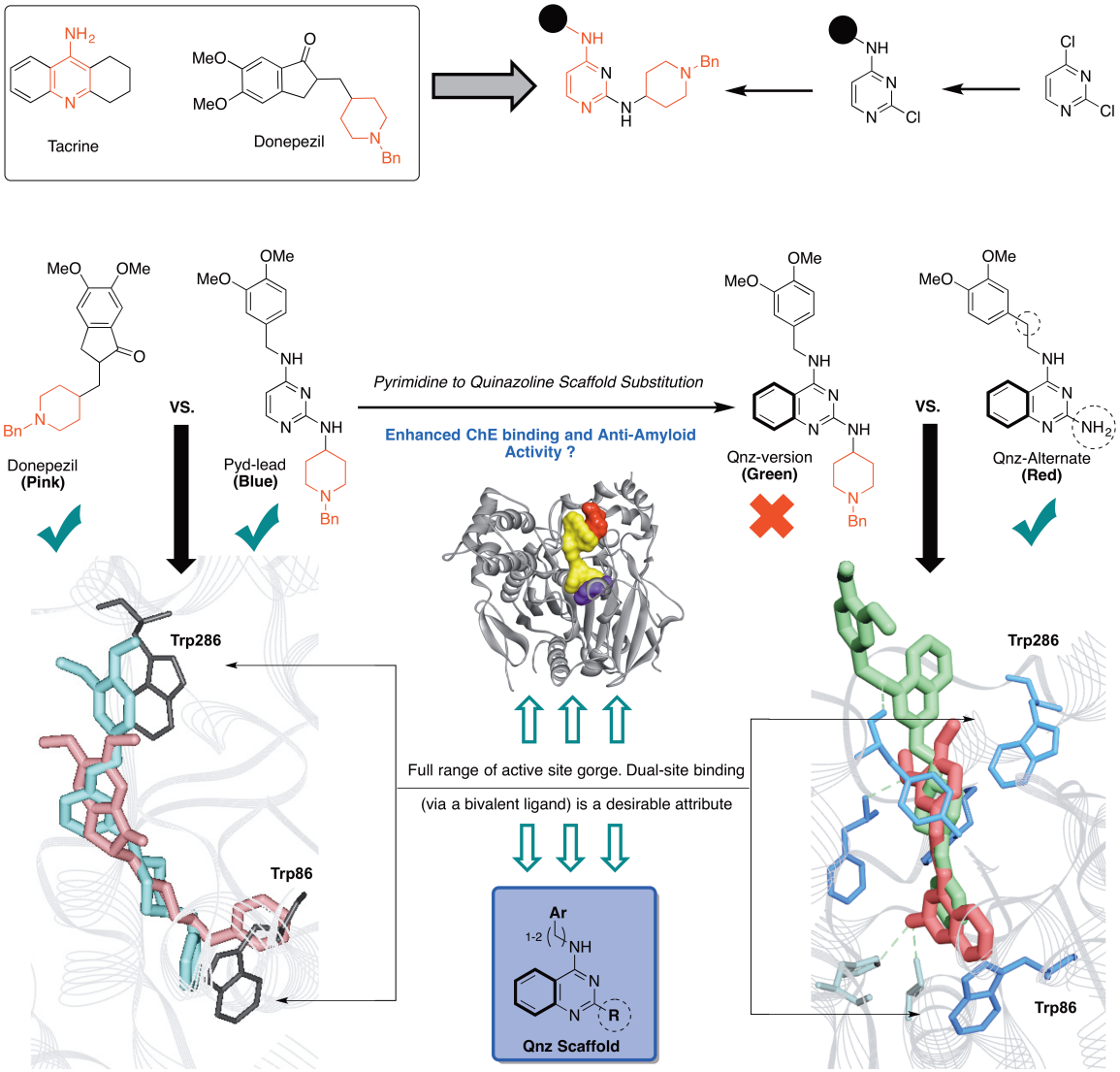


Figure 27: Summary of the design strategy leading to the disubstituted quinazoline template featuring a smaller group at the C2-position to effectively generate bivalent inhibitors.

In addition to dual cholinesterase targeting, the chosen scaffold design is hypothesized to effectively target and modulate Aβ-aggregation. With its planar and bicyclic nature, the quinazoline scaffold offers similar characteristics seen with the effective Aβ-aggregation modulator orange G, which contains a planar naphthalene scaffold. While the core template may offer intercalating or stacking interactions within the amyloid backbone structures, the nature, size and electrostatic properties of the functional groups at the C2

and C4-positions will play a critical role in varying the extent of anti-aggregation potential across the multiple domains of the dimeric and fibril structures of Aβ. Additional activity parameters, such as metal chelation and ROS scavenging, are also factored in the design strategy to meet the overall objective of developing multi-targeting candidates.

Prime focus on the incorporation of Lipinski's rules was accomplished by monitoring ClogP values (around the 3–6 range), maintaining molecular weights under 500 Da and limiting hydrogen-bonding acceptors (equal to or under 8) and donors (equal to or under 5) (Figure 28).

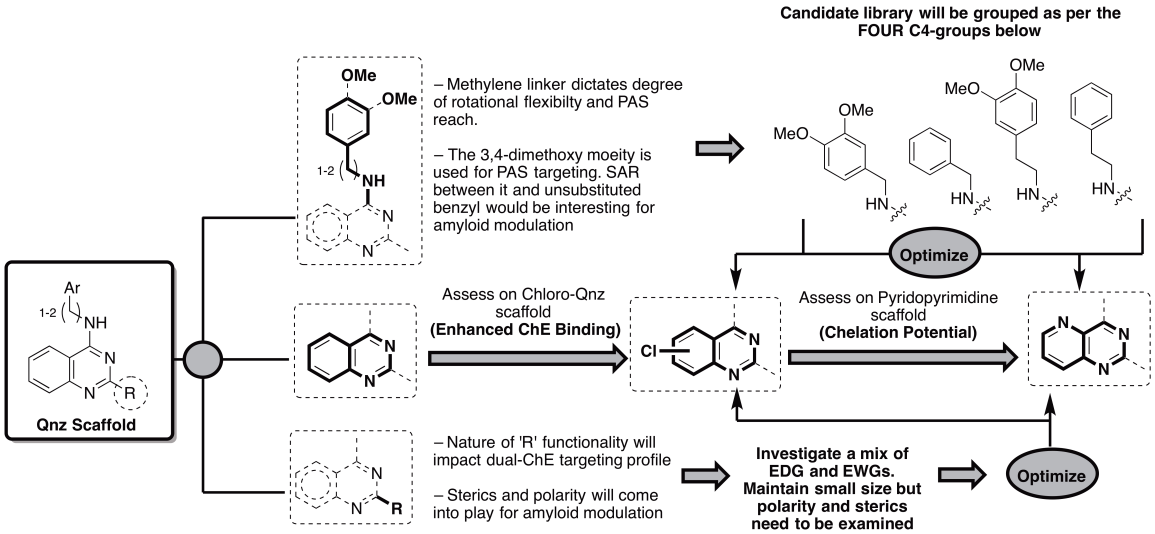


Figure 28: Overview of proposed SAR optimization on the quinazoline derivatives including template modifications.

2.3. Synthesis of quinazoline core template

In order to synthesize C2- and C4-substituted quinazoline libraries, nucleophilic aromatic substitution (NAS) reactions were utilized on chloro-substituted quinazoline or pyrido[3,2-*d*]pyrimidine intermediates (Figure 29).

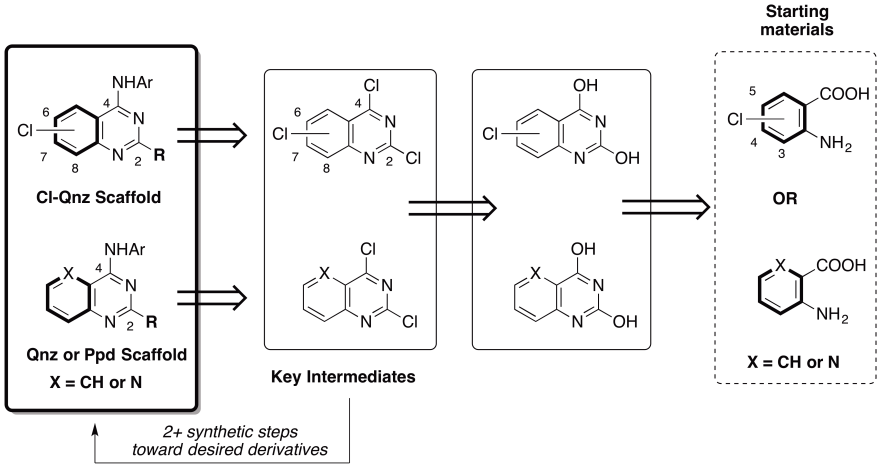


Figure 29: Retrosynthetic pathway to the key di- or trichloroquinazoline and dichloropyrido[3,2-*d*]pyrimidine intermediates.

For these applications, the synthesis of 2,4-dichloroquinazoline (2,4-DCQ) began with the condensation of anthranilic acid (2-aminobenzoic acid) with excess urea to form quinazoline-2,4-diol.[264, 289, 300] In the proceeding step, the quinazoline-2,4-diol was converted to the 2,4-dichloroquinazoline via a quinazoline-2,4-diyl-bis(phosphorodichloridate) intermediate.[301]

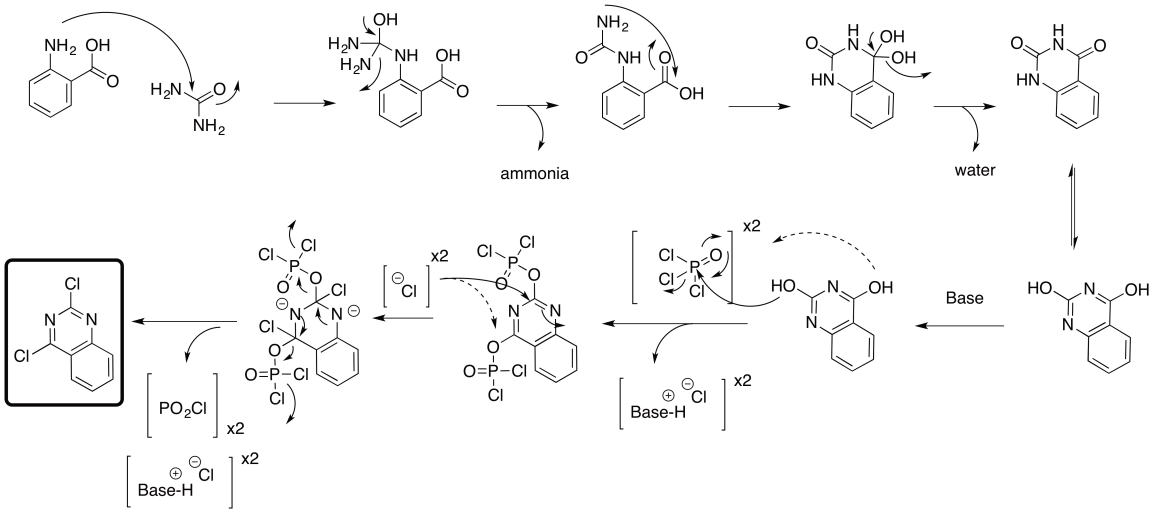


Figure 30: Reaction mechanisms for the cyclization and chlorination of 2-aminobenzoic acid to generate 2,4-DCQ.

These steps are easily transferable to afford the 2,4,6-, 2,4,7-, or 2,4,8-trichloroquinazoline or 2,4-dichloropyrido[3,2-*d*]pyrimidine intermediates required to synthesize sought-after quinazoline or pyrido[3,2-*d*]pyrimidine compound libraries. The reaction mechanisms for these known protocols are showcased in Figure 30 and the proton NMR spectral shifts for these intermediates are compared in Appendix I. The assessment of the proton spectral shift changes with chlorine placements and the change from quinazoline (Qnz) to pyrido[3,2-*d*]pyrimidine (Ppd), offered some insight into the chemical nature of these intermediates.

2.4. Target Quinazoline Library

The research program was broadly divided into two phases. The first was centered on the quinazoline scaffold, while the second was primarily based on chloroquinazolines and pyrido[3,2-*d*]pyrimidines. In phase one, a wide array of SAR data was acquired to lay the foundation for the phase two where further SAR optimization was accomplished. The following is the complete list of quinazoline and pyrido[3,2-*d*]pyrimidine compound libraries synthesized:

---

1. *N*-(3,4-Dimethoxybenzyl)quinazolin-4-amines **(Chapter 3 – 14 derivatives)**

2. *N*-Benzylquinazolin-4-amines + 1 regioisomer **(Chapter 4 – 14 derivatives)**

3. *N*-(3,4-Dimethoxyphenethyl)quinazolin-4-amines + 1 regioisomer + *N*-(3,4-Dimethoxyphenethyl) chloroquinazolin-4-amines **(Chapter 5 – 29 derivatives)**

4. *N*-Phenethylquinazolin-4-amines + 2 regioisomers + *N*-Phenethylchloroquinazolin-4-amines **(Chapter 6 – 30 derivatives)**

5. 2,4-Disubstituted Pyrido[3,2-d]pyrimidines **(Chapter 7 – 10 derivatives)**

6. Isomeric 2,4-Diaminoquinazolines **(Chapter 8 – 30 derivatives)**

In total, the thesis encompasses the design, development and biological screening of **127** quinazoline derivatives (Figure 31) with extensive SAR data for targeting the ChEs, amyloid aggregation and secondary interests such as metal chelation and ROS scavenging.

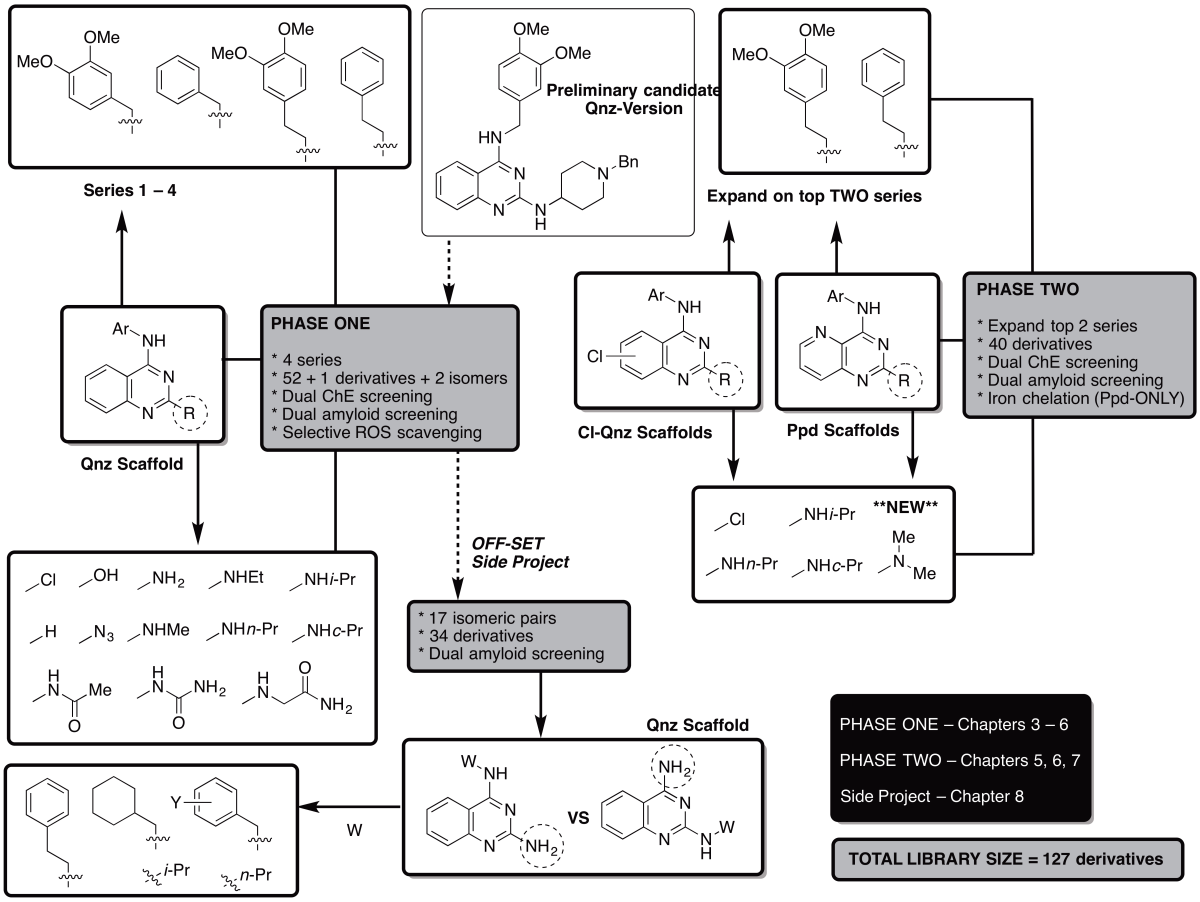
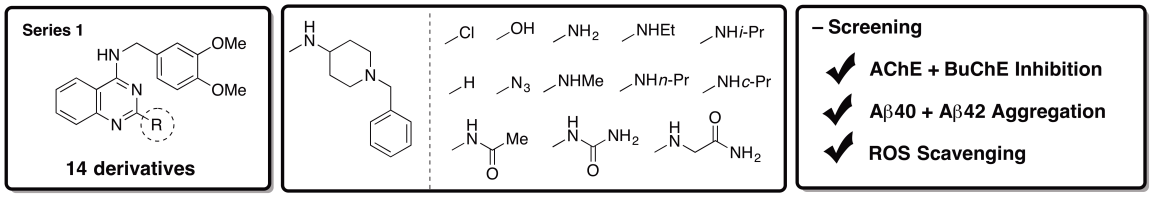


Figure 31: Outline of target derivatives in this research program.

CHAPTER 3

• Development and Evaluation of *N*-(3,4-dimethoxybenzyl)quinazolin-4-amines as Dual ChE and Aβ Aggregation Inhibitors •



* Chapter banner

3.1. Introduction

With an initial design strategy based on the Pyd-lead and the preliminary ligand (Qnz-version, Figure 27), this series features a group of derivatives bearing the 3,4-dimethoxybenzylamine group at the C4-position of the quinazoline scaffold. A combination of EWGs and EDGs was utilized to investigate and understand the role of steric and electrostatic properties in the biological profile outcomes.

This chapter discusses the synthesis and development of target derivatives (refer to the chapter banner above) along with the acquisition and assessment of the SAR data toward dual ChE and Aβ40/42 aggregation inhibition. A brief summary is provided prior to the listing of experimental data and methodology.

3.2. Hypothesis

With respect to this series of derivatives, the presence of a 3,4-dimethoxyphenyl substituent at the C4 position of the quinazoline ring scaffold was predicted to provide bivalent AChE inhibition with binding to both the catalytic and PAS of AChE. It was anticipated that this structural feature may work in favour with respect to the modulation of amyloid aggregation by interacting with monomeric species to prevent or hinder the dimerization and further oligomerization.

On the other hand, the selection of C2-groups offers wider postulations. The presence of an azide group, for example, may not be favourable in most scenarios due to its rigid conformation. In addition, the hydrophobic pockets of BuChE are likely to reject polar derivatives, although those derivatives might be capable of targeting AChE effectively. The alkylamines are strongly predicted to benefit BuChE inhibition, while effectively targeting AChE and modulating amyloid aggregation.

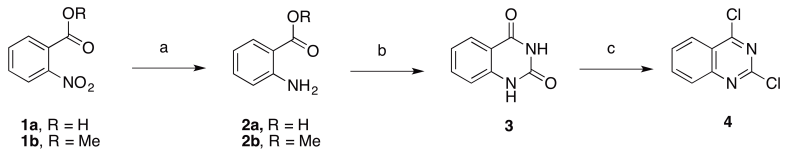
3.3. Results and Discussions

The proceeding sub-chapter describes the synthetic route to desired derivatives (**8**–**15**) along with biological assessments in the cholinesterase assay, to obtain inhibition concentrations to reduce 50% enzyme activity (IC_{50} values), and the amyloid-β aggregation assay to investigate aggregation kinetics and establish end-point IC_{50} or percent inhibition values. Select derivatives were assessed for ROS scavenging in the DPPH (2,2-diphenyl-1-picrylhydrazyl) assay. Finally, computational studies using the Discovery Studio software suite were performed to evaluate the acquired SAR data using the ChE X-ray structures and amyloid models.

3.3.1. *Synthesis*

As described earlier in Chapter 2, the synthesis of target derivatives stems from 2,4-dichloroquinazoline (**4**, Scheme 4). This key intermediate was obtained from the reduction of 2-nitrobenzoic acid (**1a**) or methyl-2-nitrobenzoate to the corresponding amine (**2a** or **2b)**,[302] followed by the cyclization with urea yielding the quinazoline-2,4-dione (**3**) and final chlorination with $POCl_3$ to provide 2,4-DCQ (**4**, Scheme 4). The reaction mechanisms pertaining to these steps were also discussed in Chapter 2.

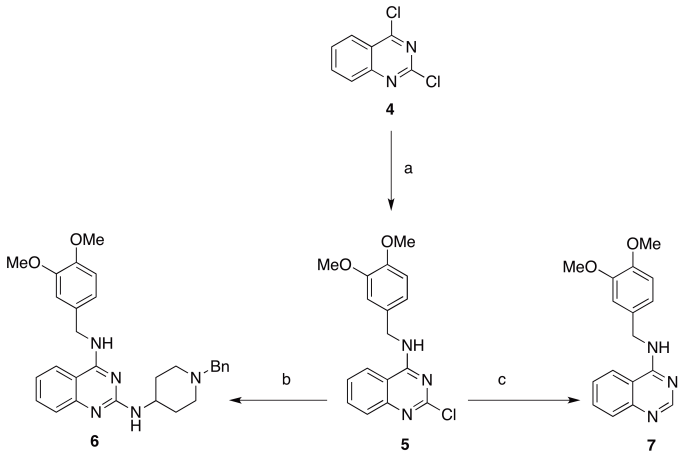
Scheme 4[a]



[a]**Reagents and conditions:** Synthetic route toward the 2,4-dichloroquinazoline intermediate. (a) Pd/C, hydrazine hydrate, EtOH, 80–85 °C, 2 h; (b) Urea, 150–155 °C, pressure vial, oil bath, 2 h; (c) $POCl_3$, toluene, *N*,*N*-diethylaniline, $POCl_3$, 0–105 °C, reflux, 14–16 h.

In the first coupling reaction, the 3,4-dimethoxybenzylamine group was added to the C4-position of 2,4-dichloroquinazoline (2,4-DCQ). This NAS reaction required moderate refluxing (3-4 h) in ethanol with an organic base, like diisopropylethylamine (DIPEA) to yield 2-chloro-*N*-(3,4-dimethoxybenzyl) quinazolin-4-amine (**5**, Scheme 5, 80–85% yield).[299, 303]

Scheme 5[a]



[a]**Reagents and conditions:** Synthetic routes toward quinazoline-based derivatives **5**-**7**. (a) 3,4-dimethoxybenzylamine, DIPEA, EtOH, reflux, 4 h; (b) 4-amino-1-benzylpiperidine, DIPEA, 1,4-dioxane, 160–165 °C, pressure vial, oil bath, 6 h.; (c) Pd/C, hydrazine hydrate, EtOH, reflux, 2 h.

Besides being a derivative of interest, **5** also played the role of "intermediate" for a number of compounds downstream. The coupling of **5** with 4-amino-1-benzylpiperidine via NAS, under harsh conditions, generated N^2-(1-benzylpiperidin-4-yl)-N^4-(3,4-dimethoxybenzyl)quinazoline-2,4-diamine (**6**, Scheme 5, ~ 50% yield), which was screened for dual ChE and amyloid-β aggregation inhibition during the initial design phase (Qnz-version, Chapter 2).[299] The C2-position SAR was explored initially by a dechlorination reaction to obtain *N*-(3,4-dimethoxybenzyl)quinazolin-4-amine (**7**, Scheme 5, ~ 45% yield) via the Pd/C and hydrazine-driven dehalogenation reaction.[304] The general reaction mechanism pertaining to NAS reactions is briefly outlined in Figure 32, while the Pd/C and hydrazine-driven dehalogenation mechanism is showcased in Figure 33.

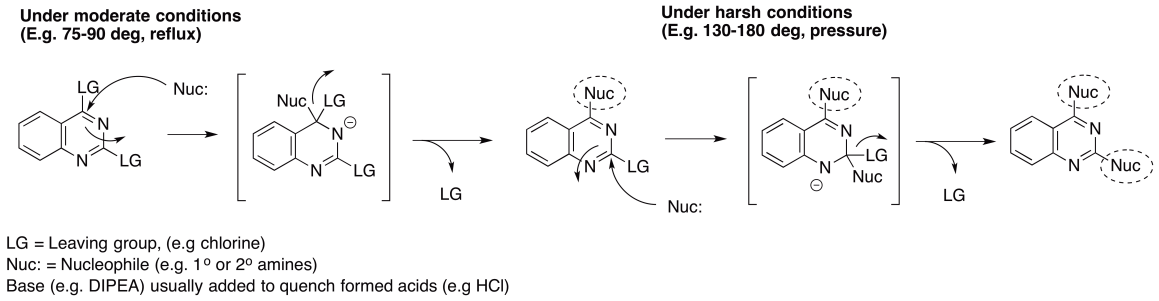


Figure 32: Mechanism for NAS reactions on the quinazoline scaffold. Coupling at the C2-position requires harsher conditions compared to C4-based coupling.

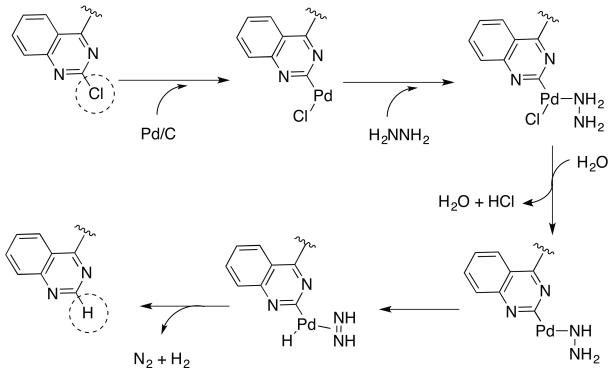
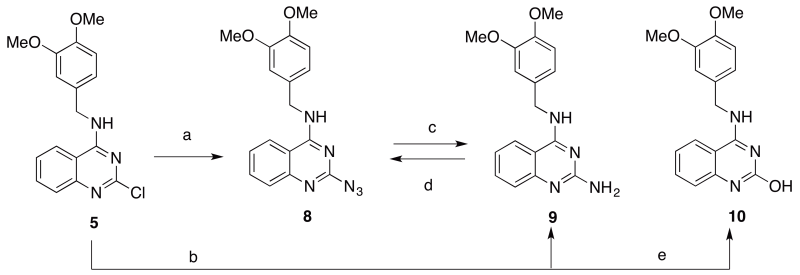


Figure 33: Mechanism for hydrazine and Pd/C driven dehalogenation via oxidative addition, β-hydrogen elimination and reductive elimination.

Further utilization of **5** was demonstrated with the nucleophilic addition of hydrazoic acid (via sodium azide) at the C2-position, under reflux conditions in ethanol and acetic acid, to yield 2-azido-*N*-(3,4-dimethoxybenzyl) quinazolin-4-amine (**8**, Scheme 6, ~ 90% yield).[305, 306] In addition to acting as a stand-alone derivative, the azide-based derivative was later utilized in the generation of the C2-amino derivative (**9**, Scheme 6, N^4-(3,4-dimethoxybenzyl)quinazoline-2,4-diamine) as an alternate method to the copper(I) oxide approach. The initial approach of direct coupling using ammonia to **5**, via the copper (I) oxide and DMEDA-ligand complex (Figure 34), proved to be inefficient.[307-311] With yields only reaching ~ 35%, the alternate approach of reducing **8** to **9**, via Pd/C and hydrazine, was acknowledged as an easier and higher-yielding (~80%) route, even when compared to the attempted triphenylphosphine approach to azide cleavage (Staudinger reaction). It is noteworthy that experimental attempts were made to convert **9** to **8**, via the diazo intermediate generated with sodium nitrite and hydrochloric acid, but outcomes were a mixture of **8** and **10** (4-((3,4-dimethoxybenzyl)amino)quinazolin-2-ol) (Figure 35).[305] An effective approach to generating **10** was developed by heating **5** in formic acid and potassium formate under reflux overnight (Scheme 6, yield ~ 65%). The reaction mechanisms pertaining to the synthesis of the azide and the C2-hydroxyl derivatives are showcased in Figures 35 and 36; respectively.

Scheme 6[a]



[a]**Reagents and conditions:** Synthetic routes toward quinazoline-based derivatives **8**-**10**. (a) Sodium azide, EtOH, acetic acid, 90–95 °C, 2 h; (b) Cu_2O, K_2CO_3, DMEDA, ethylene glycol, ammonium hydroxide, pressure vial, oil bath, 105 °C, 24 h; (c) Pd/C, hydrazine hydrate, EtOH, reflux, 2 h; (d) HCl, sodium nitrite, sodium azide, 0 °C–r.t., 1 h; (e) potassium formate, formic acid, 120–125 °C, 14–16 h.

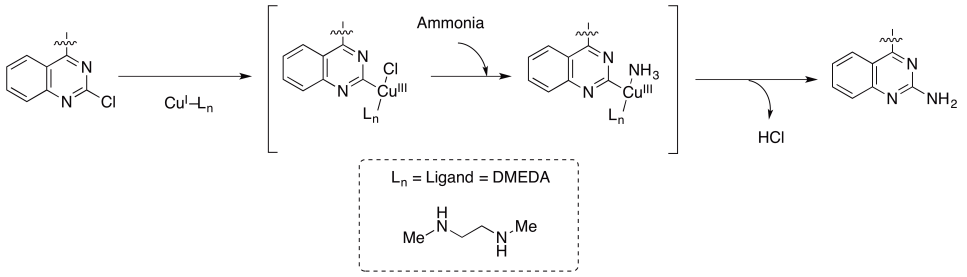


Figure 34: Copper-DMEDA complex mediating the amination of 2-chloro-N^4-substituted quinazoline derivatives using ammonium hydroxide.

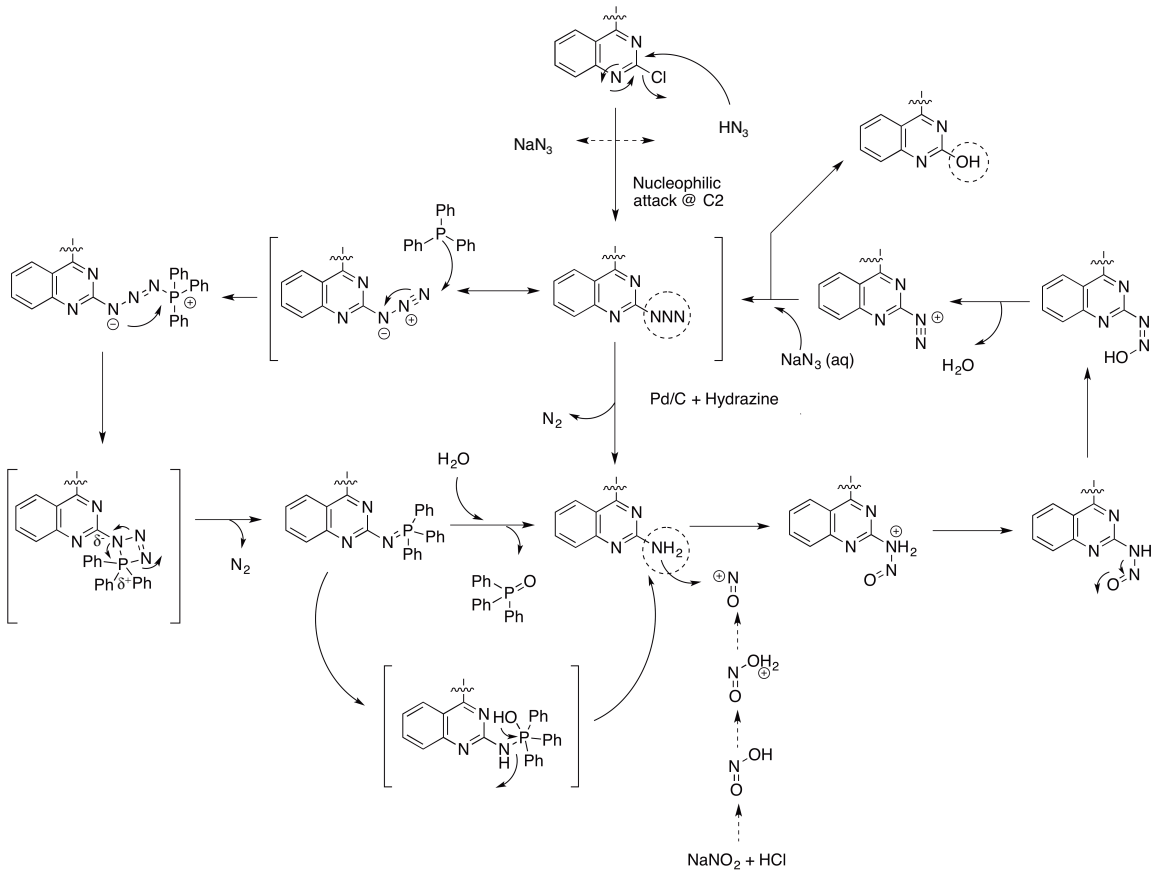


Figure 35: Reaction mechanism toward the generation and reduction of 2-azido-N^4-substituted quinazoline derivatives.

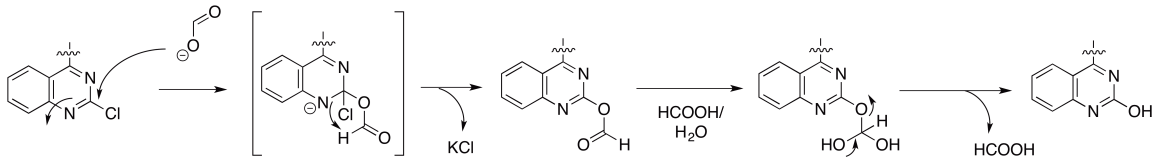
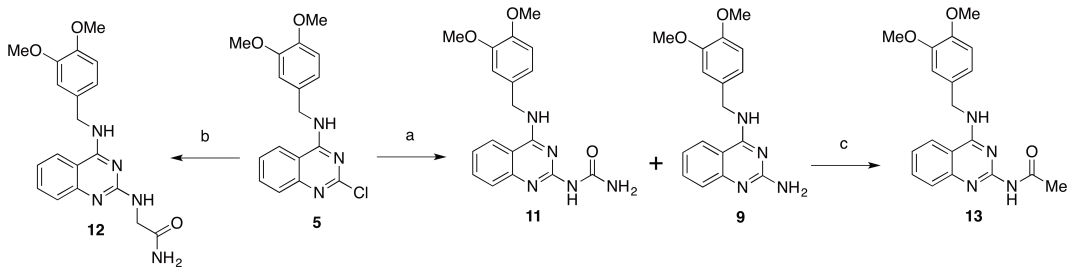


Figure 36: Reaction mechanism toward the generation of N^4-substituted quinazoline-2-ol derivatives using formic acid and potassium formate.

The development of C2-carbonyl based derivatives began with the displacement of the C2-chlorine of **5** with urea under high temperature and pressure conditions. The NAS reaction yielded derivative **11** (Scheme 7, 1-(4-((3,4-dimethoxybenzyl)amino)quinazolin-2-yl)urea, ~ 45-50% yield) along with derivative **9** (yield ~ 50%) as the hydrolyzed-urea product.[305] To enhance the SAR within the carbonyl-based derivatives, glycinamide was coupled to **5**, via a NAS reaction, to provide derivative **12** (Scheme 7, 2-((4-((3,4-dimethoxybenzyl)amino)quinazolin-2-yl)amino)acetamide, yield ~55%).[299] Interestingly, efforts to replicate the urea-coupling approach with other functional groups, like acetamide or methyl carbamate, proved unsuccessful. A replacement route to C2-acetamide was developed by refluxing **9** with acetyl chloride in acetic acid and 1,4-dioxane to yield *N*-(4-((3,4-dimethoxybenzyl)amino)quinazolin-2-yl)acetamide (**13**, Scheme 7, yield ~ 40%).[312] The acetylation of **9**, via a nucleophilic attack on the acyl chloride, is showcased in Figure 37.

Scheme 7[a]



[a]**Reagents and conditions:** Synthetic routes toward quinazoline-based derivatives **11**-**13**. (a) Urea, 1,4-dioxane, pressure vial, 160–165 °C, 24 h.; (b) glycinamide, DBU, 1,4-dioxane, pressure vial, 150–155 °C, 4 h.; (c) acetyl chloride, acetic acid, 1,4-dioxane, 120 °C, 24 h.

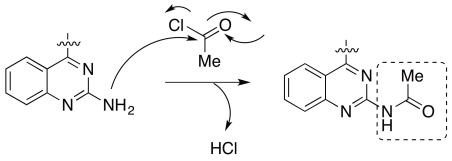
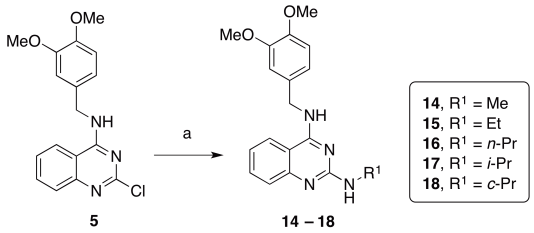


Figure 37: Reaction mechanism toward the generation of N^4-substituted quinazoline-2-acetamide derivatives using acetyl chloride and acetic acid.

The introduction of alkyl moieties at the C2-position of the quinazoline scaffold was established by coupling **5** with various alkylamines (methyl, ethyl, propyl, isopropyl and cycloproply), under previously discussed NAS conditions, to generate derivatives **14-18** (Scheme 8, ~ 60-70% yield).[288, 313, 314]

Scheme 8[a] – Synthetic routes toward quinazoline-based derivatives **14**-**18**.



[a]**Reagents and conditions:** (a) Primary amine (R^1 = Me, Et, *n*-Pr, *i*-Pr or *c*-Pr), DIPEA, 1,4-dioxane, pressure vial 150–155 °C, 2 h.

3.3.2. *Cholinesterase*

The ability of 2-substituted-*N*-(3,4-dimethoxybenzyl)-quinazolin-4-amines (**5**–**18**) to target the cholinesterases (*h*AChE/*h*BuChE) was assessed (Table 1) using the hallmark DTNB method for cholinesterase inhibition.[315] This standard assay was run in triplicate, along with assay controls (Figure 38) and blanks, using six concentrations for the drug candidates (1, 2.5, 5, 10, 25, 50 μM) and the data was processed as an average IC_{50} value of two to three independent experiments.

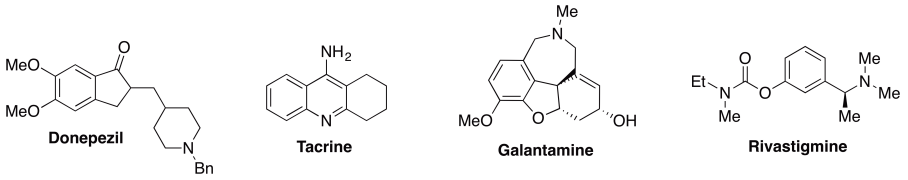
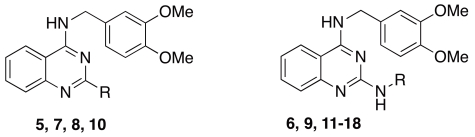


Figure 38: Standards utilized in the DTNB cholinesterase screening protocol. The broad inhibition window ensures representable and reliable data at both ends of the inhibition spectrum.

Table 1: Cholinesterase inhibition data for 2-substituted-*N*-(3,4-dimethoxybenzyl)-quinazolin-4-amines (**5**–**18**).



Derivative	R-Grp	ChE IC_{50} (μM) [a]		SI [b]	ClogP [c]	MV (Å^3) [d]	HBD:HBA [e]
		*h*AChE	*h*BuChE				
5	Cl	3.0 ± 0.2	> 50	–	3.75	213.6	1:5
6	1-BnPpd*	2.1 ± 0.1	8.3 ± 0.9	0.25	5.65	400.2	2:7
7	H	2.8 ± 0.2	> 50	–	1.84	199.6	1:5
8	N_3	8.3 ± 0.7	> 50	–	4.41	262.7	1:7
9	H	2.6 ± 0.2	> 50	–	2.98	209.5	3:6
10	OH	7.7 ± 0.9	> 50	–	3.61	248.3	2:6
11	$CONH_2$	8.6 ± 0.6	> 50	–	3.01	269.2	4:8
12	CH_2CONH_2	7.4 ± 0.8	> 50	–	2.59	289.1	4:8
13	COMe	8.5 ± 0.6	> 50	–	2.53	277.8	2:7
14	Me	7.3 ± 0.5	30.5 ± 4.0	0.24	3.80	218.8	2:6
15	Et	6.3 ± 0.4	25.0 ± 1.2	0.25	4.33	232.8	2:6
16	*n*-Pr	5.6 ± 0.4	30.4 ± 1.7	0.19	4.86	245.5	2:6
17	*i*-Pr	6.8 ± 0.5	29.8 ± 2.0	0.23	4.64	243.8	2:6
18	*c*-Pr	7.2 ± 0.6	29.8 ± 2.5	0.24	4.38	241.8	2:6
Donepezil	–	0.03 ± 0.002	3.6 ± 0.4	0.01	4.59	321.7	0:4
Tacrine	–	0.16 ± 0.01	0.04 ± 0.001	4.00	3.27	165.6	2:2
Galantamine	–	2.6 ± 0.6	> 50	–	1.18	239.4	1:4
Rivastigmine	–	6.5 ± 0.5	> 10	–	2.10	226.3	0:4

Notes: [a] IC_{50} values are an average ± SD of triplicate readings based on two to three independent experiments. [b]Selectivity index is calculated as (*h*AChE IC_{50}) ÷ (*h*BuChE IC_{50}). [c]ClogP values were determined using ChemDraw Professional 15.0. [d]Molecular volumes in Å^3 units were determined using Discovery Studio, Structure-Based Design software, BIOVIA Inc., USA. [e]Showcasing the ratio of HBD = hydrogen-bonding donors to HBA = hydrogen-bonding acceptors. *1-BnPpd = 1-benzylpiperidine.

Examination of Table 1 quickly pointed out the overall weak or no ability of this series to target BuChE (with the exception of **6**). On the other hand, AChE inhibition ranged from 2 to 9 μM placing these derivatives at level playing field with marketed compounds, galantamine and rivastigmine. Starting out with the secondary intermediate (**5**), the C2-chlorine based derivative was equipotent to galantamine in AChE (IC_{50} = 3.0 μM) but was ineffective toward BuChE. Recalling back to Section 2.2, it was interesting to observe derivative **6** (with a C2-aminobenzylpiperidine group) as being the most potent AChEI (IC_{50} = 2.1 μM) in this series, despite its not-so-favourable binding mode within the enzyme. More so, it was the most potent (albeit most active) BuChEI (IC_{50} = 8.3 μM) in the grouping surpassing rivastigmine's activity. Another interesting observation came from the equipotent profiles of **5** and **7** despite the significant change in steric and electrostatic properties at the C2-position.

As predicated earlier, the hindrance associated with the azide functionality did not serve ChE targeting as seen with **8**. Compared to the C2-unsubstituted derivative (**7**), **8** was roughly 3-fold less active toward AChE (IC_{50} = 8.3 μM) and was completely ineffective toward BuChE. Upon reduction of that azide however, AChE activity was restored as seen with derivative **9** (IC_{50} = 2.6 μM). Yet again, the observation of equipotent activity amongst C2-chlorine, C2-hydrogen and C2-amino derivatives might suggest that sterics, more so than electrostatic properties, are more important to ChE targeting with this series. This suggestion was quickly withdrawn with the results observed from **10** (IC_{50} = 7.7 μM), which was roughly 3-fold less active toward AChE compared to the amine-based bioisostere. While a small difference, NMR-studies indicated a considerable variance in the acidity of the protons at the C2-position and that would point to a big difference in the electrostatic properties between **9** and **10**.

With respect to the carbonyl-based series, derivatives **11** – **13** exhibited similar activity toward AChE and it was not a surprise to see them as ineffective toward BuChE. Of the three, the C2-glycinamide derivative (**12**, IC_{50} = 7.4 μM) was first at nearly 0.9-fold more potent compared to the urea (**11**, IC_{50} = 8.6 μM) and acetamide (**13**, IC_{50} = 8.5 μM) derivatives toward AChE.

The introduction of alkylamines at the C2-position established some level of BuChE inhibition, albeit it weak (IC_{50} ~ 30 μM), while AChE activity ranged from IC_{50} 5.6–7.3 μM. Increasing the length of the alkyl chain, from methyl (**14**) to ethyl (**15**) to propyl (**16**), resulted in roughly 1.1-fold incremental improvements in AChE potency (IC_{50} = 7.3 to 6.3 to 5.6 μM; respectively). Increasing the sterics, but not

necessarily the molecular volumes, of the propyl chain in **17** (isopropyl) and **18** (cyclopropyl) reduced potency roughly 1.2-fold in both cases (IC_{50} ~ 7 μM).

In summary, 14 derivatives were assessed for dual cholinesterase activity, of which derivative **6** (N^2-(1-benzylpiperidin-4-yl)-N^4-(3,4-dimethoxybenzyl)quinazoline-2,4-diamine) was identified as the best dual, selective ChEI. This series proved to be ineffective toward BuChE, while providing a decent range of AChE activity IC_{50} < 10 μM (Figure 39).

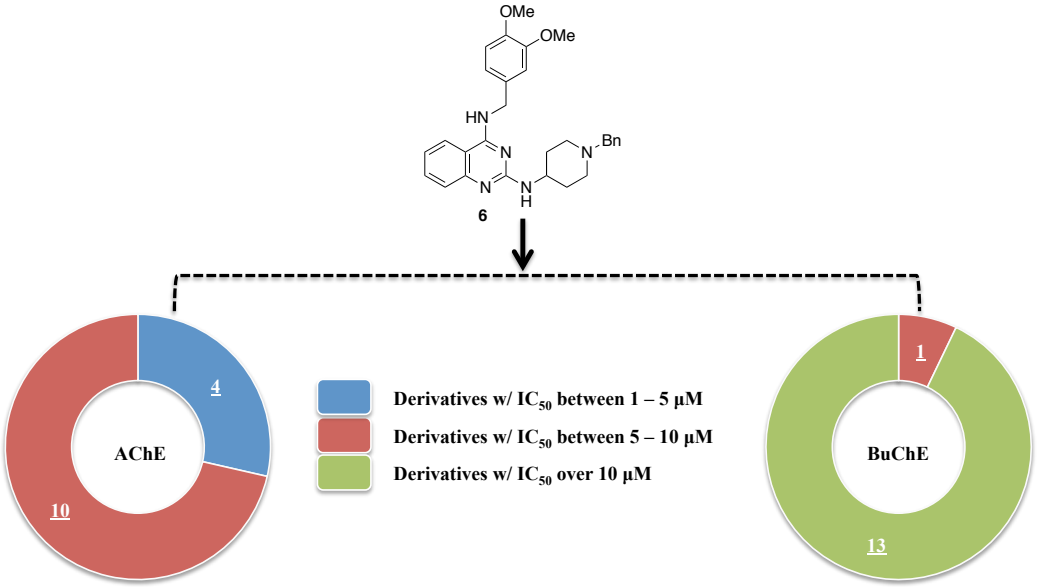


Figure 39: Cholinesterase metrics for fourteen 2-substituted-*N*-(3,4-dimethoxybenzyl)-quinazolin-4-amines (**5**–**18**).

3.3.3. *Amyloid-β Aggregation*

The ability of 2-substituted-*N*-(3,4-dimethoxybenzyl)-quinazolin-4-amines (**5-18**) to modulate the aggregation kinetics of amyloid-β was assessed (Table 2) using the standard ThT-binding method for β-sheet aggregation monitoring.[47, 203, 215, 222, 281, 316-318] This crucial assay was run in triplicate, along with assay controls (Figure 40) and blanks, using three concentrations for the drug candidates (1, 5, 25 μM) and the

data was processed as an average IC_{50} value or percent inhibition (P.I) at 25 μM of two to three independent experiments. Select derivatives were analyzed to establish aggregation kinetic plots to investigation potential modes of action in comparison to assay controls.

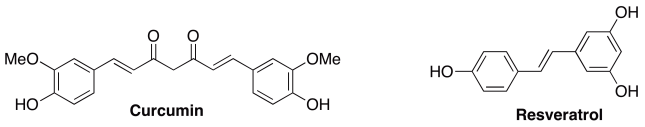
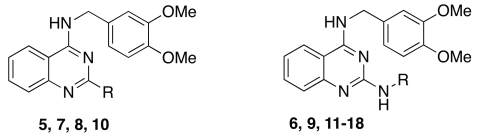


Figure 40: Standards utilized in the ThT-binding assay for β-sheet aggregation monitoring.

Table 2: Amyloid-β (Aβ40/42) inhibition data for 2-substituted-*N*-(3,4-dimethoxybenzyl)-quinazolin-4-amines (**5**–**18**).



Derivative	R-Grp	Amyloid-β IC_{50} (μM) [a]		SI [b]	ClogP [c]	MV (Å^3) [d]	HBD:HBA [e]
		Aβ40	Aβ42				
5	Cl	18%	16%	–	3.75	213.6	1:5
6	1-BnPpd[*]	2.3 ± 0.5	27%	–	5.65	400.2	2:7
7	H	31%	20%	–	1.84	199.6	1:5
8	N_3	7.2 ± 1.5	NA	–	4.41	262.7	1:7
9	H	8.4 ± 1.7	34%	–	2.98	209.5	3:6
10	OH	7.8 ± 1.2	NA	–	3.61	248.3	2:6
11	$CONH_2$	8.3 ± 1.2	40%	–	3.01	269.2	4:8
12	CH_2CONH_2	NA	NA	–	2.59	289.1	4:8
13	COMe	3.1 ± 0.4	NA	–	2.53	277.8	2:7
14	Me	36%	31%	–	3.80	218.8	2:6
15	Et	35%	30%	–	4.33	232.8	2:6
16	*n*-Pr	1.7 ± 0.3	NA	–	4.86	245.5	2:6
17	*i*-Pr	NA	NA	–	4.64	243.8	2:6
18	*c*-Pr	8.3 ± 1.6	20%	–	4.38	241.8	2:6
Curcumin	–	3.3 ± 0.45	9.9 ± 0.4	0.33	4.59	302.1	2:6
Resveratrol	–	1.1 ± 0.1	15.3 ± 1.9	0.07	2.83	187.2	3:3

Notes: [a] IC_{50} values are an average ± SD of triplicate readings based on two to three independent experiments. NA = Not active. Percent inhibition (P.I) indicates level of inhibition at highest concentration tested (25 μM). [b]Selectivity index is calculated as (Aβ40 IC_{50}) ÷ (Aβ42 IC_{50}). [c]ClogP values were determined using ChemDraw Professional 15.0. [d]Molecular volumes in Å^3 units were determined using Discovery Studio, Structure-Based Design software, BIOVIA Inc., USA. [e]Showcasing the ratio of HBD = hydrogen-bonding donors to HBA = hydrogen-bonding acceptors. [*]1-BnPpd = 1-benzylpiperidine.

Examination of Table 2 quickly pointed out the overall ability of this series to dually target Aβ aggregation (9 out of 14 derivatives as dual inhibitors). Inhibitory activity toward Aβ40 was more promising compared to Aβ42 and only two derivatives were completely inactive toward either species (**12** and **17**). When compared to assay controls, none of these derivatives matched curcumin's or resveratrol's activity toward Aβ42; however, three met or surpassed the activity observed by curcumin on Aβ40 aggregation.

Starting out with the compound (**5**), the C2-chlorine based derivative was a weak inhibitor of Aβ40/42 aggregation (P.I at 25 μM was 16%). The presence of a C2-aminobenzylpiperidine group in **6** improved Aβ42 activity by roughly 1.7-fold (P.I at 25 μM was 27%), while inhibition of Aβ40 was remarkably improved and was in between resveratrol and curcumin profiles (IC_{50} = 2.3 μM). The proposed linearity and sterics associated with **6** are likely in play, especially considering the profile of **7** (C2-hydrogen) that exhibited a dramatic loss toward Aβ40 activity (P.I at 25 μM was 30%), while relatively maintaining Aβ42 activity (P.I at 25 μM was 20%).

Despite initial anticipations regarding the azide functionality, it was disappointing to uncover derivative **8**'s moderate activity toward Aβ40 (IC_{50} = 7.3 μM) and ineffectiveness toward Aβ42. The reduction of that azide restored some level Aβ42 activity (**9**, P.I at 25 μM was 34%), while furthering the decline in Aβ40 activity (**9**, IC_{50} = 8.4 μM). Interestingly, comparing **6** and **9** suggested stronger interactions between the C2-amino group of **9** and Aβ42, while the bulkiness of **6** along with the slower aggregation rate of Aβ40, allowed for stronger inhibitory interactions. Replacement of the amino group in **9** with a hydroxyl group in **10** resulted in similar activity toward Aβ40 (**IC_{50}** = 7.8 μM) and inactivity toward Aβ42 – an equipotent profile with azide-based derivative **8**.

With respect to the carbonyl-based derivatives, C2-urea-containing derivative **11** exhibited equipotent activity toward Aβ40 and Aβ42 as **9** (C2-amino), while the gylcinamide derivative (**12**) was inactive on both fronts – Very interesting observation based on an additional methylene group at the C2-position. The acetamide derivative (**13**) on the other hand, while inactive toward Aβ42, it was roughly 3-fold more potent toward Aβ40 (IC_{50} = 3.1 μM) compared to its urea bioisostere (**11**) and amino-based derivative (**9**).

The introduction of alkylamines at the C2-position established some interesting SAR. With either a methyl or an ethyl chain, derivatives **14** and **15** exhibited weak and equipotent dual activity toward Aβ40

and Aβ42 with P.I at 25 μM roughly at 34%). An additional methylene group in **16** (C2 = propylamine) provided the most potent activity toward Aβ40 (IC_{50} = 1.7 μM), while becoming ineffective toward Aβ42. Interestingly, the isopropyl isomer of **16** was totally ineffective toward either species of Aβ, while the cyclopropyl-based derivative (**18**) provided activity toward Aβ40 similar to **9** and **11** (IC_{50} = 8.3 μM), while restoring some Aβ42 activity (P.I at 25 μM was 20%) compared to its other isomers **16** and **17**.

In summary, 14 derivatives were assessed for dual Aβ-aggregation activity, of which derivative **16** (N^4-(3,4-dimethoxybenzyl)-N^2-propylquinazoline-2,4-diamine) was identified the most potent Aβ40 aggregation inhibitor (IC_{50} = 1.7 μM). While most derivatives in this series were ineffective or weak inhibitors toward Aβ42, derivative **11** (1-(4-((3,4-dimethoxybenzyl)amino)quinazolin-2-yl)urea) was identified the most active aggregation inhibitor (P.I at 25 μM was 40%) (Figure 41).

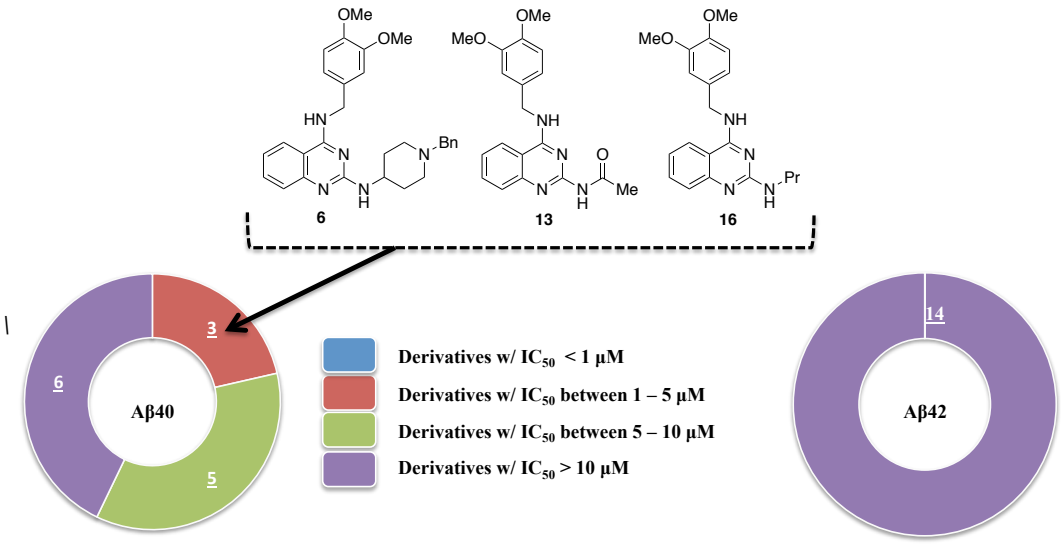


Figure 41: Amyloid-β metrics for fourteen 2-substituted-*N*-(3,4-dimethoxybenzyl)-quinazolin-4-amines (**5**-**18**).

The aggregation kinetic assessment of Aβ40 with or without series-leading derivatives is showcased in Figure 42 (due to the lack of promising data with Aβ42, kinetic assessments were not conducted for this series). As observed with resveratrol (Panel A), derivatives **6** and **16** (Panels B and C; respectively) exhibit concentration-dependent inhibition of Aβ40 aggregation. Both managed to showcase multi-type modulation

of the aggregation process, although they were not necessarily stabilizing the monomeric structure as seen with resveratrol (specifically at 25 µM). This was concluded based on the lag phase timeline that matches the Aβ40-alone curve. Nonetheless, across the three concentrations tested, both derivatives managed to reduce the rate of oligomerization (seen by the decreased slopes between the 10-15 hour mark) and lower the total amyloid load at the experiment's conclusion. In both cases, percent reduction in amyloid load (at the 1:1 ratio) surpassed the 50% mark. Based on the overall kinetic plots, it is evident that derivatives **6** and **16** act upon Aβ40 primarily at the very early stages of oligomerization.

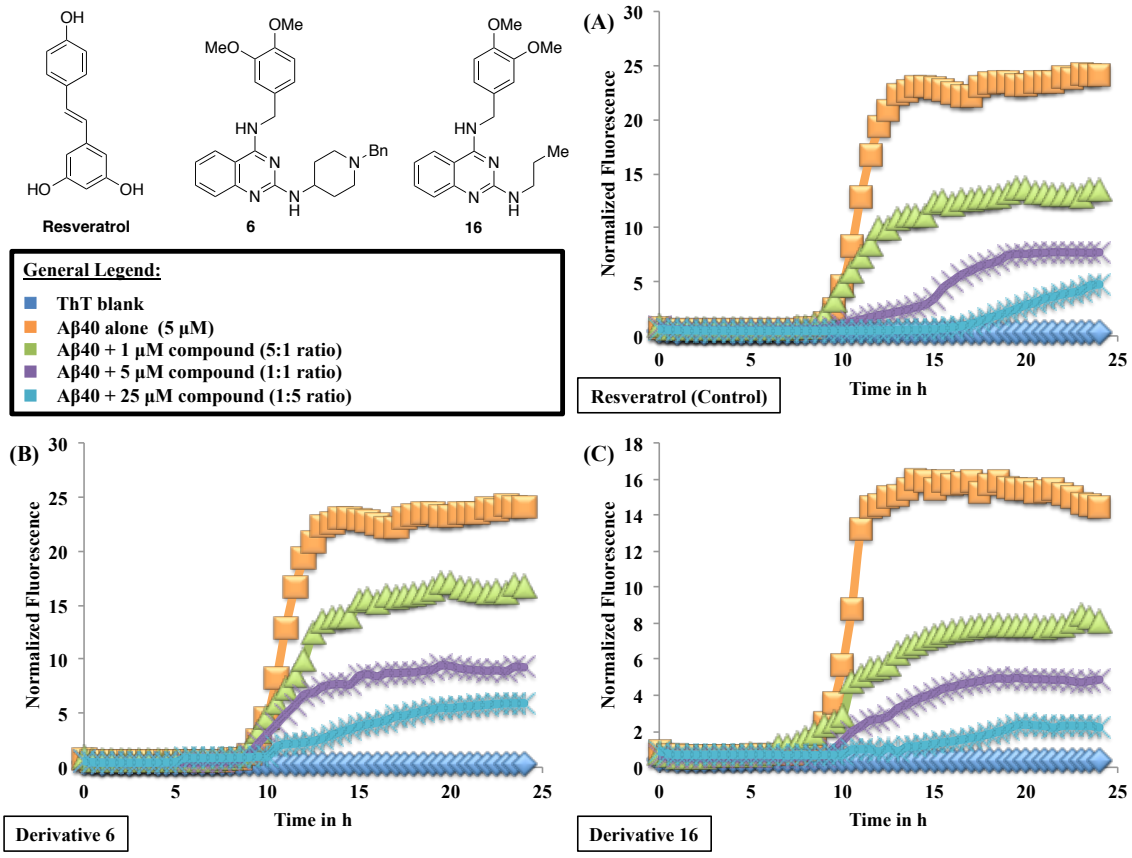


Figure 42: ThT-monitored kinetics of Aβ40 aggregation at 37 °C over a 24 h incubation period at pH 7.4 (Excitation = 440 nm, Emission = 490 nm). Panel (A): Impact of 1, 5 or 25 µM of resveratrol on the aggregation kinetics of 5 µM Aβ40. Panel (B): Impact of 1, 5 or 25 µM of N^2-(1-benzylpiperidin-4-yl)-N^4-(3,4-dimethoxybenzyl)quinazoline-2,4-diamine (**6**) on the aggregation kinetics of 5 µM Aβ40. Panel (C): Impact of 1, 5 or 25 µM of N^4-(3,4-dimethoxybenzyl)-N^2-propylquinazoline-2,4-diamine (**16**) on the aggregation kinetics of 5 µM Aβ40.

3.3.4. *Antioxidant Capacity*

The ability of select 2-substituted-*N*-(3,4-dimethoxybenzyl)-quinazolin-4-amines (**9** and **10**) to neutralize ROS was assessed using a DPPH-scavenging assay.[216, 319-321] This simple assay was run in triplicate (at 50 μM of test compound), along with assay controls (Figure 43), blanks and the data was processed as an average percent DPPH-scavenging at 50 μM of two independent experiments.

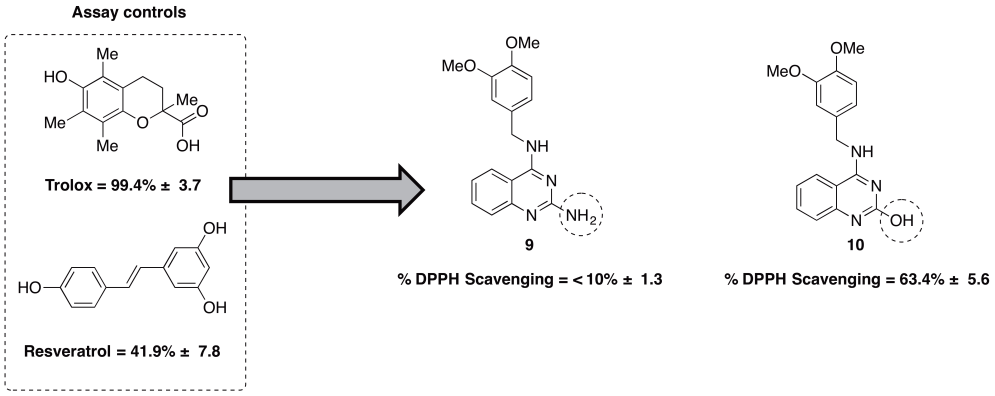


Figure 43: Standards utilized in the DPPH-scavenging along with the data for selective derivatives (**9** and **10**).

As phenolics are typically good antioxidants, especially when connected to conjugated systems, it was no surprise to observe the effectiveness of **10** at scavenging the DPPH radical. Its observed antioxidant capacity was roughly halfway in-between the capacities of resveratrol and trolox (Figure 43). While the amino bioisostere (**9**) is also conjugated, it was ineffective at DPPH-scavenging, which was expected considering the weaker potential of amines at displaying antioxidant capacity.

3.3.5. *Molecular Modeling*

The utilization of computational software is not only useful in structure-based drug design, it is also employed to understand and corroborate the acquired SAR data. The assessment of ligand-receptor

interactions was conducted between leading (or comparable) derivatives from the 2-substituted-*N*-(3,4-dimethoxybenzyl)-quinazolin-4-amine series (**5**–**18**) and the cholinesterase or amyloid targets of interest.

3.3.5.1. *Cholinesterase*

Based on the acquired anti-ChE data, presented in Table 1, the docking interactions of **6** and **9** were investigated in *h*AChE (PBD: 1B41) and superimposed in Figure 44, along with the docking interactions of **6** and **9** in *h*BuChE (PBD: 1P0I).

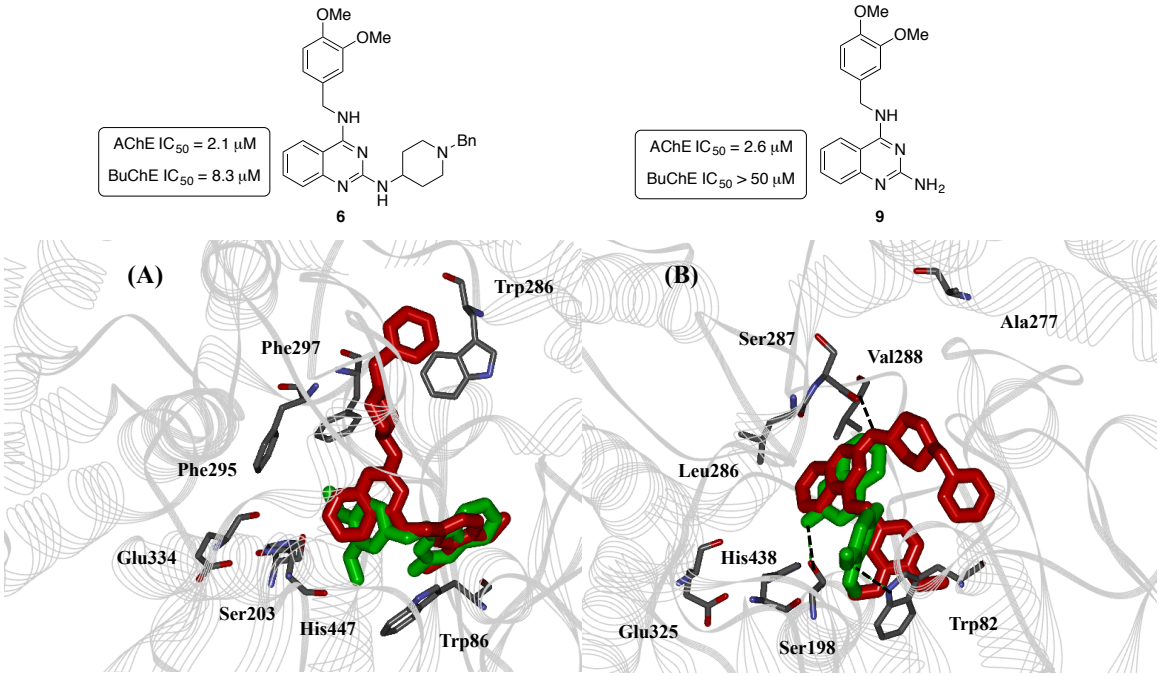


Figure 44: Superimposition of docking structures. Panel (A): Binding modes of **6** (red) and **9** (green) in the active site of *h*AChE (PDB ID: 1B41). Panel (B): Binding modes of **6** (red) and **9** (green) in the active site of *h*BuChE (PDB ID: 1P0I). Hydrogens removed to enhance visibility. Black-dashed lines indicate hydrogen-bonding interactions.

As observed in Panel A, the quinazoline scaffold of **6** was equidistantly oriented between the acyl pocket (F295/F297) and the anionic pocket (W86) at roughly 6 Å. The scaffold was also about 5 Å from the catalytic triad of *h*AChE (S203, E334 and H447). The derivative's C4-dimethoxyphenyl ring was

stacked parallel to W86 with close interactions roughly at 4–5 Å. The benzylpiperidine pharmacophore was pointed toward the PAS (W286), where the piperidine ring was oriented parallel to the acyl pocket (~ 7 Å) and the phenyl ring was stacked parallel to W286 at roughly 5–6 Å. Unlike the proposed binding orientation discussed in Chapter 2, the interactions here was collected after a wider assessment of the binding sphere identified within *h*AChE. In contrast, derivative **9** exhibited a more localized binding mode within the catalytic site as observed with its approximate distance to W286 at roughly 11 Å. The quinazoline scaffold was stacked against W86 at roughly 4–5 Å; however, the stacking was not favourably parallel to the indole ring of W86. The derivative's C4-dimethoxy phenyl ring was oriented toward the catalytic triad and sitting roughly at 6–7 Å from S203 and H447.

With respect to BuChE binding, as observed in Panel B, both derivative **6** and **9** bind with their quinazoline scaffold roughly 12 Å from A277. The scaffolds were perpendicularly stacked against the acyl pocket (L286–V288) at roughly 4–5 Å. Both derivatives' C4-dimethoxyphenyl ring were stacked parallel or semi-parallel to W82 with close interactions roughly at 5–6 Å, while one methoxy oxygen in **9** underwent hydrogen-bonding interactions with W82's indole N*H* (~ 3 Å). The benzylpiperidine pharmacophore in **6** underwent a folding arrangement with the rest of the ligand to point toward W82, allowing for hydrogen-bonding interactions between S286 carbonyl oxygen and **6**'s C2-N*H* (~ 2.8 Å). In contrast, the C2-amino group of **9** underwent hydrogen-bonding interactions with S203's hydroxyl group and H447's imidazole ring (~ 2.6–3 Å).

3.3.5.2. *Amyloid-β*

Based on the acquired anti-Aβ data, presented in Table 2, the docking interactions of **6** and **16** were investigated in both a dimeric and fibril model of Aβ ($A\beta_{9\text{-}40}$ – PDB 2LMN)[322] with superimpositions showcased in Figure 45.

In the dimer model (Panel A), the quinazoline scaffold of **6** was stacked parallel to I32–G33 roughly at 5–6 Å, compared to the perpendicular placement of **16**'s quinazoline scaffold between A21–G22 and I32–G33 on the opposite end (~ 7–8 Å). The C4-dimethoxyphenyl ring of **6** was stacked between F19/F20

of monomer 1 (~ 4–5 Å), while the benzyl ring of the C2-functionality was stacked between D23 and G29 of monomer 2 (~ 4–5 Å). With its larger volume, it was interesting to note the same planar arrangement of the quinazoline scaffold, the dimethoxyphenyl ring and the C2-benzyl ring as opposed to the piperidine ring, which was oriented in a perpendicular plane to the other ring systems. In addition, derivative **6** was capable of full interactions with both monomeric structures in the dimer spanning other regions outside of the hairpin loop domain. With **16**, the C4-dimethoxy phenyl ring was stacked parallel between D23 and A30 (~ 4 Å), while its C2-proply chain was pointed toward F19/F20 (~ 4–6 Å).

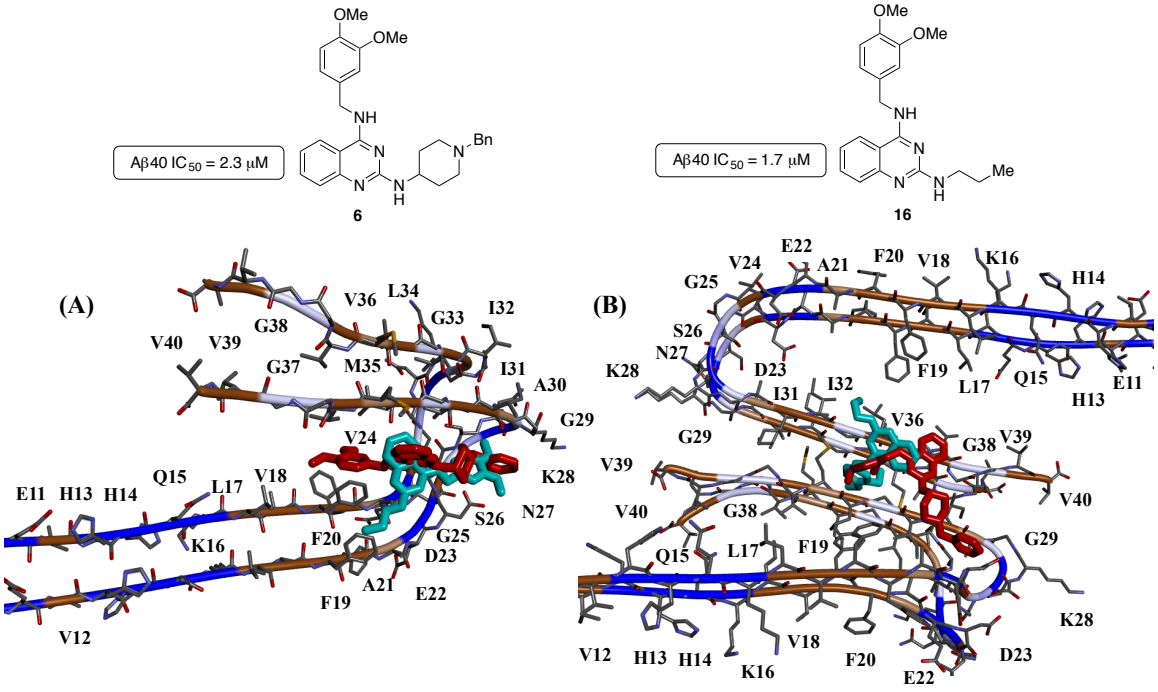


Figure 45: Superimposition of docking structures. Panel (A): Binding modes of **6** (red) and **16** (turquoise) in the Aβ ($Aβ_{9-40}$ – PDB 2LMN) dimer model or fibril model [Panel (B)]. Hydrogens removed to enhance visibility. Amino acid labels to be used as a general guide as space restrictions limited complete and accurate labeling of both structures.

In the fibril model (Panel B), the quinazoline scaffold of **6** was stacked perpendicular to a dimeric pair and exhibited close interactions with M35 and V36 roughly at 6 Å, compared to the parallel arrangement of **16**'s quinazoline scaffold against L34 and M35 (~ 4–5 Å). Both derivatives had their C4-dimethoxyphenyl rings inserted into the steric zipper domain with placement between the M35 residues roughly at 6 Å. The

benzylpiperidine pharmacophore in **6** extended to the second dimeric pair forming an anti-parallel V-shaped arrangement at the hairpin loop domain (N27–I31 ~ 6–8 Å). The propyl chain of **16** pointed inward at I32-L34 roughly at 5–6 Å).

3.4. Summary

Briefly, of the 14 derivatives in this series, all but one proved to be ineffective at targeting BuChE and to a certain extent Aβ42 aggregation. Nonetheless, the series showcased a strong DPPH-radical scavenger in **10** and a resveratrol-equivalent Aβ40 inhibitor in **16**. More so, **6** proved to be a good dual ChEI with good Aβ40 inhibitory potential at equivalent targeting potency with AChE inhibition (Figure 46).

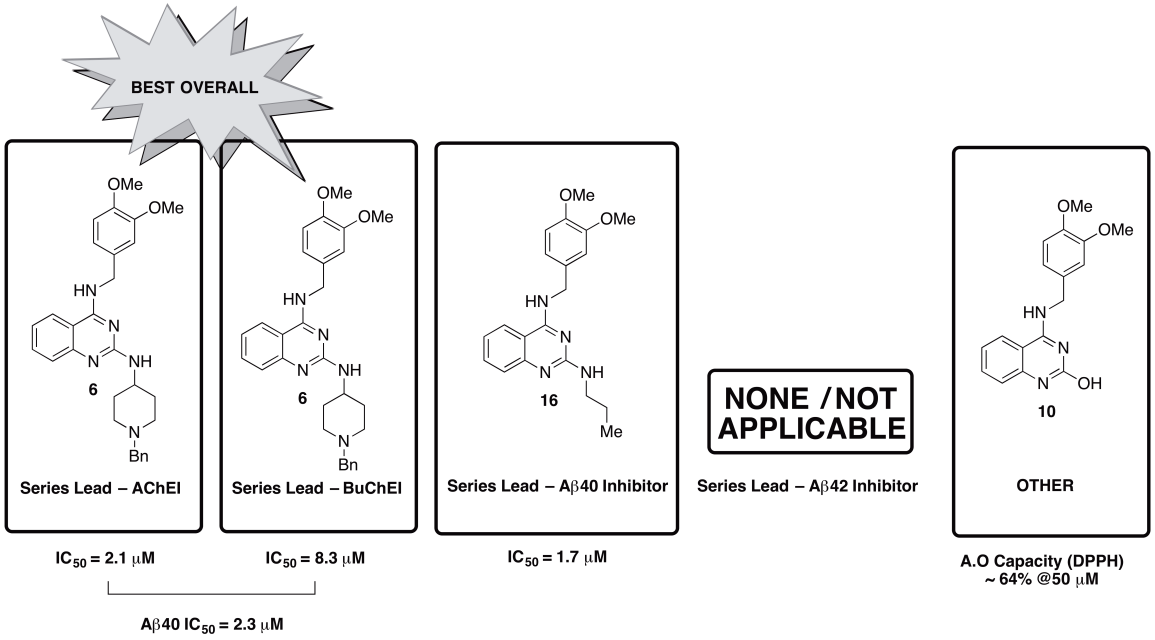


Figure 46: Cumulative chapter summary of 2-substituted-*N*-(3,4-dimethoxybenzyl)-quinazolin-4-amines (**5**–**18**).

3.5. Experimental

3.5.1. *Chemistry*

General Information. All the reagents and solvents were reagent grade purchased from various vendors (Acros Organics, Sigma-Aldrich, and Alfa Aesar, USA) with a minimum purity of 95% and were used without further purification. Melting points (mp) were determined using a Fisher-Johns apparatus and are uncorrected. Reaction progress was monitored by UV using thin-layer chromatography (TLC) using Merck 60F254 silica gel plates. Column chromatography was performed with Merck silica gel 60 (230−400 mesh) with 5:1 EtOAc:MeOH as the solvent system unless otherwise specified. Proton (^{1}H NMR) and carbon (^{13}C NMR) spectra were performed on a Bruker Avance (at 300 and 75 MHz; respectively) spectrometer using DMSO-d_6. Coupling constants (*J* values) were recorded in hertz (Hz) and the following abbreviations were used to represent multiplets of NMR signals: s = singlet, d = doublet, t = triplet, m = multiplet, br = broad. Carbon multiplicities (C, CH, CH_2 and CH_3) were assigned by DEPT 90/135 experiments. High-resolution mass spectrometry (HRMS) was determined using a Thermo Scientific Q-Exactive Orbitrap mass spectrometer (positive mode, ESI), Department of Chemistry, University of Waterloo. Compound purity (roughly 95% or over) was determined using an Agilent 1100 series HPLC equipped with an analytical column (Agilent Zorbax Eclipse XDB-C8 column, 4.6 x 150 mm, 5 μm particle size) running 50:50 Water:ACN with 0.1% TFA at a flow rate of 1.0-1.5 mL/min or an Agilent 6100 series single quad LCMS equipped with an Agilent 1.8 μm Zorbax Eclipse Plus C18 (2.1 x 50 mm) running 50:50 Water:ACN with 0.1% FA with a flow rate of 0.5mL/min. All the final compounds exhibited ≥ 95% purity.

General procedure for the synthesis of compounds 2a or 2b.[314] In a 100 mL RBF, 5 g of **1a** or **1b** (27.62–29.94 mmol) was dissolved in 30 mL of argon-degassed ethanol followed by the addition of 10 mol. % of Pd/C (2.76–2.99 mmol) and 1.5 eq. of hydrazine hydrate (41.44–44.91 mmol). Solution was refluxed at 80–85 °C for 2 h. Upon reaction completion, the hot ethanol solution was passed through dense cotton packing in a 60 mL syringe by washing with ethanol (20 mL x 3). The combined ethanol fractions were

concentrated in vacuo and purified by silica gel column chromatography using 5:1 EtOAc:MeOH as the eluent. Yield ranged from 80–85%.

General procedure for the synthesis of compound 3.[289, 323] In a 100 mL round pressure vial, 8–9 g of urea was heated at 150–155 °C till it melted. To the liquid urea solution 0.1 eq. of **2a** or **2b** (~ 2 g, 13.23-14.59 mmol) was added. The pressure vial was sealed and heated at 150–155 °C for 2 h and cooled to room temperature before adding ~ 50 mL of water and re-heating at 100–105 °C for 1 h. Upon cooling to room temperature, the reaction mixture was diluted with ~ 40 mL of EtOAc and washed brine solution (40 mL x 3). The combined aqueous layers were washed with ~ 25 mL of EtOAc. The combined EtOAc layers were dried over $MgSO_4$ and the EtOAc was removed in vacuo to yield a solid product that did not require further purification. Yield ranged from 75–85%.

General procedure for the synthesis of 4.[289, 323] In a 250 mL RBF, 5 g of **3** (30.84 mmol) was suspended in 25 mL of anhydrous toluene and allowed to stir on an ice bath. To this, 5 eq. of $POCl_3$ (154.18 mmol) was added in small aliquots followed by the slow addition of 5 eq. of DEA (154.18 mmol). The solution was kept on the ice bath for 10 min before moving to room temperature and allowed to stir for 1 h prior to refluxing at 105–110 °C for 14–16 h. Upon cooling to room temperature, the reaction mixture was added in small aliquots to a double-ice-water bath while stirring. The quenching solution was left stirring at room temperature for 5 h before vacuum filtering the yellowish-grey precipitate. The precipitate was stirred for 1 h in a saturated $NaHCO_3$ solution and then was re-filtered. This neutralization process was carried out 2–3 times until the bicarbonate solution maintains a neutral to slight basic pH. The final precipitate was dissolved in DCM and purified by a silica gel column chromatography using 100% DCM as the eluent to afford white to light grey solid.

2,4-Dichloroquinazoline (4). Yield: 80% (4.91 g, 24.77 mmol). Mp 117–119 °C; ^{1}H NMR (DMSO-d_6, 300 MHz) δ 8.20 (d, J = 8.4 Hz, 1 H), 8.08 (td, J = 7.8 Hz, 1.4 Hz, 1 H), 7.94 (d, J = 8.4 Hz, 1 H), 7.81 (td, J = 7.5 Hz, 1.2 Hz, 1 H).

General procedure for the synthesis of 2-chloro-*N*-substituted-quinazolin-4-amines.[303, 305] To a 30 mL solution of ethanol in a 100 mL round-bottom flask on ice, 5 g of **4** (25.13 mmol) was added followed by slow addition of 1.3 eq. (32.66 mmol) of the corresponding primary amine. Contents were stirred on an ice bath while 2.0 eq. of diisopropyl-ethylamine (DIPEA, 50.25 mmol) was added in drop wise fashion. The solution was then heated at 80–85 °C under reflux for 3–4 h. The reaction contents were cooled to room temperature and precipitated residues were vacuum-filtered with ethyl acetate (EtOAc) rinses. The organic supernatant was concentrated in vacuo followed by two rounds of liquid-liquid extraction using EtOAc and saturated brine solution (40–50 mL each respectively). The combined organic layers were dried over MgSO4, evaporated in vacuo and purified (1–2 times) using silica gel column chromatography with 5:1 EtOAc:MeOH as the elution solvent. Final compounds were white to beige solids with yields ranging from 70-90%.

2-Chloro-*N*-(3,4-dimethoxybenzyl)-quinazolin-4-amine (5). Yield: 90% (7.41 g, 22.50 mmol). Mp: 195–197 °C. ^{1}H NMR (300 MHz, DMSO-*d6*) δ 9.17 (t, 5.7 Hz 1H), δ 8.25 (d, J = 8.1 Hz, 1H), δ 7.74 (t, J = 7.6 Hz, 1H), δ 7.57 (d, J = 8.1 Hz, 1H), δ 7.47 (t, J = 7.6 Hz, 1H), δ 7.03 (s, 1H), δ 6.89–6.83 (m, 2H), δ 4.62 (d, J = 5.7 Hz, 2H), δ 3.70 (s, 3H), δ 3.68 (s, 3H). HRMS (ESI) m/z calcd for $C_{17}H_{16}ClN_3O_2$ $[M + H]^+$ 330.0931, found 330.0953. Purity: 97.9%

General procedure for the synthesis of compound 6.[299] In a 50 mL pressure vial (PV), 0.25 g of **5** (0.76 mmol) was dissolved in 5 mL of 1,4-dioxane followed by the addition of 4 eq. (3.03 mmol) of 4-amino-1-benzylpiperidine and 5 eq. of DIPEA (3.78 mmol). Pressure vial was sealed and stirred in an oil bath at 160–165 °C for 6 h. Upon completion and cooling to room temperature, the reaction mixture was diluted with ~ 40 mL of EtOAc and washed two to three times with equal volumes of brine solution. The combined aqueous layers were washed with ~ 25 mL of EtOAc. The combined EtOAc layers were dried

over $MgSO_4$ and the organic solvent was removed in vacuo to yield a solid product which was purified by silica gel column chromatography using 9:1 acetone:MeOH solvent system.

***N*^{2}-(1-Benzylpiperidin-4-yl)-*N*^{4}-(3,4-dimethoxybenzyl)quinazoline-2,4-diamine (6).** Yield: 42% (0.15 g, 0.32 mmol); Mp 127–129 °C. ^{1}H NMR (300 MHz, DMSO-d_6): δ 7.96 (d, J = 8.2 Hz, 1H), δ 7.42 (t, J = 7.8 Hz, 1H), δ 7.28–7.20 (m, 7H), δ 7.02–6.98 (m, 2H), δ 6.85–6.80 (m, 2H), 6.65 (br s, 1H), δ 4.58 (d, J = 5.0 Hz, 2H), δ 3.70–3.66 (m, 6H), δ 3.46 (s, 2H), δ 2.77–2.70 (m, 3H), δ 2.04–2.00 (m, 2H), δ 1.78–1.73 (m, 2H), δ 1.47–1.44 (m, 2H). HRMS (ESI) m/z calcd for $C_{29}H_{34}N_5O_2$ $[M + H]^+$ 485.2634, found 485.2705. Purity: 98.7%

General procedure for the synthesis of *N*^{4}-substituted-quinazolin-4-amines. In a 50 mL round bottom flask (RBF), 0.5 g of 2-chloro-*N*-substituted-quinazolin-4-amine (1.45–1.85 mmol) was dissolved in 20 mL of anhydrous ethanol. While stirring on ice, 10 mol. % of 10% Pd/C was added to reaction mixture followed by the drop-wise addition of 1.3 eq. of hydrazine hydrate. Solution was stirred on ice for 5 min before refluxing for 2 h at 80–85 °C. Upon completion and cooling to room temperature, the reaction mixture was passed through a tightly-packed cotton-filled syringe that has been pre-rinsed with ethanol, to remove the Pd/C catalyst. A 30 mL aliquot of ethanol was used to rinse the syringe. The combined ethanol solutions were evaporated in vacuo, diluted in EtOAc (20 mL) and washed 25 mL x 2 with equal volumes of brine solution. The combined aqueous layers were washed with 15 mL of EtOAc. The combined EtOAc layers were dried over $MgSO_4$, before removing the EtOAc in vacuo to yield a solid or semi-solid crude product that was purified by silica gel column chromatography using 5:1 EtOAc:MeOH solvent system. Final compounds were white to pale yellow solids with yields ranging from 40–47%.

***N*-(3,4-Dimethoxybenzyl)quinazolin-4-amine (7).** Yield 47% (0.21 g, 0.71 mmol); Mp 187–189 °C. ^{1}H NMR (300 MHz, DMSO-d_6): δ 8.69 (br s, 1H), δ 8.42 (s, 1H), δ 8.25 (d, J = 6.0 Hz, 1H), δ 7.71 (t, J = 9.0 Hz, 1H), δ 7.64 (d, J = 6.0 Hz, 1H), δ 7.45 (t, J = 9.0 Hz, 1H), δ 6.99 (s, 1H), δ 6.84 (s, 2H), δ 4.67 (d, J = 6.0 Hz, 2H), δ 3.68 (s, 3H), δ 3.67 (s, 3H). HRMS (ESI) m/z calcd for $C_{17}H_{18}N_3O_2$ $[M + H]^+$ 296.1321, found 296.1392. Purity: 97.3%

General procedure for the synthesis of 2-azido-*N*-substituted-quinazolin-4-amine.[305] In a 50 mL RBF, 2-chloro-*N*-substituted-quinazolin-4-amine (~1.86 mmol), 1.1 eq. NaN_3 (2.05 mmol), 4:1 EtOH (20 mL) and glacial acetic acid (5 mL) were combined and refluxed at 90–95 °C for 2 h with stirring. After cooling, the solution was vacuum-filtered to afford white solids at yields ranging from 80–85%.

2-Azido-*N*-(3,4-dimethoxybenzyl)quinazolin-4-amine (8). Yield 80% (0.41 g, 1.21 mmol); Mp 253–255 °C. ^{1}H NMR (300 MHz, DMSO-d_6): δ 9.34 (br s, 1H), δ 8.52 (d, J = 8.2 Hz, 1H), δ 8.32 (d, J = 8.3 Hz, 1H), δ 7.99 (t, J = 8.0 Hz, 1H), δ 7.73 (t, J = 8.0 Hz, 1H), δ 7.05 (s, 1H), δ 6.93–6.85 (m, 2H), δ 4.74 (d, J = 3.0 Hz, 2H), δ 3.71 (s, 3H), δ 3.67 (s, 3H). HRMS (ESI) m/z calcd for $C_{17}H_{16}N_6O_2$ $[M + H]^+$ 337.1335, found 337.1407. Purity: 98.5%

General procedure for the synthesis of N^4-substituted-quinazolin-2,4-diamine.[305]

Method 1A: In a 100 mL round-bottom pressure vial, 2-chloro-*N*-substituted-quinazolin-4-amine (3.72 mmol) was added along with 20 mol. % of CuI. To that, a mixture of 1,4-dioxane (5 mL) and 30% aqueous ammonia (15 mL) was added at room temperature. The pressure vial was sealed tightly and partially submerged in silicone oil heating at 130–135 °C. Contents were stirred in the pressure vial for 24 h (Note: in the event of pressure leakage, the contents were cooled to room temperature and additional aqueous ammonia, (10 mL) was added, sealed and heating was carried on through the 24 h period). The reaction contents were cooled to room temperature and the solution was diluted with 25 mL EtOAc, washed with saturated brine solution (10 mL x 3), and the aqueous layer was neutralized with dilute HCl, and then re-extracted with 15 mL EtOAc. The organic layers were combined, dried over MgSO4, evaporated in vacuo and purified using silica gel column chromatography with 5:1 EtOAc:MeOH as an initial elution solvent followed by transition to 5:1 EtOAc:MeOH w/ 1% TEA (triethylamine). Final compounds were obtained as white to beige solids with final yields ranging from 20-25%.

Method 1B: In a 100 mL round-bottom pressure vial, 2-chloro-*N*-substituted-quinazolin-4-amine (3.72 mmol) was dissolved and gently heated in 5 mL ethylene glycol. To that, 20 mol. % of Cu_2O and DMEDA were added followed by 20 eq. K_2CO_3 and finally, 40 eq. of 30% aqueous ammonia solution (~15-20 mL).

The pressure vial was sealed tightly, partially submerged in silicone oil and heated at 100–105 °C. Contents were stirred in the pressure vial for 24 h. After the reaction contents were cooled to room temperature, the solution was diluted with 50 mL EtOAc, washed with saturated brine solution (25 mL x 3) and the aqueous layer was neutralized with dilute HCl, and then re-extracted with 25 mL EtOAc. The residue formed was dissolved in methanol (20–25 mL). The EtOAc layers were dried over MgSO4 and evaporated in vacuo. The methanol fraction was dried with molecular sieves before evaporating the methanol in vacuo. Both EtOAc and methanol fractions were combined and purified using silica gel column chromatography with 5:1 EtOAc:MeOH as an initial elution solvent followed by transition to 5:1 EtOAc:MeOH with 1% TEA (triethylamine). Final compounds were obtained as white to beige solids with yields ranging from 35-40%.

Method 2: In a 50 mL round-bottom pressure vial, 2-chloro-*N*-substituted-quinazolin-4-amine (3.72 mmol) was combined with 6 eq. urea (22.32 mmol) and diluted with 10 mL of anhydrous 1,4-dioxane. The pressure vial was sealed tightly and partially submerged in silicone oil heating at 160–165 °C. Contents were stirred in the pressure vial for 24 h. Once the reaction contents were cooled to room temperature, the solution was diluted with 20–25 mL EtOAc. The contents were washed three times with 20 mL saturated brine solution and the aqueous layers were re-extracted twice with 20 mL EtOAc. The organic layers were combined, dried over MgSO4, evaporated in vacuo and purified using silica gel column chromatography with 5:1 EtOAc:MeOH as an initial elution solvent followed by transition to 5:1 EtOAc:MeOH w/ 1% TEA (triethylamine). Final compounds were obtained as white to light beige solids with yields ranging from 50-55%.

Method 3: In a 50 mL round-bottom flask, 2-chloro-*N*-substituted-quinazolin-4-amine (3.72 mmol) was combined with 1.1 eq. NaN_3 (4.09 mmol), before diluting with 4:1 EtOH (20 mL) and glacial acetic acid (5 mL). Flask contents were stirred under reflux at 90–95 °C for 2 h. After cooling the reaction mixture, 10 mol. % of Pd/C (10%) was added followed by slow addition of 1.5 eq. of hydrazine hydrate (5.58 mmol). Flask contents were stirred under reflux at 90–95 °C for an additional two hrs. Once complete, the warm solution was passed through a large, tightly packed cotton syringe with the aid of additional EtOH washes (2 x 20 mL). The ethanolic mixture was evaporated in vacuo. Final compounds were obtained as white to beige solids with yields ranging from 80–85%.

***N*^{4}-(3,4-Dimethoxybenzyl)quinazolin-2,4-diamine (9).** Yield 80% (0.75 g, 2.43 mmol);. Mp: 205-207 °C. ^{1}H NMR (300 MHz, DMSO-*d6*) δ 8.28 (br s, 1H), δ 7.95 (d, *J* = 7.9 Hz, 1H), δ 7.44 (t, *J* = 7.7 Hz, 1H), δ 7.15 (d, *J* = 7.7 Hz, 1H), δ 7.02–6.99 (m, 2H), δ 6.84-6.77 (m, 2H), δ 6.06 (br s, 2H), δ 4.59 (d, *J* = 5.0 Hz, 2H), δ 3.69 (s, 3H), δ 3.67 (s, 3H). HRMS (ESI) m/z calcd for $C_{17}H_{18}N_4O_2$ [M + H]+ 311.1508, found: 311.1502.

General procedure for the synthesis of *N*^{4}-substituted-quinazolin-2-ols. In a 50 mL round bottom flask (RBF), 0.5 g of 2-chloro-*N*-substituted-quinazolin-4-amine (1.45–1.85 mmol) was combined with 1.3 eq. of potassium formate (1.89–2.41 mmol) then dissolved in 20 mL of formic acid. Solution was refluxed for 14–16 h at 120–125 °C. Upon completion and cooling to room temperature, the reaction mixture was diluted with ~ 30 mL of brine solution, ~ 50 mL of saturated $NaHCO_3$ solution before extracting with ~ 25 mL (x 3) of EtOAc and washed with 25 mL (x 3) parts of brine solution. The combined aqueous layers were washed twice with 15 mL of EtOAc. The combined EtOAc layers were dried over $MgSO_4$ before removing the EtOAc in vacuo to yield a solid product that generally did not require additional purification. Additional purification as required, was accomplished by silica gel column chromatography using 5:1 EtOAc:MeOH as the eluent. The compounds were obtained as white solids with yields ranging from 58–70%.

4-((3,4-Dimethoxybenzyl)amino)quinazolin-2-ol (10). Yield 70% (0.33 g, 1.06 mmol); Mp 202–204 °C. ^{1}H NMR (300 MHz, DMSO-*d*$_6$): δ 10.61 (br s, 1H), δ 8.65 (t, *J* = 5.7 Hz, 1H), δ 8.02 (d, *J* = 8.1 Hz, 1H), δ 7.49 (t, *J* = 7.5 Hz, 1H), δ 7.11–7.05 (m, 1H), δ 6.98 (s, 1H), δ 6.88–6.85 (m, 2H), δ 4.58 (d, *J* = 5.6 Hz, 2H), δ 3.70 (s, 3H), δ 3.68 (s, 3H). HRMS (ESI) m/z calcd for $C_{17}H_{18}N_3O_3$ $[M + H]^+$ 312.1270, found 312.1342. Purity: 99.9%

General procedure for the synthesis of *N*^{4}-substituted-quinazolin-2-urea.[305] In a pressure vial, 0.5 g of 2-chloro-*N*-substituted-quinazolin-4-amine (~1.85 mmol) was mixed with 6 eq. urea (~11.2 mmol) and 10 mL of anhydrous 1,4-dioxane, sealed tightly and heated at 160–165 °C in an oil bath for 24 h. After cooling to room temperature, the solution was diluted with 20 mL EtOAc, washed three times with 20 mL

brine solution; the aqueous layers were extracted twice with 20 mL EtOAc. The combined organic layers were dried over $MgSO_4$, evaporated in vacuo and purified using silica gel column chromatography using a combination of 5:1 EtOAc:MeOH and 5:1 EtOAc:MeOH w/ 1% TEA (triethylamine) to afford target compounds as white solids with yields ranging from 45–50% and the hydrolyzed amine compounds as off white solids with yields ranging from 50–55%.

1-(4-((3,4-Dimethoxybenzyl)amino)quinazolin-2-yl)urea (11). Yield 45% (0.24 g, 0.68 mmol); Mp 263–265 °C. ^{1}H NMR (300 MHz, DMSO-d_6): δ 9.06 (br s, 1H), δ 8.80 (br s, 2H), δ 8.11 (d, J = 8.2 Hz, 1H), δ 7.59 (t, J = 7.5 Hz, 1H), δ 7.44 (d, J = 8.2 Hz, 1H), δ 7.23 (t, J = 7.3 Hz, 1H), δ 7.06 (br s, 1H), δ 6.95–6.82 (m, 3H), δ 4.60 (d, J = 5.7 Hz, 2H), δ 3.71 (s, 3H), δ 3.67 (s, 3H). HRMS (ESI) m/z calcd for $C_{18}H_{20}N_5O_3$ $[M + H]^+$ 354.1488, found 354.1560. Purity: 95.5%

General procedure for the synthesis of N^4-substituted-quinazolin-2-glycinamide.[299] In a 50 mL pressure vial, 0.25 g of 2-chloro-*N*-substituted-quinazolin-4-amine (~ 0.83 mmol) was combined with 3 eq. (~ 2.50-mmol) of glycinamide.HCl then dissolved in 5 mL of 1,4-dioxane followed by the addition of 5 eq. of DBU (~ 4.15 mmol). Pressure vial was sealed and stirred in an oil bath at 150–155 °C for 4 h. Upon completion and cooling to room temperature, the reaction mixture was diluted with ~ 40 mL of EtOAc and washed 25 mL (x 3) brine solution. The combined aqueous layers were washed with ~ 25 mL of EtOAc. The combined EtOAc layers were dried over $MgSO_4$ and EtOAc was removed in vacuo to yield solid that was purified by silica gel column chromatography using 5:1 EtOAc:MeOH as the eluent to afford target compounds as pale yellow to brown solids with yields ranging between 52–58%.

2-((4-((3,4-Dimethoxybenzyl)amino)quinazolin-2-yl)amino)acetamide (12). Yield 54% (0.15 g, 0.41 mmol); Mp 164–166 °C. ^{1}H NMR (300 MHz, DMSO-d_6) δ 8.33 (br s, 1H), δ 8.02 (d, J = 8.2 Hz, 1H), δ 7.47 (t, J = 7.5 Hz, 1H), δ 7.23 (d, J = 8.4 Hz, 2H), δ 7.09–7.03 (m, 2H), δ 6.96 (br s, 1H), δ 6.91–6.82 (m, 2H), δ 6.65 (br s, 1H), δ 4.60 (d, J = 5.6 Hz, 2H), δ 3.98 (d, J = 7.1 Hz, 2H), δ 3.70 (s, 3H), δ 3.68 (s, 3H). HRMS (ESI) m/z calcd for $C_{19}H_{22}N_5O_3$ $[M + H]^+$ 368.1644, found 368.1719. Purity: 99.4%

General procedure for the synthesis of N^4-substituted-quinazolin-2-acetamide.[312] In a 50 mL round bottom flask (RBF), 0.5 g of N^4-substituted-quinazolin-2,4-diamine (1.54–2.00 mmol) was dissolved in 15 mL of 1,4-dioxane and 10 mL of glacial acetic acid/acetyl chloride combination (4:1 ratio). Solution was refluxed for 24 h at 90–95 °C. Upon completion and cooling to room temperature, the reaction mixture was diluted with ~ 30 mL of brine solution, ~ 30 mL of concentrated $NaHCO_3$ solution before extracting with ~ 25 mL (x 3) of EtOAc and washed with 25 mL (x 2) brine solution. The combined aqueous layers were washed twice with 15 mL of EtOAc. The combined EtOAc layers were dried over $MgSO_4$ and the organic solvent was removed in vacuo to yield a solid product that generally did not require additional purification. Purification was carried out as required, by silica gel column chromatography using 5:1 EtOAc:MeOH as the eluent to afford target compounds as white solids with yields ranging from 35–42%.

***N*-(4-((3,4-Dimethoxybenzyl)amino)quinazolin-2-yl)acetamide (13).** Yield 55% (0.31 g, 0.88 mmol); Mp 263–265 °C. ^{1}H NMR (300 MHz, DMSO-d_6): δ 9.88 (br s, 1H), δ 8.67 (br s, 1H), δ 8.24 (d, J = 8.0 Hz, 1H), δ 7.64 (t, J = 7.2 Hz, 1H), δ 7.58 (d, J = 9.0 Hz, 1H), δ 7.26 (t, J = 6.0 Hz, 1H), δ 6.87–6.78 (m, 3H), δ 4.63 (d, J = 6.0 Hz, 2H), δ 3.69 (s, 3H), δ 3.67 (s, 3H), δ 2.24 (s, 3H). ESI-MS m/z calcd for $C_{19}H_{21}N_4O_3$ $[M + H]^+$ 353.15, found 353.17. Purity: 99.1%

General procedure for the synthesis of N^4-substituted-N^2-alkyl-quinazolin-2,4-diamine.[299, 313] In a 50 mL pressure vial (PV), 0.25 g of 2-chloro-*N*-substituted-quinazolin-4-amine (~ 0.83 mmol) was combined with 2 eq. (~ 1.66 mmol) of primary amine (methyl-, ethyl-, *n*-propyl-, isopropyl- or cyclopropylamine) then dissolved in 5 mL of 1,4-dioxane followed by the addition of 3 eq. of DIPEA (~ 2.40 mmol). Pressure vial was sealed and stirred in an oil bath at 150–155 °C for 2 h. Upon completion and cooling to room temperature, the reaction mixture was diluted with ~ 40 mL of EtOAc and washed with brine solution (25 mL x 2). The combined aqueous layer was washed with ~ 25 mL of EtOAc. The combined EtOAc layers were dried over $MgSO_4$ before removing EtOAc in vacuo to yield a solid product that was purified by silica gel column chromatography using 5:1 EtOAc:MeOH as the eluent to afford pale yellow to brown solids yielding at 55–70%.

***N*⁴-(3,4-Dimethoxybenzyl)-*N*²-methylquinazoline-2,4-diamine (14).** Yield 68% (0.33 g, 1.02 mmol); Mp 199–201 °C. ^{1}H NMR (300 MHz, DMSO-d_6): δ 8.23 (br s, 1H), δ 8.01 (d, J = 8.0 Hz, 1H), δ 7.41 (t, J = 7.2 Hz, 1H), δ 7.21 (m, 2H), δ 6.95 (t, J = 6.0 Hz, 1H), δ 6.84–6.80 (m, 2H), δ 6.50 (br s, 1H), δ 4.58 (d, J = 6.0 Hz, 2H), δ 3.68 (s, 3H), δ 3.66 (s, 3H), δ 2.77 (d, J = 4.5 Hz, 3H). HRMS (ESI) m/z calcd for $C_{18}H_{21}N_4O_2$ $[M + H]^+$ 325.1586, found 325.1659. Purity: 97.6%

***N*⁴-(3,4-Dimethoxybenzyl)-*N*²-ethylquinazoline-2,4-diamine (15).** Yield 67% (0.36 g, 1.06 mmol); Mp 186–188 °C. ^{1}H NMR (300 MHz, DMSO-d_6): δ 8.25 (br s, 1H), δ 7.95 (d, J = 8.0 Hz, 1H), δ 7.41 (t, J = 7.2 Hz, 1H), δ 7.20–7.18 (m, 1H), δ 7.00–6.95 (m, 2H), δ 6.84–6.72 (m, 2H), δ 6.40 (br s, 1H), δ 4.59 (d, J = 6.0 Hz, 2H), δ 3.68 (s, 3H), δ 3.66 (s, 3H), δ 3.24–3.19 (m, 2H), δ 1.06 (t, J = 7.0 Hz, 3H). HRMS (ESI) m/z calcd for $C_{19}H_{23}N_4O_2$ $[M + H]^+$ 339.1743, found 339.1817. Purity: 98.8%

***N*⁴-(3,4-Dimethoxybenzyl)-*N*²-propylquinazoline-2,4-diamine (16).** Yield 65% (0.34 g, 0.97 mmol); Mp 156–158 °C. ^{1}H NMR (300 MHz, DMSO-d_6): δ 8.20 (br s, 1H), δ 7.90 (d, J = 8.0 Hz, 1H), δ 7.40 (t, J = 7.2 Hz, 1H), δ 7.15 (d, J = 9.0 Hz, 1H), δ 7.05–6.95 (m, 2H), δ 6.82-6.74 (m, 2H), δ 6.50 (br s, 1H), δ 4.58 (d, J = 6.0 Hz, 2H), δ 3.68 (s, 3H), δ 3.66 (s, 3H), δ 3.24–3.19 (m, 2H), δ 1.46 (q, J = 7.0 Hz, 2H), δ 0.80 (t, J = 7.0 Hz, 3H). HRMS (ESI) m/z calcd for $C_{20}H_{25}N_4O_2$ $[M + H]^+$ 353.1899, found 353.1927. Purity: 98.9%

***N*⁴-(3,4-Dimethoxybenzyl)-*N*²-isopropylquinazoline-2,4-diamine (17).** Yield 68% (0.36 g, 1.02 mmol); Mp 177–179 °C. ^{1}H NMR (300 MHz, DMSO-d_6): δ 8.21 (br s, 1H), δ 7.95 (d, J = 8.0 Hz, 1H), δ 7.39 (t, J = 7.2 Hz, 1H), δ 7.20 (d, J = 9.0 Hz, 1H), δ 7.02–6.95 (m, 2H), δ 6.84–6.72 (m, 2H), δ 6.20 (br s, 1H), δ 4.58 (d, J = 6.0 Hz, 2H), δ 4.10–4.05 (m, 1H), δ 3.68 (s, 3H), δ 3.66 (s, 3H), δ 1.07 (d, J = 6.0 Hz, 6H). HRMS (ESI) m/z calcd for $C_{20}H_{25}N_4O_2$ $[M + H]^+$ 353.1899, found 353.1926. Purity: 98.6%

***N*²-Cyclopropyl-*N*⁴-(3,4-dimethoxybenzyl)quinazoline-2,4-diamine (18).** Yield 70% (0.37 g, 1.06 mmol); Mp 201–203 °C. ^{1}H NMR (300 MHz, DMSO-d_6): δ 8.20 (br s, 1H), δ 7.85 (d, J = 8.0 Hz, 1H), δ

7.40 (t, *J* = 7.2 Hz, 1H), δ 7.20 (d, *J* = 9.0 Hz, 1H), δ 7.00–6.97 (m, 2H), δ 6.84-6.70 (m, 2H), δ 6.60 (br s, 1H), δ 4.59 (d, *J* = 6.0 Hz, 2H), δ 3.67 (s, 3H), δ 3.66 (s, 3H), δ 2.46–2.42 (m, 1H), δ 0.63–0.58 (m, 2H), δ 0.48–0.41 (m, 2H). HRMS (ESI) m/z calcd for $C_{20}H_{23}N_4O_2$ $[M + H]^+$ 351.1743, found 351.1816. Purity: 98.2%

3.5.2. *Biological Screening*

3.5.2.1. *Human Cholinesterase (hChE) Assay*[299, 313]

The inhibition profile of quinazoline derivatives was evaluated using the Ellman (DTNB) reagent.[315] Human AChE and BuChE enzymes were obtained from Sigma-Aldrich, St. Louis, MO, USA (AChE product number C0663 and BuChE product number B4186 respectively). The cholinesterase inhibitors tacrine (item number 70240, Cayman Chemical Company, Ann Arbor, MI), donepezil (product number D6821, Sigma-Aldrich, St. Louis, MO), galantamine (product number G1660, Sigma-Aldrich, St. Louis, MO) and rivastigmine (product number SML0881, Sigma-Aldrich, St. Louis, MO) were used as reference agents. Quinazoline derivative stock solutions were prepared in DMSO (maximum 1% v/v in final wells) and diluted in buffer solution (50 mM Tris.HCl, pH 8.0, 0.1 M NaCl, 0.02 M $MgCl_2.6H_2O$). Then 160 µL of 5,5'-dithiobis(2-nitrobenzoic acid) (1.5 mm DTNB), 50 µL of *h*AChE (0.22 U/mL in 50 mM Tris.HCl, pH 8.0, 0.1% w/v bovine serum albumin, BSA) or 50 µL of *h*BuChE (0.12 U/mL in 50 mM Tris.HCl, pH 8.0, 0.1% w/v BSA) were added to 96–well plates after which 10 µL each of quinazoline derivatives (final concentration range 0.1–50 µM) were added and incubated for 5 min. Then 30 µL of either acetylthiocholine iodide (15 mM AThCl prepared in ultra pure water) or *S*-butyrylthiocholine iodide (15 mM BThCI prepared in ultra pure water) were added.

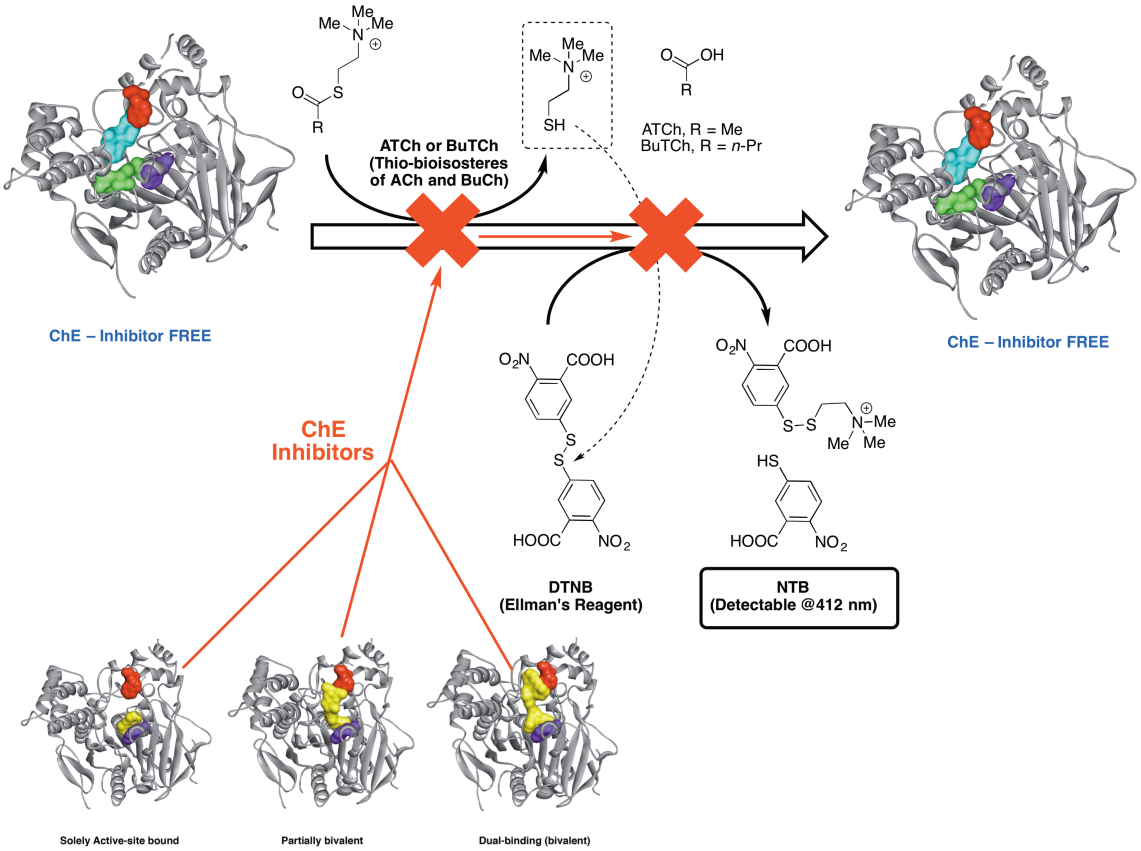


Figure 47: Principles of the DTNB-assay for assessing ChE inhibition by target quinazoline derivatives.

The absorbance was measured at different time intervals (0, 60, 120, 180, 240 and 300 s) using a wavelength of 412 nm. The inhibitory concentration (IC_{50} values) was calculated from the concentration–inhibition dose response curve on a logarithmic scale. The results were expressed as average values based on two to three independent experiments run in triplicate measurements.

3.5.2.2. *Amyloid-β (Aβ) Aggregation Assay*[317]

The ability of quinazoline-based derivatives to inhibit Aβ-aggregation kinetics was determined using a ThT-binding fluorescence assay. These assays were conducted in Costar, black-surround, clear-bottom

384–well plates with frequent shaking (30 sec. of linear shaking at 730 cpm every 5 minutes) and constant heating at 37 °C for 24 h. The ThT excitation/emission was measured at 440 nm/490 nm and readings were taken every 5 minutes using a BioTek Synergy H1 microplate reader. Quinazoline stock solutions were prepared in DMSO and diluted to 10x in 215 mM phosphate buffer at pH 7.4. Abeta.HFIP samples (Aβ40 or Aβ42, rPeptide, Bogart, USA) were dissolved in 1% ammonium hydroxide, sonicated at room temperature for 5 minutes then diluted to 50 µM in 215 mM phosphate buffer (pH 7.4). A 15 µM ThT stock solution was prepared with 50 mM glycine and adjusted to pH 7.4. The assay was carried out by adding 44 µL ThT, 20–35 µL buffer, 1 µL DMSO (for background and controls only) followed by the addition of 8 µL of 10x compound dilutions (1–25 µM concentration range). An end point reading was conducted to evaluate potential test compound interference with ThT-fluorescence before adding 8 µL of Aβ40 or Aβ42 stock solutions (5 µM final concentration). Plates were sealed with a transparent plate film before initiating the assay. RFU values were corrected for ThT-interference before calculating end point percent inhibitions or IC_{50} values and obtaining the aggregation kinetic plots. Data presented was an average of triplicate reading for two-three independent experiments.

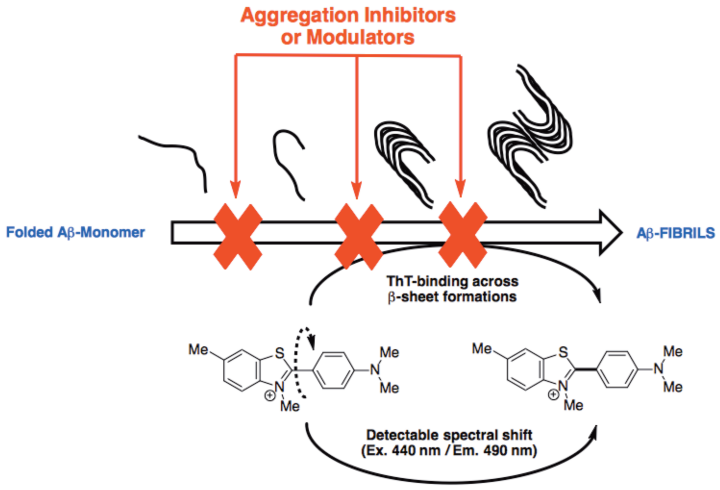


Figure 48: Principles of the ThT assay for assessing Aβ-aggregation inhibition by target quinazoline derivatives.

3.5.2.3. *DPPH Scavenging Assay*[324]

The ability of select quinazolines to scavenge the DPPH radical was utilized as a measure of antioxidant capacity, compared to trolox as the assay control. Quinazoline stock solutions were prepared in anhydrous methanol (500 µM) and the DPPH solution was also prepared in anhydrous methanol (56 µM). The addition sequence was carried out in a 96–well clear, flat bottom plate as follows: 90 µL DPPH, 10 µL test compound solution (50 µM) final concentration. Control solutions contained 90 µL anhydrous methanol and 10 µL test compound whereas DPPH control contained 90 µL of DPPH, and 10 µL anhydrous methanol. This readings were taken initially at 517 nm with 30 sec. shaking (double orbital at 530 cpm) prior to the 1 h, light restrictive, incubation period at room temperature after which readings were taken again at 517 nm after another round of 30 sec shaking (double orbital at 530 cpm) using a BioTek Synergy H1 microplate reader. The results were expressed as percentage inhibition and the data presented was an average of triplicate reading (for two independent experiments).

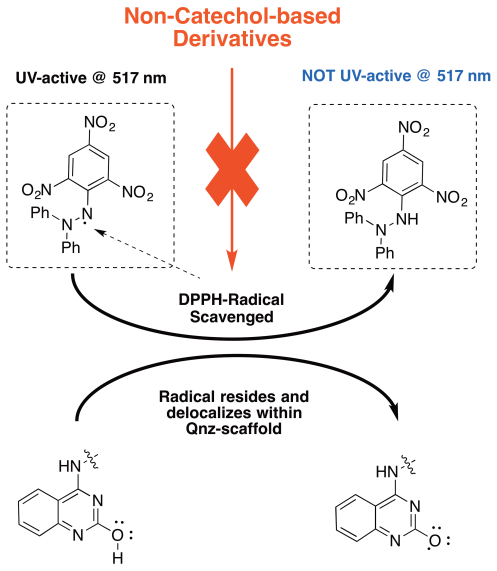


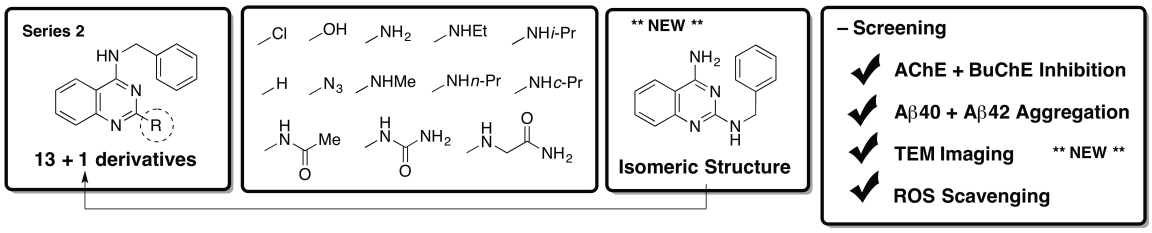
Figure 49: Principles of the DPPH-scavenging assay for assessing antioxidant capacity for select quinazolines.

3.5.3. *Computational Chemistry*[299, 313, 317, 324]

The molecular docking studies were conducted using Discovery Studio 4.0 (Structure-Based-Design program) from BIOVIA Inc. San Diego, USA. Select quinazolines derivatives were built and minimized using the *small molecules* module in Discovery Studio. X-ray coordinates of human cholinesterases were obtained from the protein data bank (*h*AChE PBD ID: 1B41 and *h*BuChE PDB ID: 1P0I) and prepared using the *macromolecules* module in Discovery Studio. Ligand binding sites were defined by selecting a 12 Å radius sphere for AChE and 15 Å radius sphere for BuChE. The molecular docking was performed using the *receptor-ligand interactions* module in Discovery Studio. The LibDock algorithm was used to find the most appropriate binding modes for select quinazoline derivatives using CHARMm force field. The docked poses obtained were ranked based on the LibDock scores and were analyzed by evaluating all the polar and nonpolar interactions. For amyloid-β docking studies, the NMR solution structure of Aβ fibrils were obtained from the protein data bank (PDB ID: 2LMN). Aβ dimer and Aβ fibril assemblies were built using the *macromolecules* module in Discovery Studio. Ligand binding site was defined by selecting a 15 Å radius sphere for both Aβ assemblies. Molecular docking was performed using the *receptor-ligand interactions* module in Discovery Studio, where the LibDock algorithm was used to find the most appropriate binding modes for select quinazoline derivatives using CHARMm force field. The docked poses obtained were ranked based on the LibDock scores and were analyzed by evaluating all the polar and nonpolar interactions.

CHAPTER 4

• Development and Evaluation of *N*-benzylquinazolin-4-amines as Dual ChE and Aβ Aggregation Inhibitors •



* Chapter banner

4.1. Introduction

The dimethoxybenzyl series (see Chapter 3) provided good insight into the requirements and restrictions toward the dual targeting of the ChEs and Aβ aggregation. While the presence of the benzylpiperidine moiety in **6** proved beneficial to that series, further exploration of the smaller C2-groups was desired. A new aspect is briefly introduced in this Chapter and that is the evaluation of a monosubstituted quinazoline-2,4-diamine regioisomer (Chapter 8 contains a larger degree of SAR pertaining to the regioisomer assessment).

This chapter highlights the synthesis and development of target derivatives (refer to the chapter banner above) along with the acquisition and assessment of the SAR data. For the most part, the synthetic approaches and mechanisms here have been previously discussed in Chapter 3. A brief summary is provided prior to the listing of experimental data and methodology.

4.2. Hypothesis

With respect to this series, the absence of the 3,4-dimethoxy moiety should reduce structural hindrance at the C4-position; however, the limited points of rotation connecting the phenyl ring and the quinazoline scaffold still exist. While the absence of the 3,4-dimethoxy moiety might benefit ChE targeting

(especially BuChE), it may reduce potential hydrogen bonding with Aβ structures impacting the modulation of amyloid aggregation.

On the other hand, continuing with the existing selection of C2-groups offers an opportunity to evaluate and compare the impact of the 3,4-dimethoxy moiety at the C4-position. Previous predications hold true with entities like the azide and carbonyl-based groups with respect to their inability to target BuChE. The reduced sterics at the C4-position, combined with alkylamines at the C2-posiiton, are predicted to improve BuChE inhibition, while effectively targeting AChE and modulating amyloid aggregation.

Lastly, the regioisomer comparison is likely to produce split observations with regards to dual ChE and amyloid aggregation targeting, primarily due to the conformational differences that each isomer takes on in the target of interest.

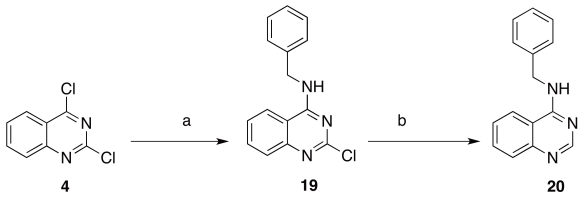
4.3. Results and Discussions

The proceeding sub-chapter discusses new synthetic methodology, while briefly highlighting previously-established routes to desired derivatives. Biological assessments in the cholinesterase and amyloid-β aggregation assay (to obtain IC_{50} values and/or investigation aggregation kinetics) are conducted. Aggregate load is corroborated via transmission electron microscopy in amyloid morphology screening and select derivatives were assessed for ROS scavenging in the DPPH assay. Computational studies were performed in the ChE X-ray structures and amyloid models to evaluate the acquired SAR data.

4.3.1. *Synthesis*

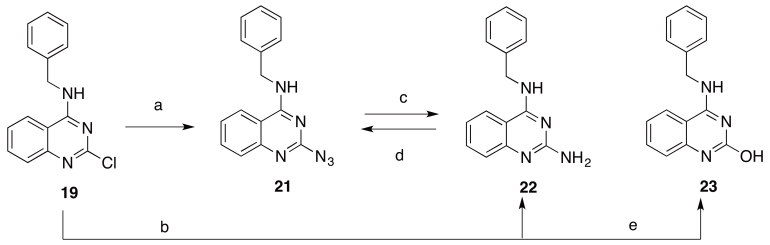
As similarly described in Chapter 3, initial coupling in this series utilized 2,4-DCQ (**4**), to add the unsubstituted benzylamine group to the C4-position of the quinazoline scaffold, via a NAS reaction, to yield *N*-(benzyl)-2-chloroquinazolin-4-amine (**19**, Scheme 9, 80–85% yield).[299, 303] The C2-unsubstituted derivative (*N*-benzylquinazolin-4-amine, **20**, Scheme 9, ~ 45% yield) was also synthesized via the Pd/C and hydrazine-driven dehalogenation reaction.[304]

Scheme 9[a]



[a]**Reagents and conditions:** Synthetic routes toward quinazoline-based derivatives **19** and **20**. (a) Benzylamine, DIPEA, EtOH, reflux, 4 h; (b) Pd/C, hydrazine hydrate, EtOH, reflux, 2 h.

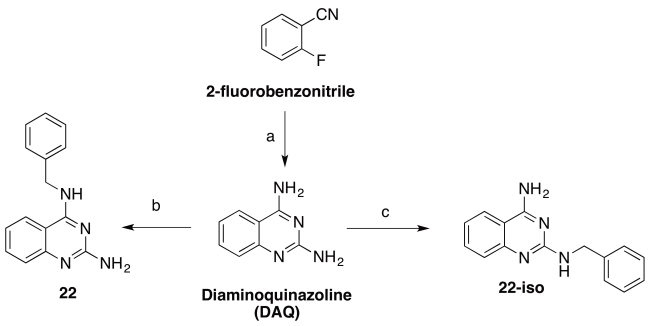
Scheme 10[a]



[a]**Reagents and conditions:** Synthetic routes toward quinazoline-based derivatives **21-23.** (a) Sodium azide, EtOH, acetic acid, 90–95 °C, 2 h; (b) Cu_2O, K_2CO_3, DMEDA, ethylene glycol, ammonium hydroxide, pressure vial, oil bath, 105 °C, 24 h; (c) Pd/C, hydrazine hydrate, EtOH, reflux, 2 h; (d) HCl, sodium nitrite, sodium azide, 0 °C–r.t., 1 h; (e) potassium formate, formic acid, 120–125 °C, 14–16 h.

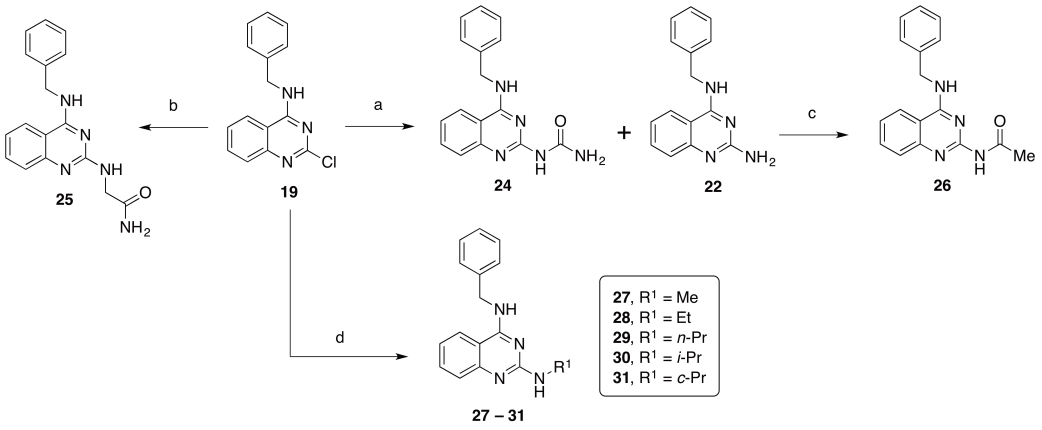
Synthesis of 2-azido-*N*-benzylquinazolin-4-amine (**21**, Scheme 10, ~ 90% yield) was accomplished as previously described utilizing sodium azide,[305, 306] while the generation of the C2-amino derivative (**22**, Scheme 10, N^4-benzylquinazoline-2,4-diamine) was primarily conducted using the azide reduction approach via Pd/C and hydrazine.[305] The effective formate/formic acid approach was utilized to generate **23** (4-(benzylamino)quinazolin-2-ol, Scheme 10, yield ~ 65%).

Scheme 11[a]



[a]**Reagents and conditions:** Synthetic routes toward quinazoline-based derivatives **22** and **22-iso.** (a) Guanidine carbonate, DMA, 150–155 °C, 14–16 h; (b) Sodium hydride, DMSO, benzyl bromide, 0 °C–r.t., 14 h; (c) DMA, potassium or cesium carbonate, benzyl bromide 80–85 °C, 5 h.

Scheme 12[a]



[a]**Reagents and conditions:** Synthetic routes toward quinazoline-based derivatives **24-31**. (a) Urea, 1,4-dioxane, pressure vial, 160–165 °C, 24 h.; (b) glycinamide, DBU, 1,4-dioxane, pressure vial, 150–155 °C, 4 h.; (c) acetyl chloride, acetic acid, 1,4-dioxane, 120 °C, 24 h.; (d) Primary amine (R^1 = Me, Et, *n*-Pr, *i*-Pr or *c*-Pr), DIPEA, 1,4-dioxane, pressure vial 150–155 °C, 2 h.

An alternate route to the synthesis of C2-amino derivatives, along with their C4-amino regioisomers, came from the utilization of 2,4-diaminoquinazoline (**DAQ**, Scheme 11). The generation of DAQ was accomplished by condensing 2-fluorobenzonitrile with guanidine carbonate in a similar fashion used to

condense urea with 2-aminobenzoic acid (Chapter 2, Figure 30). The selective alkylation of **DAQ** at the C4-position (**22**) was accomplished by utilizing sodium hydride, at equal equivalence with **DAQ**, to selectively deprotonate the C4-amino group before nucleophilic attack on the aryl bromide. For selective alkylation at the C2-position (**22-iso**) on the other hand, an inorganic quenching base was used and the more nucleophilic C2-amino group acted upon the aryl bromide, without deprotonation, to displace the halogen.[291, 317] The development of both the C2-carbonyl based derivatives **24** (C2 = urea), **25** (C2 = glycinamide), **26** (C2 = acetamide) and the C2-alkylamine based derivatives (**27**–**31**) (Scheme 12) was accomplished as previously described in Chapter 3.

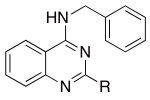
4.3.2. *Cholinesterase*

The ability of 2-substituted-*N*-benzylquinazolin-4-amines (**19**–**31**) and the C4-amino regiosiomer (**22-iso**) to target the cholinesterases (*h*AChE/*h*BuChE) was assessed using the DTNB method as described in Chapter 3 (Table 3).[315]

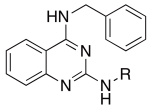
Examination of Table 3 generally pointed to the overall ability of most derivatives within this series to target BuChE. While anti-BuChE activity was not necessarily promising, it did support the hypothesis regarding the reduced sterics and polarity associated with this series and how that would benefit BuChE targeting overall. With respect to AChE targeting, IC_{50} values ranged from 5 to 14 μM and benzyl-based derivatives were, generally, less potent compared to their 3,4-dimethoxybenzyl counterparts (Chapter 3, Table 1).

Starting out with the C2-chlorine based derivative, **19** was roughly 2.5-fold less potent toward AChE (IC_{50} = 7.5 μM) compared to **5** and it was also ineffective toward BuChE. Dechlorination of **19** slightly improved AChE targeting by roughly 1.3-fold (**20**, IC_{50} = 5.8 μM); however it was also 2-fold less potent compared to its dimethoxybenzyl counterpart (**7**, Chapter 3). As expected, **20** was also ineffective toward BuChE. The azide functionality in this series (**21**) was more detrimental to AChE targeting, resulting in the least active AChEI (IC_{50} = 14.0 μM), which was also ineffective toward BuChE and roughly 1.8-fold less active compared to **8** (the dimethoxybenzyl counterpart, Chapter 3).

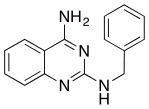
Table 3: Cholinesterase inhibition data for 2-substituted-*N*-benzylquinazolin-4-amines (**9-31**) and the C4-amino regiosiomer (**22-iso**).



19–21, 23



22, 24–31



22-iso

Derivative	R-Grp	ChE IC_{50} (μM) [a]		SI [b]	ClogP [c]	MV (Å^3) [d]	HBD:HBA [e]
		*h*AChE	*h*BuChE				
19	Cl	7.5 ± 0.8	> 50	–	4.09	174.5	1:3
20	H	5.8 ± 0.4	> 50	–	3.33	158.1	1:3
21	N_3	14.0 ± 1.1	> 50	–	4.75	210.6	1:5
22	H	5.0 ± 0.7	30.1 ± 4.0	0.17	3.32	163.9	3:4
22-iso	–	7.5 ± 0.8	11.6 ± 1.3	0.65	3.32	195.5	3:4
23	OH	9.8 ± 0.6	> 50	–	3.95	199.6	2:4
24	$CONH_2$	8.3 ± 0.9	> 50	–	3.35	221.2	4:6
25	CH_2CONH_2	7.2 ± 0.7	> 50	–	2.78	241.1	4:6
26	COMe	7.5 ± 0.5	> 50	–	2.87	228.4	2:5
27	Me	8.0 ± 0.5	18.8 ± 1.5	0.43	4.14	176.9	2:4
28	Et	7.5 ± 0.6	15.2 ± 1.0	0.49	4.67	186.5	2:4
29	*n*-Pr	7.8 ± 0.9	14.4 ± 0.9	0.54	5.20	205.1	2:4
30	*i*-Pr	6.4 ± 0.5	11.7 ± 0.8	0.55	4.98	198.5	2:4
31	*c*-Pr	6.6 ± 0.4	22.0 ± 1.6	0.30	4.73	200.9	2:4
Donepezil	–	0.03 ± 0.002	3.6 ± 0.4	0.01	4.59	321.7	0:4
Tacrine	–	0.16 ± 0.01	0.04 ± 0.001	4.00	3.27	165.6	2:2
Galantamine	–	2.6 ± 0.6	> 50	–	1.18	239.4	1:4
Rivastigmine	–	6.5 ± 0.5	> 10	–	2.10	226.3	0:4

Notes: [a] IC_{50} values are an average ± SD of triplicate readings based on two to three independent experiments. [b]Selectivity index is calculated as (*h*AChE IC_{50}) ÷ (*h*BuChE IC_{50}). [c]ClogP values were determined using ChemDraw Professional 15.0. [d]Molecular volumes in Å^3 units were determined using Discovery Studio, Structure-Based Design software, BIOVIA Inc., USA. [e]Showcasing the ratio of HBD = hydrogen-bonding donors to HBA = hydrogen-bonding acceptors.

Reducing the azide to yield **22** generated the most active AChEI in this series (IC_{50} = 5.0 μM), although it was 2-fold less potent compared to the dimethoxy counterpart in Chapter 3 (**9**). That said, **22** was the first derivative in this series to mildly target BuChE (IC_{50} ~ 30 μM) – a characteristic not seen with **9**. The assessment of **22**'s regiosiomer revealed an interesting observation where **22-iso** lost 33 % of AChE inhibitory potency (compared to **22**), while gaining a 61 % increase in BuChE potency (Table 3). Molecular volume (164 Å^3 vs. 196 Å^3; respectively) and overall conformational changes are likely to account for the observed regioisomeric effect. Similar to the bioisosteric comparison in Chapter 3, the C2-

hydroxy derivative (**23**, IC_{50} ~ 10 µM) was roughly 2-fold less potent compared to **22**, ineffective toward BuChE and less potent toward AChE (~ 1.3-fold) when compared to the dimethoxybenzyl counterpart (**10**, Chapter 3).

With respect to the carbonyl-based derivatives, similar to those in Chapter 3, derivatives **24**–**26** exhibited similar activity toward AChE (IC_{50} ~ 8 µM) and were also ineffective toward BuChE, strengthening the hypothesis that small, carbonyl-based moieties (coupled to the quinazoline scaffold) are not suitable to target BuChE.

The introduction of alkylamines at the C2-position (derivatives **27**–**31**, Table 3) established comparable activity toward AChE (IC_{50} ~ 7.1 µM) as seen with the dimethoxybenzyl counterpart (**14**–**18**, Chapter 3, IC_{50} ~ 6.6 µM). That said, the alkylamine-based derivatives in this series were anywhere from 1.3 to 3-fold more effective at targeting BuChE compared to derivatives **14**–**18**. Another interesting note, while **14**–**18** (Chapter 3) exhibited BuChE activity ranging from 25-30 µM the unsubstituted benzylamine counterparts (**27**–**31**) exhibited a wider range of BuChE activity (12–22 µM). The ranking of the alkyl side chains were: *i*-Pr > *n*-Pr > Et > Me > *c*-Pr.

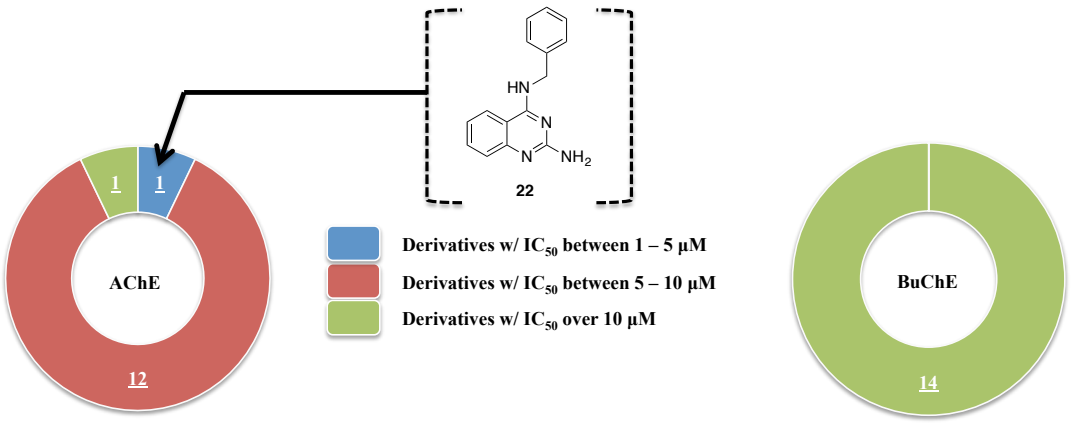


Figure 50: Cholinesterase metrics for fourteen 2-substituted-*N*-benzylquinazolin-4-amines (**19**–**31**).

In summary, 14 derivatives were assessed for dual cholinesterase activity, of which derivative **22** (N^4-benzylquinazoline-2,4-diamine) was identified as the most active AChEI (IC_{50} = 5 µM), while its

regioisomer (**22-iso**) was identified as the most active BuChEI (IC_{50} ~ 12 μM). Generally, this series proved to be less effective toward AChE, while maintaining or improving BuChE outlook compared to the dimethoxybenzyl series in Chapter 3 (Figure 50).

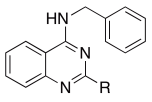
4.3.3. *Amyloid-β Aggregation*

The ability of 2-substituted-*N*-benzylquinazolin-4-amines (**19**–**31**) and the C4-amino regiosiomer (**22-iso**) to modulate the aggregation kinetics of amyloid-β was assessed using the ThT-binding method described earlier in Chapter 3 (Table 4).

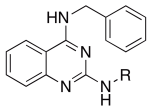
Examination of Table 2 demonstrated the overall ability of this series to dually target Aβ aggregation (12 out of 14 derivatives as dual inhibitors). In most cases, inhibitory activity toward Aβ40 was improved compared to the dimethoxybenzyl counterparts in Chapter 3. Of the 14 derivatives, only two were inactive toward Aβ42 (**22** and **25**) and **25** was also inactive toward Aβ40 – similar observation with the C2-gylcinamide as seen in Chapter 3. When compared to assay controls, only **22-iso** surpassed both curcumin's and resveratrol's activity toward Aβ42, while **23** was identified as a strong Aβ40 inhibitor that easily surpassed both controls' activity toward Aβ40. In addition, three derivatives (**21**, **22-iso** and **26**) were potent enough to be placed between resveratrol's and curcumin's ranking with respect to Aβ40 aggregation inhibition (Table 4).

Starting out with the C2-chlorine derivative, **19 (**IC_{50} ~ 17 μM) was considered a weak inhibitor of Aβ40, although it was more potent compared to its dimethoxybenzyl counterpart (**5**, Chapter 3, P.I at 25 μM was 18%). It was also equally weak as **5** toward Aβ42 (P.I at 25 μM was ~ 20%). Dechlorination of **19** worsened the activity of **20** toward Aβ40, while roughly maintaining the same P.I at 25 μM ~ 25%). When compared to **7** (Chapter 3, P.I of Aβ40/42 at 25 μM was ~ 30% and ~ 20%; respectively), **20** was more potent by ~ 7% toward both Aβ species.

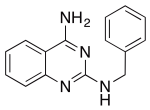
Table 4: Amyloid-β (Aβ40/42) inhibition data for 2-substituted-*N*-benzylquinazolin-4-amines (**19**–**31**) and the C4-amino regiosiomer (**22-iso**).



19–21, 23



22, 24–31



22-iso

Derivative	R-Grp	Amyloid-β IC_{50} (μM) [a]		SI [b]	ClogP [c]	MV (Å^3) [d]	HBD:HBA [e]
		Aβ40	Aβ42				
19	Cl	16.7 ± 2.5	22%	–	4.09	174.5	1:3
20	H	37%	27%	–	3.33	158.1	1:3
21	N_3	2.6 ± 0.7	37%	–	4.75	210.6	1:5
22	H	4.8 ± 1.1	NA	–	3.32	163.9	3:4
22-iso	–	2.2 ± 0.5	8.4 ± 1.1	0.26	3.32	195.5	3:4
23	OH	0.27 ± 0.02	24%	–	3.95	199.6	2:4
24	$CONH_2$	13.3 ± 2.5	48%	–	3.35	221.2	4:6
25	CH_2CONH_2	NA	NA	–	2.78	241.1	4:6
26	COMe	1.9 ± 0.3	31%	–	2.87	228.4	2:5
27	Me	48%	19%	–	4.14	176.9	2:4
28	Et	7.0 ± 1.4	24%	–	4.67	186.5	2:4
29	*n*-Pr	5.0 ± 1.0	26%	–	5.20	205.1	2:4
30	*i*-Pr	4.4 ± 0.8	13%	–	4.98	198.5	2:4
31	*c*-Pr	5.7 ± 1.1	31%	–	4.73	200.9	2:4
Curcumin	–	3.3 ± 0.45	9.9 ± 0.4	0.33	4.59	302.1	2:6
Resveratrol	–	1.1 ± 0.1	15.3 ± 1.9	0.07	2.83	187.2	3:3

Notes: [a] IC_{50} values are an average ± SD of triplicate readings based on two to three independent experiments. NA = Not active. Percent inhibition (P.I) indicates level of inhibition at highest concentration tested (25 μM). [b]Selectivity index is calculated as (Aβ40 IC_{50}) ÷ (Aβ42 IC_{50}). [c]ClogP values were determined using ChemDraw Professional 15.0. [d]Molecular volumes in Å^3 units were determined using Discovery Studio, Structure-Based Design software, BIOVIA Inc., USA. [e]Showcasing the ratio of HBD = hydrogen-bonding donors to HBA = hydrogen-bonding acceptors.

Unlike the outcome of the azide functionality in Chapter 3, **21** exhibited good activity toward Aβ40 (IC_{50} = 2.6 μM, roughly 3-fold more active compared to **8**), while providing moderate activity toward Aβ42 (P.I at 25 μM was ~ 37%). Derivative **21** was the first compound to surpass curcumin's potency toward Aβ40 in the series. Reduction of that azide caused an approximate 2-fold decrease in the activity of **22** toward Aβ40, while surrendering all inhibitory activity toward Aβ42. When compared to the dimethoxybenzyl counterpart (**9**), **22** was roughly 3-fold more potent toward Aβ40. The regioisomer of **22** was significantly more active toward Aβ40/42, starting with a 2-fold increase in potency toward Aβ40 (**22-**

iso, IC_{50} = 2.2 μM – stacked between the activities of resveratrol and curcumin) and generating the strongest inhibitory activity toward Aβ42 (IC_{50} = 8.4 μM – surpassed the activities of resveratrol and curcumin). Replacement of the amino group in **22** with a hydroxyl group in **23** resulted in a substantial improvement to the inhibitory activity toward Aβ40 **(**IC_{50} = 270 nM) with mild targeting of Aβ42 (P.I at 25 μM was 24%) – An equipotent profile with the choline- and hydrogen-based derivatives **19** and **20**. When compared to its dimethoxybenzyl counterpart, derivative **23** was also roughly 30-fold more active toward Aβ40 when compared to **10**.

With respect to the carbonyl-based derivatives, C2-urea-containing derivative **24** exhibited weak to moderate activity toward Aβ40 and Aβ42 (IC_{50} ~ 13 μM and ~ 25 μM; respectively), while the gylcinamide derivative (**25**) was inactive on both fronts – Similar outcome as that observed in Chapter 3. The acetamide derivative (**26**) on the other hand, while weakly active toward Aβ42 (P.I at 25 μM was 31%), it was roughly 7-fold more potent toward Aβ40 (IC_{50} = 1.9 μM) compared to its urea bioisostere (**24**) and roughly 3-fold more potent compared to its amino-based derivative (**22**).

The introduction of alkylamines at the C2-position established some interesting SAR. With the exception of the methyl side chain, other alkyl chains exhibited good to moderate activity toward Aβ40 (IC_{50} ~ 5–7 μM). Derivative **27** exhibited a P.I of Aβ40/42 at 25 μM of 48% and 19%; respectively, while the ethyl-base derivative (**28**) improved Aβ40 roughly 4-fold and Aβ42 by 5%. Amongst the propyl-based derivatives, ranking with respect to Aβ40 was **30** (isopropyl), **29** (propyl) then **31** (cyclopropyl) and interestingly, that ranking is reversed with respect to Aβ42.

In summary, 14 derivatives were assessed for dual Aβ-aggregation activity, of which derivative **23** (4-(benzylamino)quinazolin-2-ol) was identified the most potent Aβ40 inhibitor (IC_{50} = 270 nM). While most derivatives in this series were weak to moderate inhibitors of Aβ42, derivative **22-iso** (N^2-benzylquinazoline-2,4-diamine) was identified as the most active inhibitor (IC_{50} ~ 8 μM) (Figure 51).

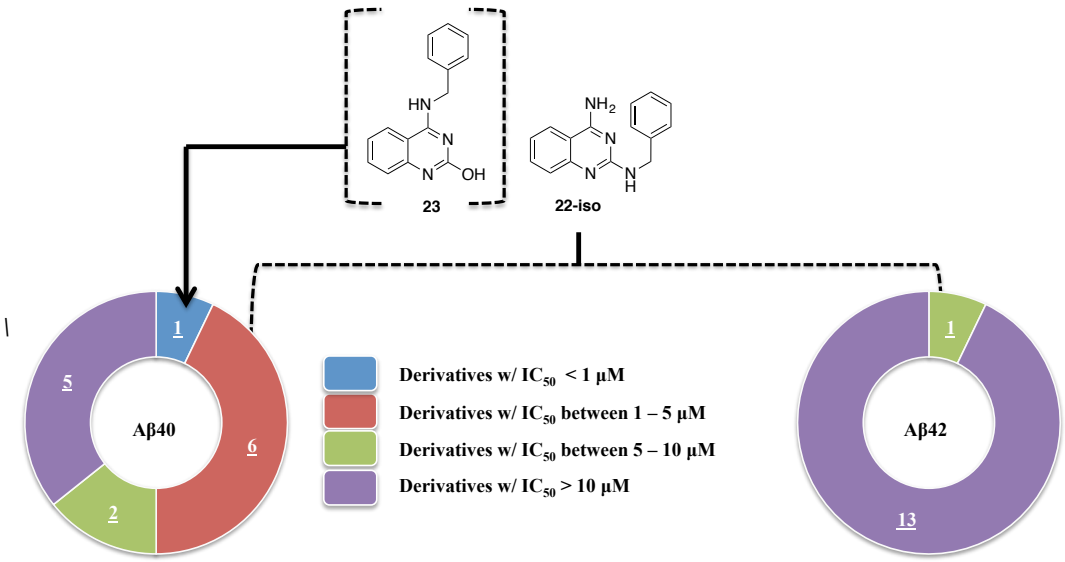


Figure 51: Amyloid-β metrics for fourteen 2-substituted-*N*-benzylquinazolin-4-amines (**19**–**31**).

The aggregation kinetic assessment of Aβ40 with or without series-leading derivatives is showcased in Figure 52. As observed with resveratrol (Panel A), derivatives **23** and **26** (Panels B and C; respectively) exhibit concentration-dependent inhibition of Aβ40 aggregation. Both managed to showcase multi-type modulation of the aggregation process, including significant monomeric structure stabilization (across all concentrations) as seen by the extended lag phase timeline as compared to the Aβ40-alone curve. Nonetheless, derivative **23** managed to stabilize the monomeric structure, reduce the rate of oligomerization and substantially hinder the total amyloid load at the 24-hour mark. At both the 1:1 and 1:5 test ratios, derivative **23** prevented significant oligomer formation as witnessed by the low RFU values across the 24 hour timeline. On the other hand, derivative **26** was very effective at monomeric structure stabilization, but did not necessarily reduce the rate of oligomerization. That said, at both the 1:1 and 1:5 test ratios, derivative **26** prevented significant fibril formation as witnessed by the lack of a plateau phase in the aggregation curves. Based on the overall kinetic plots, it is evident that derivatives **23** and **26** have the greatest impact upon Aβ40 at the very early stages of dimerization and oligomerization.

The aggregation kinetic assessment of Aβ42 with or without derivative **22-iso** is showcased in Figure 53. Compared to resveratrol (Panel A), derivative **22-iso** (Panel B) was effective at reducing the total amyloid load at all concentrations tested. In addition, at the 1:1 and 1:5 test ratios, slight stability of the monomeric structures was observed as seen by the approximate 2-hour extension in the lag phase timeline as compared to the Aβ42-alone curve. Based on the overall kinetic plot, it is evident that derivative **22-iso** has a minor role in early oligomerization process, but its impact is placed more at the fibrillation stage.

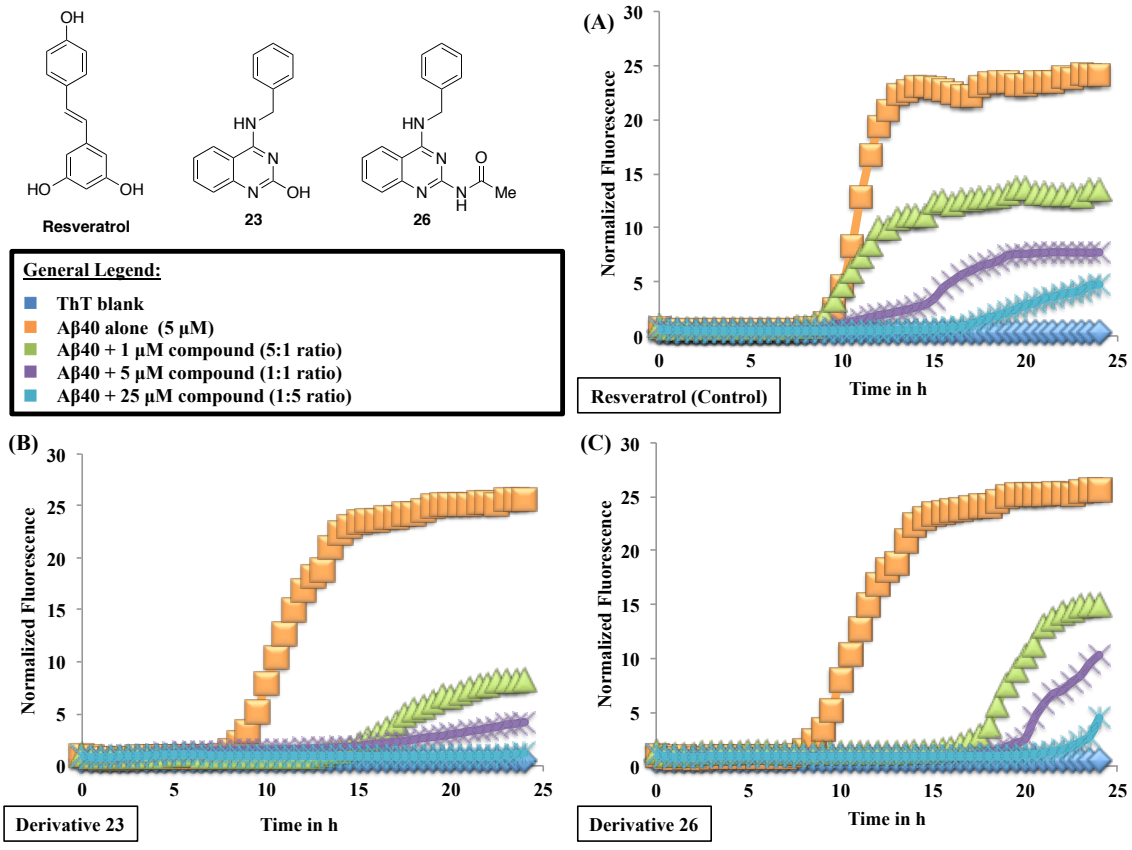


Figure 52: ThT-monitored kinetics of Aβ40 aggregation at 37 °C over a 24 h incubation period at pH 7.4 (Excitation = 440 nm, Emission = 490 nm). Panel (A): Impact of 1, 5 or 25 µM of resveratrol on the aggregation kinetics of 5 µM Aβ40. Panel (B): Impact of 1, 5 or 25 µM of 4-(benzylamino)quinazolin-2-ol (**23**) on the aggregation kinetics of 5 µM Aβ40. Panel (C): Impact of 1, 5 or 25 µM of *N*-(4-(benzylamino)quinazolin-2-yl)acetamide (**26**) on the aggregation kinetics of 5 µM Aβ40.

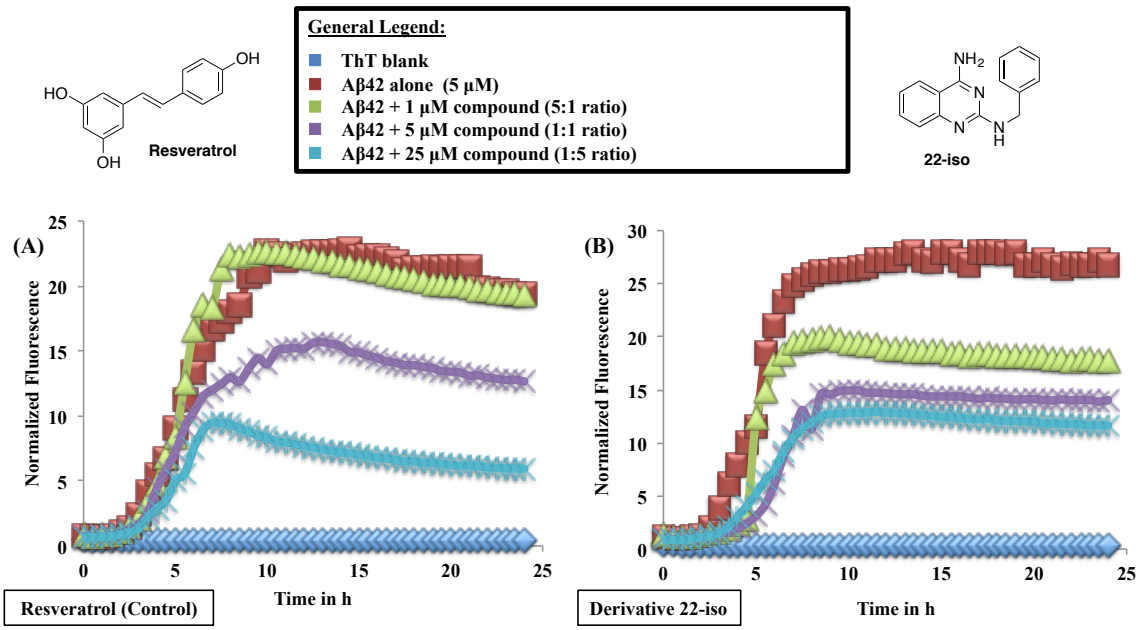


Figure 53: ThT-monitored kinetics of Aβ42 aggregation at 37 °C over a 24 h incubation period at pH 7.4 (Excitation = 440 nm, Emission = 490 nm). Panel (A): Impact of 1, 5 or 25 μM of resveratrol on the aggregation kinetics of 5 μM Aβ42. Panel (B): Impact of 1, 5 or 25 μM of N^2-benzylquinazoline-2,4-diamine (**22-iso**) on the aggregation kinetics of 5 μM Aβ42.

4.3.4. *Transmission Electron Microscopy (TEM)*

The assessment of amyloid morphology at the conclusion of a 24-hour incubation period at 37 °C was conducted on leading derivatives. This commonly employed, qualitative technique is used to corroborate the quantitative results from the ThT-binding assay.[207, 317] Experimental setup included the incubations of control and test samples, at 1:1 ratios of 25 μM, in triplicate at 37 °C (with shaking) over a 24-hour timeline. Triplicate samples were combined after the incubation period and applied to the copper-mesh grids prior to imaging in the TEM.

As observed in Figure 54, resveratrol was effective at reducing total amyloid load (Panels B and E) compared to control samples (Panels A and D). That said, derivative **23** (Panel C) surpassed the inhibitory potential of resveratrol against Aβ40, while derivative **22-iso** was more effective against Aβ42, compared to resveratrol.

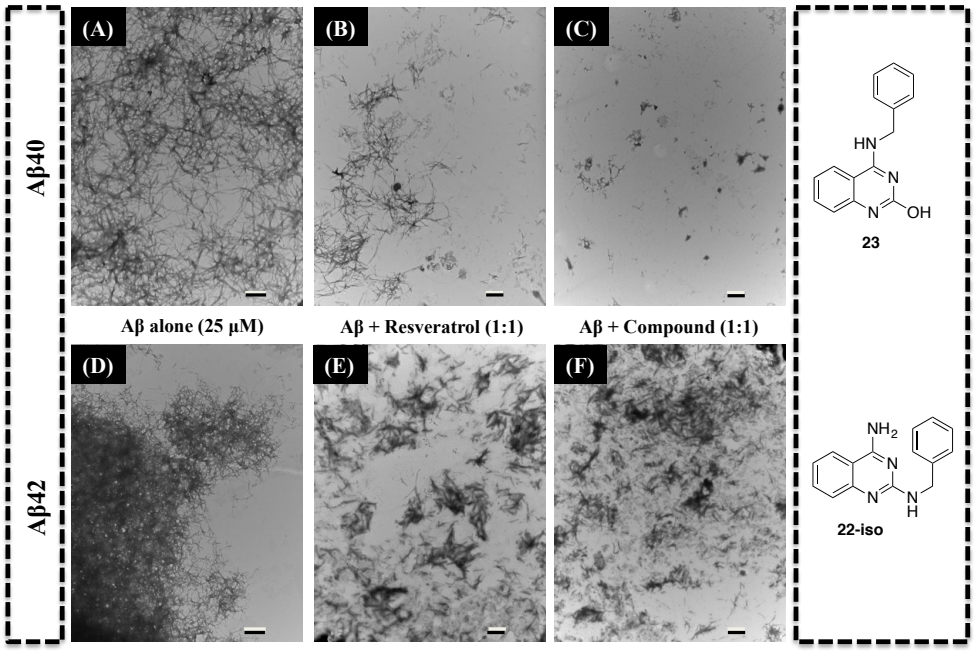


Figure 54: TEM assessment of Aβ40/42 morphology with or without test compounds at the end of a 24 h, 37 °C incubation period at pH 7.4. Panel (A–C): 25 μM Aβ40 alone or at a 1:1 ratio with resveratrol or 4-(benzylamino)quinazolin-2-ol **(23**); respectively. Panel (D–F): 25 μM Aβ42 alone or at a 1:1 ratio with resveratrol or N^2-benzylquinazoline-2,4-diamine (**22-iso**); respectively. White/black bars represent 500 nm.

4.3.5. *Antioxidant Capacity*

The ability of select 4-(benzylamino)quinazolin-2-ol (**23**) to neutralize ROS was assessed using the previously described DPPH-scavenging assay.[216, 319-321]

As a conjugated phenolic compound, it was no surprise to observe the scavenging potential of **23** in the DPPH assay. While it was equipotent to resveratrol (~ 42% DPPH-radical scavenging), the absence of the dimethoxy moiety at the C4-position impaired its antioxidant capacity by 16%, compared to **10** (Chapter 3).

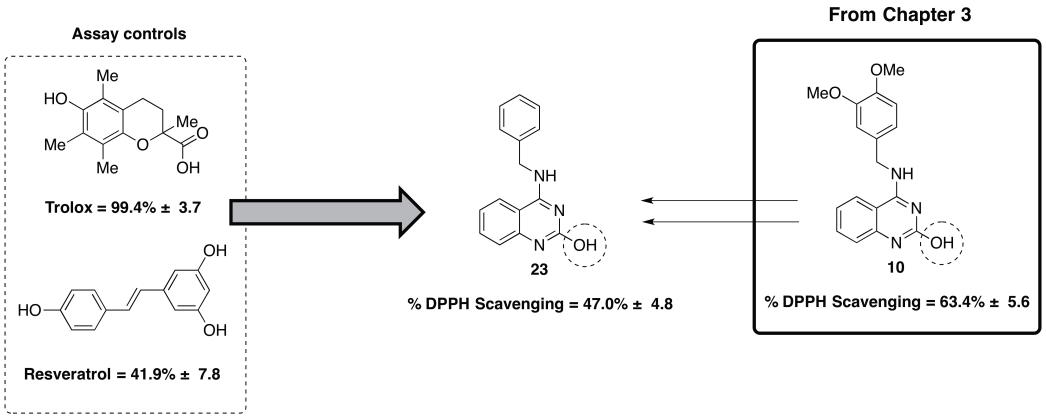


Figure 55: Standards utilized in the DPPH-scavenging along with the data for 4-(benzylamino)quinazolin-2-ol (**23**).

4.3.6. *Molecular Modeling*

The utilization of computational software is not only useful in structure-based drug design, it is also employed to understand and corroborate the acquired SAR data. The assessment of ligand-receptor interactions was conducted between leading (or comparable) derivatives from the 2-substituted-*N*-benzylquinazolin-4-amine series (**19-31**), including the **22-iso** regioisomer, and the cholinesterase or amyloid targets of interest.

4.3.6.1. *Cholinesterase*

Based on the acquired anti-ChE data, presented in Table 3, the docking interactions of **20**, **22** and **22-iso** were investigated in *h*AChE (PBD: 1B41) and superimposed in Figure 56, along with the docking interactions of **22** and **22-iso** in *h*BuChE (PBD: 1P0I).

As observed in Panel A, a perfect superimposition of **20** and **22** was observed where the quinazoline scaffold was stacked semi-parallel to W86 (~ 4 Å). Binding was deep into the active site as scaffold distance to W286 was roughly 14 Å. Both derivatives had their C4-benzyl groups wrap around W86 (~ 4

Å), while the C2- groups were directed toward the catalytic triad, allowing for **22** to undergo hydrogen-bonding interactions with S203's hydroxyl group. Transitioning to Panel B, the binding of **22-iso** was quite different compared to its regioisomer. Unlike **22**, the overall conformation of **22-iso** was more dual site binding in *h*AChE. The quinazoline scaffold was perpendicular to W86 (~ 6–7 Å) and roughly 11 Å from W286. The C2-benzyl group was running parallel to the acyl pocket at roughly 5–6 Å where the phenyl ring was pointed toward W286 (~ 7 Å). This dual site orientation allowed for the C4-amino group to undergo hydrogen-bonding interactions with both S203 and H447 (~ 2.5–3.0 Å).

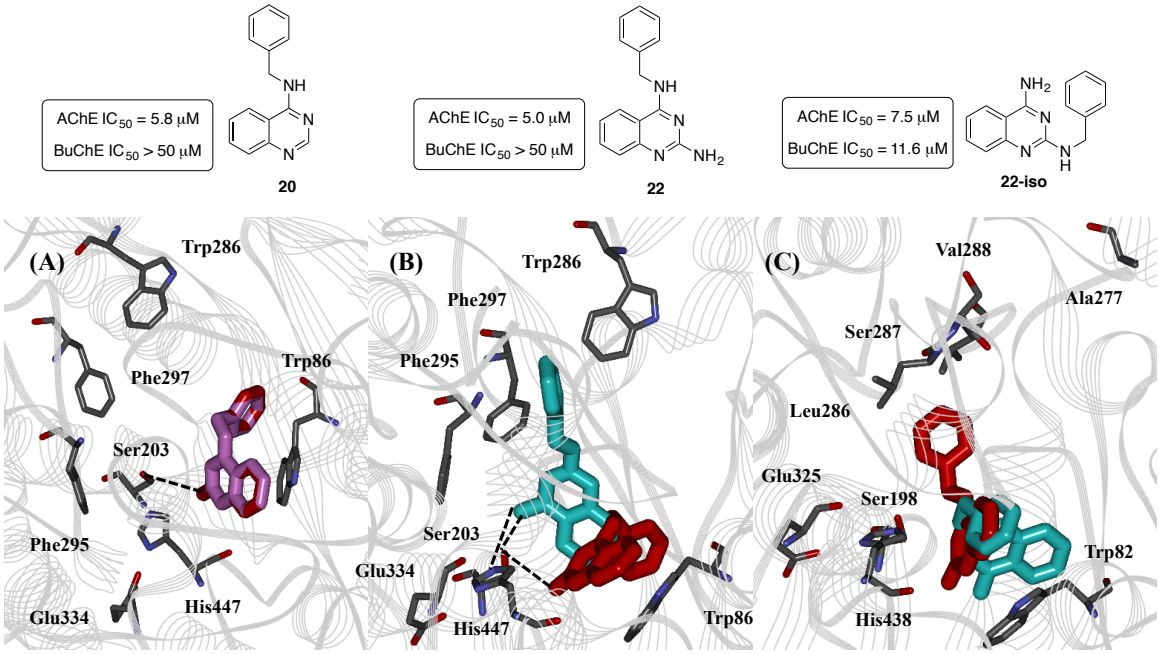


Figure 56: Superimposition of docking structures. Panel (A): Binding modes of **20** (magenta) and **22** (red) in the active site of *h*AChE (PDB ID: 1B41). Panel (B,C): Binding modes of **22** (red) and **22-iso** (turquoise) in the active sites of *h*AChE (PDB ID: 1B41) and *h*BuChE (PDB ID: 1P0I); respectively. Hydrogens removed to enhance visibility. Black-dashed lines indicate hydrogen-bonding interactions.

With respect to regioisomeric comparison in *h*BuChE, differential binding conformation was observed with **22** and **22-iso** in Panel C. Both quinazoline scaffolds were roughly 17 Å from A277, but **22**'s scaffold was stacked parallel between W82 and the catalytic triad (~ 4–5 Å), while **22-iso** had its scaffold parallel to W82. As a matter of fact, the entire ligand (**22-iso**) was mainly interacting with W82 (~ 5–6 Å), forming a

V-shaped cap over this critical residue. On the other hand, the benzyl group of **22** was directed toward the acyl pocket in a perpendicular fashion (~ 5–8 Å), while its C2-amino group was off-centrally placed near the catalytic triad with the absence of hydrogen-bonding interactions.

4.3.6.2. *Amyloid-β*

Based on the acquired anti-Aβ data, presented in Table 4, the docking interactions of **22**, **22-iso**, **23** and **26** were investigated in both dimeric and fibril model of Aβ ($Aβ_{9-40}$ – PDB 2LMN)[322] with superimpositions showcased in Figure 57. In addition, with the appreciation of the strong resonance stabilization associated with **23**, the binding of its likely resonance structures was superimposed in Figure 58.

With respect to regioisomeric comparison in amyloid dimer model, differential binding conformation was observed with **22** and **22-iso** as shown in Panel A. The quinazoline scaffold of **22** was stacked parallel to the A30-I32 region at roughly 5 Å, compared to the parallel stacking against D23-V24 (~ 6 Å) for the quinazoline scaffold of **22-iso**. Regarding the benzyl groups, derivative **22** had its C4-functionality running parallel and toward K28 at roughly 6–7 Å, allowing for hydrogen-bonding interactions with the carboxyl side chain of D23 (~ 3.2 Å) and the carbonyl-backbone of V24 (~ 3.5 Å). On the other hand, **22-iso** had its C2-benzyl group interacting parallel to G29-A30 (~ 5–6 Å), allowing for a hydrogen-bonding interaction with the carbonyl-backbone of A30 (~ 3.0 Å). With the amino groups, only derivative **22-iso** showcased hydrogen-bonding interactions between its C4-amino group and the backbone terminals of I32 (~ 1.8–3.0 Å).

Transitioning to Panel B, the binding modes of these bioisosteres (C2-NH_2 vs. C2-OH) revealed differential conformations that explain the drastic variance in potency. With **23**, the quinazoline scaffold was stacked parallel to V24-G25 (~ 5–6 Å) and was equidistantly placed between both the upstream and downstream stretches of the hairpin loop domain. This placement, resulted in the favourable positioning of the C2-OH near key residues in the hairpin loop domain and allowed for multiple hydrogen-bonding interactions (N27's backbone carbonyl at roughly 2.8 Å, S26's backbone carbonyl at roughly 2.9 Å and G29's backbone amine at roughly 3 Å). Moreover, the ligand's C4-N*H* underwent additional hydrogen-

bonding with D23's side chain carboxyl group at roughly 3 Å. Lastly, the benzyl moiety was stacked against D23-V24 at roughly ~ 5 Å, with the phenyl ring showcasing a perpendicular orientation with the peptide chain.

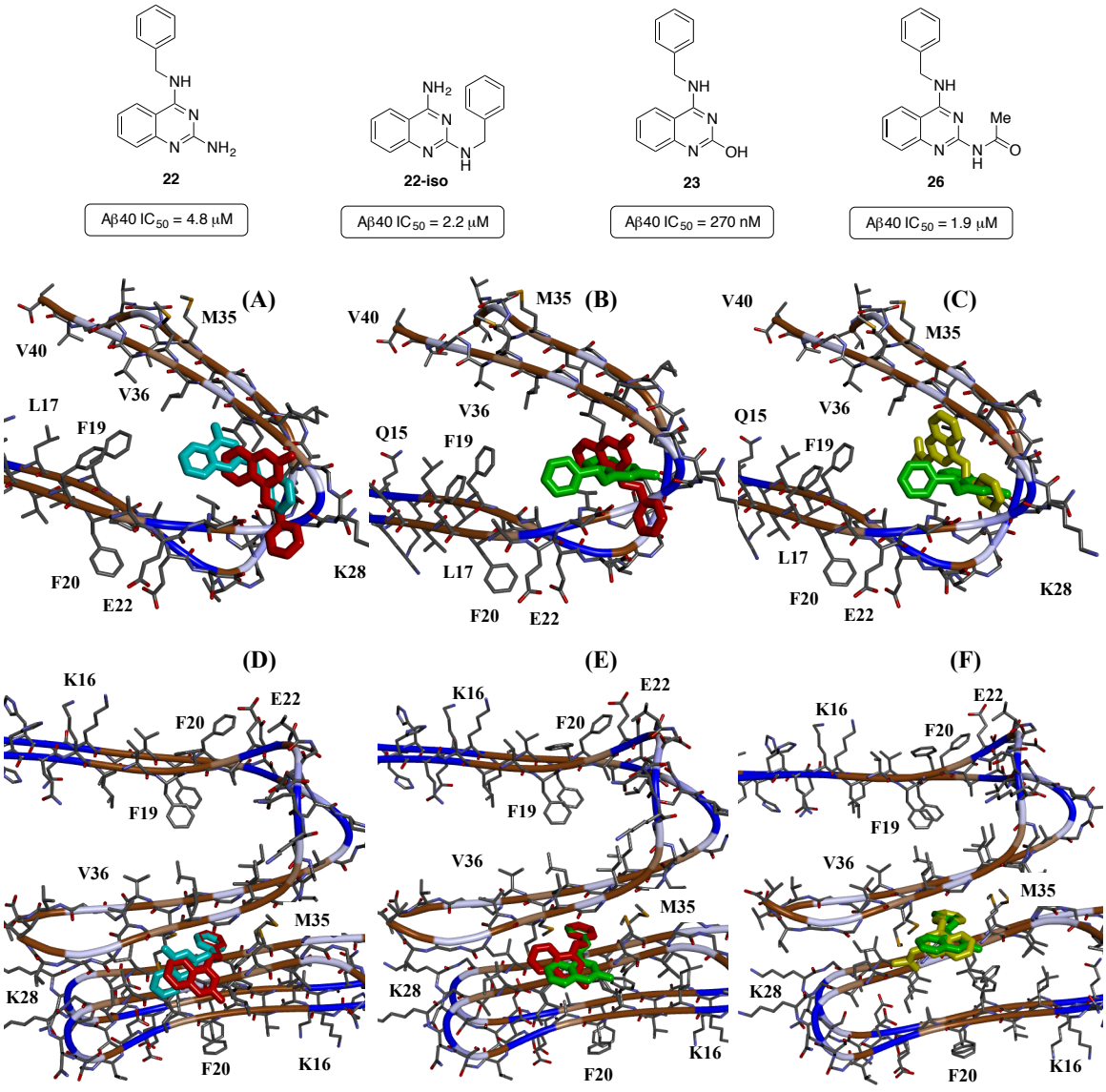


Figure 57: Superimposition of docking structures. Panels (A–C): Binding modes of **22** (red) and **22-iso** (turquoise), **22** (red) and **23** (green) or **23** (green) and **26** (gold); respectively, in the Aβ ($Aβ_{9-40}$ – PDB 2LMN) dimer model. or fibril model [Panels (D–F)]. Hydrogens removed to enhance visibility. Amino acid labels to be used as a general guide as space restrictions limited complete and accurate labeling of all peptide structures.

Collectively, these interactions at the hairpin loop domain strongly corroborate the ability of **23** to destabilize dimeric and oligomeric structures. For an overview of the resonance-structrue impact on the binding mode, *see* Figure 58.

Transitioning to Panel C (Figure 57), the first observation was the predominant interactions of **26** with the steric zipper domain of the dimeric model. The quinazoline scaffold was stacked perpendicular to A30-I32 (~ 5 Å), while the C4-benzyl group was running parallel toward K28 (~ 6–7 Å). The C2-acetamide group was equidistantly placed parallel between V24 and I32 on the opposing side (~ 4–5 Å).

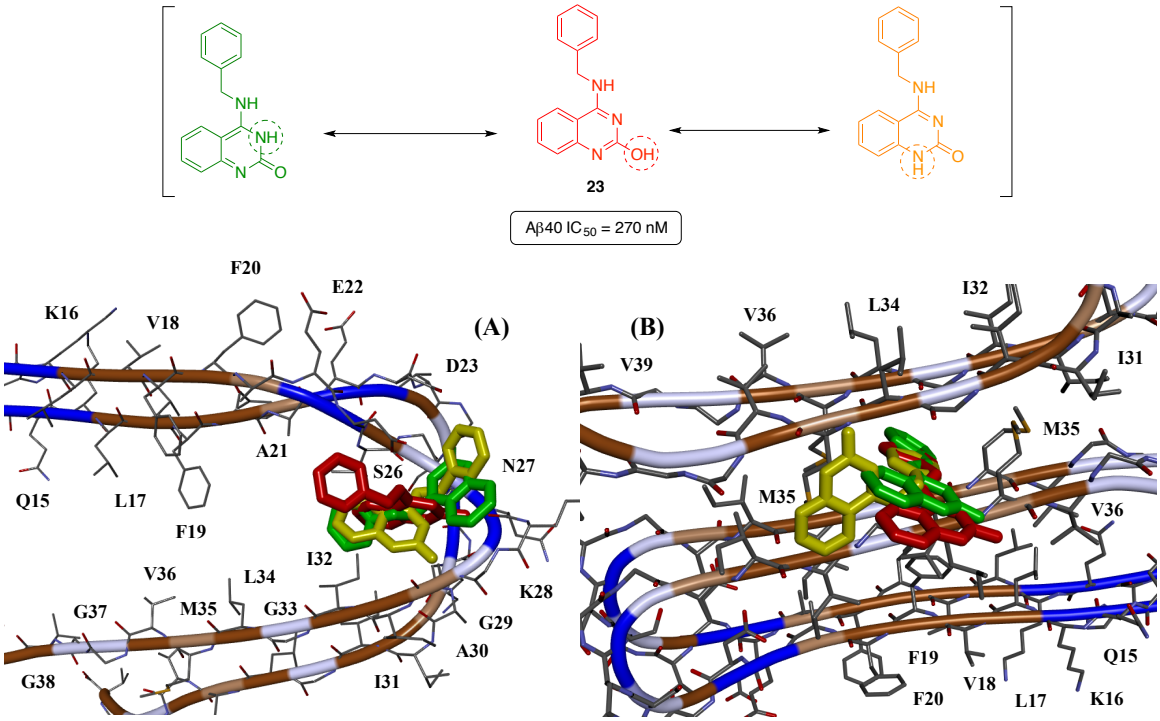


Figure 58: Superimposition of docking structures. Panel (A): Binding modes of **23** (red) and its resonance stabilized structures (green and yellow/orange) in the Aβ ($A\beta_{9\text{-}40}$ – PDB 2LMN) dimer model or fibril model [Panel (B)]. Hydrogens removed to enhance visibility. Amino acid labels to be used as a general guide as space restrictions limited complete and accurate labeling of all peptide structures.

With respect to the binding modes within the fibril model (Panels D–F, Figure 57), derivatives **22**, **22-iso**, **23** and **26** all had their benzyl groups intercalated within the steric zipper domain at roughly 5–6 Å

from the quad M35 residues and in a parallel orientation to the peptide chain. All quinazoline scaffolds extended outward from the steric zipper domain and were either stacked parallel (**23** and **26**) or perpendicular (**22** and **22-iso**), with respect to the peptide backbone, to the A30-V36 region of the domain (~ 5–6 Å). Individual ligand observations included the hydrogen-bonding interactions between: (a) **22**'s C4-N*H* and G33's backbone carbonyl (2.4 Å), (b) **22-iso**'s C4-NH_2 and M35's backbone carbonyl (2.8 Å), (c) **22-iso**'s C2-NH and G33's backbone carbonyl (2.2 Å) and (d) **26**'s carbonyl and G33's backbone amine (2.8 Å). For an overview of the resonance-structrue impact on the binding mode of **23** in the fibril model, *see* Figure 58, Panel B.

4.4. Summary

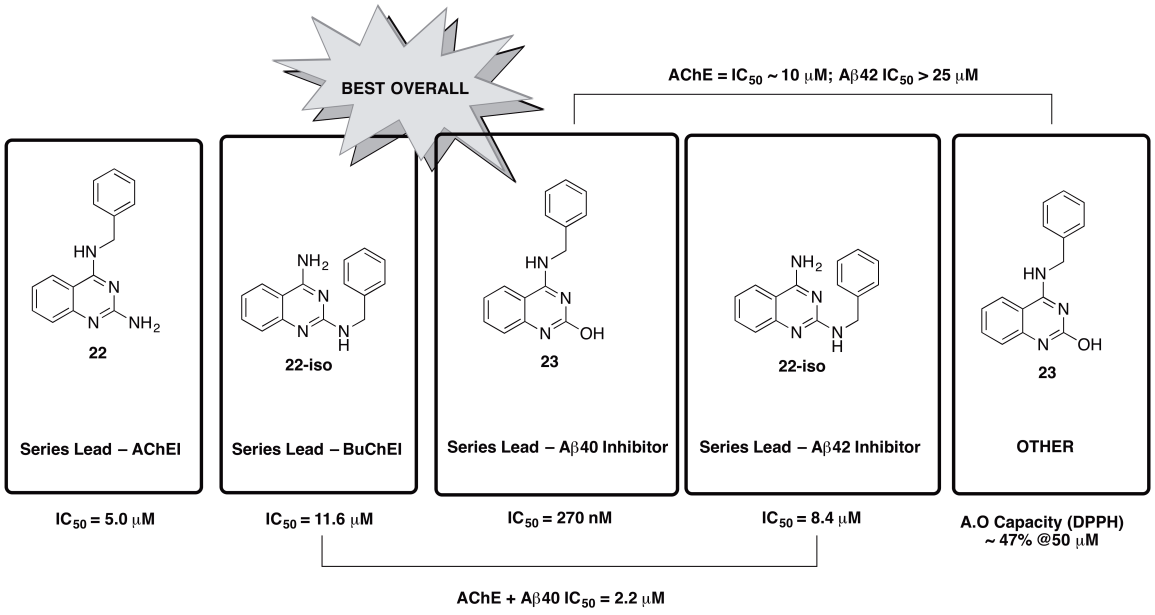


Figure 59: Cumulative chapter summary of 2-substituted-*N*-benzylquinazolin-4-amines (**19**–**31**) and related regio-isomers.

With this benzylamine-based series, an overall improvement in BuChE targeting was observed, although that came at the cost of reduced AChE potency. When compared to their dimethoxybenzyl

counterparts, the derivatives in this series were more capable of targeting Aβ42, while Aβ40 activity was a more of a mixed bag.

Nonetheless, the series showcased a potent Aβ40 aggregation inhibitor with good antioxidant capacity and moderate AChE inhibition in **23**. More so, the regioisomer of **22** proved to be a good all-round derivative with dual ChE and dual Aβ40/42 inhibitory potential (**22-iso**, Figure 59).

4.5. Experimental

Please note that this subsection includes new and re-listed methodologies from Chapter 3. For schematic representation of re-listed methodologies, if applicable, please refer to Chapter 3 – Section 3.5.

4.5.1. *Chemistry*

General Information. All the reagents and solvents were reagent grade purchased from various vendors (Acros Organics, Sigma-Aldrich, and Alfa Aesar, USA) with a minimum purity of 95% and were used without further purification. Melting points (mp) were determined using a Fisher-Johns apparatus and are uncorrected. Reaction progress was monitored by UV using thin-layer chromatography (TLC) using Merck 60F254 silica gel plates. Column chromatography was performed with Merck silica gel 60 (230−400 mesh) with 5:1 EtOAc:MeOH as the solvent system unless otherwise specified. Proton (^{1}H NMR) and carbon (^{13}C NMR) spectra were performed on a Bruker Avance (at 300 and 75 MHz; respectively) spectrometer using DMSO-d_6. Coupling constants (*J* values) were recorded in hertz (Hz) and the following abbreviations were used to represent multiplets of NMR signals: s = singlet, d = doublet, t = triplet, m = multiplet, br = broad. Carbon multiplicities (C, CH, CH_2 and CH_3) were assigned by DEPT 90/135 experiments. High-resolution mass spectrometry (HRMS) was determined using a Thermo Scientific Q-Exactive Orbitrap mass spectrometer (positive mode, ESI), Department of Chemistry, University of Waterloo. Compound purity (roughly 95% or over) was determined using an Agilent 1100 series HPLC equipped with an analytical column (Agilent Zorbax Eclipse XDB-C8 column, 4.6 x 150 mm, 5 μm particle size) running 50:50 Water:ACN with 0.1% TFA at a flow rate of 1.0-1.5 mL/min or an Agilent 6100 series single quad LCMS

equipped with an Agilent 1.8 µm Zorbax Eclipse Plus C18 (2.1 x 50 mm) running 50:50 Water:ACN with 0.1% FA with a flow rate of 0.5mL/min. All the final compounds exhibited ≥ 95% purity.

General procedure for the synthesis of 2-chloro-*N*-substituted-quinazolin-4-amines.[303, 305] To a 30 mL solution of ethanol in a 100 mL round-bottom flask on ice, 5 g of **4** (25.13 mmol) was added followed by slow addition of 1.3 eq. (32.66 mmol) of the corresponding primary amine. Contents were stirred on an ice bath while 2.0 eq. of diisopropyl-ethylamine (DIPEA, 50.25 mmol) was added in drop wise fashion. The solution was then heated at 80-85 °C under reflux for 3–4 h. The reaction contents were cooled to room temperature and precipitated residues were vacuum-filtered with ethyl acetate (EtOAc) rinses. The organic supernatant was concentrated in vacuo followed by two rounds of liquid-liquid extraction using EtOAc and saturated brine solution (40–50 mL each respectively). The combined organic layers were dried over MgSO4, evaporated in vacuo and purified (1-2 times) using silica gel column chromatography with 5:1 EtOAc:MeOH as the elution solvent. Final compounds were white to beige solids with yields ranging from 70-90%.

***N*-Benzyl-2-chloroquinazolin-4-amine (19).** Yield: 75% (5.11 g, 19.00 mmol). Mp: 169–171 °C. ^{1}H NMR (300 MHz, DMSO-*d6*) δ 9.24 (t, 6.0 Hz 1H), δ 8.27 (d, *J* = 6.0 Hz, 1H), δ 7.75 (t, *J* = 9.0 Hz, 1H), δ 7.59 (d, *J* = 6.0 Hz, 1H), δ 7.49 (t, *J* = 9.0 Hz, 1H), δ 7.34-7.20 (m, 5H), δ 4.72 (d, *J* = 6.0 Hz, 2H). HRMS (ESI) m/z calcd for $C_{15}H_{12}ClN_3$ $[M + H]^+$ 270.0720, found 270.1532. Purity: 98.8%

General procedure for the synthesis of N^4-substituted-quinazolin-4-amines. In a 50 mL round bottom flask (RBF), 0.5 g of 2-chloro-*N*-substituted-quinazolin-4-amine (1.45–1.85 mmol) was dissolved in 20 mL of anhydrous ethanol. While stirring on ice, 10 mol. % of 10% Pd/C was added to reaction mixture followed by the drop-wise addition of 1.3 eq. of hydrazine hydrate. Solution was stirred on ice for 5 min before refluxing for 2 h at 80–85 °C. Upon completion and cooling to room temperature, the reaction mixture was passed through a tightly-packed cotton-filled syringe that has been pre-rinsed with ethanol, to remove the Pd/C catalyst. A 30 mL aliquot of ethanol was used to rinse the syringe. The combined ethanol solutions were evaporated in vacuo, diluted in EtOAc (20 mL) and washed 25 mL x 2 with equal volumes of brine solution. The combined aqueous layers were washed with 15 mL of EtOAc. The combined EtOAc

layers were dried over $MgSO_4$, before removing the EtOAc in vacuo to yield a solid or semi-solid crude product that was purified by silica gel column chromatography using 5:1 EtOAc:MeOH solvent system. Final compounds were white to pale yellow solids with yields ranging from 40–47%.

***N*-Benzylquinazolin-4-amine (20).** Yield 45% (0.20 g, 0.85 mmol); Mp 142–145 °C. ^{1}H NMR (300 MHz, DMSO-d_6): δ 8.84 (t, J = 9.0 Hz, 1H), δ 8.42 (s, 1H), δ 8.26 (d, J = 6.0 Hz, 1H), δ 7.72 (t, J = 6.0 Hz, 1H), δ 7.64 (d, J = 6.0 Hz, 1H), δ 7.47 (t, J = 9.0 Hz, 1H), δ 7.31–7.19 (m, 5H), δ 4.71 (d, J = 6.0 Hz, 2H). HRMS (ESI) m/z calcd for $C_{15}H_{14}N_3$ $[M + H]^+$ 236.1109, found 236.1181. Purity: 97.9%

General procedure for the synthesis of 2-azido-*N*-substituted-quinazolin-4-amine.[305] In a 50 mL RBF, 2-chloro-*N*-substituted-quinazolin-4-amine (~1.86 mmol), 1.1 eq. NaN_3 (2.05 mmol), 4:1 EtOH (20 mL) and glacial acetic acid (5 mL) were combined and refluxed at 90–95 °C for 2 h with stirring. After cooling, the solution was vacuum-filtered to afford white solids at yields ranging from 80–85%.

2-Azido-*N*-benzylquinazolin-4-amine (21). Yield 85% (0.43 g, 1.57 mmol); Mp 224–226 °C. ^{1}H NMR (300 MHz, DMSO-d_6): δ 9.40 (br s, 1H), δ 8.48 (d, J = 8.2 Hz, 1H), δ 8.29 (d, J = 8.3 Hz, 1H), δ 7.97 (t, J = 8.0 Hz, 1H), δ 7.72 (t, J = 8.0 Hz, 1H), δ 7.40–7.21 (m, 5H), δ 4.81 (d, J = 3.0 Hz, 2H). HRMS (ESI) m/z calcd for $C_{15}H_{13}N_6$ $[M + H]^+$ 277.1123, found 277.1195. Purity: 96.3%

General procedure for the synthesis of N^4-substituted-quinazolin-2,4-diamine.[305]

Method 1A: In a 100 mL round-bottom pressure vial, 2-chloro-*N*-substituted-quinazolin-4-amine (3.72 mmol) was added along with 20 mol. % of CuI. To that, a mixture of 1,4-dioxane (5 mL) and 30% aqueous ammonia (15 mL) was added at room temperature. The pressure vial was sealed tightly and partially submerged in silicone oil heating at 130–135 °C. Contents were stirred in the pressure vial for 24 h (Note: in the event of pressure leakage, the contents were cooled to room temperature and additional aqueous

ammonia, (10 mL) was added, sealed and heating was carried on through the 24 h period). The reaction contents were cooled to room temperature and the solution was diluted with 25 mL EtOAc, washed with saturated brine solution (10 mL x 3), and the aqueous layer was neutralized with dilute HCl, and then re-extracted with 15 mL EtOAc. The organic layers were combined, dried over $MgSO_4$, evaporated in vacuo and purified using silica gel column chromatography with 5:1 EtOAc:MeOH as an initial elution solvent followed by transition to 5:1 EtOAc:MeOH w/ 1% TEA (triethylamine). Final compounds were obtained as white to beige solids with final yields ranging from 20–25%.

Method 1B: In a 100 mL round-bottom pressure vial, 2-chloro-*N*-substituted-quinazolin-4-amine (3.72 mmol) was dissolved and gently heated in 5 mL ethylene glycol. To that, 20 mol. % of Cu_2O and DMEDA were added followed by 20 eq. K_2CO_3 and finally, 40 eq. of 30% aqueous ammonia solution (~ 15–20 mL). The pressure vial was sealed tightly, partially submerged in silicone oil and heated at 100-105 °C. Contents were stirred in the pressure vial for 24 h. After the reaction contents were cooled to room temperature, the solution was diluted with 50 mL EtOAc, washed with saturated brine solution (25 mL x 3) and the aqueous layer was neutralized with dilute HCl, and then re-extracted with 25 mL EtOAc. The residue formed was dissolved in methanol (20–25 mL). The EtOAc layers were dried over $MgSO_4$ and evaporated in vacuo. The methanol fraction was dried with molecular sieves before evaporating the methanol in vacuo. Both EtOAc and methanol fractions were combined and purified using silica gel column chromatography with 5:1 EtOAc:MeOH as an initial elution solvent followed by transition to 5:1 EtOAc:MeOH with 1% TEA (triethylamine). Final compounds were obtained as white to beige solids with yields ranging from 35–40%.

Method 2: In a 50 mL round-bottom pressure vial, 2-chloro-*N*-substituted-quinazolin-4-amine (3.72 mmol) was combined with 6 eq. urea (22.32 mmol) and diluted with 10 mL of anhydrous 1,4-dioxane. The pressure vial was sealed tightly and partially submerged in silicone oil heating at 160–165 °C. Contents were stirred in the pressure vial for 24 h. Once the reaction contents were cooled to room temperature, the solution was diluted with 20–25 mL EtOAc. The contents were washed three times with 20 mL saturated brine solution and the aqueous layers were re-extracted twice with 20 mL EtOAc. The organic layers were combined, dried over $MgSO_4$, evaporated in vacuo and purified using silica gel column chromatography with 5:1 EtOAc:MeOH as an initial elution solvent followed by transition to 5:1 EtOAc:MeOH w/ 1% TEA

(triethylamine). Final compounds were obtained as white to light beige solids with yields ranging from 50–55%.

Method 3: In a 50 mL round-bottom flask, 2-chloro-*N*-substituted-quinazolin-4-amine (3.72 mmol) was combined with 1.1 eq. NaN_3 (4.09 mmol), before diluting with 4:1 EtOH (20 mL) and glacial acetic acid (5 mL). Flask contents were stirred under reflux at 90–95 °C for 2 h. After cooling the reaction mixture, 10 mol. % of Pd/C (10%) was added followed by slow addition of 1.5 eq. of hydrazine hydrate (5.58 mmol). Flask contents were stirred under reflux at 90–95 °C for an additional two hrs. Once complete, the warm solution was passed through a large, tightly packed cotton syringe with the aid of additional EtOH washes (2 x 20 mL). The ethanolic mixture was evaporated in vacuo. Final compounds were obtained as white to beige solids with yields ranging from 80–85%.

Method 4: In a 50 mL round-bottom flask, 2,4-diaminoquinazoline* (1 g, 6.24 mmol) was dissolved in 3 mL DMSO. With stirring and periodic cooling over ice-water, NaH (60%, 0.25 g, 6.24 mmol) was added over a 10–15 min. period. After complete addition of NaH, flask was stirred at room temperature with slow, dropwise addition of the appropriate alkyl/aryl halide (6.24 mmol) dissolved in 3 mL DMSO. Contents are allowed to stir at room temperature overnight (~14 h) before diluting with 20 mL of water and stirring at room temperature for 15 min. The mixture is extracted thrice with diethyl ether (40 mL x 3). The combined organic layers are washed twice with brine (20 mL x 2). Combined organic layer was dried with $MgSO_4$ and concentrated in vacuo before purifying with silica gel column chromatography using 5:1 EtOAc/MeOH to afford beige to off-white solids at 20–31% yield.

***General procedure for synthesis of 2,4-diaminoquinazoline.**[291, 317] In a 250 mL round-bottom pressure flask, 2-fluorobenzonitrile (4.6 mL, 42.32 mmol) or 2-aminobenzonitrile (5 g, 42.32 mmol) was combined with guanidine carbonate (11.43 g, 126.96 mmol) and diluted in 30 mL dimethylacetaminde (DMA). Contents are heated in an oil bath at 150 °C for overnight (~14 h) then diluted with 50mL of water before extracting thrice with EtOAc (50 mL x 3) and washing with brine (2x 20 mL). Combined organic layer was dried with $MgSO_4$ and concentrated in vacuo before purifying with silica gel column chromatography using 5:1 EtOAc/MeOH to afford an off-white solid at 80% yield. ^{1}H NMR (300 MHz,

DMSO- d_6) δ 7.91 (d, J = 7.8 Hz, 1H), δ 7.41 (t, J = 7.8 Hz, 1H), δ 7.21 (br s, 2H), δ 7.15 (d, J = 8.1 Hz, 1H), δ 6.95 (t, J = 7.2 Hz, 1H), δ 5.91 (br s, 2H). ^{13}C NMR (100 MHz, DMSO- d_6) δ 162.45, δ 160.75, δ 152.52, δ 132.30, δ 124.22, δ 123.52, δ 119.73, δ 110.34.

N^4-Benzylquinazolin-2,4-diamine (22). Yield 83% (0.77 g, 3.09 mmol); Mp: 185–187 °C. ^{1}H NMR (300 MHz, DMSO-d6) δ 8.76 (br s, 1H), 8.06 (d, J = 8.1 Hz, 1H), δ 7.50 (t, J = 8.1 Hz, 1H), δ 7.09-7.36 (m, 6H), δ 7.07 (t, J = 7.8 Hz, 1H), δ 6.48 (br s, 2H), δ 4.71 (d, J = 5.9 Hz, 2H). HRMS (ESI) m/z calcd for $C_{15}H_{14}N_4$ [M + H]+ 251.1296, found: 251.1289.

General procedure for synthesis of N^2-substituted-quinazoline-2,4-diamines.[317] In a 50 mL round-bottom flask, 2,4-diaminoquinazoline (1 g, 6.24 mmol) was dissolved in 20 mL DMA followed by the addition of potassium carbonate (0.85 g, 6.24 mmol) and the appropriate alkyl/aryl halide (6.24 mmol) at room temperature. Contents are refluxed at 85 °C for 5 h before diluting with 30 mL of water and stirring at R.T for 15 min. The mixture is extracted thrice with EtOAc (50 mL x 3). The combined organic layers are washed twice with brine (20 mL x 2). Combined organic layer was dried with $MgSO_4$ and concentrated in vacuo before purifying with silica gel column chromatography using 5:1 EtOAc/MeOH to afford beige to off-white solids at 14–26% yield.

N^2-Benzylquinazoline-2,4-diamine (22-iso). Yield 26% (0.41 g, 1.64 mmol); Mp: 159–161 °C; ^{1}H NMR (300 MHz, DMSO-d_6): δ 7.95 (d, J = 7.9 Hz, 1H), δ 7.47 (t, J = 7.4 Hz, 2H), δ 7.32–7.14 (m, 6H), δ 7.02 (t, J = 7.5 Hz ,1H), δ 4.53 (d, J = 6.3 Hz , 2H). ^{13}C NMR (100 MHz, DMSO-d_6) δ 162.75, δ 159.39, δ 141.41, δ 133.22, δ 128.54, δ 127.86, δ 127.56, δ 126.82, δ 124.68, δ 124.23, δ 120.87, δ 111.07, δ 44.23. HRMS (ESI) calcd for $C_{15}H_{14}N_4$ (M^{+1}) *m/z* 251.12912, observed 251.12907.

General procedure for the synthesis of N^4-substituted-quinazolin-2-ols. In a 50 mL round bottom flask (RBF), 0.5 g of 2-chloro-*N*-substituted-quinazolin-4-amine (1.45–1.85 mmol) was combined with 1.3

eq. of potassium formate (1.89–2.41 mmol) then dissolved in 20 mL of formic acid. Solution was refluxed for 14–16 h at 120–125 °C. Upon completion and cooling to room temperature, the reaction mixture was diluted with ~ 30 mL of brine solution, ~ 50 mL of saturated $NaHCO_3$ solution before extracting with ~ 25 mL (x3) of EtOAc and washed with 25 mL (x 3) parts of brine solution. The combined aqueous layers were washed twice with 15 mL of EtOAc. The combined EtOAc layers were dried over $MgSO_4$ before removing the EtOAc in vacuo to yield a solid product that generally did not require additional purification. Additional purification as required, was accomplished by silica gel column chromatography using 5:1 EtOAc:MeOH as the eluent. The compounds were obtained as white solids with yields ranging from 58–70%.

4-(Benzylamino)quinazolin-2-ol (23). Yield 65% (0.30 g, 1.20 mmol); Mp 198–200 °C. ^{1}H-NMR (300 MHz, DMSO-d_6): δ 10.60 (br s, 1H), δ 8.67 (t, J = 5.7 Hz, 1H), δ 8.47 (d, J = 8.1 Hz, 1H), δ 8.35 (t, J = 7.5 Hz, 1H), δ 7.31–7.09 (m, 7H), δ 4.66 (d, J = 5.6 Hz, 2H). HRMS (ESI) m/z calcd for $C_{15}H_{14}N_3O$ $[M + H]^+$ 252.1059, found 252.1130. Purity: 99.7%

General procedure for the synthesis of N^4-substituted-quinazolin-2-urea.[305] In a pressure vial, 0.5 g of 2-chloro-*N*-substituted-quinazolin-4-amine (~ 1.85 mmol) was mixed with 6 eq. urea (~ 11.2 mmol) and 10 mL of anhydrous 1,4-dioxane, sealed tightly and heated at 160–165 °C in an oil bath for 24 h. After cooling to room temperature, the solution was diluted with 20 mL EtOAc, washed three times with 20 mL brine solution; the aqueous layers were extracted twice with 20 mL EtOAc. The combined organic layers were dried over $MgSO_4$, evaporated in vacuo and purified using silica gel column chromatography using a combination of 5:1 EtOAc:MeOH and 5:1 EtOAc:MeOH w/ 1% TEA (triethylamine) to afford target compounds as white solids with yields ranging from 45–50% and the hydrolyzed amine compounds as off white solids with yields ranging from 50–55%.

1-(4-(Benzylamino)quinazolin-2-yl)urea (24). Yield 55% (0.30 g, 1.02 mmol); Mp 214–216 °C. ^{1}H NMR (300 MHz, DMSO-d_6): δ 9.11 (br s, 1H), δ 8.88 (br s, 1H), δ 8.76 (br s, 1H), δ 8.12 (d, J = 8.2 Hz, 1H), δ 7.42 (d, J = 8.2 Hz, 1H), δ 7.31–7.26 (m, 2H), δ 7.24–7.20 (m, 5H), δ 6.80 (br s, 1H), δ 4.70 (d, J = 5.7 Hz, 2H). HRMS (ESI) m/z calcd for $C_{16}H_{16}N_5O$ $[M + H]^+$ 294.1277, found 294.1348. Purity: 95.5%

General procedure for the synthesis of N^4-substituted-quinazolin-2-glycinamide.[299] In a 50 mL pressure vial, 0.25 g of 2-chloro-*N*-substituted-quinazolin-4-amine (~ 0.83 mmol) was combined with 3 eq. (~ 2.50 mmol) of glycinamide.HCl then dissolved in 5 mL of 1,4-dioxane followed by the addition of 5 eq. of DBU (~ 4.15 mmol). Pressure vial was sealed and stirred in an oil bath at 150–155 °C for 4 h. Upon completion and cooling to room temperature, the reaction mixture was diluted with ~ 40 mL of EtOAc and washed 25 mL (x 3) brine solution. The combined aqueous layers were washed with ~ 25 mL of EtOAc. The combined EtOAc layers were dried over $MgSO_4$ and EtOAc was removed in vacuo to yield solid that was purified by silica gel column chromatography using 5:1 EtOAc:MeOH as the eluent to afford target compounds as pale yellow to brown solids with yields ranging between 52–58%.

2-((4-(Benzylamino)quinazolin-2-yl)amino)acetamide (25). Yield 58% (0.16 g, 0.54 mmol); Mp 161–163 °C. ^{1}H NMR (300 MHz, DMSO-d_6): δ 8.23 (br s, 1H), δ 8.02 (d, J = 8.2 Hz, 1H), δ 7.47 (t, J = 7.5 Hz, 1H), δ 7.38–7.17 (m, 7H), δ 7.04 (t, J = 7.5 Hz, 1H), δ 6.95 (br s, 1H), δ 6.45 (br s, 1H), δ 4.68 (d, J = 5.5 Hz, 2H), δ 3.81 (d, J = 5.2 Hz, 2H). HRMS (ESI) m/z calcd for $C_{17}H_{18}N_5O$ $[M + H]^+$ 308.1433, found 308.1506. Purity: 98.8%

General procedure for the synthesis of N^4-substituted-quinazolin-2-acetamide.[312] In a 50 mL round bottom flask (RBF), 0.5 g of N^4-substituted-quinazolin-2,4-diamine (1.54–2.00 mmol) was dissolved in 15 mL of 1,4-dioxane and 10 mL of glacial acetic acid/acetyl chloride combination (4:1 ratio). Solution was refluxed for 24 h at 90–95 °C. Upon completion and cooling to room temperature, the reaction mixture was diluted with ~ 30 mL of brine solution, ~ 30 mL of concentrated $NaHCO_3$ solution before extracting with ~ 25 mL (x 3) of EtOAc and washed with 25 mL (x 2) brine solution. The combined aqueous layers were washed twice with 15 mL of EtOAc. The combined EtOAc layers were dried over $MgSO_4$ and the organic solvent was removed in vacuo to yield a solid product that generally did not require additional purification. Purification was carried out as required, by silica gel column chromatography using 5:1 EtOAc:MeOH as the eluent to afford target compounds as white solids with yields ranging from 35–42%.

***N*-(4-(Benzylamino)quinazolin-2-yl)acetamide (26).** Yield 50% (0.29 g, 0.99 mmol); Mp 219–221 °C. ^{1}H NMR (300 MHz, DMSO-d_6): δ 9.68 (br s, 1H), δ 8.18 (t, J = 6.0 Hz, 1H), δ 7.95 (d, J = 6.0 Hz, 1H), δ 7.42 (t, J = 8.4 Hz, 1H), δ 7.34–7.24 (m, 5H), δ 7.18 (d, J = 6.0 Hz, 1H), δ 6.95 (t, J = 6.0 Hz, 1H), δ 4.69 (d, J = 6.0 Hz, 2H), δ 2.22 (s, 3H). HRMS (ESI) m/z calcd for $C_{17}H_{17}N_4O$ $[M + H]^+$ 293.1324, found 293.1396. Purity: 99.9%

General procedure for the synthesis of N^4-substituted-N^2-alkyl-quinazolin-2,4-diamine.[299, 313] In a 50 mL pressure vial (PV), 0.25 g of 2-chloro-*N*-substituted-quinazolin-4-amine (~ 0.83 mmol) was combined with 2 eq. (~ 1.66 mmol) of primary amine (methyl-, ethyl-, *n*-propyl-, isopropyl- or cyclopropylamine) then dissolved in 5 mL of 1,4-dioxane followed by the addition of 3 eq. of DIPEA (~ 2.40 mmol). Pressure vial was sealed and stirred in an oil bath at 150–155 °C for 2 h. Upon completion and cooling to room temperature, the reaction mixture was diluted with ~ 40 mL of EtOAc and washed with brine solution (25 mL x 2). The combined aqueous layer was washed with ~ 25 mL of EtOAc. The combined EtOAc layers were dried over $MgSO_4$ before removing EtOAc in vacuo to yield a solid product that was purified by silica gel column chromatography using 5:1 EtOAc:MeOH as the eluent to afford pale yellow to brown solids yielding at 55–70%.

N^4-(Benzyl)-N^2-methylquinazoline-2,4-diamine (27). Yield 68% (0.33 g, 1.25 mmol); Mp 139–141 °C. ^{1}H NMR (300 MHz, DMSO-d_6): δ 8.23 (t, J = 6.0 Hz, 1H), δ 7.95 (d, J = 6.0 Hz, 1H), δ 7.55 (t, J = 9.0 Hz, 1H), δ 7.34–7.20 (m, 6H), δ 6.99 (t, J = 6.0 Hz, 1H), δ 6.53 (br s, 1H), δ 4.66 (d, J = 6.0 Hz, 2H), δ 2.74 (d, J = 4.7 Hz, 3H). HRMS (ESI) m/z calcd for $C_{16}H_{17}N_4$ $[M + H]^+$ 265.1375, found 265.1446. Purity: 100.0%

N^4-(Benzyl)-N^2-ethylquinazoline-2,4-diamine (28). Yield 70% (0.36 g, 1.29 mmol); Mp 130–132 °C. ^{1}H NMR (300 MHz, DMSO-d_6): δ 8.25 (t, J = 6.0 Hz, 1H), δ 7.96 (d, J = 6.0 Hz, 1H), δ 7.45 (t, J = 9.0 Hz, 1H), δ 7.36–7.18 (m, 6H), δ 6.99 (t, J = 6.0 Hz, 1H), δ 6.40 (br s, 1H), δ 4.67 (d, J = 6.0 Hz, 2H), δ 3.27–3.22 (m, 2H), δ 1.03 (t, J = 6.0 Hz, 3H). ^{13}C NMR (100 MHz, DMSO-d_6) δ 159.78, δ 159.57, δ 158.96, δ

151.63, δ 139.94, δ 132.33, δ 128.16, δ 127.98, δ 127.34, δ 127.26, δ 126.58, δ 126.23, δ 122.68, δ 119.90, δ 43.26, δ 35.25, δ 15.08. HRMS (ESI) m/z calcd for $C_{17}H_{19}N_4$ $[M + H]^+$ 279.1531, found 279.1602. Purity: 98.0%

***N*^{4}-(Benzyl)-*N*^{2}-propylquinazoline-2,4-diamine (29).** Yield 58% (0.31 g, 1.06 mmol); Mp 114–116 °C. ^{1}H NMR (300 MHz, DMSO-*d*$_6$): δ 8.21 (t, *J* = 6.0 Hz, 1H), δ 7.94 (d, *J* = 6.0 Hz, 1H), δ 7.42 (t, *J* = 9.0 Hz, 1H), δ 7.35–7.23 (m, 4H), δ 7.18 (m, 2H), δ 6.95 (t, *J* = 6.0 Hz, 1H), δ 6.40 (br s, 1H), δ 4.66 (d, *J* = 6.0 Hz, 2H), δ 3.14 (q, *J* = 6.0 Hz, 2H), δ 1.45–1.40 (m, *2*H), δ 0.78 (t, *J* = 7.5 Hz, 3H). HRMS (ESI) m/z calcd for $C_{18}H_{21}N_4$ $[M + H]^+$ 293.1688, found 293.1759. Purity: 98.9%

***N*^{4}-(Benzyl)-*N*^{2}-isopropylquinazoline-2,4-diamine (30).** Yield 67% (0.37 g, 1.27 mmol); Mp 135–137 °C. ^{1}H NMR (300 MHz, DMSO-*d*$_6$): δ 8.30 (t, *J* = 6.0 Hz, 1H), δ 7.90 (d, *J* = 6.0 Hz, 1H), δ 7.42 (t, *J* = 9.0 Hz, 1H), δ 7.35–7.23 (m, 4H), δ 7.20–7.18 (m, 2H), δ 6.90 (t, *J* = 6.0 Hz, 1H), δ 6.28 (br s, 1H), δ 4.67 (d, *J* = 6.0 Hz, 2H), δ 4.13–3.99 (m, 1H), δ 1.05 (d, *J* = 6.0 Hz, 6H). HRMS (ESI) m/z calcd for $C_{18}H_{21}N_4$ $[M + H]^+$ 293.1688, found 293.1759. Purity: 98.1%

***N*^{4}-(Benzyl)-*N*^{2}-cyclopropylquinazoline-2,4-diamine (31).** Yield 56% (0.30 g, 1.03 mmol); Mp 145–147 °C. ^{1}H NMR (300 MHz, DMSO-*d*$_6$): δ 8.25 (t, *J* = 6.0 Hz, 1H), δ 7.98 (d, *J* = 6.0 Hz, 1H), δ 7.40 (t, *J* = 9.0 Hz, 1H), δ 7.30–7.20 (m, 5H), δ 7.18 (d, *J* = 6.0 Hz, 1H), δ 6.95 (t, *J* = 6.0 Hz, 1H), δ 6.45 (br s, 1H), δ 4.68 (d, *J* = 6.0 Hz, 2H), δ 2.78–2.66 (m, 1H), δ 0.60 (d, *J* = 4.8 Hz, 2H), δ 0.45 (d, *J* = 4.8 Hz, 2H). HRMS (ESI) m/z calcd for $C_{18}H_{19}N_4$ $[M + H]^+$ 291.1531, found 291.1603. Purity: 99.6%

4.5.2. *Biological Screening*

4.5.2.1. *Human Cholinesterase (hChE) Assay*[299, 313]

The inhibition profile of quinazoline derivatives was evaluated using the Ellman (DTNB) reagent.[315] Human AChE and BuChE enzymes were obtained from Sigma-Aldrich, St. Louis, MO, USA (AChE product number C0663 and BuChE product number B4186 respectively). The cholinesterase inhibitors tacrine (item number 70240, Cayman Chemical Company, Ann Arbor, MI), donepezil (product number D6821, Sigma-Aldrich, St. Louis, MO), galantamine (product number G1660, Sigma-Aldrich, St. Louis, MO) and rivastigmine (product number SML0881, Sigma-Aldrich, St. Louis, MO) were used as reference agents. Quinazoline derivative stock solutions were prepared in DMSO (maximum 1% v/v in final wells) and diluted in buffer solution (50 mM Tris.HCl, pH 8.0, 0.1 M NaCl, 0.02 M $MgCl_2.6H_2O$). Then 160 µL of 5,5'-dithiobis(2-nitrobenzoic acid) (1.5 mm DTNB), 50 µL of *h*AChE (0.22 U/mL in 50 mM Tris.HCl, pH 8.0, 0.1% w/v bovine serum albumin, BSA) or 50 µL of *h*BuChE (0.12 U/mL in 50 mM Tris.HCl, pH 8.0, 0.1% w/v BSA) were added to 96-well plates after which 10 µL each of quinazoline derivatives (final concentration range 0.1–50 µM) were added and incubated for 5 min. Then 30 µL of either acetylthiocholine iodide (15 mM AThCl prepared in ultra pure water) or *S*-butyrylthiocholine iodide (15 mM BThCI prepared in ultra pure water) were added. The absorbance was measured at different time intervals (0, 60, 120, 180, 240 and 300 s) using a wavelength of 412 nm. The inhibitory concentration (IC_{50} values) was calculated from the concentration–inhibition dose response curve on a logarithmic scale. The results were expressed as average values based on two to three independent experiments run in triplicate measurements.

4.5.2.2. *Amyloid-β (Aβ) Aggregation Assay*[317]

The ability of quinazoline-based derivatives to inhibit Aβ-aggregation kinetics was determined using a ThT-binding fluorescence assay. These assays were conducted in Costar, black-surround, clear-bottom 384-well plates with frequent shaking (30 sec. of linear shaking at 730 cpm every 5 minutes) and constant

heating at 37 °C for 24 h. The ThT excitation/emission was measured at 440 nm/490 nm and readings were taken every 5 minutes using a BioTek Synergy H1 microplate reader. Quinazoline stock solutions were prepared in DMSO and diluted to 10x in 215 mM phosphate buffer at pH 7.4. Abeta.HFIP samples (Aβ40 or Aβ42, rPeptide, Bogart, USA) were dissolved in 1% ammonium hydroxide, sonicated at room temperature for 5 minutes then diluted to 50 μM in 215 mM phosphate buffer (pH 7.4). A 15 μM ThT stock solution was prepared with 50 mM glycine and adjusted to pH 7.4. The assay was carried out by adding 44 μL ThT, 20–35 μL buffer, 1 μL DMSO (for background and controls only) followed by the addition of 8 μL of 10x compound dilutions (1–25 μM concentration range). An end point reading was conducted to evaluate potential test compound interference with ThT-fluorescence before adding 8 μL of Aβ40 or Aβ42 stock solutions (5 μM final concentration). Plates were sealed with a transparent plate film before initiating the assay. RFU values were corrected for ThT-interference before calculating end point percent inhibitions or IC_{50} values and obtaining the aggregation kinetic plots. Data presented was an average of triplicate reading for two-three independent experiments.

4.5.2.3. *TEM Assay and Imaging*[142, 190, 207, 317]

In Costar 96-well, round-bottom plates were added 80 μL of 215 mM phosphate buffer, 20 μL of 10x test compound dilutions (250 μM – prepared in the same way as for the ThT assay) and 100 μL of 50 μM Aβ40 or Aβ42 respectively. For the control wells, 2 μL of DMSO and 18 μL of phosphate buffer was added. Final Aβ: test compound ratio was 1:1 (25 μM). Plates were incubated on a Fisher plate incubator set to 37 °C and the contents were shaken at 730 cpm for 24 h. To prepare the TEM grids, ~ 20 μL droplet was added using a disposable Pasteur pipette over the formvar-coated copper grids (400 mesh). Grids were air-dried for about 3 h before adding two droplets (~ 40 μL, using a disposable Pasteur pipette) of ultra-pure water and using small pieces of filter paper to wash out precipitated buffer salts. After air-drying for ~ 15-20 min, the grids were negatively stained by adding a droplet (~ 20 μL, using a disposable Pasteur pipette) of 2% phosphotungstic acid (PTA) and immediately after the grids were dried using small pieces of filter paper. Grids were further air-dried overnight. The scanning was carried out using a Philips CM 10

transmission electron microscope at 60 kV (Department of Biology, University of Waterloo) and micrographs were obtained using a 14-megapixel AMT camera.

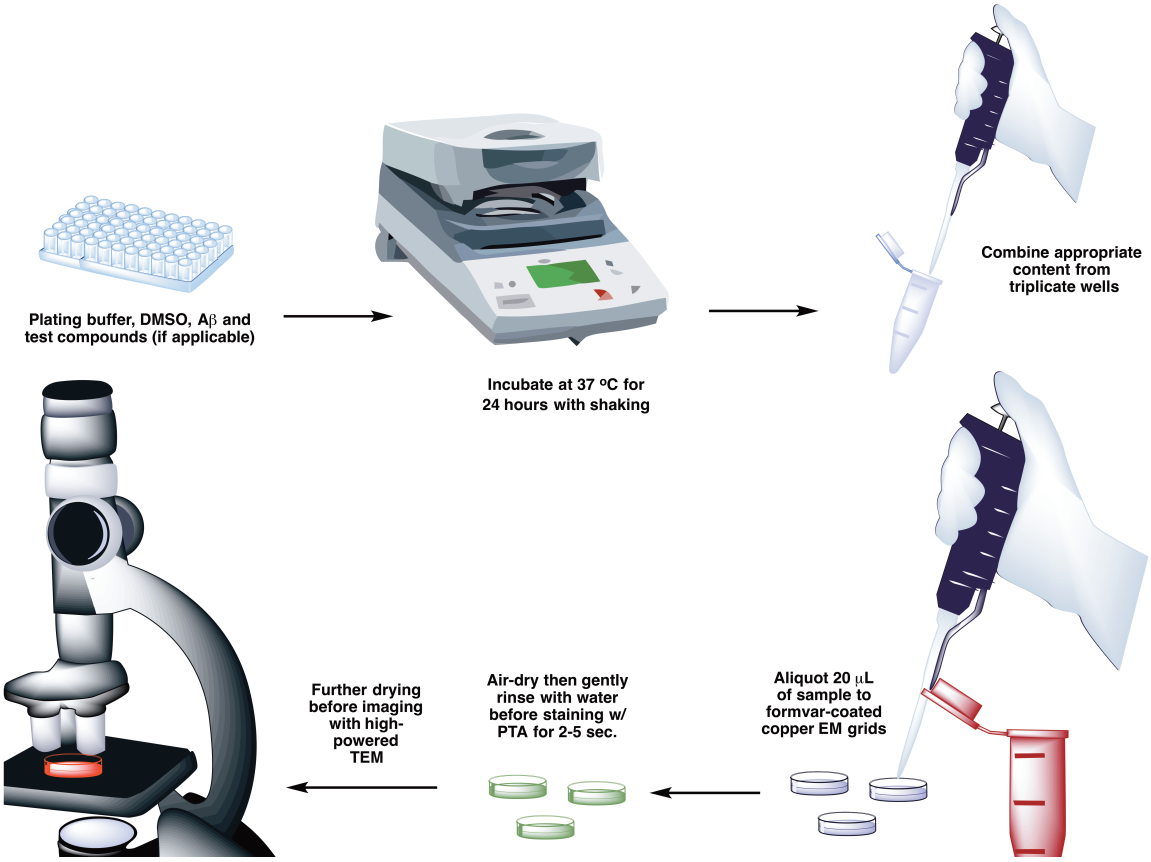


Figure 60: Principles of the TEM imaging setup for assessing amyloid morphology with or without select derivatives.

4.5.2.4. *DPPH Scavenging Assay*[324]

The ability of select quinazolines to scavenge the DPPH radical was utilized as a measure of antioxidant capacity. Quinazoline stock solutions were prepared in anhydrous methanol (500 µM) and the DPPH solution was also prepared in anhydrous methanol (56 µM). The addition sequence was carried out in a 96-well clear, flat bottom plate as follows: 90 µL DPPH, 10 µL test compound solution (50 µM) final

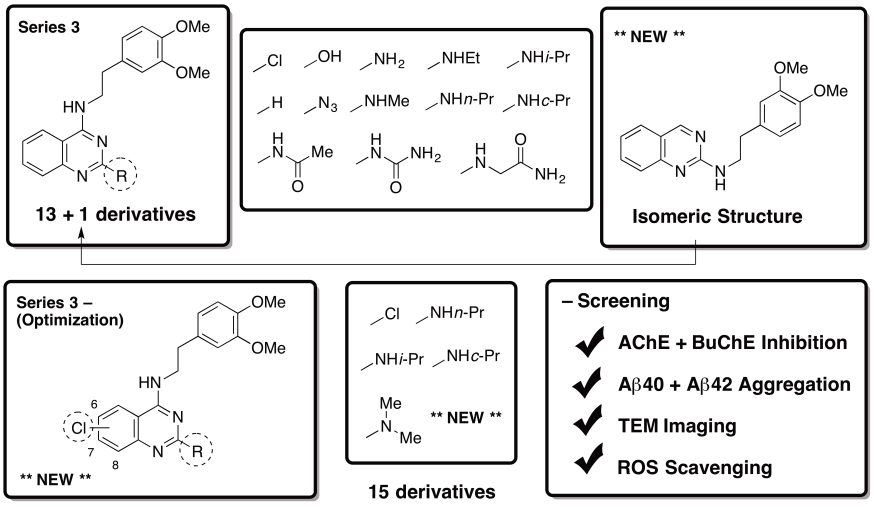
concentration. Control solutions contained 90 µL anhydrous methanol and 10 µL test compound whereas DPPH control contained 90 µL of DPPH, and 10 µL anhydrous methanol. This readings were taken initially at 517 nm with 30 sec. shaking (double orbital at 530 cpm) prior to the 1 h, light restrictive, incubation period at room temperature after which readings were taken again at 517 nm after another round of 30 sec shaking (double orbital at 530 cpm) using a BioTek Synergy H1 microplate reader. The results were expressed as percentage inhibition and the data presented was average of triplicate reading (for two independent experiments).

4.5.3. *Computational Chemistry*[299, 313, 317, 324]

The molecular docking studies were conducted using Discovery Studio 4.0 (Structure-Based-Design program) from BIOVIA Inc. San Diego, USA. Select quinazolines derivatives were built and minimized using the *small molecules* module in Discovery Studio. X-ray coordinates of human cholinesterases were obtained from the protein data bank (*h*AChE PBD ID: 1B41 and *h*BuChE PDB ID: 1P0I) and prepared using the *macromolecules* module in Discovery Studio. Ligand binding sites were defined by selecting a 12 Å radius sphere for AChE and 15 Å radius sphere for BuChE. The molecular docking was performed using the *receptor-ligand interactions* module in Discovery Studio. The LibDock algorithm was used to find the most appropriate binding modes for select quinazoline derivatives using CHARMm force field. The docked poses obtained were ranked based on the LibDock scores and were analyzed by evaluating all the polar and nonpolar interactions. For amyloid-β docking studies, the NMR solution structure of Aβ fibrils were obtained from the protein data bank (PDB ID: 2LMN). Aβ dimer and Aβ fibril assemblies were built using the *macromolecules* module in Discovery Studio. Ligand binding site was defined by selecting a 15 Å radius sphere for both Aβ assemblies. Molecular docking was performed using the *receptor-ligand interactions* module in Discovery Studio, where the LibDock algorithm was used to find the most appropriate binding modes for select quinazoline derivatives using CHARMm force field. The docked poses obtained were ranked based on the LibDock scores and were analyzed by evaluating all the polar and nonpolar interactions.

CHAPTER 5

• Development and Evaluation of *N*-(3,4-dimethoxyphenethyl)quinazolin-4-amines as Dual ChE and Aβ Aggregation Inhibitors •



* Chapter banner

5.1. Introduction

The dimethoxybenzyl series (Chapter 3) provided good insight into the requirements and restrictions toward the dual targeting of the ChEs and Aβ aggregation. The introduction of the dimethoxyphenethyl series was a direct comparison to the Chapter 3 counterparts. A regioisomeric assessment was also included with this Chapter comparing *N*-(3,4-dimethoxyphenethyl)-quinazolin-4-amine vs. *N*-(3,4-dimethoxy phenethyl)-quinazolin-2-amine, and as observed in Chapter 4, interesting SAR was projected from this assessment. An optimization phase is also presented in this Chapter, where select C2-groups, including the previously unutilized dimethylamine group, were applied to various chloroquinazoline scaffolds to acquire additional SAR data.

This chapter highlights the synthesis and development of target derivatives (refer to the chapter banner above) along with the acquisition and assessment of the SAR data. For the most part, the synthetic approaches and mechanisms here have been previously discussed in Chapter 3 and 4. A brief summary is provided prior to the listing of experimental data and methodology.

5.2. Hypothesis

With respect to this series, the re-introduction of the 3,4-dimethoxy moiety, with the additional methylene unit in the linker chain, should regain some benefit with respect to AChE targeting, while offering an additional point of rotation to enhance binding conformations.

On the other hand, continuing with the existing selection of C2-groups offers an opportunity to evaluate and compare the impact of the 3,4-dimethoxybenzyl (Chapter 3) vs. the 3,4-dimethoxyphenethyl moieties at the C4-position. Previous predications hold true with entities like the azide and carbonyl-based groups with respect to their inability to target BuChE. The increased free-rotation potential at the C4-position, combined with alkylamines at the C2-posiiton, are predicted to aid with BuChE inhibition, while effectively targeting AChE and modulating amyloid aggregation. As observed in Chapter 4, the introduction of a regioisomer provided good insight into the roles of the C2- and C4-groups with respect to dual ChE and dual amyloid targeting.

Lastly, the introduction of the chloroquinazoline scaffolds, as part of the optimization process, are predicted to significantly influence ChE binding and amyloid modulation. The new introduction of the dimethylamine group at the C2-position, as part of the optimization process, would present the only tertiary amine based quinazolines in the collective chemical library. The SAR obtained from these derivatives should provide critical insight.

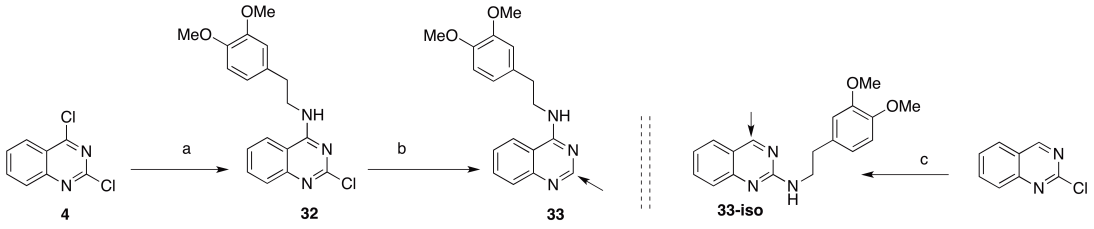
5.3. Results and Discussions

The proceeding sub-chapter discusses new synthetic methodology, while briefly highlighting previously-established routes to desired derivatives. Biological assessments in the cholinesterase and amyloid-β aggregation assay (to obtain IC_{50} values and/or investigation aggregation kinetics) are conducted. Aggregate load is corroborated via transmission electron microscopy in amyloid morphology screening and select derivatives are assessed for ROS scavenging in the DPPH assay. Computational studies are performed in the ChE X-ray structures and amyloid models to evaluate the acquisitioned SAR data.

5.3.1. *Synthesis*

As previously described in Chapters 3 and 4, initial coupling in this series utilized 2,4-DCQ (**4**) to add the 3,4-dimethoxyphenethylamine group to the C4-position of the quinazoline scaffold, via a NAS reaction, to yield 2-chloro-*N*-(3,4-dimethoxyphenethyl)quinazolin-4-amine (**32**, Scheme 13, 80–85% yield).[299, 303] The C2-unsubstituted derivative (*N*-(3,4-dimethoxyphenethyl)quinazolin-4-amine, **33**, Scheme 13, ~ 45% yield) was also attained via the Pd/C and hydrazine-driven dehalogenation reaction.[304] The regioisomer of **33** was generated by heating 2-chloroquinazoline and 3,4-dimethoxyphenethylamine, under high temperature and pressure conditions, to yield *N*-(3,4-dimethoxyphenethyl)quinazolin-2-amine, **33-iso**, Scheme 13, ~ 55% yield).

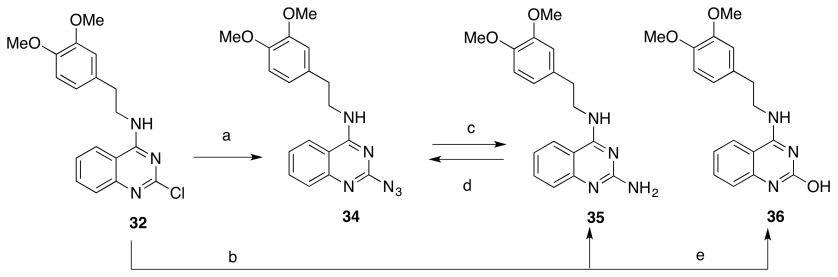
Scheme 13[a]



[a]**Reagents and conditions:** Synthetic routes toward quinazoline-based derivatives **32**, **33** and **33-iso**. (a) 3,4-dimethoxyphenethylamine, DIPEA, EtOH, reflux, 4 h; (b) Pd/C, hydrazine hydrate, EtOH, reflux, 2 h; (c) 3,4-dimethoxyphenethylamine, DIPEA, 1,4-dioxane, pressure vial, 150–155 °C, 2 h.

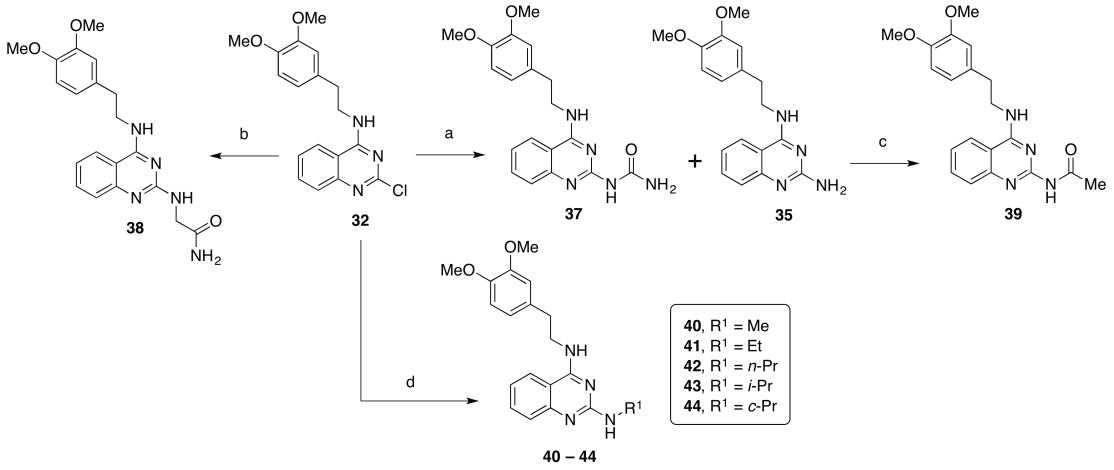
Synthesis of 2-azido-*N*-(3,4-dimethoxyphenethyl)quinazolin-4-amine (**34**, Scheme 14, ~ 90% yield) was accomplished as previously described utilizing sodium azide,[305, 306] while the generation of the C2-amino derivative (**35**, Scheme 14, N^4-(3,4-dimethoxyphenethyl)quinazoline-2,4-diamine) was primarily conducted using the azide reduction approach via Pd/C and hydrazine.[305] The effective formate/formic acid approach was utilized to generate **36** (4-(3,4-dimethoxyphenethyl)amino)quinazolin-2-ol, Scheme 14, yield ~ 65%).

Scheme 14[a]



[a]**Reagents and conditions:** Synthetic routes toward quinazoline-based derivatives **34**–**36.** (a) Sodium azide, EtOH, acetic acid, 90–95 °C, 2 h; (b) Cu_2O, K_2CO_3, DMEDA, ethylene glycol, ammonium hydroxide, pressure vial, oil bath, 105 °C, 24 h; (c) Pd/C, hydrazine hydrate, EtOH, reflux, 2 h; (d) HCl, sodium nitrite, sodium azide, 0 °C–r.t., 1 h; (e) potassium formate, formic acid, 120–125 °C, 14–16 h.

Scheme 15[a]

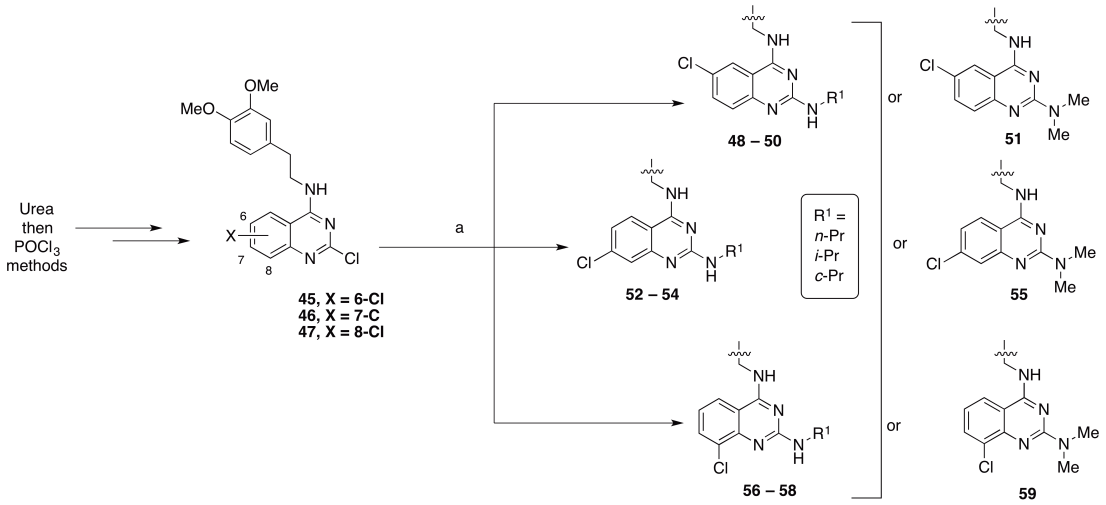


[a]**Reagents and conditions:** Synthetic routes toward quinazoline-based derivatives **37**–**44**. (a) Urea, 1,4-dioxane, pressure vial, 160–165 °C, 24 h.; (b) glycinamide, DBU, 1,4-dioxane, pressure vial, 150–155 °C, 4 h.; (c) acetyl chloride, acetic acid, 1,4-dioxane, 120 °C, 24 h. (d) Primary amine (R^1 = Me, Et, *n*-Pr, *i*-Pr or *c*-Pr), DIPEA, 1,4-dioxane, pressure vial 150–155 °C, 2 h.

The development of both the C2-carbonyl based derivatives **37** (C2 = urea), **38** (C2 = glycinamide), **39** (C2 = acetamide) and the C2-alkylamine based derivatives (**40**–**44**) was accomplished as previously described in Chapter 3 and 4 (Scheme 15).

The development of the dimethoxyphenethyl-based chloroquinazolines with various alkylamines at the C2-position (**45**–**59**) was accomplished using previously described methodologies in Chapter 3 and 4 (Scheme 16).

Scheme 16[a]



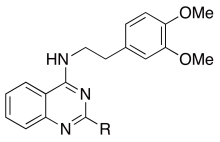
[a]**Reagents and conditions:** Synthetic routes toward quinazoline-based derivatives **45**–**59**. (a) Primary amine (R^1 = *n*-Pr, *i*-Pr or *c*-Pr) or dimethylamine, DIPEA, 1,4-dioxane, pressure vial 150–155 °C, 2 h.

5.3.2. *Cholinesterase*

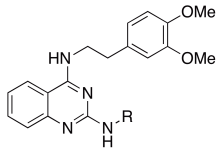
The ability of 2-substituted-*N*-(3,4-dimethoxyphenethyl)quinazolin-4-amines (**32**–**44**) and the C4-unsubstituted regiosiomer (**33-iso**) to target the cholinesterases (*h*AChE/*h*BuChE) was assessed using the DTNB method as described in Chapter 3 (Table 5). ChE data for phase-2 or optimization candidates (**45-59**) is showcased in Table 6.

Examination of Table 5 generally pointed to the overall inability of most derivatives within this series to target BuChE. When comparing the anti-BuChE activity of the alkylamine-based derivatives here (**40**–**44**) versus those in Chapter 3 (dimethoxybenzyl series, **14**–**18**), the addition of the second methylene linker at the C4-position significantly enhanced the biological activity with respect to BuChE, for the most part. With respect to AChE targeting, IC_{50} values ranged from 3 to 13 μM and that closely matched the 3 to 9 μM range seen with the dimethoxybenzyl counterparts (Chapter 3, Table 1).

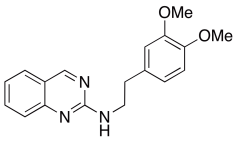
Table 5: Cholinesterase inhibition data for 2-substituted-*N*-(3,4-dimethoxyphenethyl)quinazolin-4-amines (**32**–**44**) and the C4-unsubstituted regiosiomer (**33-iso**).



32–34, 36



35, 37–44



33-iso

Derivative	R-Grp	ChE IC_{50} (μM) [a]		SI [b]	ClogP [c]	MV (Å^3) [d]	HBD:HBA [e]
		*h*AChE	*h*BuChE				
32	Cl	2.8 ± 0.3	> 50	–	4.40	225.3	1:5
33	H	2.8 ± 0.2	> 50	–	3.64	210.9	1:5
33-iso	–	8.4 ± 0.9	> 50	–	3.64	252.1	1:5
34	N_3	9.5 ± 1.0	> 50	–	5.05	271.3	1:7
35	H	2.5 ± 0.2	> 50	–	2.98	209.5	3:6
36	OH	7.6 ± 0.5	> 50	–	4.26	259.9	2:6
37	$CONH_2$	8.7 ± 0.7	> 50	–	3.65	287.0	4:8
38	CH_2CONH_2	12.5 ± 1.5	> 50	–	3.08	304.2	4:8
39	COMe	7.4 ± 0.6	> 50	–	3.18	294.6	2:7
40	Me	8.5 ± 0.5	4.5 ± 0.3	1.89	4.45	229.4	2:6
41	Et	7.5 ± 0.4	14.0 ± 1.8	0.54	4.98	245.9	2:6
42	*n*-Pr	7.0 ± 0.6	24.9 ± 3.0	0.28	5.51	258.6	2:6
43	*i*-Pr	7.6 ± 0.7	7.8 ± 0.9	0.97	5.29	259.9	2:6
44	*c*-Pr	7.2 ± 0.8	5.6 ± 0.4	1.29	5.03	252.7	2:6
Donepezil	–	0.03 ± 0.002	3.6 ± 0.4	0.01	4.59	321.7	0:4
Tacrine	–	0.16 ± 0.01	0.04 ± 0.001	4.00	3.27	165.6	2:2
Galantamine	–	2.6 ± 0.6	> 50	–	1.18	239.4	1:4
Rivastigmine	–	6.5 ± 0.5	> 10	–	2.10	226.3	0:4

Notes: [a] IC_{50} values are an average ± SD of triplicate readings based on two to three independent experiments. [b]Selectivity index is calculated as (*h*AChE IC_{50}) ÷ (*h*BuChE IC_{50}). [c]ClogP values were determined using ChemDraw Professional 15.0. [d]Molecular volumes in Å^3 units were determined using Discovery Studio, Structure-Based Design software, BIOVIA Inc., USA. [e]Showcasing the ratio of HBD = hydrogen-bonding donors to HBA = hydrogen-bonding acceptors.

Interestingly, both **32** (C2 = Cl) and **33** (C2 = H) showcased equipotent activity in AChE (IC_{50} = 2.8 μM) matching that of galantamine, while **33**'s regiosiomer was 3-fold less potent (**33-iso**, IC_{50} = 8.4 μM). The azide functionality in this series (**34**, IC_{50} = 9.5 μM) was comparable to its dimethoxybenzyl counterpart in Chapter 3 (**8**, IC_{50} = 8.3 μM, Table 1). That observation carried over to the C2-amino derivative (**35**, IC_{50} = 2.6 μM), which was roughly 4-fold more potent compared to the azide derivative and equipotent to **9** (Chapter 3, Table 1). More so, the decreased potency with a C2-hydroxy group observed in Chapter 3 with the dimethoxybenzyl series (**9** vs. **10**) was also seen here, where derivative **36** was 3-fold less potent compared to **35** but also equipotent to **10** (Chapter 3, Table 1).

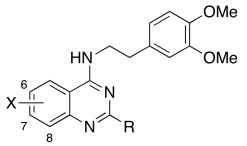
With respect to the carbonyl-based derivatives, similar to those in Chapter 3, derivatives **37**–**39** exhibited similar activity toward AChE (IC_{50} ~ 8 μM); however, the glycinamide derivative here (**38**) was less potent compared to its dimethoxybenzyl counterpart in Chapter 3 (IC_{50} ~ 13 μM vs. 7 μM). All derivatives discussed thus far within this series were inactive toward BuChE, a similar observation with those dimethoxybenzyl counterparts in Chapter 3.

The introduction of alkylamines at the C2-position (derivatives **40**–**44**, Table 5) established comparable activity toward AChE (IC_{50} ~ 7.6 μM) as seen with the dimethoxybenzyl counterpart (**14**–**18**, Chapter 3, IC_{50} ~ 6.6 μM). That said, the alkylamine-based derivatives in this series were anywhere from 1.2 to 6.8-fold more effective at targeting BuChE compared to derivatives **14**–**18**, with C2-propylamine showing the least improvement. Another interesting note, while **14–18** (Chapter 3) exhibited BuChE activity ranging from 25–30 μM the dimethoxyphenethyl counterparts (**40–44**) exhibited a wider range of BuChE activity (4.5–24.9 μM). More so, derivatives **40** and **44** were the first amongst all series discussed thus far to exhibit selective inhibition of BuChE. Those were also the most potent BuChEIs in this series (close in activity with donepezil IC_{50} ~ 4 μM), suggesting that smaller, hydrophobic groups were needed to accommodate the larger C4-dimethoxy phenethylamine group to achieve desirable inhibition. The ranking of the alkyl side chains, with respect to BuChE inhibition, were: Me > *c*-Pr > *i*-Pr > Et > *n*-Pr.

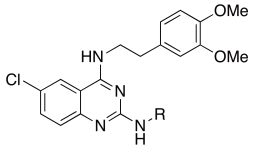
Considering the general advantage of placing alkylamines at the C2-position, along with the dimethoxyphenethylamine group at the C4-position, the optimization of **42**–**44** (C2 = *n*-Pr, *i*-Pr and *c*-Pr) was investigated on chloroquinazoline scaffolds (6-, 7- or 8-chloroquinazoline). The introduction of the new C2-group (dimethylamine, $–N(Me)_2$) was meant to correlate with the isopropylamine functionality. As

seen in Table 6, the chloroquinazoline derivatives (**45**–**59**) showcased an activity range of 6.2–13.4 μM (IC_{50}) toward AChE and 3.9– >50 μM (IC_{50}) toward BuChE. When compared to non-chloroquinazoline counterparts in Table 5, a general decrease in potency was observed suggesting that the chlorine addition was not as successful in enhancing ChE binding.

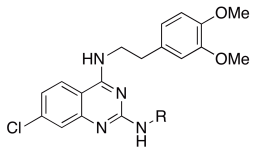
Table 6: Cholinesterase inhibition data for 2-substituted-*N*-(3,4-dimethoxyphenethyl)chloroquinazolin-4-amines (**45-59**).



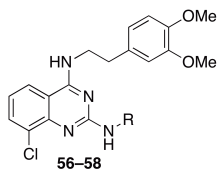
45, 51 X = 6-Cl
46, 55 X = 7-Cl
47, 59 X = 8-Cl



48–50



52–54



56–58

Derivative	R-Grp	ChE IC_{50} (μM) [a]		SI [b]	ClogP [c]	MV (Å^3) [d]	HBD:HBA [e]
		*h*AChE	*h*BuChE				
45	Cl	8.3 ± 0.9	> 50	–	5.13	281.6	1:5
46	Cl	9.0 ± 0.8	> 50	–	5.13	284.7	1:5
47	Cl	10.0 ± 0.9	> 50	–	5.13	280.9	1:5
48	*n*-Pr	6.2 ± 0.6	> 50	–	6.26	325.8	2:6
49	*i*-Pr	6.8 ± 0.7	20.34	0.34	6.04	320.4	2:6
50	*c*-Pr	8.0 ± 0.7	> 50	–	5.79	320.4	2:6
51	$N(Me)_2$	7.2 ± 0.7	31.27	0.23	5.29	311.1	1:6
52	*n*-Pr	7.2 ± 0.7	> 50	–	6.26	320.7	2:6
53	*i*-Pr	7.9 ± 0.8	3.94	2.01	6.04	324.5	2:6
54	*c*-Pr	8.7 ± 0.8	> 50	–	5.79	318.3	2:6
55	$N(Me)_2$	13.4 ± 1.1	> 50	–	5.29	311.8	1:6
56	*n*-Pr	6.5 ± 0.5	> 50	–	6.26	324.8	2:6
57	*i*-Pr	6.8 ± 0.7	19.29	0.35	6.04	324.5	2:6
58	*c*-Pr	6.6 ± 0.7	> 50	–	5.79	315.2	2:6
59	$N(Me)_2$	8.1 ± 0.8	> 50	–	5.29	310.4	1:6
Donepezil	–	0.03 ± 0.002	3.6 ± 0.4	0.01	4.59	321.7	0:4
Tacrine	–	0.16 ± 0.01	0.04 ± 0.001	4.00	3.27	165.6	2:2
Galantamine	–	2.6 ± 0.6	> 50	–	1.18	239.4	1:4
Rivastigmine	–	6.5 ± 0.5	> 10	–	2.10	226.3	0:4

Notes: [a] IC_{50} values are an average ± SD of triplicate readings based on two to three independent experiments. [b]Selectivity index is calculated as (*h*AChE IC_{50}) ÷ (*h*BuChE IC_{50}). [c]ClogP values were determined using ChemDraw Professional 15.0. [d]Molecular volumes in Å^3 units were determined using Discovery Studio, Structure-Based Design software, BIOVIA Inc., USA. [e]Showcasing the ratio of HBD = hydrogen-bonding donors to HBA = hydrogen-bonding acceptors.

Starting out with the C2-chlorine based derivatives, **45**–**47** were roughly three to four times less potent toward AChE (IC_{50} ~ 8-10 μM) compared to **32**. Placement of the chlorine atom from position 6 to 7 to 8 progressively reduced potency in AChE. Similar to **32**, none of these derivatives targeted BuChE.

When compared to **42**–**44**, the impact of chlorine placement at position 6 of the quinazoline scaffold in **48**–**50** had negligible impact on AChE inhibition (average IC_{50} ~ 7.0 vs. 7.3 μM) but significantly hindered BuChE inhibition, with the cyclopropyl-based derivative (**50**) suffering a 10-fold minimum decrease in BuChE potency (IC_{50} ~ 6 vs. > 50 μM). With the dimethylamine functionality at the C2-position (**51**), no significant impact on AChE inhibition was observed, while BuChE inhibition dropped 1.5-fold compared to the isopropylamine-based derivative (**49**) (IC_{50} ~ 31 vs. 20 μM).

Moving on, when compared to **42**–**44** and **48**–**50**, the impact of chlorine placement at position 7 in **52**–**54** had minor impact on AChE inhibition (average IC_{50} ~ 7.0 vs. 7.3 vs. 7.9 μM; respectively). In BuChE, chlorine placement (6 or 7 position) had no impact on inhibition with the propyl- and cyclopropyl-based derivatives (**52** and **54**), while the isopropyl-based derivative (**53**) displayed a 4-fold increase in potency compared to the 6-chloro isomer (**49**) (IC_{50} ~ 4 vs. 20 μM; respectively). In addition, **53** was also 2-fold more potent toward BuChE than the non-chlorinated counterpart (**43**) (IC_{50} ~ 4 vs. 8 μM; respectively). With the dimethylamine functionality however, (**55**) exhibited potency losses with both ChEs compared to **51** – AChE IC_{50} ~ 13 vs. 7 μM and BuChE IC_{50} > 50 vs. 30 μM; respectively.

Lastly, the impact of chlorine placement at position 8 in **56**-**58** elicited null or minor improvements on AChE inhibition (average IC_{50} ~ 6.6 μM) compared to other placements (**52**-**54** and **48**-**50**) and non-chlorinated (**42**-**44**) counterparts (average IC_{50} ~ 7.9 vs. 7.0 vs. 7.3 μM; respectively). In BuChE, chlorine placement at 8 position showcased comparable results as those observed with chlorine placement at position 6 and 7, with the exception of **53**. With the dimethylamine functionality, **59** exhibited similar potency to **51** in AChE (IC_{50} ~ 8 vs. 7 μM; respectively), while its inactivity toward BuChE matched that of **55**.

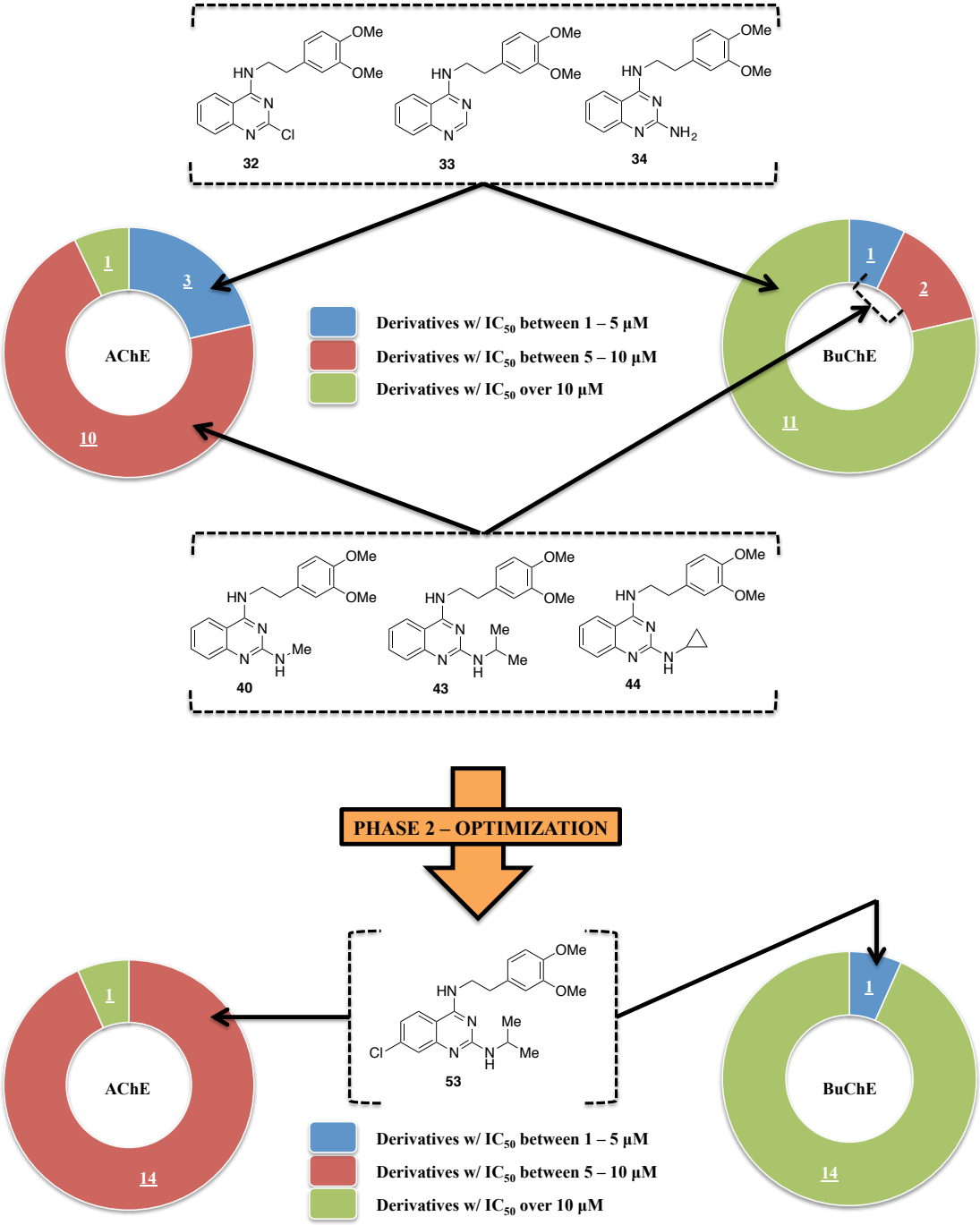


Figure 61: Cholinesterase metrics for fourteen 2-substituted-*N*-(3,4-dimethoxyphenethyl)quinazolin-4-amines (**32-44**) and 15 2-substituted-*N*-(3,4-dimethoxyphenethyl)chloroquinazolin-4-amines (**45-59**).

In summary, 29 derivatives were assessed for dual cholinesterase activity, of which derivative **35** (N^4-(3,4-dimethoxyphenethyl)quinazoline-2,4-diamine) was identified as the most active AChEI (IC_{50} = 2.6 μM), while derivative **53** (7-chloro-N^4-(3,4-dimethoxyphenethyl)-N^2-isopropylquinazoline-2,4-diamine) was identified as the most active BuChEI (IC_{50} ~ 4 μM) matching the activity level of donepezil. Generally, this series proved to be more or less as effective toward AChE as the dimethoxybenzyl series (Chapter 3). Activity toward BuChE was improved overall, while the introduction of the chloroquinazoline scaffolds and the dimethylamine functionality at the C2-position offered mixed outcomes, specifically with BuChE inhibition (Figure 61).

5.3.3. *Amyloid-β Aggregation*

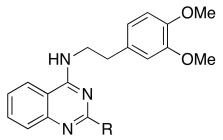
The ability of 2-substituted-*N*-(3,4-dimethoxyphenethyl)quinazolin-4-amines (**32**–**44**) and the C4-unsubstituted regiosiomer (**33-iso**) to modulate the aggregation kinetics of amyloid-β was assessed using the ThT-binding method described earlier in Chapter 3 (Table 7). Amyloid-β inhibitory data for phase-2 or optimization candidates (**45**–**59**) is showcased in Table 8.

Examination of Table 7 demonstrated the overall ability of this series to dually target Aβ aggregation (11 out of 14 derivatives as dual inhibitors). When compared to their dimethoxybenzyl counterparts in Chapter 3, inhibitory activity toward Aβ42 was improved across the board, while inhibitory activity toward Aβ40 was more of a mixed bag. Of noteworthy mention, derivatives **35** (C2 = NH_2) and **41** (C2 = NHEt) exhibited strong inhibitory activity toward Aβ40 that placed them between the activities of resveratrol and curcumin.

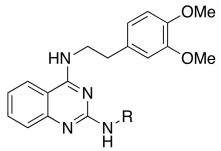
Starting out with the C2-chlorine derivative, **32** was significantly more active toward both Aβ40/42 (IC_{50} ~ 8 and 13 μM; respectively) as compared to its dimethoxybenzyl counterpart (**5**, Table 2). It was also the most active Aβ42 inhibitor in this sub-series. The dechlorination of **32** hindered Aβ42 activity significantly and also reduced Aβ40 activity by 1.5-fold. That said, **33** was still more active toward both Aβ40/42 as compared to its dimethoxybenzyl counterpart (**7**, Table 2). On the other hand, **33**'s regioisomer

was completely inactive toward both Aβ40/42, suggesting that the increased linearity of **33-iso** prevented the necessary destabilizing interactions with the amyloid structures.

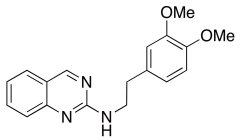
Table 7: Amyloid-β (Aβ40/42) inhibition data for 2-substituted-*N*-(3,4-dimethoxyphenethyl)quinazolin-4-amines (**32**–**44**) and the C4-unsubstituted regiosiomer (**33-iso**).



32–34, 36



35, 37–44



33-iso

Derivative	R-Grp	Amyloid-β IC_{50} (μM) [a]		SI [b]	ClogP [c]	MV (Å^3) [d]	HBD:HBA [e]
		Aβ40	Aβ42				
32	Cl	8.2 ± 1.5	13.0 ± 1.9	0.63	4.40	225.3	1:5
33	H	12.0 ± 2.4	36%	–	3.64	210.9	1:5
33-iso	–	NA	NA	–	3.64	252.1	1:5
34	N_3	40%	14%	–	5.05	271.3	1:7
35	H	2.7 ± 0.8	45%	–	2.98	209.5	3:6
36	OH	10.4 ± 1.2	32%	–	4.26	259.9	2:6
37	$CONH_2$	14.4 ± 2.9	33%	–	3.65	287.0	4:8
38	CH_2CONH_2	NA	NA	–	3.08	304.2	4:8
39	COMe	29%	22%	–	3.18	294.6	2:7
40	Me	6.6 ± 1.3	23.1 ± 2.5	–	4.45	229.4	2:6
41	Et	2.9 ± 0.5	41%	–	4.98	245.9	2:6
42	*n*-Pr	4.3 ± 0.9	14%	–	5.51	258.6	2:6
43	*i*-Pr	32%	10%	–	5.29	259.9	2:6
44	*c*-Pr	4.9 ± 1.0	25%	–	5.03	252.7	2:6
Curcumin	–	3.3 ± 0.45	9.9 ± 0.4	0.33	4.59	302.1	2:6
Resveratrol	–	1.1 ± 0.1	15.3 ± 1.9	0.07	2.83	187.2	3:3

Notes: [a] IC_{50} values are an average ± SD of triplicate readings based on two to three independent experiments. NA = Not active. Percent inhibition (P.I) indicates level of inhibition at highest concentration tested (25 μM). [b]Selectivity index is calculated as (Aβ40 IC_{50}) ÷ (Aβ42 IC_{50}). [c]ClogP values were determined using ChemDraw Professional 15.0. [d]Molecular volumes in Å^3 units were determined using Discovery Studio, Structure-Based Design software, BIOVIA Inc., USA. [e]Showcasing the ratio of HBD = hydrogen-bonding donors to HBA = hydrogen-bonding acceptors.

Compared to the outcome of the azide functionality in **9** (Chapter 3), **34** exhibited at least a 4-fold decline in activity toward Aβ40, while gaining some level of inhibition toward Aβ42. Reduction of that azide to the amino group (**35**, IC_{50} ~ 3 and ~ 31 μM; respectively) caused an approximate 9-fold increase in

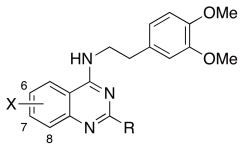
Aβ40 activity, a 3-fold increase in Aβ42 activity, while surpassing the activity levels observed with its dimethoxybenzyl counter (**10**, Chapter 3) and curcumin. Replacement of the amino group in **35** with a hydroxyl group in **36** resulted in an approximate 4-fold decline in Aβ40 activity and an approximate 1.5-fold decline in Aβ42 activity. Compared to **10** (Chapter 3), **36** was roughly 1.3 fold less active toward Aβ40 but it engaged in Aβ42 activity by providing 32% inhibition at 25 μM.

With respect to the carbonyl-based derivatives, C2-urea-containing derivative **37** was the most active amongst the three, although it was 1.7-fold and 1.2-fold less active toward Aβ40/42; respectively. Similar to the other glycinamide-containing derivatives (Chapter 3 – **12** and Chapter 4 – **25**), **38** was inactive toward Aβ40/42. The acetamide-based derivative was roughly equipotent toward both Aβ40/42 (P.I at 25 μM was ~ 26%) and while that was a gain in activity with respect to Aβ42, it was a significant decline in activity toward Aβ40 when compared to the dimethoxybenzyl counterpart (**13**, Chapter 3).

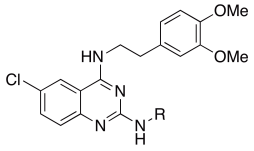
The introduction of alkylamines at the C2-position (**40**-**44**) established some interesting SAR. With the exception of the isopropyl-containing derivative (**43**, Aβ40 P.I at 25 μM was 32%), others exhibited good activity toward Aβ40 (IC_{50} ~ 3–7 μM) with **41** (C2 = NHEt) being the most potent, **42**/**44** (C2 = NH*n*-Pr and NH*c*-Pr; respectively) being roughly equipotent at IC_{50} ~ 4.6 μM, while **40** (C2 = NHMe) provided an IC_{50} value of ~ 7 μM. When compared to their dimethoxybenzyl counterparts in Chapter 3, all were more potent toward both Aβ40/42, with the exception of **42**, which was roughly 2.5-fold less potent toward Aβ40 compared to **16**.

With the introduction of the chloroquinazoline scaffolds, amyloid targeting (Aβ40/42) transitioned favourably, as showcased in Table 8, with almost all derivatives (**45**-**59**) surpassing their respective counterparts from Table 7. Activities toward Aβ40 ranged from 1.5-10.5 μM, while Aβ42 activities ranged from 1.3 μM to 33% inhibition at 25 μM. Compared to **32** (Table 7), derivatives **45**-**47** were anywhere from 2.3 to 5.5-fold more potent toward Aβ40, while also being 5 to 10-fold more potent toward Aβ42. Chlorine placement was generally in the ranking of 7-Cl > 6-Cl ~ 8-Cl. An interesting observation came out with **47** and carried on to the other derivatives in this sub-series – The placement of a C8-chlorine enabled dual Aβ targeting but with selectivity toward Aβ42 (Table 8).

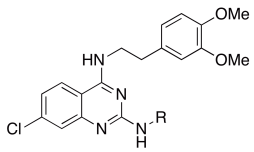
Table 8: Amyloid-β (Aβ40/42) inhibition data for 2-substituted-*N*-(3,4-dimethoxyphenethyl)chloroquinazolin-4-amines (**45**–**59**).



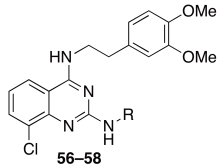
45, 51 X = 6-Cl
46, 55 X = 7-Cl
47, 59 X = 8-Cl



48–50



52–54



56–58

Derivative	R-Grp	Amyloid-β IC_{50} (μM) [a]		SI [b]	ClogP [c]	MV (Å^3) [d]	HBD:HBA [e]
		Aβ40	Aβ42				
45	Cl	2.6 ± 0.3	2.6 ± 0.2	0.99	5.13	281.6	1:5
46	Cl	1.5 ± 0.2	1.9 ± 0.2	0.81	5.13	284.7	1:5
47	Cl	3.5 ± 0.4	1.3 ± 0.8	2.76	5.13	280.9	1:5
48	*n*-Pr	4.9 ± 0.5	10.7 ± 1.1	0.46	6.26	325.8	2:6
49	*i*-Pr	5.8 ± 0.7	7.7 ± 0.8	0.76	6.04	320.4	2:6
50	*c*-Pr	8.9 ± 0.9	9.8 ± 0.8	0.91	5.79	320.4	2:6
51	$N(Me)_2$	2.5 ± 0.3	5.6 ± 0.7	0.44	5.29	311.1	1:6
52	*n*-Pr	3.1 ± 0.3	12.4 ± 1.1	0.25	6.26	320.7	2:6
53	*i*-Pr	10.6 ± 0.9	33%	–	6.04	324.5	2:6
54	*c*-Pr	5.2 ± 0.6	22.5 ± 1.9	0.23	5.79	318.3	2:6
55	$N(Me)_2$	4.3 ± 0.4	9.4 ± 0.9	0.45	5.29	311.8	1:6
56	*n*-Pr	4.9 ± 0.5	2.3 ± 0.3	2.17	6.26	324.8	2:6
57	*i*-Pr	4.0 ± 0.4	1.5 ± 0.2	2.73	6.04	324.5	2:6
58	*c*-Pr	4.6 ± 0.5	2.2 ± 0.2	2.08	5.79	315.2	2:6
59	$N(Me)_2$	2.3 ± 0.2	1.8 ± 0.3	1.27	5.29	310.4	1:6
Curcumin	–	3.3 ± 0.45	9.9 ± 0.4	0.33	4.59	302.1	2:6
Resveratrol	–	1.1 ± 0.1	15.3 ± 1.9	0.07	2.83	187.2	3:3

Notes: [a] IC_{50} values are an average ± SD of triplicate readings based on two to three independent experiments. NA = Not active. Percent inhibition (P.I) indicates level of inhibition at highest concentration tested (25 μM). [b]Selectivity index is calculated as (Aβ40 IC_{50}) ÷ (Aβ42 IC_{50}). [c]ClogP values were determined using ChemDraw Professional 15.0. [d]Molecular volumes in Å^3 units were determined using Discovery Studio, Structure-Based Design software, BIOVIA Inc., USA. [e]Showcasing the ratio of HBD = hydrogen-bonding donors to HBA = hydrogen-bonding acceptors.

With respect to Aβ40 inhibition, chlorine placement at position 6 of the quinazoline scaffold in **48**–**50**, when compared to **42**–**44**, had a positive impact with an isopropylamine at the C2 position group (IC_{50} ~ 6 vs. ~ 40+ μM) but a negative outcome with the cyclopropylamine group (IC_{50} ~ 9 vs. 5 μM), while the propylamine-based derivatives remained equipotent (IC_{50} ~ 4-5 μM). With Aβ42, derivatives **48**–**50** significantly surpassed the inhibition levels of **42**–**44**, with **49** (C2 = NH*i*-Pr) being the most active of the

three (IC_{50} ~ 8 μM). Comparing the dimethylamine-based derivative (**51**) to **49**, activity toward Aβ40/42 improved by 2.3- and 1.4-fold; respectively.

Moving on, when compared to **42–44** and **48–50**, the impact of chlorine placement at position 7 in **52–54** placed inhibitory activity toward Aβ42 between derivatives **42–44** and **48–50** (IC_{50}'s were better than non-chlorinated counterparts but worse than those with chlorine placement at position 6). With respect to Aβ40, minor improvements came with the propylamine group (**52**, IC_{50} ~ 3 vs. 4 vs. 5 μM; respectively), while middle ground placements came with the isopropyl- (**53**, IC_{50} ~ 11 vs. 40+ vs. 6 μM; respectively) and cyclopropylamine (**54**, IC_{50} ~ 5 vs. 5 vs. 9 μM; respectively) groups. Similar to **51**, with respect to **48–50**, derivative **55** was more potent toward both Aβ40/42 when compared to **52–54**. That said, **55** was roughly 1.7-fold less potent toward Aβ40/42 compared to **51**.

Lastly, the impact of chlorine placement at position 8 in **56–58** elicited major improvements with respect to Aβ42 inhibition and anywhere from minor setback to minor improvements with respect to Aβ40 inhibition, when compared to **42–44**, **48–51** and **52–55**. As mentioned earlier, derivatives **56–58** where strong, dual Aβ inhibitors with selectivity geared toward Aβ42. With these 15 chloroquinazoline derivatives, 8 surpassed the Aβ42 activity levels of resveratrol, while 5 met or surpassed the Aβ40 activity levels of curcumin.

In summary, 29 derivatives were assessed for dual Aβ activity, of which derivative **46** (2,7-dichloro-*N*-(3,4-dimethoxyphenethyl)quinazolin-4-amine) was identified as the most potent and dual Aβ inhibitor (Aβ40 IC_{50} = 1.5 μM; Aβ42 IC_{50} = 1.9 μM), while derivative **47** (2,8-dichloro-*N*-(3,4-dimethoxyphenethyl) quinazolin-4-amine) was identified as the most potent Aβ42 inhibitor (IC_{50} = 1.3 μM). Generally, this series proved to be more effective at dual Aβ targeting as compared to the dimethoxybenzyl series (Chapter 3). The introduction of the chloroquinazoline scaffolds and the dimethylamine functionality at the C2-position, offered potency improvements overall when compared to the non-chlorinated counterparts (Figure 62).

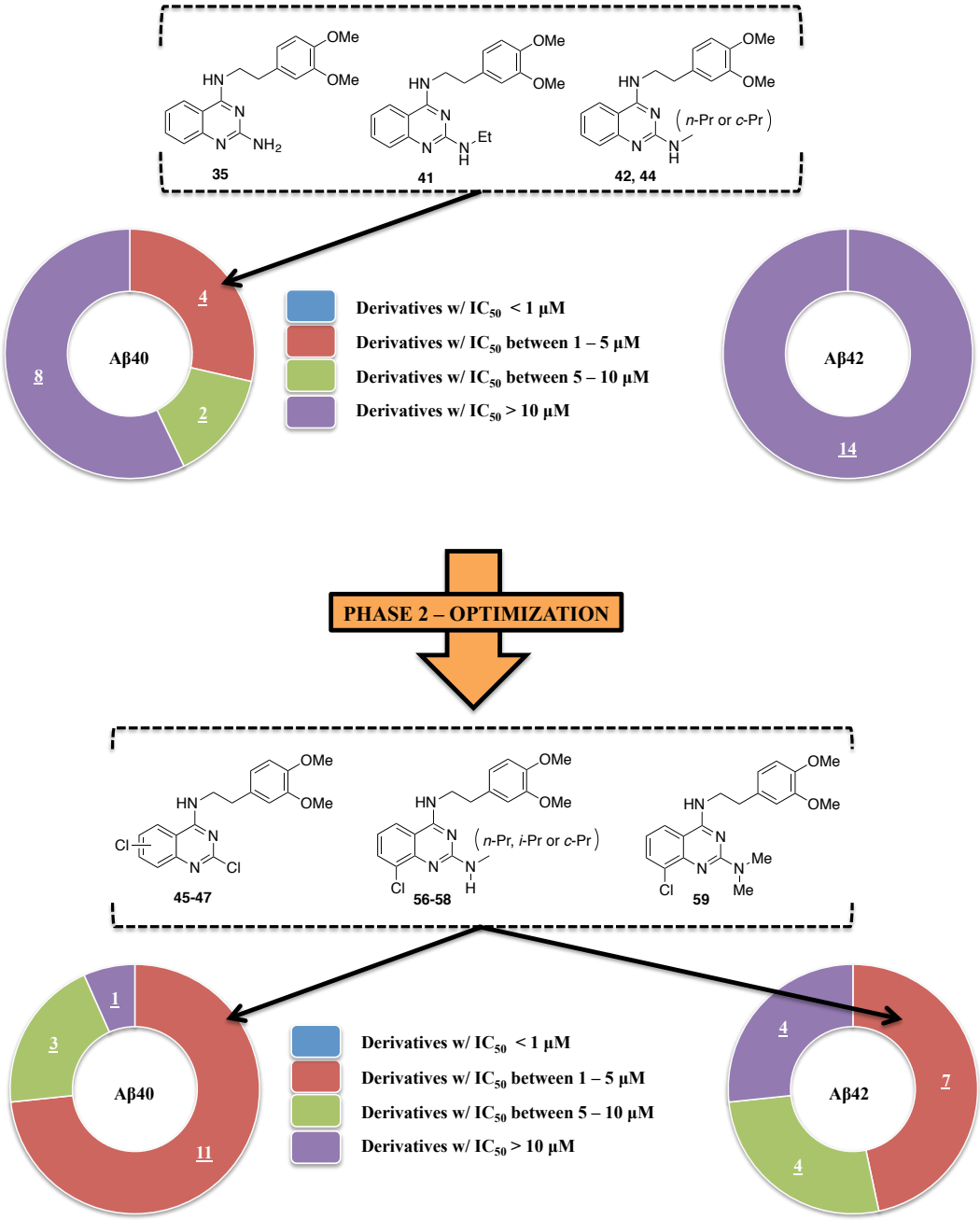


Figure 62: Amyloid-β metrics for fourteen 2-substituted-*N*-(3,4-dimethoxyphenethyl)quinazolin-4-amines (**32**–**44**) and 15 2-substituted-*N*-(3,4-dimethoxyphenethyl)chloroquinazolin-4-amines (**45**–**59**).

The aggregation kinetic assessment of Aβ40 with or without leading derivatives from this chapter is showcased in Figure 63. As observed in Panels A–D, derivatives **45**, **46**, **51** and **59** exhibited concentration-dependent inhibition of Aβ40 aggregation; however they showcased various modes of aggregation. With the dichloro-based derivatives (**45** and **46**), no monomeric structure stabilization was observed (at the 1 and 5 μM concentrations), although both managed to completely halt the aggregation process at 25 μM. Nonetheless, at 1 and 5 μM concentrations, **45** and **46** managed to reduce the rate of aggregation and the overall aggregate load after the 24 hour incubation period. On the other hand, derivatives **51** and **59** managed to showcase all three-modes of inhibition. Across all tested concentrations (1, 5 and 25 μM), both derivatives managed to systematically stabilize the monomeric peptide structures with increasing compound concentrations, although **51** was more effective compared to **59**. In addition, both derivatives managed to reduce the rate of aggregation as well as the total aggregate load after the 24 hour incubation period.

The aggregation kinetic assessment of Aβ42 with or series-leading derivatives is showcased in Figure 64. As observed in Panels A–D, derivatives **46**, **47**, **57** and **59** exhibited concentration-dependent and multi-mode inhibition of Aβ42 aggregation. At 1 and 5 μM concentrations, all derivatives managed to reduce the rate of fibrillation and overall aggregate load at the end of the 24 hour incubation period. Those capabilities extended to the 25 μM concentrations for **46** and **57**, while derivatives **47** and **59** managed to completely block the aggregation process at the 5:1 test ratio (compound: Aβ42).

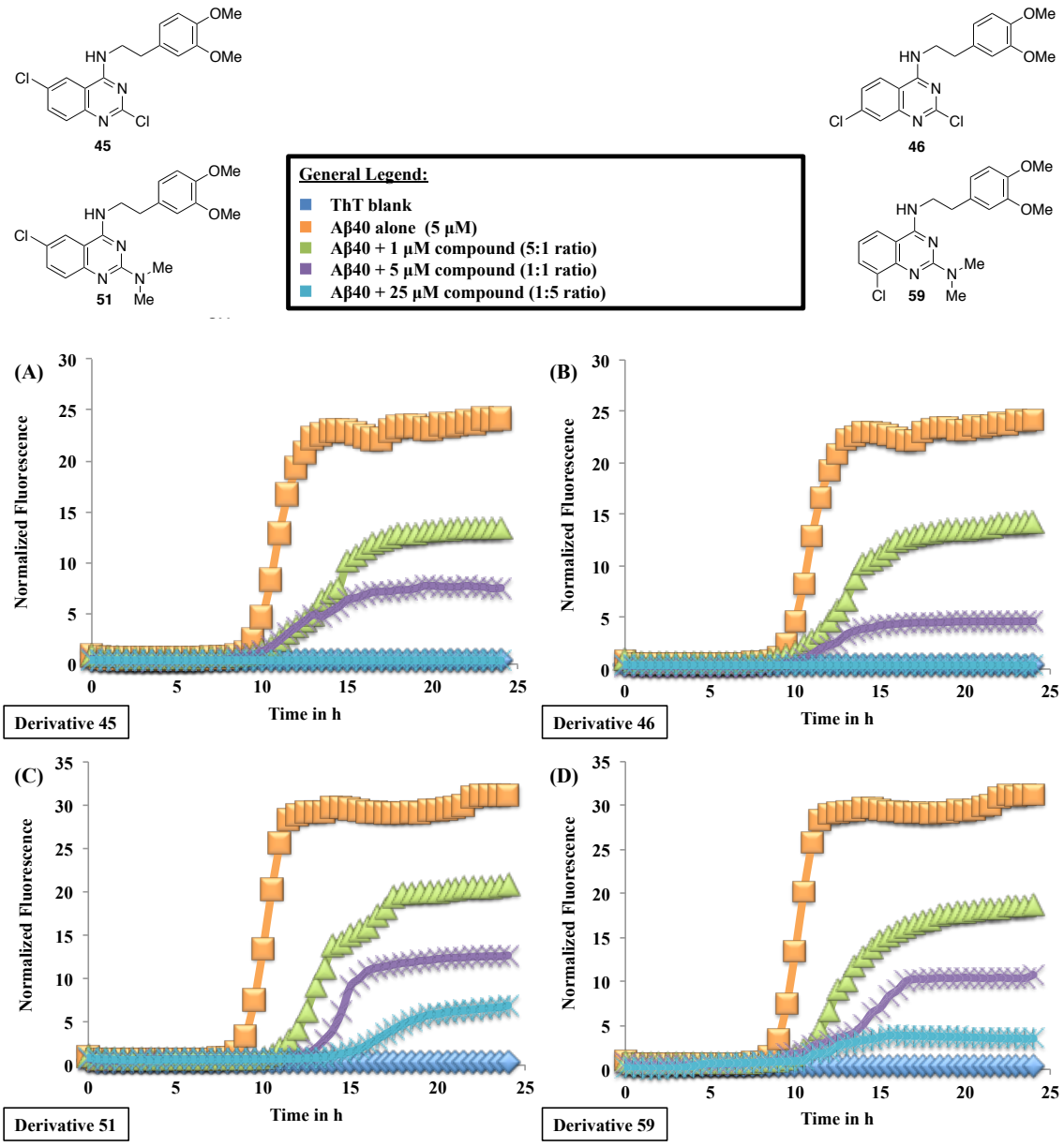


Figure 63: ThT-monitored kinetics of Aβ40 aggregation at 37 °C over a 24 h incubation period at pH 7.4 (Excitation = 440 nm, Emission = 490 nm). Panel (A): Impact of 1, 5 or 25 µM of 2,6-dichloro-*N*-(3,4-dimethoxyphenethyl)quinazolin-4-amine (**45**) on the aggregation kinetics of 5 µM Aβ40. Panel (B): Impact of 1, 5 or 25 µM of 2,7-dichloro-*N*-(3,4-dimethoxyphenethyl)quinazolin-4-amine (**46**) on the aggregation kinetics of 5 µM Aβ40. Panel (C): Impact of 1, 5 or 25 µM of 6-chloro-N^4-(3,4-dimethoxyphenethyl)-N^2,N^2-dimethylquinazoline-2,4-diamine (**51**) on the aggregation kinetics of 5 µM Aβ40. Panel (D): Impact of 1, 5 or 25 µM of 8-chloro-N^4-(3,4-dimethoxyphenethyl)-N^2,N^2-dimethylquinazoline-2,4-diamine (**59**) on the aggregation kinetics of 5 µM Aβ40.

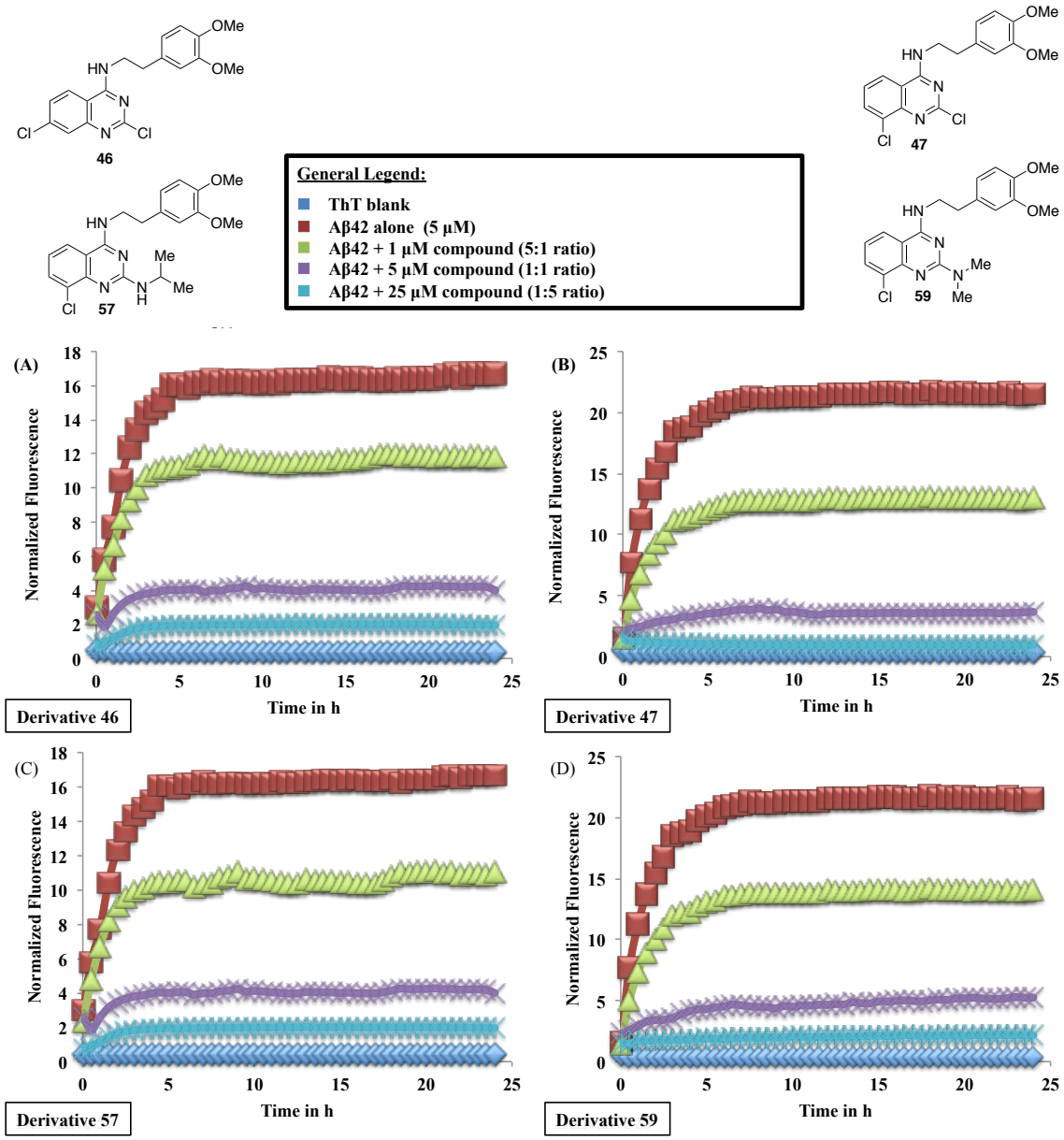


Figure 64: ThT-monitored kinetics of Aβ42 aggregation at 37 °C over a 24 h incubation period at pH 7.4 (Excitation = 440 nm, Emission = 490 nm). Panel (A): Impact of 1, 5 or 25 µM of 2,7-dichloro-*N*-(3,4-dimethoxyphenethyl)quinazolin-4-amine (**46**) on the aggregation kinetics of 5 µM Aβ42. Panel (B): Impact of 1, 5 or 25 µM of 2,8-dichloro-*N*-(3,4-dimethoxyphenethyl)quinazolin-4-amine (**47**) on the aggregation kinetics of 5 µM Aβ42. Panel (C): Impact of 1, 5 or 25 µM of 8-chloro-N^4-(3,4-dimethoxyphenethyl)-N^2-isopropylquinazoline-2,4-diamine (**57**) on the aggregation kinetics of 5 µM Aβ42. Panel (D): Impact of 1, 5 or 25 µM of 8-chloro-N^4-(3,4-dimethoxyphenethyl)-N^2,N^2-dimethylquinazoline-2,4-diamine (**59**) on the aggregation kinetics of 5 µM Aβ42.

5.3.4. *Transmission Electron Microscopy (TEM)*

The assessment of amyloid morphology at the conclusion of a 24-hour incubation period at 37 °C was conducted on leading derivatives. This commonly employed, qualitative technique is used to corroborate the quantitative results from the ThT-binding assay.[207, 317] Experimental setup included the incubations of control and test samples, at 1:1 ratios of 25 μM, in triplicate at 37 °C (with shaking) over a 24-hour timeline. Triplicate samples were combined after the incubation period and applied to the copper-mesh grids prior to imaging in the TEM.

As observed in Figure 65, resveratrol was effective at reducing total amyloid load (Panels B and E) compared to control samples (Panels A and D). That said, derivative **46** (Panel C) surpassed the inhibitory potential of resveratrol against Aβ40, while derivative **47** was more effective against Aβ42, compared to resveratrol.

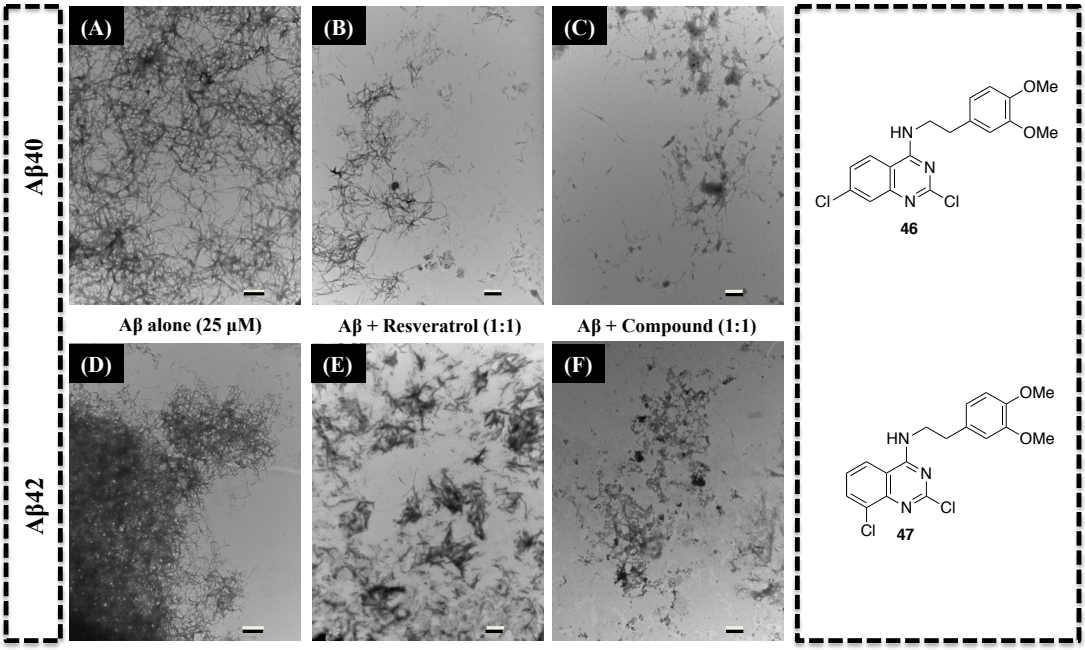


Figure 65: TEM assessment of Aβ40/42 morphology with or without test compounds at the end of a 24 h, 37 °C incubation period at pH 7.4. Panel (A–C): 25 μM Aβ40 alone or at a 1:1 ratio with resveratrol or 2,7-dichloro-*N*-(3,4-dimethoxyphenethyl)quinazolin-4-amine **(46)**; respectively. Panel (D–F): 25 μM Aβ42 alone or at a 1:1 ratio with resveratrol or 2,8-dichloro-*N*-(3,4-dimethoxyphenethyl)quinazolin-4-amine **(47)**; respectively. White/black bars represent 500 nm.

5.3.5. *Antioxidant Capacity*

The ability of 4-((3,4-dimethoxyphenethyl)amino)quinazolin-2-ol (**36**) to scavenge ROS was assessed using the previously described DPPH-scavenging assay.[216, 319-321]

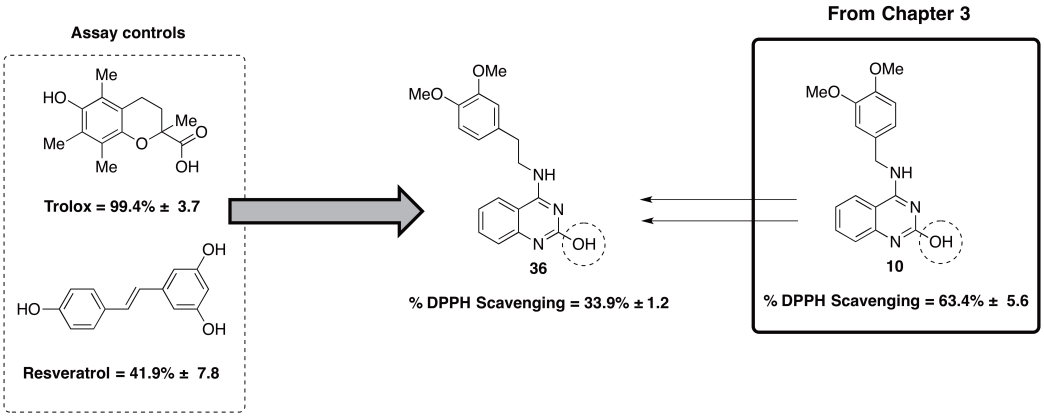


Figure 66: Standards utilized in the DPPH-scavenging along with the data for 4-((3,4-dimethoxyphenethyl)amino) quinazolin-2-ol (**36**).

While a conjugated phenolic, it was no surprise to observe the weaker (~ 1.9-fold) scavenging potential of **36** in the DPPH assay, compared to **10** (Figure 66). The benefits of the additional methylene linker at the C4-position that served ChE and amyloid inhibition (compared to 1**0**, Chapter 3) turned negatively with respect to antioxidant capacity. The overall, and likely hindered, conformation of **36** attributed to the restricted access to the C2-hydroxyl group, thus impacting radical scavenging potential.

5.3.6. *Molecular Modeling*

The utilization of computational software is not only useful in structure-based drug design, it is also employed to understand and corroborate the acquired SAR data. The assessment of ligand-receptor interactions was conducted between leading (or comparable) derivatives from the 2-substituted-*N*-(3,4-

dimethoxyphenethyl)quinazolin-4-amine series (**32**–**44**) or the 2-substituted-*N*-(3,4-dimethoxyphenethyl) chloroquinazolin-4-amine series (**45**–**59**) and the cholinesterase or amyloid targets of interest.

5.3.6.1. *Cholinesterase*

Based on the acquired anti-ChE data, presented in Tables 5 and 6, the docking interactions of **32** and **35** were investigated in *h*AChE (PBD: 1B41) and superimposed in Figure 67, along with the docking interactions of **40** and **40** or **43** and **53** in *h*BuChE (PBD: 1P0I).

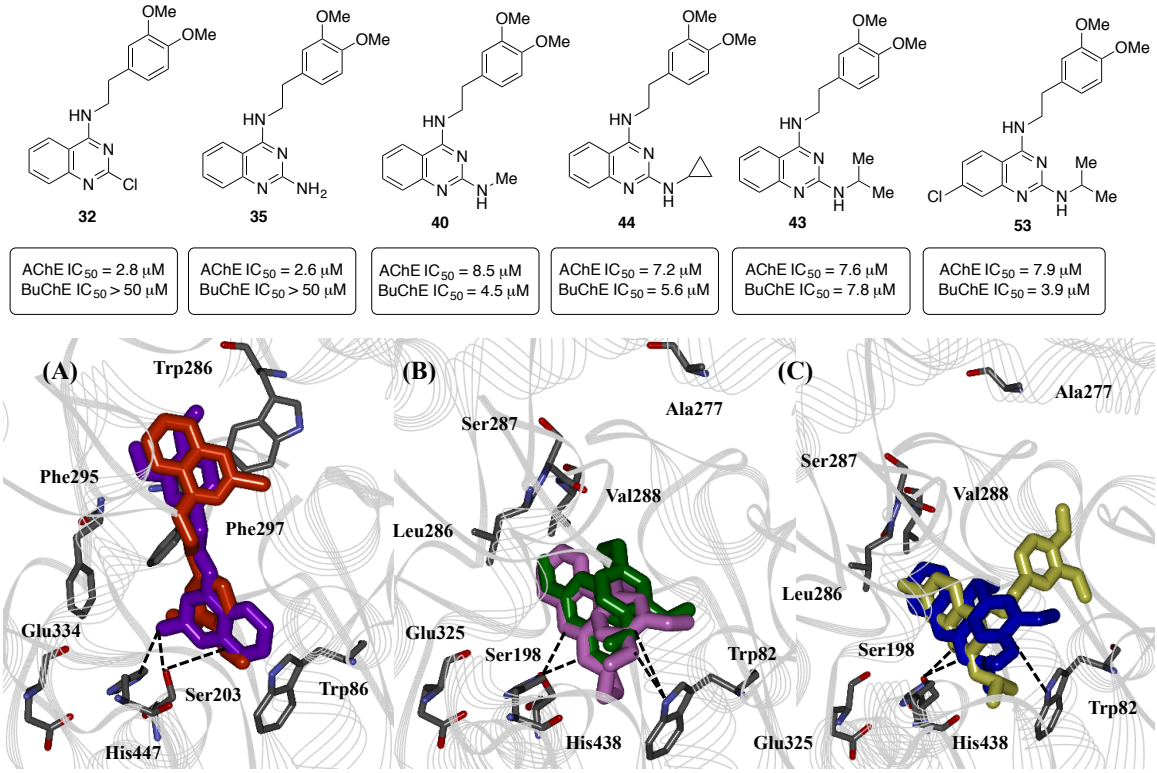


Figure 67: Superimposition of docking structures. Panel (A): Binding modes of **32** (red) and **35** (purple) in the active site of *h*AChE (PDB ID: 1B41). Panel (B): Binding modes of **40** (green) and **44** (magenta) in the active sites of *h*BuChE (PDB ID: 1P0I). Panel (C): Binding modes of **43** (blue) and **53** (gold) in the active sites of *h*BuChE (PDB ID: 1P0I). Hydrogens removed to enhance visibility. Black-dashed lines indicate hydrogen-bonding interactions.

As observed in Panel A, despite their equipotent profiles toward *h*AChE, derivatives **32** and **35** showcased vastly different binding modes. With **32**, the quinazoline scaffold was stacked against W286, roughly at 5–6 Å, while the dimethoxyphenyl group extended deep into the active site with a parallel stacking to S203 and H447. This orientation allowed for the *para*-methoxy group to undergo hydrogen-bonding interactions with S203's O*H* (~ 2.8 Å). In contrast, **35**'s quinazoline scaffold was aligned perpendicular to W86 (~ 6 Å), while the C4-dimethoxyphenethyl group ran parallel to the acyl pocket, directed toward the PAS where the dimethoxyphenyl ring was parallel to W286 (~ 6–7 Å). The ligand's C2-amino group underwent hydrogen-bonding interactions with S203 and H447 (~ 2.5–3.3 Å).

In BuChE, derivative **40** and **44** exhibited similar binding modes, where the quinazoline scaffold was stacked perpendicular between W82 and the acyl pocket (~ 6 Å) and measured roughly 15 Å from A277. This allowed for hydrogen-bonding interactions between the quinazolines' *N*1 and S203's hydroxyl group (~ 3.0 Å). With both derivatives, the C4-dimethoxyphenethyl group bent toward W82 (in a perpendicular arrangement to the quinazoline scaffolds) allowing for the *para*-methoxy group to undergo hydrogen-bonding interactions with W82's N*H* (~ 3.3 Å). The C2-alkylamines were also pointed perpendicularly toward W82, allowing for hydrogen-bonding interactions between the C2-N*H* and S203's hydroxyl group (~ 3.1 Å).

Considering the approximate 2-fold difference in potency, the impact of chlorine placement at position 7 of the quinazoline scaffold was assessed by comparing **43** and **53** in BuChE. As seen in Panel C, the quinazoline scaffolds were stacked perpendicular between W82 and the acyl pocket (~ 6 Å) and measured roughly 15 Å from A277. This allowed for hydrogen-bonding interactions between the quinazolines' *N*1 and S203's hydroxyl group (~ 3.0 Å). Similar to **40** and **44**, derivative **43**'s C4-dimethoxyphenethyl group was bent toward W82 (in a perpendicular arrangement to the quinazoline scaffolds) allowing for the *para*-methoxy group to undergo hydrogen-bonding interactions with W82's N*H* (~ 3.3 Å). The C2-isopropylamine was also pointed perpendicularly toward W82, allowing for hydrogen-bonding interactions between the C2-N*H* and S203's hydroxyl group (~ 3.3 Å). In **53**, the C2-isopropylamine possessed the same binding modes, but the C4-dimethoxyphenethyl group was directed linearly toward A277, while its C7-chlorine was directly interacting with the hydrophobic acyl pocket (L286–V288) at roughly 4–5 Å.

5.3.6.2. *Amyloid-β*

Based on the acquired anti-Aβ data, presented in Table 8, the docking interactions of **45**, **46** and **47** were investigated in both a dimeric and fibril model of Aβ ($Aβ_{9-40}$ – PDB 2LMN)[322] with superimpositions showcased in Figure 68.

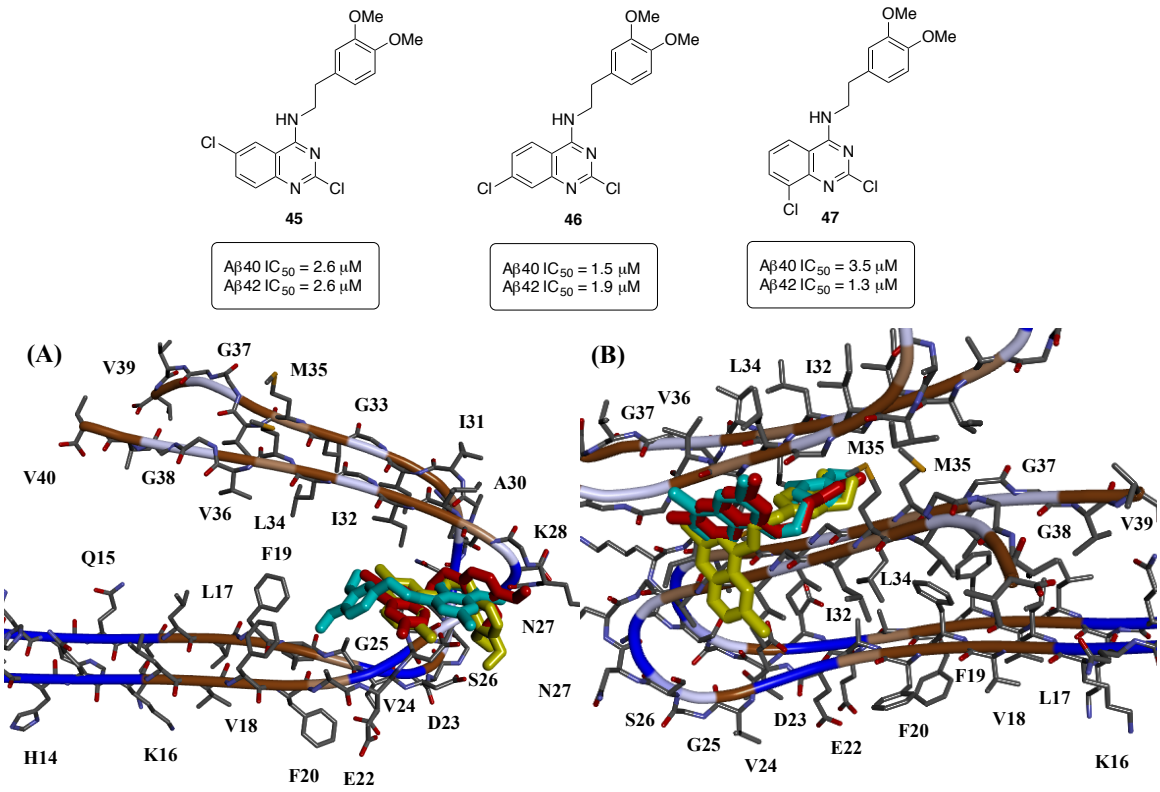


Figure 68: Superimposition of docking structures. Panels (A and B): Binding modes of **45** (gold), **46** (red) and **47** (turquoise) in the Aβ ($Aβ_{9-40}$ – PDB 2LMN) dimer model or fibril model; respectively. Hydrogens removed to enhance visibility. Amino acid labels to be used as a general guide as space restrictions limited complete and accurate labeling of all peptide structures.

As showcased in Panel A, all three dichloroquinazolines were primarily interacting within the hairpin loop domain of the amyloid dimer model. The quinazoline scaffold in **45** and **46** was stacked parallel over D23–V24 at roughly 5 Å. Both derivatives had their C4-functionality running parallel and toward K28 at roughly 6–7 Å, while their C6 or C7-chlorines were pointed toward I32–L34 of the steric zipper domain (~

8–9 Å). In contrast, **47** exhibited a reverse orientation where the quinazoline scaffold was stacked parallel over G25–S26 at roughly 7 Å. Its C4-functionality ran parallel over G22–V24 and toward F19/F20 at roughly 7–8 Å, while the C8-chlorine was stacked over D23 (~ 7 Å).

In the fibril model, derivatives **46** and **47** provided perfectly superimposed binding interactions, as showcased in Panel B. All three dichloroquinazolines (**45**-**47**) had their C4-functional groups intercalated within the steric zipper domain, where the dimethoxyphenyl rings ran parallel to the peptide backbone (~ 5–6 Å from the two pairs of M35 residues). While the quinazoline scaffold of **45** was stacked perpendicular to the peptide backbone, those of **46** and **47** were superimposed and stacked parallel to the peptide backbone (A30–I32, ~ 5 Å). All three derivatives underwent hydrogen-bonding interactions between their C4-N*H* and I32's and G33's backbone carbonyls and amine (~ 2.5–3.3 Å).

5.4. Summary

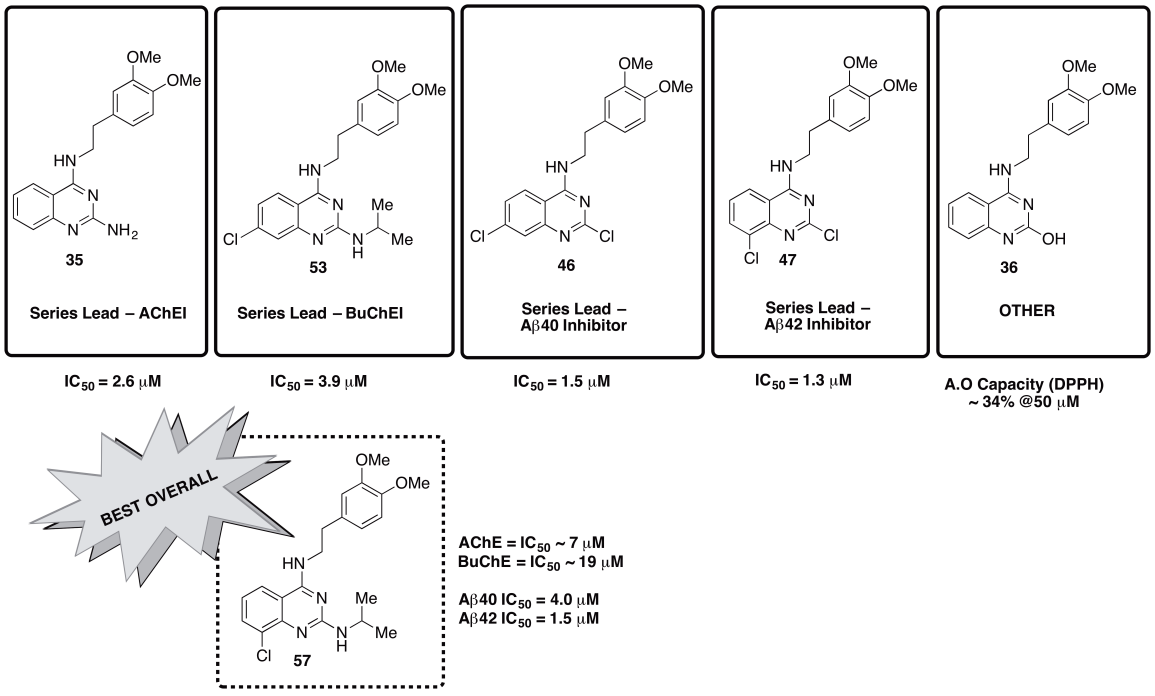


Figure 69: Cumulative chapter summary of 2-substituted-*N*-(3,4-dimethoxyphenethyl)quinazolin-4-amines (**32**-**44**) and 2-substituted-*N*-(3,4-dimethoxyphenethyl)chloroquinazolin-4-amines (**45**-**59**).

With this dimethoxyphenethylamine-based series, an overall improvement in BuChE targeting was observed, without significant losses on AChE potency. When compared to their dimethoxybenzyl counterparts, the derivatives in this series were generally more capable of targeting Aβ40/42, while the investigation into the cholorquinazoline scaffolds significantly improved dual Aβ targeting. Unlike the amino regioisomer explored in Chapter 4 (**22** vs. **22-iso**), the unsubstituted regioisomer in this series was not effective on any target of interest (**33** vs. **33-iso**). In addition, the antioxidant capacity of **36** was 2-fold weaker compared to **10** (Chapter 3), suggesting a steric hindrance concern at the C2-hydroxyl site.

Nonetheless, the series was the first to showcase selective BuChEIs (**40**, **44** and **53**) and selective Aβ42 aggregation inhibitors (**47**, **56**–**59**). While there was no clear "series leader(s)", 8-chloro-N^4-(3,4-dimethoxyphenethyl)-N^2-isopropylquinazoline-2,4-diamine (**57**) was identified was the best, overall, due to its potent and dual Aβ aggregation inhibition in addition to providing moderate but dual ChE inhibition (Figure 69).

5.5. Experimental

Please note that this subsection includes new and re-listed methodologies from Chapter 3 and 4. For schematic representation of re-listed methodologies, if applicable, please refer to Chapter 3 and 4 – Section 3.5 or 4.5.

5.5.1. *Chemistry*

General Information. All the reagents and solvents were reagent grade purchased from various vendors (Acros Organics, Sigma-Aldrich, and Alfa Aesar, USA) with a minimum purity of 95% and were used without further purification. Melting points (mp) were determined using a Fisher-Johns apparatus and are uncorrected. Reaction progress was monitored by UV using thin-layer chromatography (TLC) using Merck 60F254 silica gel plates. Column chromatography was performed with Merck silica gel 60 (230−400 mesh) with 5:1 EtOAc:MeOH as the solvent system unless otherwise specified. Proton (^{1}H NMR) and carbon (^{13}C NMR) spectra were performed on a Bruker Avance (at 300 and 75 MHz; respectively) spectrometer using

DMSO-d_6. Coupling constants (J values) were recorded in hertz (Hz) and the following abbreviations were used to represent multiplets of NMR signals: s = singlet, d = doublet, t = triplet, m = multiplet, br = broad. Carbon multiplicities (C, CH, CH_2 and CH_3) were assigned by DEPT 90/135 experiments. High-resolution mass spectrometry (HRMS) was determined using a Thermo Scientific Q-Exactive Orbitrap mass spectrometer (positive mode, ESI), Department of Chemistry, University of Waterloo. Compound purity (roughly 95% or over) was determined using an Agilent 1100 series HPLC equipped with an analytical column (Agilent Zorbax Eclipse XDB-C8 column, 4.6 x 150 mm, 5 μm particle size) running 50:50 Water:ACN with 0.1% TFA at a flow rate of 1.0-1.5 mL/min or an Agilent 6100 series single quad LCMS equipped with an Agilent 1.8 μm Zorbax Eclipse Plus C18 (2.1 x 50 mm) running 50:50 Water:ACN with 0.1% FA with a flow rate of 0.5mL/min. All the final compounds exhibited ≥ 95% purity.

General procedure for the synthesis of 2,4,6-, 2,4,7- or 2,4,8-trichloroquinazolines.[289, 323] In a 250 mL RBF, 5 g of 2-amino-5-chloro, 4-chloro, or 3-chlorobenzoic acid (29.24 mmol) was suspended in 25 mL of anhydrous toluene and allowed to stir on an ice bath. To this, 5 eq. of $POCl_3$ (146.20 mmol) was added in small aliquots followed by the slow addition of 5 eq. of DEA (146.20 mmol). The solution was kept on the ice bath for 10 min before moving to room temperature and allowed to stir for 1 h prior to refluxing at 105–110 °C for 14–16 h. Upon cooling to room temperature, the reaction mixture was added in small aliquots to a double-ice-water bath while stirring. The quenching solution was left stirring at room temperature for 5 h before vacuum filtering the yellowish-grey precipitate. The precipitate was stirred for 1 h in a saturated $NaHCO_3$ solution and then was re-filtered. This neutralization process was carried out 2–3 times until the bicarbonate solution maintains a neutral to slight basic pH. The final precipitate was dissolved in DCM and purified by a silica gel column chromatography using 100% DCM as the eluent to afford white to light grey solid.

2,4,6-Trichloroquinazoline. Yield: 75% (4.43 g, 19.12 mmol); mp 126–128 °C. ^{1}H NMR (300 MHz, DMSO-d_6) δ 8.31 (s, 1H), δ 8.15 (d, J = 9.0 Hz, 1H), δ 8.04 (d, J = 8.9 Hz, 1H). LRMS (ESI) m/z calcd for $C_8H_4Cl_3N_2$ $[M + H]^+$ 232.93, found 232.92.

2,4,7-Trichloroquinazoline. Yield: 80% (4.73 g, 20.41 mmol); mp 137–139 °C. ^{1}H NMR (300 MHz, DMSO-d_6) δ 8.30 (d, J = 9.0 Hz, 1H), δ 8.20 (s, 1H), δ 7.88 (d, J = 8.7 Hz, 1H). LRMS (ESI) m/z calcd for $C_8H_4Cl_3N_2$ $[M + H]^+$ 232.93, found 232.92.

2,4,8-Trichloroquinazoline. Yield: 65% (3.84 g, 16.56 mmol); mp 135–137 °C. ^{1}H NMR (300 MHz, DMSO-d_6) δ 8.31 (d, J = 7.7 Hz, 1H), δ 8.25 (d, J = 8.5 Hz, 1H), δ 7.78 (t, J = 7.4 Hz, 1H). LRMS (ESI) m/z calcd for $C_8H_4Cl_3N_2$ $[M + H]^+$ 232.93, found 232.92.

General procedure for the synthesis of 2-chloro-, 2,6-dichloro-, 2,7-dichloro- or 2,8-dichloro-*N*-substituted-quinazolin-4-amines.[303, 305] To a 30 mL solution of ethanol in a 100 mL round-bottom flask on ice, 5 g of **4** or a trichloroquinazoline (21.46–25.13 mmol) was added followed by slow addition of 1.3 eq. (27.90–32.66 mmol) of the corresponding primary amine. Contents were stirred on an ice bath while 2.0 eq. of diisopropyl-ethylamine (DIPEA, 42.92–50.25 mmol) was added in drop wise fashion. The solution was then heated at 80-85 °C under reflux for 3–4 h. The reaction contents were cooled to room temperature and precipitated residues were vacuum-filtered with ethyl acetate (EtOAc) rinses. The organic supernatant was concentrated in vacuo followed by two rounds of liquid-liquid extraction using EtOAc and saturated brine solution (40–50 mL each respectively). The combined organic layers were dried over $MgSO_4$, evaporated in vacuo and purified (1-2 times) using silica gel column chromatography with 5:1 EtOAc:MeOH as the elution solvent. Final compounds were white to beige solids with yields ranging from 70-90%.

2-Chloro-*N*-(3,4-dimethoxyphenethyl)-quinazolin-4-amine (**32**). Yield: 80% yield (6.89 g, 20.10 mmol). Mp: 182–184 °C. ^{1}H NMR (300 MHz, DMSO-d6) δ 8.76 (br s, 1H), δ 8.21 (d, J = 8.3 Hz, 1H), δ 7.72 (t, J = 7.5 Hz, 1H), δ 7.56 (d, J = 8.2 Hz, 1H), δ 7.45 (t, J = 7.6 Hz, 1H), δ 6.83-6.71 (m, 3H), δ 3.72-3.66 (m, 8H), δ 2.84 (t, J = 6.9 Hz, 2H). HRMS (ESI) m/z calcd for $C_{18}H_{18}ClN_3O_2$ $[M + H]^+$ 344.1088, found 344.1707. Purity: 97.4%

2,6-Dichloro-*N*-(3,4-dimethoxyphenethyl)quinazolin-4-amine (45). Yield: 80% (1.31 g, 3.45 mmol); mp 143–145 °C. ^{1}H NMR (300 MHz, DMSO-d_6) δ 8.82 (br s, 1H), δ 8.39 (s, 1H), δ 7.77 (dd, J = 8.9, 2.2 Hz, 1H), δ 7.60 (d, J = 8.7 Hz, 1H), δ 6.85–6.73 (m, 3H), δ 3.71–3.65 (m, 8H), δ 2.83 (t, J = 7.4 Hz, 2H). LRMS (ESI) m/z calcd for $C_{18}H_{18}Cl_2N_3O_2$ $[M + H]^+$ 378.06, found 378.09.

2,7-Dichloro-*N*-(3,4-dimethoxyphenethyl)quinazolin-4-amine (46). Yield: 77% (1.26 g, 3.34 mmol); mp 147–149 °C. ^{1}H NMR (300 MHz, DMSO-d_6) δ 8.92 (br s, 1H), δ 8.24 (d, J = 8.6 Hz, 1H), δ 7.66 (s, 1H), δ 7.57 (d, J = 8.9 Hz, 1H), δ 6.85–6.72 (m, 3H), δ 3.71–3.65 (m, 8H), δ 2.83 (t, J = 7.4 Hz, 2H). LRMS (ESI) m/z calcd for $C_{18}H_{18}Cl_2N_3O_2$ $[M + H]^+$ 378.06, found 378.10.

2,8-Dichloro-*N*-(3,4-dimethoxyphenethyl)quinazolin-4-amine (47). Yield: 87% (1.39 g, 3.67 mmol); mp 145–147 °C. ^{1}H NMR (300 MHz, DMSO-d_6) δ 8.97 (br s, 1H), δ 8.18 (d, J = 8.6 Hz, 1H), δ 7.92 (d, J = 8.9 Hz, 1H), δ 7.45 (t, J = 8.4 Hz, 1H), δ 6.85–6.71 (m, 3H), δ 3.71–3.65 (m, 8H), δ 2.83 (t, J = 7.4 Hz, 2H). LRMS (ESI) m/z calcd for $C_{18}H_{18}Cl_2N_3O_2$ $[M + H]^+$ 378.06, found 378.04.

General procedure for the synthesis of N^4-substituted-quinazolin-4-amines. In a 50 mL round bottom flask (RBF), 0.5 g of 2-chloro-*N*-substituted-quinazolin-4-amine (1.45–1.85 mmol) was dissolved in 20 mL of anhydrous ethanol. While stirring on ice, 10 mol. % of 10% Pd/C was added to reaction mixture followed by the drop-wise addition of 1.3 eq. of hydrazine hydrate. Solution was stirred on ice for 5 min before refluxing for 2 h at 80–85 °C. Upon completion and cooling to room temperature, the reaction mixture was passed through a tightly-packed cotton-filled syringe that has been pre-rinsed with ethanol, to remove the Pd/C catalyst. A 30 mL aliquot of ethanol was used to rinse the syringe. The combined ethanol solutions were evaporated in vacuo, diluted in EtOAc (20 mL) and washed 25 mL x 2 with equal volumes of brine solution. The combined aqueous layers were washed with 15 mL of EtOAc. The combined EtOAc layers were dried over $MgSO_4$, before removing the EtOAc in vacuo to yield a solid or semi-solid crude product that was purified by silica gel column chromatography using 5:1 EtOAc:MeOH solvent system. Final compounds were white to pale yellow solids with yields ranging from 40–47%.

***N*-(3,4-Dimethoxyphenethyl)quinazolin-4-amine (33).** Yield: 40% (0.18 g, 0.58 mmol); Mp 155–157 °C. ^{1}H NMR (300 MHz, DMSO-d_6): δ 8.44 (s, 1H), δ 8.28 (br s, 1H), δ 8.16 (d, J = 6.0 Hz, 1H), δ 7.71–7.62 (m, 2H), δ 7.46 (t, J = 9.0 Hz, 1H), δ 6.83–6.72 (m, 3H), δ 3.70 (d, J = 6.0 Hz, 2H), δ 3.67 (s, 3H), δ 3.66 (s, 3H), δ 2.84 (t, J = 9.0 Hz, 2H). HRMS (ESI) m/z calcd for $C_{18}H_{20}N_3O_2$ $[M + H]^+$ 310.1477, found 310.1549. Purity: 98.6%

General procedure for the synthesis of N^2-substituted-quinazolin-2-amines. In a 50 mL pressure vial (PV), 0.25 g of 2-chloroquinazoline (1.52 mmol) was dissolved in 5 mL of 1,4-dioxane followed by the addition of 3 eq. (4.56 mmol) of the appropriate primary amine and 5 eq. of DIPEA (7.60 mmol). Pressure vial was sealed and stirred in an oil bath at 155–160 °C for 5 h. Upon completion and cooling to room temperature, the reaction mixture was diluted with ~ 40 mL of EtOAc and washed 25 mL x 3 times with equal volumes of brine solution. The combined aqueous layers were washed with ~ 25 mL of EtOAc. The combined EtOAc layers were dried over $MgSO_4$ before removing the EtOAc in vacuo to yield a solid crude product that was purified by silica gel column chromatography using 5:1 EtOAc:MeOH as the solvent system. Final compounds were pale yellow to pale brown solids with yields ranging from 47–52%.

***N*-(3,4-Dimethoxyphenethyl)quinazolin-2-amine (33-iso).** Yield: 52% (0.18 g, 0.58 mmol); Mp 144–146 °C. ^{1}H NMR (300 MHz, DMSO-d_6): δ 9.09 (s, 1H), δ 7.72 (d, J = 8.0 Hz, 1H), δ 7.72–7.63 (m, 2H), δ 7.45–7.33 (m, 1H), δ 7.32–7.20 (m, 2H), δ 6.84–6.69 (m, 3H), δ 3.70 (s, 3H), δ 3.67 (s, 3H), δ 3.62 (q, J = 8.2 Hz, 2H), δ 2.75 (t, J = 7.6 Hz, 2H). HRMS (ESI) m/z calcd for $C_{18}H_{20}N_3O_2$ $[M + H]^+$ 310.1477, found 310.1549. Purity: 99.6%

General procedure for the synthesis of 2-azido-*N*-substituted-quinazolin-4-amine.[305] In a 50 mL RBF, 2-chloro-*N*-substituted-quinazolin-4-amine (~1.86 mmol), 1.1 eq. NaN_3 (2.05 mmol), 4:1 EtOH (20 mL) and glacial acetic acid (5 mL) were combined and refluxed at 90–95 °C for 2 h with stirring. After cooling, the solution was vacuum-filtered to afford white solids at yields ranging from 80–85%.

2-Azido-*N*-(3,4-dimethoxyphenethyl)quinazolin-4-amine (13c). Yield: 82% (0.42 g, 1.20 mmol); Mp 259–261 °C. ^{1}H NMR (300 MHz, DMSO-d_6): δ 8.91 (br s, 1H), δ 8.42 (d, J = 8.2 Hz, 1H), δ 8.31 (d, J = 8.3 Hz, 1H), δ 7.96 (t, J = 8.0 Hz, 1H), δ 7.71 (t, J = 8.0 Hz, 1H), δ 6.86–6.78 (m, 3H), δ 3.78–3.76 (m, 2H), δ 3.67 (s, 6H), δ 2.91 (t, J = 7.2 Hz, 2H). ^{13}C NMR (100 MHz, DMSO-d_6): δ 157.43, δ 153.90, δ 148.61, δ 147.28, δ 134.48, δ 132.33, δ 131.74, δ 127.72, δ 124.87, δ 120.54, δ 115.88, δ 112.61, δ 112.22, δ 111.90, δ 55.48, δ 55.32, δ 42.85, δ 33.46. HRMS (ESI) m/z calcd for $C_{18}H_{19}N_6O_2$ $[M + H]^+$ 351.1491, found 351.1564. Purity: 94.9%

General procedure for the synthesis of N^4-substituted-quinazolin-2,4-diamine.[305]

Method 1A: In a 100 mL round-bottom pressure vial, 2-chloro-*N*-substituted-quinazolin-4-amine (3.72 mmol) was added along with 20 mol. % of CuI. To that, a mixture of 1,4-dioxane (5 mL) and 30% aqueous ammonia (15 mL) was added at room temperature. The pressure vial was sealed tightly and partially submerged in silicone oil heating at 130–135 °C. Contents were stirred in the pressure vial for 24 h (Note: in the event of pressure leakage, the contents were cooled to room temperature and additional aqueous ammonia, (10 mL) was added, sealed and heating was carried on through the 24 h period). The reaction contents were cooled to room temperature and the solution was diluted with 25 mL EtOAc, washed with saturated brine solution (10 mL x 3), and the aqueous layer was neutralized with dilute HCl, and then re-extracted with 15 mL EtOAc. The organic layers were combined, dried over $MgSO_4$, evaporated in vacuo and purified using silica gel column chromatography with 5:1 EtOAc:MeOH as an initial elution solvent followed by transition to 5:1 EtOAc:MeOH w/ 1% TEA (triethylamine). Final compounds were obtained as white to beige solids with final yields ranging from 20–25%.

Method 1B: In a 100 mL round-bottom pressure vial, 2-chloro-*N*-substituted-quinazolin-4-amine (3.72 mmol) was dissolved and gently heated in 5 mL ethylene glycol. To that, 20 mol. % of Cu_2O and DMEDA were added followed by 20 eq. K_2CO_3 and finally, 40 eq. of 30% aqueous ammonia solution (~15–20 mL). The pressure vial was sealed tightly, partially submerged in silicone oil and heated at 100–105 °C. Contents were stirred in the pressure vial for 24 h. After the reaction contents were cooled to room temperature, the

solution was diluted with 50 mL EtOAc, washed with saturated brine solution (25 mL x 3) and the aqueous layer was neutralized with dilute HCl, and then re-extracted with 25 mL EtOAc. The residue formed was dissolved in methanol (20–25 mL). The EtOAc layers were dried over $MgSO_4$ and evaporated in vacuo. The methanol fraction was dried with molecular sieves before evaporating the methanol in vacuo. Both EtOAc and methanol fractions were combined and purified using silica gel column chromatography with 5:1 EtOAc:MeOH as an initial elution solvent followed by transition to 5:1 EtOAc:MeOH with 1% TEA (triethylamine). Final compounds were obtained as white to beige solids with yields ranging from 35–40%.

Method 2: In a 50 mL round-bottom pressure vial, 2-chloro-*N*-substituted-quinazolin-4-amine (3.72 mmol) was combined with 6 eq. urea (22.32 mmol) and diluted with 10 mL of anhydrous 1,4-dioxane. The pressure vial was sealed tightly and partially submerged in silicone oil heating at 160–165 °C. Contents were stirred in the pressure vial for 24 h. Once the reaction contents were cooled to room temperature, the solution was diluted with 20–25 mL EtOAc. The contents were washed three times with 20 mL saturated brine solution and the aqueous layers were re-extracted twice with 20 mL EtOAc. The organic layers were combined, dried over $MgSO_4$, evaporated in vacuo and purified using silica gel column chromatography with 5:1 EtOAc:MeOH as an initial elution solvent followed by transition to 5:1 EtOAc:MeOH w/ 1% TEA (triethylamine). Final compounds were obtained as white to light beige solids with yields ranging from 50–55%.

Method 3: In a 50 mL round-bottom flask, 2-chloro-*N*-substituted-quinazolin-4-amine (3.72 mmol) was combined with 1.1 eq. NaN_3 (4.09 mmol), before diluting with 4:1 EtOH (20 mL) and glacial acetic acid (5 mL). Flask contents were stirred under reflux at 90–95 °C for 2 h. After cooling the reaction mixture, 10 mol. % of Pd/C (10%) was added followed by slow addition of 1.5 eq. of hydrazine hydrate (5.58 mmol). Flask contents were stirred under reflux at 90–95 °C for an additional two hrs. Once complete, the warm solution was passed through a large, tightly packed cotton syringe with the aid of additional EtOH washes (2 x 20 mL). The ethanolic mixture was evaporated in vacuo. Final compounds were obtained as white to beige solids with yields ranging from 80–85%.

***N*^{4}-(3,4-Dimethoxyphenethyl)quinazolin-2,4-diamine** (**35**). Yield: 80% (0.76 g, 2.33 mmol); Mp: 179-181 °C. 1H NMR (300 MHz, DMSO-*d6*) δ 7.92–7.86 (m, 2H), δ 7.42 (t, *J* = 8.0 Hz, 1H), δ 7.15 (d, *J* = 8.0 Hz, 1H), δ 6.97 (t, *J* = 7.5 Hz, 1H), δ 6.84–6.73 (m, 3H), δ 6.05 (br s, 2H), 3.67 (s, 6H), δ 3.60-3.64 (m, 2H), δ), δ 2.83 (t, *J* = 6.9 Hz, 2H). HRMS (ESI) m/z calcd for $C_{18}H_{20}N_4O_2$ [M + H]+ 325.1664, found: 325.1657.

General procedure for the synthesis of *N*^{4}-substituted-quinazolin-2-ols. In a 50 mL round bottom flask (RBF), 0.5 g of 2-chloro-*N*-substituted-quinazolin-4-amine (1.45–1.85 mmol) was combined with 1.3 eq. of potassium formate (1.89–2.41 mmol) then dissolved in 20 mL of formic acid. Solution was refluxed for 14–16 h at 120–125 °C. Upon completion and cooling to room temperature, the reaction mixture was diluted with ~ 30 mL of brine solution, ~ 50 mL of saturated $NaHCO_3$ solution before extracting with ~ 25 mL (x 3) of EtOAc and washed with 25 mL (x 3) parts of brine solution. The combined aqueous layers were washed twice with 15 mL of EtOAc. The combined EtOAc layers were dried over $MgSO_4$ before removing the EtOAc in vacuo to yield a solid product that generally did not require additional purification. Additional purification as required, was accomplished by silica gel column chromatography using 5:1 EtOAc:MeOH as the eluent. The compounds were obtained as white solids with yields ranging from 58–70%.

4-((3,4-Dimethoxyphenethyl)amino)quinazolin-2-ol (36). Yield: 62% (0.29 g, 0.90 mmol); Mp 210–212 °C. ^{1}H NMR (300 MHz, DMSO-*d*$_6$): δ 10.60 (br s, 1H), δ 8.40 (br s, 1H), δ 8.02 (d, *J* = 8.1 Hz, 1H), δ 7.47 (t, *J* = 7.5 Hz, 1H), δ 7.12–7.02 (m, 2H), δ 6.83–6.71 (m, 3H), δ 3.70–3.60 (m, 8H), δ 2.82 (t, *J* = 7.1 Hz, 2H). HRMS (ESI) m/z calcd for $C_{18}H_{20}N_3O_3$ $[M + H]^+$ 326.1426, found 326.1499. Purity: 97.3%

General procedure for the synthesis of *N*^{4}-substituted-quinazolin-2-urea.[305] In a pressure vial, 0.5 g of 2-chloro-*N*-substituted-quinazolin-4-amine (~1.85 mmol) was mixed with 6 eq. urea (~11.2 mmol) and 10 mL of anhydrous 1,4-dioxane, sealed tightly and heated at 160–165 °C in an oil bath for 24 h. After cooling to room temperature, the solution was diluted with 20 mL EtOAc, washed three times with 20 mL

brine solution; the aqueous layers were extracted twice with 20 mL EtOAc. The combined organic layers were dried over $MgSO_4$, evaporated in vacuo and purified using silica gel column chromatography using a combination of 5:1 EtOAc:MeOH and 5:1 EtOAc:MeOH w/ 1% TEA (triethylamine) to afford target compounds as white solids with yields ranging from 45–50% and the hydrolyzed amine compounds as off white solids with yields ranging from 50–55%.

1-(4-((3,4-Dimethoxyphenethyl)amino)quinazolin-2-yl)urea (37). Yield: 47% (0.25 g, 0.68 mmol); Mp 246–248 °C. ^{1}H NMR (300 MHz, DMSO-d_6): δ 9.10 (br s, 1H), δ 8.76 (br s, 1H), δ 8.35 (br s, 1H), δ 8.03 (d, J = 8.2 Hz, 1H), δ 7.46 (t, J = 7.6 Hz, 1H), δ 7.44 (d, J = 8.2 Hz, 1H), δ 7.28 (t, J = 7.6 Hz, 1H), δ 6.90–6.78 (m, 4H), δ 3.70–3.67 (m, 8H), δ 2.86 (t, J = 7.5 Hz, 2H). HRMS (ESI) m/z calcd for $C_{19}H_{22}N_5O_3$ $[M + H]^+$ 368.1644, found 368.1718. Purity: 95.7%

General procedure for the synthesis of N^4-substituted-quinazolin-2-glycinamide.[299] In a 50 mL pressure vial, 0.25 g of 2-chloro-*N*-substituted-quinazolin-4-amine (~ 0.83 mmol) was combined with 3 eq. (~ 2.50-mmol) of glycinamide.HCl then dissolved in 5 mL of 1,4-dioxane followed by the addition of 5 eq. of DBU (~ 4.15 mmol). Pressure vial was sealed and stirred in an oil bath at 150–155 °C for 4 h. Upon completion and cooling to room temperature, the reaction mixture was diluted with ~ 40 mL of EtOAc and washed 25 mL (x 3) brine solution. The combined aqueous layers were washed with ~ 25 mL of EtOAc. The combined EtOAc layers were dried over $MgSO_4$ and EtOAc was removed in vacuo to yield solid that was purified by silica gel column chromatography using 5:1 EtOAc:MeOH as the eluent to afford target compounds as pale yellow to brown solids with yields ranging between 52–58%.

2-((4-((3,4-Dimethoxyphenethyl)amino)quinazolin-2-yl)amino)acetamide (38). Yield: 52% (0.14 g, 0.38 mmol); Mp 159–161 °C. ^{1}H NMR (300 MHz, DMSO-d_6): δ 8.13 (br s, 1H), δ 7.93 (d, J = 8.2 Hz, 1H), δ 7.45 (t, J = 7.5 Hz, 1H), δ 7.21 (d, J = 8.4 Hz, 2H), δ 7.01 (t, J = 7.5 Hz, 1H), δ 6.97 (br s, 1H), δ 6.84–6.74 (m, 3H), δ 6.42 (br s, 1H), δ 3.86 (d, J = 7.1 Hz, 2H), δ 3.68 (s, 3H), δ 3.67 (s, 3H), δ 3.64–3.59 (m,

2H), δ 2.82 (t, *J* = 7.1 Hz, 2H). HRMS (ESI) m/z calcd for $C_{20}H_{24}N_5O_3$ $[M + H]^+$ 382.1801, found 382.1873. Purity: 99.6%

General procedure for the synthesis of *N*^{4}-substituted-quinazolin-2-acetamide.[312] In a 50 mL round bottom flask (RBF), 0.5 g of N^4-substituted-quinazolin-2,4-diamine (1.54–2.00 mmol) was dissolved in 15 mL of 1,4-dioxane and 10 mL of glacial acetic acid/acetyl chloride combination (4:1 ratio). Solution was refluxed for 24 h at 90–95 °C. Upon completion and cooling to room temperature, the reaction mixture was diluted with ~ 30 mL of brine solution, ~ 30 mL of concentrated $NaHCO_3$ solution before extracting with ~ 25 mL (x 3) of EtOAc and washed with 25 mL (x 2) brine solution. The combined aqueous layers were washed twice with 15 mL of EtOAc. The combined EtOAc layers were dried over $MgSO_4$ and the organic solvent was removed in vacuo to yield a solid product that generally did not require additional purification. Purification was carried out as required, by silica gel column chromatography using 5:1 EtOAc:MeOH as the eluent to afford target compounds as white solids with yields ranging from 35–42%.

***N*-(4-((3,4-Dimethoxyphenethyl)amino)quinazolin-2-yl)acetamide (39).** Yield: 57% (0.33 g, 0.90 mmol); Mp 241–243 °C. ^{1}H NMR (300 MHz, DMSO-d_6): δ 9.83 (br s, 1H), δ 8.47 (br s, 1H), δ 8.07 (d, *J* = 8.0 Hz, 1H), δ 7.60 (t, *J* = 7.2 Hz, 1H), δ 7.43 (d, *J* = 8.2 Hz, 1H), δ 7.26 (t, *J* = 6.0 Hz, 1H), δ 6.87-6.76 (m, 3H), δ 3.66–3.63 (m, 8H), δ 2.84 (t, *J* = 7.5 Hz, 2H), δ 2.52 (s, 3H). HRMS (ESI) m/z calcd for $C_{20}H_{23}N_4O_3$ $[M + H]^+$ 367.1692, found 367.1766. Purity: 96.8%

General procedure for the synthesis of *N*^{4}-substituted-*N*^{2}-alkyl-quinazolin-2,4-diamine.[299, 313] In a 50 mL pressure vial (PV), 0.25 g of 2-chloro, 2,6-dichloro, 2,7-dichloro or 2,8-dichloro-*N*-substituted-quinazolin-4-amine (~ 0.66–0.83 mmol) was combined with 2 eq. (~ 1.32–1.66 mmol) of primary amine (methyl-, ethyl-, *n*-propyl-, isopropyl- or cyclopropylamine) or dimethylamine then dissolved in 5 mL of 1,4-dioxane followed by the addition of 3 eq. of DIPEA (~ 1.98–2.40 mmol). Pressure vial was sealed and stirred in an oil bath at 150–155 °C for 2 h. Upon completion and cooling to room temperature, the reaction

mixture was diluted with ~ 40 mL of EtOAc and washed with brine solution (25 mL x 2). The combined aqueous layer was washed with ~ 25 mL of EtOAc. The combined EtOAc layers were dried over $MgSO_4$ before removing EtOAc in vacuo to yield a solid product that was purified by silica gel column chromatography using 5:1 EtOAc:MeOH as the eluent to afford pale yellow to brown solids yielding at 55–70%.

***N*^{4}-(3,4-Dimethoxyphenethyl)-*N*^{2}-methylquinazoline-2,4-diamine (40).** Yield: 70% (0.34 g, 1.01 mmol); Mp 153–155 °C. ^{1}H NMR (300 MHz, DMSO-d_6): δ 7.87 (d, J = 8.0 Hz, 2H), δ 7.40 (t, J = 7.2 Hz, 1H), δ 7.19 (d, J = 9.0 Hz, 1H), δ 6.94 (t, J = 6.0 Hz, 1H), δ 6.83–6.72 (m, 3H), δ 6.42 (br s, 1H), δ 3.66 (s, 6H), δ 3.63–3.60 (m, 2H), δ 2.86–2.79 (m, 2H), δ 2.80 (d, J = 4.5 Hz, 3H). HRMS (ESI) m/z calcd for $C_{19}H_{23}N_4O_2$ $[M + H]^+$ 339.1743, found 339.1816. Purity: 97.8%

***N*^{4}-(3,4-Dimethoxyphenethyl)-*N*^{2}-ethylquinazoline-2,4-diamine (41).** Yield: 70% (0.33 g, 0.94 mmol); Mp 157–159 °C. ^{1}H NMR (300 MHz, DMSO-d_6): δ 7.86 (d, J = 8.0 Hz, 2H), δ 7.41 (t, J = 7.2 Hz, 1H), δ 7.19 (d, J = 9.0 Hz, 1H), δ 6.96 (t, J = 6.0 Hz, 1H), δ 6.84-6.75 (m, 3H), δ 6.40 (br s, 1H), δ 3.67 (s, 6H), δ 3.63–3.60 (m, 2H), δ 3.34–3.32 (m, 2H), δ 2.82 (t, J = 7.2 Hz, 2H), δ 1.08 (t, J = 7.0 Hz, 3H). HRMS (ESI) m/z calcd for $C_{20}H_{24}N_4O_2$ $[M + H]^+$ 353.1899, found 353.1971. Purity: 98.6%

***N*^{4}-(3,4-Dimethoxyphenethyl)-*N*^{2}-propylquinazoline-2,4-diamine (42).** Yield: 68% (0.36 g, 0.98 mmol); Mp 127–129 °C. ^{1}H NMR (300 MHz, DMSO-d_6): δ 7.87 (d, J = 8.0 Hz, 2H), δ 7.39 (t, J = 7.2 Hz, 1H), δ 7.16 (d, J = 9.0 Hz, 1H), δ 6.94 (t, J = 6.0 Hz, 1H), δ 6.83-6.72 (m, 3H), δ 6.52 (br s, 1H), δ 3.63 (s, 6H), δ 3.63–3.60 (m, 2H), δ 3.34–3.32 (m, 2H), δ 2.82 (t, J = 7.2 Hz, 2H), δ 1.59–1.46 (m, 2H), 0.83 (t, J = 7.0 Hz, 3H). HRMS (ESI) m/z calcd for $C_{21}H_{27}N_4O_2$ $[M + H]^+$ 367.2056, found 367.2132. Purity: 99.0%

***N*^{4}-(3,4-Dimethoxyphenethyl)-*N*^{2}-isopropylquinazoline-2,4-diamine (43).** Yield: 67% (0.35 g, 0.96 mmol); Mp 134–136 °C. ^{1}H NMR (300 MHz, DMSO-d_6): δ 7.90 (d, J = 8.0 Hz, 2H), δ 7.45 (t, J = 7.2 Hz,

1H), δ 7.18 (d, *J* = 9.0 Hz, 1H), δ 7.00 (t, *J* = 6.0 Hz, 1H), δ 6.84–6.72 (m, 3H), δ 6.55 (br s, 1H), δ 4.02–3.95 (m, 1H), δ 3.66 (s, 6H), δ 3.63–3.60 (m, 2H), δ 2.82 (t, *J* = 7.2 Hz, 2H), δ 1.13 (d, *J* = 6.0 Hz, 6H). HRMS (ESI) m/z calcd for $C_{21}H_{27}N_4O_2$ $[M + H]^+$ 367.2056, found 367.2131. Purity: 97.5%

***N*^{2}-Cyclopropyl-N^4-(3,4-dimethoxyphenethyl)quinazoline-2,4-diamine (44).** Yield: 67% (0.35 g, 0.96 mmol); Mp 166–168 °C. ^{1}H NMR (300 MHz, DMSO-*d*$_6$): δ 7.90 (d, *J* = 8.0 Hz, 2H), δ 7.40 (t, *J* = 7.2 Hz, 1H), δ 7.20 (d, *J* = 9.0 Hz, 1H), δ 7.00 (t, *J* = 6.0 Hz, 1H), δ 6.85–6.72 (m, 3H), δ 6.48 (br s, 1H), δ 3.68–3.65 (m, 8H), δ 2.85–2.80 (m, 3H), δ 0.63–0.55 (m, 2H), δ 0.48-0.40 (m, 2H). HRMS (ESI) m/z calcd for $C_{21}H_{25}N_4O_2$ $[M + H]^+$ 365.1899, found 365.1975. Purity: 95.8%

6-Chloro-*N*^{4}-(3,4-dimethoxyphenethyl)-*N*^{2}-propylquinazoline-2,4-diamine (48). Yield: 71% (0.37 g, 0.93 mmol); Mp 107–109 °C. ^{1}H NMR (300 MHz, DMSO-*d*$_6$) δ 8.08–8.03 (m, 2H), δ 7.40 (dd, *J* = 8.9, 2.3 Hz, 1H), δ 7.17 (d, *J* = 8.8 Hz, 1H), δ 6.84–6.71 (m, 4H), δ 3.67–3.59 (m, 8H), δ 3.27–3.23 (m, 2H), δ 2.81 (t, *J* = 7.3 Hz, 2H), δ 1.48 (sextet, *J* = 7.2 Hz, 2H), δ 0.84 (t, *J* = 7.4 Hz, 3H). HRMS (ESI) m/z calcd for $C_{21}H_{26}ClN_4O_2$ $[M + H]^+$ 401.1666, found 401.1740. Purity: 99.4%

6-Chloro-*N*^{4}-(3,4-dimethoxyphenethyl)-*N*^{2}-isopropylquinazoline-2,4-diamine (49). Yield: 75% (0.40 g, 0.99 mmol); Mp 109–111 °C. ^{1}H NMR (300 MHz, DMSO-*d*$_6$) δ 8.09–8.05 (m, 2H), δ 7.43 (dd, *J* = 8.9, 2.2 Hz, 1H), δ 7.18 (d, *J* = 9.0 Hz, 1H), δ 6.84–6.72 (m, 3H), δ 6.71 (br s, 1H), δ 4.16–4.09 (m, 1H), δ 3.67–3.59 (m, 8H), δ 2.82 (t, *J* = 7.3 Hz, 2H), δ 1.12 (d, *J* = 6.5 Hz, 6H). HRMS (ESI) m/z calcd for $C_{21}H_{26}ClN_4O_2$ $[M + H]^+$ 401.1666, found 401.1740. Purity: 98.3%

6-Chloro-*N*^{2}-cyclopropyl-*N*^{4}-(3,4-dimethoxyphenethyl)quinazoline-2,4-diamine (50). Yield: 72% (0.38 g, 0.95 mmol); Mp 104–106 °C. ^{1}H NMR (300 MHz, DMSO-*d*$_6$) δ 8.07 (d, *J* = 2.2 Hz, 1H), δ 8.00 (br s, 1H), δ 7.42 (dd, *J* = 8.9, 2.3 Hz, 1H), δ 7.22 (d, *J* = 8.9 Hz, 1H), δ 6.86–6.71 (m, 4H), δ 3.67–3.59 (m, 8H),

δ 2.87–2.75 (m, 3H), δ 0.64–0.58 (m, 2H), δ 0.48–0.43 (m, 2H). HRMS (ESI) m/z calcd for $C_{21}H_{24}ClN_4O_2$ $[M + H]^+$ 399.1510, found 399.1582. Purity: 98.5%

6-Chloro-N^4-(3,4-dimethoxyphenethyl)-N^2,N^2-dimethylquinazoline-2,4-diamine (51). Yield: 70% (0.36 g, 0.93 mmol); Mp 124–126 °C. ^{1}H NMR (300 MHz, DMSO-d_6) δ 8.08–8.05 (m, 2H), δ 7.40 (dd, J = 8.9, 2.3 Hz, 1H), δ 7.20 (d, J = 8.9 Hz, 1H), δ 6.84–6.70 (m, 3H), δ 3.67–3.58 (m, 8H), δ 3.12 (s, 6H), δ 2.82 (t, J = 7.2 Hz, 2H). ^{13}C NMR (75 MHz, DMSO-d_6) δ 159.45, δ 158.72, δ 150.76, δ 148.62, δ 147.22, δ 132.28, δ 132.06, δ 126.85, δ 123.40, δ 121.95, δ 120.43, δ 112.49, δ 111.94, δ 110.86, δ 55.47, δ 55.20, δ 42.48, δ 36.44, δ 34.00. HRMS (ESI) m/z calcd for $C_{20}H_{24}ClN_4O_2$ $[M + H]^+$ 387.1510, found 387.1581. Purity: 96.5%

7-Chloro-N^4-(3,4-dimethoxyphenethyl)-N^2-propylquinazoline-2,4-diamine (52). Yield: 71% (0.37 g, 0.93 mmol); Mp 105–107 °C. ^{1}H NMR (300 MHz, DMSO-d_6) δ 7.96–7.90 (m, 2H), δ 7.20–7.15 (m, 1H), δ 6.97 (dd, J = 8.6, 2.1 Hz, 1H), δ 6.84–6.72 (m, 4H), δ 3.67–3.59 (m, 8H), δ 2.81 (t, J = 7.3 Hz, 2H), δ 1.46 (sextet, J = 7.2 Hz, 2H), δ 0.78 (t, J = 7.4 Hz, 3H). HRMS (ESI) m/z calcd for $C_{21}H_{26}ClN_4O_2$ $[M + H]^+$ 401.1666, found 401.1738. Purity: 99.6%

7-Chloro-N^4-(3,4-dimethoxyphenethyl)-N^2-isopropylquinazoline-2,4-diamine (53). Yield: 71% (0.37 g, 0.93 mmol); Mp 111–113 °C. ^{1}H NMR (300 MHz, DMSO-d_6) δ 7.97–7.93 (m, 2H), δ 7.19–7.14 (m, 1H), δ 6.99 (dd, J = 8.7, 2.1 Hz, 1H), δ 6.84–6.72 (m, 4H), δ 4.17–4.10 (m, 1H), δ 3.67–3.59 (m, 8H), δ 2.82 (t, J = 7.3 Hz, 2H), δ 1.12 (d, J = 6.5 Hz, 6H). HRMS (ESI) m/z calcd for $C_{21}H_{26}ClN_4O_2$ $[M + H]^+$ 401.1666, found 401.1738. Purity: 95.2%

7-Chloro-N^2-cyclopropyl-N^4-(3,4-dimethoxyphenethyl)quinazoline-2,4-diamine (54). Yield: 72% (0.38 g, 0.95 mmol); Mp 108–110 °C. ^{1}H NMR (300 MHz, DMSO-d_6) δ 8.02 (br s, 1H), δ 7.93 (d, J = 8.9 Hz, 1H), δ 7.21–7.19 (m, 1H), δ 6.99 (dd, J = 8.9, 2.3 Hz, 1H), δ 6.91 (br s, 1H), δ 6.80–6.71 (m, 3H), δ 3.67–

3.59 (m, 8H), δ 2.88–2.78 (m, 3H), δ 0.64–0.58 (m, 2H), δ 0.48–0.43 (m, 2H). HRMS (ESI) m/z calcd for $C_{21}H_{24}ClN_4O_2$ $[M + H]^+$ 399.1510, found 399.1581. Purity: 99.2%

7-Chloro-*N*^{4}-(3,4-dimethoxyphenethyl)-*N*^{2},*N*^{2}-dimethylquinazoline-2,4-diamine (55). Yield: 70% (0.36 g, 0.93 mmol); Mp 128–130 °C. ^{1}H NMR (300 MHz, DMSO-d_6) δ 8.09 (br s, 1H), δ 7.90 (d, J = 8.7 Hz, 1H), δ 7.20 (d, J = 2.1 Hz, 1H), δ 6.97 (dd, J = 8.7, 2.1 Hz, 1H), δ 6.84–6.69 (m, 3H), δ 3.71–3.58 (m, 8H), δ 3.13 (s, 6H), δ 2.82 (t, J = 7.2 Hz, 2H). HRMS (ESI) m/z calcd for $C_{20}H_{24}ClN_4O_2$ $[M + H]^+$ 387.1510, found 387.1580. Purity: 98.4%

8-Chloro-*N*^{4}-(3,4-dimethoxyphenethyl)-*N*^{2}-propylquinazoline-2,4-diamine (56). Yield: 71% (0.37 g, 0.93 mmol); Mp 101–103 °C. ^{1}H NMR (300 MHz, DMSO-d_6) δ 7.92–7.86 (m, 2H), δ 7.57 (d, J = 7.0 Hz, 1H), δ 6.94–6.72 (m, 5H), δ 3.59–3.67 (m, 8H), δ 3.37–3.33 (m, 2H), δ 2.83 (t, J = 7.3 Hz, 2H), δ 1.51 (sextet, J = 7.2 Hz, 2H), δ 0.76 (t, J = 7.4 Hz, 3H). HRMS (ESI) m/z calcd for $C_{21}H_{26}ClN_4O_2$ $[M + H]^+$ 401.1666, found 401.1738. Purity: 98.3%

8-Chloro-*N*^{4}-(3,4-dimethoxyphenethyl)-*N*^{2}-isopropylquinazoline-2,4-diamine (57). Yield: 76% (0.39 g, 0.97 mmol); Mp 104–106 °C. ^{1}H NMR (300 MHz, DMSO-d_6) δ 7.92–7.86 (m, 2H), δ 7.57 (d, J = 7.0 Hz, 1H), δ 6.94–6.72 (m, 5H), δ 4.19–4.08 (m, 1H), δ 3.67–3.59 (m, 8H), δ 2.82 (t, J = 7.3 Hz, 2H), δ 1.13 (d, J = 6.5 Hz, 6H). HRMS (ESI) m/z calcd for $C_{21}H_{26}ClN_4O_2$ $[M + H]^+$ 401.1666, found 401.1737. Purity: 98.6%

8-Chloro-*N*^{2}-cyclopropyl-*N*^{4}-(3,4-dimethoxyphenethyl)quinazoline-2,4-diamine (58). Yield: 71% (0.37 g, 0.94 mmol); Mp 102–104 °C. ^{1}H NMR (300 MHz, DMSO-d_6) δ 7.92–7.86 (m, 2H), δ 7.57 (d, J = 7.0 Hz, 1H), δ 6.94–6.72 (m, 5H), δ 3.67–3.59 (m, 8H), δ 2.88–2.78 (m, 3H), δ 0.64–0.58 (m, 2H), δ 0.48–0.43 (m, 2H). HRMS (ESI) m/z calcd for $C_{21}H_{24}ClN_4O_2$ $[M + H]^+$ 399.1510, found 399.1581 Purity: 98.4%

8-Chloro-N^4-(3,4-dimethoxyphenethyl)-N^2,N^2-dimethylquinazoline-2,4-diamine (59). Yield: 68% (0.35 g, 0.91 mmol); Mp 121–123 °C. ^{1}H NMR (300 MHz, DMSO-d_6) δ 8.10 (br s, 1H), δ 7.87 (d, J = 7.6 Hz, 1H), δ 7.59 (d, J = 7.5 Hz, 1H), δ 6.90 (t, J = 7.8 Hz, 1H), δ 6.84–6.70 (m, 3H), δ 3.70–3.60 (m, 8H), δ 3.17 (s, 6H), δ 2.83 (t, J = 7.2 Hz, 2H). HRMS (ESI) m/z calcd for $C_{20}H_{24}ClN_4O_2$ $[M + H]^+$ 387.1510, found 387.1581. Purity: 99.0%

5.5.2. *Biological Screening*

5.5.2.1. *Human Cholinesterase (hChE) Assay*[299, 313]

The inhibition profile of quinazoline derivatives was evaluated using the Ellman (DTNB) reagent.[315] Human AChE and BuChE enzymes were obtained from Sigma-Aldrich, St. Louis, MO, USA (AChE product number C0663 and BuChE product number B4186 respectively). The cholinesterase inhibitors tacrine (item number 70240, Cayman Chemical Company, Ann Arbor, MI), donepezil (product number D6821, Sigma-Aldrich, St. Louis, MO), galantamine (product number G1660, Sigma-Aldrich, St. Louis, MO) and rivastigmine (product number SML0881, Sigma-Aldrich, St. Louis, MO) were used as reference agents. Quinazoline derivative stock solutions were prepared in DMSO (maximum 1% v/v in final wells) and diluted in buffer solution (50 mM Tris.HCl, pH 8.0, 0.1 M NaCl, 0.02 M $MgCl_2.6H_2O$). Then 160 µL of 5,5'-dithiobis(2-nitrobenzoic acid) (1.5 mm DTNB), 50 µL of *h*AChE (0.22 U/mL in 50 mM Tris.HCl, pH 8.0, 0.1% w/v bovine serum albumin, BSA) or 50 µL of *h*BuChE (0.12 U/mL in 50 mM Tris.HCl, pH 8.0, 0.1% w/v BSA) were added to 96-well plates after which 10 µL each of quinazoline derivatives (final concentration range 0.1–50 µM) were added and incubated for 5 min. Then 30 µL of either acetylthiocholine iodide (15 mM AThCl prepared in ultra pure water) or *S*-butyrylthiocholine iodide (15 mM BThCI prepared in ultra pure water) were added. The absorbance was measured at different time intervals (0, 60, 120, 180, 240 and 300 s) using a wavelength of 412 nm. The inhibitory concentration (IC_{50} values) was calculated from the concentration–inhibition dose response curve on a logarithmic scale. The results were expressed as average values based on two to three independent experiments run in triplicate measurements.

5.5.2.2. *Amyloid-β (Aβ) Aggregation Assay*[317]

The ability of quinazoline-based derivatives to inhibit Aβ-aggregation kinetics was determined using a ThT-binding fluorescence assay. These assays were conducted in Costar, black-surround, clear-bottom 384-well plates with frequent shaking (30 sec. of linear shaking at 730 cpm every 5 minutes) and constant heating at 37 °C for 24 h. The ThT excitation/emission was measured at 440 nm/490 nm and readings were taken every 5 minutes using a BioTek Synergy H1 microplate reader. Quinazoline stock solutions were prepared in DMSO and diluted to 10x in 215 mM phosphate buffer at pH 7.4. Abeta.HFIP samples (Aβ40 or Aβ42, rPeptide, Bogart, USA) were dissolved in 1% ammonium hydroxide, sonicated at room temperature for 5 minutes then diluted to 50 μM in 215 mM phosphate buffer (pH 7.4). A 15 μM ThT stock solution was prepared with 50 mM glycine and adjusted to pH 7.4. The assay was carried out by adding 44 μL ThT, 20–35 μL buffer, 1 μL DMSO (for background and controls only) followed by the addition of 8 μL of 10x compound dilutions (1–25 μM concentration range). An end point reading was conducted to evaluate potential test compound interference with ThT-fluorescence before adding 8 μL of Aβ40 or Aβ42 stock solutions (5 μM final concentration). Plates were sealed with a transparent plate film before initiating the assay. RFU values were corrected for ThT-interference before calculating end point percent inhibitions or IC_{50} values and obtaining the aggregation kinetic plots. Data presented was an average of triplicate reading for two-three independent experiments.

5.5.2.3. *TEM Assay and Imaging*[142, 190, 207, 317]

In Costar 96-well, round-bottom plates were added 80 μL of 215 mM phosphate buffer, 20 μL of 10x test compound dilutions (250 μM – prepared in the same way as for the ThT assay) and 100 μL of 50 μM Aβ40 or Aβ42 respectively. For the control wells, 2 μL of DMSO and 18 μL of phosphate buffer was added. Final Aβ: test compound ratio was 1:1 (25 μM). Plates were incubated on a Fisher plate incubator set to 37 °C and the contents were shaken at 730 cpm for 24 h. To prepare the TEM grids, ~ 20 μL droplet was added using a disposable Pasteur pipette over the formvar-coated copper grids (400 mesh). Grids were air-dried for about 3 h before adding two droplets (~ 40 μL, using a disposable Pasteur pipette) of ultra-

pure water and using small pieces of filter paper to wash out precipitated buffer salts. After air-drying for ~ 15-20 min, the grids were negatively stained by adding a droplet (~ 20 µL, using a disposable Pasteur pipette) of 2% phosphotungstic acid (PTA) and immediately after the grids were dried using small pieces of filter paper. Grids were further air-dried overnight. The scanning was carried out using a Philips CM 10 transmission electron microscope at 60 kV (Department of Biology, University of Waterloo) and micrographs were obtained using a 14-megapixel AMT camera.

5.5.2.4. *DPPH Scavenging Assay*[324]

The ability of select quinazolines to scavenge the DPPH radical was utilized as a measure of antioxidant capacity. Quinazoline stock solutions were prepared in anhydrous methanol (500 µM) and the DPPH solution was also prepared in anhydrous methanol (56 µM). The addition sequence was carried out in a 96-well clear, flat bottom plate as follows: 90 µL DPPH, 10 µL test compound solution (50 µM) final concentration. Control solutions contained 90 µL anhydrous methanol and 10 µL test compound whereas DPPH control contained 90 µL of DPPH, and 10 µL anhydrous methanol. This readings were taken initially at 517 nm with 30 sec. shaking (double orbital at 530 cpm) prior to the 1 h, light restrictive, incubation period at room temperature after which readings were taken again at 517 nm after another round of 30 sec shaking (double orbital at 530 cpm) using a BioTek Synergy H1 microplate reader. The results were expressed as percentage inhibition and the data presented was average of triplicate reading (for two independent experiments).

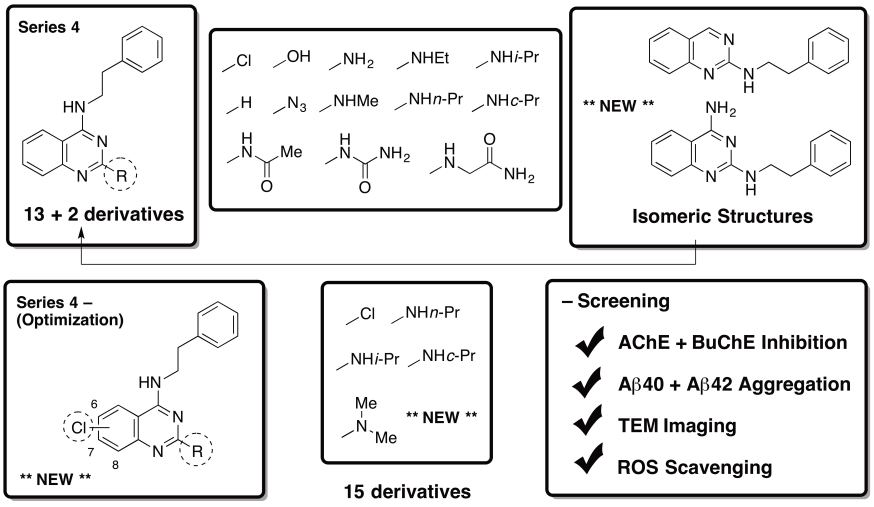
5.5.3. *Computational Chemistry*[299, 313, 317, 324]

The molecular docking studies were conducted using Discovery Studio 4.0 (Structure-Based-Design program) from BIOVIA Inc. San Diego, USA. Select quinazolines derivatives were built and minimized using the *small molecules* module in Discovery Studio. X-ray coordinates of human cholinesterases were obtained from the protein data bank (*h*AChE PBD ID: 1B41 and *h*BuChE PDB ID: 1P0I) and prepared using the *macromolecules* module in Discovery Studio. Ligand binding sites were defined by selecting a 12

Å radius sphere for AChE and 15 Å radius sphere for BuChE. The molecular docking was performed using the *receptor-ligand interactions* module in Discovery Studio. The LibDock algorithm was used to find the most appropriate binding modes for select quinazoline derivatives using CHARMm force field. The docked poses obtained were ranked based on the LibDock scores and were analyzed by evaluating all the polar and nonpolar interactions. For Amyloid-β docking studies, the NMR solution structure of Aβ fibrils were obtained from the protein data bank (PDB ID: 2LMN). Aβ dimer and Aβ fibril assemblies were built using the *macromolecules* module in Discovery Studio. Ligand binding site was defined by selecting a 15 Å radius sphere for both Aβ assemblies. Molecular docking was performed using the *receptor-ligand interactions* module in Discovery Studio, where the LibDock algorithm was used to find the most appropriate binding modes for select quinazoline derivatives using CHARMm force field. The docked poses obtained were ranked based on the LibDock scores and were analyzed by evaluating all the polar and nonpolar interactions.

CHAPTER 6

• Development and Evaluation of *N*-phenethylquinazolin-4-amines as Dual ChE and Aβ Aggregation Inhibitors •



* Chapter banner

6.1. Introduction

The preceding chapters (3–5) showcased the SAR data from 56 quinazoline and cholorquinazoline derivatives, including two regioisomeric structures. The acquired data thus far highlighted the advantages and disadvantages of introducing a dimethoxyphenyl moiety or an additional methylene linker at the C4-positon of the quinazoline scaffold, while providing clear indications of the biological outcomes based on the nature of the C2-groups. The assessment of regioisomeric structures and the impact of chlorine placements provided valuable SAR for the optimization (Phase 2) stage.

This chapter sets to further expand on the acquired SAR data by developing and assessing 30 derivatives that continue to explore the collection of the C2-groups introduced since Chapter 3. The examination of two regioisomers and chlorine placement at position 6, 7 or 8 on the quinazoline scaffold are also investigated. Highlights of the synthetic routes to target derivatives (refer to the chapter banner above) along with the acquisition and assessment of the SAR data are provided.

Generally, all synthetic approaches and mechanisms here have been previously discussed in Chapters 3–5. A brief summary is provided prior to the listing of experimental data and methodology.

6.2. Hypothesis

With respect to this series, the absence of the 3,4-dimethoxy moiety, with the additional methylene unit in the linker chain, should enhance BuChE targeting, while offering an additional point of rotation to enhance binding conformations in AChE and amongst amyloid structures.

On the other hand, continuing with the existing selection of C2-groups offers an opportunity to evaluate and compare the impact of the phenethyl moiety vs. the benzyl (Chapter 4) and the 3,4-dimethoxyphenethyl (Chapter 5) at the C4-position. Previous predications hold true with entities like the azide and carbonyl-based groups with respect to their inability to target BuChE. The increased free-rotation potential at the C4-position, combined with alkylamines at the C2-position, are predicted to aid with BuChE inhibition, while effectively targeting AChE and modulating amyloid aggregation. As these derivatives lack the dimethoxy moiety, it is predicated that their binding conformation within AChE should be primarily based at the catalytic site, with little PAS interactions.

As observed in Chapters 4 and 5, the introduction of a regioisomer provided good insight into the roles of the C2- and C4-groups with respect to dual ChE and dual amyloid targeting and here, two isomers are evaluated.

Lastly, as seen in Chapter 5, the introduction of the chloroquinazoline scaffolds, as part of the optimization process, are predicted to significantly influence ChE binding and amyloid modulation. The dimethylamine group at the C2-position, as part of the optimization process, would present the only tertiary amine based quinazolines in the collective chemical library. The SAR obtained from these derivatives should provide critical insight.

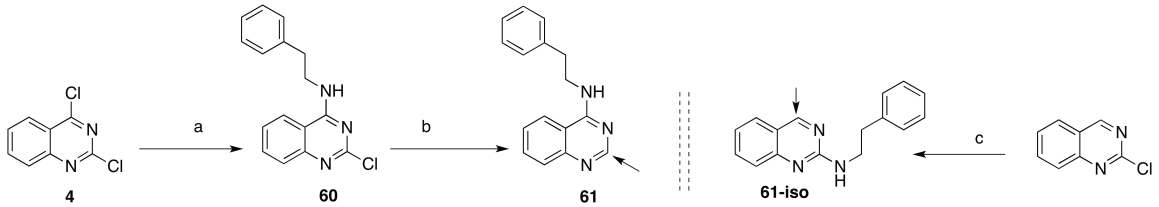
6.3. Results and Discussions

The proceeding sub-chapter briefly highlights previously-established routes to target derivatives. Biological assessments in the cholinesterase and amyloid-β aggregation assay (to obtain IC_{50} values and/or investigation aggregation kinetics) are conducted. Aggregate load is corroborated via transmission electron microscopy in amyloid morphology screening and select derivatives are assessed for ROS scavenging in the DPPH assay. Computational studies are performed in the ChE X-ray structures and amyloid models to evaluate the acquisitioned SAR data.

6.3.1. *Synthesis*

As previously described in Chapters 3–5, initial coupling in this series utilized 2,4-DCQ (**4**) to add the phenethylamine group to the C4-position of the quinazoline scaffold, via a NAS reaction, to yield 2-chloro-*N*-phenethylquinazolin-4-amine (**60**, Scheme 17, 80–85% yield).[299, 303] The C2-unsubstituted derivative (*N*-phenethylquinazolin-4-amine, **61**, Scheme 17, ~ 45% yield) was also synthesized via the Pd/C and hydrazine-driven dehalogenation reaction.[304] The regioisomer of **61** was generated by heating 2-chloroquinazoline and phenethylamine, under high temperature and pressure conditions, to yield *N*-phenethylquinazolin-2-amine, **61-iso**, Scheme 17, ~ 55% yield).

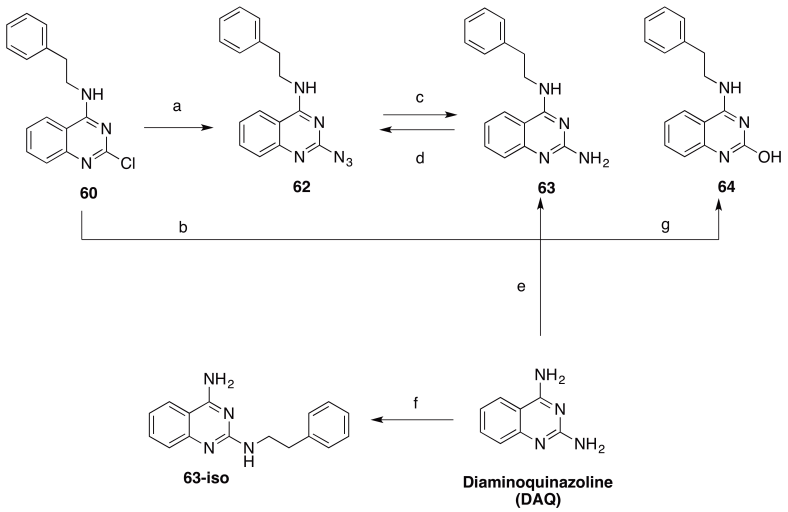
Scheme 17[a]



[a]**Reagents and conditions:** Synthetic routes toward quinazoline-based derivatives **60**, **61** and **61-iso**.(a) Phenethylamine, DIPEA, EtOH, reflux, 4 h; (b) Pd/C, hydrazine hydrate, EtOH, reflux, 2 h; (c) Phenethylamine, DIPEA, 1,4-dioxane, pressure vial, 150–155 °C, 2 h.

Synthesis of 2-azido-*N*-phenethylquinazolin-4-amine (**62**, Scheme 18, ~ 90% yield) was accomplished as previously described utilizing sodium azide,[305, 306] while the generation of the C2-amino derivative (**63**, Scheme 18, N^4-phenethylquinazoline-2,4-diamine) was primarily conducted using the azide reduction approach via Pd/C and hydrazine.[305] The synthesis of **63-iso** was accomplished from the previously described method using 2,4-diaminoquinazoline (DAQ).[317] The effective formate/formic acid approach was utilized to generate **64** (4-(phenethylamino)quinazolin-2-ol, Scheme 18, yield ~ 65%).

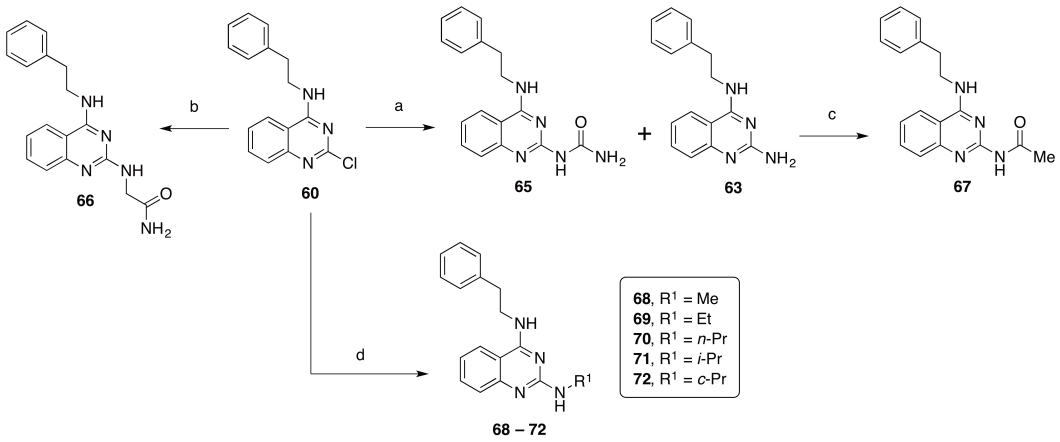
Scheme 18[a]



[a]**Reagents and conditions:** Synthetic routes toward quinazoline-based derivatives **62–64** and **63-iso.** (a) Sodium azide, EtOH, acetic acid, 90–95 °C, 2 h; (b) Cu_2O, K_2CO_3, DMEDA, ethylene glycol, ammonium hydroxide, pressure vial, oil bath, 105 °C, 24 h; (c) Pd/C, hydrazine hydrate, EtOH, reflux, 2 h; (d) HCl, sodium nitrite, sodium azide, 0 °C–r.t., 1 h; (e) Sodium hydride, DMSO, benzyl bromide, 0 °C–r.t., 14 h; (f) DMA, potassium or cesium carbonate, benzyl bromide 80–85 °C, 5 h.; (g) Potassium formate, formic acid, 120–125 °C, 14–16 h.

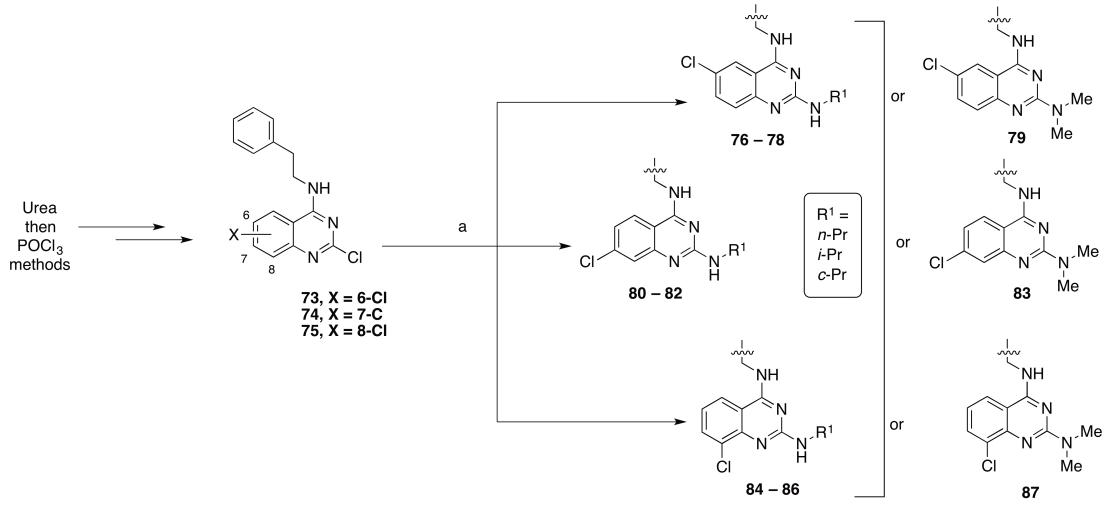
The synthesis of both the C2-carbonyl based derivatives **65** (C2 = urea), **66** (C2 = glycinamide), **67** (C2 = acetamide) and the C2-alkylamine based derivatives (**68**–**72**) was accomplished as previously described in Chapters 3–5 (Scheme 19). As previously outlined in Chapter 5, the synthesis of the phenethyl-based chloroquinazolines with various alkylamines at the C2-position (**73**–**87**) was accomplished using previously described methodologies based on N.A.S (Scheme 20).

Scheme 19[a]



[a]**Reagents and conditions:** Synthetic routes toward quinazoline-based derivatives **65**–**72**. (a) Urea, 1,4-dioxane, pressure vial, 160–165 °C, 24 h.; (b) glycinamide, DBU, 1,4-dioxane, pressure vial, 150–155 °C, 4 h.; (c) acetyl chloride, acetic acid, 1,4-dioxane, 120 °C, 24 h. (d) Primary amine (R^1 = Me, Et, *n*-Pr, *i*-Pr or *c*-Pr), DIPEA, 1,4-dioxane, pressure vial 150–155 °C, 2 h.

Scheme 20[a]

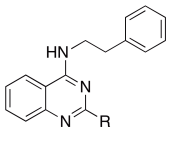


[a]**Reagents and conditions:** Synthetic routes toward quinazoline-based derivatives **73**–**87**.(a) Primary amine (R^1 = *n*-Pr, *i*-Pr or *c*-Pr) or dimethylamine, DIPEA, 1,4-dioxane, pressure vial 150–155 °C, 2 h.

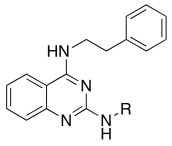
6.3.2. *Cholinesterase*

The ability of 2-substituted-*N*-phenethylquinazolin-4-amines (**60**–**72**) and the related regiosiomers (**61-iso** and **63-iso**) to target the cholinesterases (*h*AChE/*h*BuChE) was assessed using the DTNB method as described in Chapter 3 (Table 9). ChE data for phase-2 candidates (**73**–**87**) are showcased in Table 10.

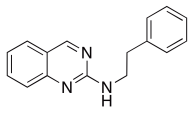
Table 9: Cholinesterase inhibition data for 2-substituted-*N*-phenethylquinazolin-4-amines (**60**–**72**) and the related regiosiomers (**61-iso** and **63-iso**).



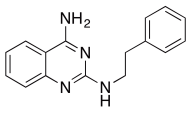
60–62, 64



63, 65–72



61-iso



63-iso

Derivative	R-Grp	ChE IC_{50} (μM) [a]		SI [b]	ClogP [c]	MV (Å^3) [d]	HBD:HBA [e]
		*h*AChE	*h*BuChE				
60	Cl	7.7 ± 0.5	> 50	–	4.74	182.1	1:3
61	H	6.2 ± 0.7	14.1 ± 1.2	0.44	3.98	168.7	1:3
61-iso	–	7.6 ± 0.5	> 50	–	3.98	197.7	1:3
62	N_3	9.7 ± 0.8	> 50	–	5.39	221.5	1:7
63	H	5.7 ± 0.7	4.9 ± 0.6	1.16	3.97	176.6	3:4
63-iso	–	7.1 ± 0.7	2.4 ± 0.1	2.96	3.97	209.2	3:4
64	OH	8.1 ± 0.6	> 50	–	4.61	208.5	2:4
65	$CONH_2$	7.9 ± 0.6	> 50	–	3.99	232.8	4:6
66	CH_2CONH_2	7.3 ± 0.9	3.5 ± 0.2	2.09	3.59	247.9	4:6
67	COMe	7.0 ± 0.5	> 50	–	3.52	245.5	2:5
68	Me	8.7 ± 1.0	5.0 ± 0.3	1.74	4.79	187.6	2:4
69	Et	7.6 ± 0.5	3.2 ± 0.3	2.38	5.32	199.2	2:4
70	*n*-Pr	7.2 ± 0.6	5.0 ± 0.4	1.44	5.85	212.3	2:4
71	*i*-Pr	7.2 ± 0.4	1.6 ± 0.05	4.51	5.63	214.3	2:4
72	*c*-Pr	8.6 ± 0.6	11.4 ± 0.9	0.75	5.38	208.5	2:4
Donepezil	–	0.03 ± 0.002	3.6 ± 0.4	0.01	4.59	321.7	0:4
Tacrine	–	0.16 ± 0.01	0.04 ± 0.001	4.00	3.27	165.6	2:2
Galantamine	–	2.6 ± 0.6	> 50	–	1.18	239.4	1:4
Rivastigmine	–	6.5 ± 0.5	> 10	–	2.10	226.3	0:4

Notes: [a] IC_{50} values are an average ± SD of triplicate readings based on two to three independent experiments. [b]Selectivity index is calculated as (*h*AChE IC_{50}) ÷ (*h*BuChE IC_{50}). [c]ClogP values were determined using ChemDraw Professional 15.0. [d]Molecular volumes in Å^3 units were determined using Discovery Studio, Structure-Based Design software, BIOVIA Inc., USA. [e]Showcasing the ratio of HBD = hydrogen-bonding donors to HBA = hydrogen-bonding acceptors.

When considered against Table 3 (Chapter 4) and Table 5 (Chapter 5), the data presented in Table 9 generally pointed to the superior ability of most derivatives within this series to target BuChE. With respect to AChE targeting, IC_{50} values ranged from 6 to 10 μM, which was a narrower range of inhibitory activity when compared to the 5–14 μM range seen with the benzyl counterparts (Chapter 4, Table 3) and the 3–13 μM range seen with the dimethoxyphenethyl counterparts (Chapter 5, Table 5).

Interestingly, both **60** (C2 = Cl; IC_{50} = 7.7 μM) and **61** (C2 = H; IC_{50} = 6.2 μM) showcased equipotent activity in AChE when compared with their C4-benzyl counterparts (**19** and **20**; respectively). While both were roughly 2.5-fold less potent in AChE compared with their C4-dimethoxyphenethyl counterparts (**32** and **33**; respectively), **61** became the first C2-substituted derivative to display moderate activity toward BuChE (IC_{50} ~ 14 μM). This was one of the initial pointers toward the favorability of the C4-phenethylamine group to target BuChE. That said, **61-iso** showcased the same pattern as seen with **33-iso** (Chapter 5) where AChE activity was reduced roughly 1.2-fold and a loss of BuChE inhibition was observed.

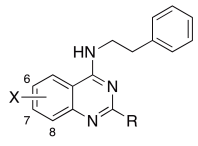
The azide functionality in this series (**62**, IC_{50} = 9.7 μM) was comparable to its dimethoxyphenethyl counterpart in Chapter 5 (**34**, IC_{50} = 8.5 μM, Table 5) and roughly 1.4-fold more potent than its benzyl counterpart in Chapter 4 (**21**, IC_{50} = 14.0 μM). That said, **62** was the least potent AChEI in this series and as with other azide-based derivatives, it was inactive toward BuChE. With a C2-amino group, **63** was equipotent to **22** with respect to AChE but, thanks to its additional methylene linker, an enhanced binding conformation was observed in BuChE yielding a 6-fold improvement in the IC_{50} (5 vs. 30 μM). The relevance of the dimethoxy moiety is showcased when comparing **63** and **35** (Chapter 5), where a 2.2-fold decline in AChE potency was observed with the absence of the 3,4-dimethoxy group. Similar to what was observed with **22** and **22-iso** in Chapter 4, **63-iso** lost some AChE potency (~ 1.2-fold) in favour of a 2-fold improvement in BuChE inhibition, with respect to **63**. When compared directly to **22-iso**, no differences were observed in AChE activity but an approximate 5-fold improvement was observed with BuChE targeting. The introduction of the C2-hydroxy group in **64** yielded comparable results to those observed in Chapter 4 (benzyl series) and Chapter 5 (dimethoxyphenethyl series) with AChE IC_{50} at roughly 8 μM and no activity toward BuChE.

With respect to the carbonyl-based derivatives, derivatives **65**–**67** exhibited activity toward AChE at IC_{50} values of 7–8 μM, which closely resemble those of **24–26** (Chapter 4, benzyl series) and **37**/**39** (Chapter 5, dimethoxyphenethyl series). While carbonyl-based derivatives have been a write-off with respect to BuChE targeting, it was a pleasant surprise to observe that **66** (C2 = glycinamide) was not only active toward BuChE, but also equipotent to donepezil (IC_{50} = 3.5 μM). As hypothesized with **61**, the additional methylene linker at the C4-position in **66** must have facilitated a substantially favourable binding conformation within BuChE to yield the 14-fold+ improvement in inhibition.

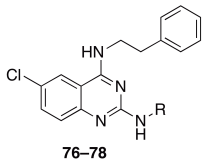
The introduction of alkylamines at the C2-position (derivatives **68**–**72**, Table 8) established comparable activity toward AChE (IC_{50} ~ 7.9 μM) as seen with both the benzyl (**27**–**31**, Chapter 4, IC_{50} ~ 7.3 μM) and the dimethoxyphenethyl counterparts (**40**–**44**, Chapter 5, IC_{50} ~ 7.6 μM). With respect to BuChE on the other hand, inhibition was generally improved with C2-Et, *n*Pr and *i*Pr derivatives (69-71) surpassing both benzyl (**28**–**30**) and dimethoxyphenethyl (**41**–**43**) counterparts. While **72** (C2-*c*Pr) was the least favourable amongst the alkylamine-based derivatives, derivative **71** (AChE IC_{50} = 7.2 μM, BuChE IC_{50} = 1.6 μM) exhibited strong AChE inhibition and was the most potent BuChE inhibitor (surpassing donepezil by 2.3- fold) amongst the subgroup.

Considering the general advantage of placing alkylamines at the C2-position, along with the benefits of a phenethylamine group at the C4-position, the optimization of **70**–**72** (C2 = *n*-Pr, *i*-Pr and *c*-Pr) was investigated on chloroquinazoline scaffolds (6-, 7- or 8-chloroquinazoline). The use of the dimethylamine group was meant to correlate with the isopropylamine functionality. As seen in Table 10, the chloroquinazoline derivatives (**73**–**87**) showcased an activity range of 5.8–8.9 μM (IC_{50}) toward AChE and 0.1–50+ μM (IC_{50}) toward BuChE. When compared to non-chloroquinazoline counterparts in Table 5, general improvements are seen in both AChE and BuChE, which was expected considering the additional hydrophobicity and electrostatic changes. This was an interesting observation considering that chlorine placement did not necessarily benefit ChE binding with the dimethoxyphenethyl series (Chapter 5).

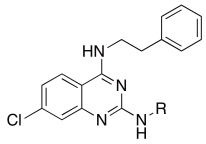
Table 10: Cholinesterase inhibition data for 2-substituted-*N*-phenethylchloroquinazolin-4-amines (**73**–**87**).



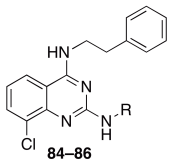
73, 79 X = 6-Cl
74, 83 X = 7-Cl
75, 87 X = 8-Cl



76–78



80–82



84–86

Derivative	R-Grp	ChE IC_{50} (μM) [a]		SI [b]	ClogP [c]	MV (Å^3) [d]	HBD:HBA [e]
		*h*AChE	*h*BuChE				
73	Cl	8.3 ± 0.8	> 50	–	5.47	231.18	1:3
74	Cl	7.6 ± 0.8	43.0 ± 3.9	0.18	5.47	234.26	1:3
75	Cl	8.9 ± 0.9	14.3 ± 1.5	0.62	5.47	232.89	1:3
76	*n*-Pr	8.9 ± 0.6	4.8 ± 0.3	1.84	6.60	275.08	2:4
77	*i*-Pr	8.7 ± 0.5	1.5 ± 0.1	5.64	6.38	274.39	2:4
78	*c*-Pr	8.7 ± 0.9	9.1 ± 0.7	0.95	6.13	266.16	2:4
79	$N(Me)_2$	7.7 ± 0.8	5.4 ± 0.6	1.41	5.63	261.02	1:4
80	*n*-Pr	7.2 ± 0.7	4.4 ± 0.4	1.66	6.6	270.96	2:4
81	*i*-Pr	6.6 ± 0.6	0.1 ± 0.02	73.3	6.38	273.37	2:4
82	*c*-Pr	7.3 ± 0.6	3.5 ± 0.4	2.09	6.13	264.1	2:4
83	$N(Me)_2$	5.8 ± 0.7	1.5 ± 0.1	3.92	5.63	258.96	1:4
84	*n*-Pr	7.7 ± 0.7	6.0 ± 0.6	1.28	6.6	272.68	2:4
85	*i*-Pr	8.6 ± 0.9	2.6 ± 0.2	3.26	6.38	275.08	2:4
86	*c*-Pr	7.6 ± 0.7	10.9 ± 0.9	0.69	6.13	265.48	2:4
87	$N(Me)_2$	7.5 ± 0.8	> 50	–	5.63	263.08	1:4
Donepezil	–	0.03 ± 0.002	3.6 ± 0.4	0.01	4.59	321.7	0:4
Tacrine	–	0.16 ± 0.01	0.04 ± 0.001	4.00	3.27	165.6	2:2
Galantamine	–	2.6 ± 0.6	> 50	–	1.18	239.4	1:4
Rivastigmine	–	6.5 ± 0.5	> 10	–	2.10	226.3	0:4

Notes: [a] IC_{50} values are an average ± SD of triplicate readings based on two to three independent experiments. [b]Selectivity index is calculated as (*h*AChE IC_{50}) ÷ (*h*BuChE IC_{50}). [c]ClogP values were determined using ChemDraw Professional 15.0. [d]Molecular volumes in Å^3 units were determined using Discovery Studio, Structure-Based Design software, BIOVIA Inc., USA. [e]Showcasing the ratio of HBD = hydrogen-bonding donors to HBA = hydrogen-bonding acceptors.

Starting out with the C2-chlorine based derivatives, **73**–**75** were roughly equipotent to **60** toward AChE (IC_{50} ~ 8–9 μM), with chlorine placement ranking as C7, C6 then C8. Interestingly, chlorine placement had significant impact on BuChE targeting considering that **73** (C6-Cl) was inactive, **74** (C7-Cl) was very weakly active, while **75** (C8-Cl) showcased moderate inhibition (IC_{50} ~ 14 μM). When compared to dimethoxyphenethyl counterparts (**45**–**47**), derivatives **73**–**75** were generally more effective or on par.

When compared to **70**–**72**, the impact of chlorine placement at position 6 of the quinazoline scaffold in **76**–**78** had negligible or minor impact on AChE inhibition (average IC_{50} ~ 7.7 vs. 8.8 μM), with C2-*c*Pr being the least impacted (derivative **72** vs. **78**). On the other hand, in BuChE, only the C2-*c*Pr derivative (**78**) showcased slight improvement (~ 1.3-fold) compared **72**, while others remain unchanged. With the dimethylamine functionality at the C2-position (**79**), an approximate 1.1-fold improvement in AChE was observed (when compared to **76**–**78**), while BuChE activity was comparable to **76**, while being roughly 4-fold less potent compared to the isopropyl-based relative, **77**. When compared to dimethoxyphenethyl counterparts (**48**–**51**), derivatives **76**–**79** were slightly less effective against AChE but much more effective toward BuChE.

Moving on, when compared to **76**–**79**, the impact of chlorine placement at position 7 in **80**–**83** had positive impact on all the derivatives (not just in a general sense) with respect to both AChE and BuChE inhibition. Most significant was the 15-fold increase in BuChE potency between **77** and **81**. As a matter of fact, derivative **81** was 40-fold more potent toward BuChE compared to donepezil and only 2-fold less potent compared to tacrine. When compared to dimethoxyphenethyl counterparts (**52**–**55**), derivatives **80**–**83** were either on par or more effective against AChE, while exhibiting superior inhibition toward BuChE.

Lastly, the impact of chlorine placement at position 8 in **84**–**87** elicited null or minor changes toward AChE inhibition (average IC_{50} ~ 7.9 μM) compared to other placements (**76**–**79** and **80**–**83**) and non-chlorinated (**70**–**72**) counterparts (average IC_{50} ~ 8.5 vs. 6.7 vs. 7.7 μM; respectively). In BuChE, chlorine placement at 8 position generally worsened or severely hindered inhibition when compared to other placements and non-chlorinated counterparts. Of greatest interest was the complete loss of BuChE inhibition with derivative **87**. That said, the isopropyl group at C2-position was always ranked in first place with respect to BuChE, while the dimethylamine group was ranked first with respect to AChE. When compared to dimethoxyphenethyl counterparts (**56**–**59**), derivatives **80**–**83** were generally as effective or slightly less effective against AChE, while BuChE activity was better (overall) but some derivatives were just as ineffective as observed in **56**–**59**.

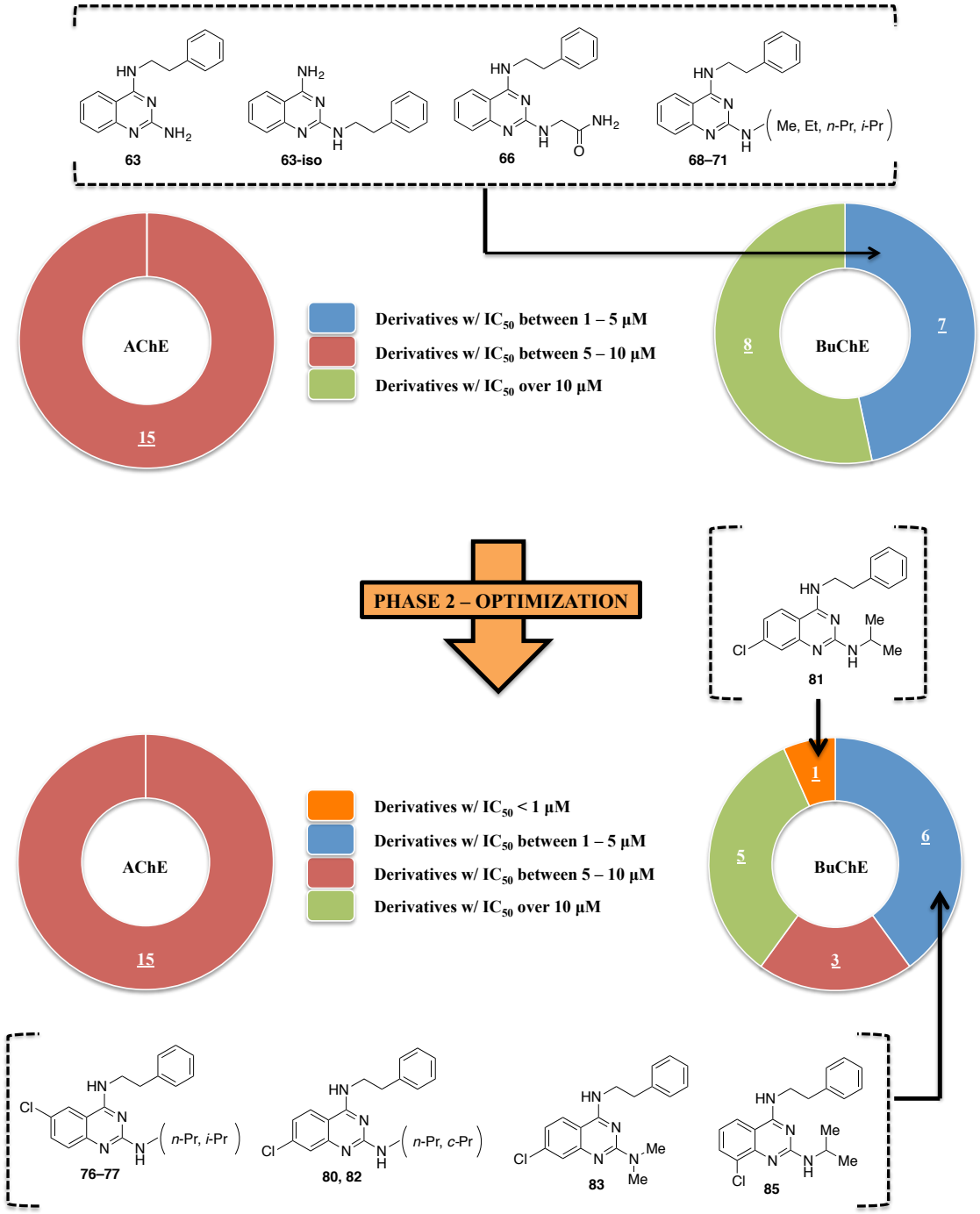


Figure 70: Cholinesterase metrics for fifteen 2-substituted-*N*-phenethylquinazolin-4-amines (**60**–**72**) and 15 2-substituted-*N*-phenethylchloroquinazolin-4-amines (**73**–**87**).

In summary, 30 derivatives were assessed for dual cholinesterase activity, of which derivative **63** (N^4-phenethylquinazoline-2,4-diamine) was identified as the most active and non-selective AChEI (Dual IC_{50} ~ 5.3 μM), while derivative **81** (7-chloro-N^2-isopropyl- N^4-phenethylquinazoline-2,4-diamine) was identified as the most active BuChEI (IC_{50} = 95 nM) surpassing the activity level of donepezil by 4-fold. Generally, this series proved to be more or less as effective toward AChE as the benzyl and dimethoxyphenethyl series (Chapter 4 and Chapter 5). Activity toward BuChE was significantly improved overall, while the introduction of the chloroquinazoline scaffolds and the dimethylamine functionality at the C2-position further improved biological activity, specifically with BuChE inhibition (Figure 70).

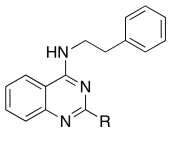
6.3.3. *Amyloid-β Aggregation*

The ability of 2-substituted-*N*-phenethylquinazolin-4-amines (**60**–**72**) and the related regiosiomer (**61-iso** and **63-iso**) to modulate the aggregation kinetics of amyloid-β was assessed using the ThT-binding method described earlier in Chapter 3 (Table 11). Amyloid-β inhibitory data for optimization candidates (**73**–**87**) is showcased in Table 12.

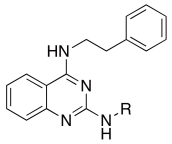
When compared to benzyl (Table 4) and dimethoxyphenethyl (Table 7) counterparts in Chapters 4 and 5, respectively, the examination of Table 11 demonstrated a higher number of inactive or weakly active derivatives toward Aβ aggregation (4 out of 15 derivatives were inactive toward both Aβ species, in addition to 2 that were inactive toward Aβ42). Overall, none of the derivatives here were considered as potent inhibitors of Aβ42 (most active had an IC_{50} ~ 25 μM); however, some were quite effective toward Aβ40 (7 out of 15 had an IC_{50} < 5 μM). Of noteworthy mention, derivatives **65** (C2 = urea), **69** (C2 = NHEt) and **72** (C2 = NH*c*Pr) exhibited strong inhibitory activity toward Aβ40 (IC_{50} 0.8–1.4 μM) that placed them on par with the activity of resveratrol.

Starting out with the C2-chlorine derivative, **60** (IC_{50} = 5 μM) was more active toward Aβ40 compared to both benzyl (**19**, IC_{50} ~ 17 μM) and dimethoxyphenethyl (**32**, IC_{50} ~ 8 μM) counterparts; however, it was only moderately active toward Aβ42 (P.I at 25 μM was ~ 36%, compared to 22% for **19**).

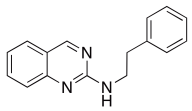
Table 11: Amyloid-β (Aβ40/42) inhibition data for 2-substituted-*N*-phenethylquinazolin-4-amines (**60**–**72**) and the related regiosiomers (**61-iso** and **63-iso**).



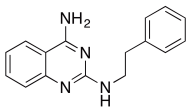
60–62, 64



63, 65–72



61-iso



63-iso

Derivative	R-Grp	Amyloid-β IC_{50} (μM) [a]		SI [b]	ClogP [c]	MV (Å^3) [d]	HBD:HBA [e]
		Aβ40	Aβ42				
60	Cl	5.0 ± 0.8	36%	–	4.74	182.1	1:3
61	H	11.9 ± 2.5	32%	–	3.98	168.7	1:3
61-iso	–	NA	NA	–	3.98	197.7	1:3
62	N_3	NA	NA	–	5.39	221.5	1:7
63	H	8.2 ± 2.0	37%	–	3.97	176.6	3:4
63-iso	–	14.9 ± 1.9	50%	–	3.97	209.2	3:4
64	OH	11.2 ± 1.4	NA	–	4.61	208.5	2:4
65	$CONH_2$	1.0 ± 0.1	46%	–	3.99	232.8	4:6
66	CH_2CONH_2	NA	NA	–	3.59	247.9	4:6
67	COMe	NA	NA	–	3.52	245.5	2:5
68	Me	2.0 ± 0.4	40%	1.74	4.79	187.6	2:4
69	Et	1.4 ± 0.3	47%	2.38	5.32	199.2	2:4
70	*n*-Pr	4.4 ± 0.6	33%	1.44	5.85	212.3	2:4
71	*i*-Pr	3.8 ± 0.7	NA	4.51	5.63	214.3	2:4
72	*c*-Pr	0.8 ± 0.03	22%	0.75	5.38	208.5	2:4
Curcumin	–	3.3 ± 0.45	9.9 ± 0.4	0.33	4.59	302.1	2:6
Resveratrol	–	1.1 ± 0.1	15.3 ± 1.9	0.07	2.83	187.2	3:3

Notes: [a] IC_{50} values are an average ± SD of triplicate readings based on two to three independent experiments. NA = Not active. Percent inhibition (P.I) indicates level of inhibition at highest concentration tested (25 μM). [b]Selectivity index is calculated as (Aβ40 IC_{50}) ÷ (Aβ42 IC_{50}). [c]ClogP values were determined using ChemDraw Professional 15.0. [d]Molecular volumes in Å^3 units were determined using Discovery Studio, Structure-Based Design software, BIOVIA Inc., USA. [e]Showcasing the ratio of HBD = hydrogen-bonding donors to HBA = hydrogen-bonding acceptors.

The dechlorination of **60** hindered Aβ40 activity nearly 2.5-fold with no impact on Aβ42 activity and derivative **61** became equipotent to its dimethoxyphenethyl counterpart (**33**). When compared to the benzyl counterpart (**20**), **61** was much more effective toward Aβ40 activity and demonstrated mild improvements toward Aβ42 activity. Its regioisomer (**61-iso**) was just as inactive toward both Aβ40/42 as **33-iso** in Chapter 5, suggesting that the lack of a functional group at the C4-position is detrimental to Aβ targeting.

Compared to the outcome of the azide functionality in **21** (Chapter 4) and **34** (Chapter 5), it was interesting to observe the abolished activity of **62** toward both Aβ40/42. This further strengthens the

incompatibility of the azide group with these quinazoline scaffolds. Reduction of that azide to the amino group (**63**, IC_{50} ~ 8 and ~ 35 μM; Aβ40/42 respectively) led to enhanced biological activity; however, it was a weaker inhibitor of Aβ40/42 compared to **35** (dimethoxyphenethyl counterpart, IC_{50} ~ 3 and ~ 28 μM; Aβ40/42 respectively). Compared to its benzyl counterpart (**22**, IC_{50} ~ 5 μM and not active; Aβ40/42 respectively), **63** was less effective toward Aβ40 only. Its regioisomer (**63-iso**) on the other hand, was less potent toward Aβ40 (~ 1.8-fold), while improving inhibitory potential toward Aβ42 by 13%. That said, direct comparison of **22-iso** and **63-iso** showcased significant hindrances in anti-Aβ40/42 activity with the additional methylene linker at the C2-position. Replacement of the C2-amino group in **63** with a hydroxyl group in **64** (IC_{50} ~ 11 μM and not active; Aβ40/42 respectively) resulted in an approximate 1.4-fold improvement in Aβ40 activity but with a total loss of Aβ42 activity. Compared to its benzyl counterpart (**23**), **64** was far less effective toward Aβ40 (~ 37-fold), while being equipotent to **36** (the dimethoxyphenethyl counterpart) with respect to Aβ40.

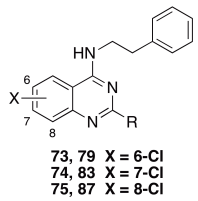
With respect to the carbonyl-based derivatives, the C2-urea-containing derivative (**65**) was the only dually active derivative in this sub-group. While no activity was anticipated for the glycinamide-based derivative (**66**), the inactivity observed with **67** was a bit unexpected considering the mild, yet dual inhibition within the dimethoxyphenethyl series (**39**) and the potent activity seen with **26** (Aβ40 IC_{50} ~ 2 μM). Compared to its benzyl and dimethoxyphenethyl counterparts (**24** and **37**; respectively), **65** was a superior inhibitor of Aβ40 (IC_{50} ~ 1 μM)., while showcasing comparable Aβ42 activity as **24**.

The introduction of alkylamines at the C2-position (**68**–**72**) provided more potent inhibitory activity toward Aβ40 (average IC_{50} ~ 2.5 μM), across the board, when compared to both benzyl (**27**–**31**, average IC_{50} ~ 5.5 μM – excluding **27**) and dimethoxyphenethyl (**40**–**44**, average IC_{50} ~ 4.8 μM – excluding **43**) counterparts. The effectiveness of alkyl chains was ranked as *c*-Pr > Et > Me > *i*-Pr > *n*-Pr, with derivative **72** being approximately 1.4-fold more potent than resveratrol (Aβ40 IC_{50} = 790 nM) and roughly 7-fold more potent compared to both benzyl and dimethoxyphenethyl counterparts (**31** and **44**; respectively).

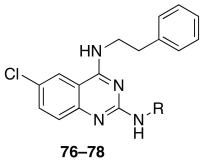
With respect to Aβ42, C2-*i*Pr or *c*Pr derivatives (**71** and **72**) were ranked lower in terms of inhibitory activity, while both C2-Et or *n*Pr derivatives (**69** and **70**) were slightly more effective compared to both benzyl and dimethoxyphenethyl counterparts. With the C2-Me derivative, **68** was ranked in between **27** and **40**.

With the introduction of the chloroquinazoline scaffolds, Aβ42 potency was enhanced overall, while activity toward Aβ40 was more of a mixed outcome, as showcased in Table 12. Compared to **60** (Table 11), only derivative **73** was 1.8-fold less potent toward Aβ40, while **74** and **75** were roughly 2.5-fold more effective. These derivatives were either 4-fold (**73**) or 20-fold (**74** and **75**) more potent toward Aβ42, compared to **60**. Chlorine placement was generally in the ranking of 7-Cl > 8-Cl > 6-Cl and interestingly, both **74** and **75** were classified as dual, non-selective inhibitors of Aβ40/42 (IC_{50} ~ 1.9 μM). When compared to dimethoxylphenethyl counterparts (**45**–**47**), **73**–**75** were either on par or slightly less effective.

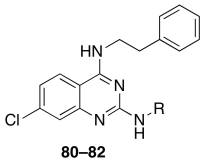
Table 12: Amyloid-β (Aβ40/42) inhibition data for 2-substituted-*N*-phenethylquinazolin-4-amines (**73**–**87**).



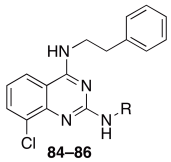
73, 79 X = 6-Cl
74, 83 X = 7-Cl
75, 87 X = 8-Cl



76–78



80–82



84–86

Derivative	R-Grp	Amyloid-β IC_{50} (μM) [a]		SI [b]	ClogP [c]	MV (Å^3) [d]	HBD:HBA [e]
		Aβ40	Aβ42				
73	Cl	9.3 ± 0.8	7.7 ± 0.8	1.21	5.47	231.18	1:3
74	Cl	1.7 ± 0.2	1.7 ± 0.2	1.00	5.47	234.26	1:3
75	Cl	2.3 ± 0.3	2.0 ± 0.4	1.15	5.47	232.89	1:3
76	*n*-Pr	44%	23%	–	6.60	275.08	2:4
77	*i*-Pr	8.6 ± 0.7	36%	–	6.38	274.39	2:4
78	*c*-Pr	8.7 ± 0.9	19%	–	6.13	266.16	2:4
79	$N(Me)_2$	6.5 ± 0.7	20%	–	5.63	261.02	1:4
80	*n*-Pr	6.9 ± 1.4	4.6 ± 0.9	1.50	6.6	270.96	2:4
81	*i*-Pr	6.1 ± 1.3	7.2 ± 1.6	0.85	6.38	273.37	2:4
82	*c*-Pr	4.8 ± 1.0	11.7 ± 2.0	0.41	6.13	264.1	2:4
83	$N(Me)_2$	5.1 ± 1.7	29%	–	5.63	258.96	1:4
84	*n*-Pr	3.7 ± 0.5	6.5 ± 0.4	0.57	6.6	272.68	2:4
85	*i*-Pr	0.9 ± 0.1	3.9 ± 0.5	0.23	6.38	275.08	2:4
86	*c*-Pr	1.3 ± 0.2	6.8 ± 1.3	0.19	6.13	265.48	2:4
87	$N(Me)_2$	1.9 ± 0.3	5.8 ± 0.7	0.33	5.63	263.08	1:4
Curcumin	–	3.3 ± 0.45	9.9 ± 0.4	0.33	4.59	302.1	2:6
Resveratrol	–	1.1 ± 0.1	15.3 ± 1.9	0.07	2.83	187.2	3:3

Notes: [a] IC_{50} values are an average ± SD of triplicate readings based on two to three independent experiments. NA = Not active. Percent inhibition (P.I) indicates level of inhibition at highest concentration tested (25 μM). [b]Selectivity index is calculated as (Aβ40 IC_{50}) ÷ (Aβ42 IC_{50}). [c]ClogP values were determined using ChemDraw Professional 15.0. [d]Molecular volumes in Å^3 units were determined using Discovery Studio, Structure-Based Design software, BIOVIA Inc., USA. [e]Showcasing the ratio of HBD = hydrogen-bonding donors to HBA = hydrogen-bonding acceptors.

With respect to Aβ40 inhibition, chlorine placement at position 6 of the quinazoline scaffold in **76**–**78**, when compared to **70**–**72**, had a significantly negative impact on inhibitory activity with **76** being the least active derivative in the sub-group. While both **77** and **78** were equipotent, they suffered a 2.3-fold and a 10.9-fold decline in Aβ40 potency; respectively, compared to **71** and **72**. With respect to Aβ42, and compared to **70**–**72**, derivative **76** lost 10% of inhibitory activity, derivative **77** gained 36%, while derivative **78** was on par with its non-chlorinated counterpart. Comparing the dimethylamine-based derivative (**79**) to **77**, activity toward Aβ40 improved by 1.4-fold, while Aβ42 inhibition was backtracked by 16%. Collective comparison to their dimethoxyphenethyl counterparts (**48**–**51**, Chapter 5), **76**–**78** were less potent across the board, although **50** and **78** were on par with respect to Aβ40.

Moving on, when compared to **76**–**79**, the impact of chlorine placement at position 7 in **80**–**83** enhanced both Aβ40/42 inhibitory activity across the board. Least impact was observed with the dimethylamine C2-group, where Aβ40 inhibition was improved 1.3-fold, while activity toward Aβ42 increased by 9%. Derivatives **82** (C2 = NH*c*-Pr) and **83** (C2 = NMe_2) were equipotent toward Aβ40 at IC_{50} ~ 5 μM, while **80** (C2 = NH*n*-Pr) and **81** (C2 = NH*n*-Pr) were also equipotent toward Aβ40 at IC_{50} ~ 6.5 μM. For Aβ42 inhibition, C2-groups ranked as NH*n*-Pr > NH*i*-Pr > NH*c*-Pr >> NMe_2. When compared to **70**-**72** (non-chlorinated counterparts), derivatives **80**–**82** were weaker toward Aβ40 but much more effective toward Aβ42. When compared to their dimethoxyphenethyl counterparts (**52**–**55**) with respect to Aβ40, derivative **80** was less potent (~ 2.2-fold), derivative **81** was more potent (~ 1.7-fold), while **82** and **83** were equipotent to **54** and **55**; respectively (IC_{50} ~ 4.9 μM). With respect to Aβ42, **80**–**82** were more potent compared to **52**–**54**, while **55** was more active compared to **83**.

Lastly, the impact of chlorine placement at position 8 in **84**–**87** elicited varying levels of improvement, toward Aβ40 inhibition compared to non-chlorinated counterparts (**70**–**72**), C6- (**76**–**79**) and C7-cholinated counterparts (**80**–**83**) and more so, their dimethoxyphenethyl counterparts (**56**–**59**). Most significant was the improvement of the C2 = NH*i*-Pr derivative (**85** – Aβ40, IC_{50} = 0.9 μM) considering the overall average Aβ40 IC_{50} of ~ 6 μM for other related counterparts. In addition, **85** was the most active Aβ42 aggregation inhibitor (IC_{50} = 3.9 μM), amongst the alkylamine-based derivatives (**70**–**72** and **76**–**87**). Overall, derivatives **84**–**87** were more effective toward Aβ42 compared to **70**–**72**, **76**–**79** and **81**–**83**.

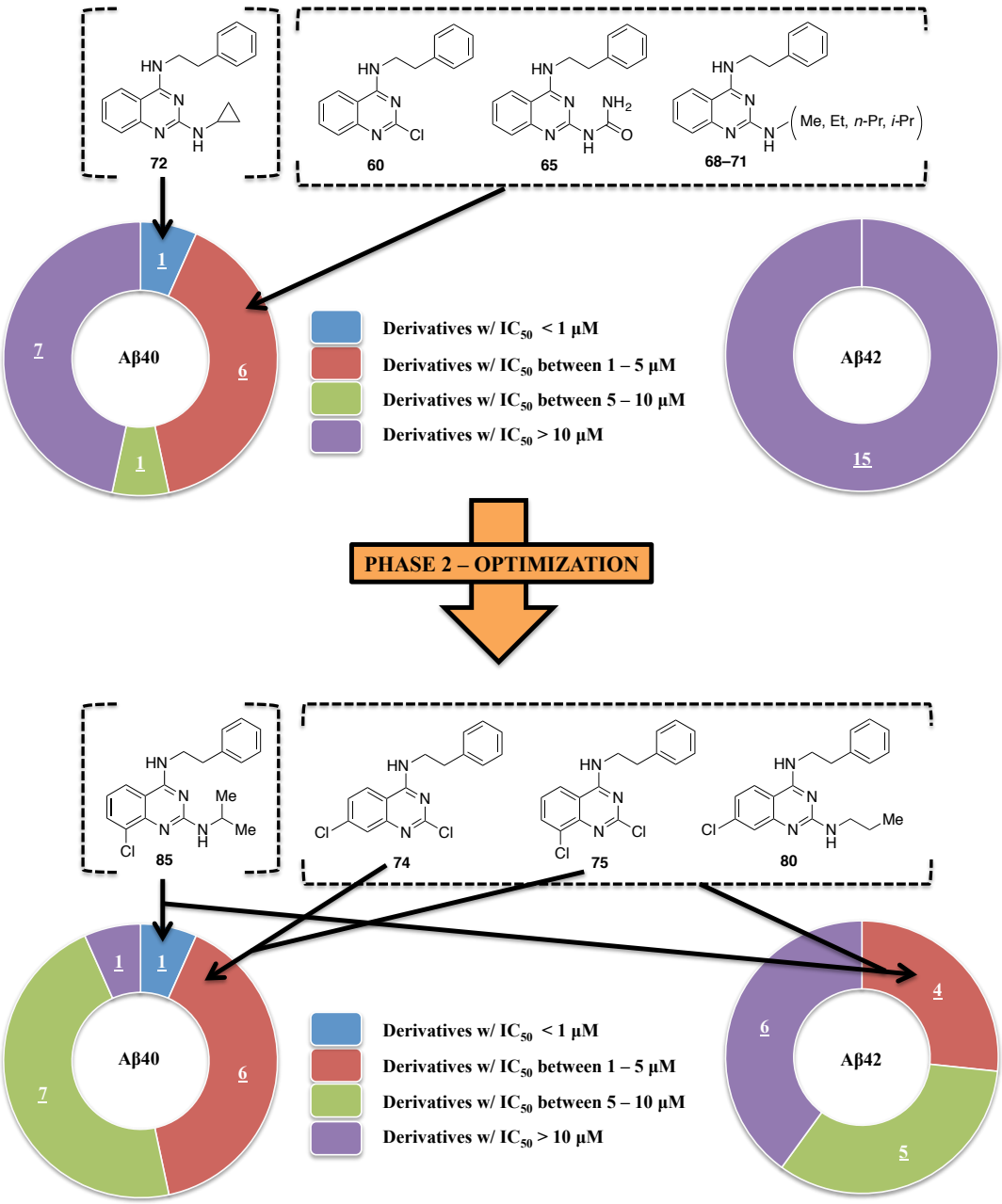


Figure 71: Amyloid-β metrics for fifteen 2-substituted-*N*-phenethylquinazolin-4-amines (**60**–**72**) and 15 2-substituted-*N*-phenethylchloroquinazolin-4-amines (**73**–**87**).

In summary, 30 derivatives were assessed for dual Aβ activity, of which derivatives **65** (1-(4-(phenethylamino)quinazolin-2-yl)urea), **72** (N^2-cyclopropyl-N^4-phenethylquinazoline-2,4-diamine) and **85** (8-chloro-N^2-isopropyl-N^4-phenethylquinazoline-2,4-diamine) were identified as comparably potent Aβ40

inhibitors (IC_{50} ~ 0.8–1.0 μM), while derivative **74** (2,7-dichloro-*N*-phenethylquinazolin-4-amine) was identified as the most potent, non-selective Aβ42 inhibitor (Aβ40/42 IC_{50} = 1.7 μM).

Generally, this series proved to be less effective at Aβ42 targeting as compared to the benzyl and dimethoxyphenethyl series (Chapter 4–5), while Aβ40 activity had mixed outcomes. The introduction of the chloroquinazoline scaffolds and the dimethylamine functionality at the C2-position, offered a mix of potency improvements and setbacks when compared to the non-chlorinated counterparts (Figure 71).

The aggregation kinetic assessment of Aβ40 with or without series-leading derivatives is showcased in Figure 72. As observed in Panels A–D, derivatives **65**, **72**, **85** and **86** exhibited concentration-dependent inhibition of Aβ40 aggregation; however they showcased various modes of aggregation. Starting with the urea-based derivative, **65** managed to induce similar levels of monomeric structure stabilization throughout the concentration range (roughly a 2 hour delay in the aggregation process). While the rate and total aggregate load differences between each concentration level was not very large, the starting out (with 1 μM) was effective enough to elicit a strong inhibitory profile. On the other hand, derivative **72** showcased all three modes of inhibitory activity, with increased potency, across all tested concentrations. Significant reductions in the start-time of the aggregation process, its rate and overall fibril load were observed with 25 μM almost halting aggregation processes completely. With the dichloro-based derivatives (**85** and **86**), no monomeric structure stabilization was observed (at the 1 and 5 μM concentrations), although both managed to completely halt the aggregation process at 25 μM. Nonetheless, at 1 and 5 μM concentrations, **85** and **86** managed to reduce the rate of aggregation and the overall aggregate load after the 24 hour incubation period. It was interesting to observe the how the 1.3-fold difference in potency between **72** and **86** manifested in the aggregation kinetics (Panel B vs. Panel D).

The aggregation kinetic assessment of Aβ42 with or series-leading derivatives is showcased in Figure 73. As observed in Panels A–B, derivatives **74** and **75** exhibited concentration-dependent and multi-mode inhibition of Aβ42 aggregation. At 1 and 5 μM concentrations, both derivatives managed to reduce the rate of fibrillation and overall aggregate load at the end of the 24 hour incubation period, with **74** almost abolishing aggregation processes all together at 1:1 ratios with Aβ42. At 25 μM concentrations, both derivatives managed to completely block the aggregation process at the 5:1 test ration (compound: Aβ42).

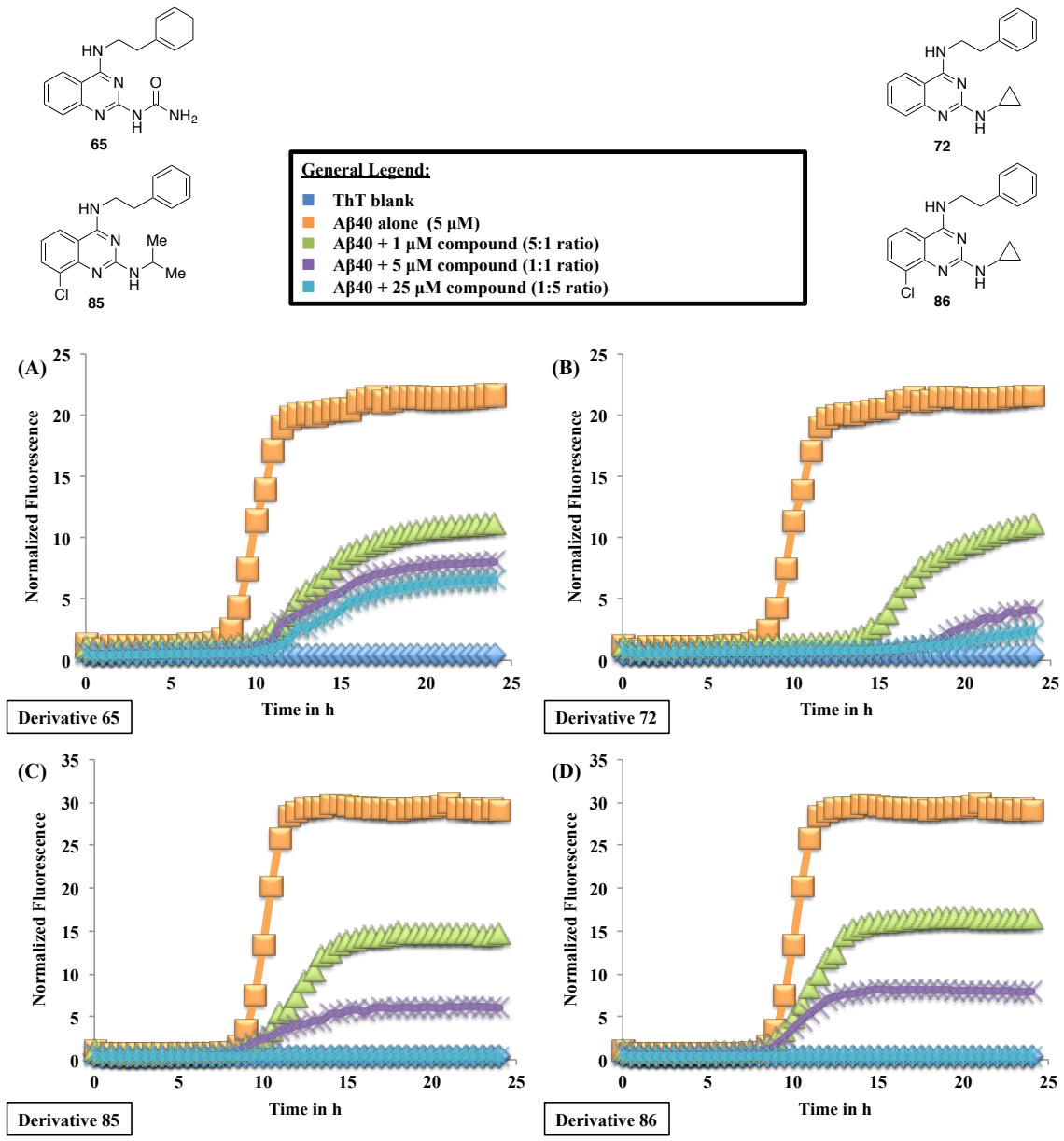


Figure 72: ThT-monitored kinetics of Aβ40 aggregation at 37 °C over a 24 h incubation period at pH 7.4 (Excitation = 440 nm, Emission = 490 nm). Panel (A): Impact of 1, 5 or 25 µM of 1-(4-(phenethylamino)quinazolin-2-yl)urea (**65**) on the aggregation kinetics of 5 µM Aβ40. Panel (B): Impact of 1, 5 or 25 µM of N^2-cyclopropyl-N^4-phenethylquinazoline-2,4-diamine (**72**) on the aggregation kinetics of 5 µM Aβ40. Panel (C): Impact of 1, 5 or 25 µM of 8-chloro-N^2-isopropyl-N^4-phenethylquinazoline-2,4-diamine (**85**) on the aggregation kinetics of 5 µM Aβ40. Panel (D): Impact of 1, 5 or 25 µM of 8-chloro-N^2-cyclopropyl-N^4-phenethylquinazoline-2,4-diamine (**86**) on the aggregation kinetics of 5 µM Aβ40.

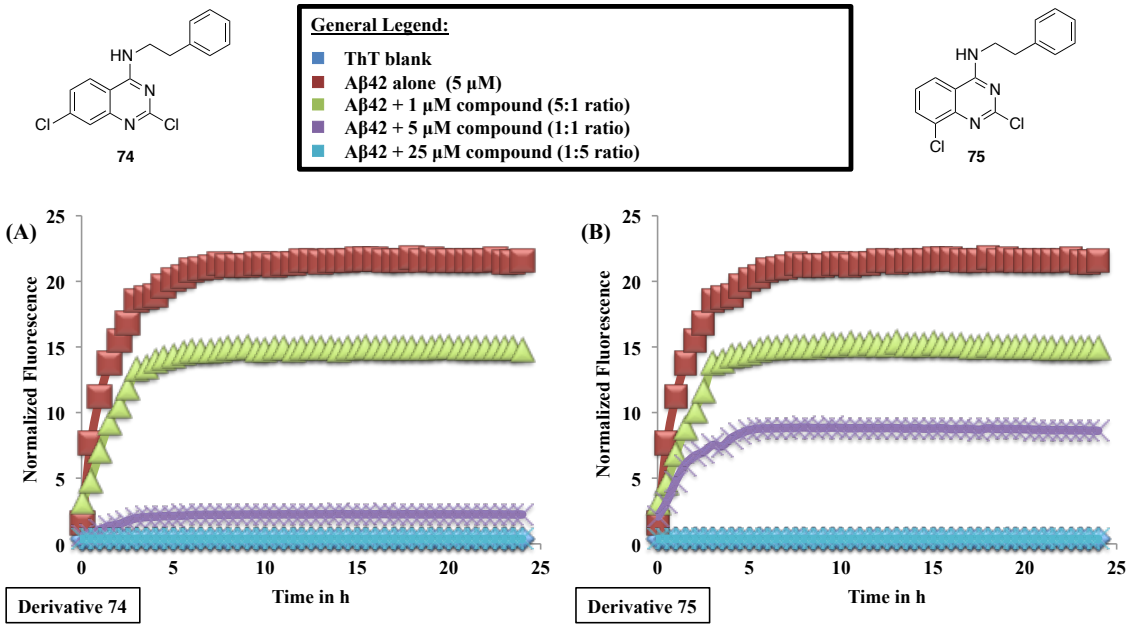


Figure 73: ThT-monitored kinetics of Aβ42 aggregation at 37 °C over a 24 h incubation period at pH 7.4 (Excitation = 440 nm, Emission = 490 nm). Panel (A): Impact of 1, 5 or 25 µM of 2,7-dichloro-*N*-phenethylquinazolin-4-amine (**74**) on the aggregation kinetics of 5 µM Aβ42. Panel (B): Impact of 1, 5 or 25 µM of 2,8-dichloro-*N*-phenethyl)quinazolin-4-amine (**75**) on the aggregation kinetics of 5 µM Aβ42.

6.3.4. *Transmission Electron Microscopy (TEM)*

The assessment of amyloid morphology at the conclusion of a 24-hour incubation period at 37 °C was conducted on series-leading derivatives. This commonly employed, qualitative technique is used to corroborate the quantitative results from the ThT-binding assay. Experimental setup included the incubations of control and test samples, at 1:1 ratios of 25 µM, in triplicate at 37 °C (with shaking) over a 24-hour timeline. Triplicate samples were combined after the incubation period and applied to the copper-mesh grids prior to imaging in the TEM.

As observed in Figure 74, resveratrol was effective at reducing total amyloid load (Panels B and E) compared to control samples (Panels A and D). That said, derivative **85** (Panel C) was more effective against Aβ40, while derivative **74** was significantly more potent toward Aβ42, compared to resveratrol.

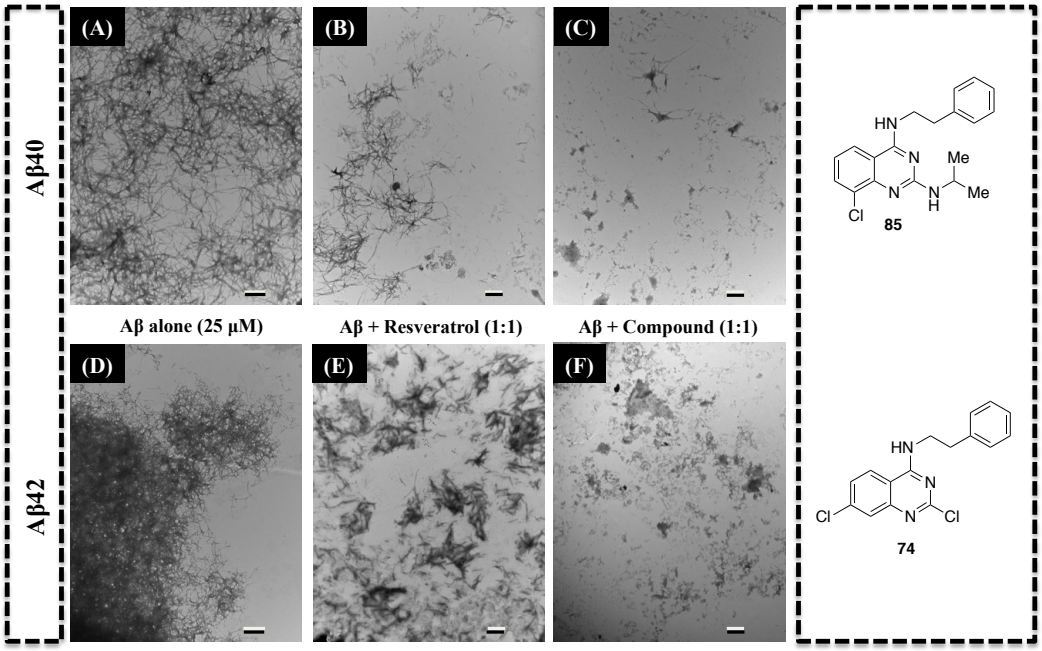


Figure 74: TEM assessment of Aβ40/42 morphology with or without test compounds at the end of a 24 h, 37 °C incubation period at pH 7.4. Panel (A–C): 25 μM Aβ40 alone or at a 1:1 ratio with resveratrol or 8-chloro-N^2-isopropyl-N^4-phenethylquinazoline-2,4-diamine (**85**); respectively. Panel (D–F): 25 μM Aβ42 alone or at a 1:1 ratio with resveratrol or 2,7-dichloro-*N*-phenethylquinazolin-4-amine **(74**); respectively. White/black bars represent 500 nm.

6.3.5. *Antioxidant Capacity*

The ability of 4-(phenethylamino)quinazolin-2-ol (**64**) to neutralize ROS was assessed using the previously described DPPH-scavenging assay.

As a conjugated, and less sterically hindered, phenolic compound, it was no surprise to observe the stronger (~1.5-fold) scavenging potential of **64** in the DPPH assay, compared to both its dimethoxyphenethyl counterpart (**36**, Figure 75). The increased flexibility of **64** also enabled it to slightly out-perform **23** by 1.1-fold. Derivative **64** was also 2-fold less potent than trolox but was 1.2-fold more effective compared to resveratrol.

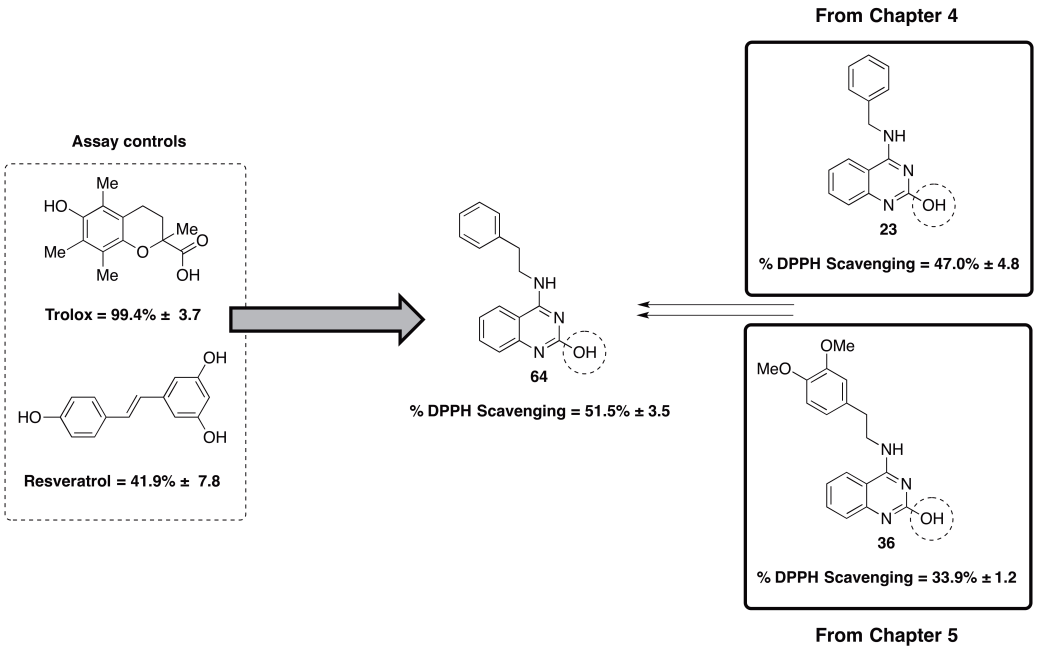


Figure 75: Standards utilized in the DPPH-scavenging along with the data for 4-(phenethylamino)quinazolin-2-ol (**64**).

6.3.6. *Molecular Modeling*

The utilization of computational software is not only useful in structure-based drug design, it is also employed to understand and corroborate the acquired SAR data. The assessment of ligand-receptor interactions was conducted between leading (or comparable) derivatives from the 2-substituted-*N*-phenethylquinazolin-4-amine series (**60**–**72**) or the 2-substituted-*N*-phenethylchloroquinazolin-4-amine series (**73**–**87**) and the cholinesterase or amyloid targets of interest.

6.3.6.1. *Cholinesterase*

Based on the acquired anti-ChE data, presented in Tables 9 and 10, the docking interactions of **63** with **63-iso** and **81** with **83** were investigated in *h*AChE (PBD: 1B41) and superimposed in Figure 76, along with the docking interactions of **63** with **63-iso** and **71**/**77**/**81**/**85** in *h*BuChE (PBD: 1P0I).

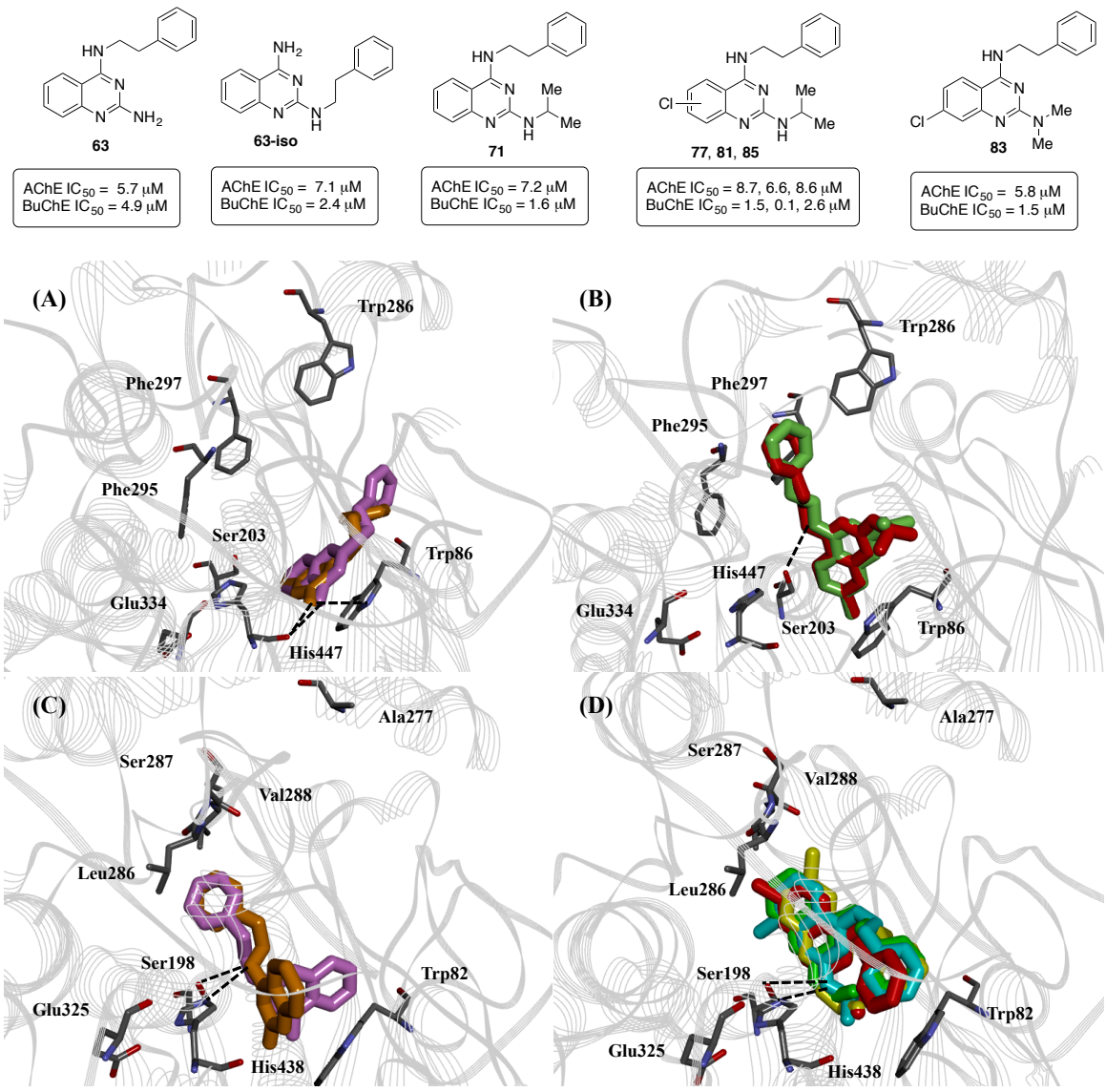


Figure 76: Superimposition of docking structures. Panel (A–B): Binding modes of **63** (orange) and **63-iso** (magenta) or **81** (red) and **83** (olive) in the active site of *h*AChE (PDB ID: 1B41); respectively. Panel (C): Binding modes of **63** (orange) and **63-iso** (magenta) in the active sites of *h*BuChE (PDB ID: 1P0I). Panel (D): Binding modes of **71** (green), **77** (gold), **81** (red) and **85** (blue) in the active sites of *h*BuChE (PDB ID: 1P0I). Hydrogens removed to enhance visibility. Black-dashed lines indicate hydrogen-bonding interactions.

As observed in Panel A, despite their isomeric structures, both quinazoline scaffolds of **63** and **63-iso** were stacked parallel over W86 at roughly 4–5 Å, orienting their C2- and C4-amino groups; respectively, to undergo hydrogen-bonding interactions with W86's indole ring (~ 3.5 Å) and H447's backbone carbonyl (~ 2.6 Å). Both ligands were localized within the active site, where the quinazoline scaffolds measured

roughly 14 Å from W286. Both ligands had their phenethylamine groups running parallel to W86 and measuring ~ 10 Å from W286.

In Panel B, very close superimpositions were observed with **81** and **83**, where the quinazoline scaffolds were roughly 11 Å from W286 and stacked perpendicular to across W86 (4–5 Å). Both ligands oriented their C7-chlorines and C2-isopropylamine or dimethylamine groups; respectively, over the indole and backbone structures of W86 (~ 4 Å). The C4-phenethylamine groups were directed, perpendicularly, toward the acyl pocket (~ 7 Å) and the phenyl rings were roughly 6 Å from the PAS. This alignment of the C4-groups allowed for hydrogen-bonding interactions (~ 3.3 Å) between the N*H* 's and the S203's hydroxyl group.

In BuChE (Panel C), the isomeric ligands (**63** and **63-iso**) exhibited unique but also similar binding modes, where the quinazoline scaffolds were primarily interacting with W82 – **63**'s quinazoline was stacked perpendicular between W82 and the catalytic triad's H437 (~ 5 Å), while **63-iso**'s quinazoline was more parallel over W82 (~ 5 Å). Both quinazolines measured roughly 18 Å from A277 and the ligands had their phenethylamines superimpose while directed toward the acyl pocket (~ 6 Å). This alignment of the phenethylamines allowed for hydrogen-bonding interactions (~ 2.3–3.5 Å) between the N*H* 's and the S198's hydroxyl group/H438's imidazole ring. With both ligands, the C2- and C4-amino groups; respectively, were directed toward the backbone of H438, but no hydrogen-bonding interactions were observed.

Lastly, in Panel D, we investigated the impact of chlorine presence and placement in **71** vs. **77**, **81** and **85**. While **81**, with C7-chlorine, was significantly more potent (~ 20-fold) compared to the other three, it was quite surprising to observe the near-perfect superimposition of all four ligands in BuChE. All took on a wide-C-shaped conformation, where the quinazoline scaffolds were stacked over the catalytic triad (~ 4 Å), placed between W82 and the acyl pocket (~ 6 Å), while the phenethylamine and isopropyl groups were oriented toward W82 in a perpendicular fashion (~ 4 Å). All ligand C2-N*H*s' underwent hydrogen-bonding with S198's hydroxyl group and H438's imidazole ring (~ 2.6 Å). The superior potency of **81** is therefore attributed to both the placement and likely binding kinetics attributed to the C7-chlorine.

6.3.6.2. *Amyloid-β*

Based on the acquired anti-Aβ data, presented in Table 12, the docking interactions of **85** and **86** were investigated in both a dimeric and fibril model of Aβ ($Aβ_{9-40}$ – PDB 2LMN) with superimpositions showcased in Figure 77.

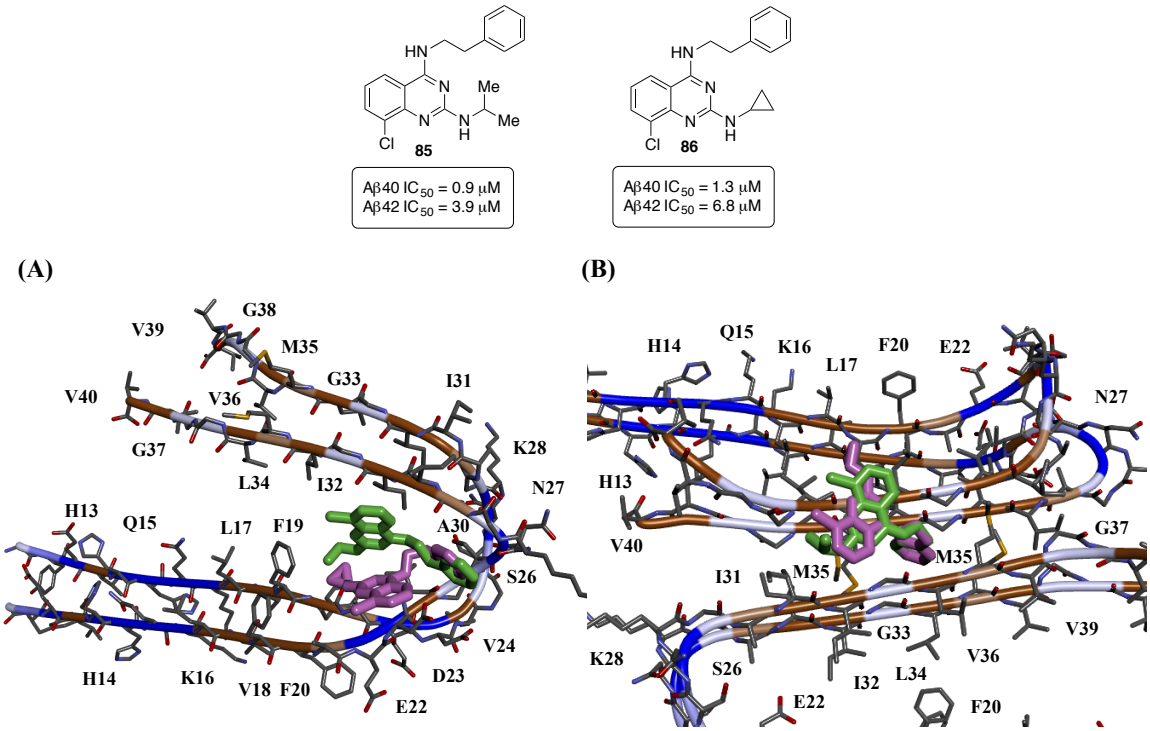


Figure 77: Superimposition of docking structures. Panels (A and B): Binding modes of **85** (olive) and **86** (magenta) in the Aβ ($Aβ_{9-40}$ – PDB 2LMN) dimer model or fibril model; respectively. Hydrogens removed to enhance visibility. Amino acid labels to be used as a general guide as space restrictions limited complete and accurate labeling of all peptide structures.

As showcased in Panel A, ligands **85** and **86** showcased different binding conformations within the dimer model, although both of their C4-phenyl rings superimpose while running parallel to K28 at roughly 6 Å. The quinazoline scaffold of **85** was perpendicularly stacked within the hairpin loop domain, measuring roughly 4 Å from I32. The ligand's C4-N*H* was undergoing hydrogen-bonding interactions with A30's backbone carbonyl (3.3 Å). On the other hand, **86**'s quinazoline scaffold was stacked parallel to D23-V24

at roughly 5 Å, allowing for hydrogen-bonding interactions between its C4-N*H* and D23's carboxyl group (~ 2.9 Å) and V24's backbone carbonyl and amine (~ 3.5 Å). Overall, both ligands oriented their C2-alkylamines toward F19/F20 and measured roughly 7 Å from the amino acid phenyl rings.

In the fibril model, both ligands oriented their C4-phenethylamine groups within the steric zipper domain, measuring roughly 5–6 Å from the quad M35 residues. Their quinazoline scaffolds were stacked perpendicular to M35 (with respect to the peptide backbone) at roughly 4–5 Å. This collective orientation allowed for both ligands' C4-N*H* to undergo hydrogen-bonding with G33's backbone carbonyl (2.7 Å). Ligand **85**'s isopropylamine was stacked parallel to I31-I32, allowing its C2-N*H* to undergo hydrogen-bonding with I31's backbone carbonyl (3.3 Å), while **86**'s cyclopropylamine group was positioned between L34-V36 at roughly 5–6 Å.

6.4. Summary

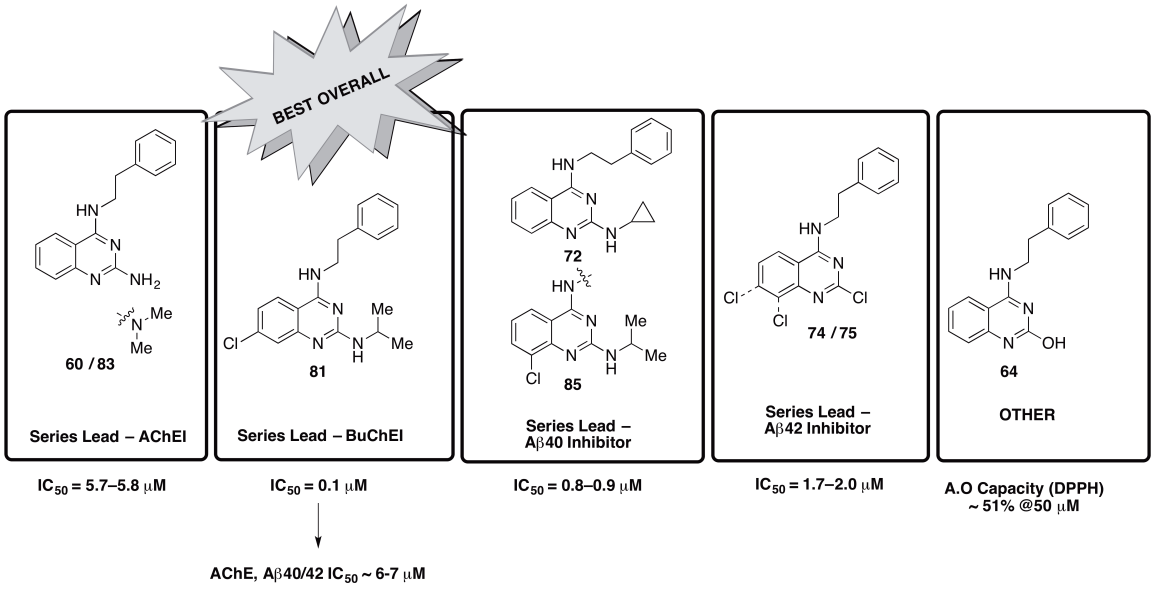


Figure 78: Cumulative chapter summary of 2-substituted-*N*-phenethylquinazolin-4-amines (**60**-**72**) and 2-substituted-*N*-phenethylchloroquinazolin-4-amines (**73**-**87**).

With this phenethylamine-based series, an overall improvement in BuChE targeting was observed, without significant losses in AChE potency. When compared to their benzyl and dimethoxyphenethyl

counterparts, the derivatives in this series were generally not as capable of targeting Aβ42, while the investigation into the cholorquinazoline scaffolds significantly improved dual Aβ targeting. The regioisomer investigations here yielded similar observations as to those observed in Chapters 4 and 5, where C4-unsubstituted derivative (**61-iso**) was not effective at either ChE or amyloid targeting, while C4-amino-based isomer (**63-iso**), enhanced BuChE binding and Aβ42 compared to **63** (which was more potent toward AChE and Aβ40). In addition, the antioxidant capacity of **64** exceeded that of both benzyl (**23**) and dimethoxyphenethyl (**36**) counterparts and resveratrol as well.

Nonetheless, the series also demonstrated a number of selective BuChEIs (**63-iso**, **66**, **68**–**71**, **76**, **77**, **79**–**85**), one selective Aβ42 aggregation inhibitor (**80**) and three non-selective Aβ inhibitors (**74**, **75** and **81**). It also had the most "inactive" derivatives toward Aβ42 aggregation, compared to previous series. Overall, a series leader was identified in 7-chloro-N^2-isopropyl-N^4-phenethylquinazoline-2,4-diamine (**81**) due to its potent activity toward BuChE (~ 95 nM, highest in entire drug library) and multi-targeting capacity toward AChE and Aβ40/42 at the equipotent concentration of ~ 7 μM (Figure 78).

6.5. Experimental

Please note that this subsection includes re-listed methodologies from Chapter 3–5. For schematic representation of re-listed methodologies, if applicable, please refer to Chapter 3 and 4 – Section 3.5 or 4.5.

6.5.1. *Chemistry*

General Information. All the reagents and solvents were reagent grade purchased from various vendors (Acros Organics, Sigma-Aldrich, and Alfa Aesar, USA) with a minimum purity of 95% and were used without further purification. Melting points (mp) were determined using a Fisher-Johns apparatus and are uncorrected. Reaction progress was monitored by UV using thin-layer chromatography (TLC) using Merck 60F254 silica gel plates. Column chromatography was performed with Merck silica gel 60 (230−400 mesh) with 5:1 EtOAc:MeOH as the solvent system unless otherwise specified. Proton (^{1}H NMR) and carbon (^{13}C NMR) spectra were performed on a Bruker Avance (at 300 and 75 MHz; respectively) spectrometer using

DMSO-d_6. Coupling constants (J values) were recorded in hertz (Hz) and the following abbreviations were used to represent multiplets of NMR signals: s = singlet, d = doublet, t = triplet, m = multiplet, br = broad. Carbon multiplicities (C, CH, CH_2 and CH_3) were assigned by DEPT 90/135 experiments. High-resolution mass spectrometry (HRMS) was determined using a Thermo Scientific Q-Exactive Orbitrap mass spectrometer (positive mode, ESI), Department of Chemistry, University of Waterloo. Compound purity (roughly 95% or over) was determined using an Agilent 1100 series HPLC equipped with an analytical column (Agilent Zorbax Eclipse XDB-C8 column, 4.6 x 150 mm, 5 μm particle size) running 50:50 Water:ACN with 0.1% TFA at a flow rate of 1.0-1.5 mL/min or an Agilent 6100 series single quad LCMS equipped with an Agilent 1.8 μm Zorbax Eclipse Plus C18 (2.1 x 50 mm) running 50:50 Water:ACN with 0.1% FA with a flow rate of 0.5mL/min. All the final compounds exhibited ≥ 95% purity.

General procedure for the synthesis of 2,4,6-, 2,4,7- or 2,4,8-trichloroquinazolines.[289, 323] In a 250 mL RBF, 5 g of 6-, 7- or 8-chloroquinazolin,2-4-diol (25.51 mmol) was suspended in 25 mL of anhydrous toluene and allowed to stir on an ice bath. To this, 5 eq. of $POCl_3$ (127.55 mmol) was added in small aliquots followed by the slow addition of 5 eq. of DEA (127.55 mmol). The solution was kept on the ice bath for 10 min before moving to room temperature and allowed to stir for 1 h prior to refluxing at 105–110 °C for 14–16 h. Upon cooling to room temperature, the reaction mixture was added in small aliquots to a double-ice-water bath while stirring. The quenching solution was left stirring at room temperature for 5 h before vacuum filtering the yellowish-grey precipitate. The precipitate was stirred for 1 h in a saturated $NaHCO_3$ solution and then was re-filtered. This neutralization process was carried out 2–3 times until the bicarbonate solution maintains a neutral to slight basic pH. The final precipitate was dissolved in DCM and purified by a silica gel column chromatography using 100% DCM as the eluent to afford white to light grey solid.

2,4,6-Trichloroquinazoline. Yield: 75% (4.43 g, 19.12 mmol); Mp 126–128 °C. ^{1}H NMR (300 MHz, DMSO-d_6) δ 8.31 (s, 1H), δ 8.15 (d, J = 9.0 Hz, 1H), δ 8.04 (d, J = 8.9 Hz, 1H). LRMS (ESI) m/z calcd for $C_8H_4Cl_3N_2$ $[M + H]^+$ 232.93, found 232.92.

2,4,7-Trichloroquinazoline. Yield: 80% (4.73 g, 20.41 mmol); Mp 137–139 °C. ^{1}H NMR (300 MHz, DMSO-d_6) δ 8.30 (d, J = 9.0 Hz, 1H), δ 8.20 (s, 1H), δ 7.88 (d, J = 8.7 Hz, 1H). LRMS (ESI) m/z calcd for $C_8H_4Cl_3N_2$ $[M + H]^+$ 232.93, found 232.92.

2,4,8-Trichloroquinazoline. Yield: 65% (3.84 g, 16.56 mmol); Mp 135–137 °C. ^{1}H NMR (300 MHz, DMSO-d_6) δ 8.31 (d, J = 7.7 Hz, 1H), δ 8.25 (d, J = 8.5 Hz, 1H), δ 7.78 (t, J = 7.4 Hz, 1H). LRMS (ESI) m/z calcd for $C_8H_4Cl_3N_2$ $[M + H]^+$ 232.93, found 232.92.

General procedure for the synthesis of 2-chloro-, 2,6-dichloro-, 2,7-dichloro- or 2,8-dichloro-*N*-substituted-quinazolin-4-amines.[303, 305] To a 30 mL solution of ethanol in a 100 mL round-bottom flask on ice, 5 g of **4** or a trichloroquinazoline (21.46–25.13 mmol) was added followed by slow addition of 1.3 eq. (27.90–32.66 mmol) of the corresponding primary amine. Contents were stirred on an ice bath while 2.0 eq. of diisopropyl-ethylamine (DIPEA, 42.92–50.25 mmol) was added in drop wise fashion. The solution was then heated at 80-85 °C under reflux for 3–4 h. The reaction contents were cooled to room temperature and precipitated residues were vacuum-filtered with ethyl acetate (EtOAc) rinses. The organic supernatant was concentrated in vacuo followed by two rounds of liquid-liquid extraction using EtOAc and saturated brine solution (40–50 mL each respectively). The combined organic layers were dried over $MgSO_4$, evaporated in vacuo and purified (1–2 times) using silica gel column chromatography with 5:1 EtOAc:MeOH as the elution solvent. Final compounds were white to beige solids with yields ranging from 70–90%.

2-Chloro-*N*-(phenethyl)-quinazolin-4-amine (**60**). Yield: 70% (4.98 g, 17.79 mmol); Mp: 145–147 °C. ^{1}H NMR (300 MHz, DMSO-d6) δ 8.81 (br s, 1H), δ 8.18 (d, J = 8.0 Hz, 1H), δ 7.73 (t, J = 7.6 Hz, 1H), δ 7.57 (d, J = 8.0 Hz, 1H), δ 7.47 (t, J = 7.6 Hz, 1H), δ 7.27–7.16 (m, 5H), δ 3.66 (q, J = 6.2 Hz, 2H), δ 2.91 (t, J = 7.2 Hz, 2H). HRMS (ESI) m/z calcd for $C_{16}H_{14}ClN_3$ $[M + H]^+$ 284.0876, found 284.1332. Purity: 96.9%

2,6-Dichloro-*N*-phenethylquinazolin-4-amine (71). Yield: 75% (1.03 g, 3.25 mmol); Mp 133–135 °C. ^{1}H NMR (300 MHz, DMSO-d_6) δ 8.88 (br s, 1H), δ 8.38 (d, J = 2.2 Hz, 1H), δ 7.77 (dd, J = 8.9, 2.2 Hz, 1H), δ 7.59 (d, J = 8.9 Hz, 1H), δ 7.30–7.16 (m, 5H), δ 3.65 (q, J = 6.1 Hz, 2H), δ 2.90 (t, J = 7.2 Hz, 2H). LRMS (ESI) m/z calcd for $C_{16}H_{14}Cl_2N_3$ $[M + H]^+$ 318.04, found 318.00.

2,7-Dichloro-*N*-phenethylquinazolin-4-amine (72). Yield: 75% (1.03 g, 3.25 mmol); Mp 137–139 °C. ^{1}H NMR (300 MHz, DMSO-d_6) δ 8.94 (br s, 1H), δ 8.22 (d, J = 8.8 Hz, 1H), δ 7.65 (s, 1H), δ 7.58 (d, J = 8.7 Hz, 1H), δ 7.28–7.17 (m, 5H), δ 3.65 (q, J = 6.1 Hz, 2H), δ 2.90 (t, J = 7.2 Hz, 2H). LRMS (ESI) m/z calcd for $C_{16}H_{14}Cl_2N_3$ $[M + H]^+$ 318.04, found 318.06.

2,8-Dichloro-*N*-phenethylquinazolin-4-amine (73). Yield: 90% (1.24 g, 3.90 mmol); Mp 136–138 °C. ^{1}H NMR (300 MHz, DMSO-d_6) δ 9.01 (br s, 1H), δ 8.16 (d, J = 8.8 Hz, 1H), δ 7.91 (d, J = 8.7 Hz, 1H), δ 7.45 (t, J = 8.0 Hz, 1H), δ 7.29–7.15 (m, 5H), δ 3.68 (q, J = 6.1 Hz, 2H), δ 2.92 (t, J = 7.2 Hz, 2H). LRMS (ESI) m/z calcd for $C_{16}H_{14}Cl_2N_3$ $[M + H]^+$ 318.04, found 318.03.

General procedure for the synthesis of N^4-substituted-quinazolin-4-amines. In a 50 mL round bottom flask (RBF), 0.5 g of 2-chloro-*N*-substituted-quinazolin-4-amine (1.45–1.85 mmol) was dissolved in 20 mL of anhydrous ethanol. While stirring on ice, 10 mol. % of 10% Pd/C was added to reaction mixture followed by the drop-wise addition of 1.3 eq. of hydrazine hydrate. Solution was stirred on ice for 5 min before refluxing for 2 h at 80–85 °C. Upon completion and cooling to room temperature, the reaction mixture was passed through a tightly-packed cotton-filled syringe that has been pre-rinsed with ethanol, to remove the Pd/C catalyst. A 30 mL aliquot of ethanol was used to rinse the syringe. The combined ethanol solutions were evaporated in vacuo, diluted in EtOAc (20 mL) and washed 25 mL x 2 with equal volumes of brine solution. The combined aqueous layers were washed with 15 mL of EtOAc. The combined EtOAc layers were dried over $MgSO_4$, before removing the EtOAc in vacuo to yield a solid or semi-solid crude

product that was purified by silica gel column chromatography using 5:1 EtOAc:MeOH solvent system. Final compounds were white to pale yellow solids with yields ranging from 40–47%.

***N*-Phenethylquinazolin-4-amine (61).** Yield: 42% (0.19 g, 0.76 mmol); Mp 137–139 °C. ^{1}H NMR (300 MHz, DMSO-d_6): δ 8.44 (s, 1H), δ 8.33 (t, J = 9.0 Hz, 1H), δ 8.16 (d, J = 6.0 Hz, 1H), δ 7.71–7.62 (m, 2H), δ 7.43 (t, J = 9.0 Hz, 1H), δ 7.26–7.16 (m, 5H), δ 3.69 (d, J = 6.0 Hz, 2H), δ 2.91 (t, J = 9.0 Hz, 2H). ^{13}C NMR (100 MHz, DMSO-d_6): δ 159.25, δ 155.12, δ 149.05, δ 139.52, δ 132.42, δ 128.65, δ 128.33, δ 127.47, δ 126.07, δ 125.51, δ 122.54, δ 114.94, δ 42.06, δ 34.46. HRMS (ESI) m/z calcd for $C_{16}H_{16}N_3$ [M + H]$^+$ 250.1266, found 250.1338. Purity: 96.6%

General procedure for the synthesis of N^2-substituted-quinazolin-2-amines. In a 50 mL pressure vial (PV), 0.25 g of 2-chloroquinazoline (1.52 mmol) was dissolved in 5 mL of 1,4-dioxane followed by the addition of 3 eq. (4.56 mmol) of the appropriate primary amine and 5 eq. of DIPEA (7.60 mmol). Pressure vial was sealed and stirred in an oil bath at 155–160 °C for 5 h. Upon completion and cooling to room temperature, the reaction mixture was diluted with ~ 40 mL of EtOAc and washed 25 mL x 3 times with equal volumes of brine solution. The combined aqueous layers were washed with ~ 25 mL of EtOAc. The combined EtOAc layers were dried over $MgSO_4$ before removing the EtOAc in vacuo to yield a solid crude product that was purified by silica gel column chromatography using 5:1 EtOAc:MeOH as the solvent system. Final compounds were pale yellow to pale brown solids with yields ranging from 47–52%.

***N*-Phenethylquinazolin-2-amine (61-iso):** Yield: 47% (0.19 g, 0.76 mmol); Mp 133–135 °C. ^{1}H NMR (300 MHz, DMSO-d_6) δ 9.06 (s, 1H), δ 7.74 (dd, J = 0.9, 8.0 Hz, 1H), δ 7.70–7.62 (m, 1H), δ 7.47–7.32 (m, 2H), δ 7.27–7.16 (m, 6H), δ 3.54 (q, J = 8.2 Hz, 2H), δ 2.88 (t, J = 7.6 Hz, 2H). HRMS (ESI) m/z calcd for $C_{16}H_{16}N_3$ [M + H]$^+$ 250.1266, found 250.1338. Purity: 98.0%

General procedure for the synthesis of 2-azido-*N*-substituted-quinazolin-4-amine.[305] In a 50 mL RBF, 2-chloro-*N*-substituted-quinazolin-4-amine (~1.86 mmol), 1.1 eq. NaN_3 (2.05 mmol), 4:1 EtOH (20 mL) and glacial acetic acid (5 mL) were combined and refluxed at 90–95 °C for 2 h with stirring. After cooling, the solution was vacuum-filtered to afford white solids at yields ranging from 80–85%.

2-Azido-*N*-phenethylquinazolin-4-amine (62). Yield: 83% (0.42 g, 1.46 mmol); Mp 233–235 °C. ^{1}H NMR (300 MHz, DMSO-d_6): δ 8.96 (br s, 1H), δ 8.40 (d, J = 8.2 Hz, 1H), δ 8.30 (d, J = 8.3 Hz, 1H), δ 7.97 (t, J = 8.0 Hz, 1H), δ 7.71 (t, J = 8.0 Hz, 1H), δ 7.27–7.16 (m, 5H), δ 3.76 (q, J = 6.6 Hz, 2H), δ 2.97 (t, J = 7.3 Hz, 2H). HRMS (ESI) m/z calcd for $C_{16}H_{15}N_6$ $[M + H]^+$ 291.1280, found 291.1351. Purity: 97.8%

General procedure for the synthesis of N^4-substituted-quinazolin-2,4-diamine.[305]

Method 1A: In a 100 mL round-bottom pressure vial, 2-chloro-*N*-substituted-quinazolin-4-amine (3.72 mmol) was added along with 20 mol. % of CuI. To that, a mixture of 1,4-dioxane (5 mL) and 30% aqueous ammonia (15 mL) was added at room temperature. The pressure vial was sealed tightly and partially submerged in silicone oil heating at 130–135 °C. Contents were stirred in the pressure vial for 24 h (Note: in the event of pressure leakage, the contents were cooled to room temperature and additional aqueous ammonia, (10 mL) was added, sealed and heating was carried on through the 24 h period). The reaction contents were cooled to room temperature and the solution was diluted with 25 mL EtOAc, washed with saturated brine solution (10 mL x 3), and the aqueous layer was neutralized with dilute HCl, and then re-extracted with 15 mL EtOAc. The organic layers were combined, dried over $MgSO_4$, evaporated in vacuo and purified using silica gel column chromatography with 5:1 EtOAc:MeOH as an initial elution solvent followed by transition to 5:1 EtOAc:MeOH w/ 1% TEA (triethylamine). Final compounds were obtained as white to beige solids with final yields ranging from 20–25%.

Method 1B: In a 100 mL round-bottom pressure vial, 2-chloro-*N*-substituted-quinazolin-4-amine (3.72 mmol) was dissolved and gently heated in 5 mL ethylene glycol. To that, 20 mol. % of Cu_2O and DMEDA

were added followed by 20 eq. K_2CO_3 and finally, 40 eq. of 30% aqueous ammonia solution (~15–20 mL). The pressure vial was sealed tightly, partially submerged in silicone oil and heated at 100–105 °C. Contents were stirred in the pressure vial for 24 h. After the reaction contents were cooled to room temperature, the solution was diluted with 50 mL EtOAc, washed with saturated brine solution (25 mL x 3) and the aqueous layer was neutralized with dilute HCl, and then re-extracted with 25 mL EtOAc. The residue formed was dissolved in methanol (20–25 mL). The EtOAc layers were dried over $MgSO_4$ and evaporated in vacuo. The methanol fraction was dried with molecular sieves before evaporating the methanol in vacuo. Both EtOAc and methanol fractions were combined and purified using silica gel column chromatography with 5:1 EtOAc:MeOH as an initial elution solvent followed by transition to 5:1 EtOAc:MeOH with 1% TEA (triethylamine). Final compounds were obtained as white to beige solids with yields ranging from 35–40%.

Method 2: In a 50 mL round-bottom pressure vial, 2-chloro-*N*-substituted-quinazolin-4-amine (3.72 mmol) was combined with 6 eq. urea (22.32 mmol) and diluted with 10 mL of anhydrous 1,4-dioxane. The pressure vial was sealed tightly and partially submerged in silicone oil heating at 160–165 °C. Contents were stirred in the pressure vial for 24 h. Once the reaction contents were cooled to room temperature, the solution was diluted with 20–25 mL EtOAc. The contents were washed three times with 20 mL saturated brine solution and the aqueous layers were re-extracted twice with 20 mL EtOAc. The organic layers were combined, dried over $MgSO_4$, evaporated in vacuo and purified using silica gel column chromatography with 5:1 EtOAc:MeOH as an initial elution solvent followed by transition to 5:1 EtOAc:MeOH w/ 1% TEA (triethylamine). Final compounds were obtained as white to light beige solids with yields ranging from 50–55%.

Method 3: In a 50 mL round-bottom flask, 2-chloro-*N*-substituted-quinazolin-4-amine (3.72 mmol) was combined with 1.1 eq. NaN_3 (4.09 mmol), before diluting with 4:1 EtOH (20 mL) and glacial acetic acid (5 mL). Flask contents were stirred under reflux at 90–95 °C for 2 h. After cooling the reaction mixture, 10 mol. % of Pd/C (10%) was added followed by slow addition of 1.5 eq. of hydrazine hydrate (5.58 mmol). Flask contents were stirred under reflux at 90–95 °C for an additional two hrs. Once complete, the warm solution was passed through a large, tightly packed cotton syringe with the aid of additional EtOH washes (2 x 20 mL). The ethanolic mixture was evaporated in vacuo. Final compounds were obtained as white to

beige solids with yields ranging from 80–85%.

Method 4: In a 50 mL round-bottom flask, 2,4-diaminoquinazoline* (1 g, 6.24 mmol) was dissolved in 3 mL DMSO. With stirring and periodic cooling over ice-water, NaH (60%, 0.25 g, 6.24 mmol) was added over a 10–15 min. period. After complete addition of NaH, flask was stirred at room temperature with slow, dropwise addition of the appropriate alkyl/aryl halide (6.24 mmol) dissolved in 3 mL DMSO. Contents are allowed to stir at room temperature overnight (~14 h) before diluting with 20 mL of water and stirring at room temperature for 15 min. The mixture is extracted thrice with diethyl ether (40 mL x 3). The combined organic layers are washed twice with brine (20 mL x 2). Combined organic layer was dried with $MgSO_4$ and concentrated in vacuo before purifying with silica gel column chromatography using 5:1 EtOAc/MeOH to afford beige to off-white solids at 20-31% yield.

***General procedure for synthesis of 2,4-diaminoquinazoline.[291, 317]** In a 250 mL round-bottom pressure flask, 2-fluorobenzonitrile (4.6 mL, 42.32 mmol) or 2-aminobenzonitrile (5 g, 42.32 mmol) was combined with guanidine carbonate (11.43 g, 126.96 mmol) and diluted in 30 mL dimethylacetaminde (DMA). Contents are heated in an oil bath at 150 °C for overnight (~ 14 h) then diluted with 50mL of water before extracting thrice with EtOAc (50 mL x 3) and washing with brine (2 x 20 mL). Combined organic layer was dried with $MgSO_4$ and concentrated in vacuo before purifying with silica gel column chromatography using 5:1 EtOAc/MeOH to afford an off-white solid at 80% yield. ^{1}H NMR (300 MHz, DMSO- *d_6*) δ 7.91 (d, 7.8 Hz, 1H), δ 7.41 (t, J = 7.8 Hz, 1H), δ 7.21 (br s, 2H), δ 7.15 (d, J = 8.1 Hz, 1H), δ 6.95 (t, J = 7.2 Hz, 1H), δ 5.91 (br s, 2H). ^{13}C NMR (100 MHz, DMSO- *d_6*) δ 162.45, δ 160.75, δ 152.52, δ 132.30, δ 124.22, δ 123.52, δ 119.73, δ 110.34.

***N*^{4}-Phenethylquinazolin-2,4-diamine (63).** Yield: 80% (0.75 g, 2.84 mmol); Mp: 168-170 °C. ^{1}H NMR (300 MHz, DMSO-*d6*), δ 8.30 (br s, 1H), 7.97 (d, *J* = 8.0 Hz, 1H), δ 7.48 (t, *J* = 9.0 Hz, 1H), δ 7.28–7.07 (m, 6H), δ 7.05 (t, *J* = 6.0 Hz, 1H), δ 6.48 (br s, 2H), δ 3.63 (q, *J* = 6.5 Hz, 2H), δ 2.90 (t, *J* = 7.4 Hz, 2H). HRMS (ESI) m/z calcd for $C_{16}H_{16}N_4$ $[M + H]^+$ 265.1453, found: 265.1446.

General procedure for synthesis of N^2-substituted-quinazoline-2,4-diamines.[317] In a 50 mL round-bottom flask, 2,4-diaminoquinazoline (1 g, 6.24 mmol) was dissolved in 20 mL DMA followed by the addition of potassium carbonate (0.85 g, 6.24 mmol) and the appropriate alkyl/aryl halide (6.24 mmol) at room temperature. Contents are refluxed at 85 °C for 5 h before diluting with 30 mL of water and stirring at R.T for 15 min. The mixture is extracted thrice with EtOAc (50 mL x 3). The combined organic layers are washed twice with brine (20 mL x 2). Combined organic layer was dried with $MgSO_4$ and concentrated in vacuo before purifying with silica gel column chromatography using 5:1 EtOAc/MeOH to afford beige to off-white solids at 14–26% yield.

N^2-Phenethylquinazoline-2,4-diamine (22-iso). Yield 19% (0.31 g, 1.17 mmol); Mp: 151–153 °C; ^{1}H NMR (300 MHz, DMSO-d_6): δ 8.11 (d, J = 8.2 Hz, 1H), δ 7.67 (s, 1H), δ 7.40 (d, J = 8.0 Hz, 1H), δ 7.32 – 7.11 (m, 9H), δ 3.59 (d, J = 7.0 Hz, 2H), δ 2.88 (d, J = 7.4 Hz, 2H). HRMS (ESI) m/z calcd for $C_{16}H_{16}N_4$ $[M + H]^+$ 265.1448, observed 265.1447.

General procedure for the synthesis of N^4-substituted-quinazolin-2-ols. In a 50 mL round bottom flask (RBF), 0.5 g of 2-chloro-*N*-substituted-quinazolin-4-amine (1.45–1.85 mmol) was combined with 1.3 eq. of potassium formate (1.89–2.41 mmol) then dissolved in 20 mL of formic acid. Solution was refluxed for 14–16 h at 120–125 °C. Upon completion and cooling to room temperature, the reaction mixture was diluted with ~ 30 mL of brine solution, ~ 50 mL of saturated $NaHCO_3$ solution before extracting with ~ 25 mL (x 3) of EtOAc and washed with 25 mL (x 3) parts of brine solution. The combined aqueous layers were washed twice with 15 mL of EtOAc. The combined EtOAc layers were dried over $MgSO_4$ before removing the EtOAc in vacuo to yield a solid product that generally did not require additional purification. Additional purification as required, was accomplished by silica gel column chromatography using 5:1 EtOAc:MeOH as the eluent. The compounds were obtained as white solids with yields ranging from 58–70%.

4-(Phenethylamino)quinazolin-2-ol (64). Yield: 58% (0.27 g, 1.02 mmol); Mp 189–191 °C. ^{1}H NMR (300 MHz, DMSO-d_6): δ 10.60 (br s, 1H), δ 8.57 (br s, 1H), δ 8.06 (d, J = 8.1 Hz, 1H), δ 7.47 (t, J = 7.5

Hz, 1H), δ 7.29–7.02 (m, 7H), δ 3.60 (q, *J* = 7.6 Hz, 2H), δ 2.89 (t, *J* = 7.4 Hz, 2H). HRMS (ESI) m/z calcd for $C_{16}H_{16}N_3O$ $[M + H]^+$ 266.1215, found 266.1287. Purity: 96.9%

General procedure for the synthesis of *N*^{4}-substituted-quinazolin-2-urea.[305] In a pressure vial, 0.5 g of 2-chloro-*N*-substituted-quinazolin-4-amine (~1.85 mmol) was mixed with 6 eq. urea (~11.2 mmol) and 10 mL of anhydrous 1,4-dioxane, sealed tightly and heated at 160–165 °C in an oil bath for 24 h. After cooling to room temperature, the solution was diluted with 20 mL EtOAc, washed three times with 20 mL brine solution; the aqueous layers were extracted twice with 20 mL EtOAc. The combined organic layers were dried over $MgSO_4$, evaporated in vacuo and purified using silica gel column chromatography using a combination of 5:1 EtOAc:MeOH and 5:1 EtOAc:MeOH w/ 1% TEA (triethylamine) to afford target compounds as white solids with yields ranging from 45–50% and the hydrolyzed amine compounds as off white solids with yields ranging from 50–55%.

1-(4-(Phenethylamino)quinazolin-2-yl)urea (65). Yield: 51% (0.27 g, 0.90 mmol); Mp 197–199 °C. ^{1}H NMR (300 MHz, DMSO-*d*$_6$): δ 9.08 (br s, 1H), δ 8.83 (br s, 1H), δ 8.45 (br s, 1H), δ 8.05 (d, *J* = 8.2 Hz, 1H), δ 7.58 (t, *J* = 7.6 Hz, 1H), δ 7.44 (d, *J* = 8.2 Hz, 1H), δ 7.32–7.17 (m, 6H), δ 6.87 (br s, 1H), δ 3.67–3.62 (m, 2H), δ 2.90 (t, *J* = 7.5 Hz, 2H). HRMS (ESI) m/z calcd for $C_{17}H_{18}N_5O$ $[M + H]^+$ 308.1433, found 308.1505. Purity: 95.9%

General procedure for the synthesis of *N*^{4}-substituted-quinazolin-2-glycinamide.[299] In a 50 mL pressure vial, 0.25 g of 2-chloro-*N*-substituted-quinazolin-4-amine (~ 0.83 mmol) was combined with 3 eq. (~ 2.50 mmol) of glycinamide.HCl then dissolved in 5 mL of 1,4-dioxane followed by the addition of 5 eq. of DBU (~ 4.15 mmol). Pressure vial was sealed and stirred in an oil bath at 150–155 °C for 4 h. Upon completion and cooling to room temperature, the reaction mixture was diluted with ~ 40 mL of EtOAc and washed 25 mL (x 3) brine solution. The combined aqueous layers were washed with ~ 25 mL of EtOAc. The combined EtOAc layers were dried over $MgSO_4$ and EtOAc was removed in vacuo to yield solid that

was purified by silica gel column chromatography using 5:1 EtOAc:MeOH as the eluent to afford target compounds as pale yellow to brown solids with yields ranging between 52–58%.

2-((4-(Phenethylamino)quinazolin-2-yl)amino)acetamide (66). Yield: 55% (0.16 g, 0.48 mmol); Mp 149–151 °C. ^{1}H NMR (300 MHz, DMSO-d_6): δ 8.06 (br s, 1H), δ 7.92 (d, J = 8.2 Hz, 1H), δ 7.45 (t, J = 7.5 Hz, 1H), δ 7.28–7.16 (m, 7H), δ 7.01 (t, J = 7.5 Hz, 1H), δ 6.97 (br s, 1H), δ 6.37 (br s, 1H), δ 3.86 (d, J = 7.1 Hz, 2H), δ 3.61 (q, J = 5.9 Hz, 2H), δ 2.89 (t, J = 7.1 Hz, 2H). HRMS (ESI) m/z calcd for $C_{18}H_{20}N_5O$ $[M + H]^+$ 322.1590, found 322.1662. Purity: 99.2%

General procedure for the synthesis of N^4-substituted-quinazolin-2-acetamide.[312] In a 50 mL round bottom flask (RBF), 0.5 g of N^4-substituted-quinazolin-2,4-diamine (1.54-2.00 mmol) was dissolved in 15 mL of 1,4-dioxane and 10 mL of glacial acetic acid/acetyl chloride combination (4:1 ratio). Solution was refluxed for 24 h at 90–95 °C. Upon completion and cooling to room temperature, the reaction mixture was diluted with ~ 30 mL of brine solution, ~ 30 mL of concentrated $NaHCO_3$ solution before extracting with ~ 25 mL (x 3) of EtOAc and washed with 25 mL (x 2) brine solution. The combined aqueous layers were washed twice with 15 mL of EtOAc. The combined EtOAc layers were dried over $MgSO_4$ and the organic solvent was removed in vacuo to yield a solid product that generally did not require additional purification. Purification was carried out as required, by silica gel column chromatography using 5:1 EtOAc:MeOH as the eluent to afford target compounds as white solids with yields ranging from 35–42%.

***N*-(4-(Phenethylamino)quinazolin-2-yl)acetamide (67):** Yield: 49% (0.28 g, 0.92 mmol); Mp 187–189 °C. ^{1}H NMR (300 MHz, DMSO-d_6): δ 9.45 (br s, 1H), δ 7.86 (m, 2H), δ 7.39 (t, J = 9.0 Hz, 1H), δ 7.27–7.16 (m, 6H), δ 6.93 (t, J = 6.0 Hz, 1H), δ 3.63 (q, J = 6.0 Hz, 2H), δ 2.92 (t, J = 7.5 Hz, 2H), δ 2.26 (s, 3H). HRMS (ESI) m/z calcd for $C_{18}H_{19}N_4O$ $[M + H]^+$ 307.1481, found 307.1553. Purity: 99.9%

General procedure for the synthesis of N^4-substituted-N^2-alkyl-quinazolin-2,4-diamine.[299, 313] In a 50 mL pressure vial (PV), 0.25 g of 2-chloro, 2,6-dichloro, 2,7-dichloro or 2,8-dichloro-*N*-substituted-quinazolin-4-amine (~ 0.66–0.83 mmol) was combined with 2 eq. (~ 1.32–1.66 mmol) of primary amine (methyl-, ethyl-, *n*-propyl-, isopropyl- or cyclopropylamine) or dimethylamine then dissolved in 5 mL of 1,4-dioxane followed by the addition of 3 eq. of DIPEA (~ 1.98–2.40 mmol). Pressure vial was sealed and stirred in an oil bath at 150–155 °C for 2 h. Upon completion and cooling to room temperature, the reaction mixture was diluted with ~ 40 mL of EtOAc and washed with brine solution (25 mL x 2). The combined aqueous layer was washed with ~ 25 mL of EtOAc. The combined EtOAc layers were dried over $MgSO_4$ before removing EtOAc in vacuo to yield a solid product that was purified by silica gel column chromatography using 5:1 EtOAc:MeOH as the eluent to afford pale yellow to brown solids yielding at 55–70%.

N^2-Methyl-N^4-(phenethyl)quinazoline-2,4-diamine (68). Yield: 65% (0.32 g, 1.15 mmol); Mp 121–123 °C. ^{1}H NMR (300 MHz, DMSO-d_6): δ 7.97 (m, 2H), δ 7.42 (t, J = 9.0 Hz, 1H), δ 7.29–7.16 (m, 6H), δ 6.93 (t, J = 6.0 Hz, 1H), δ 6.35 (br s, 1H), δ 3.60 (q, J = 6.0 Hz, 2H), δ 2.80 (t, J = 9.0 Hz, 2H), δ 2.70 (d, J = 3.0 Hz, 3H). HRMS (ESI) m/z calcd for $C_{17}H_{19}N_4$ $[M + H]^+$ 279.1531, found 279.1603. Purity: 98.6%

N^2-Ethyl-N^4-(phenethyl)quinazoline-2,4-diamine (69). Yield: 61% (0.31 g, 1.06 mmol); Mp 117–119 °C. ^{1}H NMR (300 MHz, DMSO-d_6): δ 7.86 (m, 2H), δ 7.43 (t, J = 9.0 Hz, 1H), δ 7.30–7.16 (m, 6H), δ 6.97 (t, J = 6.0 Hz, 1H), δ 6.50 (br s, 1H), δ 3.61 (q, J = 6.0 Hz, 2H), δ 3.32 (d, J = 9.0 Hz, 2H), δ 2.92 (t, J = 9.0 Hz, 2H), δ 1.09 (t, J = 6.0 Hz, 3H). HRMS (ESI) m/z calcd for $C_{18}H_{21}N_4$ $[M + H]^+$ 293.1688, found 293.1795. Purity: 98.0%

N^4-(Phenethyl)-N^2-propylquinazoline-2,4-diamine (70). Yield: 55% (0.30 g, 0.98 mmol); Mp 102–104 °C. ^{1}H NMR (300 MHz, DMSO-d_6): δ 7.86 (m, 2H), δ 7.39 (t, J = 9.0 Hz, 1H), δ 7.27–7.16 (m, 6H), δ 6.93 (t, J = 6.0 Hz, 1H), δ 6.40 (br s, 1H), δ 3.60 (q, J = 6.0 Hz, 2H), δ 3.30–3.24 (m, 2H), δ 2.89 (t, J = 7.5 Hz,

2H), δ 1.56–1.49 (sextet, *J* = 6.0 Hz, 2H), δ 0.84 (t, *J* = 7.5 Hz, 3H). HRMS (ESI) m/z calcd for $C_{19}H_{23}N_4$ $[M + H]^+$ 307.1844, found 307.1916. Purity: 100.0%

***N*²-Isopropyl-*N*⁴-(phenethyl)quinazoline-2,4-diamine (71).** Yield: 58% (0.32 g, 1.06 mmol); Mp 112–114 °C. ^{1}H NMR (300 MHz, DMSO-d_6): δ 7.89 (m, 2H), δ 7.40 (t, *J* = 9.0 Hz, 1H), δ 7.27–7.17 (m, 6H), δ 6.98 (t, *J* = 6.0 Hz, 1H), δ 6.30 (br s, 1H), δ 4.12 (m, 1H), δ 3.60 (q, *J* = 6.0 Hz, 2H), δ 2.91 (t, *J* = 7.5 Hz, 2H), δ 1.12 (d, *J* = 6.0 Hz, 6H). HRMS (ESI) m/z calcd for $C_{19}H_{23}N_4$ $[M + H]^+$ 307.1844, found 307.1916. Purity: 98.5%

***N*²-Cyclopropyl-*N*⁴-(phenethyl)quinazoline-2,4-diamine (72).** Yield: 58% (0.32 g, 1.05 mmol); Mp 116–118 °C. ^{1}H NMR (300 MHz, DMSO-d_6): δ 7.87 (m, 2H), δ 7.40 (t, *J* = 9.0 Hz, 1H), δ 7.30–7.12 (m, 6H), δ 6.90 (t, *J* = 6.0 Hz, 1H), δ 6.60 (br s, 1H), δ 3.63 (q, *J* = 6.0 Hz, 2H), δ 2.92 (t, *J* = 7.5 Hz, 2H), δ 2.82 (m, 1H), δ 0.59 (d, *J* = 4.8 Hz, 2H), δ 0.44 (d, *J* = 4.8 Hz, 2H). HRMS (ESI) m/z calcd for $C_{19}H_{21}N_4$ $[M + H]^+$ 305.1688, found 305.1759. Purity: 100.0%

6-Chloro-*N*⁴-phenethyl-*N*²-propylquinazoline-2,4-diamine (76). Yield: 71% (0.38 g, 1.12 mmol); Mp 107–109 °C. ^{1}H NMR (300 MHz, DMSO-d_6) δ 8.09–8.02 (m, 2H), δ 7.41 (dd, *J* = 8.9, 2.3 Hz, 1H), δ 7.30–7.14 (m, 6H), δ 6.72 (br s, 1H), δ 3.60 (q, *J* = 7.5 Hz, 2H), δ 3.23–3.20 (m, 2H), δ 2.89 (t, *J* = 7.3 Hz, 2H), δ 1.47 (sextet, *J* = 7.2 Hz, 2H), δ 0.84 (t, *J* = 7.4 Hz, 3H). HRMS (ESI) m/z calcd for $C_{19}H_{22}ClN_4$ $[M + H]^+$ 341.1455, found 341.1527. Purity: 99.7%

6-Chloro-*N*²-isopropyl-*N*⁴-phenethylquinazoline-2,4-diamine (77). Yield: 75% (0.40 g, 1.18 mmol); Mp 104–106 °C. ^{1}H NMR (300 MHz, DMSO-d_6) δ 8.10–8.04 (m, 2H), δ 7.44 (dd, *J* = 8.9, 2.3 Hz, 1H), δ 7.30–7.15 (m, 6H), δ 6.65 (br s, 1H), δ 4.18–4.07 (m, 1H), δ 3.60 (q, *J* = 7.5 Hz, 2H), δ 2.89 (t, *J* = 7.3 Hz, 2H), δ 1.13 (d, *J* = 6.5 Hz, 6H). HRMS (ESI) m/z calcd for $C_{19}H_{22}ClN_4$ $[M + H]^+$ 341.1455, found 341.1527. Purity: 98.6%

6-Chloro-N^2-cyclopropyl-N^4-phenethylquinazoline-2,4-diamine (78). Yield: 73% (0.39 g, 1.15 mmol); Mp 108–110 °C. ^{1}H NMR (300 MHz, DMSO-d_6) δ 8.07–8.04 (m, 2H), δ 7.43 (dd, J = 8.9, 2.3 Hz, 1H), δ 7.29–7.14 (m, 6H), δ 6.87 (br s, 1H), 3.67–3.60 (m, 2H), δ 2.89 (t, J = 7.6 Hz, 2H), δ 2.81–2.75 (m, 1H), δ 0.65–0.58 (m, 2H), δ 0.48–0.43 (m, 2H). HRMS (ESI) m/z calcd for $C_{19}H_{20}ClN_4$ $[M + H]^+$ 338.1298, found 339.1371. Purity: 99.6%

6-Chloro-N^2,N^2-dimethyl-N^4-phenethylquinazoline-2,4-diamine (79). Yield: 76% (0.39 g, 1.20 mmol); Mp 122–124 °C. ^{1}H NMR (300 MHz, DMSO-d_6) δ 8.11 (br s, 1H), δ 8.04 (d, J = 2.3 Hz, 1H), δ 7.41 (dd, J = 8.9, 2.3 Hz, 1H), δ 7.28–7.16 (m, 6H), δ 3.61 (q, J = 5.6 Hz, 2H), δ 3.12 (s, 6H), δ 2.90 (t, J = 7.2 Hz, 2H). HRMS (ESI) m/z calcd for $C_{18}H_{20}ClN_4$ $[M + H]^+$ 327.1298, found 327.1370. Purity: 99.5%

7-Chloro-N^4-phenethyl-N^2-propylquinazoline-2,4-diamine (80). Yield: 70% (0.37 g, 1.10 mmol); Mp 105–107 °C. ^{1}H NMR (300 MHz, DMSO-d_6) δ 8.03 (br s, 1H), δ 7.89 (d, J = 8.7 Hz, 1H), δ 7.30–7.15 (m, 6H), δ 6.96 (dd, J = 8.9, 2.3 Hz, 1H), δ 6.71 (br s, 1H), δ 3.60 (q, J = 7.5 Hz, 2H), δ 3.23–3.20 (m, 2H), δ 2.89 (t, J = 7.3 Hz, 2H), δ 1.46 (sextet, J = 7.2 Hz, 2H), δ 0.84 (t, J = 7.4 Hz, 3H). HRMS (ESI) m/z calcd for $C_{19}H_{22}ClN_4$ $[M + H]^+$ 341.1455, found 341.1528. Purity: 99.4%

7-Chloro-N^2-isopropyl-N^4-phenethylquinazoline-2,4-diamine (81). Yield: 75% (0.40 g, 1.18 mmol); Mp 106–108 °C. ^{1}H NMR (300 MHz, DMSO-d_6) δ 8.07 (br s, 1H), δ 7.91 (d, J = 8.7 Hz, 1H), δ 7.30–7.15 (m, 6H), δ 6.98 (dd, J = 8.9, 2.3 Hz, 1H), δ 6.62 (br s, 1H), δ 4.16–4.09 (m, 1H), δ 3.60 (q, J = 7.5 Hz, 2H), δ 2.89 (t, J = 7.3 Hz, 2H), δ 1.13 (d, J = 6.5 Hz, 6H). HRMS (ESI) m/z calcd for $C_{19}H_{22}ClN_4$ $[M + H]^+$ 341.1455, found 341.1528. Purity: 99.6%

7-Chloro-N^2-cyclopropyl-N^4-phenethylquinazoline-2,4-diamine (82). Yield: 73% (0.39 g, 1.15 mmol); Mp 111–113 °C. ^{1}H NMR (300 MHz, DMSO-d_6) δ 8.07 (br s, 1H), δ 7.92 (d, J = 8.7 Hz, 1H), δ 7.29–7.14 (m, 6H), δ 6.99 (dd, J = 8.7, 2.0 Hz, 1H), δ 6.92 (br s, 1H), δ 3.67–3.60 (m, 2H), δ 2.89 (t, J = 7.6 Hz, 2H), δ 2.85–2.77 (m, 1H), δ 0.65–0.59 (m, 2H), δ 0.48–0.45 (m, 2H). ^{13}C NMR (75 MHz, DMSO-d_6) δ 160.94,

δ 159.43, δ 152.96, δ 139.64, δ 136.75, δ 128.65, δ 128.29, δ 126.03, δ 124.75, δ 123.14, δ 122.43, δ 119.97, δ 109.87, δ 42.14, δ 34.53, δ 23.85, δ 6.37. HRMS (ESI) m/z calcd for $C_{19}H_{20}ClN_4$ $[M + H]^+$ 338.1298, found 339.1371. Purity: 98.5%

7-Chloro-*N*^{2},*N*^{2}-dimethyl-*N*^{4}-phenethylquinazoline-2,4-diamine (83). Yield: 72% (0.37 g, 1.15 mmol); Mp 127–129 °C. ^{1}H NMR (300 MHz, DMSO-d_6) δ 8.12 (br s, 1H), δ 7.90 (d, J = 8.7 Hz, 1H), δ 7.29–7.14 (m, 6H), δ 6.97 (dd, J = 8.9, 2.3 Hz, 1H), δ 3.60 (q, J = 5.6 Hz, 2H), δ 3.12 (s, 6H), δ 2.89 (t, J = 7.2 Hz, 2H). HRMS (ESI) m/z calcd for $C_{18}H_{20}ClN_4$ $[M + H]^+$ 327.1298, found 327.1371. Purity: 94.5%

8-Chloro-*N*^{4}-phenethyl-*N*^{2}-propylquinazoline-2,4-diamine (84). Yield: 70% (0.37 g, 1.10 mmol); Mp 102–104 °C. ^{1}H NMR (300 MHz, DMSO-d_6) δ 8.03 (br s, 1H), δ 7.85 (d, J = 8.6 Hz, 1H), δ 7.57 (d, J = 8.6 Hz, 1H), δ 7.30–7.15 (m, 5H), δ 6.89 (t, J = 7.9 Hz, 1H), δ 6.79 (br s, 1H), δ 3.61 (q, J = 7.5 Hz, 2H), δ 3.23–3.20 (m, 2H), δ 2.89 (t, J = 7.3 Hz, 2H), δ 1.50 (sextet, J = 7.2 Hz, 2H), δ 0.84 (t, J = 7.4 Hz, 3H). HRMS (ESI) m/z calcd for $C_{19}H_{22}ClN_4$ $[M + H]^+$ 341.1455, found 341.1528. Purity: 98.8%

8-Chloro-*N*^{2}-isopropyl-*N*^{4}-phenethylquinazoline-2,4-diamine (85). Yield: 70% (0.37 g, 1.10 mmol); Mp 107–109 °C. ^{1}H NMR (300 MHz, DMSO-d_6) δ 8.99 (br s, 1H), δ 8.16 (d, J = 8.6 Hz, 1H), δ 7.88 (d, J = 8.6 Hz, 1H), δ 7.44 (t, J = 7.9 Hz, 1H), δ 7.30-7.09 (m, 5H), δ 6.97 (br s, 1H), δ 4.25-4.14 (m, 1H), δ 3.67 (q, J = 7.5 Hz, 2H), δ 2.89 (t, J = 7.3 Hz, 2H), δ 1.16 (d, J = 6.5 Hz, 6H). HRMS (ESI) m/z calcd for $C_{19}H_{22}ClN_4$ $[M + H]^+$ 341.1455, found 341.1527. Purity: 100.0%

8-Chloro-*N*^{2}-cyclopropyl-*N*^{4}-phenethylquinazoline-2,4-diamine (86). Yield: 69% (0.37 g, 1.09 mmol); Mp 111–113 °C. ^{1}H NMR (300 MHz, DMSO-d_6) δ 8.17–8.15 (m, 1H), δ 7.92–7.87 (m, 1H), δ 7.63–7.59 (m, 1H), δ 7.31–7.04 (m, 5H), δ 6.98–6.92 (m, 2H), δ 3.75–3.64 (m, 2H), δ 2.97–2.88 (m, 3H), δ 0.65–0.59 (m, 2H), δ 0.48–0.45 (m, 2H). HRMS (ESI) m/z calcd for $C_{19}H_{20}ClN_4$ $[M + H]^+$ 338.1298, found 338.1372. Purity: 98.7%

8-Chloro-N^2,N^2-dimethyl-N^4-phenethylquinazoline-2,4-diamine (87). Yield: 72% (0.37 g, 1.15 mmol); Mp 122–124 °C. ^{1}H NMR (300 MHz, DMSO-d_6) δ 8.15 (br s, 1H), δ 7.86 (d, J = 8.7 Hz, 1H), δ 7.60 (d, J = 8.7 Hz, 1H), δ 7.30–7.15 (m, 5H), δ 6.91 (t, J = 9.0 Hz, 1H), δ 3.63 (q, J = 5.6 Hz, 2H), δ 3.18 (s, 6H), δ 2.91 (t, J = 7.2 Hz, 2H). HRMS (ESI) m/z calcd for $C_{18}H_{19}ClN_4$ $[M + H]^+$ 327.1298, found 327.1371. Purity: 96.3%

6.5.2. *Biological Screening*

6.5.2.1. *Human Cholinesterase (hChE) Assay*[299, 313]

The inhibition profile of quinazoline derivatives was evaluated using the Ellman (DTNB) reagent.[315] Human AChE and BuChE enzymes were obtained from Sigma-Aldrich, St. Louis, MO, USA (AChE product number C0663 and BuChE product number B4186 respectively). The cholinesterase inhibitors tacrine (item number 70240, Cayman Chemical Company, Ann Arbor, MI), donepezil (product number D6821, Sigma-Aldrich, St. Louis, MO), galantamine (product number G1660, Sigma-Aldrich, St. Louis, MO) and rivastigmine (product number SML0881, Sigma-Aldrich, St. Louis, MO) were used as reference agents. Quinazoline derivative stock solutions were prepared in DMSO (maximum 1% v/v in final wells) and diluted in buffer solution (50 mM Tris.HCl, pH 8.0, 0.1 M NaCl, 0.02 M $MgCl_2.6H_2O$). Then 160 µL of 5,5'-dithiobis(2-nitrobenzoic acid) (1.5 mm DTNB), 50 µL of *h*AChE (0.22 U/mL in 50 mM Tris.HCl, pH 8.0, 0.1% w/v bovine serum albumin, BSA) or 50 µL of *h*BuChE (0.12 U/mL in 50 mM Tris.HCl, pH 8.0, 0.1% w/v BSA) were added to 96-well plates after which 10 µL each of quinazoline derivatives (final concentration range 0.1–50 µM) were added and incubated for 5 min. Then 30 µL of either acetylthiocholine iodide (15 mM AThCl prepared in ultra pure water) or *S*-butyrylthiocholine iodide (15 mM BThCI prepared in ultra pure water) were added. The absorbance was measured at different time intervals (0, 60, 120, 180, 240 and 300 s) using a wavelength of 412 nm. The inhibitory concentration (IC_{50} values) was calculated from the concentration–inhibition dose response curve on a logarithmic scale. The

results were expressed as average values based on two to three independent experiments run in triplicate measurements.

6.5.2.2. *Amyloid-β (Aβ) Aggregation Assay*[317]

The ability of quinazoline-based derivatives to inhibit Aβ-aggregation kinetics was determined using a ThT-binding fluorescence assay. These assays were conducted in Costar, black-surround, clear-bottom 384-well plates with frequent shaking (30 sec. of linear shaking at 730 cpm every 5 minutes) and constant heating at 37 °C for 24 h. The ThT excitation/emission was measured at 440 nm/490 nm and readings were taken every 5 minutes using a BioTek Synergy H1 microplate reader. Quinazoline stock solutions were prepared in DMSO and diluted to 10x in 215 mM phosphate buffer at pH 7.4. Abeta.HFIP samples (Aβ40 or Aβ42, rPeptide, Bogart, USA) were dissolved in 1% ammonium hydroxide, sonicated at room temperature for 5 minutes then diluted to 50 μM in 215 mM phosphate buffer (pH 7.4). A 15 μM ThT stock solution was prepared with 50 mM glycine and adjusted to pH 7.4. The assay was carried out by adding 44 μL ThT, 20–35 μL buffer, 1 μL DMSO (for background and controls only) followed by the addition of 8 μL of 10x compound dilutions (1–25 μM concentration range). An end point reading was conducted to evaluate potential test compound interference with ThT-fluorescence before adding 8 μL of Aβ40 or Aβ42 stock solutions (5 μM final concentration). Plates were sealed with a transparent plate film before initiating the assay. RFU values were corrected for ThT-interference before calculating end point percent inhibitions or IC_{50} values and obtaining the aggregation kinetic plots. Data presented was an average of triplicate reading for two-three independent experiments.

6.5.2.3. *TEM Assay and Imaging*[142, 190, 207, 317]

In Costar 96-well, round-bottom plates were added 80 μL of 215 mM phosphate buffer, 20 μL of 10x test compound dilutions (250 μM – prepared in the same way as for the ThT assay) and 100 μL of 50 μM Aβ40 or Aβ42 respectively. For the control wells, 2 μL of DMSO and 18 μL of phosphate buffer was added. Final Aβ: test compound ratio was 1:1 (25 μM). Plates were incubated on a Fisher plate incubator

set to 37 °C and the contents were shaken at 730 cpm for 24 h. To prepare the TEM grids, ~ 20 µL droplet was added using a disposable Pasteur pipette over the formvar-coated copper grids (400 mesh). Grids were air-dried for about 3 h before adding two droplets (~ 40 µL, using a disposable Pasteur pipette) of ultra-pure water and using small pieces of filter paper to wash out precipitated buffer salts. After air-drying for ~ 15-20 min, the grids were negatively stained by adding a droplet (~ 20 µL, using a disposable Pasteur pipette) of 2% phosphotungstic acid (PTA) and immediately after the grids were dried using small pieces of filter paper. Grids were further air-dried overnight. The scanning was carried out using a Philips CM 10 transmission electron microscope at 60 kV (Department of Biology, University of Waterloo) and micrographs were obtained using a 14-megapixel AMT camera.

6.5.2.4. *DPPH Scavenging Assay*[324]

The ability of select quinazolines to scavenge the DPPH radical was utilized as a measure of antioxidant capacity. Quinazoline stock solutions were prepared in anhydrous methanol (500 µM) and the DPPH solution was also prepared in anhydrous methanol (56 µM). The addition sequence was carried out in a 96-well clear, flat bottom plate as follows: 90 µL DPPH, 10 µL test compound solution (50 µM) final concentration. Control solutions contained 90 µL anhydrous methanol and 10 µL test compound whereas DPPH control contained 90 µL of DPPH, and 10 µL anhydrous methanol. This readings were taken initially at 517 nm with 30 sec. shaking (double orbital at 530 cpm) prior to the 1 h, light restrictive, incubation period at room temperature after which readings were taken again at 517 nm after another round of 30 sec shaking (double orbital at 530 cpm) using a BioTek Synergy H1 microplate reader. The results were expressed as percentage inhibition and the data presented was average of triplicate reading (for two independent experiments).

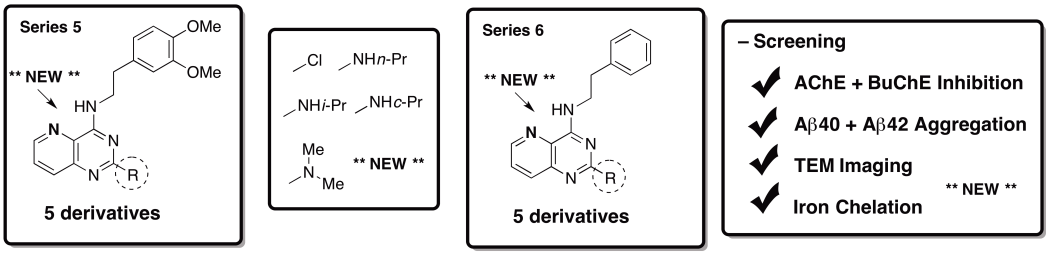
6.5.3. *Computational Chemistry*[299, 313, 317, 324]

The molecular docking studies were conducted using Discovery Studio 4.0 (Structure-Based-Design program) from BIOVIA Inc. San Diego, USA. Select quinazolines derivatives were built and minimized

using the *small molecules* module in Discovery Studio. X-ray coordinates of human cholinesterases were obtained from the protein data bank (*h*AChE PBD ID: 1B41 and *h*BuChE PDB ID: 1P0I) and prepared using the *macromolecules* module in Discovery Studio. Ligand binding sites were defined by selecting a 12 Å radius sphere for AChE and 15 Å radius sphere for BuChE. The molecular docking was performed using the *receptor-ligand interactions* module in Discovery Studio. The LibDock algorithm was used to find the most appropriate binding modes for select quinazoline derivatives using CHARMm force field. The docked poses obtained were ranked based on the LibDock scores and were analyzed by evaluating all the polar and nonpolar interactions. For Amyloid-β docking studies, the NMR solution structure of Aβ fibrils were obtained from the protein data bank (PDB ID: 2LMN). Aβ dimer and Aβ fibril assemblies were built using the *macromolecules* module in Discovery Studio. Ligand binding site was defined by selecting a 15 Å radius sphere for both Aβ assemblies. Molecular docking was performed using the *receptor-ligand interactions* module in Discovery Studio, where the LibDock algorithm was used to find the most appropriate binding modes for select quinazoline derivatives using CHARMm force field. The docked poses obtained were ranked based on the LibDock scores and were analyzed by evaluating all the polar and nonpolar interactions.

CHAPTER 7

• Development and Evaluation of 2,4-Disubstituted Pyridopyrimidines as Dual ChE and Aβ Aggregation Inhibitors with Chelation Capacity •



* Chapter banner

7.1. Introduction

The preceding chapters (3–6) showcased the SAR data from 86 quinazoline and cholorquinazoline derivatives, including four regioisomeric structures. The acquired data thus far highlighted the advantages and disadvantages of introducing a dimethoxyphenyl moiety or an additional methylene linker at the C4-positon of the quinazoline scaffold, while providing clear indications of the biological outcomes based on the nature of the C2-groups. The assessment of regioisomeric structures and the impact of chlorine placements provided valuable SAR for the optimization (Phase 2) stage.

This chapter sets to further expand on the acquired SAR data, of the C4-dimethoxypheneyl and C4-phenethylamine series, by developing and assessing 10 derivatives based on the quinazoline-related scaffold – pyridopyrimidine (Ppd). From the cumulative assessment of the C2-groups utilized throughout the project, the following alkylamines (*n*-propyl, *i*-proply, *c*-propyl and dimethylamines) were utilized in this chapter.

Generally, all synthetic approaches and mechanisms here have been previously discussed in Chapters 3–6. A brief summary is provided prior to the listing of experimental data and methodology.

7.2. Hypothesis

With respect to this series, the focus on the dimethoxyphenethyl and phenethyl moieties at C4-position was based on the overall benefits observed with the additional methylene unit in the linker chain. While the 3,4-dimethoxy groups were more suitable for AChE targeting, their absence proved more effective at BuChE targeting, so these observations are likely to carry forward here. On the other hand, honing in on the aliphatic alkylamines was based on their superior ability to generate dual ChE inhibitors, while offering strong potentials toward dual Aβ targeting.

The strategy behind the pyridopyrimidine scaffold is established on the introduction of a chelation center within the scaffold (pyridine nitrogen and C4-NH) and decreasing the overall hydrophobicity of the derivatives. While the chelation center would enhance the overall multi-targeting capacity of the derivatives, the reduced hydrophobicity associated with the more polar scaffold is predicated to deter BuChE activity. The SAR obtained from these derivatives should provide critical insight, especially when compared to their non-chlorinated, quinazoline-based counterparts in Chapters 5 and 6.

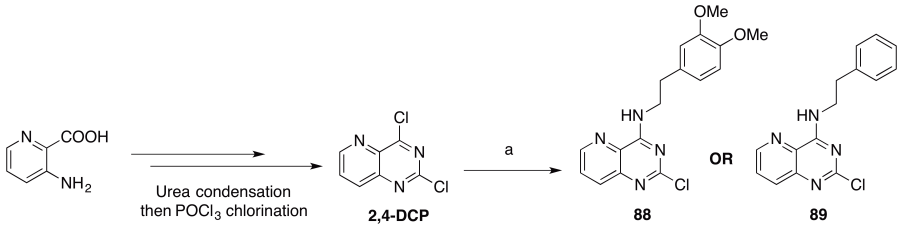
7.3. Results and Discussions

The proceeding sub-chapter briefly highlights previously-established routes to target derivatives. Biological assessments in the cholinesterase and amyloid-β aggregation assay (to obtain IC_{50} values and/or investigation aggregation kinetics) are conducted. Aggregate load is corroborated via transmission electron microscopy in amyloid morphology screening and derivatives are assessed for iron chelation potential in the competition-based ferrozine assay. Computational studies are performed in the ChE X-ray structures and amyloid models to evaluate the acquisitioned SAR data.

7.3.1. *Synthesis*

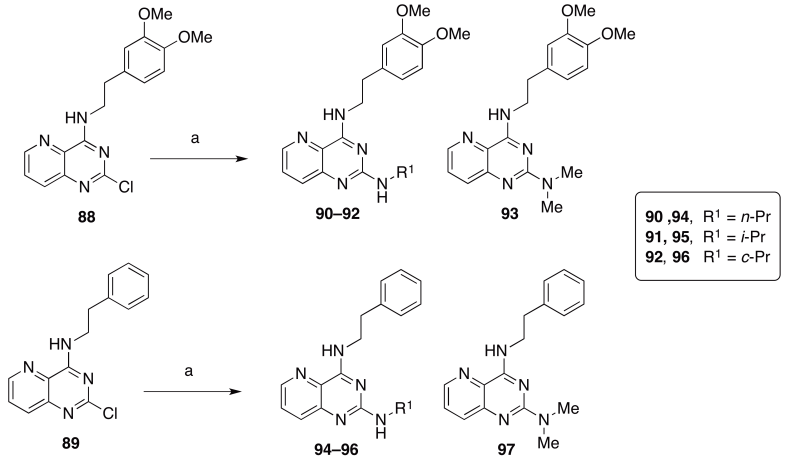
As previously described, initial coupling in this series utilized 2,4-dichloropyridopyrimidine (2,4-DCP) to add the 3,4-dimethoxyphenethylamine or the phenethylamine group to the C4-position of the pyrido[3,2-*d*]pyrimidine (Ppd) scaffold, via a NAS reaction, to yield 2-chloro-*N*-(3,4-dimethoxyphenethyl) pyrido[3,2-*d*]pyrimidin-4-amine or 2-chloro-*N*-phenethylpyrido[3,2-*d*]pyrimidin-4-amine (**88**–**89**, Scheme 21). The coupling of the alkylamines at the C2-position to **88** or **89** was accomplished using previously described methodologies based on N.A.S (**90**–**97**, Scheme 22).

Scheme 21[a]



[a]**Reagents and conditions:** Synthetic routes toward pyridopyrimidine-based derivatives **88** and **89**. (a) 3,4-dimethoxyphenethylamine or phenethylamine, DIPEA, EtOH, reflux, 4 h.

Scheme 22[a]

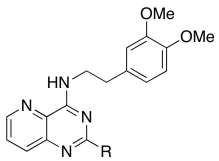


[a]**Reagents and conditions:** Synthetic routes toward pyridopyrimidine-based derivatives **90**–**97**.(a) Primary amine (R^1 = *n*-Pr, *i*-Pr or *c*-Pr) or dimethylamine, DIPEA, 1,4-dioxane, pressure vial 150–155 °C, 2 h.

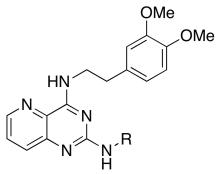
7.3.2. *Cholinesterase*

The ability of 2,4-disubstituted pyridopyrimidines (**88**–**97**) to target the cholinesterases (*h*AChE/ *h*BuChE) was assessed using the DTNB method as described in Chapter 3 (Table 13).

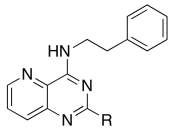
Table 13: Cholinesterase inhibition data for 2,4-disubstituted pyridopyrimidines (**88**–**97**).



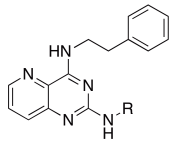
88, 93



90–92



89, 97



94–96

Derivative	R-Grp	ChE IC_{50} (μM) [a]		SI [b]	ClogP [c]	MV (Å^3) [d]	HBD:HBA [e]
		*h*AChE	*h*BuChE				
88	Cl	9.0 ± 0.9	> 50	–	3.59	267.53	1:6
89	Cl	7.2 ± 0.7	> 50	–	3.93	209.57	1:4
90	*n*-Pr	7.2 ± 0.8	> 50	–	4.81	308.35	2:7
91	*i*-Pr	7.4 ± 0.7	> 50	–	4.59	303.21	2:7
92	*c*-Pr	7.2 ± 0.5	> 50	–	4.34	299.09	2:7
93	$N(Me)_2$	6.7 ± 0.5	> 50	–	3.81	290.52	1:7
94	*n*-Pr	8.1± 0.8	30.3 ± 2.8	0.27	5.16	251.41	2:5
95	*i*-Pr	7.8 ± 0.8	29.3 ± 2.1	0.27	4.94	255.87	2:5
96	*c*-Pr	7.6 ± 0.6	> 50	–	4.68	244.21	2:5
97	$N(Me)_2$	6.8 ± 0.7	> 50	–	4.15	242.84	1:5
Donepezil	–	0.03 ± 0.002	3.6 ± 0.4	0.01	4.59	321.7	0:4
Tacrine	–	0.16 ± 0.01	0.04 ± 0.001	4.00	3.27	165.6	2:2
Galantamine	–	2.6 ± 0.6	> 50	–	1.18	239.4	1:4
Rivastigmine	–	6.5 ± 0.5	> 10	–	2.10	226.3	0:4

Notes: [a] IC_{50} values are an average ± SD of triplicate readings based on two to three independent experiments. [b]Selectivity index is calculated as (*h*AChE IC_{50}) ÷ (*h*BuChE IC_{50}). [c]ClogP values were determined using ChemDraw Professional 15.0. [d]Molecular volumes in Å^3 units were determined using Discovery Studio, Structure-Based Design software, BIOVIA Inc., USA. [e]Showcasing the ratio of HBD = hydrogen-bonding donors to HBA = hydrogen-bonding acceptors.

When considered against non-chlorinated quinazoline counterparts in Table 5 (Chapter 5) and Table 9 (Chapter 6), the data presented in Table 13 generally pointed to the significant inability of the derivatives within this pyridopyrimidine series to target BuChE. With respect to AChE targeting, IC_{50} values remained static at ~ 7.5 μM, compared to ~ 6.2 μM for dimethoxyphenethylamine-based quinazolines and ~ 7.7 for

phenethylamine-based quinazolines counterparts. Starting with the C2-chlorine-based derivatives, **88** was roughly 3-fold less potent toward AChE compared to its quinazoline counterpart (**32**, IC_{50} ~ 3 μM) and roughly 1.3-fold less potent compared to its phenethylamine counterpart (**89**, IC_{50} ~ 7 μM). Interestingly, **89** was equipotent to its quinazoline counterpart (**60**) toward AChE.

The introduction of secondary alkylamines at the C2-position of the dimethoxyphenethylamine-based pyridopyrimidines (**90**–**92**, Table 13) established equipotent activity toward AChE (IC_{50} ~ 7.3 μM) as seen with their quinazoline counterparts (**42**–**44**); however, BuChE activity was totally suppressed with the pyridopyrimidine scaffold. The tertiary dimethylamine-based derivative (**93**) was also inactive toward BuChE and was more or less comparable to **90**–**92** toward AChE. Compared to **90**–**93**, the phenethylamine-based pyridopyrimidines (**94**–**97**) were also equipotent toward AChE (although **94** was slightly less potent compared to **90**), while BuChE was either very weak (**94** and **95**, IC_{50} ~ 30 μM) to non-existent (**96** and **97**). When extending the comparison to their quinazoline counterparts (**70**–**72**), the pyridopyrimidine-based derivatives were no match on the BuChE front and, yet again, were roughly equivalent in their activity toward AChE (IC_{50} 7.7 μM vs. 7.8 μM).

In summary, the investigation into the impact of the pyridopyrimidine scaffold on dual ChE inhibition simply revealed that while AChE targeting potential was not impacted, these derivatives (**88**–**97**) were not suitable for BuChE targeting, based on their polar ring scaffold. Overall, AChE targeting was based on an average IC_{50} value of 7.5 μM.

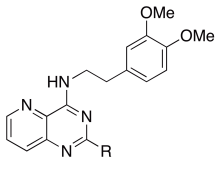
7.3.3. *Amyloid-β Aggregation*

The ability of 2,4-disubstituted pyridopyrimidines (**88**–**97**) to modulate the aggregation kinetics of amyloid-β was assessed using the ThT-binding method described earlier in Chapter 3 (Table 14).

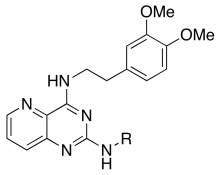
When considered against non-chlorinated quinazoline counterparts in Table 7 (Chapter 5) and Table 11 (Chapter 6), the data presented in Table 14 generally pointed to the reduced capacity of **88**–**97** to target Aβ40 (with the exception of **95** being ~ 4-fold more potent compared to **71**), while also demonstrating enhanced capacity to inhibit Aβ42.

Starting with the C2-chlorine-based derivatives, **88** was roughly 4-fold less potent toward Aβ40 compared to its quinazoline counterpart (**32**, IC_{50} ~ 8 μM), but was roughly 5-fold more potent toward Aβ42 (IC_{50} ~ 3 μM). The phenethylamine counterpart (**89**) was 18% less potent toward Aβ40, while also being ~ 10-fold less potent toward Aβ42. Interestingly, **89** was roughly 10-fold less potent toward Aβ40 and ~ 1.5-fold more potent toward Aβ42 compared to its quinazoline counterpart (**60**).

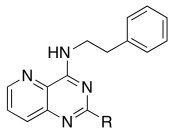
Table 14: Amyloid-β (Aβ40/42) inhibition data for 2,4-disubstituted pyridopyrimidines (**88**–**97**).



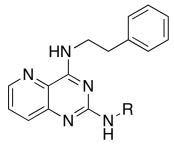
88, 93



90–92



89, 97



94–96

Derivative	R-Grp	Amyloid-β IC_{50} (μM) [a]		SI [b]	ClogP [c]	MV (Å^3) [d]	HBD:HBA [e]
		Aβ40	Aβ42				
88	Cl	44%	2.7 ± 0.3	–	3.59	267.53	1:6
89	Cl	26%	22.6 ± 2.8	–	3.93	209.57	1:4
90	*n*-Pr	NA	41%	–	4.81	308.35	2:7
91	*i*-Pr	NA	33%	–	4.59	303.21	2:7
92	*c*-Pr	NA	46%	–	4.34	299.09	2:7
93	$N(Me)_2$	23%	38%	–	3.81	290.52	1:7
94	*n*-Pr	NA	13.7 ± 2.0	–	5.16	251.41	2:5
95	*i*-Pr	1.1 ± 0.1	50%	–	4.94	255.87	2:5
96	*c*-Pr	6.8 ± 1.0	11.5 ± 1.5	–	4.68	244.21	2:5
97	$N(Me)_2$	NA	12.7 ± 2.0	–	4.15	242.84	1:5
Curcumin	–	3.3 ± 0.45	9.9 ± 0.4	0.33	4.59	302.1	2:6
Resveratrol	–	1.1 ± 0.1	15.3 ± 1.9	0.07	2.83	187.2	3:3

Notes: [a] IC_{50} values are an average ± SD of triplicate readings based on two to three independent experiments. NA = Not active. Percent inhibition (P.I) indicates level of inhibition at highest concentration tested (25 μM). [b]Selectivity index is calculated as (Aβ40 IC_{50}) ÷ (Aβ42 IC_{50}). [c]ClogP values were determined using ChemDraw Professional 15.0. [d]Molecular volumes in Å^3 units were determined using Discovery Studio, Structure-Based Design software, BIOVIA Inc., USA. [e]Showcasing the ratio of HBD = hydrogen-bonding donors to HBA = hydrogen-bonding acceptors.

The introduction of secondary alkylamines at the C2-position of the dimethoxyphenethylamine-based pyridopyrimidines (**90**–**92**, Table 13) demonstrated a total loss of Aβ40 activity (compared to IC_{50} ~ 4–39 μM, **42**–**44**) while exhibiting an estimated 40% inhibition toward Aβ42 (compared to ~ 16% inhibition at

25 μM). The tertiary dimethylamine-based derivative (**93**) was weakly active toward Aβ40 (P.I ~ 23% at 25 μM), while exhibiting P.I of Aβ42 similar to **90**–**92** (38% vs. ~ 40% at 25 μM). Compared to **90**–**93**, the phenethylamine-based pyridopyrimidines (**94**–**97**) were more active toward Aβ42 (IC_{50} ~ 16 μM), while only **95** and **96** exhibited potent to moderate (IC_{50} ~ 1 and 7 μM; respectively) inhibition of Aβ40. When extending the comparison to their quinazoline counterparts (**70**–**72**), the pyridopyrimidine-based derivatives were more active toward Aβ42 (IC_{50} ~ 48 vs. ~ 16 μM; respectively), while activity toward Aβ40 was of mixed outcomes. While the quinazoline scaffold favoured the *n*-Pr (**70**, IC_{50} ~ 4 μM) and *c*-Pr (**72**, IC_{50} ~ 1 μM) C2-groups, the pyridopyrimidine favoured the *i*-Pr group (**95**, IC_{50} ~ 1 μM).

In summary, the investigation into the impact of the pyridopyrimidine scaffold on dual Aβ targeting simply revealed that while the pyridopyrimidine scaffold was not as effective toward Aβ40, it generally enhanced Aβ42 targeting potential. Overall, derivative **95** (N^2-isopropyl-N^4-phenethylpyrido[3,2-*d*]pyrimidine-2,4-diamine) was identified as the leading Aβ40 aggregation inhibitor (IC_{50} ~ 1 μM, equipotent to resveratrol), while **88** (2-chloro-*N*-(3,4-dimethoxyphenethyl)pyrido[3,2-*d*]pyrimidin-4-amine) was identified as the leading Aβ42 aggregation inhibitor (IC_{50} ~ 3 μM).

The aggregation kinetic assessment of Aβ40/42 with or without series-leading derivatives is showcased in Figure 79. As observed in Panel A, derivative **95** exhibited concentration-dependent inhibition of Aβ40 aggregation while showcasing multi-mode anti-aggregation characteristics. Starting with 1 μM test concentration, **95** managed to induce some level of monomeric structure stabilization (roughly a 1–2 hour delay in the aggregation process), while reducing both the rate and total aggregate load to roughly 50%. These patterns were extended to both the 5 and 25 μM test concentrations, but at higher levels exemplified by the 4–5 delay in the aggregation process.

In Panel B, derivative **88** exhibited concentration-dependent inhibition of Aβ42 aggregation, with both 5 and 25 μM test concentrations halting the aggregation processes completely. At the 1 μM test concentration, the only observable impact was focused on slight reductions of the total aggregate load at the end of the 24 hour incubation process.

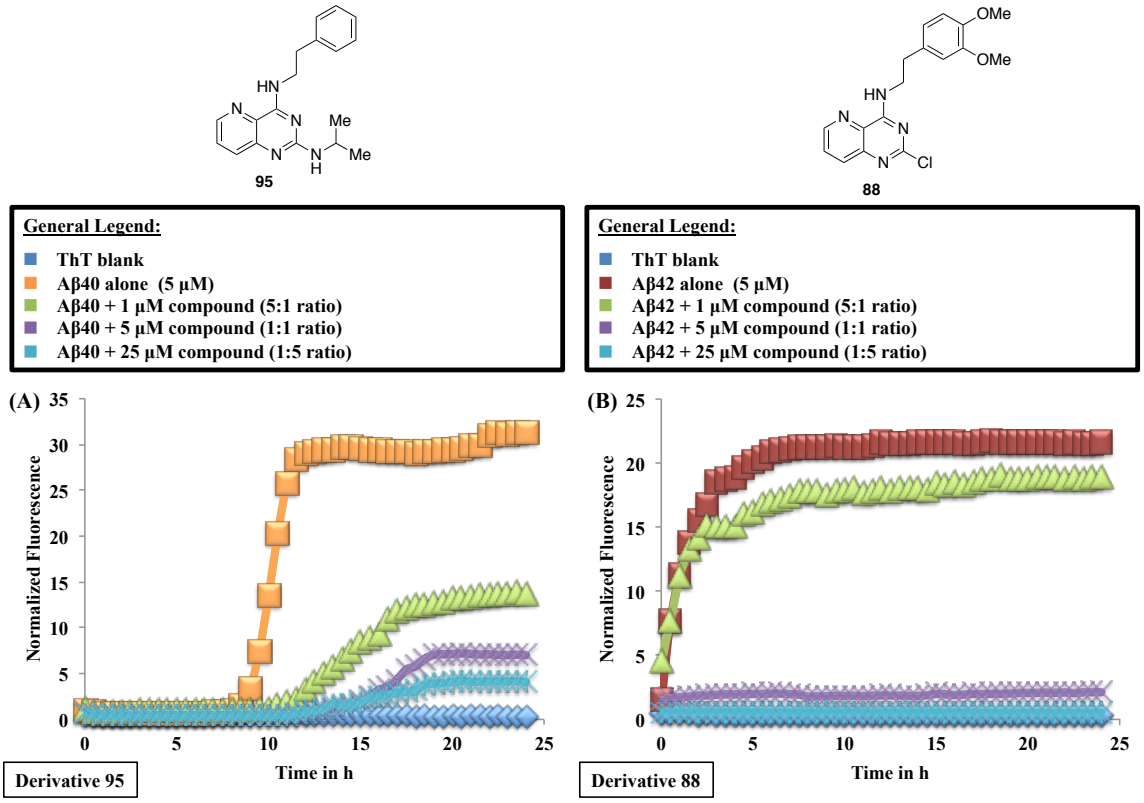


Figure 79: ThT-monitored kinetics of Aβ40/42 aggregation at 37 °C over a 24 h incubation period at pH 7.4 (Excitation = 440 nm, Emission = 490 nm). Panel (A): Impact of 1, 5 or 25 μM of N^2-isopropyl-N^4-phenethylpyrido[3,2-*d*]pyrimidine-2,4-diamine (**95**) on the aggregation kinetics of 5 μM Aβ40. Panel (B): Impact of 1, 5 or 25 μM of 2-chloro-*N*-(3,4-dimethoxyphenethyl) pyrido[3,2-*d*]pyrimidin-4-amine (**88**) on the aggregation kinetics of 5 μM Aβ42.

7.3.4. *Transmission Electron Microscopy (TEM)*

The assessment of amyloid morphology at the conclusion of a 24-hour incubation period at 37 °C was conducted on leading derivatives. This commonly employed, qualitative technique is used to corroborate the quantitative results from the ThT-binding assay. Experimental setup included the incubations of control and test samples, at 1:1 ratios of 25 μM, in triplicate at 37 °C (with shaking) over a 24-hour timeline. Triplicate samples were combined after the incubation period and applied to the copper-mesh grids prior to imaging in the TEM.

As observed in Figure 80, resveratrol was effective at reducing total amyloid load (Panels B and E) compared to control samples (Panels A and D). That said, derivative **95** (Panel C) was similarly effective against Aβ40, while derivative **88** was significantly more potent toward Aβ42, compared to resveratrol.

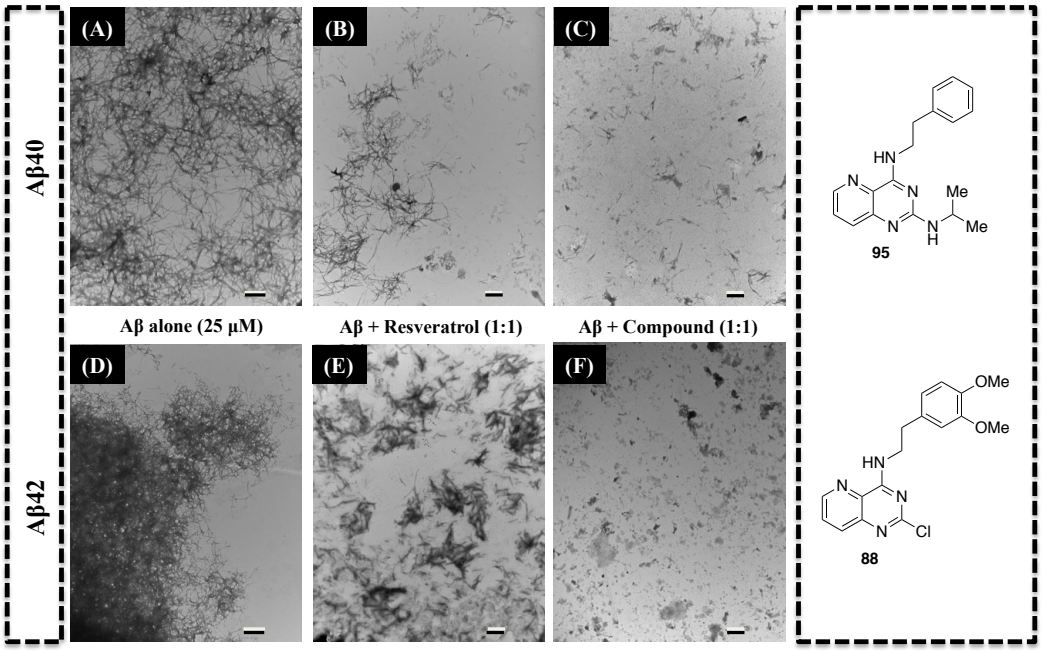


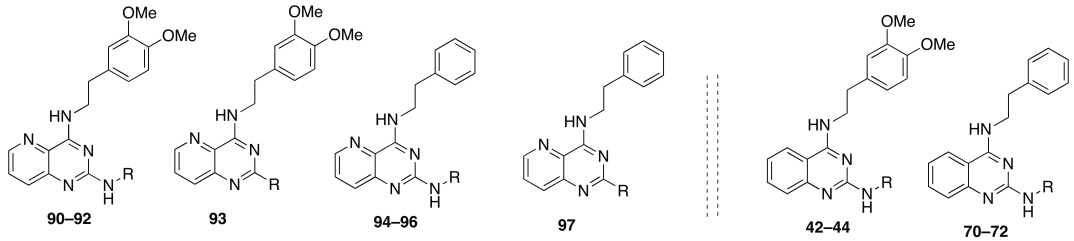
Figure 80: TEM assessment of Aβ40/42 morphology with or without test compounds at the end of a 24-hour, 37 °C incubation period at pH 7.4. Panel (A–C): 25 μM Aβ40 alone or at a 1:1 ratio with resveratrol or N^2-isopropyl-N^4-phenethylpyrido[3,2-*d*]pyrimidine-2,4-diamine (**95**); respectively. Panel (D–F): 25 μM Aβ42 alone or at a 1:1 ratio with resveratrol or 2-chloro-*N*-(3,4-dimethoxyphenethyl)pyrido[3,2-*d*]pyrimidin-4-amine **(88)**; respectively. White/ black bars represent 500 nm.

7.3.5. *Iron Chelation Capacity*

The ability of these 2,4-disubstituted pyridopyrimidines to chelate iron (Fe^{2+}) was conducted in comparison to their respective quinazoline counterparts, as part of the initial chelation center hypothesis, using the competition-based ferrozine assay (Table 15).[319] This commonly employed assay is based on the observed ferrozine absorbance shift upon iron-binding (562 nm) and the reduction in ferrozine-iron complex absorbance with a competitive chelator (such as a pyridopyrimidine-based derivative). Experimental setup included the incubations of ferrozine and iron-(II)-sulphate (at 2.5:1 ratio – 100 μM: 40

μM) at room temperature followed by the addition of assay controls (clioquinol and deferoxamine) or test samples (**90**–**97**) at 50 μM, in triplicate. The 96-well plates were covered and incubated, with shaking, for 15-30 minutes prior to reading at 562 nm.

Table 15: Iron (Fe^{2+}) chelation capacity for 2,4-disubstituted pyridopyrimidines (**90**–**97**) in relation to quinazoline counterparts (**42**–**44** and **70**–**72**).



Derivative	R-Grp	% Fe^{2+} Chelation [a]	% Fe^{2+} Chelation [a]	R-Grp	Qnz-Counterpart
90	*n*-Pr	24%	3%	*n*-Pr	**42**
91	*i*-Pr	22%	2%	*i*-Pr	**43**
92	*c*-Pr	27%	NA	*c*-Pr	**44**
93	$N(Me)_2$	23%	–	–	–
94	*n*-Pr	29%	4%	*n*-Pr	**70**
95	*i*-Pr	24%	2%	*i*-Pr	**71**
96	*c*-Pr	37%	3%	*c*-Pr	**72**
97	$N(Me)_2$	23%	–	–	–
Clioquinol	–	39%			
Deferroxamine	–	88%			

Notes: [a] Percent inhibition values are an average of triplicate readings based on two independent experiments. NA = Not active.

As observed in Table 15, the pyridopyrimidines managed to inflict an average 26% chelating capacity for iron. When compared to their quinazoline counterparts, the pyridopyrimidine-chelating hypothesis was supported considering the inability of the quinazoline-based derivatives to chelate iron. That said, the only potential chelating quinazolines were those featuring the urea moiety at the C2-position (**11**, **24**, **37** and **65**) and in fact, those demonstrated an average of 15% chelating capacity (Figure 81). Overall, **96** (N^2-

cyclopropyl-N^4-phenethylpyrido[3,2-*d*]pyrimidine-2,4-diamine) was identified as the most active iron chelator, equipotent to clioquinol (37% vs. 39%; respectively).

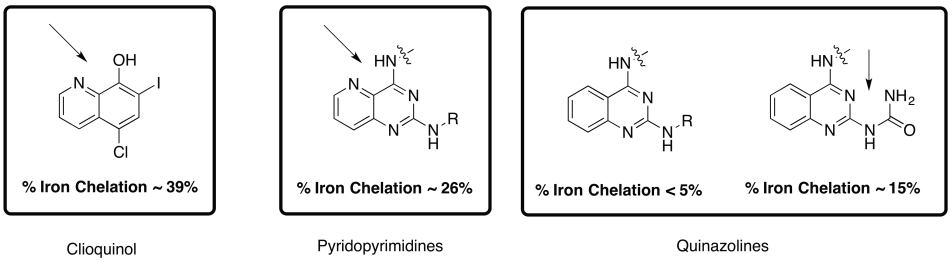


Figure 81: Overall summary of the scaffold evaluation toward iron chelation capacity.

7.3.6. *Molecular Modeling*

The utilization of computational software is not only useful in structure-based drug design, it is also employed to understand and corroborate the acquired SAR data. The assessment of ligand-receptor interactions was conducted between leading (or comparable) derivatives from the 2,4-disubstituted pyridopyrimidine series (**88**–**97**) and the cholinesterase or amyloid targets of interest.

7.3.6.1. *Cholinesterase*

Based on the acquired anti-ChE data, presented in Table 13, the docking interactions of **93** and **97** were investigated in *h*AChE (PBD: 1B41) and superimposed in Figure 82. While both derivatives are equipotent, they exhibited opposite binding interactions within AChE. With **93**, the pyridopyrimidine scaffold was dominantly PAS localized (~ 5–6 Å from W286), allowing for the C4-dimethoxy phenethylamine to extend deep toward the active site. This orientation facilitated the *para*-methoxy group to undergo hydrogen-bonding interactions with W86's indole N*H* (~ 3.3 Å). In contrast, **97** exhibited stronger active site binding interactions with its pyridopyrimidine scaffold stacked semi-parallel over W86

(~ 5 Å) and the pyridine ring oriented toward the catalytic triad, facilitating hydrogen-bonding interactions between the pyridine nitrogen and S203's O*H* (~ 3.4 Å). The C4-phenethylamine ran parallel to the acyl pocket and was pointed toward W286 (~ 6–7 Å). With both derivatives, no hydrogen-bonding interactions were observed with dimethylamine groups, but it was interesting to observe the orientation of these groups with respect to the pyridopyrimidine scaffold – In **93**, the dimethylamine group was oriented in a planar manner, while **97** was running anti-planar with the pyridopyrimidine scaffold.

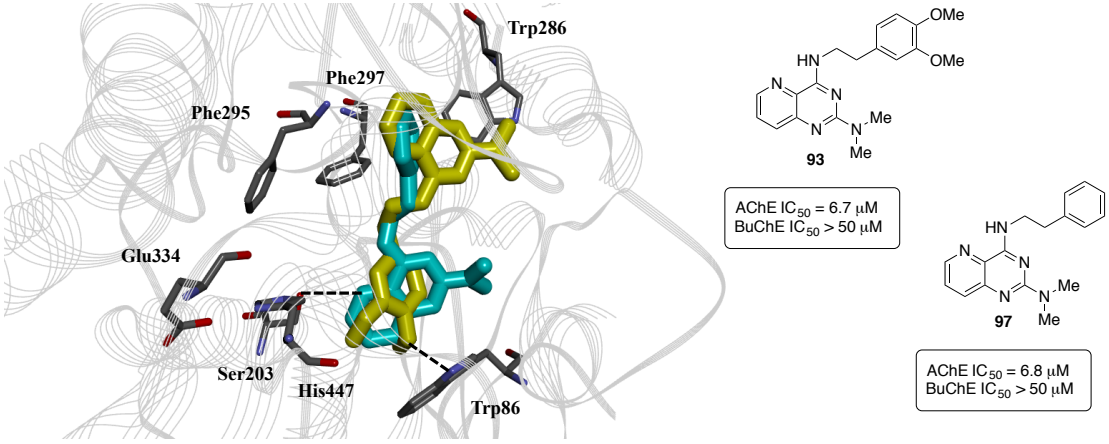


Figure 82: Superimposition of docking structures of **93** (gold) and **97** (turquoise) in the active site of *h*AChE (PDB ID: 1B41). Hydrogens removed to enhance visibility. Black-dashed lines indicate hydrogen-bonding interactions.

7.3.6.2. *Amyloid-β*

Based on the acquired anti-Aβ data, presented in Table 14, the docking interactions of **95** and **96** were investigated in both a dimeric and fibril model of Aβ ($A\beta_{9\text{-}40}$ – PDB 2LMN) with superimpositions showcased in Figure 83.

Considering the approximate 7-fold gap in potency toward Aβ40, the unique binding interactions of **95** (C2 = *i*-Pr) and **96** (C2 = *c*-Pr) explain the potency gap. In a general sense, ligand **95** exhibited close interactions at three regions of the dimeric structure, compared to just two regions with ligand **96**. The pyridopyrimidine scaffold of **95** was equidistantly placed between the V24 and I32 (~ 5–6 Å), allowing the

C4-phenethlyamine group to interact within the hairpin loop domain, where the phenyl ring was roughly 4 Å from S26–N27 and the C4–N*H* was ~ 3.4 Å from E22's carboxyl group (hydrogen-bonding interaction). The ligand's isopropyl group was directed toward the aliphatic regions L34 (~ 4–5 Å), allowing for hydrogen-bonding interactions between the C2-N*H* and the backbone carbonyl of I32 (~ 3.5 Å). In contrast, the pyridopyrimidine scaffold of **96** was perpendicularly stacked against I31 (~ 4–5 Å), while the C2-cyclopropylamine group was suspended over I32, allowing for hydrogen-bonding interactions between the C2-N*H* and the backbone carbonyl of I32 (~ 2.9 Å). The ligand's C4-phenethylamine was running parallel along A30-I31 with the phenyl ring oriented toward the backbones of N27-K28 (~ 3–4 Å).

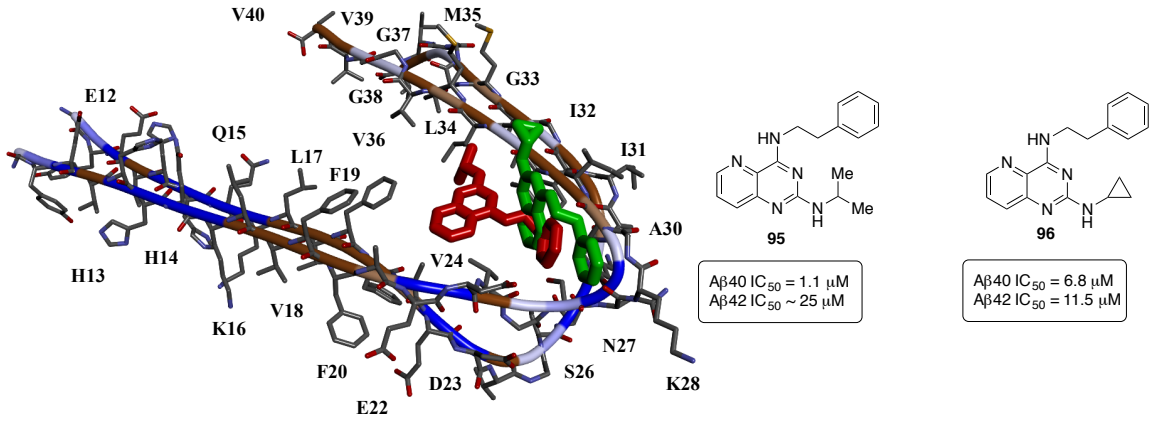


Figure 83: Superimposition of docking structures. Binding modes of **95** (red) and **96** (green) in the Aβ ($Aβ_{9-40}$ – PDB 2LMN) dimer model. Hydrogens removed to enhance visibility. Amino acid labels to be used as a general guide as space restrictions limited complete and accurate labeling of all peptide structures.

7.4. Summary

With this collection of 2,4-disubstituted pyrido[3,2-*d*]pyrimidines, AChE targeting potential was not impacted while BuChE inhibition was basically non-existent, as initially anticipated. When compared to their non-chlorinated quinazoline counterparts, the pyridopyrimidines demonstrated improvements in Aβ42 targeting, while inhibitory activity toward Aβ40 revealed more of a mixed outcome. In addition, the pyridopyrimidine scaffold itself enabled the derivatives within this series to impose anywhere from 22–37% iron chelating capacity.

Overall, a series leader was identified in N^2-cyclopropyl-N^4-phenethylpyrido[3,2-*d*]pyrimidine-2,4-diamine (**96**) due to its greater chelating capacity (~ 37% at 50 μM) and multi-targeting capacity toward AChE and Aβ40 at the equipotent concentration of ~ 7 μM (Figure 84). That said, **96** was capable of targeting Aβ42 (IC_{50} ~ 12 μM), but not BuChE.

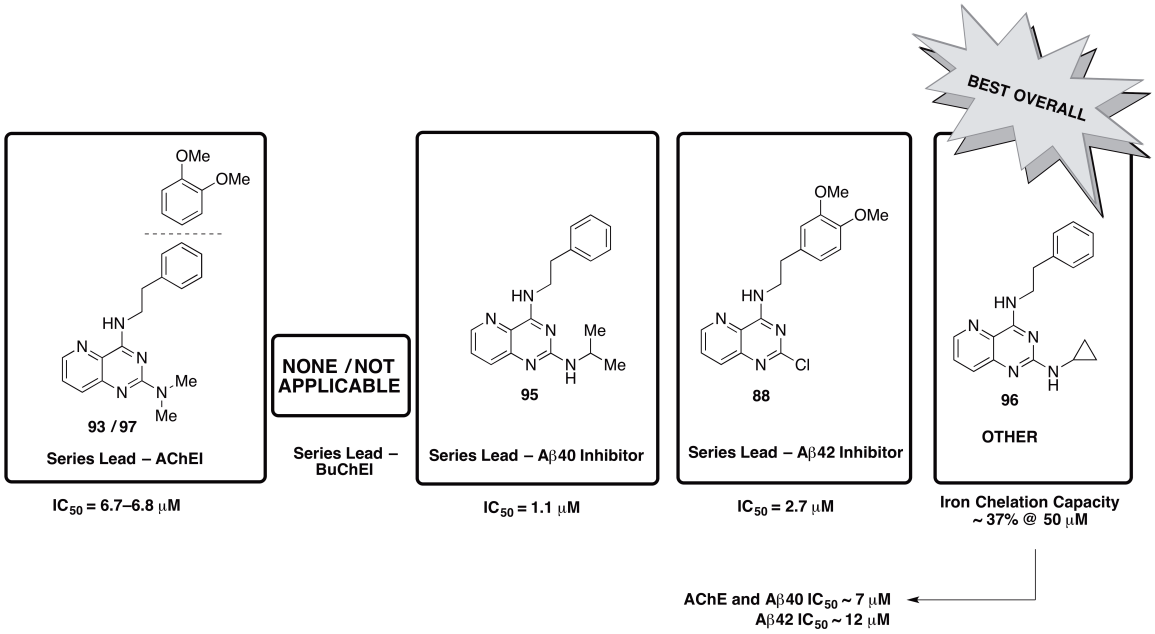


Figure 84: Cumulative chapter summary of 2,4-disubstituted pyridopyrimidines (**88**–**97**).

7.5. Experimental

Please note that this subsection includes re-listed methodologies from Chapter 3–5 and one new method (iron chelation) with a schematic representation. For schematic representation of re-listed methodologies, if applicable, please refer to Chapter 3 and 4 – Section 3.5 or 4.5.

7.5.1. *Chemistry*

General Information. All the reagents and solvents were reagent grade purchased from various vendors (Acros Organics, Sigma-Aldrich, and Alfa Aesar, USA) with a minimum purity of 95% and were used

without further purification. Melting points (mp) were determined using a Fisher-Johns apparatus and are uncorrected. Reaction progress was monitored by UV using thin-layer chromatography (TLC) using Merck 60F254 silica gel plates. Column chromatography was performed with Merck silica gel 60 (230−400 mesh) with 5:1 EtOAc:MeOH as the solvent system unless otherwise specified. Proton (^{1}H NMR) and carbon (^{13}C NMR) spectra were performed on a Bruker Avance (at 300 and 75 MHz; respectively) spectrometer using DMSO-d_6. Coupling constants (*J* values) were recorded in hertz (Hz) and the following abbreviations were used to represent multiplets of NMR signals: s = singlet, d = doublet, t = triplet, m = multiplet, br = broad. Carbon multiplicities (C, CH, CH_2 and CH_3) were assigned by DEPT 90/135 experiments. High-resolution mass spectrometry (HRMS) was determined using a Thermo Scientific Q-Exactive Orbitrap mass spectrometer (positive mode, ESI), Department of Chemistry, University of Waterloo. Compound purity (roughly 95% or over) was determined using an Agilent 1100 series HPLC equipped with an analytical column (Agilent Zorbax Eclipse XDB-C8 column, 4.6 x 150 mm, 5 μm particle size) running 50:50 Water:ACN with 0.1% TFA at a flow rate of 1.0-1.5 mL/min or an Agilent 6100 series single quad LCMS equipped with an Agilent 1.8 μm Zorbax Eclipse Plus C18 (2.1 x 50 mm) running 50:50 Water:ACN with 0.1% FA with a flow rate of 0.5mL/min. All the final compounds exhibited ≥ 95% purity.

General procedure for the synthesis of 2,4-dichloro[3,2-*d*]pyriopyrimidine.[289, 323] In a 250 mL RBF, 5 g of pyrido[3,2*d*]pyrimidin-2,4-diol (30.67 mmol) was suspended in 25 mL of anhydrous toluene and allowed to stir on an ice bath. To this, 5 eq. of $POCl_3$ (153.37 mmol) was added in small aliquots followed by the slow addition of 5 eq. of DEA (153.37 mmol). The solution was kept on the ice bath for 10 min before moving to room temperature and allowed to stir for 1 h prior to refluxing at 105–110 °C for 14–16 h. Upon cooling to room temperature, the reaction mixture was added in small aliquots to a double-ice-water bath while stirring. The quenching solution was left stirring at room temperature for 5 h before vacuum filtering the yellowish-grey precipitate. The precipitate was stirred for 1 h in a saturated $NaHCO_3$ solution and then was re-filtered. This neutralization process was carried out 2–3 times until the bicarbonate solution maintains a neutral to slight basic pH. The final precipitate was dissolved in DCM and purified by a silica gel column chromatography using 100% DCM as the eluent to afford white to light grey solid.

2,4-Dichloropyrido[3,2-*d*]pyrimidine. Yield: 65% (3.97 g, 19.94 mmol); Mp 197–199 °C. ^{1}H NMR (300 MHz, DMSO-d_6) δ 9.17 (d, J = 4.1 Hz, 1H), δ 8.44 (d, J = 8.4 Hz, 1H), δ 8.10 (dd, J = 8.6, 4.1 Hz, 1H). LRMS (ESI) m/z calcd for $C_7H_4Cl_2N_3$ $[M + H]^+$ 199.97, found 199.96.

General procedure for the synthesis of 2-chloro-*N*-substituted-pyrido[3,2-*d*]pyrimidin-4-amines.[303, 305] To a 30 mL solution of ethanol in a 100 mL round-bottom flask on ice, 5 g of 2,4-dichloropyrido[3,2-*d*]pyrimidine (25.13 mmol) was added followed by slow addition of 1.3 eq. (32.66 mmol) of the corresponding primary amine. Contents were stirred on an ice bath while 2.0 eq. of diisopropylethylamine (DIPEA, 50.25 mmol) was added in drop wise fashion. The solution was then heated at 80–85 °C under reflux for 3–4 h. The reaction contents were cooled to room temperature and precipitated residues were vacuum-filtered with ethyl acetate (EtOAc) rinses. The organic supernatant was concentrated in vacuo followed by two rounds of liquid-liquid extraction using EtOAc and saturated brine solution (40–50 mL each respectively). The combined organic layers were dried over MgSO4, evaporated in vacuo and purified (1–2 times) using silica gel column chromatography with 5:1 EtOAc:MeOH as the elution solvent. Final compounds were white to beige solids with yields ranging from 82–84%.

2-Chloro-*N*-(3,4-dimethoxyphenethyl)pyrido[3,2-*d*]pyrimidin-4-amine (88). Yield: 84% (1.45 g, 4.22 mmol); Mp 156–158 °C. ^{1}H NMR (300 MHz, DMSO-d_6) δ 8.96 (br s, 1H), δ 8.73 (s, 1H), δ 7.99 (d, J = 8.6 Hz, 1H), δ 7.78 (dd, J = 8.6, 4.3 Hz, 1H), δ 6.83–6.71 (m, 3H), δ 3.74–3.67 (m, 8H), δ 2.84 (t, J = 7.4 Hz, 2H). LRMS (ESI) m/z calcd for $C_{17}H_{18}ClN_4O_2$ $[M + H]^+$ 345.10, found 345.11.

2-Chloro-*N*-phenethylpyrido[3,2-*d*]pyrimidin-4-amine (89). Yield: 82% (1.17 g, 4.12 mmol). ^{1}H NMR (300 MHz, DMSO-d_6) δ 9.02 (br s, 1H), δ 8.74 (s, 1H),, δ 7.99 (d, J = 8.8 Hz, 1H), δ 7.78 (dd, J = 8.5, 4.2 Hz, 1H), δ 7.28–7.13 (m, 5H), δ 3.68 (q, J = 6.1 Hz, 2H), δ 2.91 (t, J = 7.2 Hz, 2H). LRMS (ESI) m/z calcd for $C_{15}H_{14}ClN_4$ $[M + H]^+$ 285.08, found 285.09.

General procedure for the synthesis of N^4-substituted-N^2-alkyl-pyrido[3,2-*d*]pyrimidin-2,4-diamines.[299, 313] In a 50 mL pressure vial (PV), 0.25 g of 2-chloro-*N*-(3,4-dimethoxyphenethyl)pyrido[3,2-*d*]pyrimidin-4-amine or 2-chloro-*N*-phenethylpyrido[3,2-*d*]pyrimidin-4-amine (~ 0.73–0.88 mmol) was combined with 2 eq. (~ 1.46–1.76 mmol) of primary amine (*n*-propyl-, isopropyl- or cyclopropylamine) or dimethylamine then dissolved in 5 mL of 1,4-dioxane followed by the addition of 3 eq. of DIPEA (~ 2.19–2.64 mmol). Pressure vial was sealed and stirred in an oil bath at 150–155 °C for 2 h. Upon completion and cooling to room temperature, the reaction mixture was diluted with ~ 40 mL of EtOAc and washed with brine solution (25 mL x 2). The combined aqueous layer was washed with ~ 25 mL of EtOAc. The combined EtOAc layers were dried over $MgSO_4$ before removing EtOAc in vacuo to yield a solid product that was purified by silica gel column chromatography using 5:1 EtOAc:MeOH as the eluent to afford pale yellow to brown solids yielding at 71–78%.

N^4-(3,4-Dimethoxyphenethyl)-N^2-propylpyrido[3,2-*d*]pyrimidine-2,4-diamine (90). Yield: 76% (0.40 g, 1.10 mmol); mp 121–123 °C. ^{1}H NMR (300 MHz, DMSO-d_6) δ 8.22 (dd, J = 4.8, 1.2 Hz, 1H), δ 7.85 (br s, 1H), δ 7.53 (br s, 1H), δ 7.43 (dd, J = 8.4, 4.1 Hz, 1H), δ δ 6.84–6.72 (m, 4H), δ 3.67–3.61 (m, 8H), δ 3.30–3.24 (m, 2H), δ 2.82 (t, J = 7.3 Hz, 2H), δ 1.46 (sextet, J = 7.2 Hz, 2H), δ 0.84 (t, J = 7.4 Hz, 3H). HRMS (ESI) m/z calcd for $C_{20}H_{26}N_5O_2$ $[M + H]^+$ 368.2008, found 368.2081. Purity: 99.6%

N^4-(3,4-Dimethoxyphenethyl)-N^2-isopropylpyrido[3,2-*d*]pyrimidine-2,4-diamine (91). Yield: 73% (0.39 g, 1.06 mmol); mp 127–129 °C. ^{1}H NMR (300 MHz, DMSO-d_6) δ 8.22 (dd, J = 4.8, 1.2 Hz, 1H), δ 7.86 (brs, 1H), δ 7.53 (br s, 1H), δ 7.44 (dd, J = 8.4, 4.1 Hz, 1H), δ 6.84–6.72 (m, 3H), δ 6.57 (br s, 1H), 4.16–4.09 (m, 1H), δ 3.67–3.61 (m, 8H), δ 2.82 (t, J = 7.3 Hz, 2H), δ 1.12 (d, J = 6.5 Hz, 6H). HRMS (ESI) m/z calcd for $C_{20}H_{26}N_5O_2$ $[M + H]^+$ 368.2008, found 368.2081. Purity: 98.4%

N^2-Cyclopropyl-N^4-(3,4-dimethoxyphenethyl)pyrido[3,2-*d*]pyrimidine-2,4-diamine (92). Yield: 71% (0.38 g, 1.03 mmol); mp 117–119 °C. ^{1}H NMR (300 MHz, DMSO-d_6) δ 8.25 (dd, J = 4.8, 1.2 Hz, 1H), δ 7.94 (br s, 1H), δ 7.59 (br s, 1H), δ 7.45 (dd, J = 8.4, 4.1 Hz, 1H), δ 6.94 (br s, 1H), δ 6.84–6.72 (m, 3H), δ 3.68–3.65 (m, 8H), δ 2.88–2.80 (m, 3H), δ 0.63–0.59 (m, 2H), δ 0.48–0.46 (m, 2H). HRMS (ESI) m/z calcd for $C_{20}H_{24}N_5O_2$ $[M + H]^+$ 366.1852, found 366.1927. Purity: 99.4%

N^4-(3,4-Dimethoxyphenethyl)-N^2,N^2-dimethylpyrido[3,2-*d*]pyrimidine-2,4-diamine (93). Yield: 77% (0.40 g, 1.12 mmol). ^{1}H NMR (300 MHz, DMSO-d_6) δ 8.24 (dd, J = 4.2, 1.5 Hz, 1H), δ 8.03 (br s, 1H), δ 7.57 (dd, J = 8.5, 1.5 Hz, 1H), δ 7.44 (dd, J = 8.5, 4.2 Hz, 1H), δ 6.83–6.70 (m, 3H), δ 3.67–3.62 (m, 8H), δ 3.14 (s, 6H), δ 2.82 (t, J = 7.2 Hz, 2H). HRMS (ESI) m/z calcd for $C_{19}H_{24}N_5O_2$ $[M + H]^+$ 354.1852, found 354.1924. Purity: 97.3%

N^4-Phenethyl-N^2-propylpyrido[3,2-*d*]pyrimidine-2,4-diamine (94). Yield: 76% (0.41 g, 1.34 mmol); Mp 132–134 °C. ^{1}H NMR (300 MHz, DMSO-d_6) δ 8.22 (dd, J = 4.1, 1.6 Hz, 1H), δ 7.95 (br s, 1H), δ 7.54 (br s, 1H), δ 7.44 (dd, J = 8.4, 4.1 Hz, 1H), δ 7.29–7.14 (m, 5H), δ 6.78 (br s, 1H), δ 3.62 (q, J = 7.5 Hz, 2H), δ 3.23–3.20 (m, 2H), δ 2.89 (t, J = 7.3 Hz, 2H), δ 1.48 (sextet, J = 7.2 Hz, 2H), δ 0.84 (t, J = 7.4 Hz, 3H). ^{13}C NMR (75 MHz, DMSO-d_6) δ 159.32, δ 146.53, δ 142.32, δ 141.98, δ 139.52, δ 131.99, δ 131.41, δ 128.60, δ 128.30, δ 127.53, δ 126.4, δ 42.67, δ 41.39, δ 34.63, δ 22.34, δ 11.53. HRMS (ESI) m/z calcd for $C_{18}H_{22}N_5$ $[M + H]^+$ 308.1797, found 308.1869. Purity: 99.4%

N^2-Isopropyl-N^4-phenethylpyrido[3,2-*d*]pyrimidine-2,4-diamine (95). Yield: 76% (0.41 g, 1.34 mmol). ^{1}H NMR (300 MHz, DMSO-d_6) δ 8.23 (dd, J = 4.1, 1.6 Hz, 1H), δ 7.99 (br s, 1H), δ 7.55 (br s, 1H), δ 7.44 (dd, J = 8.4, 4.1 Hz, 1H), δ 7.30–7.14 (m, 5H), δ 6.60 (br s, 1H), δ 4.19–4.08 (m, 1H), δ 3.63 (q, J = 7.5 Hz, 2H), δ 2.89 (t, J = 7.3 Hz, 2H), δ 1.13 (d, J = 6.5 Hz, 6H). HRMS (ESI) m/z calcd for $C_{18}H_{22}N_5$ $[M + H]^+$ 308.1797, found 308.1869. Purity: 99.7%

N^2-Cyclopropyl-N^4-phenethylpyrido[3,2-*d*]pyrimidine-2,4-diamine (96). Yield: 72% (0.39 g, 1.27 mmol). ^{1}H NMR (300 MHz, DMSO-d_6) δ 8.26 (dd, J = 4.1, 1.6 Hz, 1H), δ 8.02 (br s, 1H), δ 7.55 (br s, 1H), δ 7.46 (dd, J = 8.4, 4.1 Hz, 1H), δ 7.27–7.16 (m, 5H), δ 6.93 (br s, 1H), δ 3.63 (q, J = 7.5 Hz, 2H), δ 2.89 (t, J = 7.3 Hz, 2H), δ 2.81–2.77 (m, 1H), δ 0.63–0.59 (m, 2H), δ 0.49–0.46 (m, 2H). HRMS (ESI) m/z calcd for $C_{18}H_{20}N_5$ $[M + H]^+$ 306.1640, found 306.1711. Purity: 99.8%

N^2,N^2-Dimethyl-N^4-phenethylpyrido[3,2-*d*]pyrimidine-2,4-diamine (97). Yield: 78% (0.40 g, 1.37 mmol). ^{1}H NMR (300 MHz, DMSO-d_6) δ 8.25 (dd, J = 4.2, 1.5 Hz, 1H), δ 8.09 (br s, 1H), δ 7.57 (dd, J = 8.5, 1.5 Hz, 1H), δ 7.44 (dd, J = 8.5, 4.2 Hz, 1H), δ 7.26–7.16 (m, 5H), δ 3.63 (q, J = 5.6 Hz, 2H), δ 3.14 (s, 6H), δ 2.90 (t, J = 7.2 Hz, 2H). HRMS (ESI) m/z calcd for $C_{17}H_{20}N_5$ $[M + H]^+$ 294.1640, found 294.1712. Purity: 99.8%

7.5.2. *Biological Screening*

7.5.2.1. *Human Cholinesterase (hChE) Assay*[299, 313]

The inhibition profile of quinazoline derivatives was evaluated using the Ellman (DTNB) reagent.[315] Human AChE and BuChE enzymes were obtained from Sigma-Aldrich, St. Louis, MO, USA (AChE product number C0663 and BuChE product number B4186 respectively). The cholinesterase inhibitors tacrine (item number 70240, Cayman Chemical Company, Ann Arbor, MI), donepezil (product number D6821, Sigma-Aldrich, St. Louis, MO), galantamine (product number G1660, Sigma-Aldrich, St. Louis, MO) and rivastigmine (product number SML0881, Sigma-Aldrich, St. Louis, MO) were used as reference agents. Quinazoline derivative stock solutions were prepared in DMSO (maximum 1% v/v in final wells) and diluted in buffer solution (50 mM Tris.HCl, pH 8.0, 0.1 M NaCl, 0.02 M $MgCl_2.6H_2O$). Then 160 µL of 5,5'-dithiobis(2-nitrobenzoic acid) (1.5 mm DTNB), 50 µL of *h*AChE (0.22 U/mL in 50 mM Tris.HCl, pH 8.0, 0.1% w/v bovine serum albumin, BSA) or 50 µL of *h*BuChE (0.12 U/mL in 50 mM Tris.HCl, pH 8.0, 0.1% w/v BSA) were added to 96-well plates after which 10 µL each of quinazoline derivatives (final concentration range 0.1–50 µM) were added and incubated for 5 min. Then 30 µL of either acetylthiocholine iodide (15 mM AThCl prepared in ultra pure water) or *S*-butyrylthiocholine iodide (15 mM BThCI prepared in ultra pure water) were added. The absorbance was measured at different time intervals (0, 60, 120, 180, 240 and 300 s) using a wavelength of 412 nm. The inhibitory concentration (IC_{50} values) was calculated from the concentration–inhibition dose response curve on a logarithmic scale. The

results were expressed as average values based on two to three independent experiments run in triplicate measurements.

7.5.2.2. *Amyloid-β (Aβ) Aggregation Assay*[317]

The ability of quinazoline-based derivatives to inhibit Aβ-aggregation kinetics was determined using a ThT-binding fluorescence assay. These assays were conducted in Costar, black-surround, clear-bottom 384-well plates with frequent shaking (30 sec. of linear shaking at 730 cpm every 5 minutes) and constant heating at 37 °C for 24 h. The ThT excitation/emission was measured at 440 nm/490 nm and readings were taken every 5 minutes using a BioTek Synergy H1 microplate reader. Quinazoline stock solutions were prepared in DMSO and diluted to 10x in 215 mM phosphate buffer at pH 7.4. Abeta.HFIP samples (Aβ40 or Aβ42, rPeptide, Bogart, USA) were dissolved in 1% ammonium hydroxide, sonicated at room temperature for 5 minutes then diluted to 50 μM in 215 mM phosphate buffer (pH 7.4). A 15 μM ThT stock solution was prepared with 50 mM glycine and adjusted to pH 7.4. The assay was carried out by adding 44 μL ThT, 20–35 μL buffer, 1 μL DMSO (for background and controls only) followed by the addition of 8 μL of 10x compound dilutions (1–25 μM concentration range). An end point reading was conducted to evaluate potential test compound interference with ThT-fluorescence before adding 8 μL of Aβ40 or Aβ42 stock solutions (5 μM final concentration). Plates were sealed with a transparent plate film before initiating the assay. RFU values were corrected for ThT-interference before calculating end point percent inhibitions or IC_{50} values and obtaining the aggregation kinetic plots. Data presented was an average of triplicate reading for two-three independent experiments.

7.5.2.3. *TEM Assay and Imaging*[142, 190, 207, 317]

In Costar 96-well, round-bottom plates were added 80 μL of 215 mM phosphate buffer, 20 μL of 10x test compound dilutions (250 μM – prepared in the same way as for the ThT assay) and 100 μL of 50 μM

Aβ40 or Aβ42 respectively. For the control wells, 2 μL of DMSO and 18 μL of phosphate buffer was added. Final Aβ: test compound ratio was 1:1 (25 μM). Plates were incubated on a Fisher plate incubator set to 37 °C and the contents were shaken at 730 cpm for 24 h. To prepare the TEM grids, ~ 20 μL droplet was added using a disposable Pasteur pipette over the formvar-coated copper grids (400 mesh). Grids were air-dried for about 3 h before adding two droplets (~ 40 μL, using a disposable Pasteur pipette) of ultra-pure water and using small pieces of filter paper to wash out precipitated buffer salts. After air-drying for ~ 15-20 min, the grids were negatively stained by adding a droplet (~ 20 μL, using a disposable Pasteur pipette) of 2% phosphotungstic acid (PTA) and immediately after the grids were dried using small pieces of filter paper. Grids were further air-dried overnight. The scanning was carried out using a Philips CM 10 transmission electron microscope at 60 kV (Department of Biology, University of Waterloo) and micrographs were obtained using a 14-megapixel AMT camera.

7.5.2.4. *Iron Chelation Assay*[319]

The ability of select pyridopyrimidines to chelate iron was utilized as a measure of overall chelation capacity and the effectiveness of the scaffold as a chelating center. This was determined using the ferrozine (Sigma-Aldrich, USA) based competitive colorimetic assay. Test compounds were initially dissolved in anhydrous methanol to 10 mM and diluted down to 105 μM using 100 mM tris buffer (pH 7.4). Then 95 μL of test compound solutions (50 μM final concentration) were added to clear 96-well plates, followed by a 10 μL aliquot of iron-(II)-sulphate ($FeSO_4 \cdot 7H_2O$) stock solution (from 800 μM stock solution prepared in methanol). After a 5-minute incubation period at room temperature, 95 μL ferrozine solution (from 210 μM stock solution prepared in tris buffer) was added. After incubating at room temperature for 30 minutes the absorbance was measured at 562 nm and subtracted from compound blanks (95 μL of compound solutions + 105 μL of tris buffer) and compared to the ferrozine-only positive control (95 μL of tris buffer + 10 μL of iron sulphate + 95 μL of ferrozine). The results obtained were compared with known iron chelators clioquinol (50 μM) and desferoxamine (50 μM). The results were reported as average % iron-chelation ± SD in triplicate measurements based on two independent experiments.

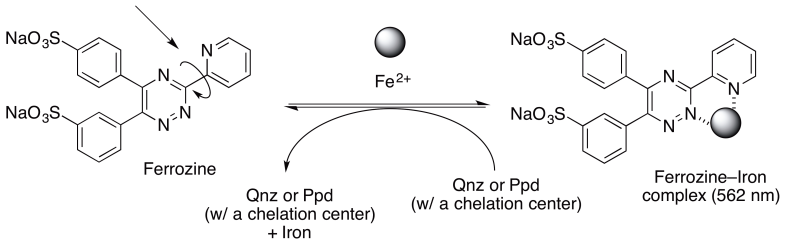


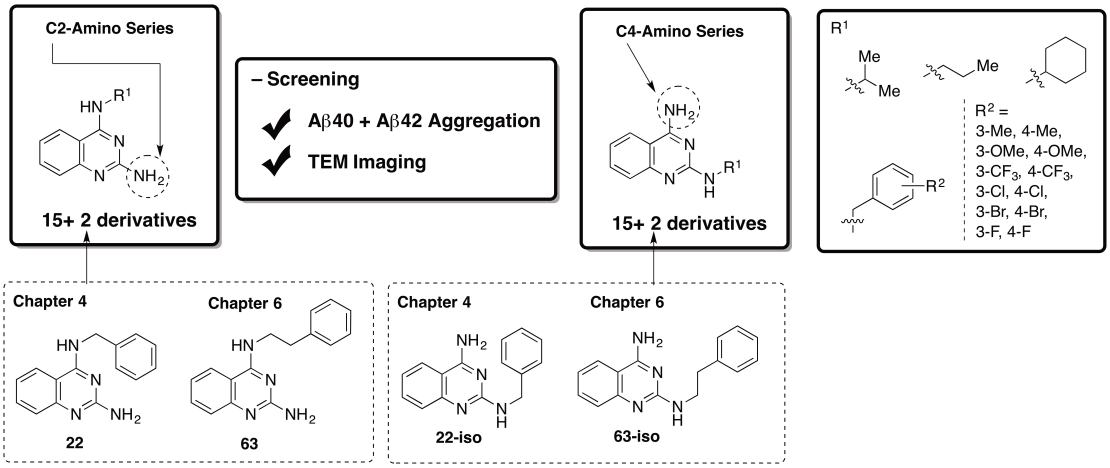
Figure 85: Principles of the ferrozine-based iron chelation assay.

7.5.3. *Computational Chemistry*[299, 313, 317, 324]

The molecular docking studies were conducted using Discovery Studio 4.0 (Structure-Based-Design program) from BIOVIA Inc. San Diego, USA. Select quinazolines derivatives were built and minimized using the *small molecules* module in Discovery Studio. X-ray coordinates of human cholinesterases were obtained from the protein data bank (*h*AChE PBD ID: 1B41 and *h*BuChE PDB ID: 1P0I) and prepared using the *macromolecules* module in Discovery Studio. Ligand binding sites were defined by selecting a 12 Å radius sphere for AChE and 15 Å radius sphere for BuChE. The molecular docking was performed using the *receptor-ligand interactions* module in Discovery Studio. The LibDock algorithm was used to find the most appropriate binding modes for select quinazoline derivatives using CHARMm force field. The docked poses obtained were ranked based on the LibDock scores and were analyzed by evaluating all the polar and nonpolar interactions. For Amyloid-β docking studies, the NMR solution structure of Aβ fibrils were obtained from the protein data bank (PDB ID: 2LMN). Aβ dimer and Aβ fibril assemblies were built using the *macromolecules* module in Discovery Studio. Ligand binding site was defined by selecting a 15 Å radius sphere for both Aβ assemblies. Molecular docking was performed using the *receptor-ligand interactions* module in Discovery Studio, where the LibDock algorithm was used to find the most appropriate binding modes for select quinazoline derivatives using CHARMm force field. The docked poses obtained were ranked based on the LibDock scores and were analyzed by evaluating all the polar and nonpolar interaction.

CHAPTER 8

• Development and Evaluation of Isomeric Monosubstituted 2,4-diaminoquinazolines as Aβ Aggregation Inhibitors •



* Chapter banner

8.1. Introduction

The notion of regioisomeric comparison was examined in Chapters 4, 5 and 6. The SAR data from these 4 isomer pairs (**22** vs. **22-iso**, **33** vs. **33-iso**, **61** vs. **61-iso** and **63** vs. **63-iso**) showcased interesting activities and selectivities with respect to both ChE and Aβ targeting.

With the enhanced value of the quinazolin-2,4-diamine scaffold in dual Aβ targeting , this Chapter sets to further expand on the acquired SAR data, of the C2-amino and C4-amino series, by developing and assessing 15 isomer pairs based on the quinazoline scaffold. While initial derivatives were based on unsubstituted benzyl or phenethyl moieties, the library within this Chapter explores three aliphatic moieties (*n*-propyl, *i*-proply, and cyclohexyl) and a collection of substituted benzyl groups (EDGs and EWGs) – see Chapter banner above.

Generally, all synthetic approaches and mechanisms here have been previously discussed in Chapters 3–6. A brief summary is provided prior to the listing of experimental data and methodology.

8.2. Hypothesis

With respect to these series, the focus is on modulating Aβ aggregation by evaluating the selectivity factor regarding the placement of the amino ($–NH_2$) group. With the benzyl moiety in Chapter 4, the amino placement at the C4-position (**22-iso**) benefited both Aβ40/42 targeting, while the phenethyl moiety in Chapter 6 only benefited Aβ40 targeting with a C2-amino placement (**63**) and benefited Aβ42 targeting with a C4-amino placement (**63-iso**).

While no clear hypothesis can be outlined, the safe prediction is that the smaller derivatives (i.e featuring either the isopropyl or propyl chains) are likely to provide no inhibitory capacity toward Aβ40/42. In addition, past chapters showcased that chlorine could serve as an anti-fibrillation moiety, so it was proposed to observe the effect of the halogen-based benzyl groups here.

8.3. Results and Discussions

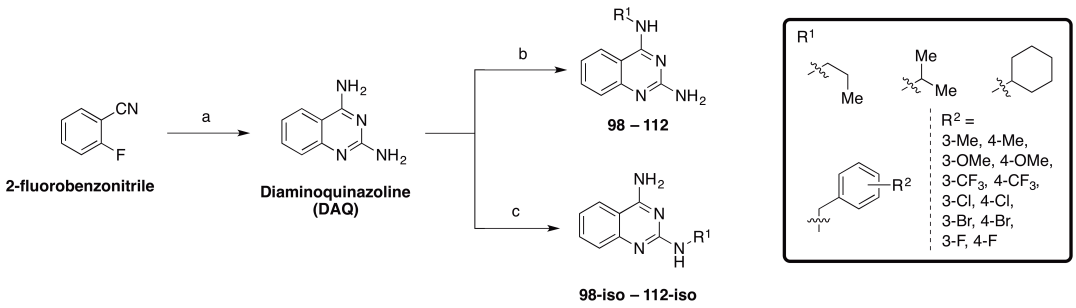
The proceeding sub-chapter briefly highlights previously-established routes to target derivatives. Biological assessments in the amyloid-β aggregation assay (to obtain IC_{50} values and/or investigation aggregation kinetics) were conducted. Aggregate load is corroborated via TEM in amyloid morphology screening. Computational studies are performed in the ChE X-ray structures and amyloid models to evaluate the acquisitioned SAR data.

8.3.1. *Synthesis*

As initially described in Chapter 4, the synthetic schemes pertaining to this chapter revolve around the DAQ starting material. The generation of DAQ was accomplished by condensing 2-fluorobenzonitrile with guanidine carbonate and the selective alkylation of **DAQ** at the C4-position, generating the C2-amino series, was accomplished by utilizing sodium hydride, at equal equivalence with **DAQ**, to selectively deprotonate the C4-amino group before nucleophilic attack on the aryl bromide. For selective alkylation at the C2-

position on the other hand, an inorganic quenching base was used and the more nucleophilic C2-amino group acted upon the aryl bromide, without deprotonation, to displace the halogen (Scheme 23).[291, 317]

Scheme 23[a]



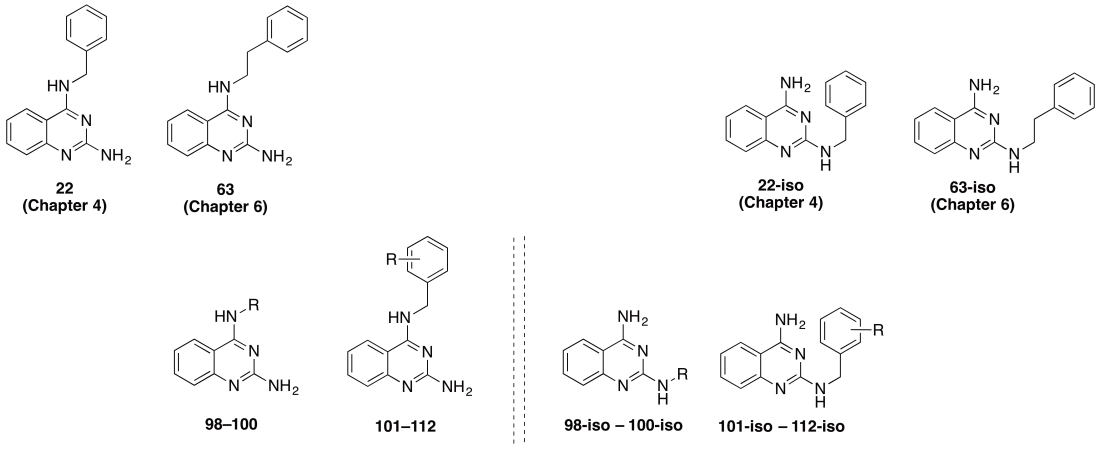
[a]**Reagents and conditions:** Synthetic routes toward isomeric quinazoline-2,4-diamine derivatives **98–112.** (a) Guanidine carbonate, DMA, 150–155 °C, 14–16 h; (b) Sodium hydride, DMSO, benzyl bromide, 0 °C–r.t., 14 h; (c) DMA, potassium or cesium carbonate, benzyl bromide 80–85 °C, 5 h.

8.3.2. *Amyloid-β Aggregation*

The ability of the 2,4-diaminoquinazolines (**98**–**112** and their respective regioisomers) to modulate the aggregation kinetics of amyloid-β was assessed using the ThT-binding method described earlier in Chapter 3 (Table 16).

Quite interestingly, the data revealed that C2-amino quinazolines were more active toward Aβ40 compared to their C4-amino regioisomers, while toward Aβ42, the observation shifted in favour of the C4-amino quinazolines – regardless of the nature of the alkyl or aryl group attached. The sole deviant from these observations is the **22**/**22-iso** pair, considering that **22-iso** was more potent toward both Aβ40/42 compared to **22**. Overall, all derivatives were capable of targeting one or both Aβ species, with four surpassing curcumin's inhibitory potential toward Aβ42 and nine equaling or surpassing resveratrol's inhibitory potential toward Aβ40.

Table 16: Amyloid-β (Aβ40/42) inhibition data for 2,4-diaminoquinazolines (**98**–**112**) and their regioisomers.



C2-amino Derivative	Amyloid-β IC_{50} (μM) [a]		R-Group	Amyloid-β IC_{50} (μM) [a]		C4-amino Derivative
	Aβ40	Aβ42		Aβ40	Aβ42	
98	15.0 ± 1.3	NA	*n*-Pr	26%	10%	**98-iso**
99	10.2 ± 1.0	NA	*i*-Pr	NA	15%	**99-iso**
100	13.6 ± 1.3	37%	Cyclohexylmethyl	18%	46%	**100-iso**
101	3.7 ± 0.4	10%	3-Me	39%	48%	**101-iso**
102	4.0 ± 0.4	41%	4-Me	13.1 ± 1.2	22.5 ± 2.3	**102-iso**
103	20.6 ± 2.1	NA	3-OMe	20%	39%	**103-iso**
104	1.1 ± 0.1	32%	4-OMe	6.8 ± 0.5	47%	**104-iso**
105	3.6 ± 0.4	21.0 ± 1.8	3-CF_3	12.5 ± 1.3	13.9 ± 1.5	**105-iso**
106	2.0 ± 0.1	37%	4-CF_3	2.3 ± 0.3	5.3 ± 0.4	**106-iso**
107	1.9 ± 0.1	32%	3-Cl	5.9 ± 0.3	13.4 ± 1.2	**107-iso**
108	0.6 ± 0.1	43%	4-Cl	0.9 ± 0.1	8.1 ± 0.9	**108-iso**
109	0.6 ± 0.1	22.3 ± 2.2	3-Br	1.5 ± 0.2	2.8 ± 0.3	**109-iso**
110	0.08 ± 0.01	14.8 ± 1.5	4-Br	1.7 ± 0.2	1.7 ± 0.2	**110-iso**
111	2.9 ± 0.3	23%	3-F	11.3 ± 0.9	14.8 ± 1.5	**111-iso**
112	3.1 ± 0.3	38%	4-F	37%	46%	**112-iso**
⬇ ⬇	– Previously reported –					⬇ ⬇
22	4.8 ± 1.1	NA	*Chapter 4*	2.2 ± 0.5	8.4 ± 1.1	**22-iso**
63	8.2 ± 2.0	37%	*Chapter 6*	14.9 ± 1.9	50%	**63-iso**
Curcumin	3.3 ± 0.45	9.9 ± 0.4	–	1.1 ± 0.1	15.3 ± 1.9	**Resveratrol**

Notes: [a] IC_{50} values are an average ± SD of triplicate readings based on two to three independent experiments. NA = Not active. Percent inhibition (P.I) indicates level of inhibition at highest concentration tested (25 μM).

Starting with the aliphatic additions to the DAQ scaffold, increasing the sterics and size (from *n*-Pr to *i*-Pr to cyclohexylmethyl) benefited Aβ42, regardless of placement, although C4-amino derivatives (**98-iso** – **100-iso**) were more active. Toward Aβ40, C2-amino derivatives (**98**–**100**) were roughly equipotent at an

IC_{50} of 13 μM, while their regioisomers were considerably weaker – maxing 26% inhibition at 25 μM for the *n*-Pr group. Compared to their aromatic counterparts (**22**/**22-iso**), **100**/**100-iso** were generally less active toward Aβ40/42, with the exception of **100** demonstrating Aβ42 activity, when **22** did not.

Transitioning to the substituted benzyl-based derivatives, the presence of either a *para*- or a *meta*-methyl group on a C4-placed benzyl group (**101–102**, IC_{50} ~ 4 μM) did not impact Aβ40 inhibition, compared to the unsubstituted-benzyl derivative (**22**, IC_{50} ~ 5 μM). The addition; however, did impact Aβ42 inhibition, taking it from no activity with **22** to 10% with **101** and then to 41% with **102**. When methyl addition was done on a C2-placed benzyl group, both Aβ40/42 activities dropped compared to **22-iso**, although the impact was greater seen with *meta*-methyl (**101**). Enhancing the EDG properties of the benzyl group with a methoxy group reduced the inhibitory profiles when placed at the *meta*-position, regardless of isomeric identity (i.e.: **103** < **101** and **22** in addition to **103-iso** < **101-iso** and **22-iso**). However, *para*-placement of the methoxy group (**104** and **104-iso**) improved Aβ40 activity by 4-fold and 2-fold; respectively, compared to *para*-methyl-based derivatives (**102** and **102-iso**). That observation did not extend to Aβ42 activity as **104** ranked between **22** (NA) and **102** (41%), while **104-iso** (47%) was weaker than both **22-iso** (IC_{50} ~ 8 μM) and **102-iso** (IC_{50} ~ 23 μM). The change from methyl (**101**/**101-iso** and **102**/**102-iso**) to trifluoromethyl (**105**/**105-iso** and **106**/**106-iso**) was unanimously positive, or at least elicited similar inhibitory outcomes. Of notable mention, **106-iso** was the first derivative to showcase dual potency toward Aβ40/42 with IC_{50}'s of ~ 2 and 5 μM; respectively. These positive turnouts transitioned to the comparison with **22** and **22-iso**, although that excluded **105-iso** (*meta*-CF_3) as it was less active compared to **22-iso**.

The introduction of *meta*- or *para*-positioned halides (bromo, chloro or fluoro) to the C4-placed benzyl moiety, as in **107**–**112**, resulted in unanimous Aβ40/42 inhibitory improvements when compared to **22**. The regioisomers **107-iso** – **112-iso**, on the other hand, showcased mixed outcomes on both Aβ40/42 fronts when compared to **22-iso**. Focusing in on the C4-placed benzyl halides (**107**–**112**), with respect to both Aβ40/42, halide ranking was as follows: Br (*para* > *meta*) > Cl (*para* > *meta*) > F (*para* ~ *meta*). Of noteworthy mention, derivative **110** (*para*-Br) was the most potent Aβ40 inhibitor in not only this Chapter but amongst all derivatives tested. At 80 nM, it was 14-fold more potent compared to resveratrol and 60-fold more potent compared to its unsubstituted counterpart (**22**). In addition, it was the most active Aβ40

inhibitor (IC_{50} ~ 15 μM) in the C2-amino series of derivatives (**98-112**) – Which in itself, points to the strong selectivity of these isomer for Aβ40 >> Aβ42. In second place, derivatives **108** (*para*-Cl) and **109** (*meta*-Br) share an IC_{50} of 0.6 μM toward Aβ40, although both were almost as effective toward Aβ42 as well (IC_{50} ~ 22-29 μM). Shifting toward the C2-placed benzyl halides (**107-iso** – **112-iso**), with respect to both Aβ40/42, halide ranking was almost similar: Br (*para* ~ *meta*) > Cl (*para* > *meta*) > F (*para* < *meta*). Of noteworthy mention, derivative **110-iso** (*para*-Br) was the most potent and dual Aβ inhibitor (IC_{50} ~ 2 μM), while **108-iso** (*para*-Cl) was the most potent Aβ40 inhibitor (IC_{50} ~ 1 μM) in the C4-amino series.

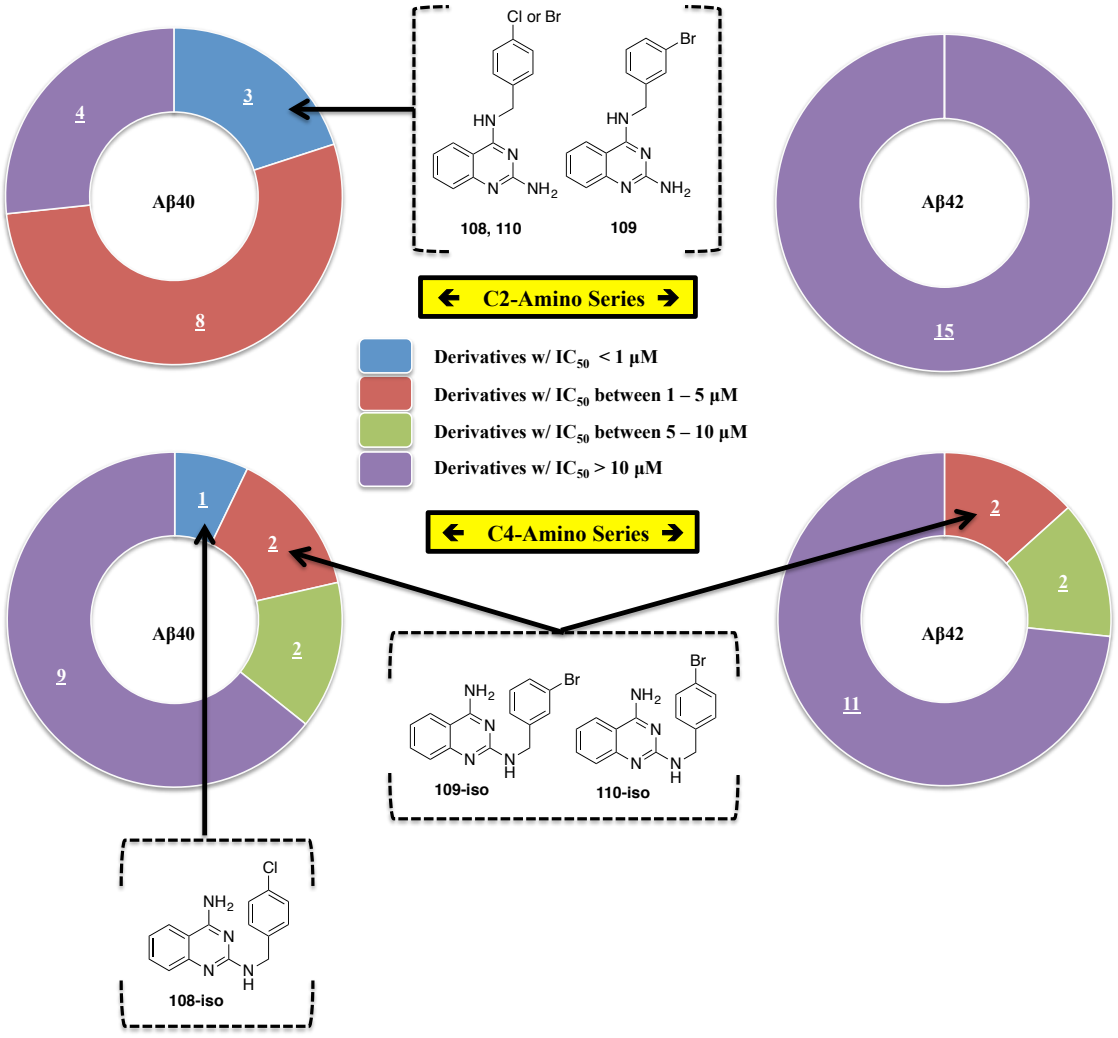


Figure 86: Amyloid-β metrics for thirty 2,4-diaminoquinazolines (**98-112**) including their regioisomers.

In summary, the expansion into the regioisomeric investigation with respect to Aβ inhibition was quite interesting. The initial data obtained from Chapter 4 (**22**/**22-iso**) and Chapter 6 (**63**/**63-iso**) led to the utilization of substituted benzyl (and not phenethyl) groups and the unanimous observation of preferred targeting (C2-amino derivatives preferably targeted Aβ40, while C4-amino derivatives preferably targeted Aβ42) was unexpected but intriguing. Overall, aliphatic groups were not favourable in terms of Aβ inhibition and in a very broad sense (with some expectations), *para*-substituted benzyl groups were more active compared to *meta*-substituted benzyl groups. Best results, on both Aβ40/42 fronts, were observed with 3- and 4-bromobenzyl groups (Figure 86).

The aggregation kinetic assessment of Aβ40 with or without series-leading derivatives is showcased in Figure 87. As observed in Panel A–D, derivatives **109/109-iso** and **110/110-iso** exhibited concentration-dependent inhibition of Aβ40 aggregation while showcasing multi-mode anti-aggregation characteristics. Both C2-amino derivatives (**109** and **110**; Panels A and C) managed to delay the onset of aggregation 2-fold (t = 20 h. vs. 10 h for the Aβ40 control), while reducing the rate of aggregation. As very potent inhibitors, both kinetic plots showcased no plateau phase, which was indicative of ultra low fibril concentrations at the end of the 24 h incubation period. The C4-amino isomers (Panels B and D), on the other hand, did not showcase a delay in the aggregation process (at least at the 1 and 5 μM concentrations), but did showcase a reduction in the rates of aggregation and overall fibril load at the end of the 24 h incubation period. Interestingly, at the 5:1 ratio of **110-iso**: Aβ40, the complete aggregation process was halted. Comparing **109-iso** and **110-iso**, it would appear that the placement of the bromine impacted the mode of inhibition across the concentration range – With a *meta*-bromine, monomeric stabilization was attainable with increasing concentration as seen by the time point of aggregation (10 h. vs. 12 h. vs. 15 h.), while *para*-bromine was more effective at reducing fibrillation.

The aggregation kinetic assessment of Aβ42 with or without series-leading derivatives is showcased in Figure 88. As observed in Panel A–D, derivatives **109/109-iso** and **110/110-iso** exhibited concentration-dependent inhibition of Aβ40 aggregation while showcasing multi-mode anti-aggregation characteristics. Both C2-amino derivatives (**109** and **110**; Panels A and C) managed to reduce the rate of aggregation and overall aggregate load. The kinetic plots demonstrate the greater ability of **110** to reduce Aβ42 fibrils compared to **109**.

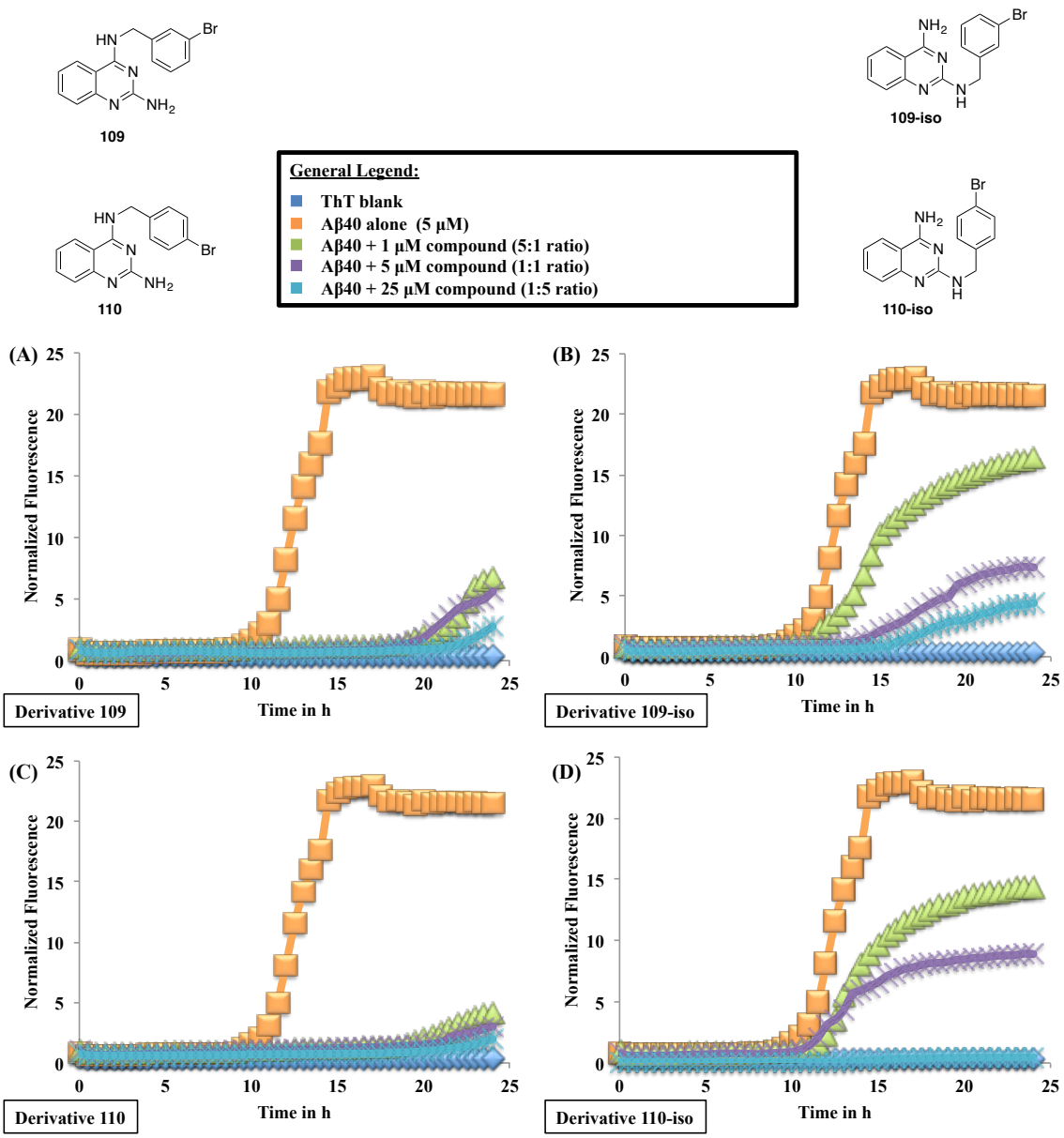


Figure 87: ThT-monitored kinetics of Aβ40 aggregation at 37 °C over a 24 h incubation period at pH 7.4 (Excitation = 440 nm, Emission = 490 nm). Panel (A): Impact of 1, 5 or 25 μM of N^4-(3-bromobenzyl)quinazoline-2,4-diamine (**109**) on the aggregation kinetics of 5 μM Aβ40. Panel (B): Impact of 1, 5 or 25 μM of N^2-(3-bromobenzyl)quinazoline-2,4-diamine (**109-iso**) on the aggregation kinetics of 5 μM Aβ40. Panel (C): Impact of 1, 5 or 25 μM of N^4-(4-bromobenzyl)quinazoline-2,4-diamine (**110**) on the aggregation kinetics of 5 μM Aβ40. Panel (D): Impact of 1, 5 or 25 μM of N^2-(4-bromobenzyl)quinazoline-2,4-diamine (**110-iso**) on the aggregation kinetics of 5 μM Aβ40.

The C4-amino isomers (Panels B and D), on the other hand, did showcase minor delays in the aggregation process (roughly 1.5-2 h delay compared to control), but a reduction in the rates of aggregation was more dominant with **109-iso** vs. **110-iso**. While overall fibril load was reduced in a concentration-

dependent manner with both derivatives, **110-iso**: managed to completely halt Aβ42 aggregation at the 5:1 ratio tested (**110-iso**: Aβ42).

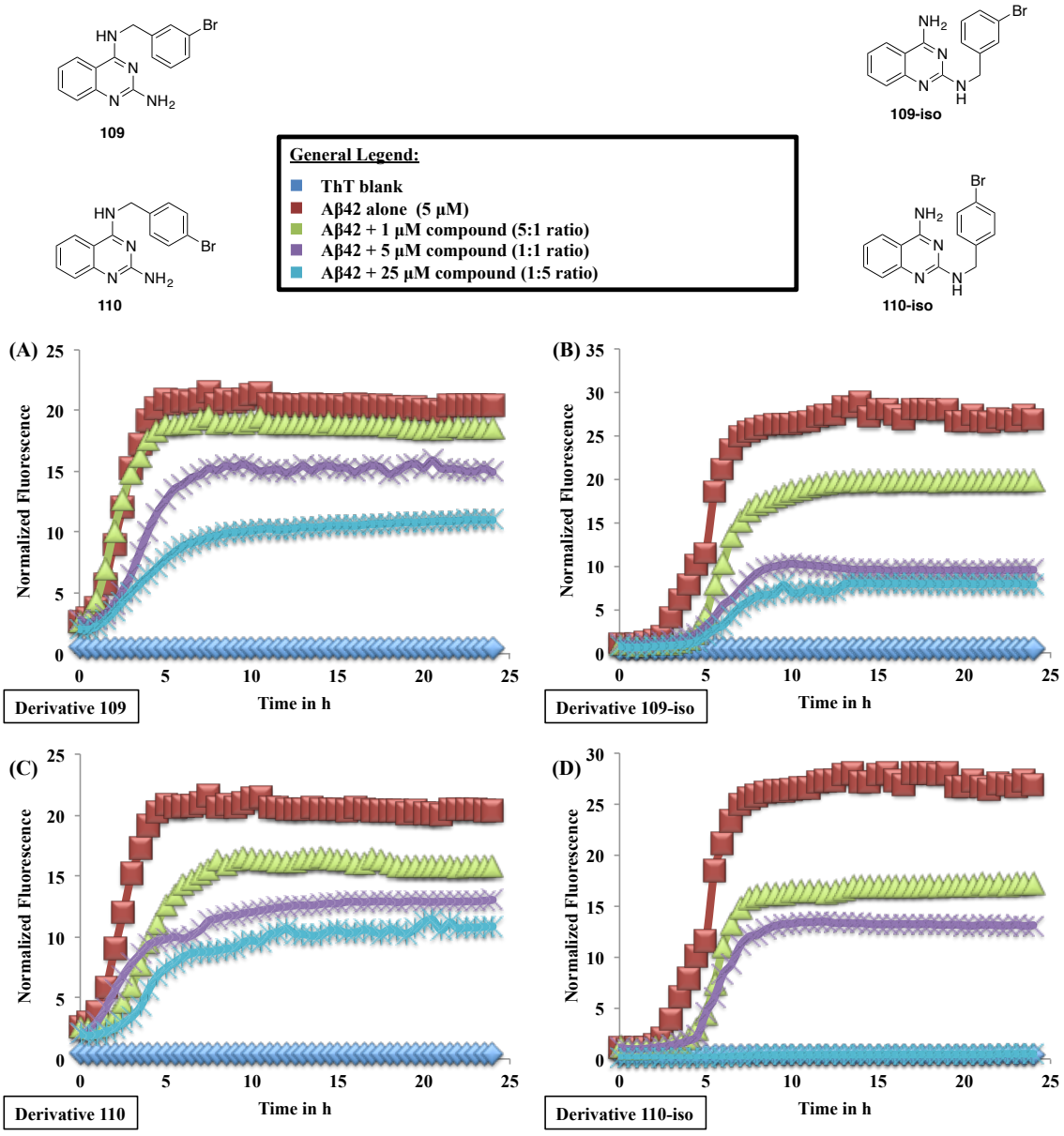


Figure 88: ThT-monitored kinetics of Aβ42 aggregation at 37 °C over a 24 h incubation period at pH 7.4 (Excitation = 440 nm, Emission = 490 nm). Panel (A): Impact of 1, 5 or 25 µM of N^4-(3-bromobenzyl)quinazoline-2,4-diamine (**109**) on the aggregation kinetics of 5 µM Aβ42. Panel (B): Impact of 1, 5 or 25 µM of N^2-(3-bromobenzyl)quinazoline-2,4-diamine (**109-iso**) on the aggregation kinetics of 5 µM Aβ42. Panel (C): Impact of 1, 5 or 25 µM of N^4-(4-bromobenzyl)quinazoline-2,4-diamine (**110**) on the aggregation kinetics of 5 µM Aβ42. Panel (D): Impact of 1, 5 or 25 µM of N^2-(4-bromobenzyl)quinazoline-2,4-diamine (**110-iso**) on the aggregation kinetics of 5 µM Aβ42.

8.3.3. *Transmission Electron Microscopy (TEM)*

The assessment of amyloid morphology at the conclusion of a 24-hour incubation period at 37 °C was conducted on leading derivatives. This commonly employed, qualitative technique is used to corroborate the quantitative results from the ThT-binding assay.[207, 317] Experimental setup included the incubations of control and test samples, at 1:1 ratios of 25 μM, in triplicate at 37 °C (with shaking) over a 24-hour timeline. Triplicate samples were combined after the incubation period and applied to the copper-mesh grids prior to imaging in the TEM.

As observed in Figure 89, resveratrol was effective at reducing total amyloid load (Panels B and E) compared to control samples (Panels A and D). That said, derivative **110** (Panel C) abolished the aggregation process and far exceeded the inhibitory potential of resveratrol against Aβ40, while derivative **110-iso** was far more effective against Aβ42, compared to resveratrol.

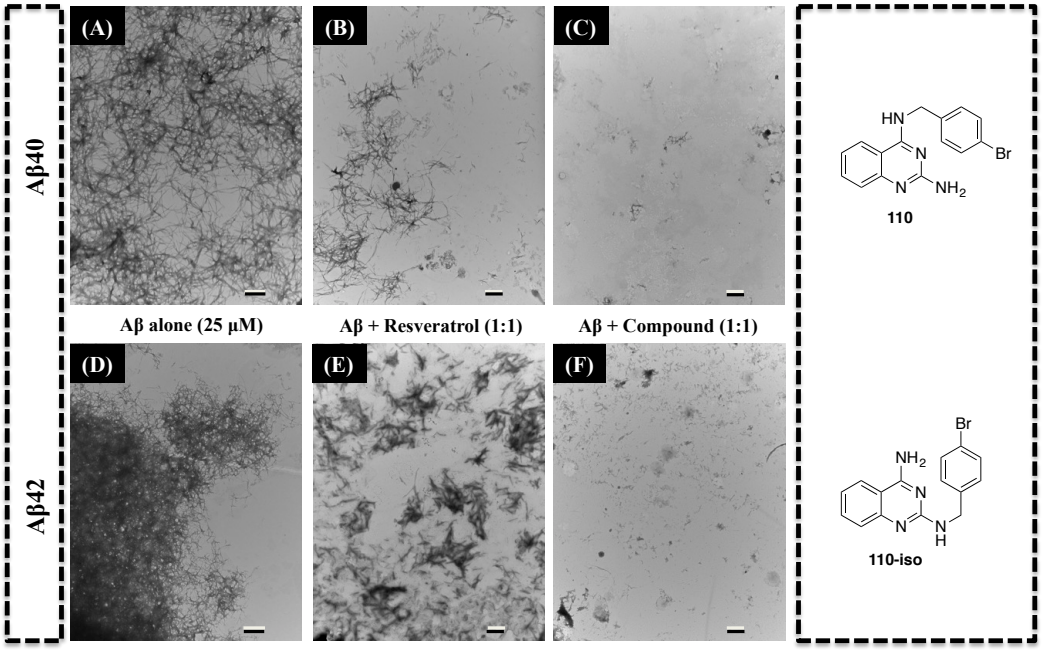


Figure 89: TEM assessment of Aβ40/42 morphology with or without test compounds at the end of a 24 h, 37 °C incubation period at pH 7.4. Panel (A–C): 25 μM Aβ40 alone or at a 1:1 ratio with resveratrol or N^4-(4-bromobenzyl)quinazoline-2,4-diamine (**110**); respectively. Panel (D–F): 25 μM Aβ42 alone or at a 1:1 ratio with resveratrol or N^2-(4-bromobenzyl)quinazoline-2,4-diamine (**110-iso**); respectively. White/black bars represent 500 nm.

8.3.4. *Amyloid-β Molecular Modeling*

The utilization of computational software is not only useful in structure-based drug design, it is also employed to understand and corroborate the acquired SAR data. The assessment of ligand-receptor interactions was conducted between leading (or comparable) derivatives from the 2,4-diaminoquinazolines (**98-112** and respective isomers) and the amyloid targets of interest. Based on the acquired anti-Aβ data, presented in Table 16, the docking interactions of **109/109-iso** and **100/100-iso** were investigated in both the dimeric and fibril model of Aβ ($A\beta_{9\text{-}40}$ – PDB 2LMN) with superimpositions showcased in Figure 90.

Considering the 2.5-fold gap in potency toward Aβ40, the unique binding interactions of **109** (C2-amino) within the KLVFFA region (vs. **109-iso**) explain the potency gap. The quinazoline scaffold of **109** (Panel A) was stacked perpendicular over V18-F20 (~ 4–5 Å), with the 3-bromobenzyl moiety oriented toward the hairpin loop domain. The bromine was pointed toward the hydrophobic region of I32-L34 (~ 5–7 Å). The ligand's C2-amino was close to the carboxyl group of D23, but did not undergo hydrogen-bonding interactions. In contrast, the regioisomer (**109-iso,** Panel A) was dominantly interacting within the hairpin loop domain, where the quinazoline scaffold was suspended parallel over the peptide chain, between D23 and K29 (~ 4–5 Å). The ligand's C4-amino group was undergoing hydrogen-bonding interactions with D23's carboxyl side chain (~ 3.2 Å), while the 3-bromobenzyl moiety was oriented over V24–S26 (~ 4–6 Å). Transitioning to Panel B, the observed 21-fold potency gap between **110** and **110-iso**, along with the kinetic plot patterns in Figure 87, is corroborated in the dimer model docking. While both isomers are dominantly interacting within the hairpin loop domain, stronger interactions were demonstrated by **110** compared to **110-iso**. Starting with the quinazoline scaffold, that of **110** is stacked semi-parallel over the S26-K28 region (~ 4–5 Å), with the C2-amino group directed toward D23-G25, although no hydrogen-bonding interactions were observed. The ligand's 4-bromobenzyl moiety extends outward from the hairpin loop domain, running parallel to the peptide backbone with the bromophenyl ring equidistantly placed between D23-G25 and I31-G33 (~ 6–7 Å). On the other hand, the quinazoline scaffold of **110-iso** was perpendicularly stacked over I31-I32 (~ 4–5 Å), allowing the C4-amino group to hydrogen-bond with carbonyl backbone of G33 (~ 3.1 Å), while the 4-bromobenzyl moiety extended perpendicularly toward N27-K28 (~ 4–6 Å).

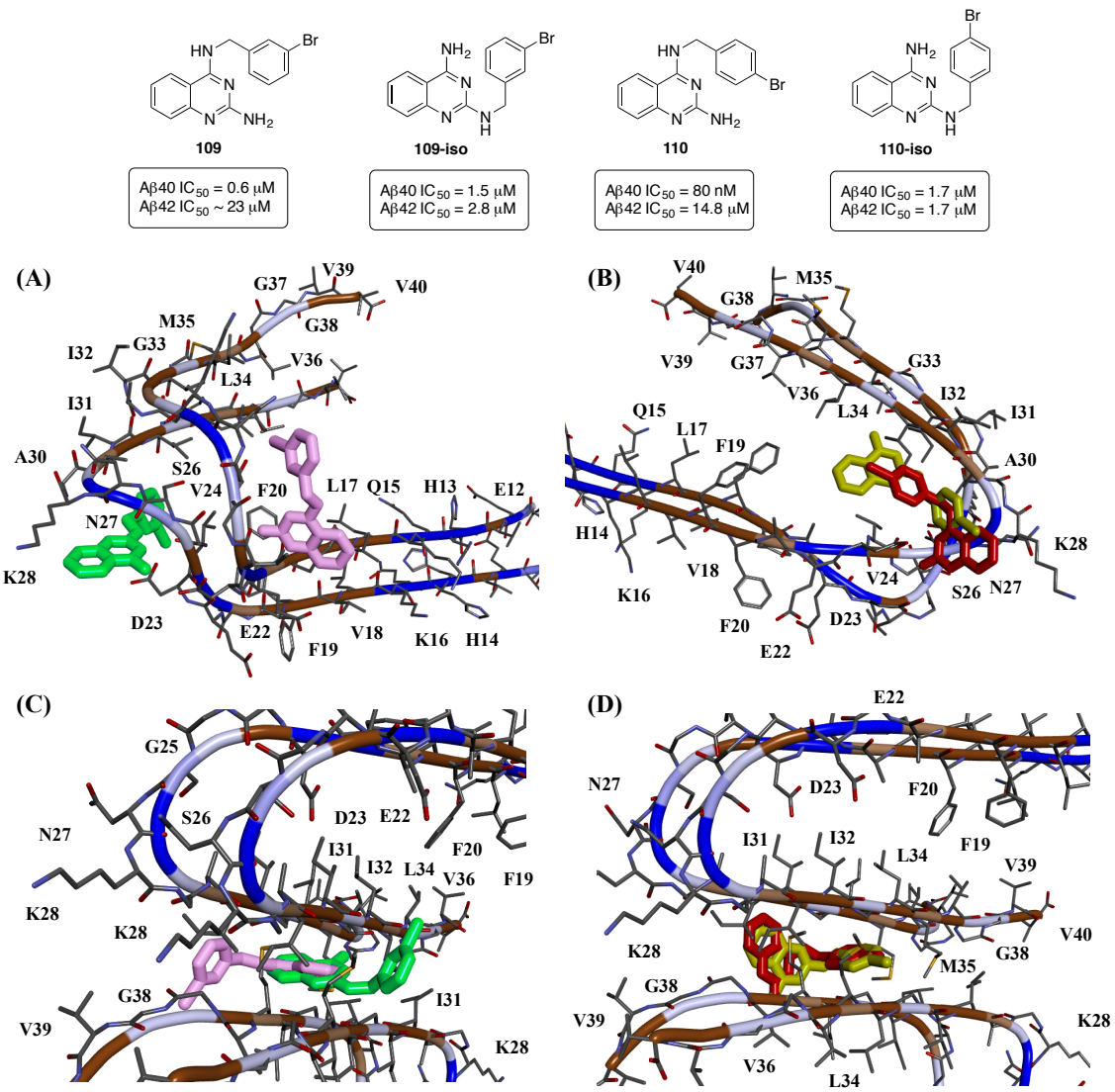


Figure 90: Superimposition of docking structures. Panel (A, C): Binding modes of **109** (pink) and **109-iso** (green) in the Aβ ($Aβ_{9-40}$ – PDB 2LMN) dimer or fibril model; respectively. Panel (B, D): Binding modes of **110** (red) and **110-iso** (gold) in the Aβ ($Aβ_{9-40}$ – PDB 2LMN) dimer or fibril model; respectively Hydrogens removed to enhance visibility. Amino acid labels to be used as a general guide as space restrictions limited complete and accurate labeling of all peptide structures.

The collective comparison of both isomeric pairs in the fibril model (Figure 90, Panel C and D) revealed one particularly interesting observation. With a 3-bromobenzyl moiety, regardless of C2- or C4-placement, the quinazoline scaffolds were directly intercalated within the steric zipper domain, while with a 4-bromobenzyl moiety, it was the 4-bromophenyl rings that were directly intercalated within the steric zipper domain.

8.4. Summary

With this collection of 2,4-diaminoquinazolines, Aβ targeting preferences emerged with the C2-amino derivatives surpassing the activity of their regioisomers against Aβ40, while the C4-amino derivatives surpassed the activity of their regioisomers against Aβ42.

Overall, leading candidates were identified in N^4-(4-bromobenzyl)quinazoline-2,4-diamine (**100**) due to its superior inhibitory potential toward Aβ40 (IC_{50} ~ 80 nM), while its regioisomer was the most potent and dual, non-selective Aβ inhibitor (IC_{50} ~ 2 μM). While bromo-based quinazolin-diamines were most potent overall, chloro-based bioisosteres were ranked in second place (Figure 91).

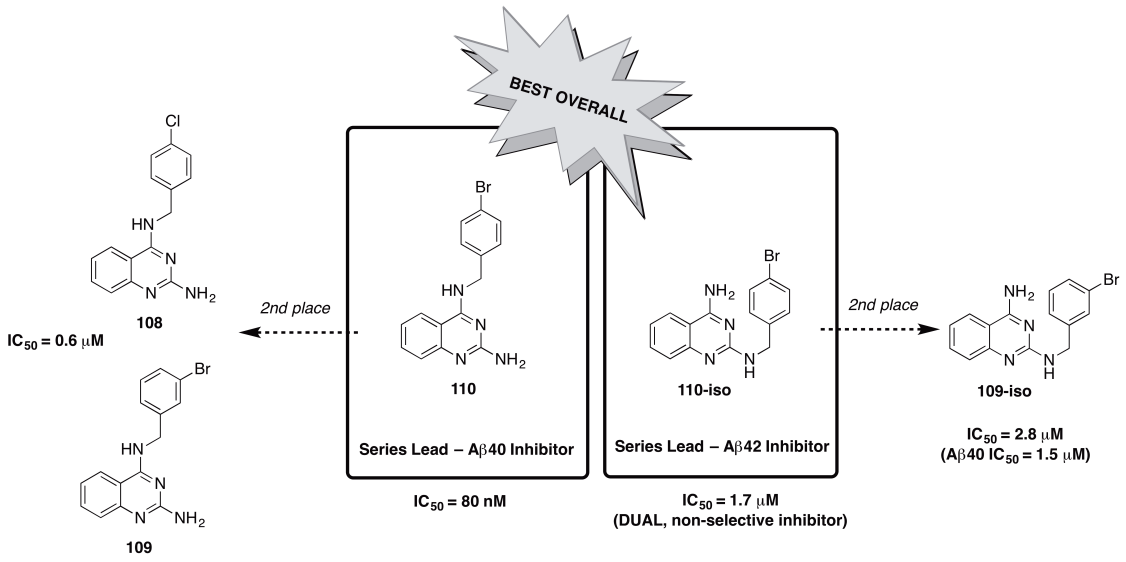


Figure 91: Cumulative chapter summary of 2,4-diaminoquinazolines (**98–112**) and their respective regioisomers.

8.5. Experimental

Please note that this subsection includes re-listed methodologies from Chapter 3–7. For schematic representation of re-listed methodologies, if applicable, please refer to Chapter 3 and 4 – Section 3.5 or 4.5.

8.5.1. *Chemistry*

General Information. All the reagents and solvents were reagent grade purchased from various vendors (Acros Organics, Sigma-Aldrich, and Alfa Aesar, USA) with a minimum purity of 95% and were used without further purification. Melting points (mp) were determined using a Fisher-Johns apparatus and are uncorrected. Reaction progress was monitored by UV using thin-layer chromatography (TLC) using Merck 60F254 silica gel plates. Column chromatography was performed with Merck silica gel 60 (230−400 mesh) with 5:1 EtOAc:MeOH as the solvent system unless otherwise specified. Proton (^{1}H NMR) and carbon (^{13}C NMR) spectra were performed on a Bruker Avance (at 300 and 75 MHz; respectively) spectrometer using DMSO-d_6. Coupling constants (*J* values) were recorded in hertz (Hz) and the following abbreviations were used to represent multiplets of NMR signals: s = singlet, d = doublet, t = triplet, m = multiplet, br = broad. Carbon multiplicities (C, CH, CH_2 and CH_3) were assigned by DEPT 90/135 experiments. High-resolution mass spectrometry (HRMS) was determined using a Thermo Scientific Q-Exactive Orbitrap mass spectrometer (positive mode, ESI), Department of Chemistry, University of Waterloo. Compound purity (roughly 95% or over) was determined using an Agilent 1100 series HPLC equipped with an analytical column (Agilent Zorbax Eclipse XDB-C8 column, 4.6 x 150 mm, 5 μm particle size) running 50:50 Water:ACN with 0.1% TFA at a flow rate of 1.0-1.5 mL/min or an Agilent 6100 series single quad LCMS equipped with an Agilent 1.8 μm Zorbax Eclipse Plus C18 (2.1 x 50 mm) running 50:50 Water:ACN with 0.1% FA with a flow rate of 0.5mL/min. All the final compounds exhibited ≥ 95% purity.

General procedure for synthesis of 2,4-diaminoquinazoline.[291, 317] In a 250 mL round-bottom pressure flask, 2-fluorobenzonitrile (4.6 mL, 42.32 mmol) or 2-aminobenzonitrile (5 g, 42.32 mmol) was combined with guanidine carbonate (11.43 g, 126.96 mmol) and diluted in 30 mL dimethylacetaminde (DMA). Contents are heated in an oil bath at 150 °C for overnight (~14 h) then diluted with 50mL of water before extracting thrice with EtOAc (50 mL x 3) and washing with brine (2x 20 mL). Combined organic layer was dried with $MgSO_4$ and concentrated in vacuo before purifying with silica gel column chromatography using 5:1 EtOAc/MeOH to afford an off-white solid at 80% yield. ^{1}H NMR (300 MHz, DMSO- d_6) δ 7.91 (d, 7.8 Hz, 1H), δ 7.41 (t, J = 7.8 Hz, 1H), δ 7.21 (br s, 2H), δ 7.15 (d, J = 8.1 Hz, 1H), δ

6.95 (t, J = 7.2 Hz, 1H), δ 5.91 (br s, 2H). ^{13}C NMR (100 MHz, DMSO- d_6) δ 162.45, δ 160.75, δ 152.52, δ 132.30, δ 124.22, δ 123.52, δ 119.73, δ 110.34.

General procedure for synthesis of N^4-substituted-quinazoline-2,4-diamines.[317] In a 50 mL round-bottom flask, 2,4-diaminoquinazoline* (1 g, 6.24 mmol) was dissolved in 3 mL DMSO. With stirring and periodic cooling over ice-water, NaH (60%, 0.25 g, 6.24 mmol) was added over a 10–15 min. period. After complete addition of NaH, flask was stirred at room temperature with slow, dropwise addition of the appropriate alkyl/aryl halide (6.24 mmol) dissolved in 3 mL DMSO. Contents are allowed to stir at room temperature overnight (~14 h) before diluting with 20 mL of water and stirring at room temperature for 15 min. The mixture is extracted thrice with diethyl ether (40 mL x 3). The combined organic layers are washed twice with brine (20 mL x 2). Combined organic layer was dried with $MgSO_4$ and concentrated in vacuo before purifying with silica gel column chromatography using 5:1 EtOAc/MeOH to afford beige to off-white solids at 20-31% yield.

N^4-Propylquinazoline-2,4-diamine (98). Yield: 20% (0.25 g, 1.24 mmol); Mp: 121–123 °C; ^{1}H NMR (300 MHz, DMSO- d_6): δ 8.09–7.95 (m, 2H), δ 7.47 (ddd, J = 8.3, 6.9, 1.4 Hz, 1H), δ 7.19 (dd, J = 8.4, 1.2 Hz, 1H), δ 7.03 (ddd, J = 8.2, 6.9, 1.2 Hz, 1H), δ 6.28 (s, 2H), δ 3.43–3.36 (m, 2H), δ 1.61 (h, J = 7.4 Hz, 2H), δ 0.89 (t, J = 7.4 Hz, 3H). HRMS (ESI) m/z calcd for $C_{11}H_{14}N_4$ $[M+1]^+$ 203.12912, observed 203.12911.

N^4-Isopropylquinazoline-2,4-diamine (99). Yield: 19% (0.24 g, 1.19 mmol); Mp: 131–133 °C; ^{1}H NMR (300 MHz, DMSO- d_6): δ 8.25–8.02 (m, 2H), δ 7.54 (ddd, J = 8.3, 7.0, 1.3 Hz, 1H), δ 7.24 (dd, J = 8.4, 1.1 Hz, 1H), δ 7.12 (ddd, J = 8.2, 7.0, 1.2 Hz, 1H), δ 6.72 (s, 2H), δ 4.47 (h, J = 6.7 Hz, 1H), δ 1.22 (d, J = 6.6 Hz, 6H). HRMS (ESI) m/z calcd for $C_{11}H_{14}N_4$ $[M+1]^+$ 203.12912, observed 203.12908.

N^4-(Cyclohexylmethyl)quinazoline-2,4-diamine (100). Yield: 20% (0.32 g, 1.25 mmol); Mp: 108–110 °C; ^{1}H NMR (300 MHz, DMSO-d_6): δ 8.48 (s, 1H), δ 8.12 (d, J = 8.2 Hz, 1H), δ 7.57 (t, J = 7.7 Hz, 1H), δ 7.27 (d, J = 8.3 Hz, 1H), δ 7.15 (t, J = 7.6 Hz, 1H), δ 6.82 (s, 2H), δ 1.74 – 1.56 (m, 7H), δ 1.16 (t, J = 10.6

Hz, 4H), δ 0.94 (t, *J* = 11.3 Hz, 2H). HRMS (ESI) m/z calcd for $C_{15}H_{20}N_4$ $[M+1]^+$ 257.17607, observed 257.17589.

***N*^{4}-(3-Methylbenzyl)quinazoline-2,4-diamine (101)**. Yield: 24% (0.39 g, 1.48 mmol); Mp: 117–119 °C; ^{1}H NMR (300 MHz, DMSO-d_6): δ 8.80 (s, 1H), δ 8.09 (d, *J* = 8.2 Hz, 1H), δ 7.53 (ddd, *J* = 8.3, 7.0, 1.3 Hz, 1H), δ 7.25 (dd, *J* = 8.4, 1.1 Hz, 1H), δ 7.21–7.05 (m, 4H), δ 7.02 (dd, *J* = 5.5, 3.3 Hz, 1H), δ 6.56 (s, 2H), δ 4.69 (d, *J* = 5.7 Hz, 2H), δ 2.25 (s, 3H). HRMS (ESI) m/z calcd for $C_{16}H_{16}N_4$ $[M+1]^+$ 265.14477, observed 265.14469.

***N*^{4}-(4-Methylbenzyl)quinazoline-2,4-diamine (102)**. Yield: 21% (0.35 g, 1.33 mmol); Mp: 113-115 °C; ^{1}H NMR (300 MHz, DMSO-d_6): δ 8.95 (s, 1H), δ 8.11 (d, *J* = 8.0 Hz, 1H), δ 7.56 (ddd, *J* = 8.4, 7.0, 1.3 Hz, 1H), δ 7.24 (d, *J* = 8.3 Hz, 3H), δ 7.11 (t, *J* = 8.9 Hz, 3H), δ 6.74 (s, 2H), δ 4.68 (d, *J* = 5.8 Hz, 2H), δ 2.24 (s, 3H). HRMS (ESI) m/z calcd for $C_{16}H_{16}N_4$ $[M+1]^+$ 265.14477, observed 265.14467.

***N*^{4}-(3-Methoxybenzyl)quinazoline-2,4-diamine (103)**. Yield: 20% (0.35 g, 1.25 mmol); Mp: 132–134 °C; ^{1}H NMR (300 MHz, DMSO-d_6): δ 8.89 (s, 1H), δ 8.11 (d, *J* = 8.2 Hz, 1H), δ 7.55 (ddd, *J* = 8.4, 6.9, 1.3 Hz, 1H), δ 7.31–7.06 (m, 3H), δ 6.97–6.87 (m, 2H), δ 6.78 (ddd, *J* = 8.2, 2.5, 1.2 Hz, 1H), δ 6.64 (s, 2H), δ 4.70 (d, *J* = 5.6 Hz, 2H), δ 3.69 (s, 3H). HRMS (ESI) m/z calcd for $C_{16}H_{16}N_4O$ $[M+1]^+$ 281.13969, observed 281.13964.

***N*^{4}-(4-Methoxybenzyl)quinazoline-2,4-diamine (104)**. Yield: 25% (0.44 g, 1.57 mmol); Mp: 140–142 °C; ^{1}H NMR (300 MHz, DMSO-d_6): δ 9.77 (d, *J* = 6.2 Hz, 1H), δ 8.29 (d, *J* = 8.2 Hz, 1H), δ 7.69 (t, *J* = 7.7 Hz, 1H), δ 7.62 (s, 1H), δ 7.44–7.23 (m, 5H), δ 6.86 (d, *J* = 8.3 Hz, 2H), δ 4.68 (d, *J* = 5.7 Hz, 2H), 3.69 (s, 3H). HRMS (ESI) m/z calcd for $C_{16}H_{16}N_4O$ $[M+1]^+$ 281.13969, observed 281.13963.

***N*^{4}-(3-(Trifluoromethyl)benzyl)quinazoline-2,4-diamine (105)**. Yield: 19% (0.37 g, 1.16 mmol); Mp: 104–106 °C; ^{1}H NMR (300 MHz, DMSO-d_6): δ 9.00 (d, *J* = 6.5 Hz, 1H), δ 8.10 (d, *J* = 8.1 Hz, 1H), δ 7.75–

7.64 (m, 2H), δ 7.61–7.49 (m, 3H), δ 7.27 (d, *J* = 8.2 Hz, 1H), δ 7.14 (t, *J* = 7.5 Hz, 1H), δ 6.69 (s, 2H), δ 4.80 (d, *J* = 5.6 Hz, 2H). HRMS (ESI) m/z calcd for $C_{16}H_{13}F_3N_4$ $[M+1]^+$ 319.11651, observed 319.11637.

***N*^{4}-(4-(Trifluoromethyl)benzyl)quinazoline-2,4-diamine (106)**. Yield: 20% (0.40 g, 1.26 mmol); Mp: 110–112 °C; ^{1}H NMR (300 MHz, DMSO-d_6): δ 8.51 (s, 1H), δ 8.00 (d, *J* = 8.1 Hz, 1H), δ 7.65 (d, *J* = 8.1 Hz, 2H), δ 7.59–7.37 (m, 3H), δ 7.19 (d, *J* = 8.0 Hz, 1H), δ 7.03 (t, *J* = 7.6 Hz, 1H), δ 6.07 (s, 2H), δ 4.77 (d, *J* = 5.9 Hz, 2H). HRMS (ESI) m/z calcd for $C_{16}H_{13}F_3N_4$ $[M+1]^+$ 319.11651, observed 319.11647.

***N*^{4}-(3-Chlorobenzyl)quinazoline-2,4-diamine (107)**. Yield: 23% (0.41 g, 1.44 mmol); Mp: 117-119 °C; ^{1}H NMR (300 MHz, DMSO-d_6): δ 9.12 (s, 1H), δ 8.14 (dd, *J* = 8.3, 1.3 Hz, 1H), δ 7.59 (ddd, *J* = 8.4, 7.1, 1.3 Hz, 1H), δ 7.42 (d, *J* = 1.9 Hz, 1H), δ 7.35 – 7.28 (m, 4H), δ 7.23 – 7.11 (m, 1H), δ 6.86 (s, 2H), δ 4.73 (d, *J* = 5.4 Hz, 2H). HRMS (ESI) m/z calcd for $C_{15}H_{13}ClN_4$ $[M+1]^+$ 285.09015, observed 285.09006.

***N*^{4}-(4-Chlorobenzyl)quinazoline-2,4-diamine (108)**. Yield: 26% (0.46 g, 1.62 mmol); Mp: 132–134 °C; ^{1}H NMR (300 MHz, DMSO-d_6): δ 9.11 (t, *J* = 6.0 Hz, 1H), δ 8.13 (dd, *J* = 8.3, 1.3 Hz, 1H), δ 7.58 (ddd, *J* = 8.3, 7.0, 1.2 Hz, 1H), δ 7.44–7.31 (m, 4H), δ 7.28 (d, *J* = 8.3 Hz, 1H), δ 7.24–7.10 (m, 1H), δ 6.81 (s, 2H), δ 4.70 (d, *J* = 5.5 Hz, 2H). HRMS (ESI) m/z calcd for $C_{15}H_{13}ClN_4$ $[M+1]^+$ 285.09015, observed 285.09005.

***N*^{4}-(3-Bromobenzyl)quinazoline-2,4-diamine (109)**. Yield: 24% (0.49 g, 1.49 mmol); Mp: 127-129 °C; ^{1}H NMR (300 MHz, DMSO-d_6): δ 8.99 (s, 1H), δ 8.10 (dd, *J* = 8.2, 1.4 Hz, 1H), δ 7.60–7.51 (m, 2H), δ 7.44–7.33 (m, 2H), δ 7.27 (d, *J* = 7.9 Hz, 2H), δ 7.15 (s, 1H), δ 6.72 (s, 2H), δ 4.71 (d, *J* = 5.7 Hz, 2H). HRMS (ESI) m/z calcd for $C_{15}H_{13}BrN_4$ $[M+1]^+$ 329.03964, observed 329.03968.

***N*^{4}-(4-Bromobenzyl)quinazoline-2,4-diamine (110)**. Yield: 29% (0.60 g, 1.83 mmol); Mp: 116–118 °C; ^{1}H NMR (300 MHz, DMSO-d_6): δ 7.95 (d, *J* = 8.1 Hz, 1H), δ 7.46 (q, *J* = 12.2, 10.0 Hz, 2H), δ 7.36–7.10 (m, 7H), δ 7.02 (t, *J* = 7.5 Hz, 1H), δ 4.54 (d, *J* = 6.3 Hz, 2H). HRMS (ESI) m/z calcd for $C_{15}H_{13}BrN_4$ $[M+1]^+$ 329.03964, observed 329.03965.

***N*^{4}-(3-Fluorobenzyl)quinazoline-2,4-diamine (111)**. Yield: 24% (0.40 g, 1.49 mmol); Mp: 118–120 °C; ^{1}H NMR (300 MHz, DMSO-d_6): δ 8.92 (t, *J* = 5.9 Hz, 1H), δ 8.10 (dd, *J* = 8.3, 1.3 Hz, 1H), δ 7.55 (ddd, *J* = 8.3, 6.9, 1.3 Hz, 1H), δ 7.40–6.97 (m, 6H), δ 6.62 (s, 2H), δ 4.72 (d, *J* = 5.6 Hz, 2H). HRMS (ESI) m/z calcd for $C_{15}H_{13}FN_4$ $[M+1]^+$ 269.11970, observed 269.11956.

***N*^{4}-(4-Fluorobenzyl)quinazoline-2,4-diamine (112)**. Yield: 28% (0.47 g, 1.75 mmol); Mp: 123–125 °C; ^{1}H NMR (300 MHz, DMSO-d_6): δ 9.08 (d, *J* = 7.0 Hz, 1H), δ 8.12 (d, *J* = 8.1 Hz, 1H), δ 7.58 (t, *J* = 7.6 Hz, 1H), δ 7.45–7.37 (m, 2H), δ 7.28 (d, *J* = 8.3 Hz, 1H), δ 7.17–7.08 (m, 3H), δ 6.85 (s, 2H), δ 4.70 (d, *J* = 5.7 Hz, 2H). HRMS (ESI) m/z calcd for $C_{15}H_{13}FN_4$ $[M+1]^+$ 269.11970, observed 269.11958.

General procedure for synthesis of *N*^{2}-substituted-quinazoline-2,4-diamines.[317] In a 50 mL round-bottom flask, 2,4-diaminoquinazoline (1 g, 6.24 mmol) was dissolved in 20 mL DMA followed by the addition of potassium carbonate (0.85 g, 6.24 mmol) and the appropriate alkyl/aryl halide (6.24 mmol) at room temperature. Contents are refluxed at 80–85 °C for 5 h before diluting with 30 mL of water and stirring at R.T for 15 min. The mixture is extracted thrice with EtOAc (50 mL x 3). The combined organic layers are washed twice with brine (20 mL x 2). Combined organic layer was dried with $MgSO_4$ and concentrated in vacuo before purifying with silica gel column chromatography using 5:1 EtOAc/MeOH to afford beige to off-white solids at 14–26% yield.

***N*^{2}-Propylquinazoline-2,4-diamine (98-iso)**. Yield: 16% (0.20 g, 0.99 mmol); Mp: 159–161 °C; ^{1}H NMR (300 MHz, DMSO-d_6): δ 8.05 (d, *J* = 8.2 Hz, 1H), δ 7.57 (d, *J* = 7.9 Hz, 1H), δ 7.35 (d, *J* = 8.4 Hz, 1H), δ 7.14 (s, 1H), δ 3.32–3.26 (m, 2H), δ 1.53 (h, *J* = 7.4 Hz, 2H), δ 0.87 (t, *J* = 7.4 Hz, 3H). HRMS (ESI) m/z calcd for $C_{11}H_{14}N_4$ $[M+1]^+$ 203.12912, observed 203.12912.

***N*^{2}-Isopropylquinazoline-2,4-diamine (99-iso)**. Yield: 14% (0.18 g, 0.89 mmol); Mp: 127–129 °C; ^{1}H NMR (300 MHz, DMSO-d_6): δ 8.07 (d, *J* = 8.1 Hz, 1H), δ 7.60 (t, *J* = 7.7 Hz, 1H), δ 7.35 (d, *J* = 8.4 Hz,

1H), δ 7.16 (t, *J* = 7.7 Hz, 1H), δ 4.16 (h, *J* = 6.7 Hz, 1H), δ 1.15 (d, *J* = 6.5 Hz, 6H). HRMS (ESI) m/z calcd for $C_{11}H_{14}N_4$ $[M+1]^+$ 203.12912, observed 203.12912.

***N*^{2}-(Cyclohexylmethyl)quinazoline-2,4-diamine (100-iso)**. Yield: 25% (0.40 g, 1.56 mmol); Mp: 193–195 °C; ^{1}H NMR (300 MHz, DMSO-d_6): δ 9.00 (d, *J* = 31.9 Hz, 1H), δ 8.17 (d, *J* = 8.1 Hz, 1H), δ 7.76 (t, *J* = 7.7 Hz, 1H), δ 7.36 (t, *J* = 7.7 Hz, 1H), δ 1.63 (dd, *J* = 22.6, 10.7 Hz, 6H), δ 1.18 (d, *J* = 12.5 Hz, 5H), δ 0.93 (q, *J* = 10.7, 10.1 Hz, 2H). HRMS (ESI) m/z calcd for $C_{15}H_{20}N_4$ $[M+1]^+$ 257.17607, observed 257.17598.

***N*^{2}-(3-Methylbenzyl)quinazoline-2,4-diamine (101-iso)**. Yield: 18% (0.30 g, 1.14 mmol); Mp: 104-106 °C; ^{1}H NMR (300 MHz, DMSO-d_6): δ 8.03 (d, *J* = 8.2 Hz, 1H), 7.57 (s, 1H), 7.31 (d, *J* = 8.3 Hz, 1H), 7.19–7.08 (m, 4H), 7.00 (d, *J* = 7.3 Hz, 1H), 4.54 (d, *J* = 6.2 Hz, 2H), 2.24 (s, 3H). HRMS (ESI) m/z calcd for $C_{16}H_{16}N_4$ $[M+1]^+$ 265.14477, observed 265.14465.

***N*^{2}-(4-Methylbenzyl)quinazoline-2,4-diamine (102-iso)**. Yield: 20% (0.33 g, 1.25 mmol); Mp: 109–111 °C; ^{1}H NMR (300 MHz, DMSO-d_6): δ 7.96 (d, *J* = 8.1 Hz, 1H), δ 7.48 (t, *J* = 7.7 Hz, 1H), δ 7.27–7.15 (m, 3H), δ 7.10–6.97 (m, 4H), δ 4.49 (d, *J* = 6.2 Hz, 2H), δ 2.22 (s, 3H). HRMS (ESI) m/z calcd for $C_{16}H_{16}N_4$ $[M+1]^+$ 265.14477, observed 265.14465.

***N*^{2}-(3-Methoxybenzyl)quinazoline-2,4-diamine (103-iso)**. Yield: 17% (0.29 g, 1.04 mmol); Mp: 147–149 °C; ^{1}H NMR (300 MHz, DMSO-d_6): δ 7.97 (d, *J* = 8.1 Hz, 1H), δ 7.50 (t, *J* = 7.8 Hz, 1H), δ 7.28–7.12 (m, 2H), δ 7.05 (t, *J* = 7.5 Hz, 1H), δ 6.93–6.78 (m, 2H), δ 6.78–6.69 (m, 1H), δ 4.51 (d, *J* = 6.3 Hz, 2H), δ 3.68 (s, 3H). HRMS (ESI) m/z calcd for $C_{16}H_{16}N_4O$ $[M+1]^+$ 281.13969, observed 281.13964.

***N*^{2}-(4-Methoxybenzyl)quinazoline-2,4-diamine (104-iso)**. Yield: 21% (0.36 g, 1.29 mmol); Mp: 139–141 °C; ^{1}H NMR (300 MHz, DMSO-d_6): δ 8.01 (d, *J* = 8.1 Hz, 1H), δ 7.81–6.92 (m, 7H), δ 6.89–6.77 (m, 2H), δ 4.48 (d, *J* = 6.0 Hz, 2H), δ 3.68 (d, *J* = 1.3 Hz, 3H). HRMS (ESI) m/z calcd for $C_{16}H_{16}N_4O$ $[M+1]^+$ 281.13969, observed 281.13961.

***N*^{2}-(3-(Trifluoromethyl)benzyl)quinazoline-2,4-diamine (105-iso)**. Yield: 15% (0.30 g, 0.94 mmol); Mp: 118–120 °C; ^{1}H NMR (300 MHz, DMSO-d_6): δ 7.99 (d, J = 8.1 Hz, 1H), δ 7.69 – 7.62 (m, 3H), δ 7.55–7.47 (m, 5H), δ 7.24 (d, J = 8.3 Hz, 1H), δ 7.05 (d, J = 7.6 Hz, 1H), δ 4.62 (d, J = 6.2 Hz, 2H). HRMS (ESI) m/z calcd for $C_{16}H_{13}F_3N_4$ $[M+1]^+$ 319.11651, observed 319.11638.

***N*^{2}-(4-(Trifluoromethyl)benzyl)quinazoline-2,4-diamine (106-iso)**. Yield: 16% (0.32 g, 1.00 mmol); Mp: 124–126 °C; ^{1}H NMR (300 MHz, DMSO-d_6): δ 7.98 (d, J = 8.2 Hz, 1H), δ 7.63 (d, J = 8.1 Hz, 2H), δ 7.53 (d, J = 8.2 Hz, 4H), δ 7.24 (d, J = 8.3 Hz, 1H), δ 7.08 (d, J = 8.2 Hz, 1H), δ 4.62 (d, J = 6.2 Hz, 2H). HRMS (ESI) m/z calcd for $C_{16}H_{13}F_3N_4$ $[M+1]^+$ 319.11651, observed 319.11647.

***N*^{2}-(3-Chlorobenzyl)quinazoline-2,4-diamine (107-iso)**. Yield: 16% (0.28 g, 0.99 mmol); Mp: 121–123 °C; ^{1}H NMR (300 MHz, DMSO-d_6): δ 7.95 (s, 1H), δ 7.49 (s, 1H), δ 7.36 (s, 1H), δ 7.28–7.21 (m, 6H), δ 7.03 (t, J = 7.5 Hz, 2H), δ 4.52 (s, 2H). HRMS (ESI) m/z calcd for $C_{15}H_{13}ClN_4$ $[M+1]^+$ 285.09015, observed 285.09008.

***N*^{2}-(4-Chlorobenzyl)quinazoline-2,4-diamine (108-iso)**. Yield: 19% (0.34 g, 1.20 mmol); Mp: 128-130 °C; ^{1}H NMR (300 MHz, DMSO-d_6): δ 7.97 (d, J = 8.1 Hz, 1H), δ 7.49 (t, J = 7.9 Hz, 1H), δ 7.42 – 7.13 (m, 7H), δ 7.04 (t, J = 7.5 Hz, 2H), δ 4.51 (d, J = 6.3 Hz, 2H). HRMS (ESI) m/z calcd for $C_{15}H_{13}ClN_4$ $[M+1]^+$ 285.09015, observed 285.09007.

***N*^{2}-(3-Bromobenzyl)quinazoline-2,4-diamine (109-iso)**. Yield: 21% (0.43 g, 1.31 mmol); Mp: 108–110 °C; ^{1}H NMR (300 MHz, DMSO-d_6): δ 7.95 (d, J = 8.1 Hz, 1H), δ 7.49 (d, J = 6.0 Hz, 2H), δ 7.34 (dd, J = 12.6, 7.6 Hz, 3H), δ 7.27–7.19 (m, 3H), δ 7.03 (t, J = 7.5 Hz, 2H), δ 4.52 (d, J = 6.4 Hz, 2H). HRMS (ESI) m/z calcd for $C_{15}H_{13}BrN_4$ $[M+1]^+$ 329.03964, observed 329.03958.

***N*^{2}-(4-Bromobenzyl)quinazoline-2,4-diamine (110-iso)**. Yield: 22% (0.46 g, 1.40 mmol); Mp: 119–121 °C; ^{1}H NMR (300 MHz, DMSO-d_6): δ 7.98 (d, J = 8.2 Hz, 1H), δ 7.58–7.18 (m, 8H), δ 7.14–7.00 (m, 2H), δ 4.50 (d, J = 6.3 Hz, 2H). HRMS (ESI) m/z calcd for $C_{15}H_{13}BrN_4$ $[M+1]^+$ 329.03964, observed 329.03952.

***N*^{2}-(3-Fluorobenzyl)quinazoline-2,4-diamine (111-iso)**. Yield: 20% (0.33 g, 1.23 mmol); Mp: 138–140 °C; ^{1}H NMR (300 MHz, DMSO-d_6): δ 8.01–7.91 (m, 1H), δ 7.48 (t, J = 7.7 Hz, 1H), δ 7.30 (td, J = 7.9, 6.1 Hz, 1H), δ 7.27–6.93 (m, 6H), δ 4.54 (d, J = 6.3 Hz, 2H). HRMS (ESI) m/z calcd for $C_{15}H_{13}FN_4$ $[M+1]^+$ 269.11970, observed 269.11954.

***N*^{2}-(4-Fluorobenzyl)quinazoline-2,4-diamine (112-iso)**. Yield: 20% (0.34 g, 1.27 mmol); Mp: 144–146 °C; ^{1}H NMR (300 MHz, DMSO-d_6): δ 7.97 (d, J = 8.1 Hz, 1H), δ 7.49 (t, J = 7.7 Hz, 1H), δ 7.35 (dd, J = 8.3, 5.6 Hz, 2H), δ 7.23 (d, J = 8.4 Hz, 1H), δ 7.07 (dd, J = 10.4, 7.5 Hz, 3H), δ 4.51 (d, J = 6.1 Hz, 2H). HRMS (ESI) m/z calcd for $C_{15}H_{13}FN_4$ $[M+1]^+$ 269.11970, observed 269.11953.

8.5.2. *Biological Screening*

8.5.2.1. *Amyloid-β (Aβ) Aggregation Assay*[317]

The ability of quinazoline-based derivatives to inhibit Aβ-aggregation kinetics was determined using a ThT-binding fluorescence assay. These assays were conducted in Costar, black-surround, clear-bottom 384-well plates with frequent shaking (30 sec. of linear shaking at 730 cpm every 5 minutes) and constant heating at 37 °C for 24 h. The ThT excitation/emission was measured at 440 nm/490 nm and readings were taken every 5 minutes using a BioTek Synergy H1 microplate reader. Quinazoline stock solutions were prepared in DMSO and diluted to 10x in 215 mM phosphate buffer at pH 7.4. Abeta.HFIP samples (Aβ40 or Aβ42, rPeptide, Bogart, USA) were dissolved in 1% ammonium hydroxide, sonicated at room temperature for 5 minutes then diluted to 50 μM in 215 mM phosphate buffer (pH 7.4). A 15 μM ThT stock solution was prepared with 50 mM glycine and adjusted to pH 7.4. The assay was carried out by adding 44 μL ThT, 20–35 μL buffer, 1 μL DMSO (for background and controls only) followed by the addition of 8 μL of 10x compound dilutions (1–25 μM concentration range). An end point reading was conducted to evaluate potential test compound interference with ThT-fluorescence before adding 8 μL of Aβ40 or Aβ42 stock solutions (5 μM final concentration). Plates were sealed with a transparent plate film before initiating

the assay. RFU values were corrected for ThT-interference before calculating end point percent inhibitions or IC_{50} values and obtaining the aggregation kinetic plots. Data presented was an average of triplicate reading for two-three independent experiments.

8.5.2.2. *TEM Assay and Imaging*[142, 190, 207, 317]

In Costar 96-well, round-bottom plates were added 80 μL of 215 mM phosphate buffer, 20 μL of 10x test compound dilutions (250 μM – prepared in the same way as for the ThT assay) and 100 μL of 50 μM Aβ40 or Aβ42 respectively. For the control wells, 2 μL of DMSO and 18 μL of phosphate buffer was added. Final Aβ: test compound ratio was 1:1 (25 μM). Plates were incubated on a Fisher plate incubator set to 37 °C and the contents were shaken at 730 cpm for 24 h. To prepare the TEM grids, ~ 20 μL droplet was added using a disposable Pasteur pipette over the formvar-coated copper grids (400 mesh). Grids were air-dried for about 3 h before adding two droplets (~ 40 μL, using a disposable Pasteur pipette) of ultra-pure water and using small pieces of filter paper to wash out precipitated buffer salts. After air-drying for ~ 15-20 min, the grids were negatively stained by adding a droplet (~ 20 μL, using a disposable Pasteur pipette) of 2% phosphotungstic acid (PTA) and immediately after the grids were dried using small pieces of filter paper. Grids were further air-dried overnight. The scanning was carried out using a Philips CM 10 transmission electron microscope at 60 kV (Department of Biology, University of Waterloo) and micrographs were obtained using a 14-megapixel AMT camera.

8.5.3. *Computational Chemistry*[299, 313, 317, 324]

The molecular docking studies were conducted using Discovery Studio 4.0 (Structure-Based-Design program) from BIOVIA Inc. San Diego, USA. Select quinazolines derivatives were built and minimized using the *small molecules* module in Discovery Studio. X-ray coordinates of human cholinesterases were obtained from the protein data bank (*h*AChE PBD ID: 1B41 and *h*BuChE PDB ID: 1P0I) and prepared

using the *macromolecules* module in Discovery Studio. Ligand binding sites were defined by selecting a 12 Å radius sphere for AChE and 15 Å radius sphere for BuChE. The molecular docking was performed using the *receptor-ligand interactions* module in Discovery Studio. The LibDock algorithm was used to find the most appropriate binding modes for select quinazoline derivatives using CHARMm force field. The docked poses obtained were ranked based on the LibDock scores and were analyzed by evaluating all the polar and nonpolar interactions. For Amyloid-β docking studies, the NMR solution structure of Aβ fibrils were obtained from the protein data bank (PDB ID: 2LMN). Aβ dimer and Aβ fibril assemblies were built using the *macromolecules* module in Discovery Studio. Ligand binding site was defined by selecting a 15 Å radius sphere for both Aβ assemblies. Molecular docking was performed using the *receptor-ligand interactions* module in Discovery Studio, where the LibDock algorithm was used to find the most appropriate binding modes for select quinazoline derivatives using CHARMm force field. The docked poses obtained were ranked based on the LibDock scores and were analyzed by evaluating all the polar and nonpolar interactions.

CHAPTER 9

• Conclusions and Future Outlook •

Over its hundred plus years of research history, the field of dementia sciences has accomplished numerous milestones in furthering our knowledge of neurodegenerative disease. That history is also flagged with countless setbacks with respect to diagnosis and therapeutic interventions. As with many aspects of life, one grows stronger when acknowledging and learning from any given setbacks or failures. The dementia research community has seen a paradigm-shift with respect to developing therapeutic interventions for Alzheimer's disease. As our understanding of disease pathology continues to grow, it has become more relevant to develop multi-targeting therapeutics considering their higher probability of demonstrating disease-modifying effects.

Over the course of the research program, a chemical library of **127 derivatives** based on the quinazoline ring scaffold (and related templates) were developed and screened against multiple targets associated with AD pathology (AChE, BuChE, Aβ40/42 aggregation, ROS species and metal ions such as Fe^{2+}).

The design strategy was influenced by the diversity and vast utility of quinazoline and quinazoline-related scaffolds in medicinal chemistry, along with previously reported studies on the smaller pyrimidine ring scaffold. Synthetic methodology was N.A.S-dominant, but included some cyclization reactions, catalyst-dependent reductions and hydrolysis steps). By far the most challenging aspect of the synthetic scheme was the $POCl_3$-based chlorination step that yielded the critical di- or tri-chloroquinazoline intermediates. Biological assessments were accomplished using previously established or refurbished methods to obtain the necessary SAR data. Molecular modeling studies were conducted to investigate the docking of lead derivatives within the target enzymes and to corroborate their biological profiles. A collective summary of the various parameters for library characterization is presented below:

- **Molecular Weights (MWs):** 202.3 – 483.6 $gmol^{-1}$
- **Molecular Volumes:** 132.9 – 400.3 $Å^3$
- **Partition Coefficients (ClogPs):** 1.8 – 6.6
- ***h*AChE Inhibition Range (IC_{50}):** 2.1 μM – 15.0 μM
- ***h*BuChE Inhibition Range (IC_{50}):** 90 nM – 50+ μM
- **Aβ40 Aggregation Inhibition:** 80 nM – Not active
- **Aβ42 Aggregation Inhibition:** 1.3 μM – Not active
- **Antioxidant Capacity:** 33% – 63% at 50 μM
- **Iron Chelating Capacity:** 15% – 37% at 50 μM

While appropriate chapters included their particular metrics with respect to cholinesterase and/or amyloid-β data, the cumulative metrics are displayed below to assist in the identification of lead candidates from the collective library (Figure 92).

As indicated through the cumulative metrics, no single derivative (out of the 97) exhibited IC_{50} values within the 0–5 μM range across the four primary targets. In addition, derivatives showcasing antioxidant or iron chelating capacities were moderate to weak AChE inhibitors, inactive toward BuChE and moderate to weakAβ40/42 aggregation inhibitors. That said, 4 of the 5 leading candidates in Figure 92 were derived from Chapter 7 – the phenethylamine-based series. Of those 4 top leading candidates, **85** (8-chloro-N^2-isopropyl-N^4-phenethylquinazoline-2,4-diamine) exhibited IC_{50} values within the 0–5 μMrange for Aβ40/42 and BuChE, while the AChE IC_{50} was ~ 9 μM. While the quinazoline library contained 35–40 candidates (~ 30% of library size) with nanomolar to low micromolar IC_{50} values toward Aβ40 aggregation, it was essential to recall the primary goal of identifying multi-targeting derivatives.

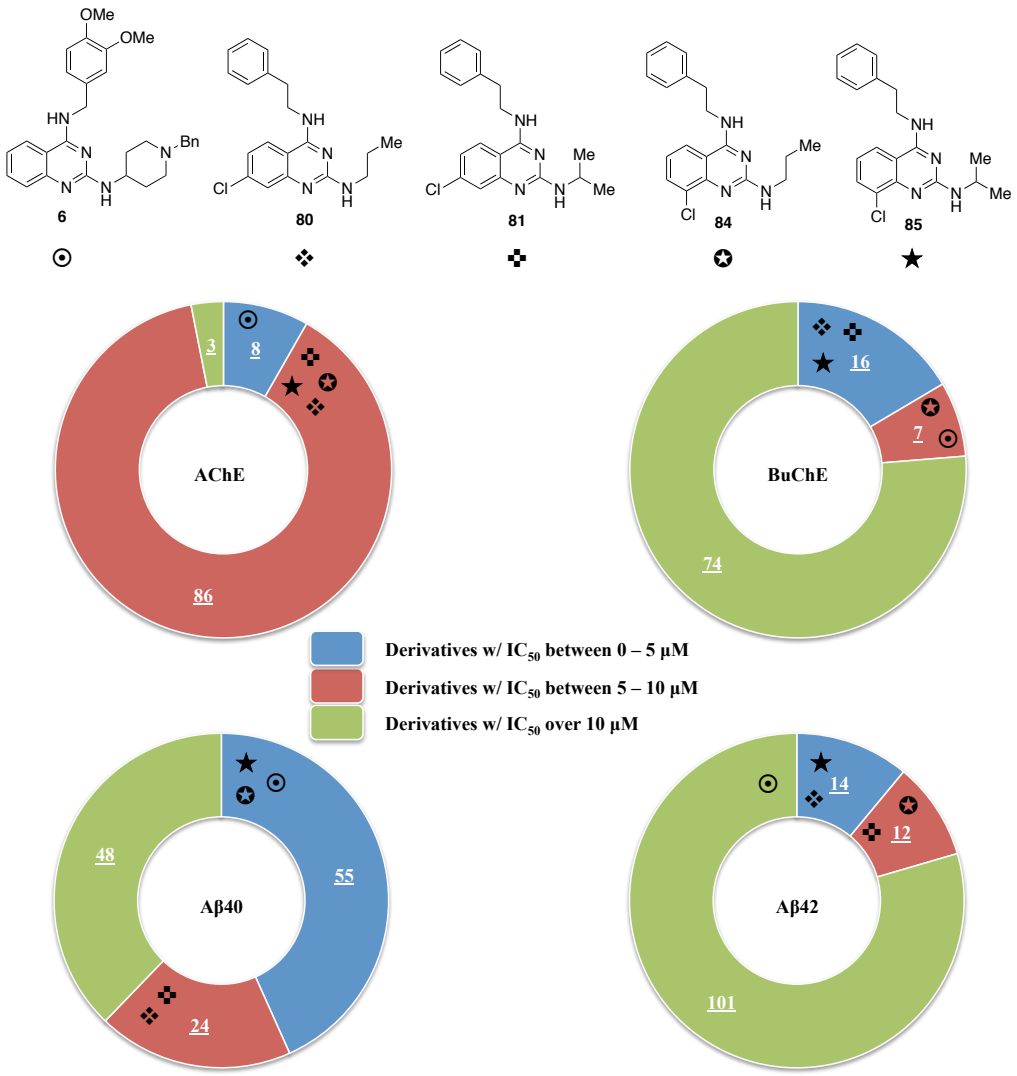


Figure 92: Collective metrics for complete quinazoline-based library. Selections were based on good to moderate activity against all 4 primary targets. (Notes: As Chapter 8 diaminoquinazolines were only assessed for Aβ aggregation, they were included in the Aβ pie charts but not considered during leading candidate selection. Derivatives screened for antioxidant and chelation capacities were not identified as complete multi-targeting candidates; hence those metrics were not included here).

➔ In terms of general observations:

- While placement of an azide moiety at the C2-position of the quinazoline scaffold was not particularly favourable toward ChE inhibition, few derivatives showed good activity toward Aβ aggregation

inhibition. It is plausible that, they may offer a more desirable outcome if placed elsewhere in the molecule.

- While placement of carbonyl moieties (at least amides) at the C2-position of the quinazoline scaffold was not useful against BuChE, they did provide valuable SAR toward other targets of interest.
- The 3,4-dimethoxy moiety at the C4-position was favoured for enhancing AChE targeting but that usually came at the cost of BuChE inhibition.
- The additional methylene linker at the C4-position yielded more positive outcomes compared its absence.
- The transition from the quinazoline scaffold to the chlorinated quinazoline scaffolds yielded more positive outcomes, especially toward Aβ targeting.
- The transition from the quinazoline scaffold to the pyridopyrimidine scaffold was not effective considering the null effects on AChE, loss of BuChE activity and reduced activities toward Aβ40. While they did provide moderate levels of Fe^{2+} chelation, further optimization with that scaffold is required.
- Regioisomeric investigations highlighted the preference/selectivity of C2-alkylated derivatives toward more hydrophobic targets, like BuChE and Aβ42 (compared to their C4-alkylated isomers).

➔With respect to future studies regarding this research program, some short/mid-term goals include:

- Cholinesterase assessment of diaminoquinazolines (from Chapter 8) as that could alter existing leading candidate selections. Halogen-based derivatives, in particular, would be of keen interest considering their strong anti-Aβ activities.
- Establishing MTT toxicity profiles for leading candidates, especially considering their higher ClogP values. Furthermore, establishing co-incubation toxicity profiles with Aβ and leading derivatives would provide key insight into their anti-Aβ-induced toxicity potential.
- Assessment of top candidates toward tau aggregation as a 5^{th} primary target.
- Establishing some pharmacokinetic profiles for leading candidates to assess preclinical eligibility.

- Potential re-purposing of weaker candidates toward oncology targets.

➔ On the other hand, further optimization and/or project expansion could incorporate:

- Assessments of other quinazoline-related scaffolds, such as quinoline or tetrahydroquinazoline.
- Expansions to the nature and size of the alkylamines utilized at the C2-position. Small cyclic amines would be worthy of assessment.
- Off-scaffold chelation centers and/or phenolic moieties for antioxidant capacity.
- Comparisons of quinazoline-2,4-diols or quinazoline-2,4-dithiols to the quinazoline-2,4-diamines.

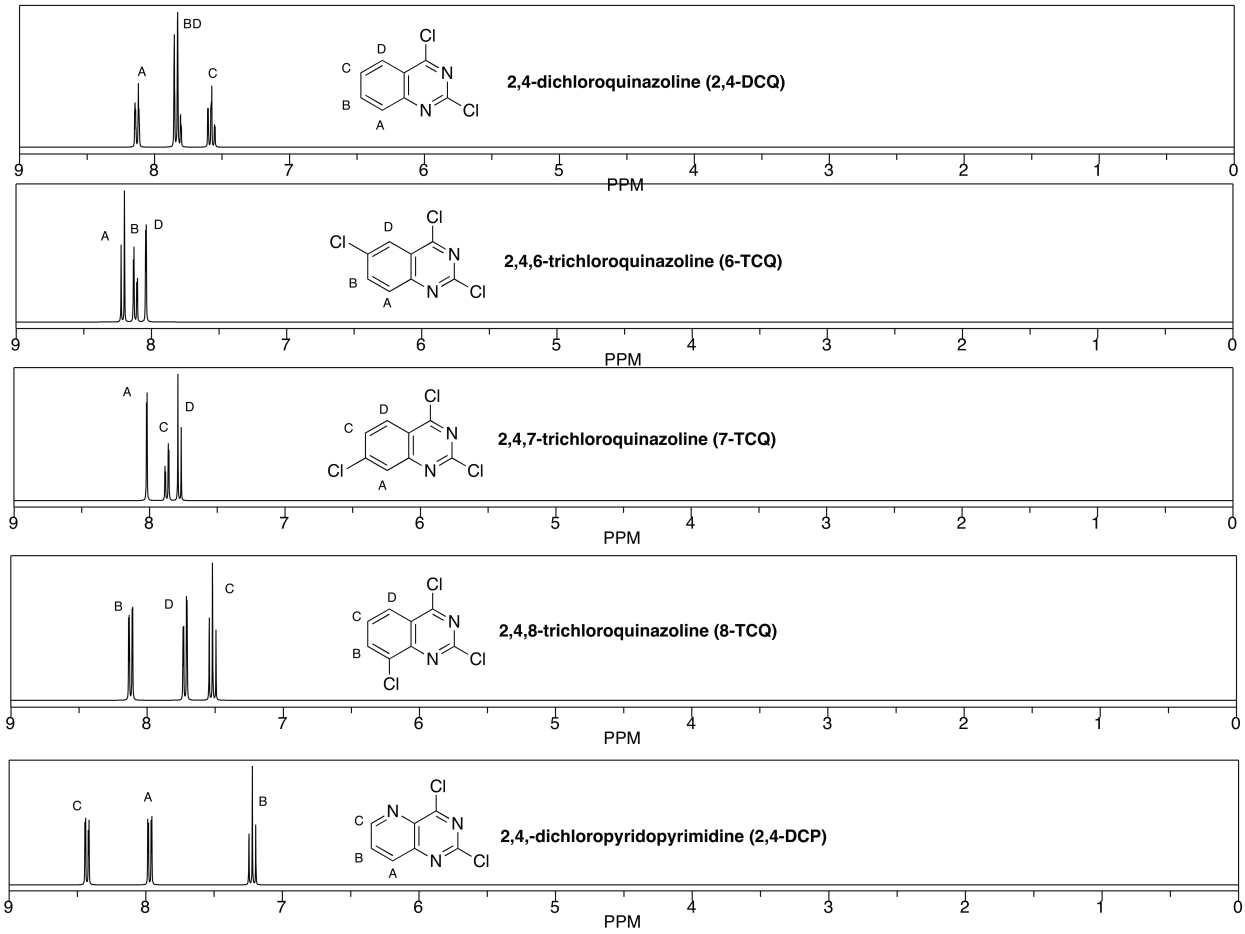
It was interesting to observe the narrower inhibitory window of these derivatives toward AChE (as compared to BuChE) and perhaps performing some molecular dynamic studies or competitive-binding assays would help explain these observations. With respect to Aβ activity, a wide range of inhibitory activity was observed., indicating that these quinazoline scaffolds can be further explored and utilized in anti-Aβ research programs.

In summary, the SAR data obtained for the quinazoline libraries (3,4-dimethoxybenzyl, benzyl, 3,4-dimethoxyphenethyl and phenethyl series) yielded several interesting findings and validated the hypothesis that a quinazoline-scaffold is a versatile ring system that can be modified to design small molecules as potential multi-targeting agents to treat AD. In addition, these quinazoline based small molecules have the potential to be used as pharmacological tools to investigate and understand the mechanisms of protein aggregation. With current evidence strongly supporting the mandate to develop multi-pronged approaches to achieve the desired disease-modifying effects, the results discussed here could aid in the formulation of new drug development strategies to the deviate from the “one drug, one target” approach and yield newer generation therapies for AD patients.

• Appendices •

Appendix I: Sample spectra for Chapter 2

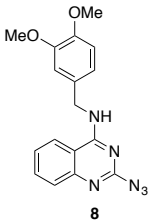
Section A: NMR



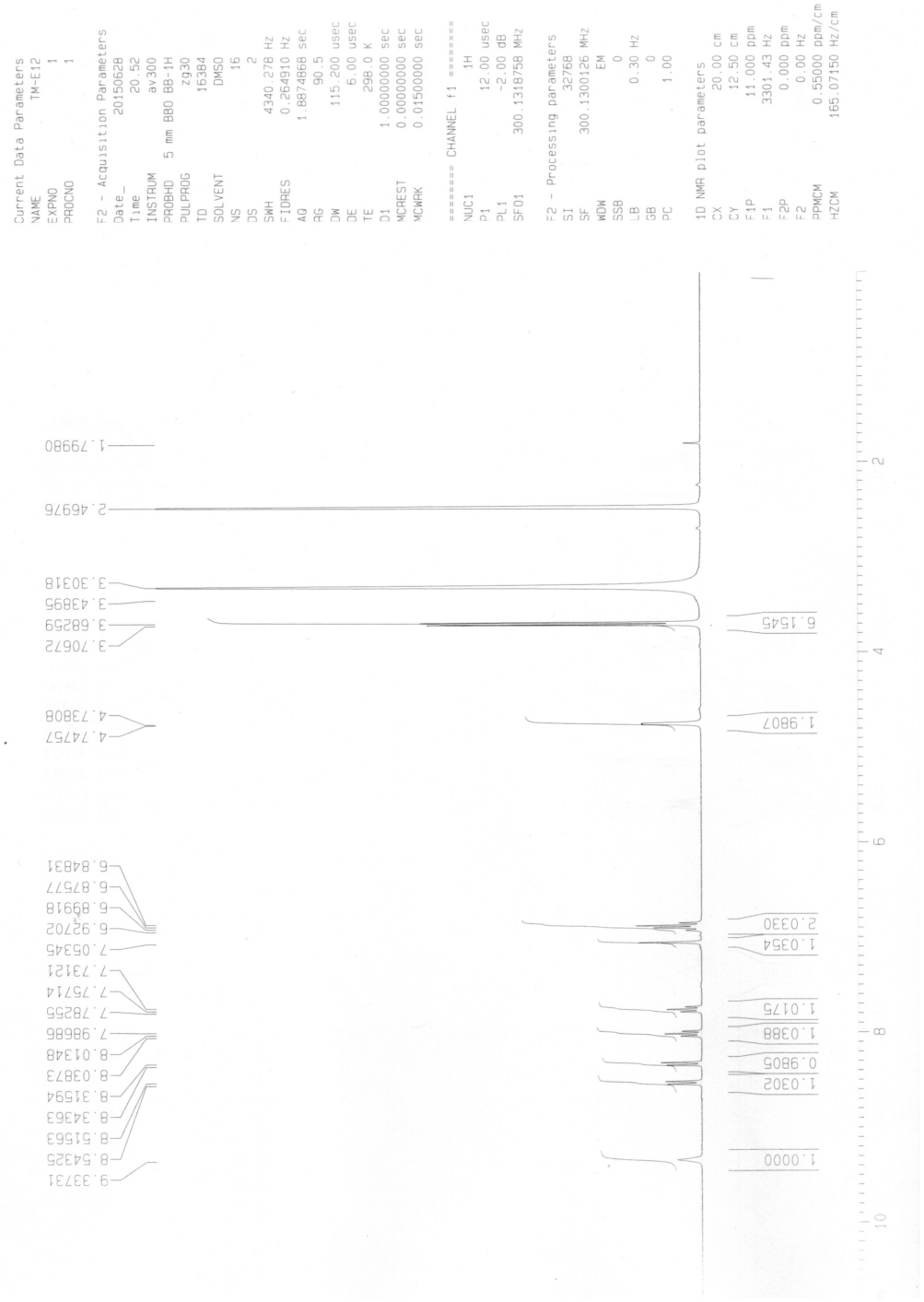
**** Spectra generated using ChemDraw Professional 15.0***

Appendix II: Sample spectra for Chapter 3

Section A: NMR

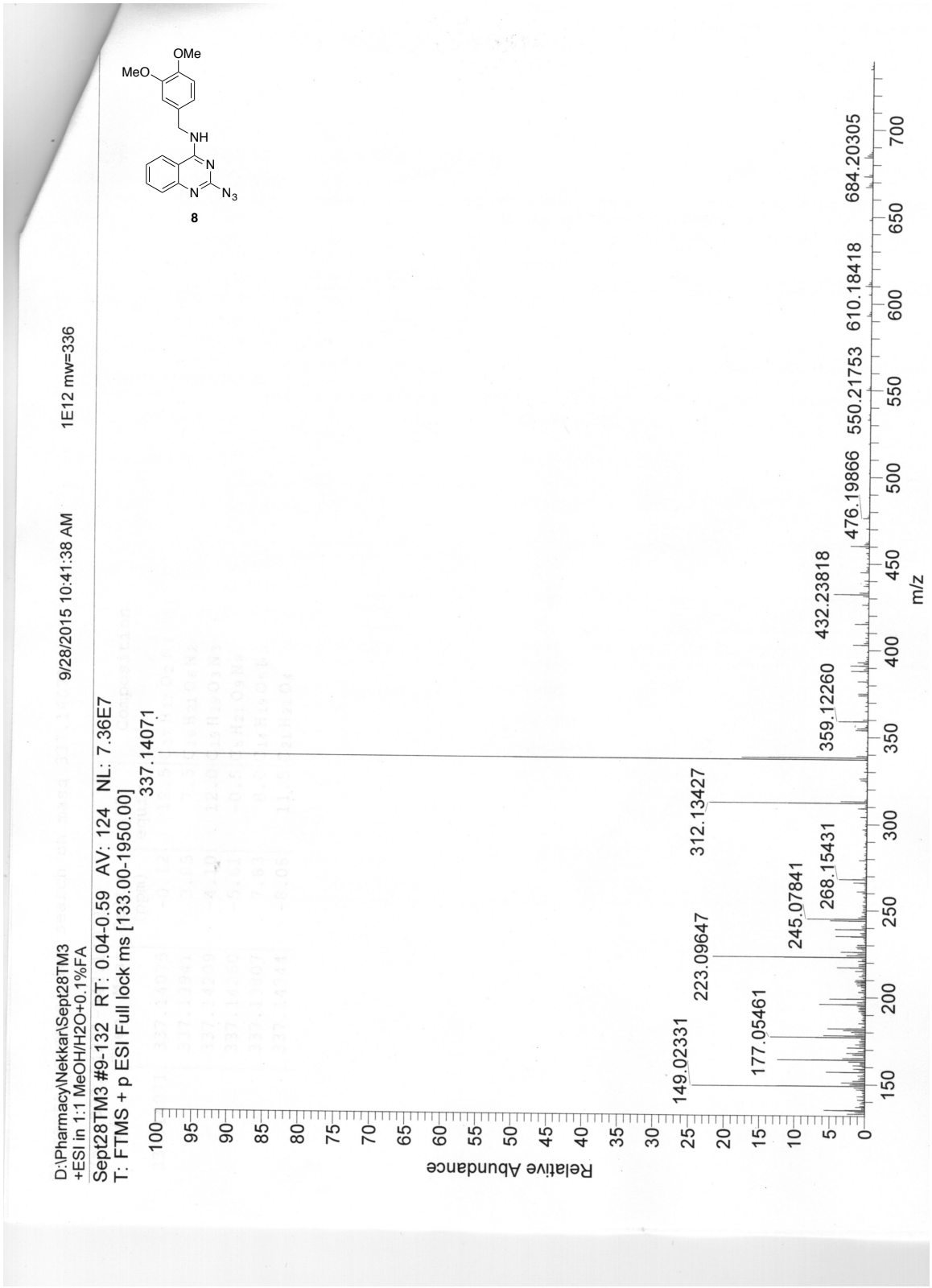


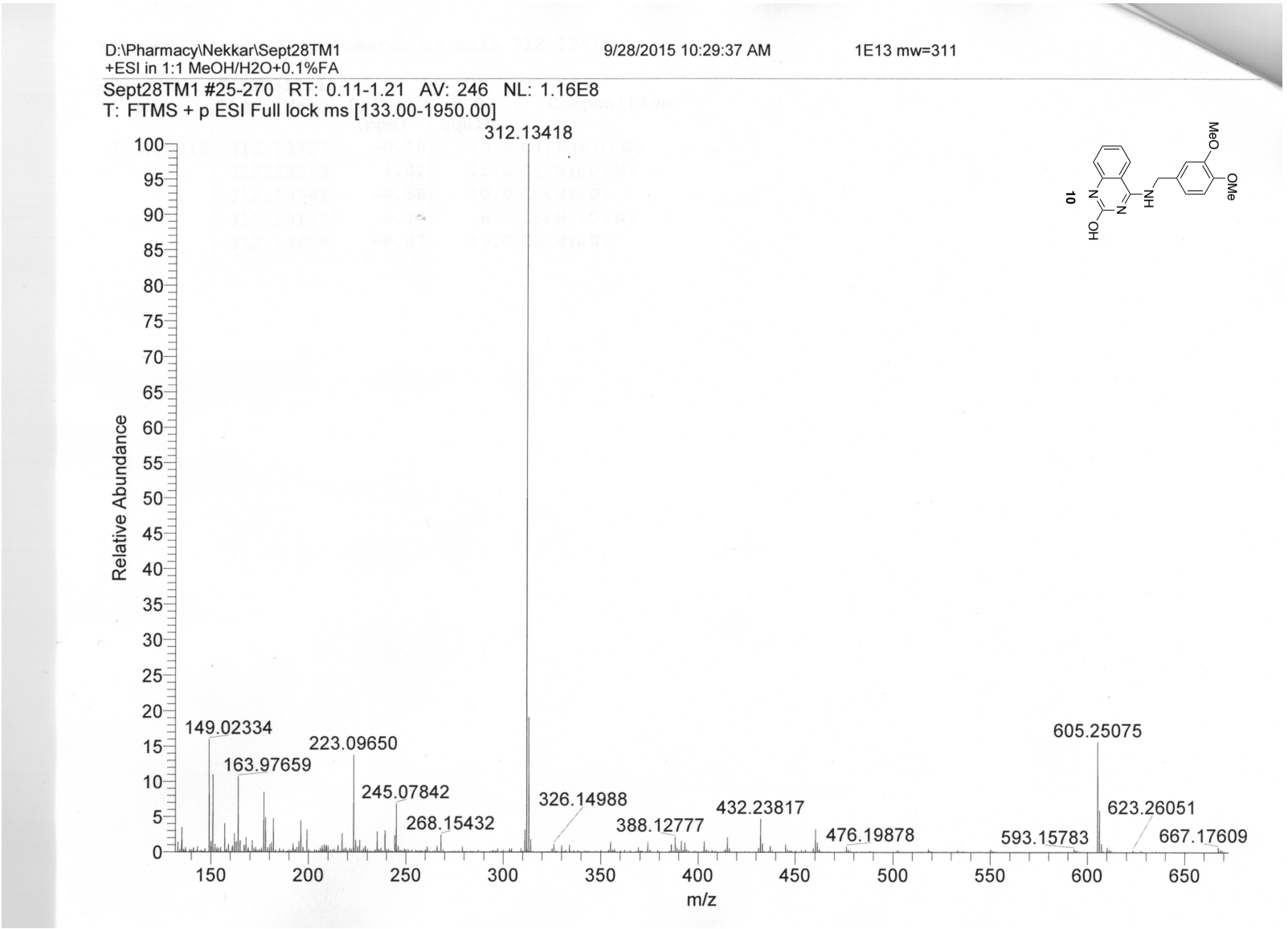
8



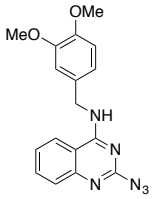

OMe
MeO
NH
N
N
OH
10
Current Data Parameters
NAME TM-qnz1E-OH-fromazide
EXPNO 1
PROCNO 1
F2 - Acquisition Parameters
Date_ 20150704
Time 22.54
INSTRUM av300
PROBHD 5 mm BBO BB-1H
PULPROG zg30
TD 16384
SOLVENT DMSO
NS 16
DS 2
SWH 4340.278 Hz
FIDRES 0.264910 Hz
AQ 1.8874868 sec
RG 161.3
DW 115.200 usec
DE 6.00 usec
TE 298.0 K
D1 1.00000000 sec
MCREST 0.00000000 sec
MCWRK 0.01500000 sec
======== CHANNEL f1 ========
NUC1 1H
P1 12.00 usec
PL1 -2.00 dB
SFO1 300.1318758 MHz
F2 - Processing parameters
SI 32768
SF 300.1300126 MHz
WDW EM
SSB 0
LB 0.30 Hz
GB 0
PC 1.00
1D NMR plot parameters
CX 20.00 cm
CY 12.50 cm
F1P 12.000 ppm
F1 3601.56 Hz
F2P -0.000 ppm
F2 -0.00 Hz
PPMCM 0.60000 ppm/cm
HZCM 180.07800 Hz/cm
1.2037
1.9557
2.0525
2.4686
3.2862
3.5838
3.6991
4.5844
4.6030
6.8054
6.8336
6.8494
6.8767
6.9838
7.0479
7.0731
7.0931
7.1189
7.4914
7.5165
7.5418
7.5581
7.5804
7.5958
7.6195
8.0229
8.0498
8.6487
8.6676
8.6860
10.5108
6.1924
2.1190
2.1261
0.9994
2.0994
2.2008
1.0478
1.0000
0.9517

Section B: HRMS

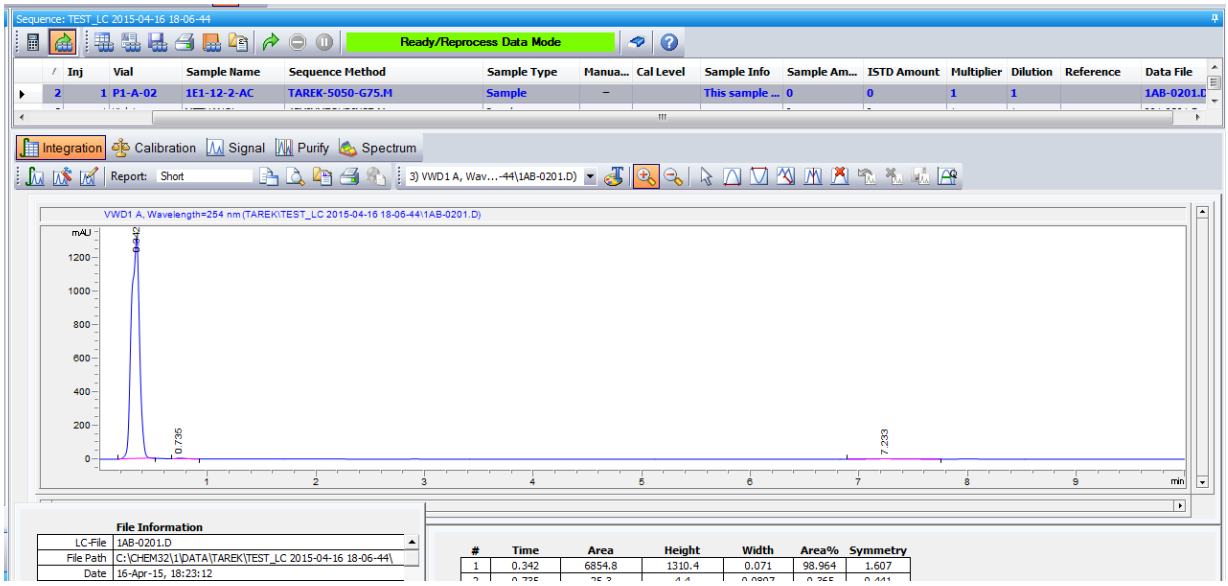


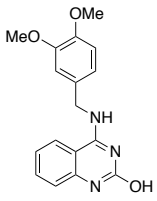

D:\Pharmacy\Nekkar\Sept28TM1
+ESI in 1:1 MeOH/H2O+0.1%FA
9/28/2015 10:29:37 AM
1E13 mw=311
Sept28TM1 #25-270 RT: 0.11-1.21 AV: 246 NL: 1.16E8
T: FTMS + p ESI Full lock ms [133.00-1950.00]
312.13418
149.02334
163.97659
223.09650
245.07842
268.15432
326.14988
388.12777
432.23817
476.19878
593.15783
605.25075
623.26051
667.17609
Relative Abundance
m/z
MeO
OMe
NH
N
N
OH
10

Section C: HPLC

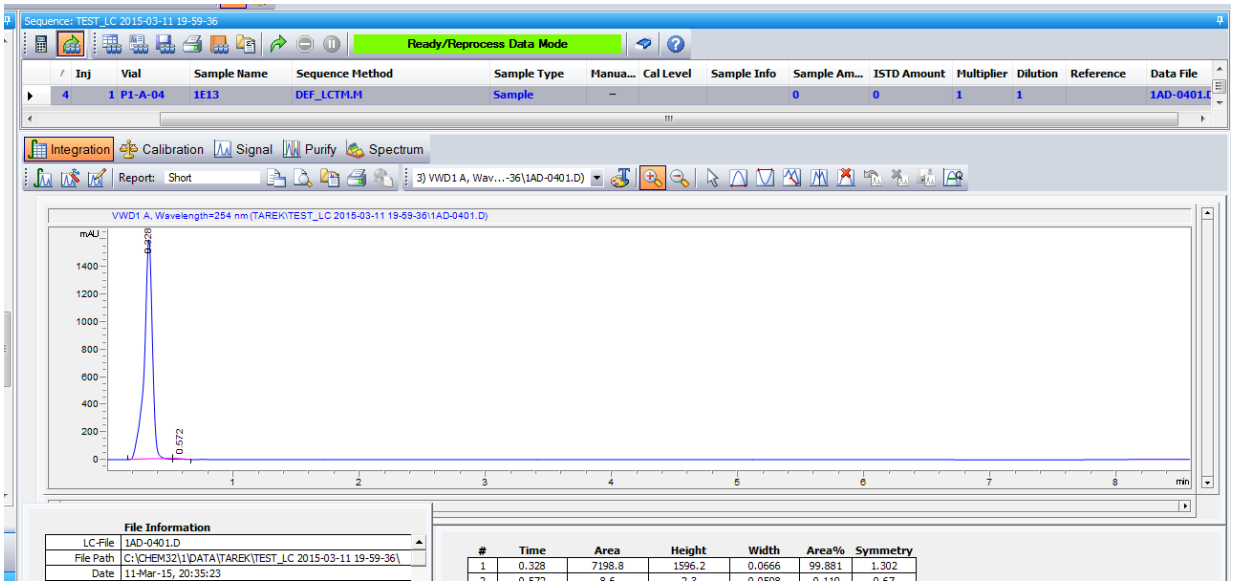


8



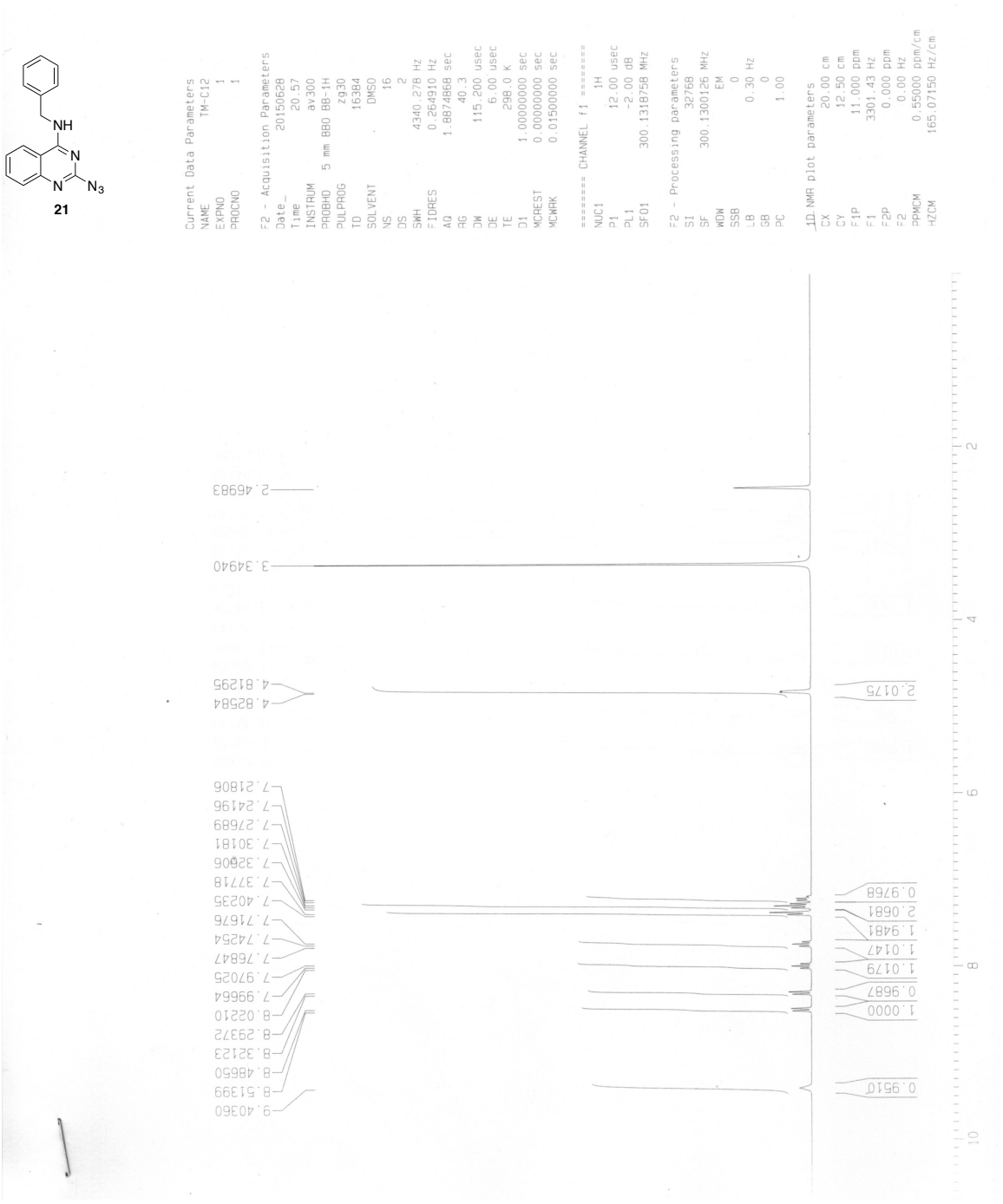


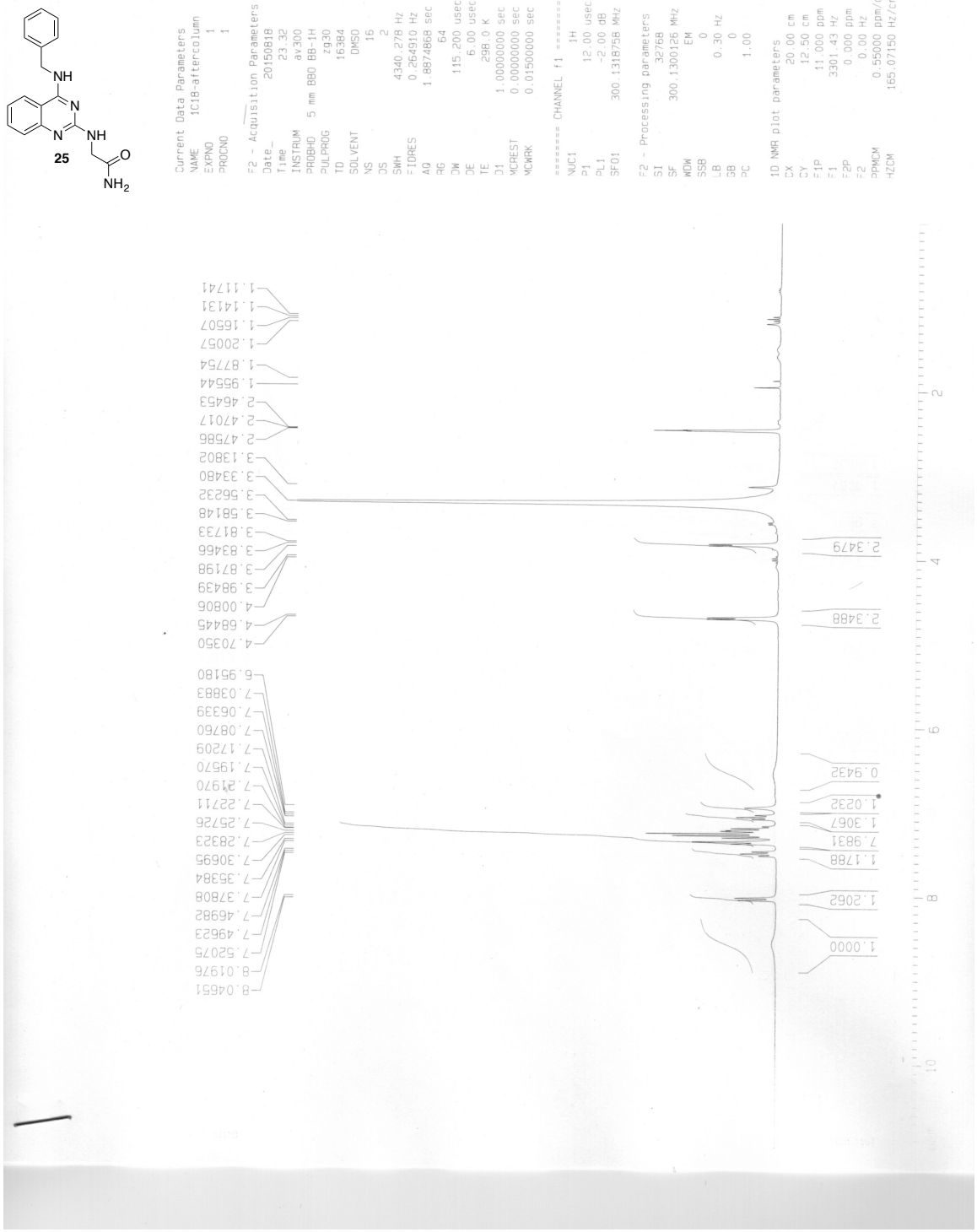
10



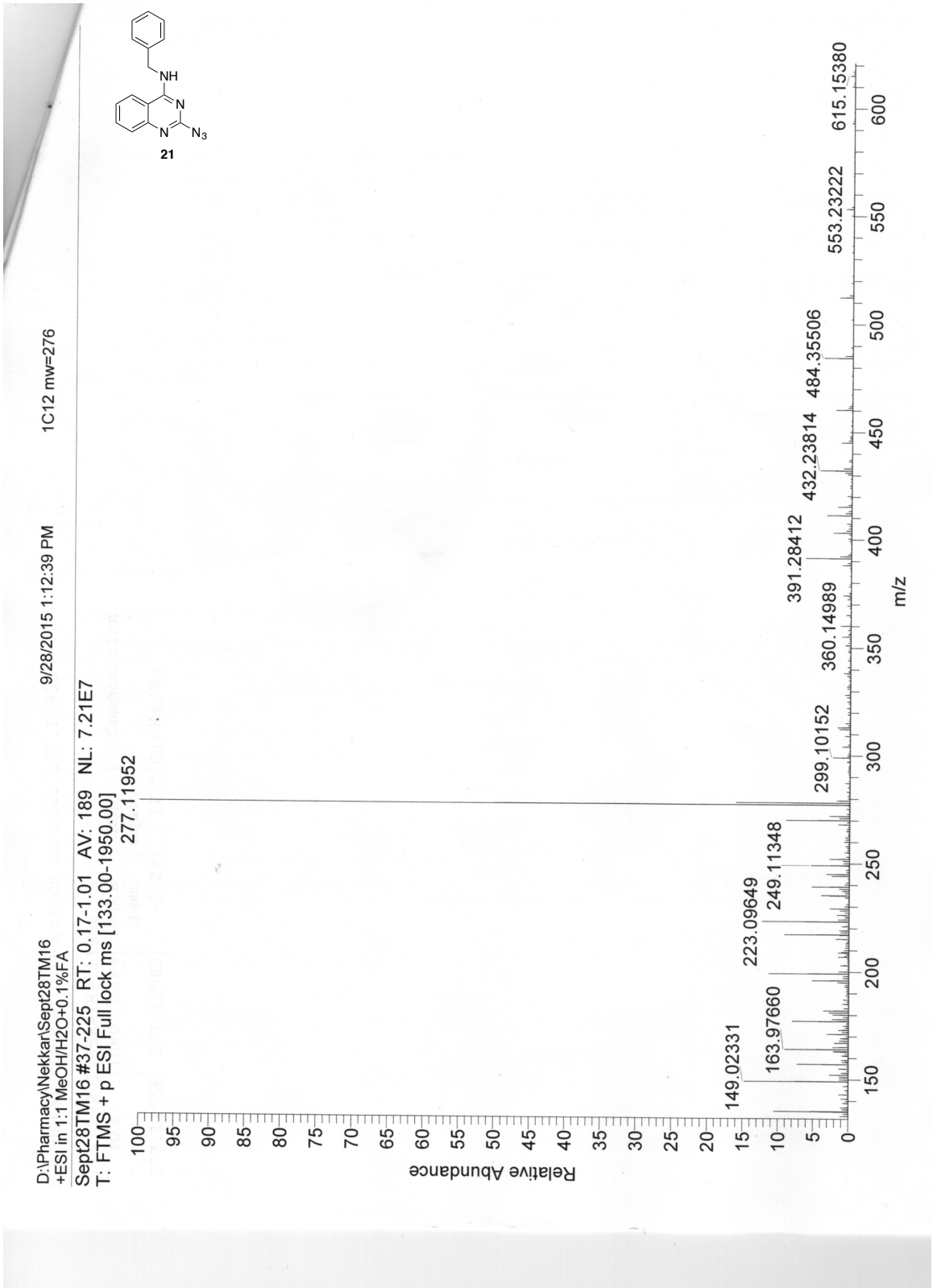
Appendix III: Sample spectra for Chapter 4

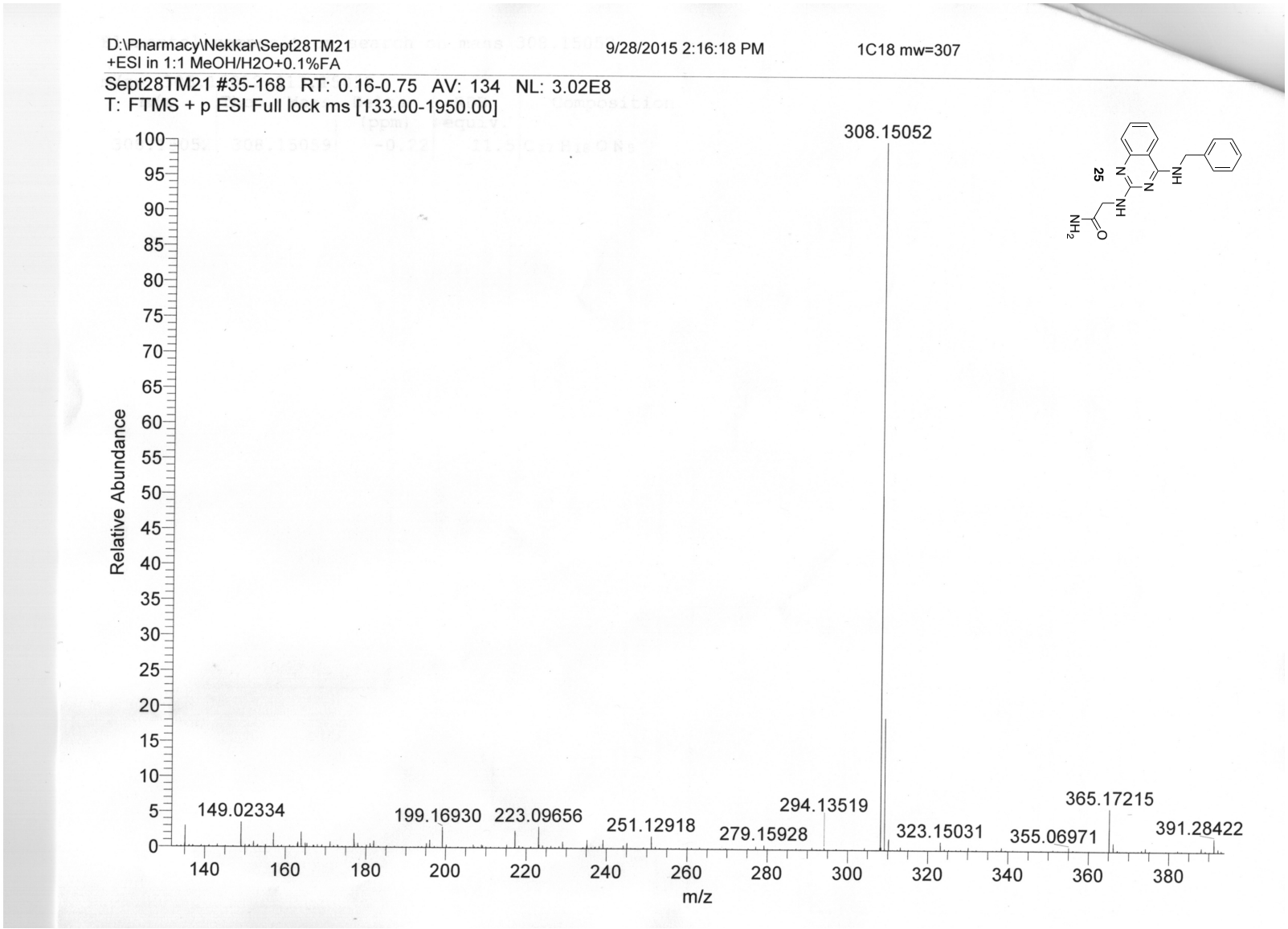
Section A: NMR



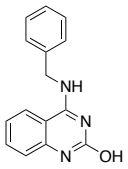

25
Current Data Parameters
NAME 1C18-aftercolumn
EXPNO 1
PROCNO 1
F2 - Acquisition Parameters
Date_ 20150818
Time 23.32
INSTRUM av300
PROBHD 5 mm BBO BB-1H
PULPROG zg30
TD 16384
SOLVENT DMSO
NS 16
DS 2
SWH 4340.278 Hz
FIDRES 0.264910 Hz
AQ 1.8874868 sec
RG 64
DW 115.200 usec
DE 6.00 usec
TE 298.0 K
D1 1.00000000 sec
WCREST 0.00000000 sec
WCWRK 0.01500000 sec
======= CHANNEL f1 =======
NUC1 1H
P1 12.00 usec
PL1 -2.00 dB
SF01 300.1318758 MHz
F2 - Processing parameters
SI 32768
SF 300.1300125 MHz
WDW EM
SSB 0
LB 0.30 Hz
GB 0
PC 1.00
1D NMR plot parameters
CX 20.00 cm
CY 12.50 cm
F1P 11.000 ppm
F1 3301.43 Hz
F2P 0.000 ppm
F2 0.00 Hz
PPMCM 0.55000 ppm/cm
HZCM 165.07150 Hz/cm
1.11741
1.14131
1.16507
1.20057
1.87754
1.95544
2.46453
2.47017
2.47586
3.13802
3.33480
3.56232
3.58148
3.81733
3.83466
3.87198
3.98439
4.00806
4.68445
4.70350
6.95180
7.03883
7.06339
7.08760
7.17209
7.19570
7.21970
7.22711
7.25726
7.28323
7.30695
7.33684
7.37808
7.46982
7.49623
7.52075
8.01976
8.04651
2.3479
2.3488
0.9432
1.0232
1.3067
7.9831
1.1788
1.2062
1.0000

Section B: HRMS

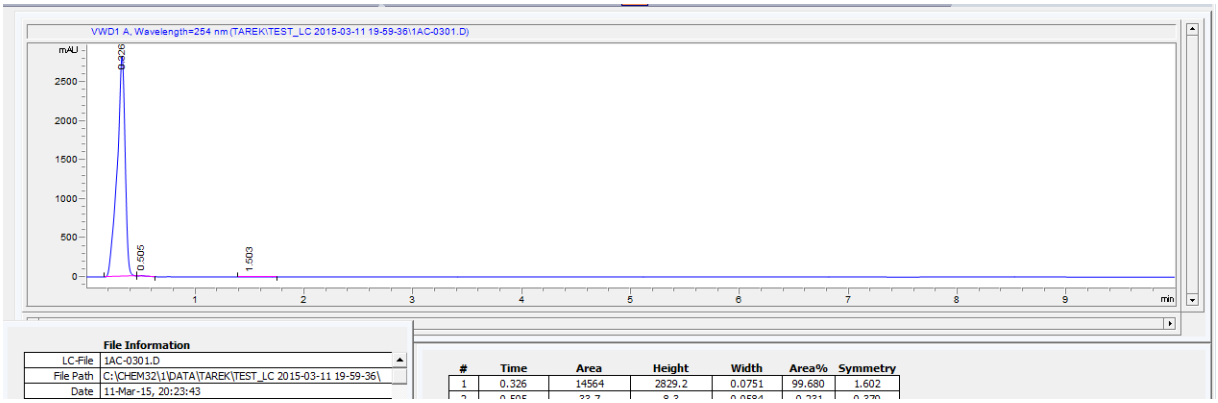



D:\Pharmacy\Nekkar\Sept28TM21
+ESI in 1:1 MeOH/H2O+0.1%FA
9/28/2015 2:16:18 PM
1C18 mw=307
Sept28TM21 #35-168 RT: 0.16-0.75 AV: 134 NL: 3.02E8
T: FTMS + p ESI Full lock ms [133.00-1950.00]
308.15052
149.02334
199.16930
223.09656
251.12918
279.15928
294.13519
323.15031
355.06971
365.17215
391.28422
Relative Abundance
m/z
25

Section C: HPLC

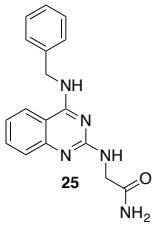


23

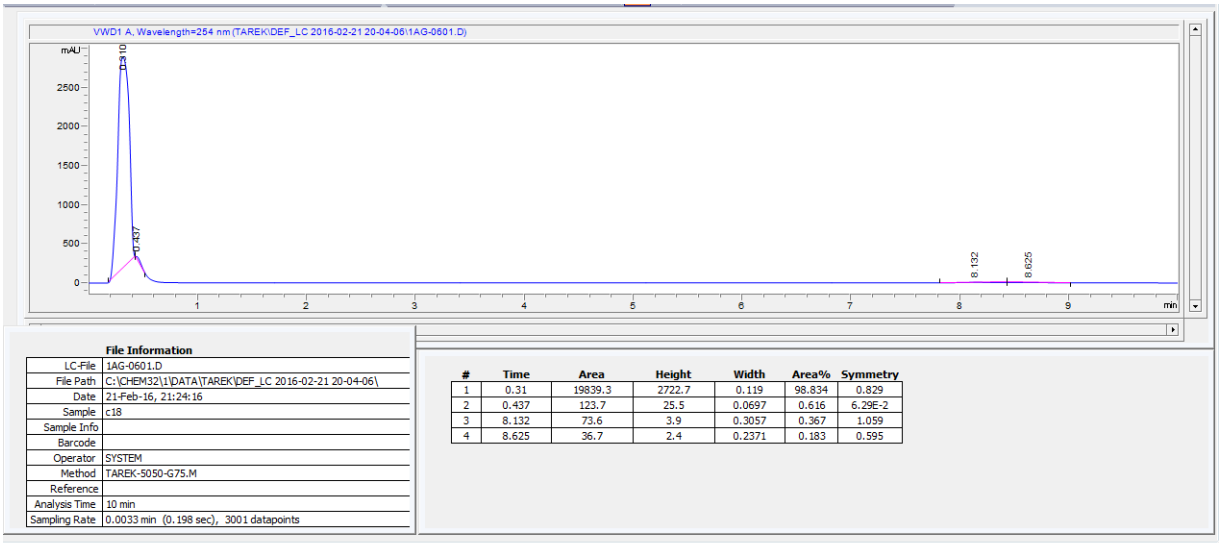


File Information	
LC-File	1AC-0301.D
File Path	C:\CHEM32\1\DATA\TAREK\TEST_LC 2015-03-11 19-59-36\
Date	11-Mar-15, 20:23:43

#	Time	Area	Height	Width	Area%	Symmetry
1	0.326	14564	2829.2	0.0751	99.680	1.602



25

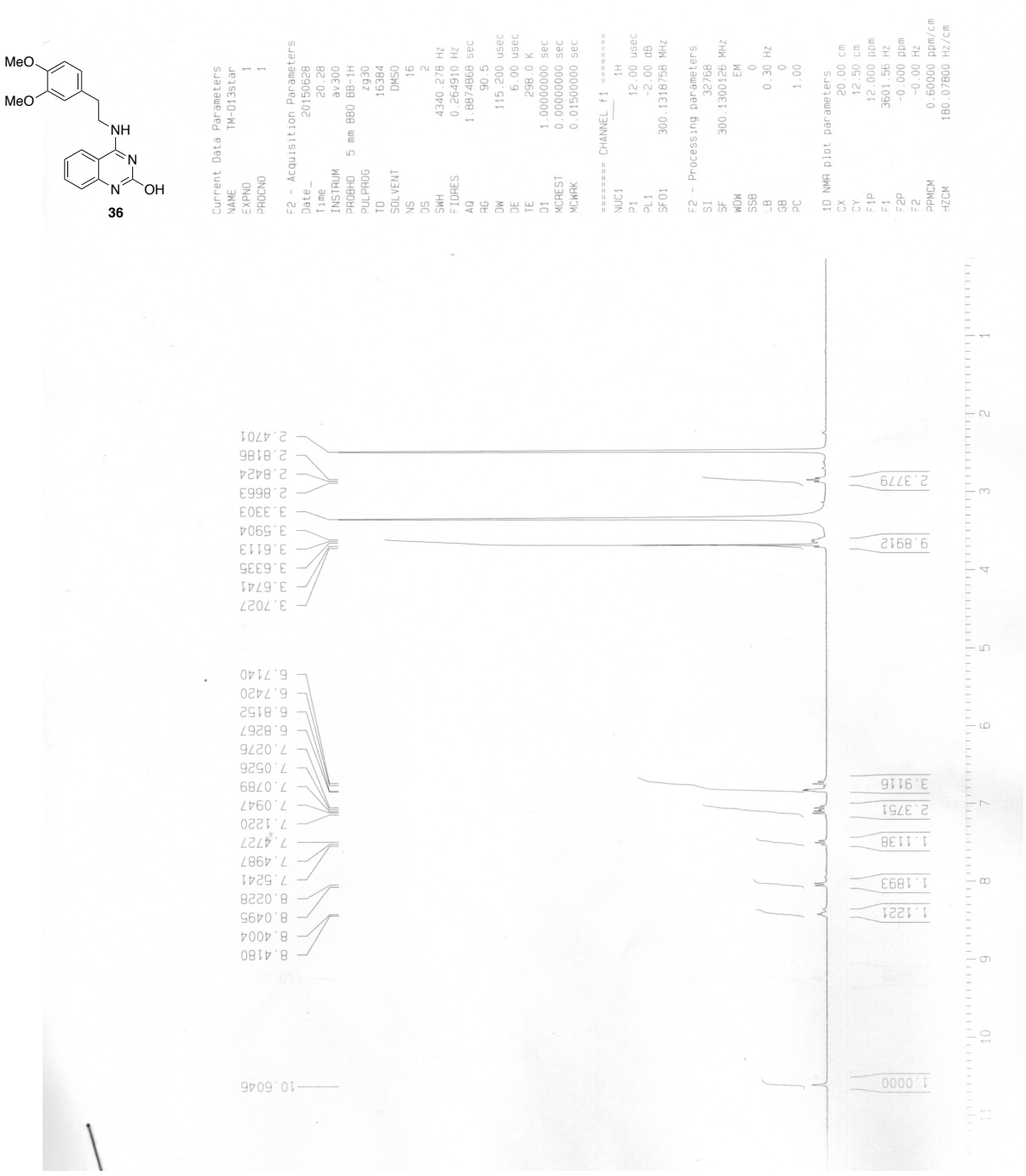


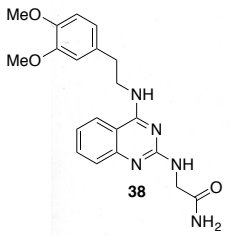
File Information	
LC-File	1AG-0601.D
File Path	C:\CHEM32\1\DATA\TAREK\DEF_LC 2016-02-21 20-04-06\
Date	21-Feb-16, 21:24:16
Sample	c18
Sample Info	
Barcode	
Operator	SYSTEM
Method	TAREK-5050-G75.M
Reference	
Analysis Time	10 min
Sampling Rate	0.0033 min (0.198 sec), 3001 datapoints

#	Time	Area	Height	Width	Area%	Symmetry
1	0.31	19839.3	2722.7	0.119	98.834	0.829
2	0.437	123.7	25.5	0.0697	0.616	6.29E-2
3	8.132	73.6	3.9	0.3057	0.367	1.059
4	8.625	36.7	2.4	0.2371	0.183	0.595

Appendix IV: Sample spectra for Chapter 5

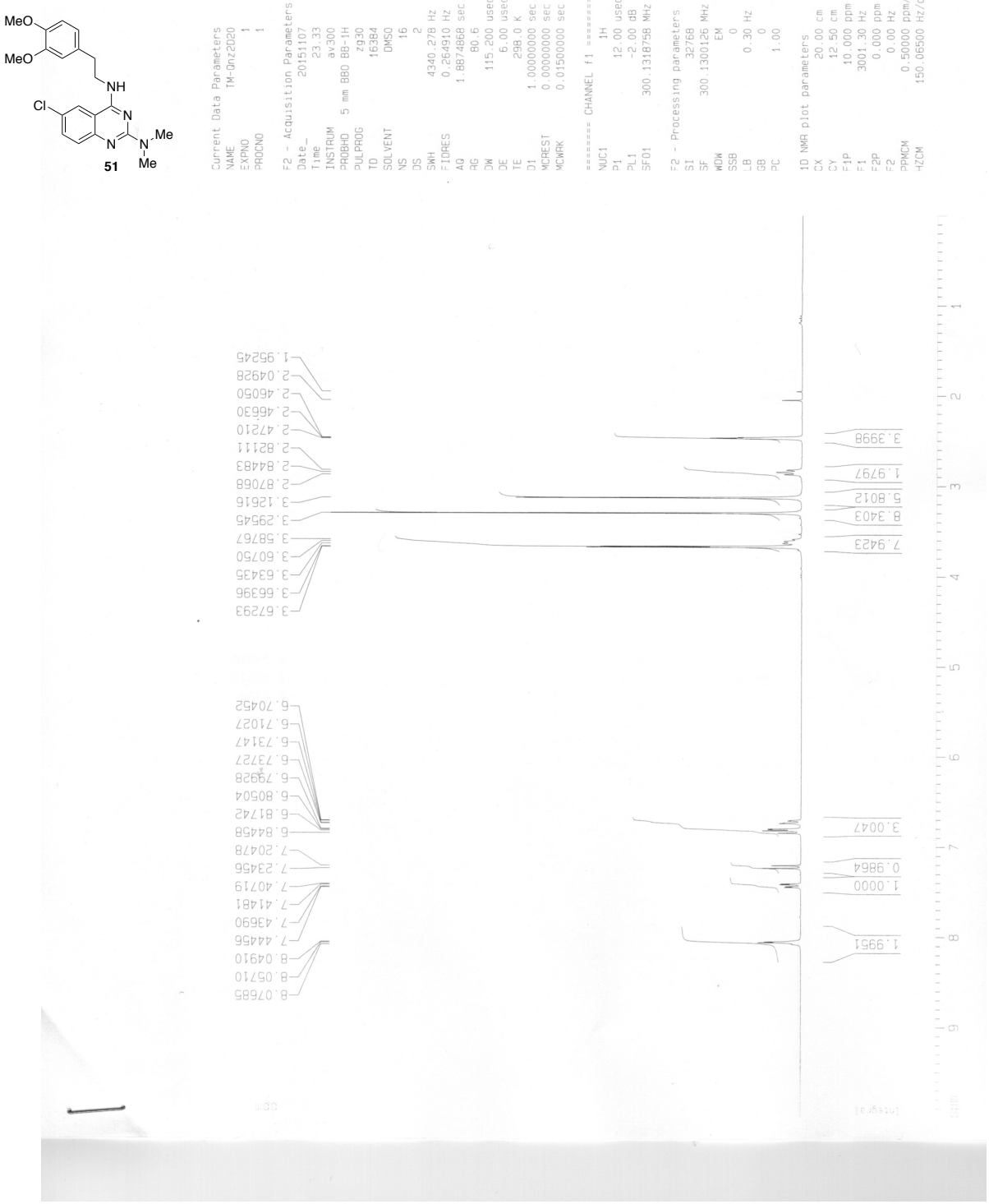
Section A: NMR

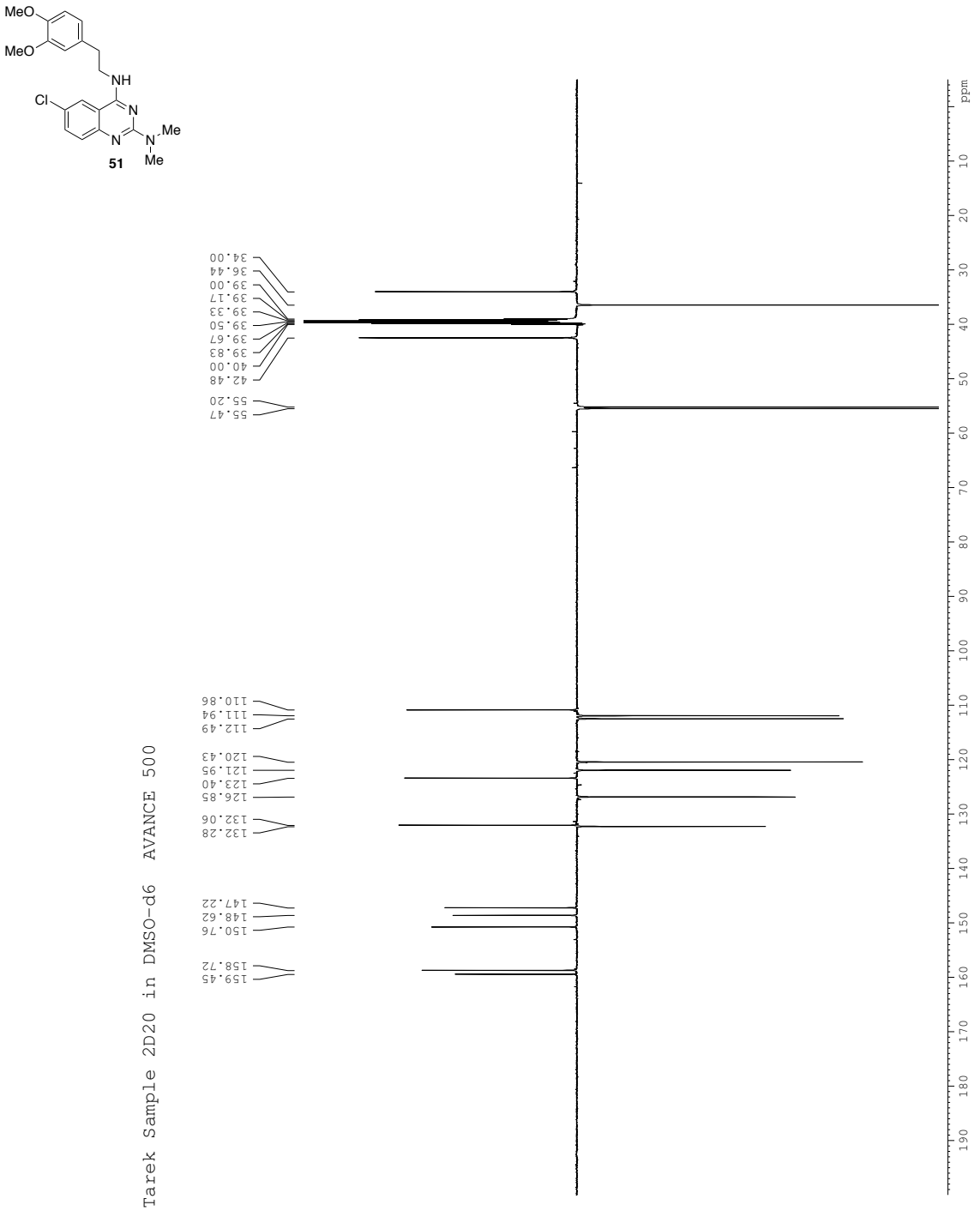


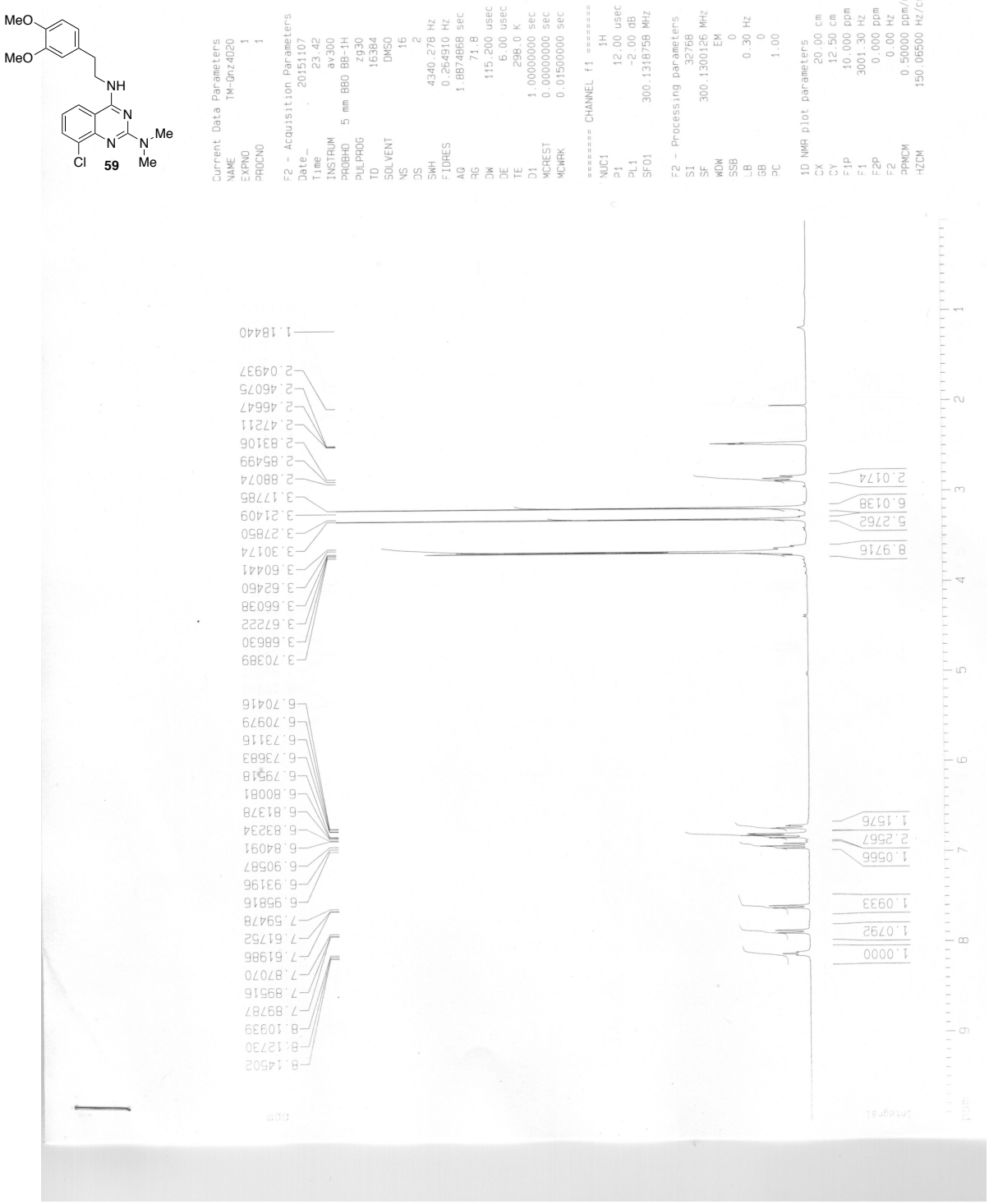

MeO
MeO
NH
N
N
NH
O
NH2

38

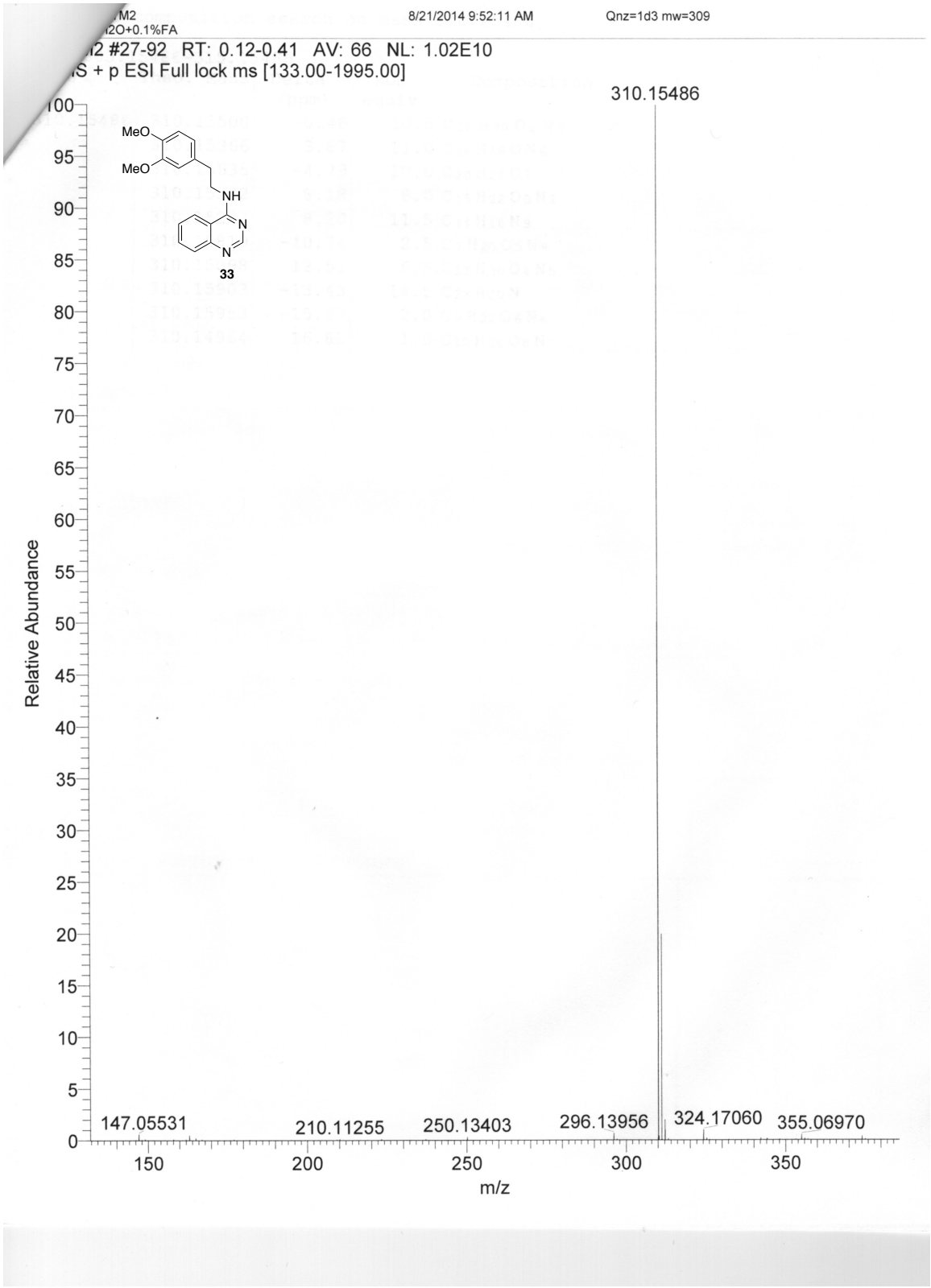
Current Data Parameters
NAME 1D18-aftercolumn
EXPNO 1
PROCNO 1
F2 - Acquisition Parameters
Date_ 20150818
Time 23.37
INSTRUM av300
PROBHD 5 mm BBO BB-1H
PULPROG zg30
TD 16384
SOLVENT DMSO
NS 16
DS 2
SWH 4340.278 Hz
FIDRES 0.264910 Hz
AQ 1.8874868 sec
RG 64
DW 115.200 usec
DE 6.00 usec
TE 298.0 K
D1 1.00000000 sec
MCREST 0.00000000 sec
MCWRK 0.01500000 sec
======== CHANNEL f1 ========
NUC1 1H
P1 12.00 usec
PL1 -2.00 dB
SF01 300.1318758 MHz
F2 - Processing parameters
SI 32768
SF 300.1300126 MHz
WDW EM
SSB 0
LB 0.30 Hz
GB 0
PC 1.00
1D NMR plot parameters
CX 20.00 cm
CY 12.50 cm
F1P 11.000 ppm
F1 3301.43 Hz
F2P 0.000 ppm
F2 0.00 Hz
PPMCM 0.55000 ppm/cm
HZCM 165.07150 Hz/cm
2.46482
2.47033
2.47595
2.82370
2.84727
2.87289
3.33038
3.59167
3.61201
3.63764
3.67738
3.68478
3.85467
3.87260
6.74016
6.74526
6.76766
6.77239
6.81487
6.82936
6.83461
6.84140
6.97240
7.01403
7.03960
7.06413
7.21501
7.24221
7.45198
7.47771
7.50260
7.93302
7.95992
1.7292
1.9117
5.3236
1.7692
0.7127
0.9658
1.7371
0.8079
0.9059
1.6404
0.8446
1.0000
0.5183

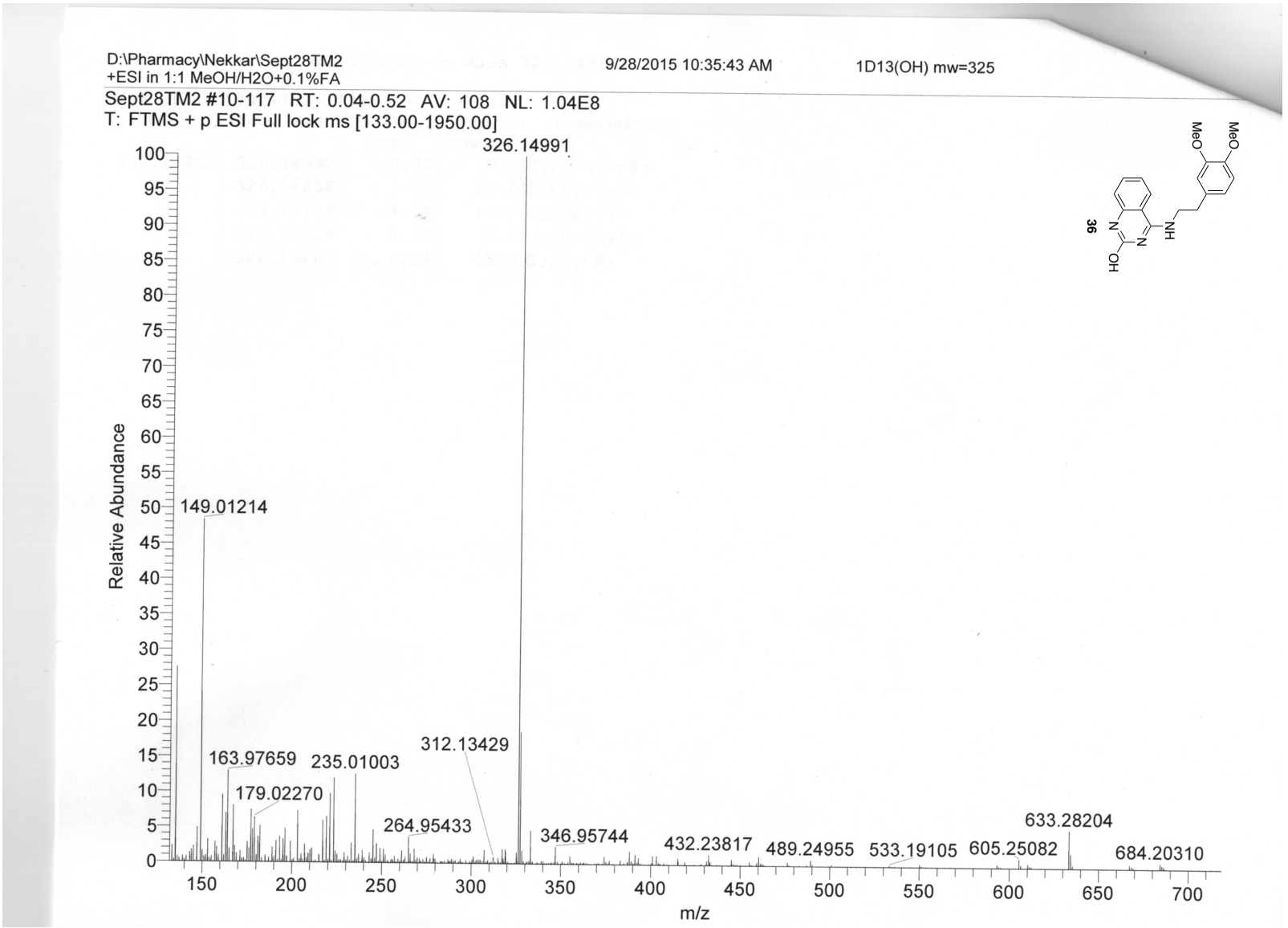

MeO
MeO
NH
Cl
N
N
N
Me
Me
51
Current Data Parameters
NAME TM-Qnz2020
EXPNO 1
PROCNO 1
F2 - Acquisition Parameters
Date_ 20151107
Time 23.33
INSTRUM av300
PROBHD 5 mm BBO BB-1H
PULPROG zg30
TD 16384
SOLVENT DMSO
NS 16
DS 2
SWH 4340.278 Hz
FIDRES 0.264910 Hz
AQ 1.8874868 sec
RG 80.6
DW 115.200 usec
DE 6.00 usec
TE 298.0 K
D1 1.00000000 sec
WCREST 0.00000000 sec
WCWRK 0.01500000 sec
======== CHANNEL f1 ========
NUC1 1H
P1 12.00 usec
PL1 -2.00 dB
SFO1 300.1318758 MHz
F2 - Processing parameters
SI 32768
SF 300.1300125 MHz
WDW EM
SSB 0
LB 0.30 Hz
GB 0
PC 1.00
1D NMR plot parameters
CX 20.00 cm
CY 12.50 cm
F1P 10.000 ppm
F1 3001.30 Hz
F2P 0.000 ppm
F2 0.00 Hz
PPMCM 0.50000 ppm/cm
HZCM 150.06500 Hz/cm
1.95245
2.04928
2.46050
2.46530
2.47210
2.82111
2.84483
2.87068
3.12616
3.29545
3.58767
3.60750
3.63435
3.66396
3.67293
6.70452
6.71027
6.73147
6.73727
6.79928
6.80504
6.81742
6.84458
7.20478
7.23456
7.40719
7.41481
7.43690
7.44456
8.04910
8.05710
8.07685
3.3998
1.9797
5.8012
8.3403
7.9423
3.0047
0.9864
1.0000
1.9951

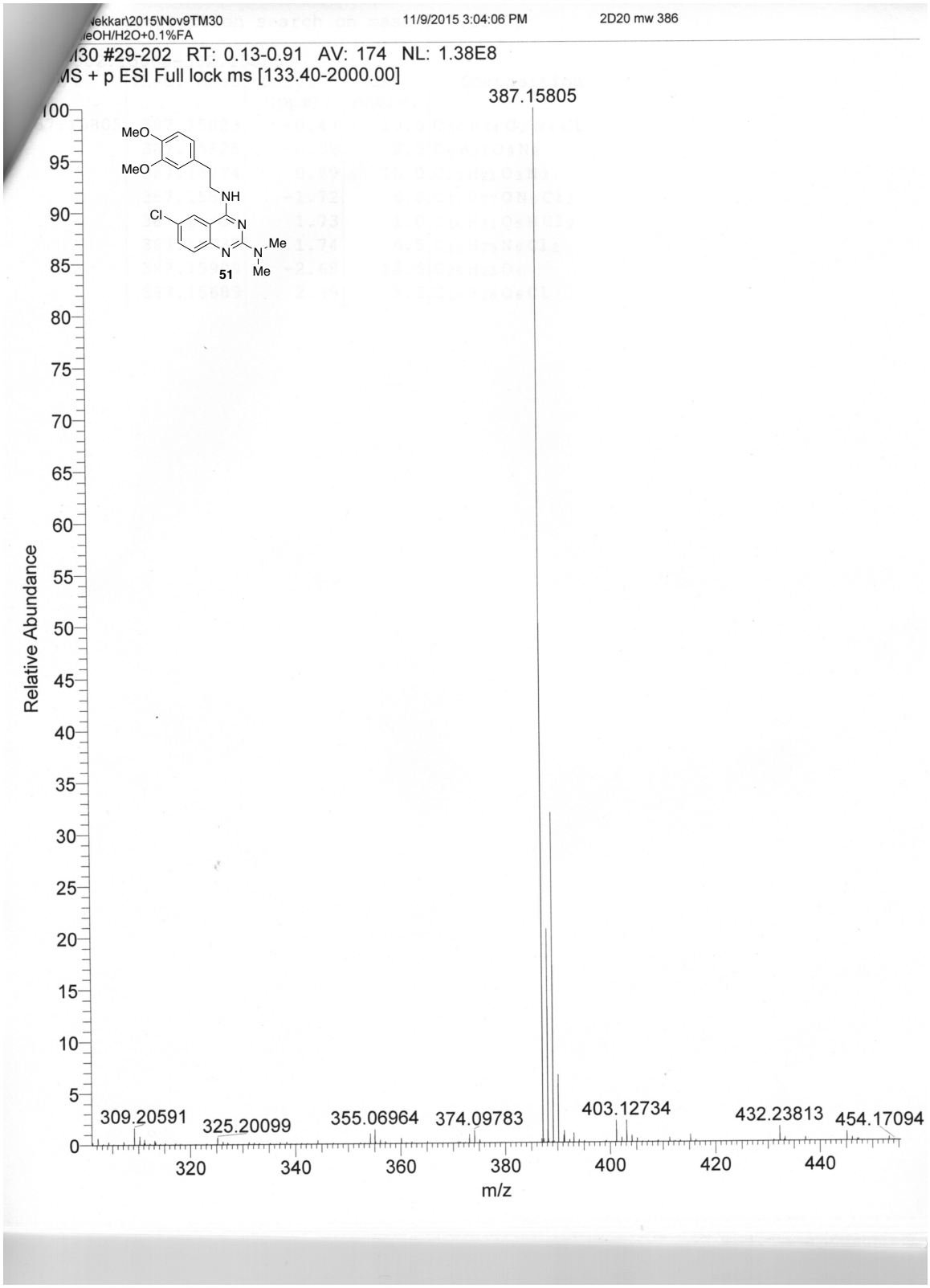

MeO
MeO
NH
Cl
N
N
N
Me
Me
51
Tarek Sample 2D20 in DMSO-d6 AVANCE 500
34.00
36.44
39.00
39.17
39.33
39.50
39.67
39.83
40.00
42.48
55.20
55.47
110.86
111.94
112.49
120.43
121.95
123.40
126.85
132.06
132.28
147.22
148.62
150.76
158.72
159.45
ppm

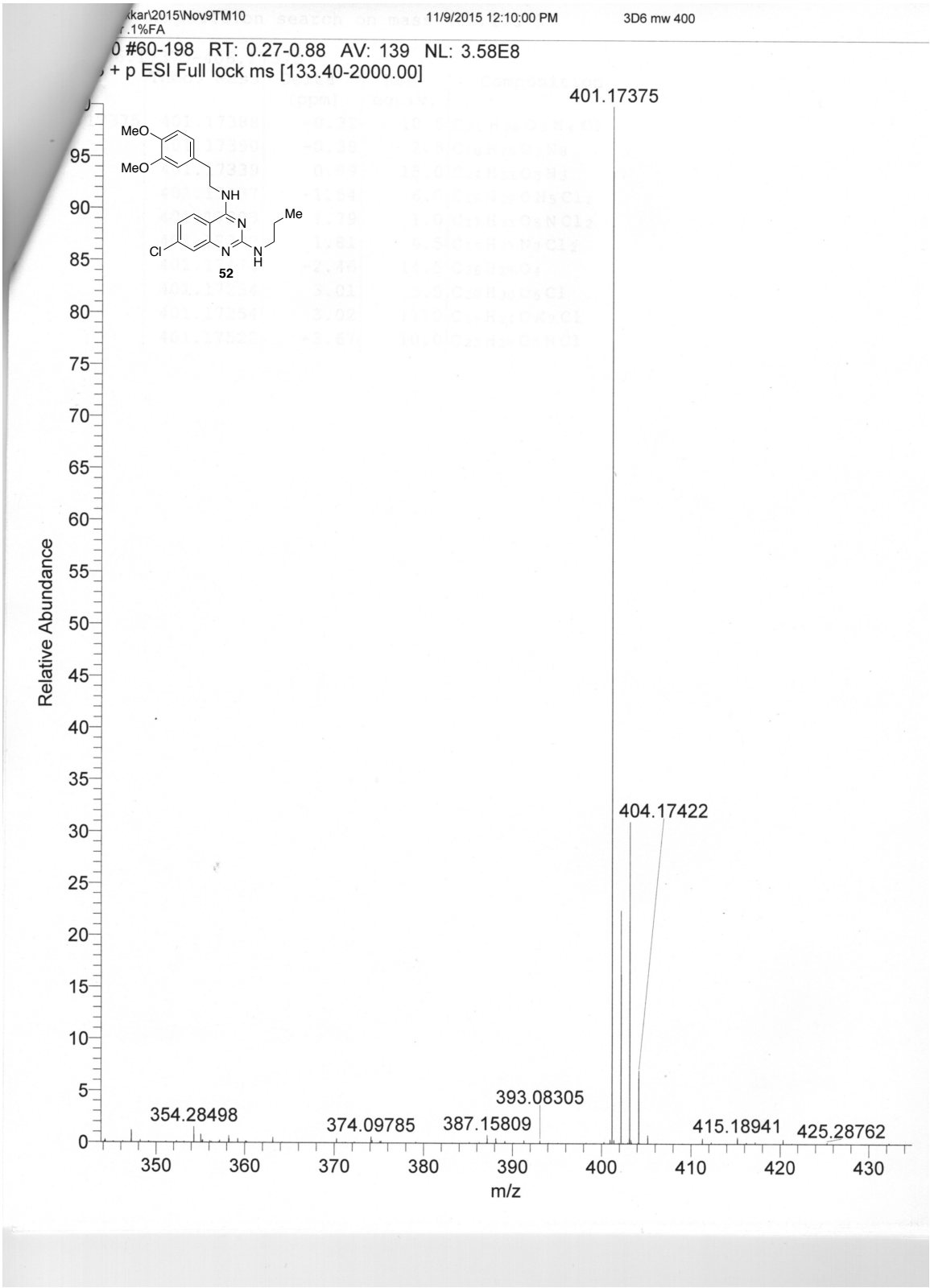

MeO
MeO
NH
N
N
N
Me
Me
Cl
59

Section B: HRMS

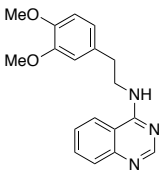



D:\Pharmacy\Nekkar\Sept28TM2
+ESI in 1:1 MeOH/H2O+0.1%FA
9/28/2015 10:35:43 AM
1D13(OH) mw=325
Sept28TM2 #10-117 RT: 0.04-0.52 AV: 108 NL: 1.04E8
T: FTMS + p ESI Full lock ms [133.00-1950.00]
326.14991
149.01214
163.97659
235.01003
312.13429
179.02270
264.95433
346.95744
432.23817
489.24955
533.19105
605.25082
633.28204
684.20310
Relative Abundance
m/z
MeO
MeO
NH
N
N
OH
36

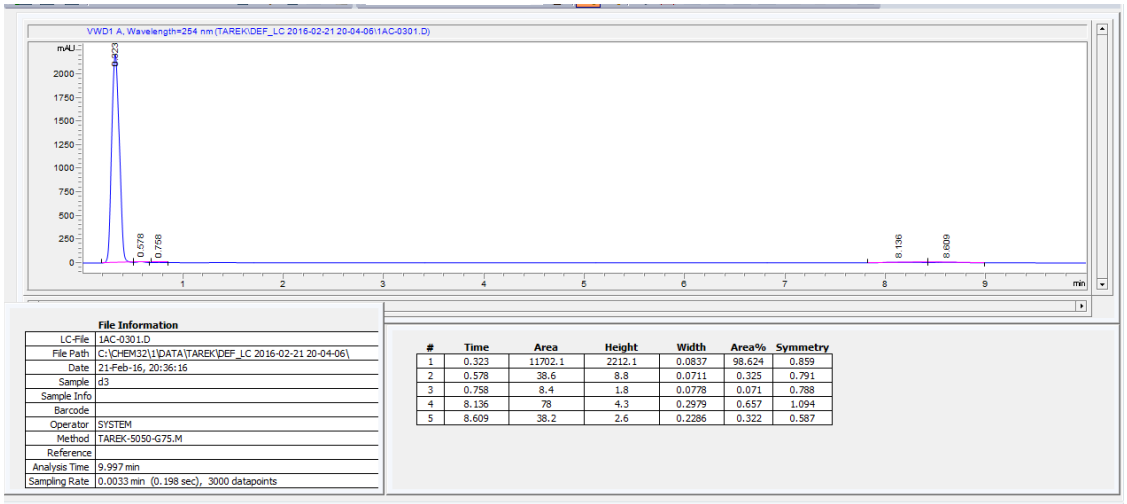

ekkar\2015\Nov9TM30
11/9/2015 3:04:06 PM
2D20 mw 386
eOH/H2O+0.1%FA
30 #29-202 RT: 0.13-0.91 AV: 174 NL: 1.38E8
MS + p ESI Full lock ms [133.40-2000.00]
387.15805
MeO
MeO
NH
Cl
N
N
N
Me
Me
51
Relative Abundance
m/z
309.20591
325.20099
355.06964
374.09783
403.12734
432.23813
454.17094


kkar\2015\Nov9TM10
r.1%FA
11/9/2015 12:10:00 PM
3D6 mw 400
0 #60-198 RT: 0.27-0.88 AV: 139 NL: 3.58E8
+ p ESI Full lock ms [133.40-2000.00]
401.17375
404.17422
393.08305
354.28498
374.09785
387.15809
415.18941
425.28762
MeO
MeO
NH
N
Me
Cl
N
N
H
52
Relative Abundance
m/z
0
5
10
15
20
25
30
35
40
45
50
55
60
65
70
75
80
85
90
95
350
360
370
380
390
400
410
420
430

Section C: HPLC



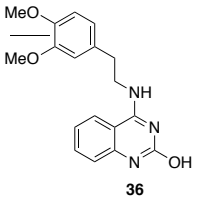
33



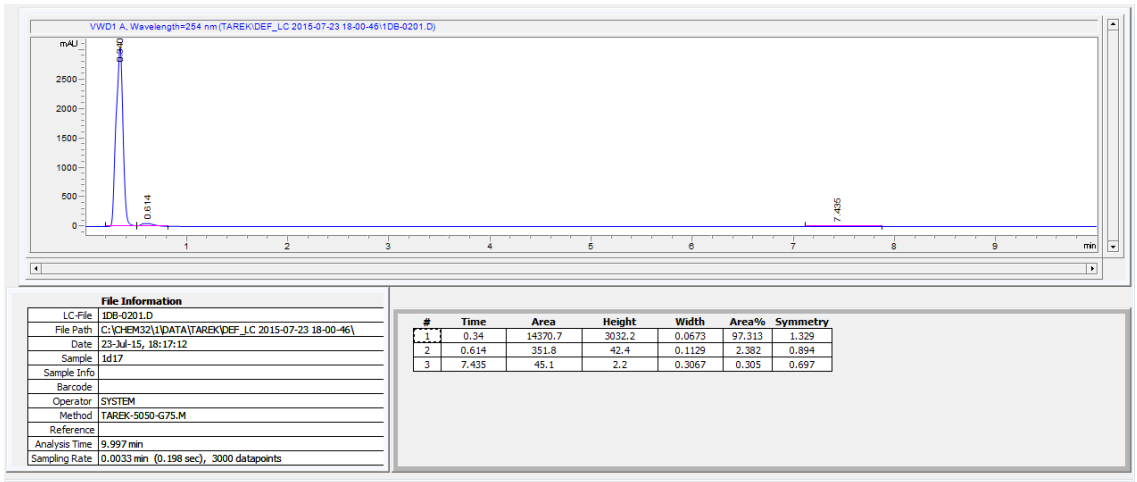
File Information

LC-File	1AC-0301.D
File Path	C:\CHEM32\1\DATA\TAREK\DEF_LC 2016-02-21 20-04-06\
Date	21-Feb-16, 20:36:16
Sample	d3
Sample Info	
Barcode	
Operator	SYSTEM
Method	TAREK-5050-G75.M
Reference	
Analysis Time	9.997 min
Sampling Rate	0.0033 min (0.198 sec), 3000 datapoints

#	Time	Area	Height	Width	Area%	Symmetry
1	0.323	11702.1	2212.1	0.0837	98.624	0.859
2	0.578	38.6	8.8	0.0711	0.325	0.791
3	0.758	8.4	1.8	0.0778	0.071	0.788
4	8.136	78	4.3	0.2979	0.657	1.094
5	8.609	38.2	2.6	0.2286	0.322	0.587



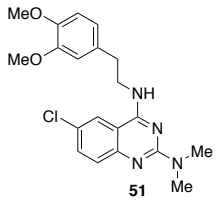
36



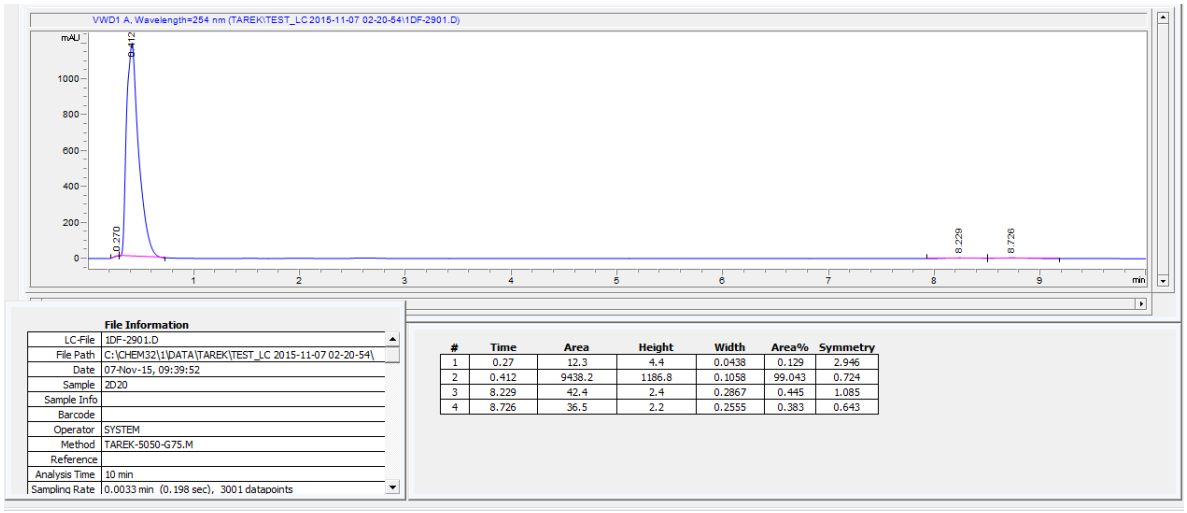
File Information

LC-File	1DB-0201.D
File Path	C:\CHEM32\1\DATA\TAREK\DEF_LC 2015-07-23 18-00-46\
Date	23-Jul-15, 18:17:12
Sample	1d17
Sample Info	
Barcode	
Operator	SYSTEM
Method	TAREK-5050-G75.M
Reference	
Analysis Time	9.997 min
Sampling Rate	0.0033 min (0.198 sec), 3000 datapoints

#	Time	Area	Height	Width	Area%	Symmetry
1	0.34	14370.7	3032.2	0.0673	97.313	1.329
2	0.614	351.8	42.4	0.1129	2.382	0.894
3	7.435	45.1	2.2	0.3067	0.305	0.697



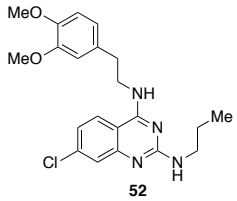
51



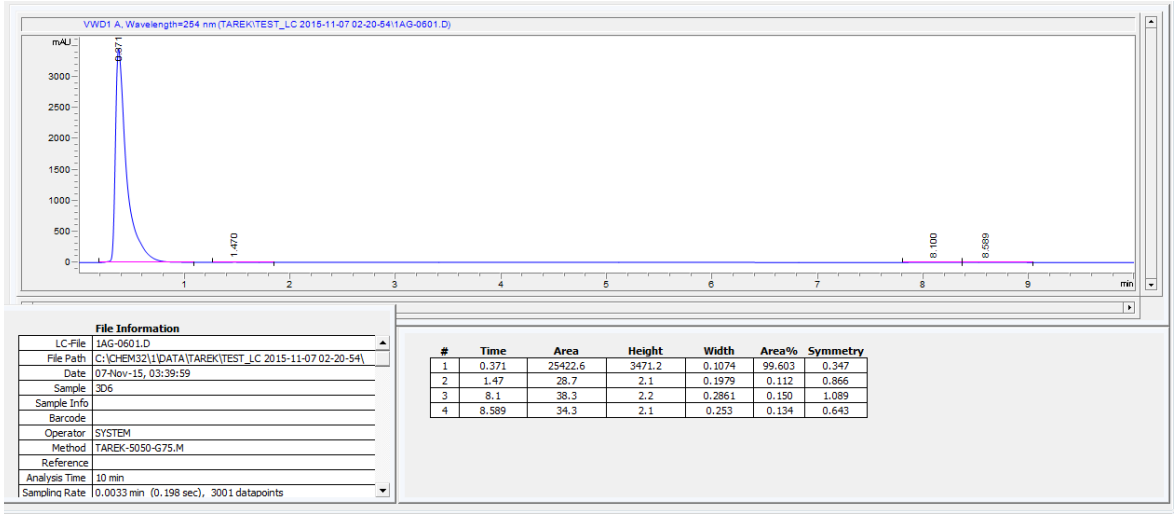
File Information

LC-File	1DF-2901.D
File Path	C:\CHEM32\1\DATA\TAREK\TEST_LC 2015-11-07 02-20-54\
Date	07-Nov-15, 09:39:52
Sample	2D20
Sample Info	
Barcode	
Operator	SYSTEM
Method	TAREK-5050-G75.M
Reference	
Analysis Time	10 min
Sampling Rate	0.0033 min (0.198 sec), 3001 datapoints

#	Time	Area	Height	Width	Area%	Symmetry
1	0.27	12.3	4.4	0.0438	0.129	2.946
2	0.412	9438.2	1186.8	0.1058	99.043	0.724
3	8.229	42.4	2.4	0.2867	0.445	1.085
4	8.726	36.5	2.2	0.2555	0.383	0.643



52



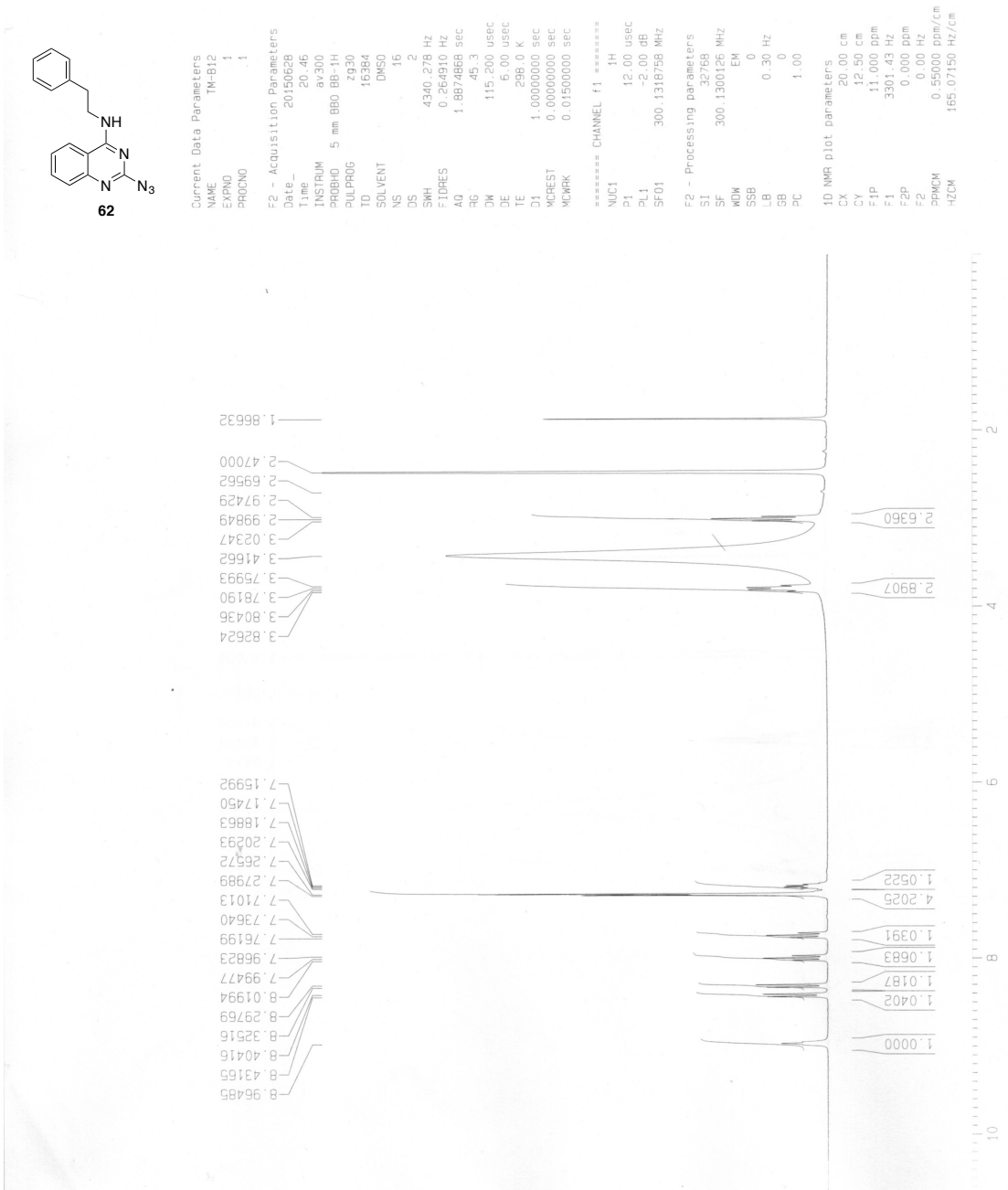
File Information

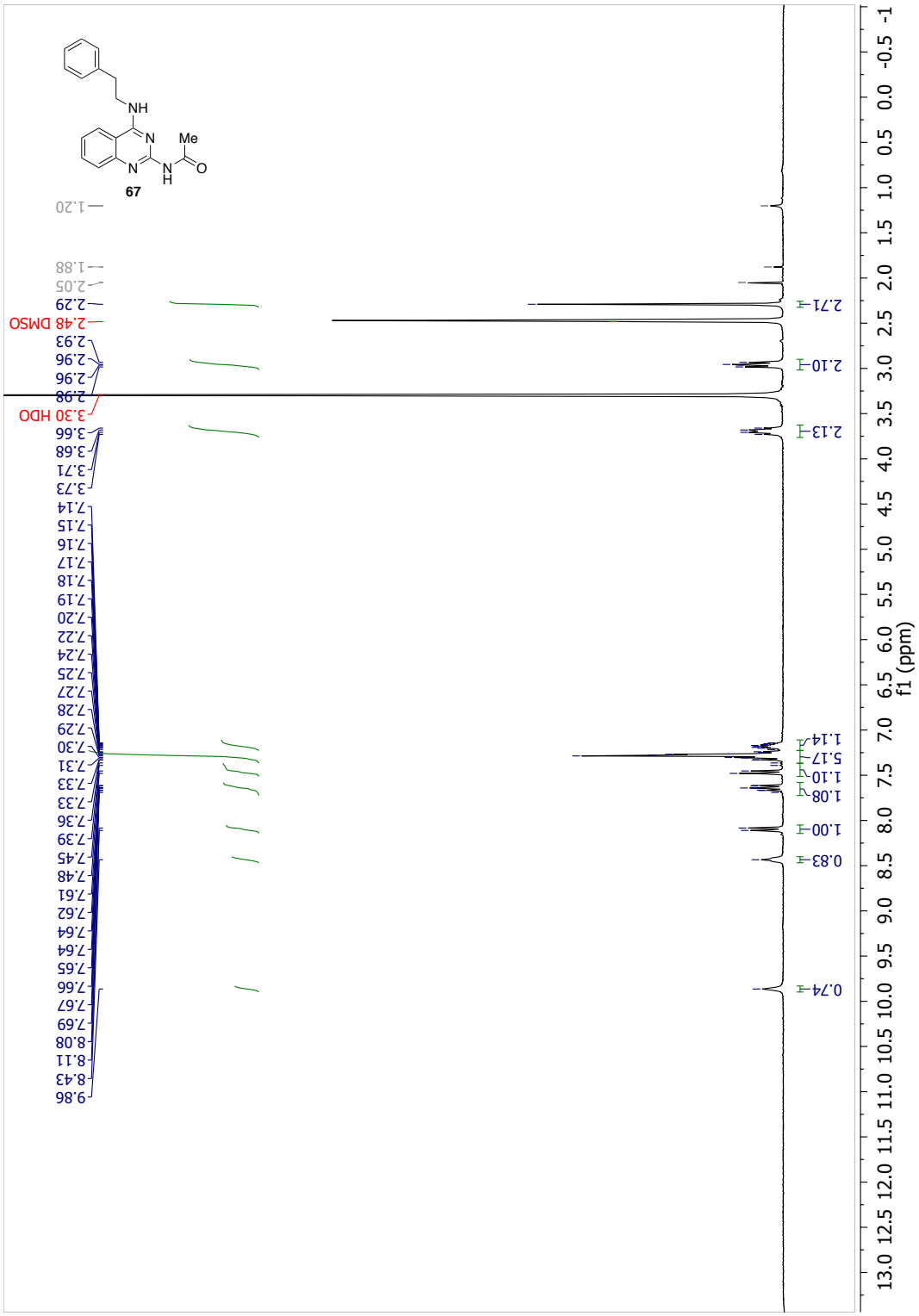
LC-File	1AG-0601.D
File Path	C:\CHEM32\1\DATA\TAREK\TEST_LC 2015-11-07 02-20-54\
Date	07-Nov-15, 03:39:59
Sample	3D6
Sample Info	
Barcode	
Operator	SYSTEM
Method	TAREK-5050-G75.M
Reference	
Analysis Time	10 min
Sampling Rate	0.0033 min (0.198 sec), 3001 datapoints

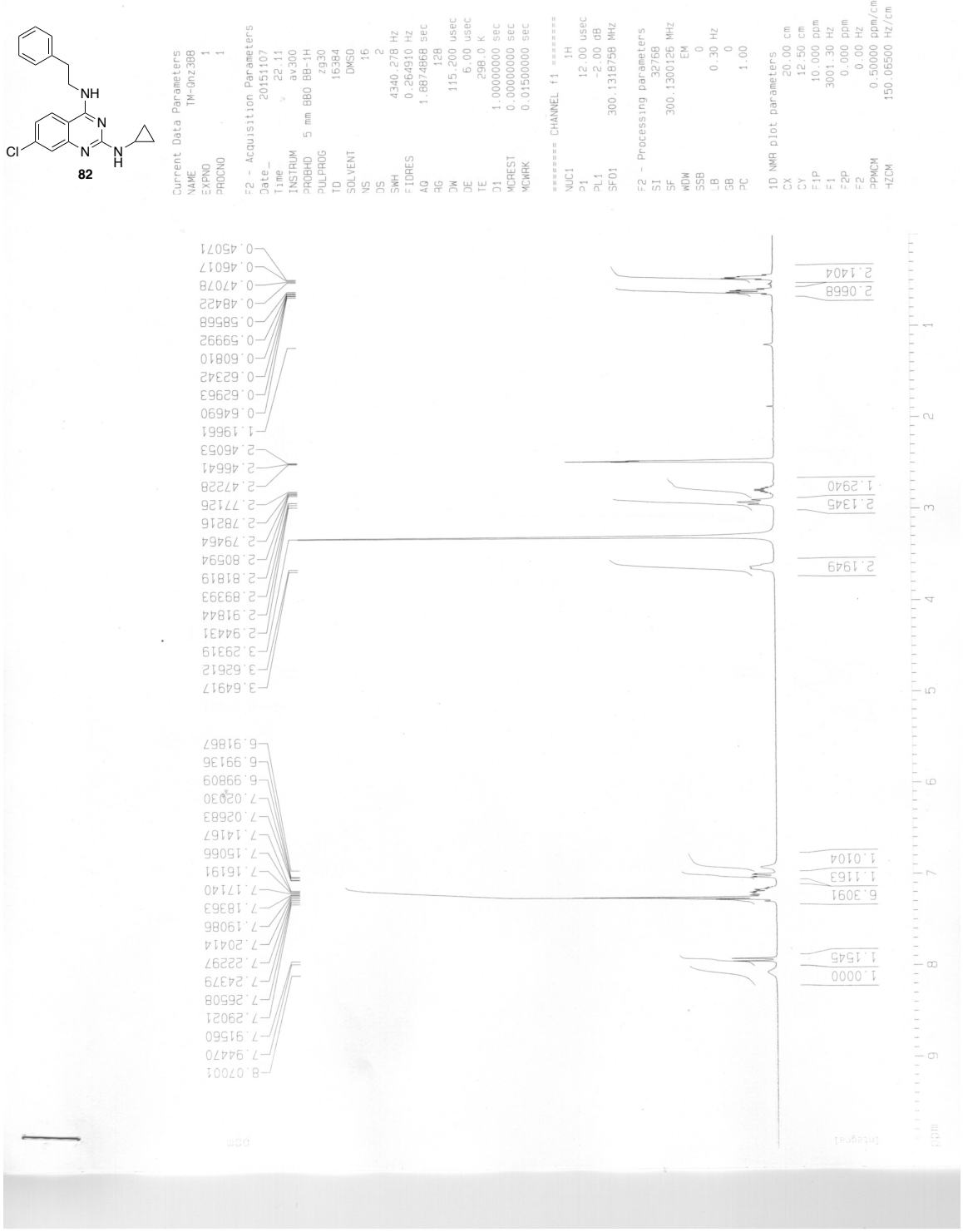
#	Time	Area	Height	Width	Area%	Symmetry
1	0.371	25422.6	3471.2	0.1074	99.603	0.347
2	1.47	28.7	2.1	0.1979	0.112	0.866
3	8.1	38.3	2.2	0.2861	0.150	1.089
4	8.589	34.3	2.1	0.253	0.134	0.643

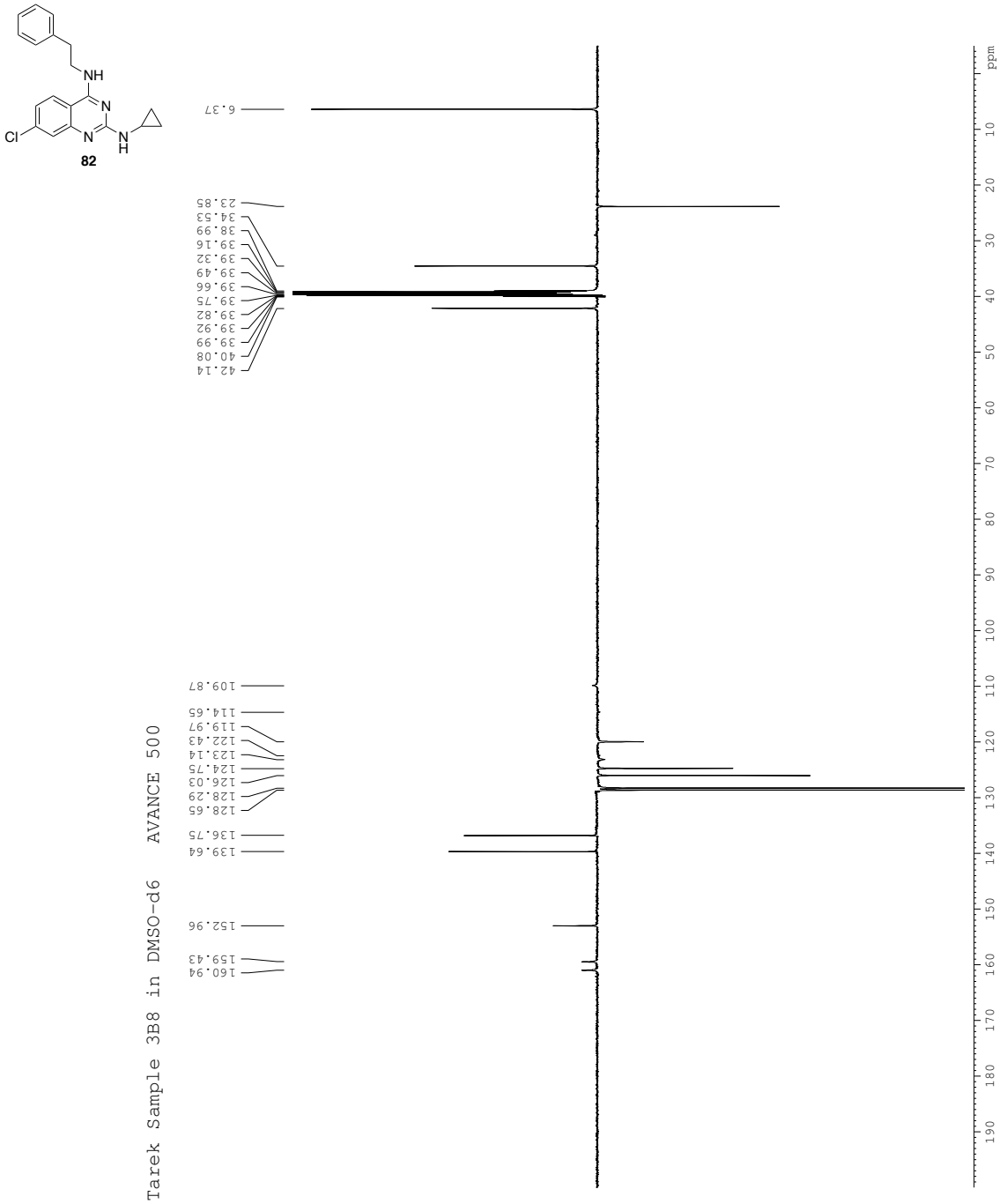
Appendix V: Sample spectra for Chapter 6

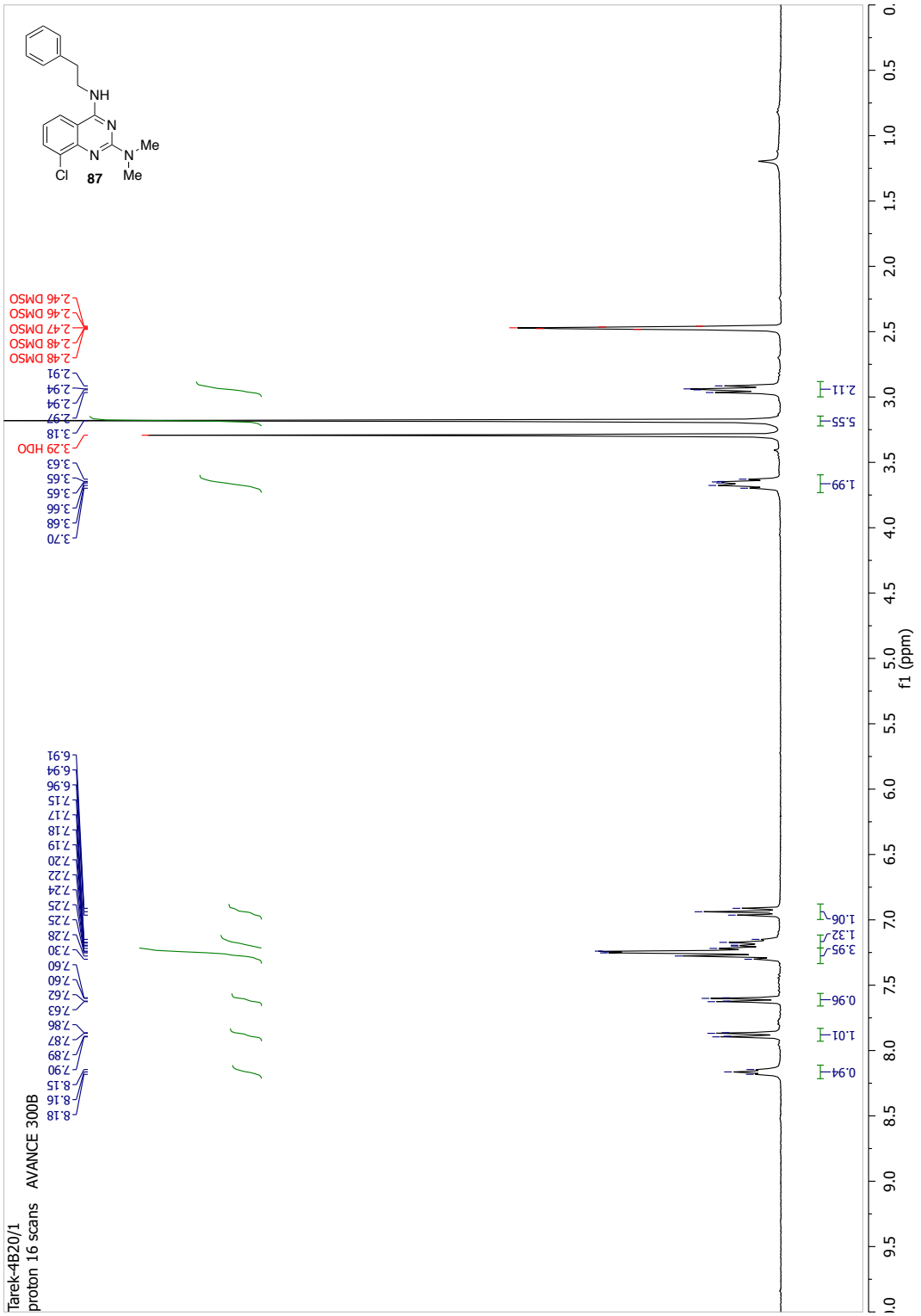
Section A: NMR



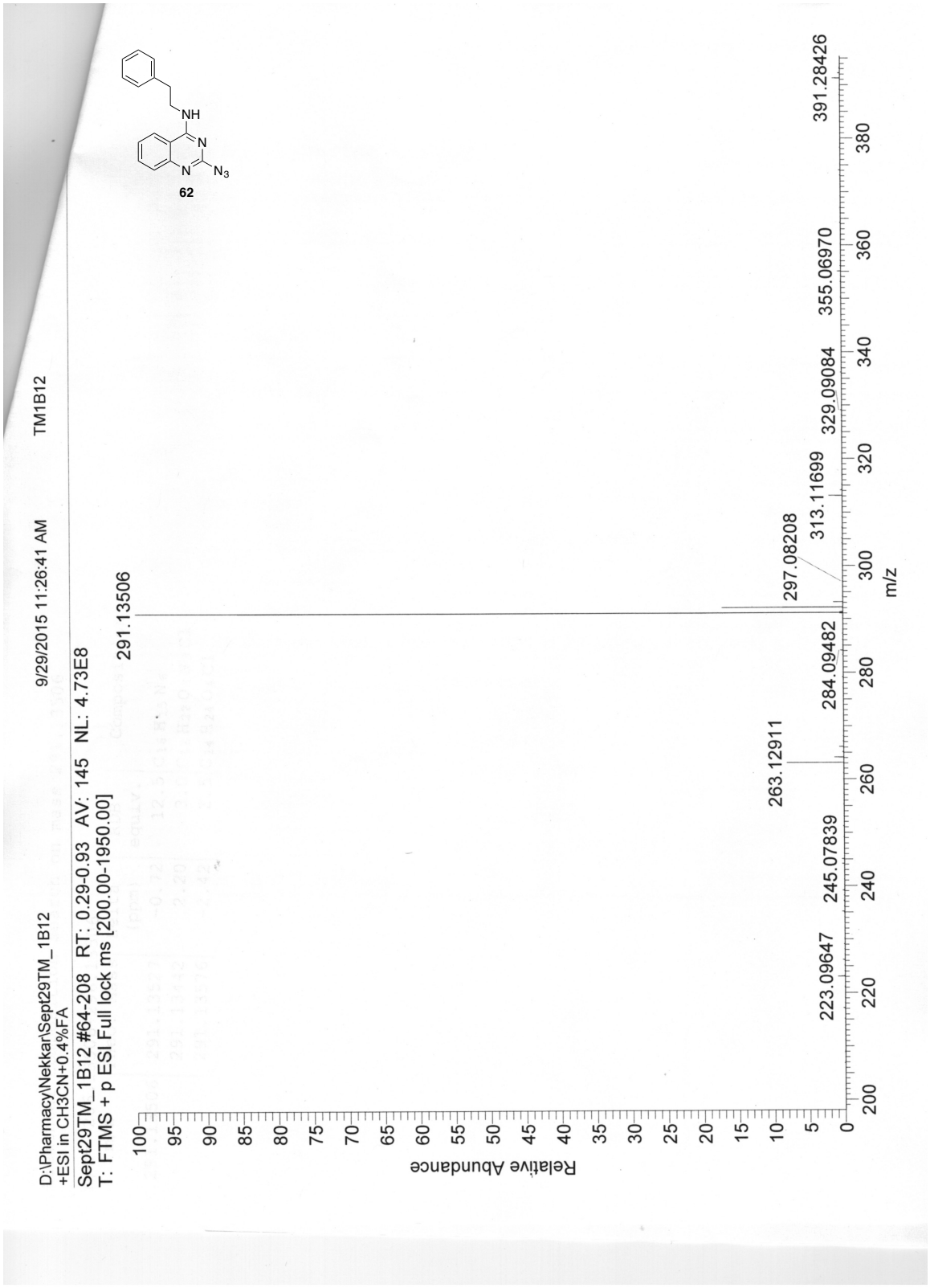

NH
N
N
Me
N
H
O
67
f1 (ppm)

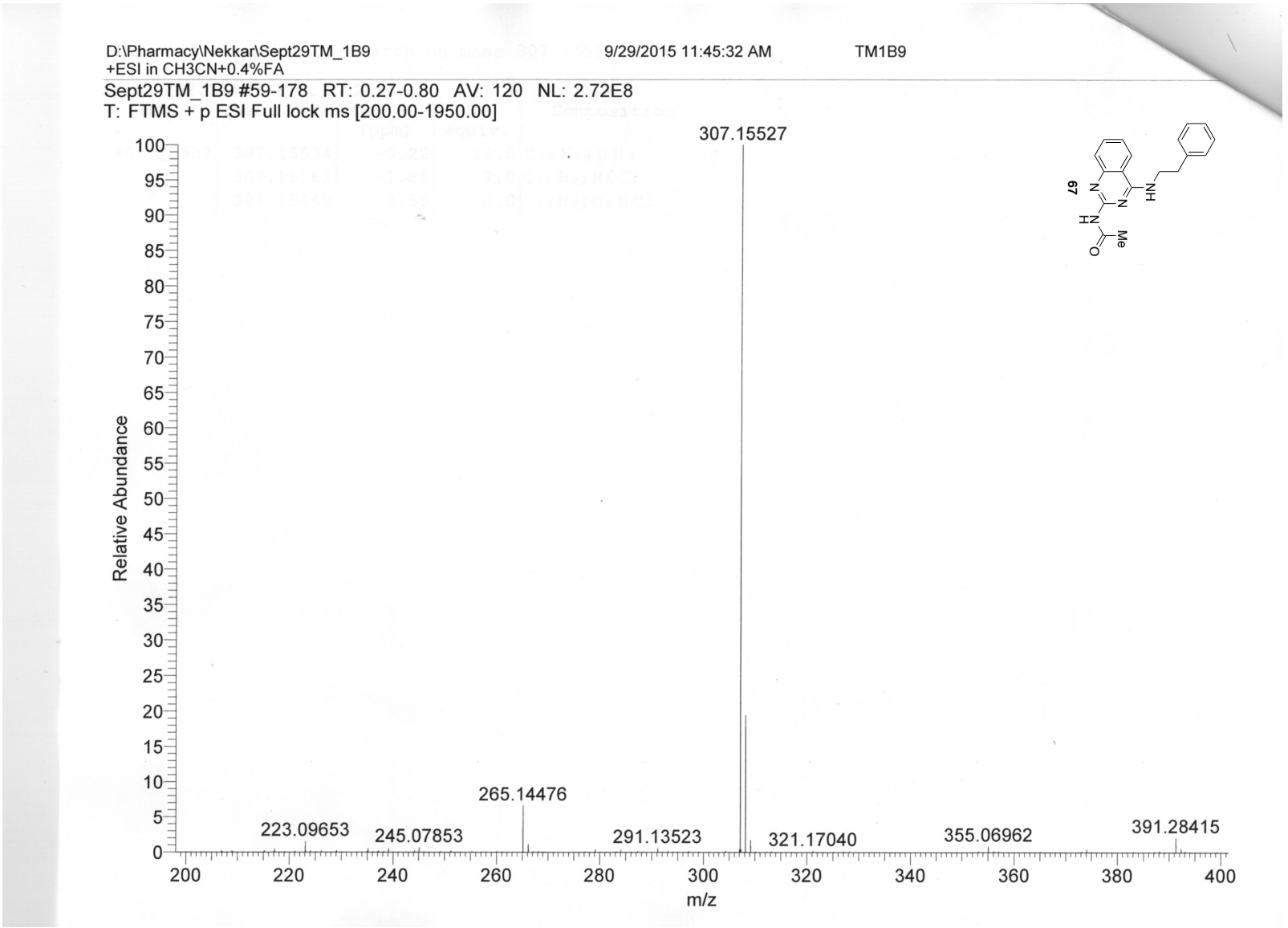

NH
N
Cl
N
N
H
82
Current Data Parameters
NAME TM-Gnz38B
EXPNO 1
PROCNO 1
F2 - Acquisition Parameters
Date_ 20151107
Time 22.11
INSTRUM av300
PROBHD 5 mm BBO BB-1H
PULPROG zg30
TD 16384
SOLVENT DMSO
NS 16
DS 2
SWH 4340.278 Hz
FIDRES 0.264910 Hz
AQ 1.8874868 sec
RG 128
DW 115.200 usec
DE 6.00 usec
TE 298.0 K
D1 1.00000000 sec
MCREST 0.00000000 sec
MCWRK 0.01500000 sec
======== CHANNEL f1 ========
NUC1 1H
P1 12.00 usec
PL1 -2.00 dB
SF01 300.1318758 MHz
F2 - Processing parameters
SI 32768
SF 300.1300126 MHz
WDW EM
SSB 0
LB 0.30 Hz
GB 0
PC 1.00
1D NMR plot parameters
CX 20.00 cm
CY 12.50 cm
F1P 10.000 ppm
F1 3001.30 Hz
F2P 0.000 ppm
F2 0.00 Hz
PPMCM 0.50000 ppm/cm
HZCM 150.06500 Hz/cm
0.45071
0.46017
0.47078
0.48422
0.58568
0.59992
0.60810
0.62342
0.62963
0.64690
1.19661
2.46053
2.46641
2.47228
2.77126
2.78216
2.79464
2.80594
2.81819
2.89393
2.91844
2.94431
3.29319
3.62612
3.64917
6.91867
6.99136
6.99809
7.02030
7.02683
7.14167
7.15066
7.16191
7.17140
7.18363
7.19086
7.20414
7.22297
7.24379
7.26508
7.29021
7.91560
7.94470
8.07001
2.1404
2.0668
1.2940
2.1345
2.1949
1.0104
1.1163
6.3091
1.1545
1.0000

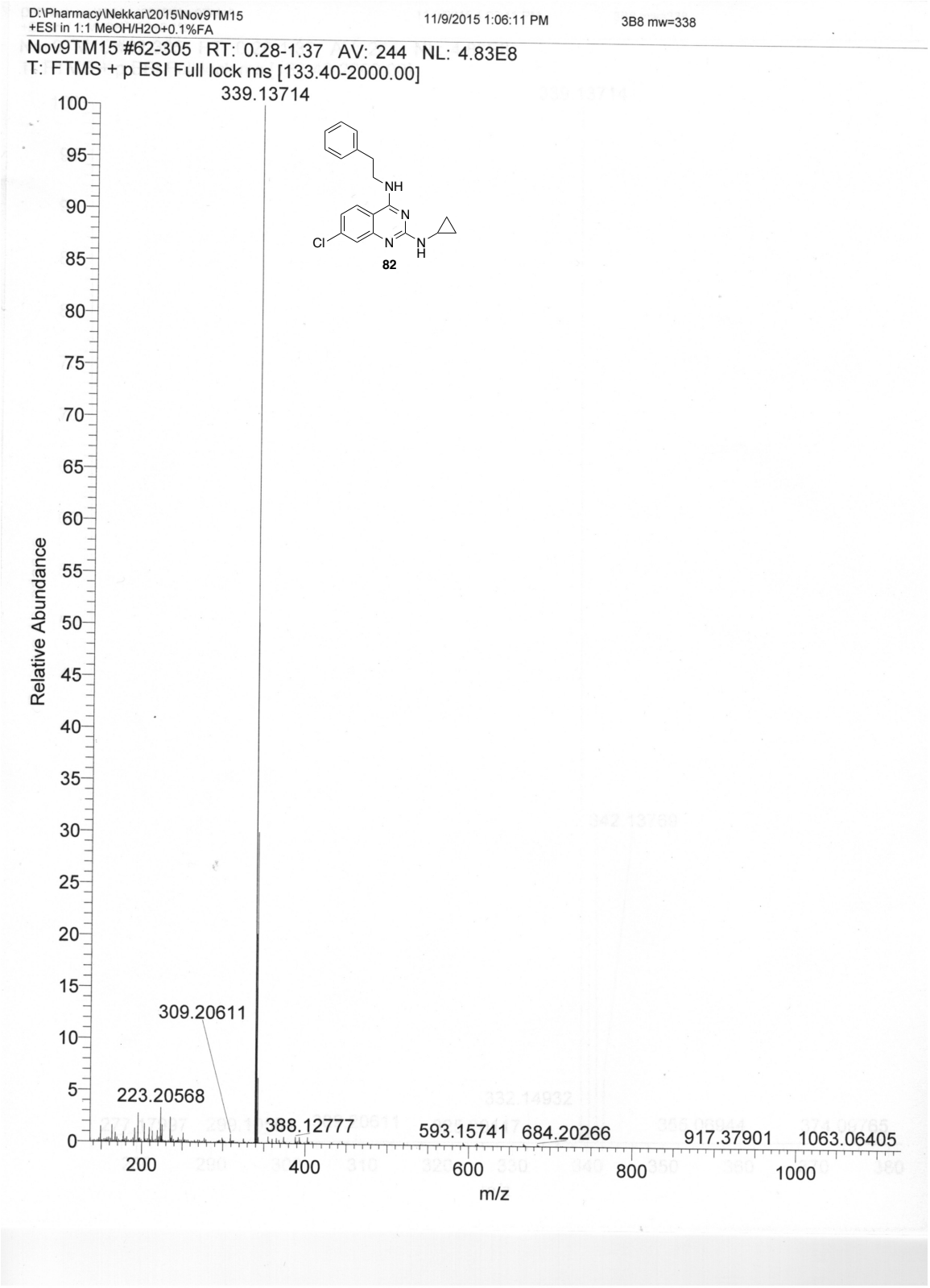

NH
N
Cl
N
N
H
82
6.37
23.85
34.53
38.99
39.16
39.32
39.49
39.66
39.75
39.82
39.92
39.99
40.08
42.14
109.87
114.65
119.97
122.43
123.14
124.75
126.03
128.29
128.65
136.75
139.64
152.96
159.43
160.94
Tarek Sample 3B8 in DMSO-d6 AVANCE 500
ppm

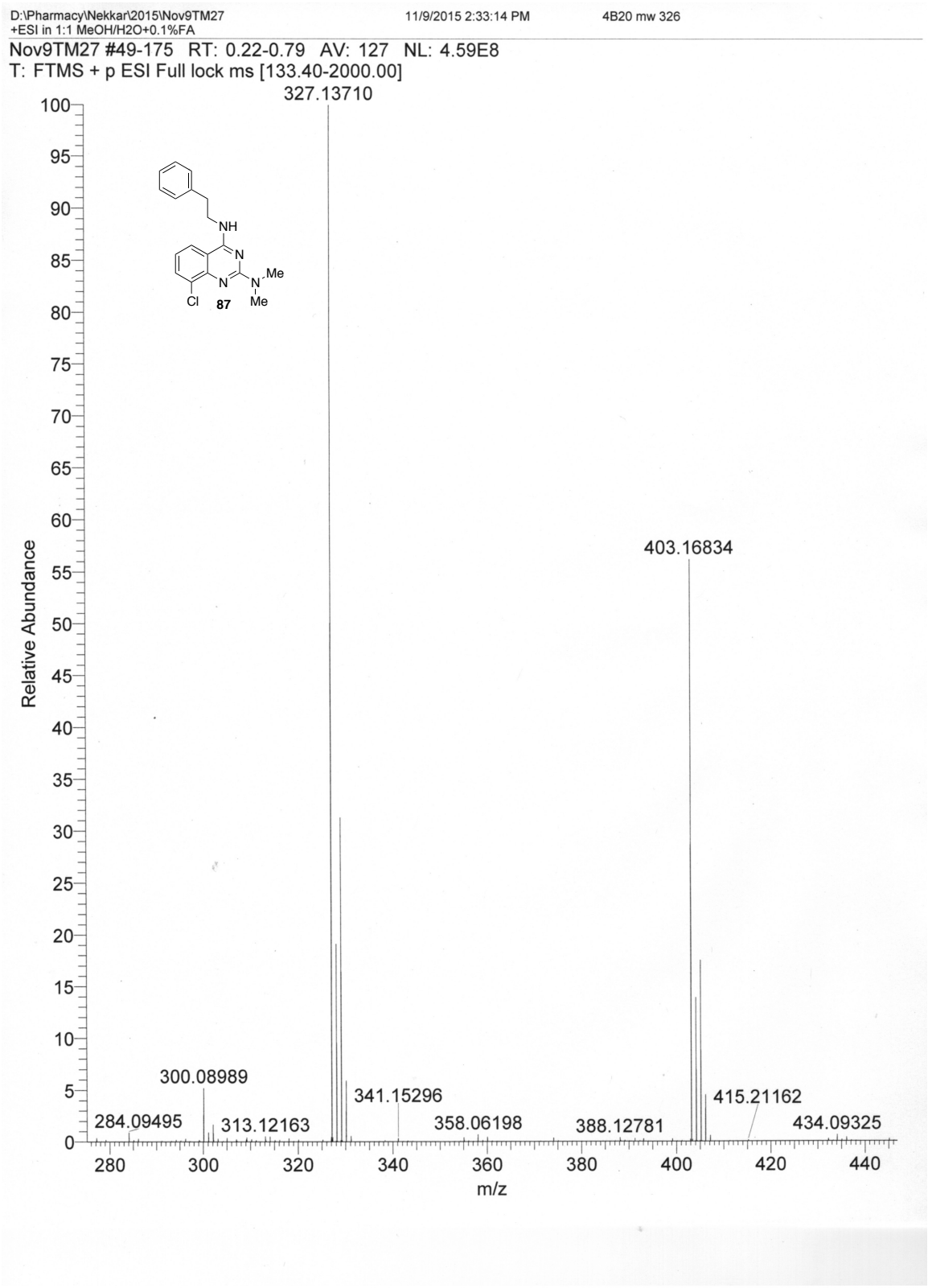

NH
N
N
N
Me
Me
Cl
87
Tarek-4B20/1
proton 16 scans
AVANCE 300B
f1 (ppm)

Section B: HRMS

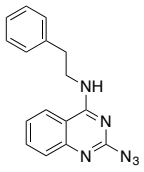



D:\Pharmacy\Nekkar\Sept29TM_1B9
9/29/2015 11:45:32 AM
TM1B9
+ESI in CH3CN+0.4%FA
Sept29TM_1B9 #59-178 RT: 0.27-0.80 AV: 120 NL: 2.72E8
T: FTMS + p ESI Full lock ms [200.00-1950.00]
307.15527
265.14476
223.09653
245.07853
291.13523
321.17040
355.06962
391.28415
Relative Abundance
m/z
67
Me

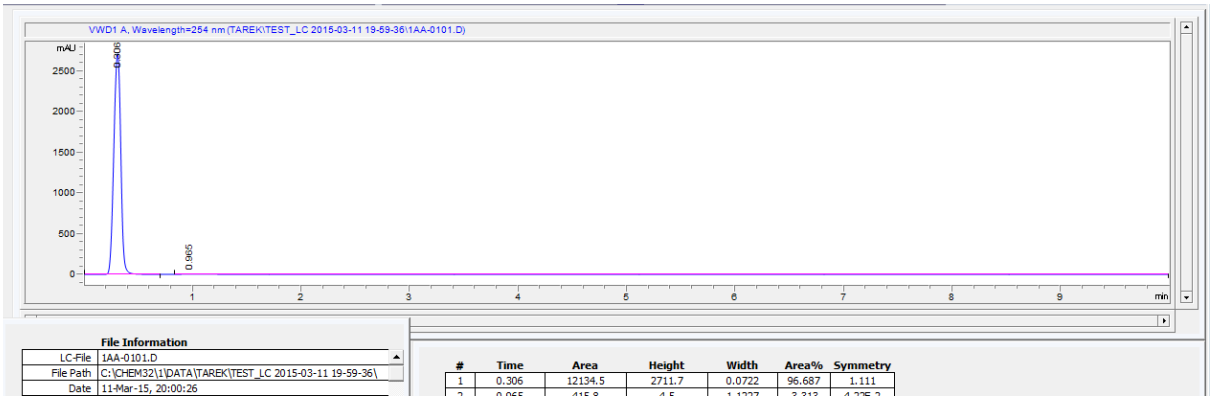

D:\Pharmacy\Nekkar\2015\Nov9TM15
+ESI in 1:1 MeOH/H2O+0.1%FA
11/9/2015 1:06:11 PM
3B8 mw=338
Nov9TM15 #62-305 RT: 0.28-1.37 AV: 244 NL: 4.83E8
T: FTMS + p ESI Full lock ms [133.40-2000.00]
339.13714
NH
N
Cl
N
N
H
82
Relative Abundance
m/z
309.20611
223.20568
388.12777
593.15741
684.20266
917.37901
1063.06405


D:\Pharmacy\Nekkar\2015\Nov9TM27
11/9/2015 2:33:14 PM
4B20 mw 326
+ESI in 1:1 MeOH/H2O+0.1%FA
Nov9TM27 #49-175 RT: 0.22-0.79 AV: 127 NL: 4.59E8
T: FTMS + p ESI Full lock ms [133.40-2000.00]
327.13710
403.16834
300.08989
341.15296
415.21162
284.09495
313.12163
358.06198
388.12781
434.09325
Relative Abundance
m/z
87

Section C: HPLC



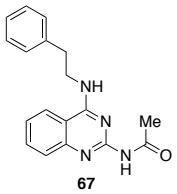
62



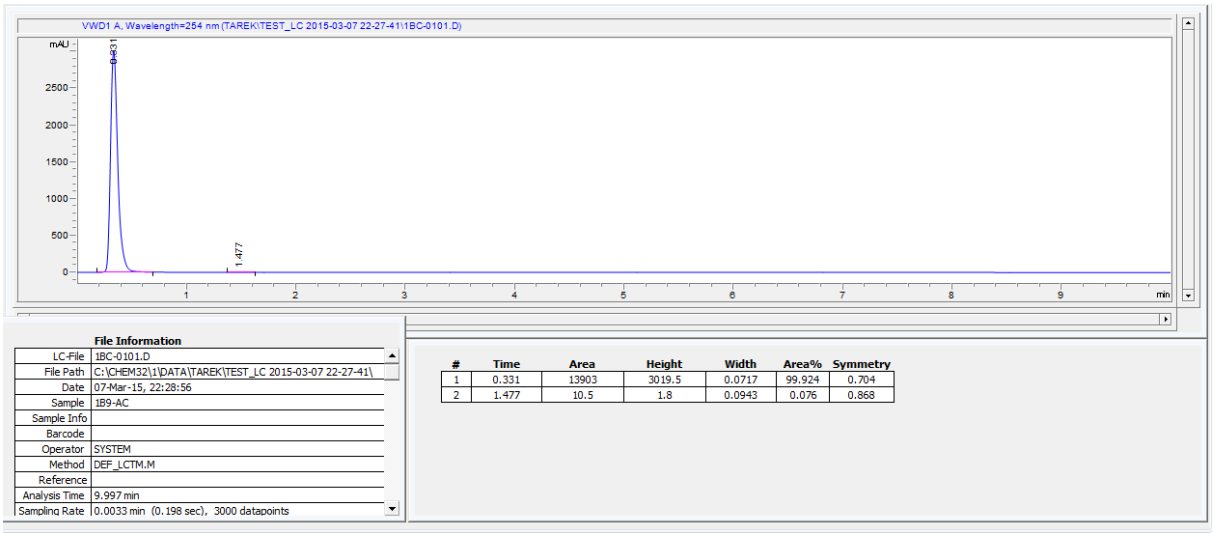
File Information

LC-File	1AA-0101.D
File Path	C:\CHEM32\1\DATA\TAREK\TEST_LC 2015-03-11 19-59-36\
Date	11-Mar-15, 20:00:26

#	Time	Area	Height	Width	Area%	Symmetry
1	0.306	12134.5	2711.7	0.0722	96.687	1.111



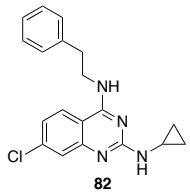
67



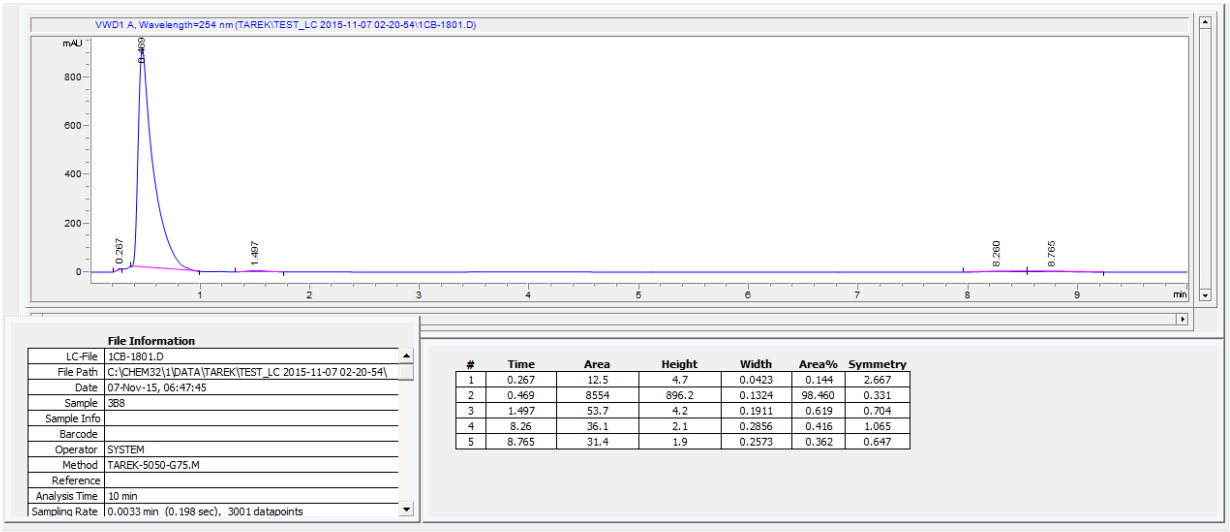
File Information

LC-File	1BC-0101.D
File Path	C:\CHEM32\1\DATA\TAREK\TEST_LC 2015-03-07 22-27-41\
Date	07-Mar-15, 22:28:56
Sample	1B9-AC
Sample Info	
Barcode	
Operator	SYSTEM
Method	DEF_LCTM.M
Reference	
Analysis Time	9.997 min
Sampling Rate	0.0033 min (0.198 sec), 3000 datapoints

#	Time	Area	Height	Width	Area%	Symmetry
1	0.331	13903	3019.5	0.0717	99.924	0.704
2	1.477	10.5	1.8	0.0943	0.076	0.868



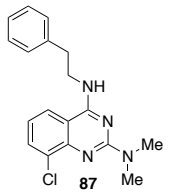
82



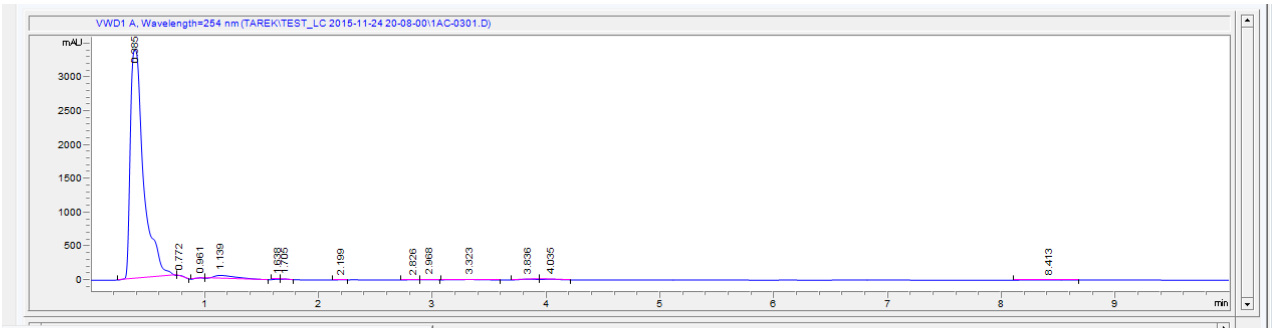
File Information

LC-File	1CB-1801.D
File Path	C:\CHEM32\1\DATA\TAREK\TEST_LC 2015-11-07 02-20-54\
Date	07-Nov-15, 06:47:45
Sample	3B8
Sample Info	
Barcode	
Operator	SYSTEM
Method	TAREK-5050-G75.M
Reference	
Analysis Time	10 min
Sampling Rate	0.0033 min (0.198 sec), 3001 datapoints

#	Time	Area	Height	Width	Area%	Symmetry
1	0.267	12.5	4.7	0.0423	0.144	2.667
2	0.469	8554	896.2	0.1324	98.460	0.331
3	1.497	53.7	4.2	0.1911	0.619	0.704
4	8.26	36.1	2.1	0.2856	0.416	1.065
5	8.765	31.4	1.9	0.2573	0.362	0.647



87



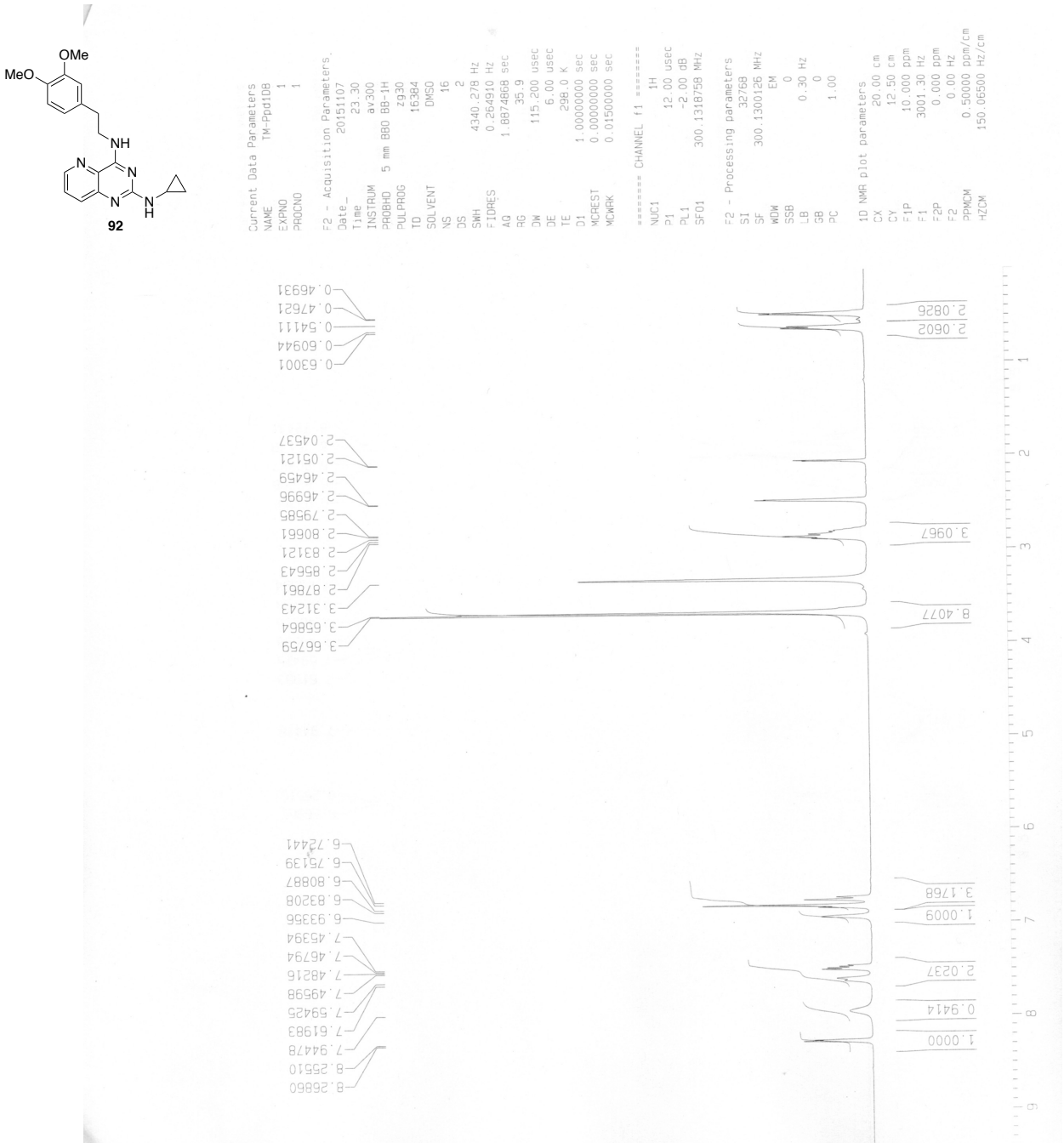
File Information

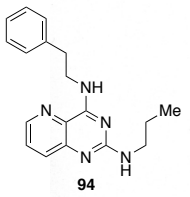
LC-File	1AC-0301.D
File Path	C:\CHEM32\1\DATA\TAREK\TEST_LC 2015-11-24 20-08-00\
Date	24-Nov-15, 20:40:07
Sample	4b20-1
Sample Info	
Barcode	
Operator	SYSTEM
Method	TAREK-5050-G75.M
Reference	
Analysis Time	9.997 min
Sampling Rate	0.0033 min (0.198 sec), 3000 datapoints

#	Time	Area	Height	Width	Area%	Symmetry
1	0.385	27655	3401.7	0.1218	96.294	0.487
2	0.772	49.2	8.5	0.0851	0.171	9.22E-2
3	0.961	54.6	12.1	0.0638	0.190	2.555
4	1.139	681.6	47.6	0.2091	2.373	0.396
5	1.638	10.3	3.5	0.0482	0.036	2.229
6	1.705	15	4.6	0.0522	0.052	0.506
7	2.199	7.8	1.8	0.0721	0.027	1.324
8	2.826	14.7	2.7	0.0916	0.051	1.732
9	2.968	15.1	2.9	0.0849	0.052	0.75

Appendix VI: Sample spectra for Chapter 7

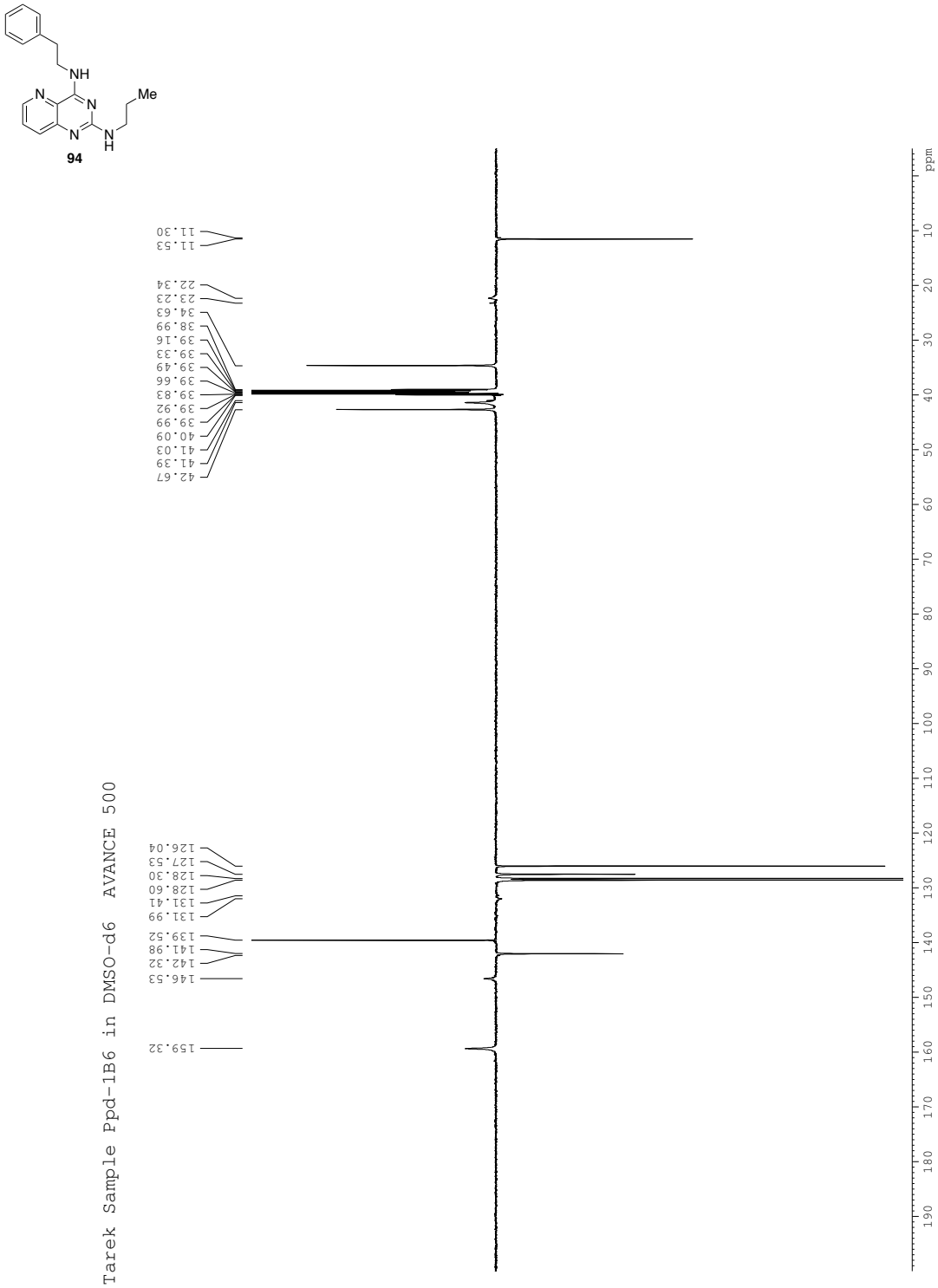
Section A: NMR




NH
N
N
N
N
H
Me

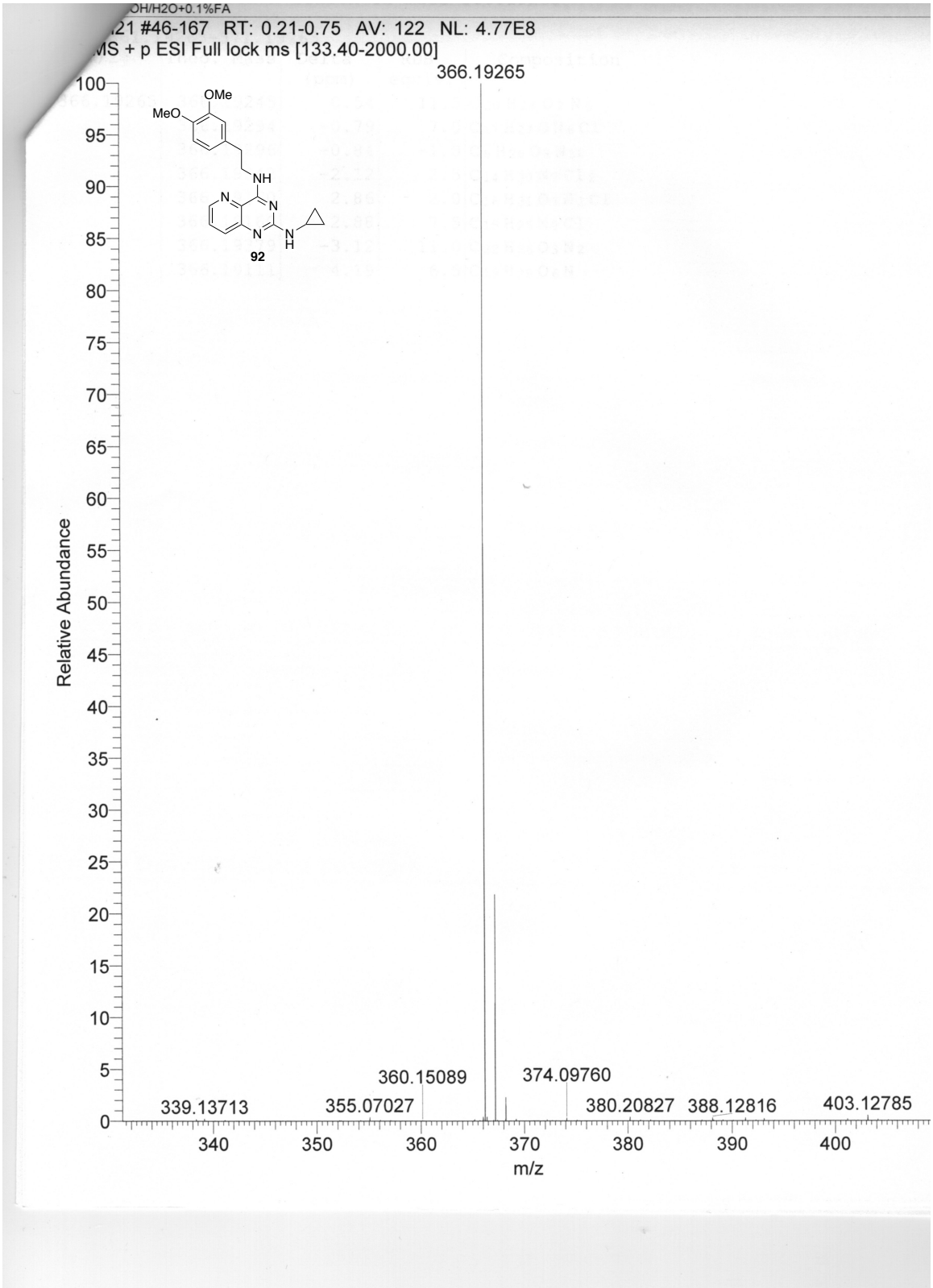
94

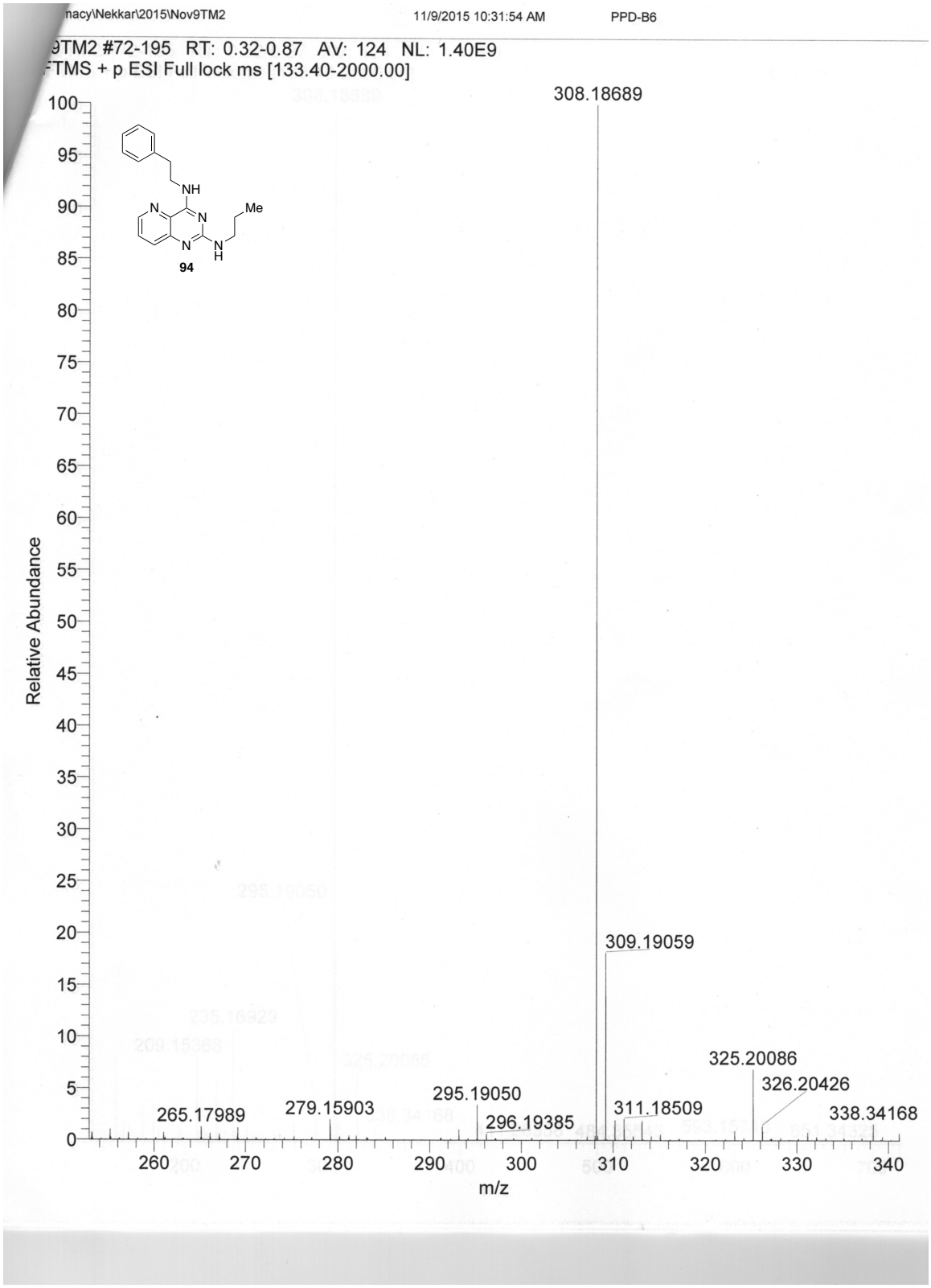
Current Data Parameters
NAME TM-Pp01B6
EXPNO 1
PROCNO 1
F2 - Acquisition Parameters
Date_ 20151107
Time 21.45
INSTRUM av300
PROBHD 5 mm BBO BB-1H
PULPROG zg30
TD 16384
SOLVENT DMSO
NS 16
DS 2
SWH 4340.278 Hz
FIDRES 0.264910 Hz
AQ 1.8874868 sec
RG 128
DW 115.200 usec
DE 6.00 usec
TE 298.0 K
D1 1.00000000 sec
MCREST 0.00000000 sec
MCWRK 0.01500000 sec
======== CHANNEL f1 ========
NUC1 1H
P1 12.00 usec
PL1 -2.00 dB
SFO1 300.1318756 MHz
F2 - Processing parameters
SI 32768
SF 300.1300126 MHz
WDW EM
SSB 0
LB 0.30 Hz
GB 0
PC 1.00
1D NMR plot parameters
CX 20.00 cm
CY 12.50 cm
F1P 10.000 ppm
F1 3001.30 Hz
F2P 0.000 ppm
F2 0.00 Hz
PPMCM 0.50000 ppm/cm
HZCM 150.06500 Hz/cm
2.9576
1.9521
2.0425
2.2656
1.9899
0.9340
4.7803
0.3627
0.7005
0.8707
0.8136
1.0000

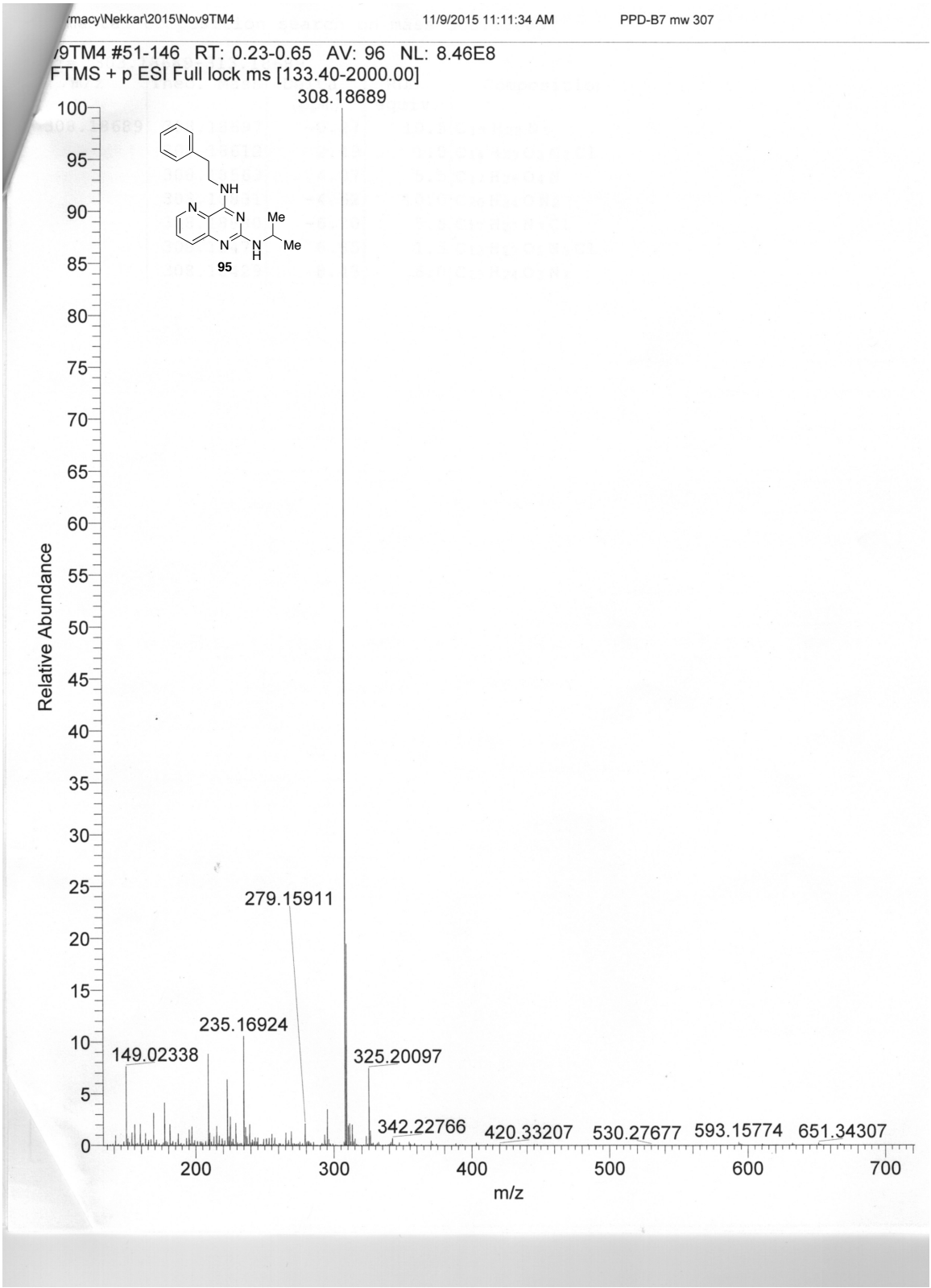

NH
N
N
Me
N
N
H
94
11.30
11.53
22.34
23.23
34.63
38.99
39.16
39.33
39.49
39.66
39.83
39.92
39.99
40.09
41.03
41.39
42.67
126.04
127.53
128.30
128.60
131.41
131.99
139.52
141.98
142.32
146.53
159.32
Tarek Sample Ppd-1B6 in DMSO-d6 AVANCE 500
ppm
10
20
30
40
50
60
70
80
90
100
110
120
130
140
150
160
170
180
190


NH
N
N
Me
N
N
H
Me
95
Current Data Parameters
NAME TM-Ppd1B7
EXPNO 1
PROCNO 1
F2 - Acquisition Parameters
Date_ 20151107
Time 22.02
INSTRUM av300
PROBHD 5 mm BBO BB-1H
PULPROG zg30
TD 16384
SOLVENT DMSO
NS 16
DS 2
SWH 4340.278 Hz
FIDRES 0.264910 Hz
AQ 1.8874668 sec
RG 71.8
DW 115.200 usec
DE 6.00 usec
TE 298.0 K
D1 1.00000000 sec
MCREST 0.00000000 sec
MCWRK 0.01500000 sec
======== CHANNEL f1 ========
NUC1 1H
P1 12.00 usec
PL1 -2.00 dB
SFO1 300.1318758 MHz
F2 - Processing parameters
SI 32768
SF 300.1300126 MHz
WDW EM
SSB 0
LB 0.30 Hz
GB 0
PC 1.00
1D NMR plot parameters
CX 20.00 cm
CY 12.50 cm
F1P 10.000 ppm
F1 3001.30 Hz
F2P 0.000 ppm
F2 0.00 Hz
PPMCM 0.50000 ppm/cm
HZCM 150.06500 Hz/cm
1.13077
1.15247
1.18710
2.46025
2.46623
2.47219
2.89446
2.91858
2.94488
3.30052
3.62879
3.64919
3.67778
3.69898
4.07572
4.09768
4.11967
4.14548
4.16740
4.18958
6.60455
7.14463
7.15381
7.18519
7.17471
7.18668
7.19369
7.22902
7.24987
7.27110
7.29618
7.44198
7.45580
7.47017
7.48398
7.54327
7.57040
8.23282
8.23800
8.24651
8.25166
6.0051
2.0112
1.9402
0.9554
0.9793
4.8403
1.0421
0.8758
0.8153
1.0000

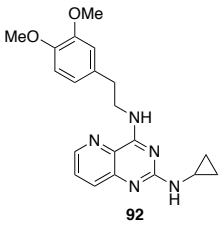
Section B: HRMS



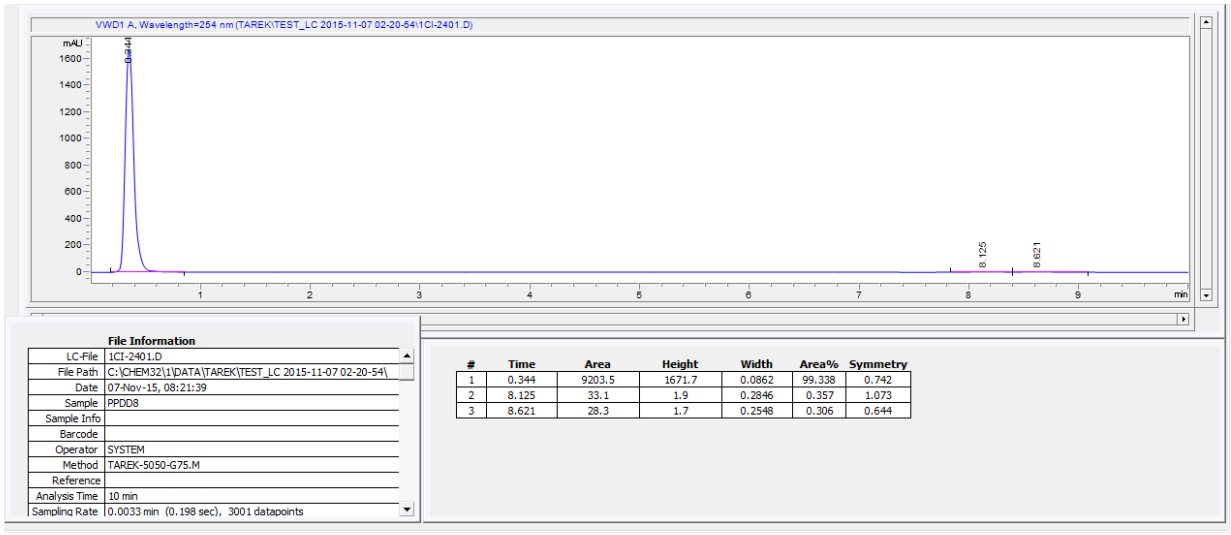

nacy\Nekkar\2015\Nov9TM2
11/9/2015 10:31:54 AM
PPD-B6
9TM2 #72-195 RT: 0.32-0.87 AV: 124 NL: 1.40E9
FTMS + p ESI Full lock ms [133.40-2000.00]
NH
N
N
Me
N
N
H
94
308.18689
309.19059
325.20086
326.20426
338.34168
311.18509
295.19050
296.19385
279.15903
265.17989
Relative Abundance
m/z
100
95
90
85
80
75
70
65
60
55
50
45
40
35
30
25
20
15
10
5
0
260
270
280
290
300
310
320
330
340


rmacy\Nekkar\2015\Nov9TM4
11/9/2015 11:11:34 AM
PPD-B7 mw 307
/9TM4 #51-146 RT: 0.23-0.65 AV: 96 NL: 8.46E8
FTMS + p ESI Full lock ms [133.40-2000.00]
308.18689
279.15911
235.16924
149.02338
325.20097
342.22766
420.33207
530.27677
593.15774
651.34307
Relative Abundance
m/z
95
NH
N
N
Me
Me
N
H

Section C: HPLC

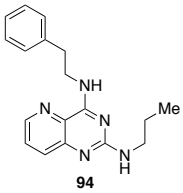


92

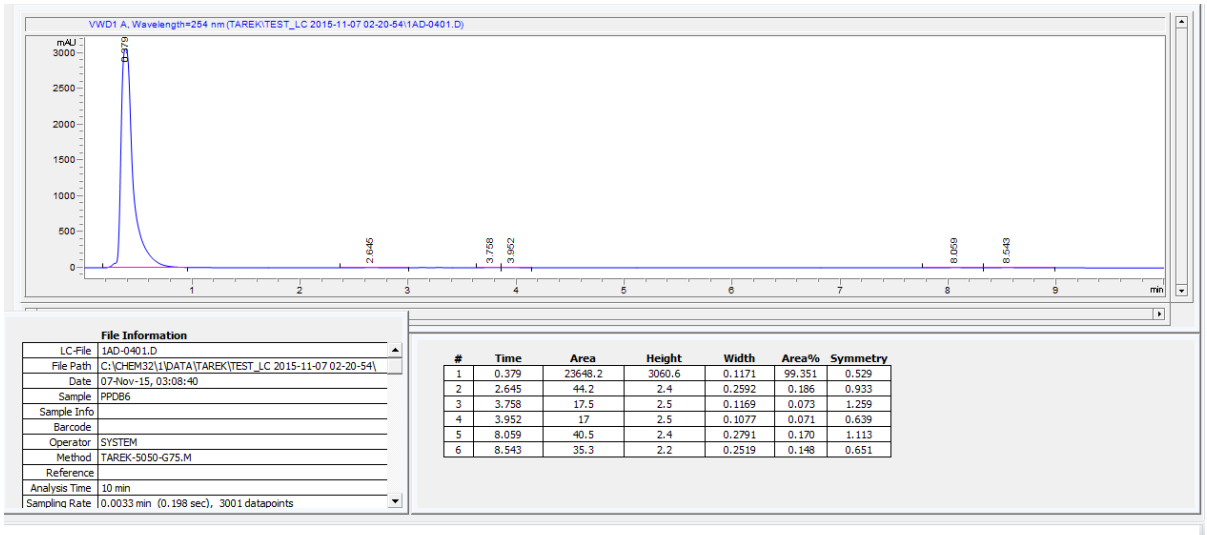


File Information	
LC-File	1CI-2401.D
File Path	C:\CHEM32\1\DATA\TAREK\TEST_LC 2015-11-07 02-20-54\
Date	07-Nov-15, 08:21:39
Sample	PPDD8
Sample Info	
Barcode	
Operator	SYSTEM
Method	TAREK-5050-G75.M
Reference	
Analysis Time	10 min
Sampling Rate	0.0033 min (0.198 sec), 3001 datapoints

#	Time	Area	Height	Width	Area%	Symmetry
1	0.344	9203.5	1671.7	0.0862	99.338	0.742
2	8.125	33.1	1.9	0.2846	0.357	1.073
3	8.621	28.3	1.7	0.2548	0.306	0.644



94

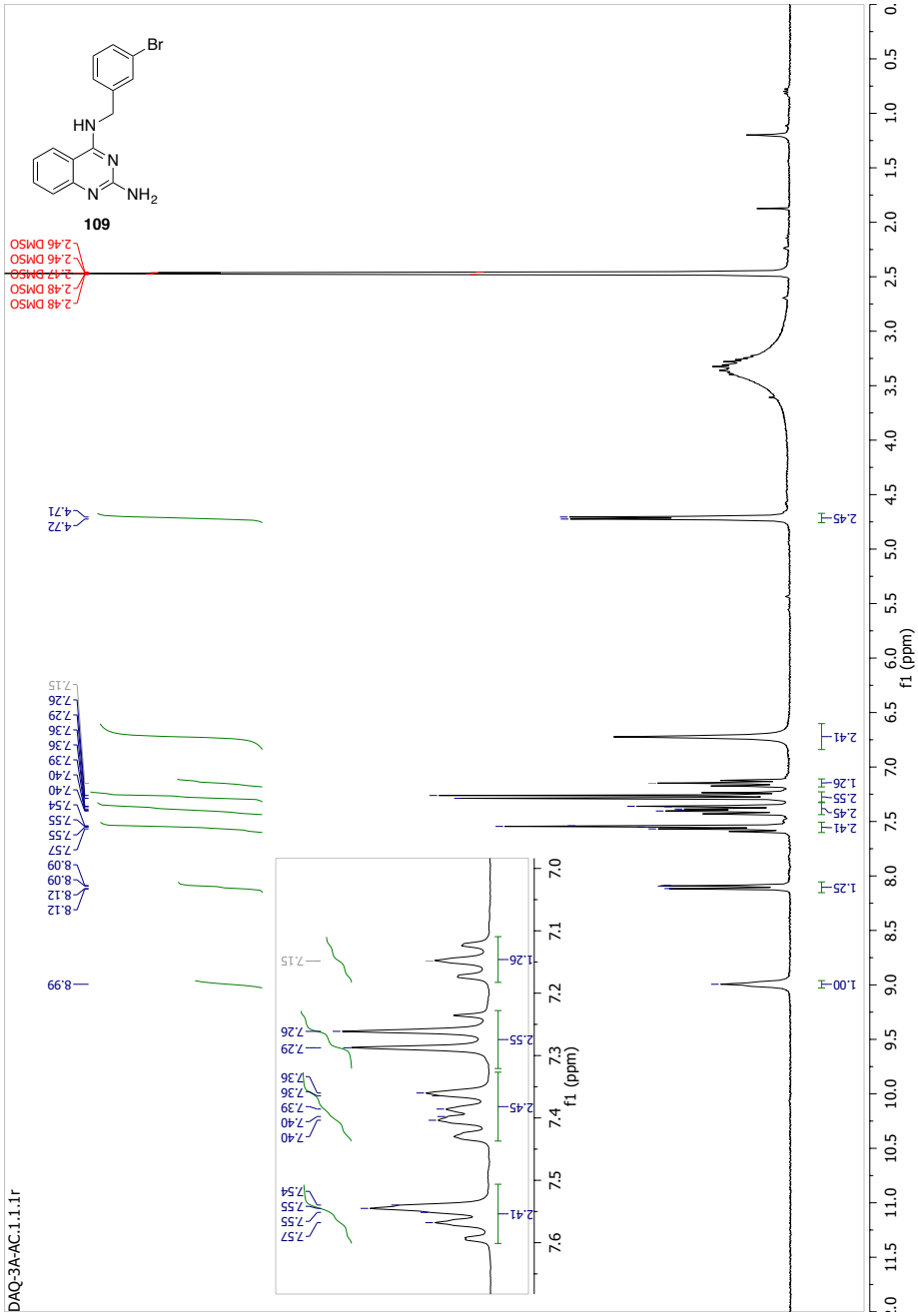


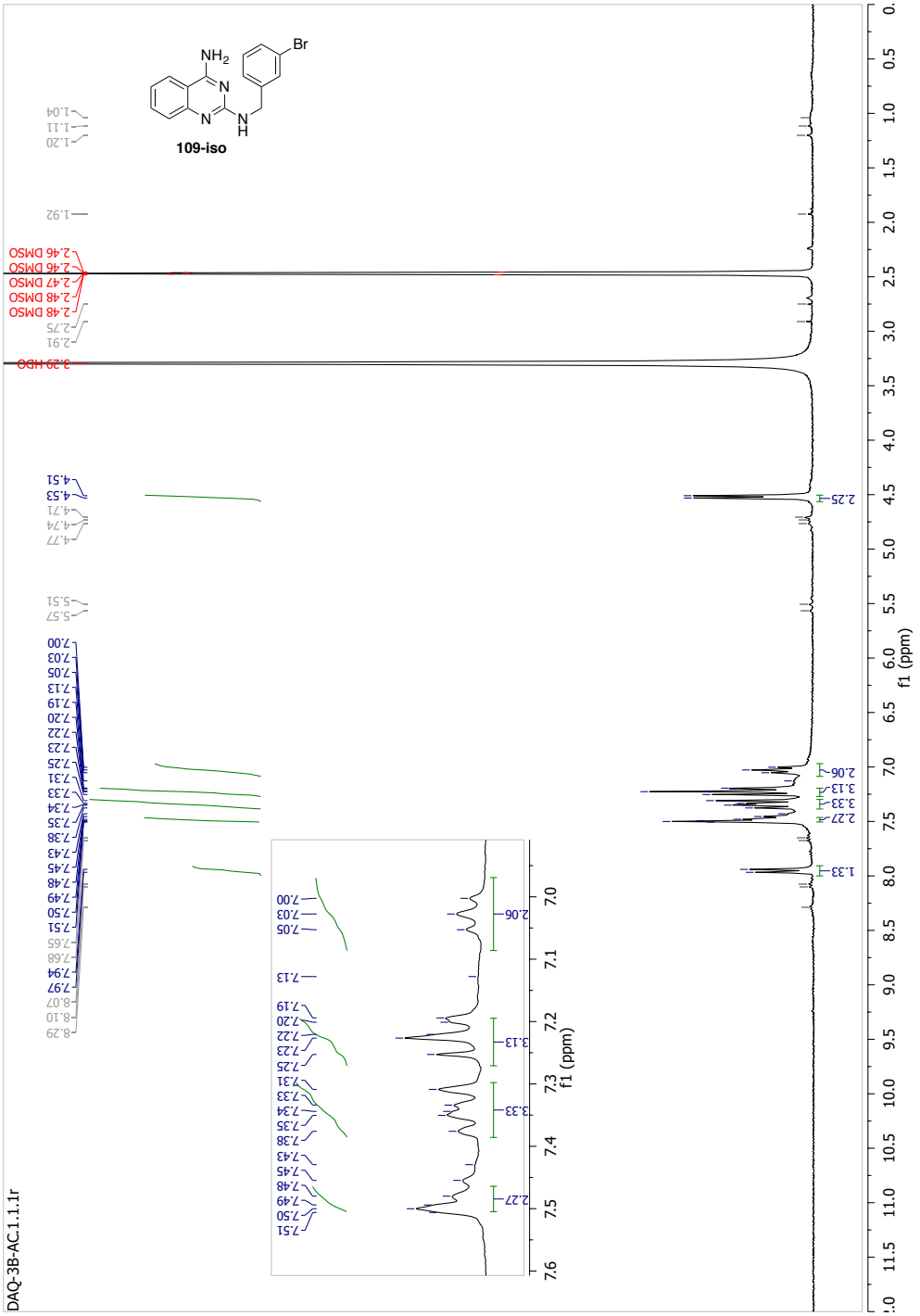
File Information	
LC-File	1AD-0401.D
File Path	C:\CHEM32\1\DATA\TAREK\TEST_LC 2015-11-07 02-20-54\
Date	07-Nov-15, 03:08:40
Sample	PPDB6
Sample Info	
Barcode	
Operator	SYSTEM
Method	TAREK-5050-G75.M
Reference	
Analysis Time	10 min
Sampling Rate	0.0033 min (0.198 sec), 3001 datapoints

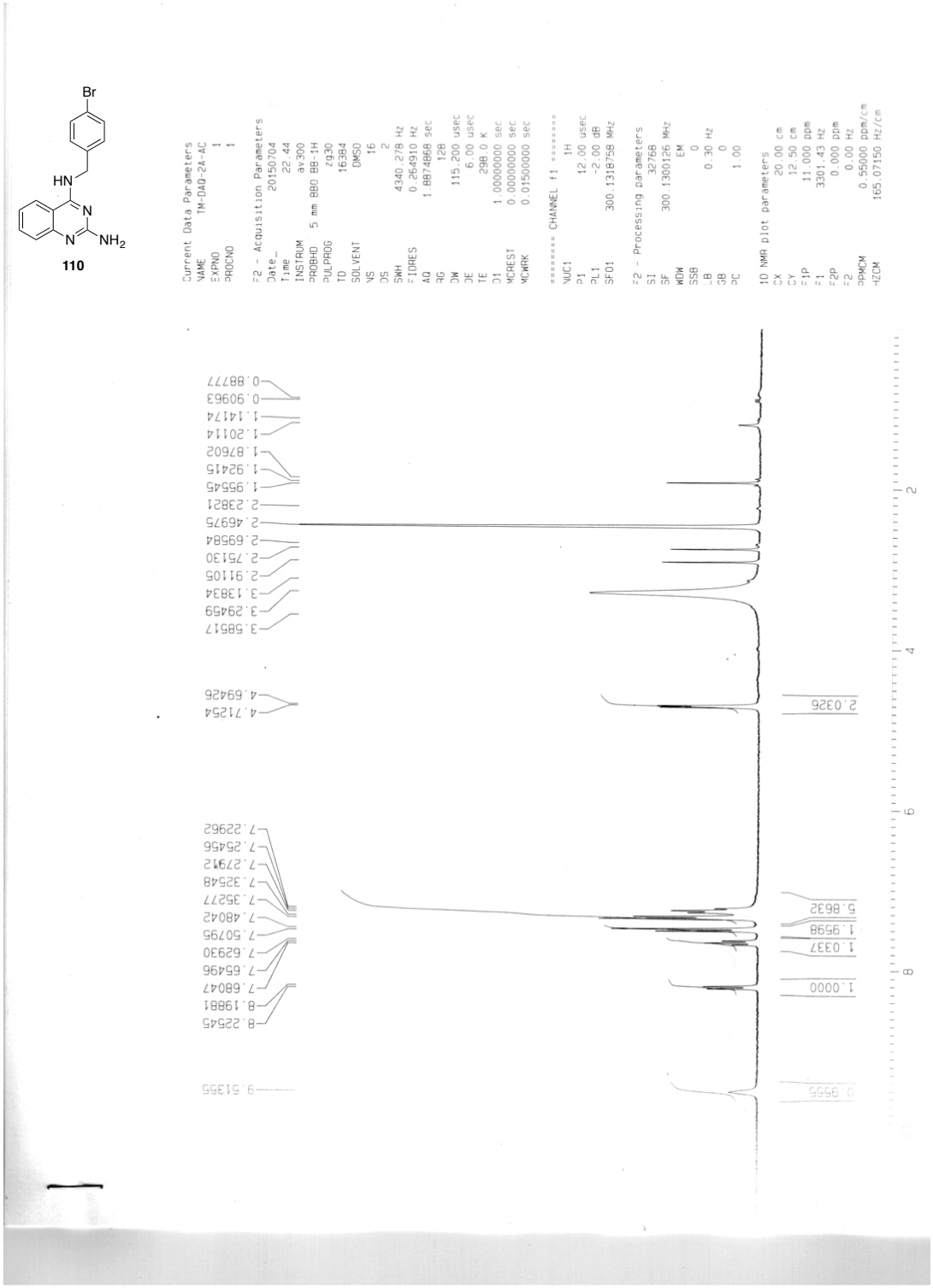
#	Time	Area	Height	Width	Area%	Symmetry
1	0.379	23648.2	3060.6	0.1171	99.351	0.529
2	2.645	44.2	2.4	0.2592	0.186	0.933
3	3.758	17.5	2.5	0.1169	0.073	1.259
4	3.952	17	2.5	0.1077	0.071	0.639
5	8.059	40.5	2.4	0.2791	0.170	1.113
6	8.543	35.3	2.2	0.2519	0.148	0.651

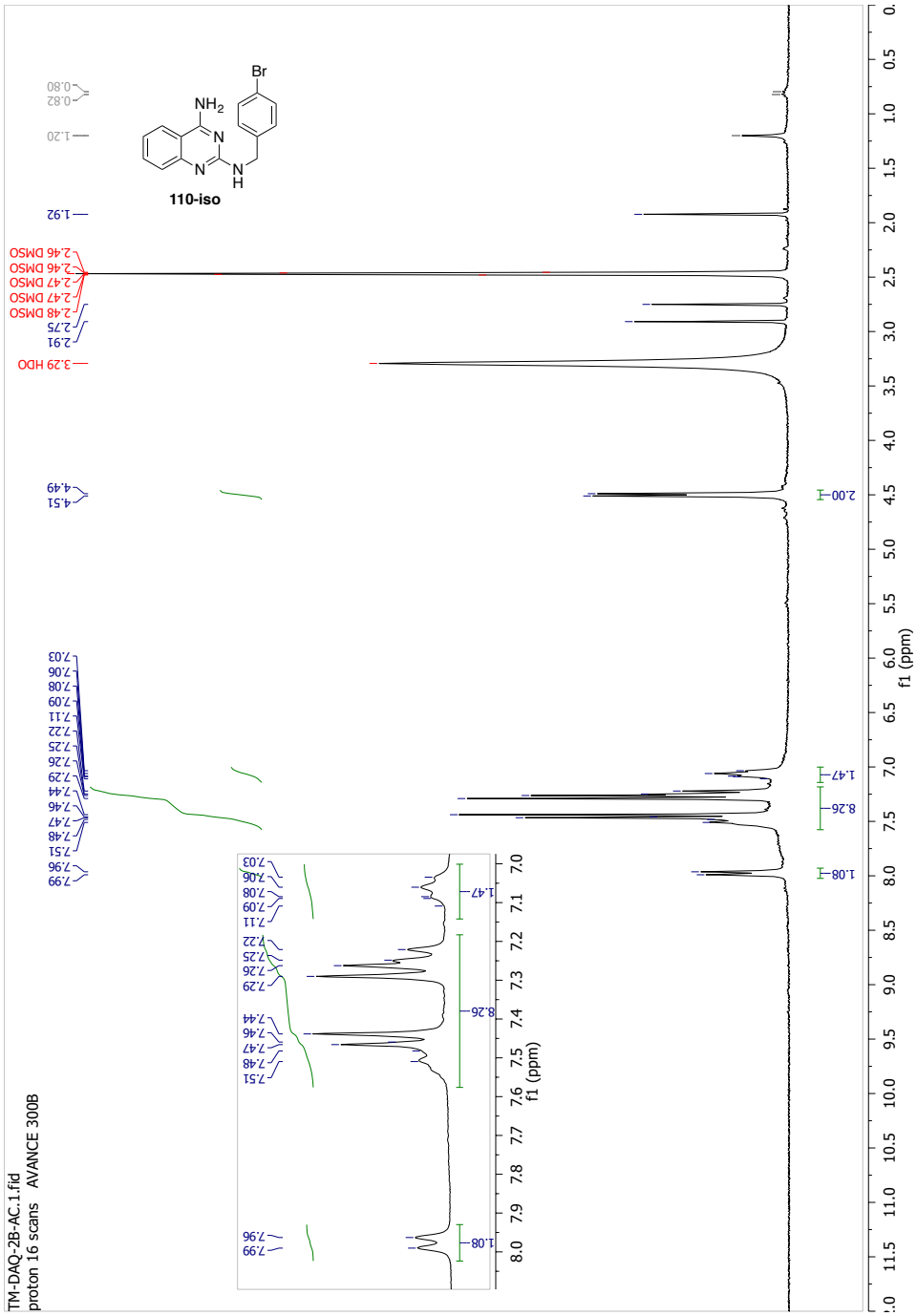
Appendix VII: Sample spectra for Chapter 8

Section A: NMR

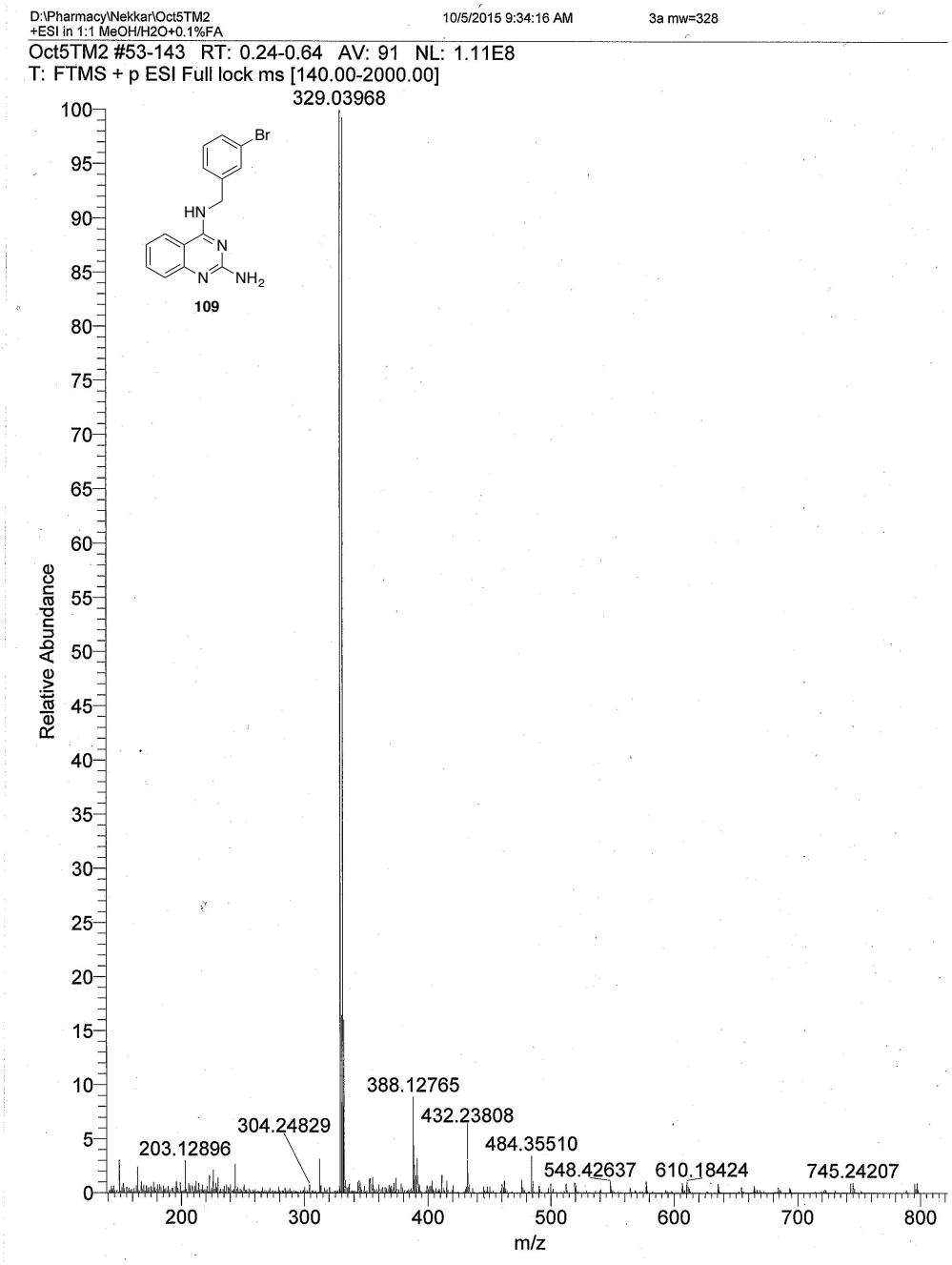


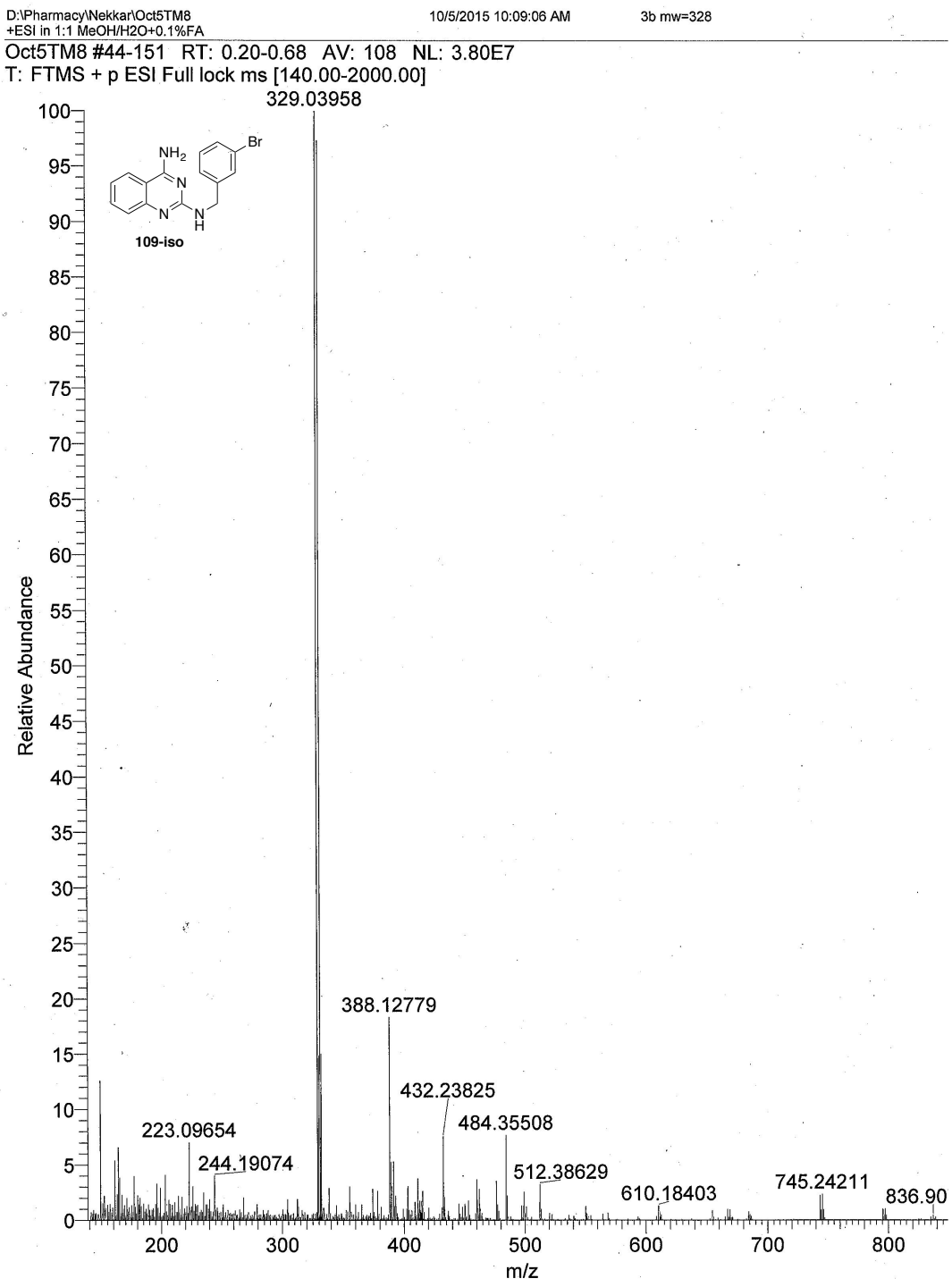

109-iso
DAQ-3B-AC1.1.1r
f1 (ppm)

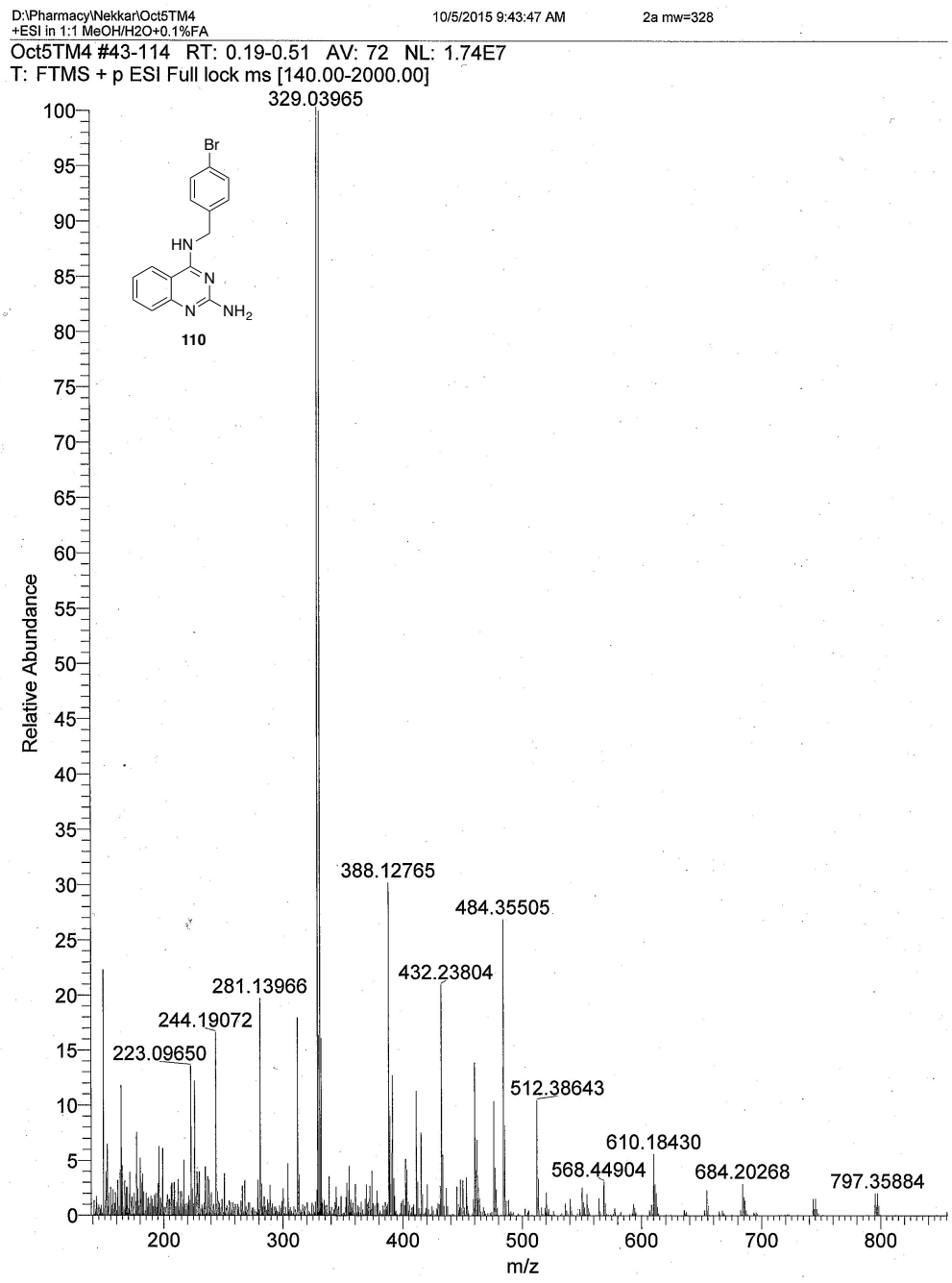

Br
HN
N
N
NH2
110
Current Data Parameters
NAME TM-DAQ-24-AC
EXPNO 1
PROCNO 1
F2 - Acquisition Parameters
Date_ 20150704
Time 22.44
INSTRUM av300
PROBHD 5 mm BBO BB-1H
PULPROG zg30
TD 16384
SOLVENT DMSO
NS 16
DS 2
SWH 4340.278 Hz
FIDRES 0.264910 Hz
AQ 1.8874868 sec
RG 128
DW 115.200 usec
DE 6.00 usec
TE 298.0 K
D1 1.00000000 sec
MCREST 0.00000000 sec
MCWRK 0.01500000 sec
======== CHANNEL f1 ========
NUC1 1H
P1 12.00 usec
PL1 -2.00 dB
SFO1 300.1318758 MHz
F2 - Processing parameters
SI 32768
SF 300.1300126 MHz
WDW EM
SSB 0
LB 0.30 Hz
GB 0
PC 1.00
1D NMR plot parameters
CX 20.00 cm
CY 12.50 cm
F1P 11.000 ppm
F1 3301.43 Hz
F2P 0.000 ppm
F2 0.00 Hz
PPMCM 0.55000 ppm/cm
HZCM 165.07150 Hz/cm
0.88777
0.90963
1.14174
1.20114
1.87602
1.92415
1.95545
2.23821
2.46975
2.69584
2.75130
2.91105
3.13834
3.29459
3.58517
4.69426
4.71254
7.22962
7.25456
7.27912
7.32548
7.35277
7.48042
7.50795
7.62930
7.65496
7.68047
8.19881
8.22545
9.51355
2.0326
5.8632
1.9598
1.0337
1.0000
0.9555
2
4
6
8

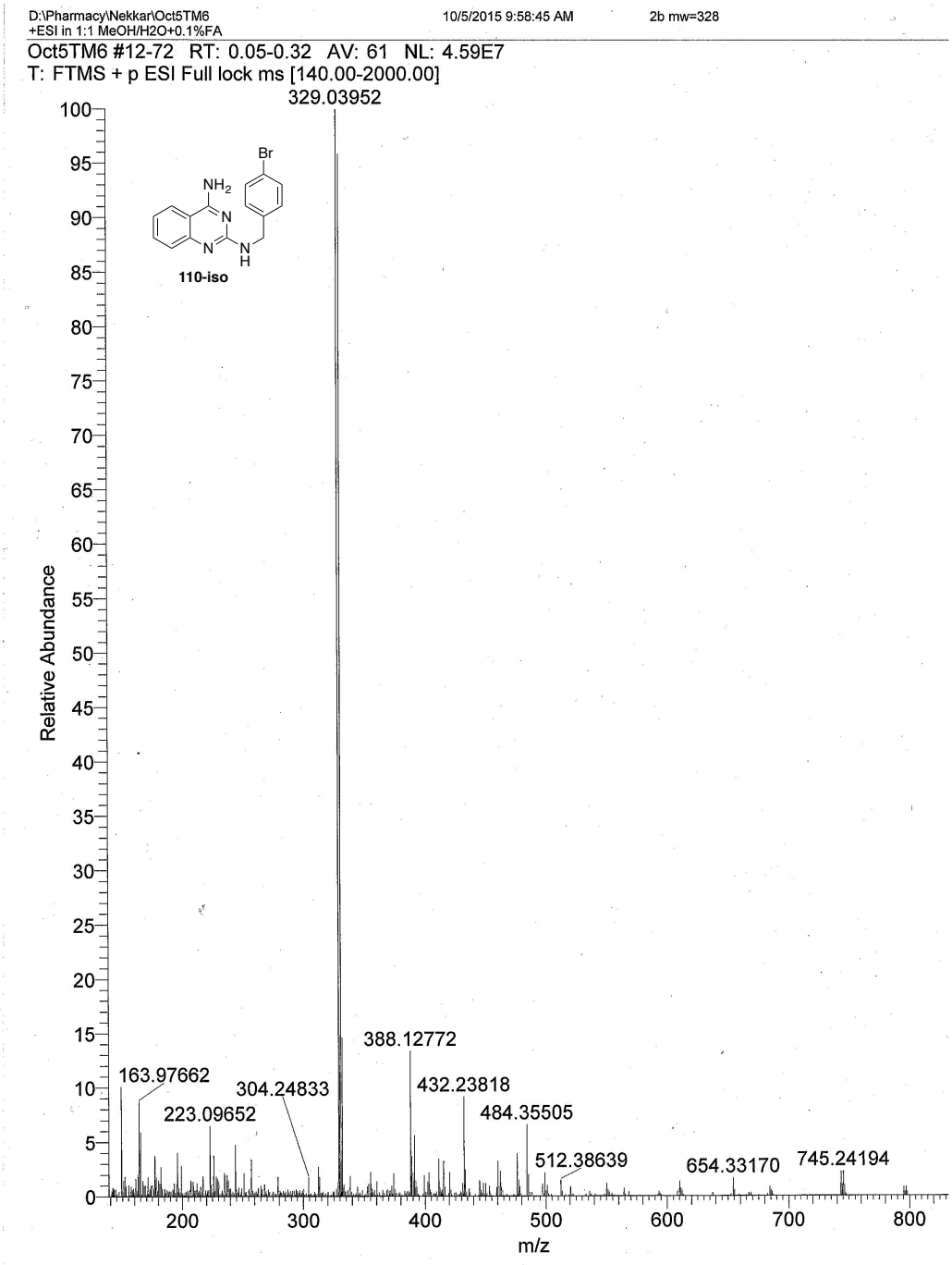

Br
NH2
N
N
N
H
110-iso
TM-DAQ-2B-AC.1.fid
proton 16 scans AVANCE 300B
f1 (ppm)

Section B: HRMS

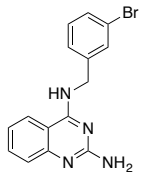



D:\Pharmacy\Nekkar\Oct5TM8
+ESI in 1:1 MeOH/H2O+0.1%FA
10/5/2015 10:09:06 AM
3b mw=328
Oct5TM8 #44-151 RT: 0.20-0.68 AV: 108 NL: 3.80E7
T: FTMS + p ESI Full lock ms [140.00-2000.00]
329.03958
388.12779
432.23825
484.35508
512.38629
610.18403
745.24211
836.90
223.09654
244.19074
109-iso
Relative Abundance
m/z

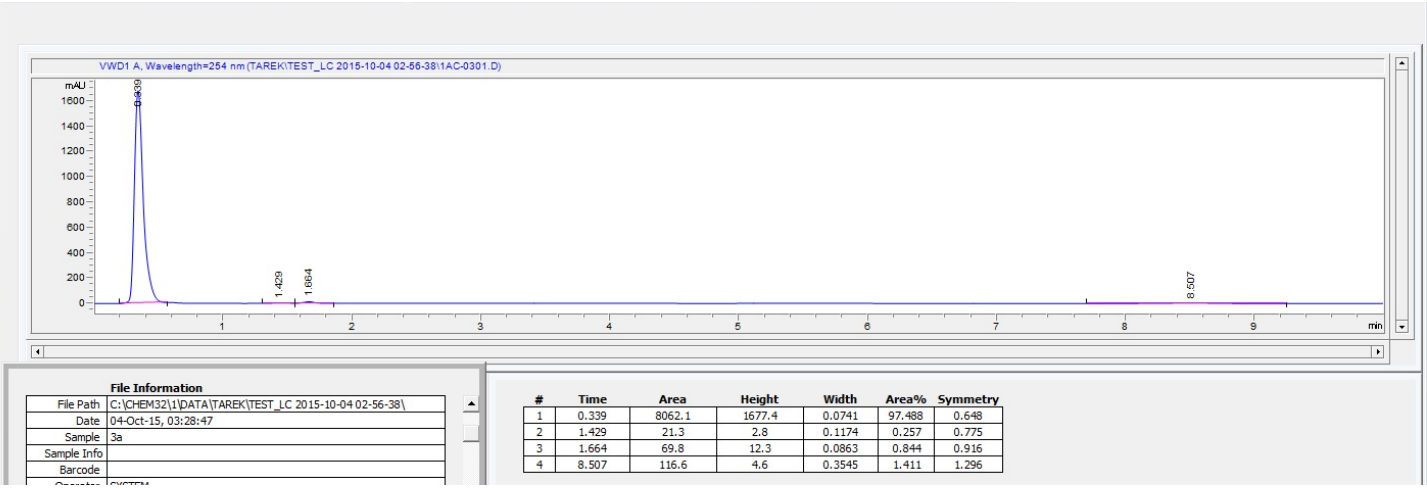

D:\Pharmacy\Nekkar\Oct5TM4
+ESI in 1:1 MeOH/H2O+0.1%FA
10/5/2015 9:43:47 AM
2a mw=328
Oct5TM4 #43-114 RT: 0.19-0.51 AV: 72 NL: 1.74E7
T: FTMS + p ESI Full lock ms [140.00-2000.00]
329.03965
388.12765
484.35505
432.23804
281.13966
244.19072
223.09650
512.38643
610.18430
568.44904
684.20268
797.35884
Relative Abundance
m/z
110


D:\Pharmacy\Nekkar\Oct5TM6
+ESI in 1:1 MeOH/H2O+0.1%FA
10/5/2015 9:58:45 AM
2b mw=328
Oct5TM6 #12-72 RT: 0.05-0.32 AV: 61 NL: 4.59E7
T: FTMS + p ESI Full lock ms [140.00-2000.00]
110-iso
Relative Abundance
m/z
329.03952
388.12772
163.97662
304.24833
432.23818
223.09652
484.35505
512.38639
654.33170
745.24194

Section C: HPLC



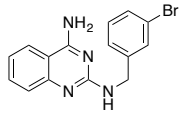
109



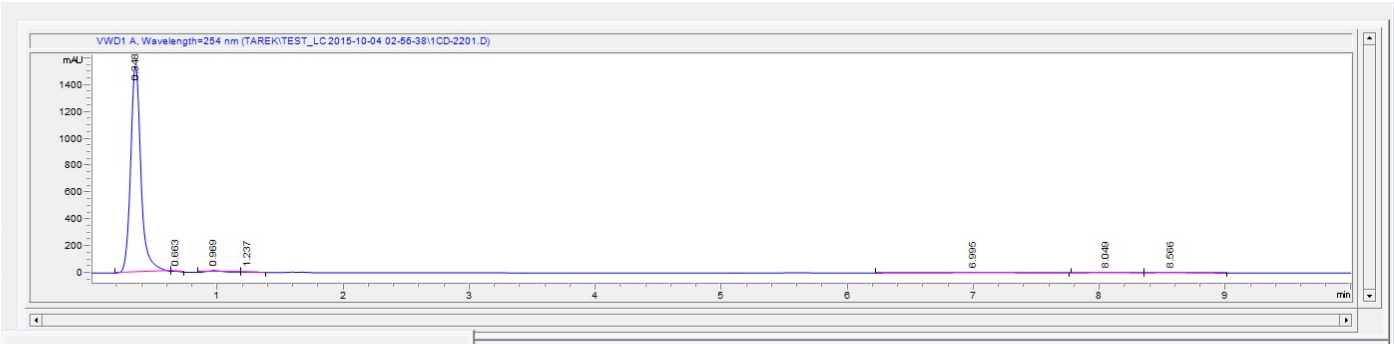
File Information

File Path	C:\CHEM32\1\DATA\TAREK\TEST_LC 2015-10-04 02-56-38\
Date	04-Oct-15, 03:28:47
Sample	3a
Sample Info	
Barcode	

#	Time	Area	Height	Width	Area%	Symmetry
1	0.339	8062.1	1677.4	0.0741	97.488	0.648
2	1.429	21.3	2.8	0.1174	0.257	0.775
3	1.664	69.8	12.3	0.0863	0.844	0.916
4	8.507	116.6	4.6	0.3545	1.411	1.296



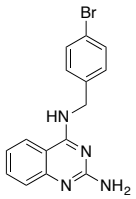
109-iso



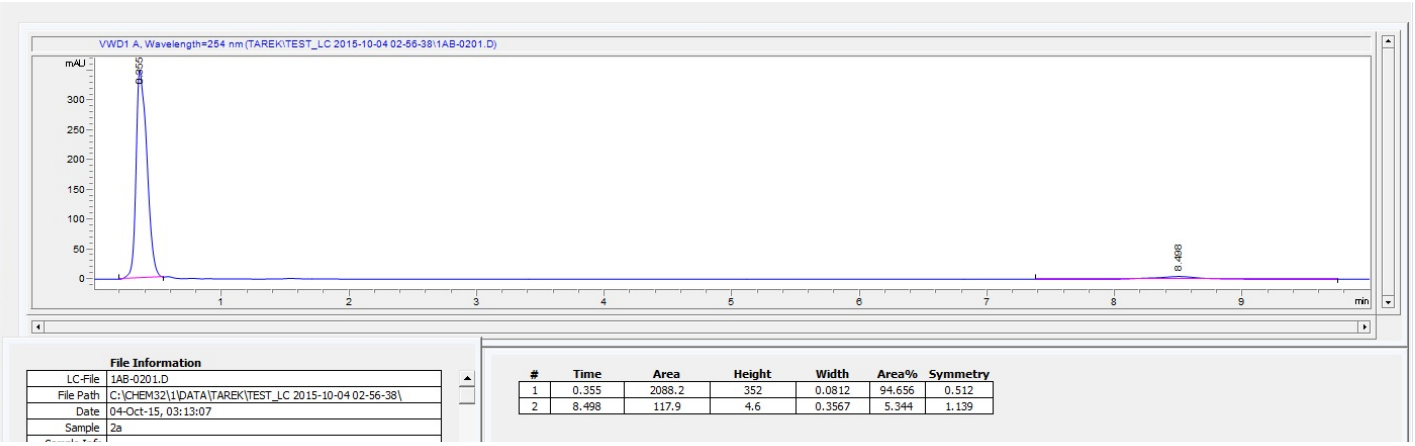
File Information

LC-File	1CD-2201.D
File Path	C:\CHEM32\1\DATA\TAREK\TEST_LC 2015-10-04 02-56-38\
Date	04-Oct-15, 08:26:09
Sample	3b
Sample Info	
Barcode	
Operator	SYSTEM
Method	TAREK-5050-G75.M

#	Time	Area	Height	Width	Area%	Symmetry
1	0.348	8827.5	1543.4	0.0877	96.717	0.803
2	0.663	11.8	3.2	0.0606	0.130	0.38
3	0.969	93.5	12.1	0.118	1.024	0.777
4	1.237	13.6	1.8	0.1019	0.149	0.251
5	6.995	111.7	2.2	0.6582	1.223	1.142
6	8.049	36.3	2.2	0.2686	0.397	0.849
7	8.566	32.9	2.1	0.2462	0.360	0.638



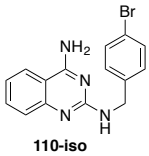
110



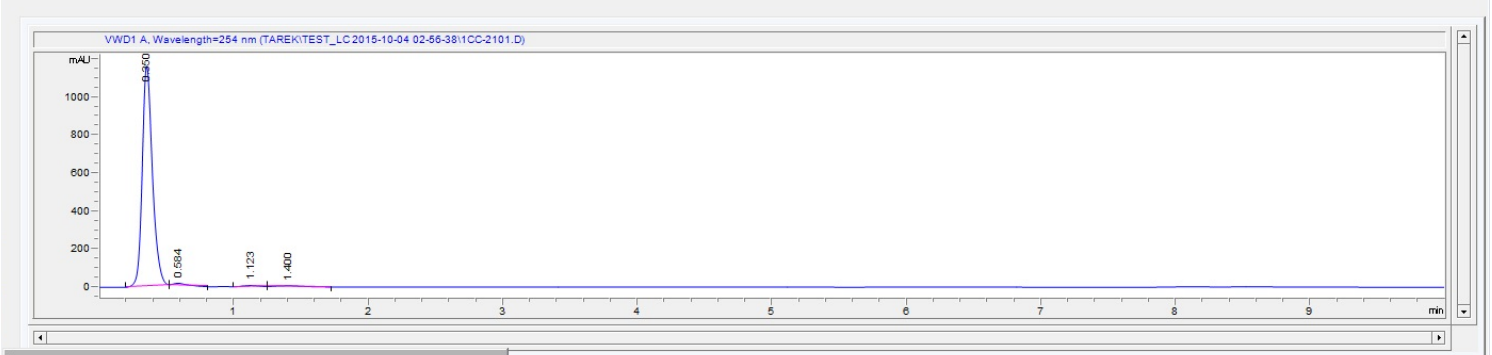
File Information

LC-File	1AB-0201.D
File Path	C:\CHEM32\1\DATA\TAREK\TEST_LC 2015-10-04 02-56-38\
Date	04-Oct-15, 03:13:07
Sample	2a

#	Time	Area	Height	Width	Area%	Symmetry
1	0.355	2088.2	352	0.0812	94.656	0.512
2	8.498	117.9	4.6	0.3567	5.344	1.139



110-iso



File Information

File Path	C:\CHEM32\1\DATA\TAREK\TEST_LC 2015-10-04 02-56-38\
Date	04-Oct-15, 08:10:30
Sample	2b
Sample Info	
Barcode	

#	Time	Area	Height	Width	Area%	Symmetry
1	0.35	6086.5	1159.8	0.0792	97.314	0.738
2	0.584	61.8	9.7	0.0974	0.988	0.467
3	1.123	46.7	6	0.1173	0.747	1.079
4	1.4	59.5	4.7	0.1803	0.951	0.696

• References •

1. Maurer, K.; Volk, S.; Gerbaldo, H. Auguste D and Alzheimer's disease. *Lancet* **1997,** 349, 1546-1549.

2. Felician, O.; Sandson, T. A. The neurobiology and pharmacotherapy of Alzheimer's disease. *J Neuropschiatry Clin Neurosci* **1999,** 11, 19-31.

3. 2015 Alzheimer's disease facts and figures. *Alzheimer's & Dementia* **2015,** 11, 332-384.

4. World Alzheimer Report 2015. *Alzheimer's Disease International* **2015**.

5. Annual Report 2015. *Alzheimer's Society of Canada* **2015**.

6. Dubois, B.; Padovani, A.; Scheltens, P.; Rossi, A.; Dell'Agnello, G. Timely diagnosis for Alzheimer's disease: A literature review on benefits and challenges. *J Alzheimers Dis* **2015,** 49, 617-631.

7. De Felice, F. G.; Munoz, D. P. Opportunities and challenges in developing relevant animal models for Alzheimer's disease. *Ageing Res Rev* **2016,** 26, 112-114.

8. Golde, T. E. The therapeutic importance of understanding mechanisms of neuronal cell death in neurodegenerative disease. *Mol Neurodegener* **2009,** 4, 8-14.

9. Selkoe, D. J. Alzheimer's disease is a synaptic failure. *Science* **2002,** 298, 789-791.

10. Mattson, M. P. Pathways towards and away from Alzheimer's disease. *Nature* **2004,** 430, 631-639.

11. Shankar, G. M.; Walsh, D. M. Alzheimer's disease: synaptic dysfunction and Abeta. *Mol Neurodegener* **2009,** 4, 48-60.

12. Brunnstrom, H. R.; Englund, E. M. Cause of death in patients with dementia disorders. *Eur J Neurol* **2009,** 16, 488-492.

13. Poirier, J. Apolipoprotein E in animal models of CNS injury and in Alzheimer's disease. *Trends Neurosci* **1994,** 17, 525-530.

14. Hirono, N.; Hashimoto, M.; Yasuda, M.; Kazui, H.; Mori, E. Accelerated memory decline in Alzheimer's disease With apolipoprotein e4 allele. *J Neuropschiatry Clin Neurosci* **2003,** 15, 354-358.

15. Bereczki, E.; Bernát, G.; Csont, T.; Ferdinandy, P.; Scheich, H.; Sántha, M. Overexpression of human apolipoprotein B-100 induces severe neurodegeneration in transgenic mice. *J Proteome Res* **2008,** 7, 2246-2252.

16. Hardy, J. Amyloid, the presenilins and Alzheimer's disease. *Trends Neurosci* **1997,** 20, 154-159.

17. Suh, Y.-H.; Checler, F. Amyloid precursor protein, presenilins, and α-synuclein molecular pathogenesis and pharmacological applications in Alzheimer 's disease. *Pharmacol Rev* **2002,** 54, 469-525.

18. Förstl, H.; Kurz, A. Clinical features of Alzheimer's disease. *Eur Arch Psychiatry Clin Neurosci* **1999,** 249, 288-290.

19. Kurz, A.; Perneczky, R. Novel insights for the treatment of Alzheimer's disease. *Prog Neuropsychopharmacol Biol Psychiatry* **2011,** 35, 373-379.

20. De Strooper, B.; Karran, E. The cellular phase of Alzheimer's disease. *Cell* **2016,** 164, 603-615.

21. Valera, E.; Spencer, B.; Masliah, E. Immunotherapeutic approaches targeting amyloid-beta, alpha-Synuclein, and tau for the treatment of neurodegenerative disorders. *Neurotherapeutics* **2015**, 179-189.

22. Hampel, H.; Schneider, L. S.; Giacobini, E.; Kivipelto, M.; Sindi, S.; Dubois, B.; Broich, K.; Nistico, R.; Aisen, P. S.; Lista, S. Advances in the therapy of Alzheimer's disease: targeting amyloid beta and tau and perspectives for the future. *Expert Rev Neurother* **2015,** 15, 83-105.

23. Lloret, A.; Fuchsberger, T.; Giraldo, E.; Vina, J. Molecular mechanisms linking amyloid beta toxicity and Tau hyperphosphorylation in Alzheimers disease. *Free Radic Biol Med* **2015,** 83, 186-191.

24. Holden, M.; Kelly, C. Use of cholinesterase inhibitors in dementia. *Adv Psychiatr Treat* **2002,** 8, 89-96.

25. Francis, P. T.; Ramirez, M. J.; Lai, M. K. Neurochemical basis for symptomatic treatment of Alzheimer's disease. *Neuropharmacology* **2010,** 59, 221-229.

26. Terry, A. V., Jr.; Buccafusco, J. J. The cholinergic hypothesis of age and Alzheimer's disease-related cognitive deficits: recent challenges and their implications for novel drug development. *J Pharmacol Exp Ther* **2003,** 306, 821-827.

27. Chiti, F.; Dobson, C. M. Protein misfolding, functional amyloid, and human disease. *Ann Rev Biochem* **2006,** 75, 333-366.

28. Correia, S. C.; Resende, R.; Moreira, P. I.; Pereira, C. M. Alzheimer's disease-related misfolded proteins and dysfunctional organelles on autophagy menu. *DNA Cell Biol* **2015,** 34, 261-273.

29. Thinakaran, G.; Koo, E. H. Amyloid precursor protein trafficking, processing, and function. *J Biol Chem* **2008,** 283, 29615-29619.

30. Guo, L.; Salt, T. E.; Luong, V.; Wood, N.; Cheung, W.; Maass, A.; Ferrari, G.; Russo-Marie, F.; Sillito, A. M.; Cheetham, M. E.; Moss, S. E.; Fitzke, F. W.; Cordeiro, M. F. Targeting amyloid-beta in glaucoma treatment. *Proc Natl Acad Sci U S A* **2007,** 104, 13444-13449.

31. Holmes, B. B.; Furman, J. L.; Mahan, T. E.; Yamasaki, T. R.; Mirbaha, H.; Eades, W. C.; Belaygorod, L.; Cairns, N. J.; Holtzman, D. M.; Diamond, M. I. Proteopathic tau seeding predicts tauopathy in vivo. *Proc Natl Acad Sci U S A* **2014,** 111, E4376-4385.

32. Ávila, J.; Lim, F.; Moreno, F.; Belmonte, C.; Cuello, C. Tau function and dysfunction in neurons. *Mol Neurobio* **2002,** 25, 213-231.

33. Buée, L.; Bussière, T.; Buée-Scherrer, V.; Delacourte, A.; Hof, P. R. Tau protein isoforms, phosphorylation and role in neurodegenerative disorders. *Brain Res Rev* **2000,** 33, 95-130.

34. Gendron, T. F.; Petrucelli, L. The role of tau in neurodegeneration. *Mol Neurodegener* **2009,** 4, 2-19.

35. Wischik, C. M.; Harrington, C. R.; Storey, J. M. Tau-aggregation inhibitor therapy for Alzheimer's disease. *Biochem Pharmacol* **2014,** 88, 529-539.

36. Nisbet, R. M.; Polanco, J. C.; Ittner, L. M.; Gotz, J. Tau aggregation and its interplay with amyloid-beta. *Acta Neuropathol* **2015,** 129, 207-220.

37. LaFerla, F. M. Pathways linking Abeta and tau pathologies. *Biochem Soc Trans* **2010,** 38, 993-995.

38. Bush, A. I. The metallobiology of Alzheimer's disease. *Trends Neurosci* **2003,** 26, 207-214.

39. Bandyopadhyay, S.; Huang, X.; Lahiri, D. K.; Rogers, J. T. Novel drug targets based on metallobiology of Alzheimer's disease. *Expert Opin Ther Targets* **2010,** 14, 1177-1197.

40. White, A. R.; Faller, P.; Atwood, C. S.; Zatta, P. Metals and AD. *Int J Alzheimers Dis* **2011**.

41. Suh, W. H.; Suslick, K. S.; Suh, Y.-H. Therapeutic agents for Alzheimer's disease. *Curr Med Chem* **2005,** 5, 259-269.

42. Klafki, H. W.; Staufenbiel, M.; Kornhuber, J.; Wiltfang, J. Therapeutic approaches to Alzheimer's disease. *Brain* **2006,** 129, 2840-55.

43. Zheng, H.; Fridkin, M.; Youdim, M. New approaches to treating Alzheimer's disease. *Perspect Medicin Chem* **2015,** 7, 1-8.

44. Bajic, V.; Milocanovic, E. S.; Spremo-Potparevic, B.; Zivkovic, L.; Milicevic, Z.; Stanimirovic, J.; Bogdanovic, N.; Isenovic, E. R. Treatment of Alzheimer's disease: Classical therapeutic approach. *Curr Pharm Anal* **2016,** 12, ASAP.

45. Guzior, N.; Więckowska, A.; Panek, D.; Malawska, B. Recent development of multifunctional agents as potential drug candidates for the treatment of Alzheimer's disease. *Curr Med Chem* **2015,** 22, 373-404.

46. Leon, R.; Garcia, A. G.; Marco-Contelles, J. Recent advances in the multitarget-directed ligands approach for the treatment of Alzheimer's disease. *Med Res Rev* **2013,** 33, 139-189.

47. Guzior, N.; Bajda, M.; Skrok, M.; Kurpiewska, K.; Lewinski, K.; Brus, B.; Pislar, A.; Kos, J.; Gobec, S.; Malawska, B. Development of multifunctional, heterodimeric isoindoline-1,3-dione derivatives as cholinesterase and beta-amyloid aggregation inhibitors with neuroprotective properties. *Eur J Med Chem* **2015,** 92, 738-749.

48. Jin, H.; Randazzo, J.; Zhang, P.; Kador, P. F. Multifunctional antioxidants for the treatment of age-related diseases. *J Med Chem* **2010,** 53, 1117-1127.

49. Cavalli, A.; Bolognesi, M. L.; Minarini, A.; Rosini, M.; Tumiatti, V.; Recanatini, M.; Carlo, M. Multi-target-directed ligands to combat neurodegenerative diseases. *J Med Chem* **2008,** 51, 347-372.

50. Hernandez-Rodriguez, M.; Correa-Basurto, J.; Martinez-Ramos, F.; Padilla, M., II; Benitez-Cardoza, C. G.; Mera-Jimenez, E.; Rosales-Hernandez, M. C. Design of multi-target compounds as AChE, BACE1, and amyloid-beta(1-42) oligomerization inhibitors: in silico and in vitro studies. *J Alzheimers Dis* **2014,** 41, 1073-1085.

51. Green, K. D.; Fridman, M.; Garneau-Tsodikova, S. hChAT: a tool for the chemoenzymatic generation of potential acetyl/butyrylcholinesterase inhibitors. *Chembiochem* **2009,** 10, 2191-2194.

52. Weinbroum, A. A. Pathophysiological and clinical aspects of combat anticholinesterase poisoning. *Br Med Bull* **2004,** 72, 119-133.

53. Cygler, M.; Schrag, J. D.; Sussman, J. L.; Harel, M.; Silman, I.; Gentry, M. K.; Doctor, B. P. Relationship between sequence conservation and three-dimensional structure in a large family of esterases, lipases, and related proteins. *Protein Sci* **1993,** 2, 366-382.

54. Taylor, P.; Radić, Z. The cholinesterases: From genes to proteins *Ann Rev. Pharmacol Toxicol* **1994,** 34, 281-320.

55. Bourne, Y.; Taylor, P.; Bougis, P. E.; Marchot, P. Crystal structure of mouse acetylcholinesterase. *J Biol Chem* **1999,** 274, 2963-2970.

56. Bartolucci, C.; Siotto, M.; Ghidini, E.; Amari, G.; Bolzoni, P. T.; Racchi, M.; Villetti, G.; Delcanale, M.; Lamba, D. Structural determinants of Torpedo californica acetylcholinesterase inhibition by the novel and orally active carbamate based anti-Alzheimer drug ganstigmine (CHF-2819). *J Med Chem* **2006,** 49, 5051-5058.

57. Dvir, H.; Silman, I.; Harel, M.; Rosenberry, T. L.; Sussman, J. L. Acetylcholinesterase: from 3D structure to function. *Chem Biol Interact* **2010,** 187, 10-22.

58. Radic, Z.; Manetsch, R.; Krasinski, A.; Raushel, J.; Yamauchi, J.; Garcia, C.; Kolb, H.; Sharpless, K. B.; Taylor, P. Molecular basis of interactions of cholinesterases with tight binding inhibitors. *Chem Biol Interact* **2005,** 157-158, 133-141.

59. Chatonnet, A.; Lockridge, O. Comparison of butyrylcholinesterase and acetylcholinesterase. *Biochem J* **1989,** 260, 625-634.

60. Savini, L.; Gaeta, A.; Fattorusso, C.; Catalanotti, B.; Campiani, G.; Chiasserini, L.; Pellerano, C.; Novellino, E.; McKissic, D.; Saxena, A. Specific targeting of acetylcholinesterase and butyrylcholinesterase recognition sites. Rational design of novel, selective, and highly potent cholinesterase inhibitors. *J Med Chem* **2003,** 46, 1-4.

61. Soreq, H.; Seidman, S. Acetylcholinesterase – New roles for an old actor. *Nature Rev Neurosci* **2001,** 2, 295-302.

62. Saxena, A.; Redman, A. M. G.; Jiang, X.; Lockridge, O.; Doctor, B. P. Differences in active-site gorge dimensions of cholinesterases revealed by binding of inhibitors to human butyrylcholinesterase. *Chem Biol Interact* **1999,** 119-120, 61-69.

63. Bartolucci, C.; Perola, E.; Pilger, C.; Fels, G.; Lamba, D. Three-dimensional structure of a complex of galanthamine (Nivalin) with acetylcholinesterase from Torpedo californica: Implications for the design of new anti-Alzheimer drugs. *Proteins* **2001,** 42, 182-191.

64. Vellom, D. C.; Radić, Z.; Li, Y.; Pickering, N. A.; Camp, S.; Taylor, P. Amino acid residues controlling acetylcholinesterase and butyrylcholinesterase specificity. *Biochemistry* **1993,** 32, 12-17.

65. Barak, D.; Ordentlich, A.; Kaplan, D.; Kronman, C.; Velan, B.; Shafferman, A. Lessons from functional analysis of AChE covalent and noncovalent inhibitors for design of AD therapeutic agents. *Chem Biol Interact* **2005,** 157-158, 219-226.

66. Harel, M.; Schalk, I.; Ehret-Sabatier, L.; Bouet, F.; Goeldner, M.; Hirth, C.; Axelsen, P. H.; Silman, I.; Sussman, J. L. Quaternary ligand binding to aromatic residues in the active-site gorge of acetylcholinesterase. *Proc Natl Acad Sci U S A* **1993,** 90, 9031-9035.

67. Bourne, Y.; Radic, Z.; Kolb, H. C.; Sharpless, K. B.; Taylor, P.; Marchot, P. Structural insights into conformational flexibility at the peripheral site and within the active center gorge of AChE. *Chem Biol Interact* **2005,** 157-158, 159-165.

68. Dickerson, T. J.; Beuscher IV, A. E.; Rogers, C. J.; Hixon, M. S.; Yamamoto, N.; Xu, Y.; Olson, A. J.; Janda, K. D. Discovery of acetylcholinesterase peripheral anionic site ligands through computational refinement of a directed library. *Biochemistry* **2005,** 44, 14845-14853.

69. Chen, X.; Wehle, S.; Kuzmanovic, N.; Merget, B.; Holzgrabe, U.; Konig, B.; Sotriffer, C. A.; Decker, M. Acetylcholinesterase inhibitors with photoswitchable inhibition of beta-amyloid aggregation. *ACS Chem Neurosci* **2014,** 5, 377-389.

70. Dinamarca, M. C.; Sagal, J. P.; Quintanilla, R. A.; Godoy, J. A.; Arrazola, M. S.; Inestrosa, N. C. Amyloid-β-acetylcholinesterase complexes potentiate neurodegenerative changes induced by the Abeta peptide. Implications for the pathogenesis of Alzheimer's disease. *Mol Neurodegener* **2010,** 5, 4-19.

71. Su, T.; Xie, S.; Wei, H.; Yan, J.; Huang, L.; Li, X. Synthesis and biological evaluation of berberine-thiophenyl hybrids as multi-functional agents: Inhibition of acetylcholinesterase, butyrylcholinesterase, and Abeta aggregation and antioxidant activity. *Bioorg Med Chem* **2013,** 21, 5830-5840.

72. Rodriguez-Franco, M. I.; Fernandez-Bachiller, M. I.; Perez, C.; Hernandez-Ledesma, B.; Bartolome, B. Novel tacrine-melatonin hybrids as dual-acting drugs for Alzheimer disease, with improved acetylcholinesterase inhibitory and antioxidant properties. *J Med Chem* **2006,** 49, 459-462.

73. Camps, P.; Formosa, X.; Galdeano, C.; Munoz-Torrero, D.; Ramirez, L.; Gomez, E.; Isambert, N.; Lavilla, R.; Badia, A.; Clos, M. V.; Bartolini, M.; Mancini, F.; Andrisano, V.; Arce, M. P.; Rodriguez-Franco, M. I.; Huertas, O.; Dafni, T.; Luque, F. J. Pyrano[3,2-c]quinoline-6-chlorotacrine hybrids as a novel family of acetylcholinesterase- and beta-amyloid-directed anti-Alzheimer compounds. *J Med Chem* **2009,** 52, 5365-5379.

74. Di Pietro, O.; Perez-Areales, F. J.; Juarez-Jimenez, J.; Espargaro, A.; Clos, M. V.; Perez, B.; Lavilla, R.; Sabate, R.; Luque, F. J.; Munoz-Torrero, D. Tetrahydrobenzo[h][1,6]naphthyridine-6-chlorotacrine hybrids as a new family of anti-Alzheimer agents targeting beta-amyloid, tau, and cholinesterase pathologies. *Eur J Med Chem* **2014,** 84, 107-117.

75. Lan, J. S.; Xie, S. S.; Li, S. Y.; Pan, L. F.; Wang, X. B.; Kong, L. Y. Design, synthesis and evaluation of novel tacrine-(beta-carboline) hybrids as multifunctional agents for the treatment of Alzheimer's disease. *Bioorg Med Chem* **2014,** 22, 6089-6104.

76. Li, S. Y.; Jiang, N.; Xie, S. S.; Wang, K. D.; Wang, X. B.; Kong, L. Y. Design, synthesis and evaluation of novel tacrine-rhein hybrids as multifunctional agents for the treatment of Alzheimer's disease. *Org Biomol Chem* **2014,** 12, 801-814.

77. Rizzo, S.; Rivière, C.; Piazzi, L.; Bisi, A.; Gobbi, S.; Bartolini, M.; Andrisano, V.; Morroni, F.; Tarozzi, A.; Monti, J.-P.; Rampa, A. Benzofuran-based hybrid compounds for the inhibition of cholinesterase activity, beta amyloid aggregation, and abeta neurotoxicity. *J Med Chem* **2008,** 51, 2883-2886.

78. Recanatini, M.; Cavalli, A.; Belluti, F.; Piazzi, L.; Rampa, A.; Bisi, A.; Gobbi, S.; Valenti, P.; Andrisano, V.; Bartolini, M.; Cavrini, V. SAR of 9-Amino-1,2,3,4-tetrahydroacridine-Based acetylcholinesterase Inhibitors: Synthesis, enzyme inhibitory activity, QSAR, and structure-based CoMFA of tacrine analogues. *J Med Chem* **2000,** 43, 2007-2018.

79. Huang, L.; Miao, H.; Sun, Y.; Meng, F.; Li, X. Discovery of indanone derivatives as multi-target-directed ligands against Alzheimer's disease. *Eur J Med Chem* **2014,** 87, 429-439.

80. Allderdice, P. W.; Gardner, H. A. R.; Galutira, D.; Lockridge, O.; LaDu, B. N.; McAlpine, P. J. The cloned butyrylcholinesterase (BCHE) gene maps to a single chromosome site, 3q26. *Genomics* **1991,** 11, 452-454.

81. Darvesh, S.; Hopkins, D. A.; Geula, C. Neurobiology of butyrylcholinesterase. *Nat Rev Neurosci* **2003,** 4, 131-138.

82. Nicolet, Y.; Lockridge, O.; Masson, P.; Fontecilla-Camps, J. C.; Nachon, F. Crystal structure of human butyrylcholinesterase and of its complexes with substrate and products. *J Biol Chem* **2003,** 278, 41141-41147.

83. Greig, N. H.; Utsuki, T.; Ingram, D. K.; Wang, Y.; Pepeu, G.; Scali, C.; Yu, Q. S.; Mamczarz, J.; Holloway, H. W.; Giordano, T.; Chen, D.; Furukawa, K.; Sambamurti, K.; Brossi, A.; Lahiri, D. K. Selective butyrylcholinesterase inhibition elevates brain acetylcholine, augments learning and lowers Alzheimer beta-amyloid peptide in rodent. *Proc Natl Acad Sci U S A* **2005,** 102, 17213-17218.

84. Garcia-Ayllon, M. S.; Riba-Llena, I.; Serra-Basante, C.; Alom, J.; Boopathy, R.; Saez-Valero, J. Altered levels of acetylcholinesterase in Alzheimer plasma. *PLoS One* **2010,** 5, e8701.

85. Zhang, Y. W.; Thompson, R.; Zhang, H.; Xu, H. APP processing in Alzheimer's disease. *Mol Brain* **2011,** 4, 3-17.

86. Zheng, H.; Koo, E. H. The amyloid precursor protein: beyond amyloid. *Mol Neurodegener* **2006,** 1, 5-18.

87. Priller, C.; Bauer, T.; Mitteregger, G.; Krebs, B.; Kretzschmar, H. A.; Herms, J. Synapse formation and function is modulated by the amyloid precursor protein. *J Neurosci* **2006,** 26, 7212-7221.

88. Muresan, V.; Ladescu Muresan, Z. Amyloid-beta precursor protein: Multiple fragments, numerous transport routes and mechanisms. *Exp Cell Res* **2015,** 334, 45-53.

89. Selkoe, D. J. Alzheimer's disease genes, proteins, and therapy. *Am J Physiol* **2001,** 81, 741-766.

90. Selkoe, D. J. Physiological produdion of the β-amyloid protein and the mechanism of AIzheimer's disease. *Trends Neurosci* **1993,** 16, 403-409.

91. Wang, H.; Barreyro, L.; Provasi, D.; Djemil, I.; Torres-Arancivia, C.; Filizola, M.; Ubarretxena-Belandia, I. Molecular determinants and thermodynamics of the amyloid precursor protein transmembrane domain implicated in Alzheimer's disease. *J Mol Biol* **2011,** 408, 879-895.

92. Dahms, S. O.; Hoefgen, S.; Roeser, D.; Schlott, B.; Guhrs, K. H.; Than, M. E. Structure and biochemical analysis of the heparin-induced E1 dimer of the amyloid precursor protein. *Proc Natl Acad Sci U S A* **2010,** 107, 5381-5386.

93. Wang, L. S.; Naj, A. C.; Graham, R. R.; Crane, P. K.; Kunkle, B. W.; Cruchaga, C.; Murcia, J. D.; Cannon-Albright, L.; Baldwin, C. T.; Zetterberg, H.; Blennow, K.; Kukull, W. A.; Faber, K. M.; Schupf, N.; Norton, M. C.; Tschanz, J. T.; Munger, R. G.; Corcoran, C. D.; Rogaeva, E.; Lin, C. F.; Dombroski, B. A.; Cantwell, L. B.; Partch, A.; Valladares, O.; Hakonarson, H.; St George-Hyslop, P.; Green, R. C.; Goate, A. M.; Foroud, T. M.; Carney, R. M.; Larson, E. B.; Behrens, T. W.; Kauwe, J. S.; Haines, J. L.; Farrer, L. A.; Pericak-Vance, M. A.; Mayeux, R.; Schellenberg, G. D. Rarity of the Alzheimer disease-protective APP A673T variant in the United States. *JAMA Neurol* **2015,** 72, 209-216.

94. Kokawa, A.; Ishihara, S.; Fujiwara, H.; Nobuhara, M.; Iwata, M.; Ihara, Y.; Funamoto, S. The A673T mutation in the amyloid precursor protein reduces the production of beta-amyloid protein from its beta-carboxyl terminal fragment in cells. *Acta Neuropathol Commun* **2015,** 3, 66.

95. Nhan, H. S.; Chiang, K.; Koo, E. H. The multifaceted nature of amyloid precursor protein and its proteolytic fragments: friends and foes. *Acta Neuropathol* **2015,** 129, 1-19.

96. Karran, E.; Mercken, M.; De Strooper, B. The amyloid cascade hypothesis for Alzheimer's disease: an appraisal for the development of therapeutics. *Nat Rev Drug Discov* **2011,** 10, 698-712.

97. Parvathy, S.; Hussain, I.; Karran, E. H.; Turner, A. J.; Hooper, N. M. Cleavage of Alzheimer's amyloid precursor protein by α-secretase occurs at the surface of neuronal cell. *Biochemistry* **1999,** 38, 9728-9734.

98. Lichtenthaler, S. F. Alpha-secretase in Alzheimer's disease: molecular identity, regulation and therapeutic potential. *J Neurochem* **2011,** 116, 10-21.

99. Lichtenthaler, S. F.; Haass, C. Amyloid at the cutting edge: activation of α-secretase prevents amyloidogenesis in an Alzheimer disease mouse model. *J Clin Invest* **2004,** 113, 1384-1387.

100. Cai, H.; Wang, Y.; Mccarthy, D.; Wen, H.; Borchelt, D. R.; Price, D. L.; Wong, P. C. BACE1 is the major β-secretase for generation of Aβ peptides by neurons. *Nat Neurosci* **2001,** 4, 233-234.

101. Hemming, M. L.; Elias, J. E.; Gygi, S. P.; Selkoe, D. J. Identification of beta-secretase (BACE1) substrates using quantitative proteomics. *PLoS One* **2009,** 4, e8477.

102. Citron, M. β-secretase inhibition for the treatment of Alzheimer's disease--promise and challenge. *Trends Pharmacol Sci* **2004,** 25, 92-97.

103. Skovronsky, D. M.; Lee, V. M.-Y. β-Secretase revealed: starting gate for race to novel therapies for Alzheimer's disease. *Trends in Pharmacol Sci* **2000,** 21, 161-163.

104. Hartl, D.; Klatt, S.; Roch, M.; Konthur, Z.; Klose, J.; Willnow, T. E.; Rohe, M. Soluble alpha-APP (sAPPalpha) regulates CDK5 expression and activity in neurons. *PLoS One* **2013,** 8, e65920.

105. Deng, J.; Habib, A.; Obregon, D. F.; Barger, S. W.; Giunta, B.; Wang, Y. J.; Hou, H.; Sawmiller, D.; Tan, J. Soluble amyloid precursor protein alpha inhibits tau phosphorylation through modulation of GSK3beta signaling pathway. *J Neurochem* **2015,** 135, 630-637.

106. Obregon, D.; Hou, H.; Deng, J.; Giunta, B.; Tian, J.; Darlington, D.; Shahaduzzaman, M.; Zhu, Y.; Mori, T.; Mattson, M. P.; Tan, J. Soluble amyloid precursor protein-alpha modulates beta-secretase activity and amyloid-beta generation. *Nat Commun* **2012,** 3, 777-797.

107. Randall, A. D.; Witton, J.; Booth, C.; Hynes-Allen, A.; Brown, J. T. The functional neurophysiology of the amyloid precursor protein (APP) processing pathway. *Neuropharmacology* **2010,** 59, 243-267.

108. Kuhn, P. H.; Wang, H.; Dislich, B.; Colombo, A.; Zeitschel, U.; Ellwart, J. W.; Kremmer, E.; Rossner, S.; Lichtenthaler, S. F. ADAM10 is the physiologically relevant, constitutive α-secretase of the amyloid precursor protein in primary neurons. *EMBO J* **2010,** 29, 3020-3032.

109. Szczepanik, A. M.; Rampe, D.; Ringheim, G. E. Amyloid-β peptide fragments p3 and p4 induce pro-inflammatory cytokine and chemssokine production in vitro and in vivo. *J Neurochem* **2001,** 77, 304-317.

110. Hunter, S.; Brayne, C. Relationships between the amyloid precursor protein and its various proteolytic fragments and neuronal systems. *Alz Res Ther* **2010,** 4, 10-25.

111. Ohkawara, T.; Nagase, H.; Koh, C. S.; Nakayama, K. The amyloid precursor protein intracellular domain alters gene expression and induces neuron-specific apoptosis. *Gene* **2011,** 475, 1-9.

112. Słomnicki, Ł. P.; Leśniak, W. A putative role of the Amyloid Precursor Protein Intracellular Domain (AICD) in transcription. *Acta Neurobiol Exp* **2008,** 68, 219-228.

113. Branca, C.; Sarnico, I.; Ruotolo, R.; Lanzillotta, A.; Viscomi, A. R.; Benarese, M.; Porrini, V.; Lorenzini, L.; Calza, L.; Imbimbo, B. P.; Ottonello, S.; Pizzi, M. Pharmacological targeting of the beta-amyloid precursor protein intracellular domain. *Sci Rep* **2014,** 4, 4618-4627.

114. Muller, T.; Meyer, H. E.; Egensperger, R.; Marcus, K. The amyloid precursor protein intracellular domain (AICD) as modulator of gene expression, apoptosis, and cytoskeletal dynamics-relevance for Alzheimer's disease. *Prog Neurobiol* **2008,** 85, 393-406.

115. Cappai, R. Making sense of the amyloid precursor protein: its tail tells an interesting tale. *J Neurochem* **2014,** 130, 325-327.

116. Sisodia, S. S.; St George-Hyslop, P. H. *Nat Rev Neurosci* **2002,** 3, 281-290.

117. Nakamura, M.; Shishido, N.; Nunomura, A.; Smith, M. A.; Perry, G.; Hayashi, Y.; Nakayama, K.; Hayashi, T. Three histidine residues of amyloid-β peptide control the redox activity of copper and iron. *Biochemistry* **2007,** 46, 12737-12743.

118. Smith, D. G.; Cappai, R.; Barnham, K. J. The redox chemistry of the Alzheimer's disease amyloid beta peptide. *Biochim Biophys Acta* **2007,** 1768, 1976-1990.

119. Hane, F.; Tran, G.; Attwood, S. J.; Leonenko, Z. Cu(2+) affects amyloid-beta (1-42) aggregation by increasing peptide-peptide binding forces. *PLoS One* **2013,** 8, e59005.

120. Tougu, V.; Tiiman, A.; Palumaa, P. Interactions of Zn(II) and Cu(II) ions with Alzheimer's amyloid-beta peptide. Metal ion binding, contribution to fibrillization and toxicity. *Metallomics* **2011,** 3, 250-261.

121. Landau, M.; Sawaya, M. R.; Faull, K. F.; Laganowsky, A.; Jiang, H.; Sievers, S. a.; Liu, J.; Barrio, J. R.; Eisenberg, D. Towards a pharmacophore for amyloid. *PLoS Biology* **2011,** 9, 1-13.

122. Gazit, E. Mechanisms of amyloid fibril self-assembly and inhibition. Model short peptides as a key research tool. *FEBS J* **2005,** 272, 5971-5978.

123. Colletier, J. P.; Laganowsky, A.; Landau, M.; Zhao, M.; Soriaga, A. B.; Goldschmidt, L.; Flot, D.; Cascio, D.; Sawaya, M. R.; Eisenberg, D. Molecular basis for amyloid-beta polymorphism. *Proc Natl Acad Sci U S A* **2011,** 108, 16938-16943.

124. Zheng, J.; Ma, B.; Nussinov, R. Consensus features in amyloid fibrils: sheet-sheet recognition via a (polar or nonpolar) zipper structure. *Phys Biol* **2006,** 3, 1-4.

125. Marr, R. A.; Hafez, D. M. Amyloid-beta and Alzheimer's disease: the role of neprilysin-2 in amyloid-beta clearance. *Front Aging Neurosci* **2014,** 6, 187-195.

126. Palop, J. J.; Mucke, L. Amyloid-β-induced neuronal dysfunction in Alzheimer's disease: from synapses toward neural networks. *Nat Neurosci* **2010,** 13, 812-818.

127. Giuffrida, M. L.; Tomasello, M. F.; Pandini, G.; Caraci, F.; Battaglia, G.; Busceti, C.; Di Pietro, P.; Pappalardo, G.; Attanasio, F.; Chiechio, S.; Bagnoli, S.; Nacmias, B.; Sorbi, S.; Vigneri, R.; Rizzarelli, E.; Nicoletti, F.; Copani, A. Monomeric β-amyloid interacts with type-1 insulin-like growth factor receptors to provide energy supply to neurons. *Front Cell Neurosci* **2015,** 9, 297-313.

128. Koudinov, A. R.; Berezov, T. T. Alzheimer's amyloid-beta (Aβ) is an essential synaptic protein, not neurotoxic junk. *Acta Neurobiol Exp* **2004,** 64, 71-79.

129. Pearson, H. A.; Peers, C. Physiological roles for amyloid beta peptides. *J Physiol* **2006,** 575, 5-10.

130. Xiang, Y.; Bu, X. L.; Liu, Y. H.; Zhu, C.; Shen, L. L.; Jiao, S. S.; Zhu, X. Y.; Giunta, B.; Tan, J.; Song, W. H.; Zhou, H. D.; Zhou, X. F.; Wang, Y. J. Physiological amyloid-beta clearance in the periphery and its therapeutic potential for Alzheimer's disease. *Acta Neuropathol* **2015,** 130, 487-499.

131. Wang, Y. J.; Zhou, H. D.; Zhou, X. F. Clearance of amyloid-beta in Alzheimer's disease: progress, problems and perspectives. *Drug Discov Today* **2006,** 11, 931-938.

132. Marr, R. A.; Masliah, E. Amyloid-beta clearance in Alzheimer's disease. *Front Aging Neurosci* **2015,** 6, 1-112.

133. Kim, Y. E.; Hipp, M. S.; Bracher, A.; Hayer-Hartl, M.; Hartl, F. U. Molecular chaperone functions in protein folding and proteostasis. *Annu Rev Biochem* **2013,** 82, 323-355.

134. Evans, C. G.; Chang, L.; Gestwicki, J. E. Heat shock protein 70 (hsp70) as an emerging drug target. *J Med Chem* **2010,** 53, 4585-4602.

135. Valastyan, J. S.; Lindquist, S. Mechanisms of protein-folding diseases at a glance. *Dis Model Mech* **2014,** 7, 9-14.

136. Stefani, M.; Dobson, C. M. Protein aggregation and aggregate toxicity: new insights into protein folding, misfolding diseases and biological evolution. *J Mol Med (Berl)* **2003,** 81, 678-699.

137. Miller, Y.; Ma, B.; Nussinov, R. Zinc ions promote Alzheimer Abeta aggregation via population shift of polymorphic states. *Proc Natl Acad Sci U S A* **2010,** 107, 9490-9495.

138. Ahmed, M.; Davis, J.; Aucoin, D.; Sato, T.; Ahuja, S.; Aimoto, S.; Elliott, J. I.; Van Nostrand, W. E.; Smith, S. O. Structural conversion of neurotoxic amyloid-beta(1-42) oligomers to fibrils. *Nat Struct Mol Biol* **2010,** 17, 561-567.

139. Lee, C.; Ham, S. Characterizing amyloid-beta protein misfolding from molecular dynamics simulations with explicit water. *J Comput Chem* **2011,** 32, 349-355.

140. Knowles, T. P.; Vendruscolo, M.; Dobson, C. M. The amyloid state and its association with protein misfolding diseases. *Nat Rev Mol Cell Biol* **2014,** 15, 384-396.

141. Breydo, L.; Uversky, V. N. Structural, morphological, and functional diversity of amyloid oligomers. *FEBS Lett* **2015,** 589, 2640-2648.

142. Mold, M.; Ouro-Gnao, L.; Wieckowski, B. M.; Exley, C. Copper prevents amyloid-beta(1-42) from forming amyloid fibrils under near-physiological conditions in vitro. *Sci Rep* **2013,** 3, 1256-1261.

143. Hane, F.; Leonenko, Z. Effect of metals on kinetic pathways of amyloid-beta aggregation. *Biomolecules* **2014,** 4, 101-116.

144. Bitan, G.; Kirkitadze, M. D.; Lomakin, A.; Vollers, S. S.; Benedek, G. B.; Teplow, D. B. Amyloid β-protein (Aβ) assembly: Aβ40 and Aβ42 oligomerize through distinct pathways. *Proc Natl Acad Sci U S A* **2003,** 100, 330-335.

145. Rambaran, R. N.; Serpell, L. C. Amyloid fibrils. *Prion* **2014,** 2, 112-117.

146. Dovidchenko, N. V.; Glyakina, A. V.; Selivanova, O. M.; Grigorashvili, E. I.; Suvorina, M. Y.; Dzhus, U. F.; Mikhailina, A. O.; Shiliaev, N. G.; Marchenkov, V. V.; Surin, A. K.; Galzitskaya, O. V. One of the possible mechanisms of amyloid fibrils formation based on the sizes of primary and secondary folding nuclei of Abeta40 and Abeta42. *J Struct Biol* **2016**, ASAP.

147. Jan, A.; Hartley, D. M.; Lashuel, H. A. Preparation and characterization of toxic Abeta aggregates for structural and functional studies in Alzheimer's disease research. *Nat Protoc* **2010,** 5, 1186-1209.

148. Dobson, C. M. Protein folding and misfolding. *Nature* **2003,** 426, 884-890.

149. Meier, B. H.; Bockmann, A. The structure of fibrils from 'misfolded' proteins. *Curr Opin Struct Biol* **2014,** 30C, 43-49.

150. Fandrich, M.; Schmidt, M.; Grigorieff, N. Recent progress in understanding Alzheimer's β-amyloid structures. *Trends Biochem Sci* **2011,** 36, 338-345.

151. Gaspar, R. C.; Villarreal, S. A.; Bowles, N.; Hepler, R. W.; Joyce, J. G.; Shughrue, P. J. Oligomers of beta-amyloid are sequestered into and seed new plaques in the brains of an AD mouse model. *Exp Neurol* **2010,** 223, 394-400.

152. Krafft, G. A.; Klein, W. L. ADDLs and the signaling web that leads to Alzheimer's disease. *Neuropharmacology* **2010,** 59, 230-242.

153. Shughrue, P. J.; Acton, P. J.; Breese, R. S.; Zhao, W. Q.; Chen-Dodson, E.; Hepler, R. W.; Wolfe, A. L.; Matthews, M.; Heidecker, G. J.; Joyce, J. G.; Villarreal, S. A.; Kinney, G. G. Anti-ADDL antibodies differentially block oligomer binding to hippocampal neurons. *Neurobiol Aging* **2010,** 31, 189-202.

154. Pozueta, J.; Lefort, R.; Shelanski, M. L. Synaptic changes in Alzheimer's disease and its models. *Neuroscience* **2013,** 251, 51-65.

155. Deshpande, A.; Mina, E.; Glabe, C.; Busciglio, J. Different conformations of amyloid beta induce neurotoxicity by distinct mechanisms in human cortical neurons. *J Neurosci* **2006,** 26, 6011-6018.

156. Soto, C. Unfolding the role of protein misfolding in neurodegenerative diseases. *Nat Rev Neurosci* **2003,** 4, 49-60.

157. Quist, A.; Doudevski, I.; Lin, H.; Azimova, R.; Ng, D.; Frangione, B.; Kagan, B.; Ghiso, J.; Lal, R. Amyloid ion channels: a common structural link for protein-misfolding disease. *Proc Natl Acad Sci U S A* **2005,** 102, 10427-32.

158. Viola, K. L.; Klein, W. L. Amyloid beta oligomers in Alzheimer's disease pathogenesis, treatment, and diagnosis. *Acta Neuropathol* **2015,** 129, 183-206.

159. Klein, W. L. Synaptotoxic amyloid-β oligomers: A molecular basis for the cause, diagnosis, and treatment of Alzheimer's disease? *J Alzheimers Dis* **2013,** 33, S49-S65.

160. Kayed, R.; Lasagna-Reeves, C. A. Molecular mechanisms of amyloid oligomers toxicity. *J Alzheimers Dis* **2013,** 33, S67-S78.

161. Fandrich, M. Oligomeric intermediates in amyloid formation: structure determination and mechanisms of toxicity. *J Mol Biol* **2012,** 421, 427-440.

162. Benilova, I.; Karran, E.; De Strooper, B. The toxic Abeta oligomer and Alzheimer's disease: an emperor in need of clothes. *Nat Neurosci* **2012,** 15, 349-357.

163. Umeda, T.; Tomiyama, T.; Sakama, N.; Tanaka, S.; Lambert, M. P.; Klein, W. L.; Mori, H. Intraneuronal amyloid beta oligomers cause cell death via endoplasmic reticulum stress, endosomal/lysosomal leakage, and mitochondrial dysfunction in vivo. *J Neurosci Res* **2011,** 89, 1031-1042.

164. Hartmann, T. Cholesterol, Aβ and Alzheimer's disease. *Trends Neurosci* **2001,** 24, 45-48.

165. Kamenetz, F.; Tomita, T.; Hsieh, H.; Seabrook, G.; Borchelt, D. R.; Iwatsubo, T.; Sangram, S.; Malinow, R. APP processing and synaptic function. *Neuron* **2003,** 37, 925-937.

166. Pagani, L.; Eckert, A. Amyloid-Beta interaction with mitochondria. *Int J Alzheimers Dis* **2011,** 2011, 1-12.

167. Di Carlo, M. Beta amyloid peptide: from different aggregation forms to the activation of different biochemical pathways. *Eur Biophys J* **2010,** 39, 877-888.

168. Reddy, P. H. Amyloid beta, mitochondrial structural and functional dynamics in Alzheimer's disease. *Exp Neurol* **2009,** 218, 286-292.

169. Lashuel, H. A.; Hartley, D. M.; Petre, B. M.; Walz, T.; Lansbury, P. T. Amyloid pores from pathogenic mutations. *Nature* **2002,** 418, 291.

170. Menting, K. W.; Claassen, J. A. β-secretase inhibitor; a promising novel therapeutic drug in Alzheimer's disease. *Front Aging Neurosci* **2014,** 6, 165-174.

171. Kreft, A. F.; Martone, R.; Porte, A. Recent advances in the identification of gamma-secretase inhibitors to clinically test the Abeta oligomer hypothesis of Alzheimer's disease. *J Med Chem* **2009,** 52, 6169-6188.

172. Shelton, C. C.; Zhu, L.; Chau, D.; Yang, L.; Wang, R.; Djaballah, H.; Zheng, H.; Li, Y. M. Modulation of gamma-secretase specificity using small molecule allosteric inhibitors. *Proc Natl Acad Sci U S A* **2009,** 106, 20228-20233.

173. Al-Tel, T. H.; Al-Qawasmeh, R. A.; Schmidt, M. F.; Al-Aboudi, A.; Rao, S. N.; Sabri, S. S.; Voelter, W. Rational design and synthesis of potent dibenzazepine motifs as beta-secretase inhibitors. *J Med Chem* **2009,** 52, 6484-6488.

174. Ghosh, A. K.; Gemma, S.; Tang, J. β-secretase as a therapeutic target for Alzheimer's disease. *Neurotherapeutics* **2008,** 5, 399-408.

175. Malamas, M. S.; Barnes, K.; Hui, Y.; Johnson, M.; Lovering, F.; Condon, J.; Fobare, W.; Solvibile, W.; Turner, J.; Hu, Y.; Manas, E. S.; Fan, K.; Olland, A.; Chopra, R.; Bard, J.; Pangalos, M. N.; Reinhart, P.; Robichaud, A. J. Novel pyrrolyl 2-aminopyridines as potent and selective human beta-secretase (BACE1) inhibitors. *Bioorg Med Chem Lett* **2010,** 20, 2068-2073.

176. Rueeger, H.; Lueoend, R.; Rogel, O.; Rondeau, J. M.; Mobitz, H.; Machauer, R.; Jacobson, L.; Staufenbiel, M.; Desrayaud, S.; Neumann, U. Discovery of cyclic sulfone hydroxyethylamines as potent and selective beta-site APP-cleaving enzyme 1 (BACE1) inhibitors: structure-based design and in vivo reduction of amyloid beta-peptides. *J Med Chem* **2012,** 55, 3364-3386.

177. Malamas, M. S.; Erdei, J.; Gunawan, I.; Turner, J.; Hu, Y.; Wagner, E.; Fan, K.; Chopra, R.; Olland, A.; Bard, J.; Jacobsen, S.; Magolda, R. L.; Pangalos, M.; Robichaud, A. J. Design and synthesis of 5,5'-disubstituted aminohydantoins as potent and selective human beta-secretase (BACE1) inhibitors. *J Med Chem* **2010,** 53, 1146-1158.

178. John, V.; Beck, J. P.; Bienkowski, M. J.; Sinha, S.; Heinrikson, R. L. Human β-secretase (BACE) and BACE Inhibitors. *J Med Chem* **2003,** 46, 4625-4630.

179. Zhou, S.; Zhou, H.; Walian, P. J.; Jap, B. K. Regulation of γ-Secretase Activity in Alzheimer's Disease. *Biochemistry* **2007,** 46, 2553-2563.

180. Keown, L. E.; Collins, I.; Cooper, L. C.; Harrison, T.; Madin, A.; Mistry, J.; Reilly, M.; Shaimi, M.; Welch, C. J.; Clarke, E. E.; Lewis, H. D.; Wrigley, J. D. J.; Best, J. D.; Murray, F.; Shearman, M. S. Novel orally bioavailable γ-secretase inhibitors with excellent in vivo activity. *J Med Chem* **2009,** 52, 3441-3444.

181. Doody, R. S.; Raman, R.; Farlow, M.; Iwatsubo, T.; Vellas, B.; Joffe, S.; Kieburtz, K.; He, F.; Sun, X.; Thomas, R. G.; Aisen, P. S.; Alzheimer's Disease Cooperative Study Steering, C.; Siemers, E.; Sethuraman, G.; Mohs, R.; Semagacestat Study, G. A phase 3 trial of semagacestat for treatment of Alzheimer's disease. *N Engl J Med* **2013,** 369, 341-350.

182. De Strooper, B. Lessons from a failed gamma-secretase Alzheimer trial. *Cell* **2014,** 159, 721-726.

183. Doody, R. S.; Thomas, R. G.; Farlow, M.; Iwatsubo, T.; Vellas, B.; Joffe, S.; Kieburtz, K.; Raman, R.; Sun, X.; Aisen, P. S.; Siemers, E.; Liu-Seifert, H.; Mohs, R.; Alzheimer's Disease Cooperative Study Steering, C.; Solanezumab Study, G. Phase 3 trials of solanezumab for mild-to-moderate Alzheimer's disease. *N Engl J Med* **2014,** 370, 311-321.

184. Mikulca, J. A.; Nguyen, V.; Gajdosik, D. A.; Teklu, S. G.; Giunta, E. A.; Lessa, E. A.; Tran, C. H.; Terak, E. C.; Raffa, R. B. Potential novel targets for Alzheimer pharmacotherapy: II. Update on secretase inhibitors and related approaches. *J Clin Pharm Ther* **2014,** 39, 25-37.

185. Schneider, L. S.; Mangialasche, F.; Andreasen, N.; Feldman, H.; Giacobini, E.; Jones, R.; Mantua, V.; Mecocci, P.; Pani, L.; Winblad, B.; Kivipelto, M. Clinical trials and late-stage drug development for Alzheimer's disease: an appraisal from 1984 to 2014. *J Intern Med* **2014,** 275, 251-283.

186. Racchi, M.; Mazzucchelli, M.; Lenzken, S. C.; Porrello, E.; Lanni, C.; Govoni, S. Role of acetylcholinesterase inhibitors in the regulation of amyloid beta precursor protein (AbetaPP) metabolism. *Chem Biol Interact* **2005,** 157-158, 335-338.

187. Pakaski, M.; Kalman, J. Interactions between the amyloid and cholinergic mechanisms in Alzheimer's disease. *Neurochem Int* **2008,** 53, 103-111.

188. Fang, L.; Jumpertz, S.; Zhang, Y.; Appenroth, D.; Fleck, C.; Mohr, K.; Trankle, C.; Decker, M. Hybrid molecules from xanomeline and tacrine: enhanced tacrine actions on cholinesterases and muscarinic M1 receptors. *J Med Chem* **2010,** 53, 2094-2103.

189. Zhao, X.; Marszalec, W.; Toth, P. T.; Huang, J.; Yeh, J. Z.; Narahashi, T. In vitro galantamine-memantine co-application: mechanism of beneficial action. *Neuropharmacology* **2006,** 51, 1181-1191.

190. Matharu, B.; Gibson, G.; Parsons, R.; Huckerby, T. N.; Moore, S. A.; Cooper, L. J.; Millichamp, R.; Allsop, D.; Austen, B. Galantamine inhibits beta-amyloid aggregation and cytotoxicity. *J Neurol Sci* **2009,** 280, 49-58.

191. Sinha, S. The metabolism of the amyloid precursor protein and its relevance to Alzheimer's disease. *Perspect Drug Discov Des* **1995,** 2, 363-369.

192. Bucciantini, M.; Giannoni, E.; Chiti, F.; Baroni, F.; Formigll, L.; Zurdo, J.; Taddel, N.; Ramponi, G.; Dobson, C. M.; Stefani, M. Inherent toxicity of aggregates implies a common mechanism for protein misfolding diseases. *Nature* **2002,** 416, 507-511.

193. Bieschke, J.; Herbst, M.; Wiglenda, T.; Friedrich, R. P.; Boeddrich, A.; Schiele, F.; Kleckers, D.; Lopez del Amo, J. M.; Gruning, B. A.; Wang, Q.; Schmidt, M. R.; Lurz, R.; Anwyl, R.; Schnoegl, S.; Fandrich, M.; Frank, R. F.; Reif, B.; Gunther, S.; Walsh, D. M.; Wanker, E. E. Small-molecule conversion of toxic oligomers to nontoxic beta-sheet-rich amyloid fibrils. *Nat Chem Biol* **2012,** 8, 93-101.

194. Feng, Y.; Yang, S.-g.; Du, X.-t.; Zhang, X.; Sun, X.-x.; Zhao, M.; Sun, G.-y.; Liu, R.-t. Ellagic acid promotes Aβ42 fibrillization and inhibits Aβ42-induced neurotoxicity. *Biochem Biophys Res Comm* **2009,** 390, 1250-1254.

195. Petrushina, I.; Ghochikyan, A.; Mktrichyan, M.; Mamikonyan, G.; Movsesyan, N.; Davtyan, H.; Patel, A.; Head, E.; Cribbs, D. H.; Agadjanyan, M. G. Alzheimer's disease peptide epitope vaccine reduces insoluble but not soluble/oligomeric Abeta species in amyloid precursor protein transgenic mice. *J Neurosci* **2007,** 27, 12721-12731.

196. Friedrich, R. P.; Tepper, K.; Ronicke, R.; Soom, M.; Westermann, M.; Reymann, K.; Kaether, C.; Fandrich, M. Mechanism of amyloid plaque formation suggests an intracellular basis of Abeta pathogenicity. *Proc Natl Acad Sci U S A* **2010,** 107, 1942-1947.

197. Rajasekhar, K.; Suresh, S. N.; Manjithaya, R.; Govindaraju, T. Rationally designed peptidomimetic modulators of abeta toxicity in Alzheimer's disease. *Sci Rep* **2015,** 5, 8139-8148.

198. Thal, D. R.; Walter, J.; Saido, T. C.; Fandrich, M. Neuropathology and biochemistry of Abeta and its aggregates in Alzheimer's disease. *Acta Neuropathol* **2015,** 129, 167-182.

199. Necula, M.; Kayed, R.; Milton, S.; Glabe, C. G. Small molecule inhibitors of aggregation indicate that amyloid beta oligomerization and fibrillization pathways are independent and distinct. *J Biol Chem* **2007,** 282, 10311-10324.

200. Wong, H. E.; Kwon, I. Xanthene food dye, as a modulator of Alzheimer's disease amyloid-beta peptide aggregation and the associated impaired neuronal cell function. *PLoS One* **2011,** 6, e25752.

201. Wong, H. E.; Qi, W.; Choi, H. M.; Fernandez, E. J.; Kwon, I. A safe, blood-brain barrier permeable triphenylmethane dye inhibits amyloid-beta neurotoxicity by generating nontoxic aggregates. *ACS Chem Neurosci* **2011,** 2, 645-657.

202. Wu, C.; Scott, J.; Shea, J. E. Binding of Congo red to amyloid protofibrils of the Alzheimer Abeta(9-40) peptide probed by molecular dynamics simulations. *Biophys J* **2012,** 103, 550-557.

203. Khurana, R.; Coleman, C.; Ionescu-Zanetti, C.; Carter, S. A.; Krishna, V.; Grover, R. K.; Roy, R.; Singh, S. Mechanism of thioflavin T binding to amyloid fibrils. *J Struct Biol* **2005,** 151, 229-238.

204. Hamley, I. W. The amyloid beta peptide: a chemist's perspective. Role in Alzheimer's and fibrillization. *Chem Rev* **2012,** 112, 5147-5192.

205. Jameson, L. P.; Smith, N. W.; Dzyuba, S. V. Dye-binding assays for evaluation of the effects of small molecule inhibitors on amyloid (abeta) self-assembly. *ACS Chem Neurosci* **2012,** 3, 807-819.

206. Vázquez, J. A. Modeling of chemical inhibition from amyloid protein aggregation kinetics. *BMC Pharmacol Toxicol* **2014,** 15, 9-19.

207. Gras, S. L.; Waddington, L. J.; Goldie, K. N. Transmission electron microscopy of amyloid fibrils. *Methods Mol Biol* **2011,** 752, 197-214.

208. Kaminski Schierle, G. S.; van de Linde, S.; Erdelyi, M.; Esbjorner, E. K.; Klein, T.; Rees, E.; Bertoncini, C. W.; Dobson, C. M.; Sauer, M.; Kaminski, C. F. In situ measurements of the formation and morphology of intracellular beta-amyloid fibrils by super-resolution fluorescence imaging. *J Am Chem Soc* **2011,** 133, 12902-12905.

209. Juszczyk, P.; Kołodziejczyk, A. S.; Grzonka, Z. Circular dichroism and aggregation studies of amyloid β (11–28) fragment and its variants. *Acta Biochimica Polonica* **2005,** 52, 425-431.

210. Zheng, J.; Liu, C.; Sawaya, M. R.; Vadla, B.; Khan, S.; Woods, R. J.; Eisenberg, D.; Goux, W. J.; Nowick, J. S. Macrocyclic beta-sheet peptides that inhibit the aggregation of a tau-protein-derived hexapeptide. *J Am Chem Soc* **2011,** 133, 3144-3157.

211. Patterson, B. W.; Elbert, D. L.; Mawuenyega, K. G.; Kasten, T.; Ovod, V.; Ma, S.; Xiong, C.; Chott, R.; Yarasheski, K.; Sigurdson, W.; Zhang, L.; Goate, A.; Benzinger, T.; Morris, J. C.; Holtzman, D.; Bateman, R. J. Age and amyloid effects on human central nervous system amyloid-beta kinetics. *Ann Neurol* **2015,** 78, 439-453.

212. Tiiman, A.; Krishtal, J.; Palumaa, P.; Tõugu, V. In vitro fibrillization of Alzheimer's amyloid-β peptide (1-42). *AIP Advan* **2015,** 5, 1-12.

213. Bu, X. L.; Rao, P. P.; Wang, Y. J. Anti-amyloid aggregation activity of natural compounds: Implications for Alzheimer's drug discovery. *Mol Neurobiol* **2015**.

214. Yang, F.; Lim, G. P.; Begum, A. N.; Ubeda, O. J.; Simmons, M. R.; Ambegaokar, S. S.; Chen, P. P.; Kayed, R.; Glabe, C. G.; Frautschy, S. A.; Cole, G. M. Curcumin inhibits formation of amyloid beta oligomers and fibrils, binds plaques, and reduces amyloid in vivo. *J Biol Chem* **2005,** 280, 5892-5901.

215. Feng, Y.; Wang, X. P.; Yang, S. G.; Wang, Y. J.; Zhang, X.; Du, X. T.; Sun, X. X.; Zhao, M.; Huang, L.; Liu, R. T. Resveratrol inhibits beta-amyloid oligomeric cytotoxicity but does not prevent oligomer formation. *Neurotoxicology* **2009,** 30, 986-995.

216. Li, S. Y.; Wang, X. B.; Kong, L. Y. Design, synthesis and biological evaluation of imine resveratrol derivatives as multi-targeted agents against Alzheimer's disease. *Eur J Med Chem* **2014,** 71, 36-45.

217. Lu, C.; Guo, Y.; Yan, J.; Luo, Z.; Luo, H. B.; Yan, M.; Huang, L.; Li, X. Design, synthesis, and evaluation of multitarget-directed resveratrol derivatives for the treatment of Alzheimer's disease. *J Med Chem* **2013,** 56, 5843-5859.

218. He, J.; Xing, Y. F.; Huang, B.; Zhang, Y. Z.; Zeng, C. M. Tea catechins induce the conversion of preformed lysozyme amyloid fibrils to amorphous aggregates. *J Agric Food Chem* **2009,** 57, 11391-11396.

219. Kim, J.; Lee, H. J.; Lee, K. W. Naturally occurring phytochemicals for the prevention of Alzheimer's disease. *J Neurochem* **2010,** 112, 1415-1430.

220. Cheng, B.; Gong, H.; Xiao, H.; Petersen, R. B.; Zheng, L.; Huang, K. Inhibiting toxic aggregation of amyloidogenic proteins: a therapeutic strategy for protein misfolding diseases. *Biochim Biophys Acta* **2013,** 1830, 4860-4871.

221. Cao, C.; Cirrito, J. R.; Lin, X.; Wang, L.; Verges, D. K.; Dickson, A.; Mamcarz, M.; Zhang, C.; Mori, T.; Arendash, G. W.; Holtzman, D. M.; Potter, H. Caffeine suppresses amyloid-beta levels in plasma and brain of Alzheimer's disease transgenic mice. *J Alzheimers Dis* **2009,** 17, 681-697.

222. Yang, S. G.; Wang, W. Y.; Ling, T. J.; Feng, Y.; Du, X. T.; Zhang, X.; Sun, X. X.; Zhao, M.; Xue, D.; Yang, Y.; Liu, R. T. alpha-Tocopherol quinone inhibits beta-amyloid aggregation and cytotoxicity, disaggregates preformed fibrils and decreases the production of reactive oxygen species, NO and inflammatory cytokines. *Neurochem Int* **2010,** 57, 914-922.

223. Mori, T.; Koyama, N.; Segawa, T.; Maeda, M.; Maruyama, N.; Kinoshita, N.; Hou, H.; Tan, J.; Town, T. Methylene blue modulates beta-secretase, reverses cerebral amyloidosis, and improves cognition in transgenic mice. *J Biol Chem* **2014,** 289, 30303-30317.

224. Stoddard, S. V.; Hamann, M. T.; Wadkins, R. M. Insights and ideas garnered from marine metabolites for development of dual-function acetylcholinesterase and amyloid-beta aggregation inhibitors. *Mar Drugs* **2014,** 12, 2114-2131.

225. Meena, P.; Nemaysh, V.; Khatri, M.; Manral, A.; Luthra, P. M.; Tiwari, M. Synthesis, biological evaluation and molecular docking study of novel piperidine and piperazine derivatives as multi-targeted agents to treat Alzheimer's disease. *Bioorg Med Chem* **2015,** 23, 1135-1148.

226. Hasegawa, M. Molecular mechanisms in the pathogenesis of Alzheimer's disease and tauopathies-prion-like seeded aggregation and phosphorylation. *Biomolecules* **2016,** 6, 24-35.

227. Drubin, D. G.; Kirschner, M. W. Tau protein function in living cells. *J Cell Biology* **1986,** 103, 2739-2746.

228. Spires-Jones, T. L.; Hyman, B. T. The intersection of amyloid beta and tau at synapses in Alzheimer's disease. *Neuron* **2014,** 82, 756-771.

229. Perez, M.; Santa-Maria, I.; Tortosa, E.; Cuadros, R.; Del Valle, M.; Hernandez, F.; Moreno, F. J.; Avila, J. The role of the VQIVYK peptide in tau protein phosphorylation. *J Neurochem* **2007,** 103, 1447-1460.

230. Chaudhary, N.; Singh, S.; Nagaraj, R. Morphology of self-assembled structures formed by short peptides from the amyloidogenic protein tau depends on the solvent in which the peptides are dissolved. *J Pept Sci* **2009,** 15, 675-684.

231. Goux, W. J.; Kopplin, L.; Nguyen, A. D.; Leak, K.; Rutkofsky, M.; Shanmuganandam, V. D.; Sharma, D.; Inouye, H.; Kirschner, D. A. The formation of straight and twisted filaments from short tau peptides. *J Biol Chem* **2004,** 279, 26868-26875.

232. Hu, X.; Li, X.; Zhao, M.; Gottesdiener, A.; Luo, W.; Paul, S. Tau pathogenesis is promoted by Aβ1-42 but not Aβ1-40. *Mol Neurodegen* **2014,** 9, 52-62.

233. Rhein, V.; Song, X.; Wiesner, A.; Ittner, L. M.; Baysang, G.; Meier, F.; Ozmen, L.; Bluethmann, H.; Drose, S.; Brandt, U.; Savaskan, E.; Czech, C.; Gotz, J.; Eckert, A. Amyloid-beta and tau synergistically impair the oxidative phosphorylation system in triple transgenic Alzheimer's disease mice. *Proc Natl Acad Sci U S A* **2009,** 106, 20057-20062.

234. Chang, E.; Congdon, E. E.; Honson, N. S.; Duff, K. E.; Kuret, J. Structure-activity relationship of cyanine tau aggregation inhibitors. *J Med Chem* **2009,** 52, 3539-3547.

235. Chirita, C.; Necula, M.; Kuret, J. Ligand-dependent inhibition and reversal of tau filament formation. *Biochemistry* **2004,** 43, 2879-2887.

236. Ballatore, C.; Brunden, K. R.; Piscitelli, F.; James, M. J.; Crowe, A.; Yao, Y.; Hyde, E.; Trojanowski, J. Q.; Lee, V. M.; Smith, A. B., 3rd. Discovery of brain-penetrant, orally bioavailable aminothienopyridazine inhibitors of tau aggregation. *J Med Chem* **2010,** 53, 3739-3747.

237. Proctor, C. J.; Gray, D. A. GSK3 and p53 - is there a link in Alzheimer's disease? *Mol Neurodegener* **2010,** 5, 7-21.

238. Oumata, N.; Bettayeb, K.; Ferandin, Y.; Demange, L.; Lopez-Giral, A.; Goddard, M.-L.; Myrianthopoulos, V.; Mikros, E.; Flajolet, M.; Greengard, P.; Meijer, L.; Galons, H. Roscovitine-derived, dual-specificity inhibitors of cyclin-dependent kinases and casein kinases 1. *J Med Chem* **2008,** 51, 5229-5242.

239. Mariano, M.; Schmitt, C.; Miralinaghi, P.; Catto, M.; Hartmann, R. W.; Carotti, A.; Engel, M. First selective dual inhibitors of tau phosphorylation and Beta-amyloid aggregation, two major pathogenic mechanisms in Alzheimer's disease. *ACS Chem Neurosci* **2014,** 5, 1198-1202.

240. Muthaiyah, B.; Essa, M. M.; Chauhan, V.; Chauhan, A. Protective effects of walnut extract against amyloid beta peptide-induced cell death and oxidative stress in PC12 cells. *Neurochem Res* **2011,** 36, 2096-2103.

241. Frank-Cannon, T. C.; Alto, L. T.; McAlpine, F. E.; Tansey, M. G. Does neuroinflammation fan the flame in neurodegenerative diseases? *Mol Neurodegener* **2009,** 4, 47-59.

242. Rosales-Corral, S. A.; Acuña-Castroviejo, D.; Coto-Montes, A.; Boga, J. A.; Manchester, L. C.; Fuentes-Broto, L.; Korkmaz, A.; MA, S.; Tan, D.; Reiter, R. J. Alzheimer's disease: pathological mechanisms and the beneficial role of melatonin. *J. Pineal Res.* **2012,** 52, 167-202.

243. Hu, N. W.; Klyubin, I.; Anwyl, R.; Rowan, M. J. GluN2B subunit-containing NMDA receptor antagonists prevent Abeta-mediated synaptic plasticity disruption in vivo. *Proc Natl Acad Sci U S A* **2009,** 106, 20504-20509.

244. Katayama, S.; Ae, N.; Kodo, T.; Masumoto, S.; Hourai, S.; Tamamura, C.; Tanaka, H.; Nagata, R. Tricyclic indole-2-carboxylic acids highly in vivo active and selective antagonists for the glycine binding site of the NMDA receptor. *J Med Chem* **2003,** 46, 691-701.

245. Zhou, Z.-l.; Navratil, J. M.; Cai, S. X.; Whittemore, E. R.; Espitia, S. A.; Hawkinson, J. E.; Tran, M.; Woodward, R. M.; Weber, E.; Keana, J. F. W. Synthesis and SAR of 5-, 6-, 7- and 8-Aza Analogues of 3-Aryl-4- hydroxyquinolin-2(1H)-one as NMDA/Glycine Site Antagonists. *Bioorg Med Chem* **2001,** 9, 2061-2071.

246. Sterling, J.; Herzig, Y.; Goren, T.; Finkelstein, N.; Lerner, D.; Goldenberg, W.; Miskolczi, I.; Molnar, S.; Rantal, F.; Tamas, T.; Toth, G.; Zagyva, A.; Zekany, A.; Lavian, G.; Gross, A.; Friedman, R.; Razin, M.; Huang, W.; Krais, B.; Chorev, M.; Youdim, M. B. H.; Weinstock, M. Novel dual inhibitors of AChE and MAO derived from hydroxy aminoindan and phenethylamine as potential treatment for Alzheimer's disease. *J Med Chem* **2002,** 45, 5260-5279.

247. Pisani, L.; Muncipinto, G.; Miscioscia, T. F.; Nicolotti, O.; Leonetti, F.; Catto, M.; Caccia, C.; Salvati, P.; Soto-Otero, R.; Mendez-Alvarez, E.; Passeleu, C.; Carotti, A. Discovery of a novel class of potent coumarin monoamine oxidase B inhibitors: development and biopharmacological profiling of 7-[(3-chlorobenzyl)oxy]-4-[(methylamino)methyl]-2H-chromen-2-one methanesulfonate (NW-1772) as a highly potent, selective, reversible, and orally active monoamine oxidase B inhibitor. *J Med Chem* **2009,** 52, 6685-6706.

248. Brühlmann, C.; Ooms, F.; Carrupt, P.-A.; Testa, B.; Catto, M.; Leonetti, F.; Altomare, C.; Carotti, A. Coumarins derivatives as dual inhibitors of acetylcholinesterase and monoamine oxidase. *J Med Chem* **2001,** 44, 3195-3198.

249. Lim, G. P.; Yang, F.; Chu, T.; Chen, P.; Beech, W.; Teter, B.; Tran, T.; Ubeda, O.; Ashe, K. H.; Frautschy, S. A.; Cole, G. M. Ibuprofen suppresses plaque pathology and inflammation in a mouse model for Alzheimer’s disease. *J Neuro Sci* **2000,** 20, 5709-5714.

250. Hirohata, M.; Ono, K.; Naiki, H.; Yamada, M. Non-steroidal anti-inflammatory drugs have anti-amyloidogenic effects for Alzheimer's beta-amyloid fibrils in vitro. *Neuropharmacology* **2005,** 49, 1088-1099.

251. Chen, Y. P.; Zhang, Z. Y.; Li, Y. P.; Li, D.; Huang, S. L.; Gu, L. Q.; Xu, J.; Huang, Z. S. Syntheses and evaluation of novel isoliquiritigenin derivatives as potential dual inhibitors for amyloid-beta aggregation and 5-lipoxygenase. *Eur J Med Chem* **2013,** 66, 22-31.

252. Medeiros, R.; Figueiredo, C. P.; Pandolfo, P.; Duarte, F. S.; Prediger, R. D.; Passos, G. F.; Calixto, J. B. The role of TNF-alpha signaling pathway on COX-2 upregulation and cognitive decline induced by beta-amyloid peptide. *Behav Brain Res* **2010,** 209, 165-173.

253. Irannejad, H.; Unsal Tan, O.; Ozadali, K.; Dadashpour, S.; Tuylu Kucukkilinc, T.; Ahangar, N.; Ahmadnejad, M.; Emami, S. 1,2-Diaryl-2-hydroxyiminoethanones as dual COX-1 and beta-amyloid aggregation inhibitors: biological evaluation and in silico study. *Chem Biol Drug Des* **2015,** 85, 494-503.

254. Rosini, M.; Simoni, E.; Bartolini, M.; Cavalli, A.; Ceccarini, L.; Pascu, N.; Mcclymont, D. W.; Tarozzi, A.; Bolognesi, M. L.; Minarini, A.; Tumiatti, V.; Andrisano, V.; Mellor, I. R.; Melchiorre, C. Inhibition of acetylcholinesterase, β-amyloid aggregation, and NMDA receptors in Alzheimer's disease: A promising direction for the multi-target-directed ligands gold. *J Med Chem* **2008,** 51, 4381-4384.

255. Mahajan, A.; Hans, R.; Chibale, K.; Kumar, V. Synthesis and medicinal chemistry of selected antitubercular natural products and natural product derivatives. *RSC Advances* **2014,** 4, 15180-15215.

256. Joshi, B. K.; Gloer, J. B.; Wicklow, D. T.; Dowd, P. F. Sclerotigenin: A new antiinsectan benzodiazepine from the sclerotia of Penicillium sclerotigenum. *J Nat Prod* **1999,** 62, 650-652.

257. Khan, I.; Ibrar, A.; Abbas, N.; Saeed, A. Recent advances in the structural library of functionalized quinazoline and quinazolinone scaffolds: synthetic approaches and multifarious applications. *Eur J Med Chem* **2014,** 76, 193-244.

258. Michael, J. P. Quinoline, quinazoline and acridone alkaloids. *Nat Prod Rep* **2002,** 19, 742-760.

259. Blunt, J. W.; Copp, B. R.; Keyzers, R. A.; Munro, M. H.; Prinsep, M. R. Marine natural products. *Nat Prod Rep* **2014,** 31, 160-258.

260. Ravez, S.; Castillo-Aguilera, O.; Depreux, P.; Goossens, L. Quinazoline derivatives as anticancer drugs: a patent review (2011 - present). *Expert Opin Ther Pat* **2015,** 25, 789-804.

261. Burgdorf, L.; Kuhn, D.; Ross, T.; Deutsch, C. U. h. w. g. c. p. U. S. Pyridopyrimidine derivatives as protein kinase inhibitors. In Patent WO2014023385A1: 2015.

262. Chauhan, J. S.; Dhanda, S. K.; Singla, D.; Open Source Drug Discovery, C.; Agarwal, S. M.; Raghava, G. P. QSAR-based models for designing quinazoline/imidazothiazoles/pyrazolopyrimidines based inhibitors against wild and mutant EGFR. *PLoS One* **2014,** 9, e101079.

263. Marzaro, G.; Giuotto, A.; Chilin, A. Quinazoline derivatives as potential anticancer agents: A patent review (2007 – 2010). *Expert Opin Ther Patents* **2012,** 22, 223-252.

264. Zhu, L.; Jin, J.; Liu, C.; Zhang, C.; Sun, Y.; Guo, Y.; Fu, D.; Chen, X.; Xu, B. Synthesis and biological evaluation of novel quinazoline-derived human Pin1 inhibitors. *Bioorg Med Chem* **2011,** 19, 2797-2807.

265. Jafari, E.; Khajouei, M. R.; Hassanzadeh, F.; Hakimelahi, G. H.; Khodarahmi, G. A. Quinazolinone and quinazoline derivatives: recent structures with potent antimicrobial and cytotoxic activities. *Res Pharm Sci* **2016,** 11, 1-14.

266. Guiles, J. W.; Toro, A.; Ochsner, U. A.; Bullard, J. M. Development of 4H-pyridopyrimidines: a class of selective bacterial protein synthesis inhibitors. *Org Med Chem Lett* **2012,** 2, 5-12.

267. Rajesh, K.; Reddy, B. P.; Sarveswari, S.; Vijayakumar, V. Regioselective synthesis and biological evaluation of novel bis(2-chloroquinolines). *Res Chem Intermed* **2013,** 39, 4259-4267.

268. Zheng, X.; Wang, L.; Wang, B.; Miao, K.; Xiang, K.; Feng, S.; Gao, L.; Shen, H. C.; Yun, H. Discovery of piperazinylquinoline derivatives as novel respiratory syncytial virus fusion inhibitors. *ACS Med Chem Letters* **2016,** ASAP.

269. Smits, R. a.; de Esch, I. J. P.; Zuiderveld, O. P.; Broeker, J.; Sansuk, K.; Guaita, E.; Coruzzi, G.; Adami, M.; Haaksma, E.; Leurs, R. Discovery of auinazolines as histamine H4 receptor inverse agonists using a scaffold hopping approach. *J Med Chem* **2008,** 51, 7855-7865.

270. Orjales, A.; Mosquera, R.; Lopez, B.; Olivera, R.; Labeaga, L.; Nunez, M. T. Novel 2-(4-methylsulfonylphenyl)pyrimidine derivatives as highly potent and specific COX-2 inhibitors. *Bioorg Med Chem* **2008,** 16, 2183-2199.

271. Lin, Z.; Murray, P. M.; Ding, Y.; Denny, W. A.; Ferguson, L. R. Quinazolines as novel anti-inflammatory histone deacetylase inhibitors. *Mut Res* **2010,** 690, 81-88.

272. Kanuma, K.; Omodera, K.; Nishiguchi, M.; Funakoshi, T.; Chaki, S.; Nagase, Y.; Iida, I.; Yamaguchi, J.; Semple, G.; Tran, T. A.; Sekiguchi, Y. Identification of 4-amino-2-cyclohexylaminoquinazolines as metabolically stable melanin-concentrating hormone receptor 1 antagonists. *Bioorg Med Chem* **2006,** 14, 3307-3319.

273. Rao, Y.; Liu, H.; Gao, L.; Yu, H.; Ou, T. M.; Tan, J. H.; Huang, S. L.; Wang, H. G.; Li, D.; Gu, L. Q.; Ye, J. M.; Huang, Z. S. Synthesis and biological evaluation of novel bouchardatine derivatives as potential adipogenesis/lipogenesis inhibitors for antiobesity treatment. *J Med Chem* **2015,** 58, 9395-9413.

274. Wu, M.; Li, Y.; Fu, X.; Wang, J.; Zhang, S.; Yang, L. Profiling the interaction mechanism of quinoline/quinazoline derivatives as MCHR1 antagonists: an in silico method. *Int J Mol Sci* **2014,** 15, 15475-15502.

275. Ugale, V. G.; Bari, S. B. Quinazolines: new horizons in anticonvulsant therapy. *Eur J Med Chem* **2014,** 80, 447-501.

276. Ghosh, A. K. U. h. w. g. c. p. U. S. Quinazoline inhibitors of BACE 1 and methods of using. In Patent WO2010059953A1: 2013.

277. Khattab, S. N.; Haiba, N. S.; Asal, A. M.; Bekhit, A. A.; Amer, A.; Abdel-Rahman, H. M.; El-Faham, A. Synthesis and evaluation of quinazoline amino acid derivatives as mono amine oxidase (MAO) inhibitors. *Bioorg Med Chem* **2015,** 23, 3574-3585.

278. Gil, A. M.; Ayuso-Gontan, C. G.; Martín, C. P.; Castillo, A. P.; García, J. M.; Sancho, M. R.; Cristóbal, M. S. S. U. h. w. g. c. p. U. S. Use of quinazoline derivatives for neurodegenerative diseases. In Patent US20120129877: 2015.

279. Elkamhawy, A.; Lee, J.; Park, B. G.; Park, I.; Pae, A. N.; Roh, E. J. Novel quinazoline-urea analogues as modulators for Abeta-induced mitochondrial dysfunction: design, synthesis, and molecular docking study. *Eur J Med Chem* **2014,** 84, 466-475.

280. O'Hare, E.; Scopes, D. I.; Kim, E. M.; Palmer, P.; Spanswick, D.; McMahon, B.; Amijee, H.; Nerou, E.; Treherne, J. M.; Jeggo, R. Novel 5-aryloxypyrimidine SEN1576 as a candidate for the treatment of Alzheimer's disease. *Int J Neuropsychopharmacol* **2014,** 17, 117-126.

281. Xu, Z. C.; Wang, X. B.; Yu, W. Y.; Xie, S. S.; Li, S. Y.; Kong, L. Y. Design, synthesis and biological evaluation of benzylisoquinoline derivatives as multifunctional agents against Alzheimer's disease. *Bioorg Med Chem Lett* **2014,** 24, 2368-2373.

282. Selvam, T. P.; Kumar, P. V. Quinazoline marketed drugs - A review. *Research in Pharmacy* **2011,** 1, 1-21.

283. Bilbro, J.; Mart, M.; Kyprianou, N. Therapeutic value of quinazoline-based compounds in prostate cancer. *Anticancer Res* **2013,** 32, 4695-4700.

284. Buron, F.; Mérour, J. Y.; Akssira, M.; Guillaumet, G.; Routier, S. Recent advances in the chemistry and biology of pyridopyrimidines. *Eur J Med Chem* **2015,** 95, 76-95.

285. Al-Ebaisat, H. A review on synthesis and spectral properties of quinazolines and pyrimidines. *Am Chem Sci J* **2015,** 6, 213-223.

286. Selvam, T. P.; James, C. R.; Driandev, P. V.; Valzita, S. K. A mini review of pyrimidine and fused pyrimidine marketed drugs. *Res Pharm* **2012,** 2, 1-9.

287. Wnag, D.; Gao, F. Quinazoline derivatives: synthesis and bioactivities. *Chemistry Central Journal* **2013,** 7.

288. Odingo, J.; O'Malley, T.; Kesicki, E. A.; Alling, T.; Bailey, M. A.; Early, J.; Ollinger, J.; Dalai, S.; Kumar, N.; Singh, R. V.; Hipskind, P. A.; Cramer, J. W.; Ioerger, T.; Sacchettini, J.; Vickers, R.; Parish, T. Synthesis and evaluation of the 2,4-diaminoquinazoline series as anti-tubercular agents. *Bioorg Med Chem* **2014,** 22, 6965-6979.

289. Jiang, N.; Zhai, X.; Zhao, Y.; Liu, Y.; Qi, B.; Tao, H.; Gong, P. Synthesis and biological evaluation of novel 2-(2-arylmethylene)hydrazinyl-4-aminoquinazoline derivatives as potent antitumor agents. *Eur J Med Chem* **2012,** 54, 534-541.

290. Khan, I.; Ibrar, A.; Ahmed, W.; Saeed, A. Synthetic approaches, functionalization and therapeutic potential of quinazoline and quinazolinone skeletons: The advances continue. *Eur J Med Chem* **2015,** 90, 124-169.

291. Chao, B.; Tong, X. K.; Tang, W.; Li, D. W.; He, P. L.; Garcia, J. M.; Zeng, L. M.; Gao, A. H.; Yang, L.; Li, J.; Nan, F. J.; Jacobs, M.; Altmeyer, R.; Zuo, J. P.; Hu, Y. H. Discovery and optimization of 2,4-diaminoquinazoline derivatives as a new class of potent dengue virus inhibitors. *J Med Chem* **2012,** 55, 3135-3143.

292. Wang, J.; Zha, S.; Chen, K.; Zhang, F.; Song, C.; Zhu, J. Quinazoline synthesis via Rh(III)-catalyzed intermolecular C-H functionalization of benzimidates with dioxazolones. *Org Lett* **2016,** 18, 2062-2065.

293. Wang, D.; Gao, F. Quinazoline derivatives: synthesis and bioactivities. *Chem Cent J* **2013,** 7, 95-109.

294. Yin, P.; Liu, N.; Deng, Y. X.; Chen, Y.; Deng, Y.; He, L. Synthesis of 2,4-diaminoquinazolines and tricyclic quinazolines by cascade reductive cyclization of methyl N-cyano-2-nitrobenzimidates. *J Org Chem* **2012,** 77, 2649-2658.

295. Lam, T.; Hilgers, M. T.; Cunningham, M. L.; Kwan, B. P.; Nelson, K. J.; Brown-Driver, V.; Ong, V.; Trzoss, M.; Hough, G.; Shaw, K. J.; Finn, J. Structure-based design of new dihydrofolate reductase antibacterial agents: 7-(benzimidazol-1-yl)-2,4-diaminoquinazolines. *J Med Chem* **2014,** 57, 651-668.

296. Li, Z.; Wang, B.; Hou, J. Q.; Huang, S. L.; Ou, T. M.; Tan, J. H.; An, L. K.; Li, D.; Gu, L. Q.; Huang, Z. S. 2-(2-indolyl-)-4(3H)-quinazolines derivates as new inhibitors of AChE: design, synthesis, biological evaluation and molecular modelling. *J Enzyme Inhib Med Chem* **2013,** 28, 583-592.

297. Smith, B.; Medda, F.; Gokhale, V.; Dunckley, T.; Hulme, C. Recent advances in the design, synthesis, and biological evaluation of selective DYRK1A inhibitors: a new avenue for a disease modifying treatment of Alzheimer's? *ACS Chem Neurosci* **2012,** 3, 857-872.

298. Kumar, A.; Nisha, C. M.; Silakari, C.; Sharma, I.; Anusha, K.; Gupta, N.; Nair, P.; Tripathi, T.; Kumar, A. Current and novel therapeutic molecules and targets in Alzheimer's disease. *J Formos Med Assoc* **2016,** 115, 3-10.

299. Mohamed, T.; Yeung, J. C.; Vasefi, M. S.; Beazely, M. A.; Rao, P. P. Development and evaluation of multifunctional agents for potential treatment of Alzheimer's disease: application to a pyrimidine-2,4-diamine template. *Bioorg Med Chem Lett* **2012,** 22, 4707-4712.

300. Ife, R. J.; Brown, T. H.; Blurton, P.; Keeling, D. J.; Leach, C. a.; Meeson, M. L.; Parsons, M. E.; Theobald, C. J. Reversible inhibitors of the gastric (H+/K+)-ATPase.5. Substituted 2,4-diaminoquinazolines and thienopyrimidines. *J Med Chem* **1995,** 38, 2763-2773.

301. Arnott, E. A.; Chan, L. C.; Cox, B. G.; Meyrick, B.; Phillips, A. POCl3 chlorination of 4-quinazolones. *J Org Chem* **2011,** 76, 1653-1661.

302. Lauwiner, M.; Wissmann, J. Reduction of aromatic nitro compounds with hydrazine hydrate in the presence of an iron oxide hydroxide catalyst. I. The reduction of monosubstituted nitrobenzenes with hydrazine hydrate in the presence of ferrihydrite. *Applied Catalysis A: General* **1998,** 172, 141-148.

303. Mohamed, T.; Assoud, A.; Rao, P. P. N-Benzyl-2-chloro-quinazolin-4-amine. *Acta Crystallogr Sect E Struct Rep Online* **2014,** 70, o554.

304. Cellier, P. P.; Spindler, J.-F.; Taillefer, M.; Cristau, H.-J. Pd/C-catalyzed room-temperature hydrodehalogenation of aryl halides with hydrazine hydrochloride. *Tetrahedron Lett* **2003,** 44, 7191-7195.

305. Mohamed, T.; Rao, P. P. N. Facile approaches toward the synthesis of N4-monosubstituted quinazolin-2,4-diamines. *Tetrahedron Lett* **2015,** 56, 6882-6885.

306. Scriven, E. F. V.; Turnbull, K. Azides: Their preparation and synthetic uses. *Chem Reviews* **1988,** 88, 297-368.

307. Aillerie, A.; Pellegrini, S.; Bousquet, T.; Pélinski, L. In situ generation of ammonia for the copper-catalyzed synthesis of primary aminoquinolines. *New J Chem* **2014,** 38, 1389-1391.

308. Okano, K.; Tokuyama, H.; Fukuyama, T. Copper-mediated aromatic amination reaction and its application to the total synthesis of natural products. *Chem Commun (Camb)* **2014,** 50, 13650-13663.

309. Sambiagio, C.; Marsden, S. P.; Blacker, A. J.; McGowan, P. C. Copper catalysed Ullmann type chemistry: from mechanistic aspects to modern development. *Chem Soc Rev* **2014,** 43, 3525-3550.

310. Aubin, Y.; Fischmeister, C.; Thomas, C. M.; Renaud, J. L. Direct amination of aryl halides with ammonia. *Chem Soc Rev* **2010,** 39, 4130-4145.

311. Elmkaddem, M. K.; Fischmeister, C.; Thomas, C. M.; Renaud, J. L. Efficient synthesis of aminopyridine derivatives by copper catalyzed amination reactions. *Chem Commun (Camb)* **2010,** 46, 925-927.

312. Helgen, C.; Bochet, C. G. Pyridine-derived heterocycles as potential photoacylating reagents. *Heterocycles* **2006,** 67, 797-805.

313. Mohamed, T.; Zhao, X.; Habib, L. K.; Yang, J.; Rao, P. P. Design, synthesis and structure-activity relationship (SAR) studies of 2,4-disubstituted pyrimidine derivatives: dual activity as cholinesterase and Abeta-aggregation inhibitors. *Bioorg Med Chem* **2011,** 19, 2269-2281.

314. Zeng, Z. S.; He, Q. Q.; Liang, Y. H.; Feng, X. Q.; Chen, F. E.; De Clercq, E.; Balzarini, J.; Pannecouque, C. Hybrid diarylbenzopyrimidine non-nucleoside reverse transcriptase inhibitors as promising new leads for improved anti-HIV-1 chemotherapy. *Bioorg Med Chem* **2010,** 18, 5039-5047.

315. Ellman, G. L.; Courtney, K. D.; Andres, V.; Featherstone, R. M. A New and Rapid Colormetric Determination of Acetylcholinesterase Activity. *Biochem Pharmacol* **1961,** 7, 88-95.

316. Chen, S. Y.; Chen, Y.; Li, Y. P.; Chen, S. H.; Tan, J. H.; Ou, T. M.; Gu, L. Q.; Huang, Z. S. Design, synthesis, and biological evaluation of curcumin analogues as multifunctional agents for the treatment of Alzheimer's disease. *Bioorg Med Chem* **2011,** 19, 5596-5604.

317. Mohamed, T.; Shakeri, A.; Tin, G.; Rao, P. P. Structure-activity relationship studies of isomeric 2,4-diaminoquinazolines on beta-amyloid aggregation kinetics. *ACS Med Chem Lett* **2016,** 7, 502-507.

318. Bourhim, M.; Kruzel, M.; Srikrishnan, T.; Nicotera, T. Linear quantitation of Abeta aggregation using Thioflavin T: reduction in fibril formation by colostrinin. *J Neurosci Methods* **2007,** 160, 264-268.

319. Yang, L. X.; Huang, K. X.; Li, H. B.; Gong, J. X.; Wang, F.; Feng, Y. B.; Tao, Q. F.; Wu, Y. H.; Li, X. K.; Wu, X. M.; Zeng, S.; Spencer, S.; Zhao, Y.; Qu, J. Design, synthesis, and examination of neuron protective properties of alkenylated and amidated dehydro-silybin derivatives. *J Med Chem* **2009,** 52, 7732-7752.

320. Catto, M.; Arnesano, F.; Palazzo, G.; De Stradis, A.; Calo, V.; Losacco, M.; Purgatorio, R.; Campagna, F. Investigation on the influence of (Z)-3-(2-(3-chlorophenyl)hydrazono)-5,6-dihydroxyindolin-2-one (PT2) on beta-amyloid(1-40) aggregation and toxicity. *Arch Biochem Biophys* **2014,** 560, 73-82.

321. Li, S. Y.; Wang, X. B.; Xie, S. S.; Jiang, N.; Wang, K. D.; Yao, H. Q.; Sun, H. B.; Kong, L. Y. Multifunctional tacrine-flavonoid hybrids with cholinergic, beta-amyloid-reducing, and metal chelating properties for the treatment of Alzheimer's disease. *Eur J Med Chem* **2013,** 69, 632-646.

322. Petkova, A. T.; Yau, W.; Tycko, R. Experimental constraints on quaternary strucutre in Alzheimer's β-Amyloid fibrils. *Biochemistry* **2006,** 45, 498-512.

323. Paul, K.; Sharma, A.; Luxami, V. Synthesis and in vitro antitumor evaluation of primary amine substituted quinazoline linked benzimidazole. *Bioorg Med Chem Lett* **2014,** 24, 624-629.

324. Tin, G.; Mohamed, T.; Gondora, N.; Beazely, M. A.; Rao, P. P. N. Tricyclic phenothiazine and phenoselenazine derivatives as potential multi-targeting agents to treat Alzheimer's disease. *Med. Chem. Commun.* **2015,** 6, 1930-1941.